Advanced Structured Materials

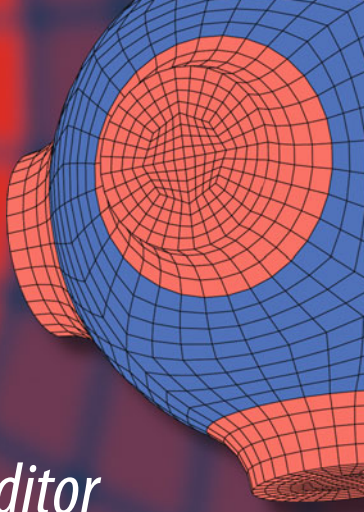

Pablo Andrés Muñoz-Rojas *Editor*

Computational Modeling, Optimization and Manufacturing Simulation of Advanced Engineering Materials

Springer

Advanced Structured Materials

Volume 49

More information about this series at http://www.springer.com/series/8611

Pablo Andrés Muñoz-Rojas
Editor

Computational Modeling, Optimization and Manufacturing Simulation of Advanced Engineering Materials

Springer

Editor
Pablo Andrés Muñoz-Rojas
Department of Mechanical Engineering
Santa Catarina State University—UDESC
Joinville, Santa Catarina
Brazil

ISSN 1869-8433 ISSN 1869-8441 (electronic)
Advanced Structured Materials
ISBN 978-3-319-04264-0 ISBN 978-3-319-04265-7 (eBook)
DOI 10.1007/978-3-319-04265-7

Library of Congress Control Number: 2016934665

Printed on acid-free paper

This Springer imprint is published by Springer Nature
The registered company is Springer International Publishing AG Switzerland

Preface

At the time this book is published, the world is experiencing the most spectacular rate of technological developments ever seen in history. This scenario demands a continuous enhancement of engineering materials in order to obtain improved or new mechanical, electrical or, in a more comprehensive sense, thermo-physical properties. Technological achievements usually rely on previous scientific developments and give support to engineering needs. Thus, we can talk of *engineering tailored materials* (*ETM*) or *advanced engineering materials* (*AEM*), which include the former.

This book presents 14 chapters centered in AEMs, covering subjects such as new manufacturing processes or aspects of their computational modeling, optimization procedures aimed at the obtainment of tailored properties, and computational modeling of constitutive behavior. In particular, the book is divided into four different parts: Part I—Micro and Nanoscale Modeling (3 chapters), Part II—Biological Tissues (4 chapters), Part III—Porous and Multiphase Materials (4 chapters) and Part IV—Polymers (3 chapters). The contributions belong to researchers from nine countries: Argentina, Australia, Brazil, Canada, Chile, Colombia, Germany, Poland, and Spain.

I would like to express my gratitude to all the people who contributed to the elaboration of this compendium. The list is long and I cannot mention them all, I apologize for that. Notwithstanding, in addition to all the authors, I feel indebted to André Kühl, André J. Torii, Carla T.M. Anflor, Carlos A. dos Santos, Clovis S. de Barcellos, Edgar N. Mamiya, Eduardo Bittencourt, Eduardo L. Cardoso, José A.M. Carrer, Jun S.O. Fonseca†, Júlio M. Pureza, Lucival Malcher, Miguel Vaz Jr., Roberto D. Machado, Rodnny J. Mendoza Fakhye, Severino P.C. Marques, and Thiago A. Carniel.

Finally, I wish to dedicate this book to the memory of Prof. Domingos Boechat Alves, from the Federal University of Santa Catarina and Prof. Jun Sérgio Ono Fonseca, from the Federal University of Rio Grande do Sul, both in Brazil. Their decease in 2015 was a great loss to the Brazilian computational mechanics

community. They were engineering researchers of the highest level, who conducted their lives in the most ethical way both in academy and as individuals. They inspired generations of young researchers in Brazil and will be remembered for the legacy they left.

February 2016 Pablo Andrés Muñoz-Rojas

Contents

Part I
Micro and Nanoscale Modeling

On the Variational Analysis of Vibrations of Prestressed Six-Parameter Shells

Holm Altenbach and Victor A. Eremeyev

Abstract We discuss the variational statements of the theory of linear vibrations of prestressed six-parameter shells. Initial or residual stresses can significantly influence buckling and oscillations of thin-walled structures. Within the six-parameter theory of shells a shell is modeled as a deformed material each point of it has six degrees f freedom, that is three translational and three rotational ones. Starting with the governing equations of the six-parameter shell theory the constitutive equations are analyzed. The linearization of the boundary-value problem is realized. After a brief discussion of the eigen-vibrations of the prestressed six-parameter shells the Rayleigh principle is introduced and discussed.

1 Introduction

Residual or initial stresses play an important role in engineering because such stresses can change the behavior of solids and structures. It is well-known that residual stresses result in failures even if they are much smaller in comparison with applied stresses. In addition, residual stresses can significantly influence buckling and oscillations of thin-walled structures, such as plates and shells. Investigations of prestressed solids are discussed, for example, in [36, 37, 39, 48, 55, 62]. Mechanical models of thin prestressed structures are studied in [2, 7, 10, 38, 40, 41, 44, 63, 68, 69] within the framework of various theories of plates and shells.

H. Altenbach (✉)
Lehrstuhl für Technische Mechanik, Fakultät für Maschinenbau,
Institut für Mechanik, Otto-von-Guericke-Universität Magdeburg,
Universitätsplatz 2, 39106 Magdeburg, Germany
e-mail: holm.altenbach@ovgu.de

V.A. Eremeyev
Department of Applied Mechanics and Robotics, Faculty of Mechanical Engineering and Avionics, Rzeszów University of Technology,
Al. Powstańców Warszawy 8, 35-959 Rzeszów, Poland
e-mail: veremeyev@prz.edu.pl

P.A. Muñoz-Rojas (ed.), *Computational Modeling, Optimization and Manufacturing Simulation of Advanced Engineering Materials*,
Advanced Structured Materials 49, DOI 10.1007/978-3-319-04265-7_1

Here we consider the eigen-oscillations of prestressed shells using the non-linear micropolar shell theory. This variant of the shell theory which is called also six-parameter theory of shells is presented in [18, 20, 27–29, 31, 32, 45–47, 58, 61, 70] among others, see also the reviews [4, 5] and the references therein. Similar models of shells are discussed in [52–54]. Within the micropolar shell theory the kinematics of the shell is determined by two kinematically independent fields of translations and rotations. Each point of the micropolar shell base surface has six degrees of freedom as in rigid body dynamics. This means that the drilling moment is taken in account. The surface stress and couple stress tensors are introduced in the theory. The advantage of the 6-parameter shell model is the correct description of multifolded shells, of interaction of a shell with a rigid body, etc., see [43, 60] and the references therein. The full micropolar kinematics may be important for proper modeling of piezoelectric or piezomagnetic shells since electromagnetic fields produce forces and moments including the drilling ones, see [34, 49]. In addition, this gives the possibility of description of the contact interaction of shells with distributed on its surface nano-objects [24, 33] or sensors, actuators, absorbers, etc., see [1, 6, 14, 15, 22, 23, 42, 50, 67].

Using certain constraints one can reduce the micropolar shell theory to Kirchhoff-Love-type or Reissner-Mindlin-type shell models. Mathematical studies of linear boundary-value problems of statics, dynamics and eigen-oscillations are performed in [26] within the framework of the functional analysis methods and the theory of Sobolev's spaces. First existence results for statics of nonlinear micropolar shells have been given in [11–13, 52] based on direct methods of the calculus of variations.

The chapter is based on the recent publications [3, 25]. It is organized as follows. In Sect. 2 we introduce briefly the basic equations of micropolar shells. Then in Sect. 3 we derive linearized boundary-value problems. In Sect. 4 we formulate boundary-value problems for eigen-oscillations. Finally, in Sect. 5 we give the variational statement of the problems using the Rayleigh variational principle. Let us also note that the Rayleigh principle allows us to optimize the form and change the distribution of shell properties to find in an extremal way the least or higher eigenfrequencies, see, e.g., [8]. We introduce the Rayleigh quotient for the shell with initial stresses and compare it with the Rayleigh quotient of the shell without initial stresses. This gives the possibility to analyze the influence of initial stresses. We show that the eigen-frequencies of the prestressed shells change by two reasons:

1. by changes of the elastic moduli tensors and
2. by terms depending on the initial stresses only.

The last reason is more important in the case of flexible thin structures for which instability may occur.

2 Dynamics and Statics of Micropolar Plates and Shells

Within the framework of the direct approach the micropolar shell is represented as a deformable material surface in each point of which three orthogonal unit vectors called directors are attached. The deformation of the micropolar shell is described by mapping from one state called the reference configuration to another one called the actual configuration. Let Σ be a base surface of the shell in the reference configuration $\varkappa$. The position vector of Σ is $\mathbf{P}(q^1, q^2)$, where q^α, $\alpha = 1, 2$, are Gaussian coordinates on Σ. The actual configuration χ describes the state of the shell at instant of time t. In χ the base surface of the shell is denoted by σ and described by the position vector $\boldsymbol{\rho}(q^1, q^2, t)$. In the reference and actual configurations we also introduce directors $\mathbf{D}_k(q^1, q^2)$ and $\mathbf{d}_k(q^1, q^2, t)$, $k = 1, 2, 3$. These two sets of vectors describe the orientation of shell material points in the reference and actual configurations, respectively. Then the relative change of the orientation of the shell is determined by the proper orthogonal tensor $\mathbf{Q} = \mathbf{d}_k \otimes \mathbf{D}_k$. Hence, the micropolar shell is described by two kinematically independent fields

$$\boldsymbol{\rho} = \boldsymbol{\rho}(q^1, q^2, t) \quad \text{and} \quad \mathbf{Q} = \mathbf{Q}(q^1, q^2, t). \tag{1}$$

Let us introduce for the micropolar hyper-elastic shell the strain energy density W. According to the local action principle [66], W takes the form

$$W = W(\boldsymbol{\rho}, \nabla_\varkappa \boldsymbol{\rho}, \mathbf{Q}, \nabla_\varkappa \mathbf{Q}),$$

where

$$\nabla_\varkappa \stackrel{\triangle}{=} \mathbf{P}^\alpha \frac{\partial}{\partial q^\alpha} \quad (\alpha, \beta = 1, 2), \qquad \mathbf{P}^\alpha \cdot \mathbf{P}_\beta = \delta^\alpha_\beta, \quad \mathbf{P}^\alpha \cdot \mathbf{N} = 0, \quad \mathbf{P}_\beta = \frac{\partial \mathbf{P}}{\partial q^\beta}.$$

Here vectors $\mathbf{P}_\beta$ and $\mathbf{P}^\alpha$ denote the natural and reciprocal bases on Σ, respectively, $\mathbf{N}$ is the unit normal to Σ and δ^α_β is the Kronecker symbol.

From the principle of material frame-indifference [66] it follows that W depends on two surface strain measures $\mathbf{E}$ and $\mathbf{K}$:

$$W = W(\mathbf{E}, \mathbf{K}), \tag{2}$$

where

$$\mathbf{E} = \mathbf{F} \cdot \mathbf{Q}^\top - \mathbf{A}, \qquad \mathbf{K} = \frac{1}{2} \mathbf{P}^\alpha \otimes \left(\frac{\partial \mathbf{Q}}{\partial q^\alpha} \cdot \mathbf{Q}^\top \right)_\times. \tag{3}$$

Here $\mathbf{F} = \nabla_\varkappa \boldsymbol{\rho}$ is the surface deformation gradient, and $\mathbf{A} \triangleq \mathbf{I} - \mathbf{N} \otimes \mathbf{N}$, $\mathbf{I}$ is the unit 3D tensor, $\mathbf{T}_\times$ is the vectorial invariant of the second-order tensor $\mathbf{T}$ defined by

$$\mathbf{T}_\times = (\mathsf{T}^{mn} \mathbf{i}_m \otimes \mathbf{i}_n)_\times = \mathsf{T}^{mn} \mathbf{i}_m \times \mathbf{i}_n$$

for any base $\mathbf{i}_m$, $\times$ denotes the vector product, see e.g. [45].

Introducing the translation vector $\mathbf{u} = \boldsymbol{\rho} - \mathbf{P}$, which is also named displacement vector, and the finite rotation vector $\boldsymbol{\theta} = 2\mathbf{e}\tan\varphi/2$ we can express $\mathbf{Q}$, $\mathbf{E}$ and $\mathbf{K}$ as follows (see [59] for details)

$$\mathbf{Q} = \frac{1}{(4+\theta^2)}\left[(4-\theta^2)\mathbf{I} + 2\boldsymbol{\theta}\otimes\boldsymbol{\theta} - 4\mathbf{I}\times\boldsymbol{\theta}\right], \tag{4}$$

$$\mathbf{E} = (\mathbf{A} + \nabla_x\mathbf{u})\cdot\mathbf{Q}^{\top} - \mathbf{A}, \quad \mathbf{K} = \frac{4}{4+\theta^2}\nabla_x\boldsymbol{\theta}\cdot\left(\mathbf{I} + \frac{1}{2}\mathbf{I}\times\boldsymbol{\theta}\right), \tag{5}$$

where $\theta^2 = \boldsymbol{\theta}\cdot\boldsymbol{\theta}$. $\mathbf{Q}$ describes the rotation about the axis with the unit vector $\mathbf{e}$ trough an angle φ.

The Lagrangian equations of motion of the micropolar shell are (cf. for example [18, 31, 47])

$$\nabla_x\cdot\mathbf{T}_x + \mathbf{f} = \rho_x\frac{\mathrm{d}\mathbf{K}_1}{\mathrm{d}t}, \tag{6}$$

$$\nabla_x\cdot\mathbf{M}_x + \left[\mathbf{F}^{\top}\cdot\mathbf{T}_x\right]_{\times} + \mathbf{m} = \rho_x\left(\frac{\mathrm{d}\mathbf{K}_2}{\mathrm{d}t} + \mathbf{v}\times\boldsymbol{\Theta}_1^{\top}\cdot\boldsymbol{\omega}\right), \tag{7}$$

where

$$\mathbf{T}_x = \mathbf{S}_1\cdot\mathbf{Q}, \qquad \mathbf{M}_x = \mathbf{S}_2\cdot\mathbf{Q}, \tag{8}$$

$$\mathbf{S}_1 = \frac{\partial W}{\partial\mathbf{E}}, \qquad \mathbf{S}_2 = \frac{\partial W}{\partial\mathbf{K}}, \tag{9}$$

$$\mathbf{K}_1 = \frac{\partial \mathrm{K}}{\partial\mathbf{v}} = \mathbf{v} + \boldsymbol{\Theta}_1^{\top}\cdot\boldsymbol{\omega}, \qquad \mathbf{K}_2 = \frac{\partial \mathrm{K}}{\partial\boldsymbol{\omega}} = \boldsymbol{\Theta}_1\cdot\mathbf{v} + \boldsymbol{\Theta}_2\cdot\boldsymbol{\omega}, \tag{10}$$

$$\mathrm{K}(\mathbf{v},\boldsymbol{\omega}) = \frac{1}{2}\mathbf{v}\cdot\mathbf{v} + \boldsymbol{\omega}\cdot\boldsymbol{\Theta}_1\cdot\mathbf{v} + \frac{1}{2}\boldsymbol{\omega}\cdot\boldsymbol{\Theta}_2\cdot\boldsymbol{\omega}. \tag{11}$$

Here $\mathbf{T}_x$ and $\mathbf{M}_x$ are the surface stress and couple stress tensors of the first Piola-Kirchhoff type while the stress measures $\mathbf{S}_1$ and $\mathbf{S}_2$ are the referential stress and couple stress tensors, respectively, $\mathbf{f}$ and $\mathbf{m}$ are the surface force and couple densities distributed on Σ,

$$\mathbf{v} = \frac{\mathrm{d}\boldsymbol{\rho}}{\mathrm{d}t}, \qquad \boldsymbol{\omega} = \frac{1}{2}\left(\mathbf{Q}^{\top}\cdot\frac{\mathrm{d}\mathbf{Q}}{\mathrm{d}t}\right)_{\times}$$

are the linear and angular velocities, respectively, ρ_x is the surface mass density in the reference configuration, $\rho_x\,\mathrm{K}$ is the surface density of the kinetic energy, and $\rho_x\,\boldsymbol{\Theta}_1$, $\rho_x\,\boldsymbol{\Theta}_2$ are the rotatory inertia tensors, $\boldsymbol{\Theta}_2 = \boldsymbol{\Theta}_2^{\top}$.

In what follows we use the simplest relations for $\boldsymbol{\Theta}_1$ and $\boldsymbol{\Theta}_2$, see [58],

$$\mathbf{\Theta}_1 = \mathbf{0}, \quad \mathbf{\Theta}_2 = \gamma\,\mathbf{I}, \tag{12}$$

where γ is a scalar measure of the rotatory inertia. With Eqs. (12) the equations of motion (6) and (7) take more simple form

$$\boldsymbol{\nabla}_{\varkappa}\cdot\mathbf{T}_{\varkappa} + \mathbf{f} = \rho_{\varkappa}\frac{\mathrm{d}\mathbf{v}}{\mathrm{d}t}, \tag{13}$$

$$\boldsymbol{\nabla}_{\varkappa}\cdot\mathbf{M}_{\varkappa} + \left[\mathbf{F}^{\top}\cdot\mathbf{T}_{\varkappa}\right]_{\times} + \mathbf{m} = \rho_{\varkappa}\,\gamma\,\frac{\mathrm{d}\boldsymbol{\omega}}{\mathrm{d}t}. \tag{14}$$

Equations (6) and (7) or (13) and (14) are supplemented by following boundary conditions:

$$\begin{aligned} &\text{on } \omega_1 \,:\, \boldsymbol{\rho} = \mathbf{r}_0(\mathrm{s}), \quad &&\text{on } \omega_2 \,:\, \boldsymbol{\nu}\cdot\mathbf{T}_{\varkappa} = \mathbf{t}(\mathrm{s}),\\ &\text{on } \omega_3 \,:\, \mathbf{Q} = \mathbf{h}(\mathrm{s}), \quad &&\text{on } \omega_4 \,:\, \boldsymbol{\nu}\cdot\mathbf{M}_{\varkappa} = \boldsymbol{\mu}(\mathrm{s}). \end{aligned} \tag{15}$$

Here $\mathbf{r}_0(\mathrm{s})$, $\mathbf{h}(\mathrm{s})$ are given vector and tensor functions, $\mathbf{h}\cdot\mathbf{h}^{\top} = \mathbf{I}$, and $\boldsymbol{\nu}$ is the external unit normal to the boundary contour $\omega = \partial\Sigma$, $\boldsymbol{\nu}\cdot\mathbf{N} = 0$, $\mathbf{t}$ and $\boldsymbol{\mu}$ are the linear densities of forces and couples distributed along corresponding parts of the shell contour ω, respectively. The contour ω is divided into two parts in such a way that

$$\omega = \omega_1 \cup \omega_2 = \omega_3 \cup \omega_4.$$

The corresponding initial conditions are

$$\boldsymbol{\rho}\big|_{t=0} = \boldsymbol{\rho}^{\circ}, \quad \mathbf{v}\big|_{t=0} = \mathbf{v}^{\circ}, \quad \mathbf{Q}\big|_{t=0} = \mathbf{Q}^{\circ}, \quad \boldsymbol{\omega}\big|_{t=0} = \boldsymbol{\omega}^{\circ} \tag{16}$$

with given initial values $\boldsymbol{\rho}^{\circ}$, $\mathbf{v}^{\circ}$, $\mathbf{Q}^{\circ}$, $\boldsymbol{\omega}^{\circ}$.

Following [18, 28, 31] let us consider the model of physically linear isotropic shells, whose strain energy density is given by the quadratic form

$$\begin{aligned} 2W = {} & \alpha_1 \mathrm{tr}^{\,2}\mathbf{E}_{\|} + \alpha_2 \mathrm{tr}\,\mathbf{E}_{\|}^2 + \alpha_3 \mathrm{tr}\left(\mathbf{E}_{\|}\cdot\mathbf{E}_{\|}^{\top}\right) + \alpha_4 \mathbf{N}\cdot\mathbf{E}^{\top}\cdot\mathbf{E}\cdot\mathbf{N} \\ & + \beta_1\,\mathrm{tr}^{\,2}\mathbf{K}_{\|} + \beta_2\,\mathrm{tr}\,\mathbf{K}_{\|}^2 + \beta_3\,\mathrm{tr}\left(\mathbf{K}_{\|}\cdot\mathbf{K}_{\|}^{\top}\right) + \beta_4\,\mathbf{N}\cdot\mathbf{K}^{\top}\cdot\mathbf{K}\cdot\mathbf{N}, \end{aligned} \tag{17}$$

$$\mathbf{E}_{\|} \triangleq \mathbf{E}\cdot\mathbf{A}, \qquad \mathbf{K}_{\|} \triangleq \mathbf{K}\cdot\mathbf{A}.$$

Equation (17) contains 8 elastic stiffness parameters, α_k, β_k, $k = 1, 2, 3, 4$. With respect to Eq. (17) $\mathbf{S}_1$ and $\mathbf{S}_2$ have the form

$$\mathbf{S}_1 = \alpha_1(\mathrm{tr}\,\mathbf{E}_{\|})\mathbf{A} + \alpha_2\mathbf{E}_{\|}^{\top} + \alpha_3\mathbf{E}_{\|} + \alpha_4(\mathbf{E}\cdot\mathbf{N})\otimes\mathbf{N}, \tag{18}$$

$$\mathbf{S}_2 = \beta_1(\mathrm{tr}\,\mathbf{K}_{\|})\mathbf{A} + \beta_2\mathbf{K}_{\|}^{\top} + \beta_3\mathbf{K}_{\|} + \beta_4(\mathbf{K}\cdot\mathbf{N})\otimes\mathbf{N}. \tag{19}$$

Introducing the fourth-order tensors $\mathbf{C}_1$ and $\mathbf{C}_2$ by the formulae

$$\mathbf{C}_1 = \alpha_1 \mathbf{A} \otimes \mathbf{A} + \alpha_2 \mathbf{P}_\alpha \otimes \mathbf{A} \otimes \mathbf{P}^\alpha + \alpha_4 \mathbf{P}_\alpha \otimes \mathbf{N} \otimes \mathbf{P}^\alpha \otimes \mathbf{N},$$
$$\mathbf{C}_2 = \beta_1 \mathbf{A} \otimes \mathbf{A} + \beta_2 \mathbf{P}_\alpha \otimes \mathbf{A} \otimes \mathbf{P}^\alpha \mathbf{P}^\beta + \beta_4 \mathbf{P}_\alpha \otimes \mathbf{N} \otimes \mathbf{P}^\alpha \otimes \mathbf{N},$$

we re-write (18) and (19) in a more compact form

$$\mathbf{S}_1 = \mathbf{C}_1 : \mathbf{E}, \quad \mathbf{S}_2 = \mathbf{C}_2 : \mathbf{K}, \tag{20}$$

where ":" denotes the inner product in the space of second-order tensors, for example

$$(\mathbf{a} \otimes \mathbf{b} \otimes \mathbf{c} \otimes \mathbf{d}) : (\mathbf{x} \otimes \mathbf{y}) = (\mathbf{c} \cdot \mathbf{x})(\mathbf{d} \cdot \mathbf{y})\mathbf{a} \otimes \mathbf{b}.$$

For parameters α_k, β_k the following values are proposed in [18]

$$\alpha_1 = C\nu,\ \alpha_2 = 0,\ \alpha_3 = C(1-\nu),\ \alpha_4 = \alpha_s C(1-\nu),$$
$$\beta_1 = D\nu,\ \beta_2 = 0,\ \beta_3 = D(1-\nu),\ \beta_4 = \alpha_t D(1-\nu),$$

where

$$C = \frac{\mathsf{E}h}{1-\nu^2}, \quad D = \frac{\mathsf{E}h^3}{12(1-\nu^2)}.$$

Here E, ν are the Young's modulus and the Poisson's ratio of the bulk material, h is the shell thickness. α_s is an analogy to the shear correction factor introduced in [64, 65] where the value $\alpha_s = 5/6$ is used or in [51] with $\alpha_s = \pi^2/12$. In [56, 57] $\alpha_t = 0.7$ is suggested, see also [19]. Extensive numerical analysis of the influence of α_s and α_t on the solutions' behavior is presented in [18].

The boundary-value problem (6), (7), (15), and (16) supplemented by the constitutive equation (17) describes finite deformations of the isotropic micropolar shell. Numerical solutions of few examples are presented in [16–19] among others.

The equations of motion (6) and (7) can be transformed to the Eulerian form

$$\boldsymbol{\nabla}_\chi \cdot \mathbf{T} + \mathrm{J}^{-1}\mathbf{f} = \rho \frac{\mathrm{d}\mathbf{K}_1}{\mathrm{dt}}, \tag{21}$$

$$\boldsymbol{\nabla}_\chi \cdot \mathbf{M} + \mathbf{T}_\times + \mathrm{J}^{-1}\mathbf{m} = \rho \left(\frac{\mathrm{d}\mathbf{K}_2}{\mathrm{dt}} + \mathbf{v} \times \boldsymbol{\Theta}_1^\top \cdot \boldsymbol{\omega} \right), \tag{22}$$

where

$$\boldsymbol{\nabla}_\chi = \boldsymbol{\rho}^\alpha \frac{\partial}{\partial \mathrm{q}^\alpha}, \quad \boldsymbol{\rho}^\alpha \cdot \boldsymbol{\rho}_\beta = \delta^\alpha_\beta, \quad \boldsymbol{\rho}^\alpha \cdot \mathbf{n} = 0, \quad \boldsymbol{\rho}_\beta = \frac{\partial \boldsymbol{\rho}}{\partial \mathrm{q}^\beta},$$

$$\mathbf{T} = \mathrm{J}^{-1}\mathbf{F}^\top \cdot \mathbf{T}_\chi, \quad \mathbf{M} = \mathrm{J}^{-1}\mathbf{F}^\top \cdot \mathbf{M}_\chi, \tag{23}$$

$$\mathrm{J} = \mathrm{J}(\mathbf{F}) = \sqrt{\frac{1}{2}\left\{ \left[\mathrm{tr}\ (\mathbf{F} \cdot \mathbf{F}^\top)\right]^2 - \mathrm{tr}\left[(\mathbf{F} \cdot \mathbf{F}^\top)^2\right] \right\}}.$$

Here $\mathbf{T}$ and $\mathbf{M}$ are Cauchy-type surface stress and couple stress tensors, ρ is the surface mass density in the actual configuration, $\boldsymbol{\nabla}_\chi$ is the surface nabla operator on σ related with $\boldsymbol{\nabla}_\varkappa$ by the formula $\boldsymbol{\nabla}_\varkappa = \mathbf{F} \cdot \boldsymbol{\nabla}_\chi$, and $\mathbf{n}$ is the unit normal to σ.

3 Linearized Boundary-Value Problems

Let $\boldsymbol{\rho}_0$ and $\mathbf{Q}_0$ are the known static solution of (6), (7), and (15). The corresponding state of the shell we will call the basic actual configuration and denote it by χ_0. In addition, let us consider the actual configuration χ_*, which differs from χ_0 by infinitesimal deformation, and derive the linearized boundary-value problem. Denoting quantities related to χ_* by the lower index $*$ we have

$$\boldsymbol{\rho}_* = \boldsymbol{\rho}_0 + \delta\boldsymbol{\rho}, \quad \mathbf{Q}_* = \mathbf{Q}_0 + \delta\mathbf{Q},$$

where we use the symbol δ for infinitesimal increments of corresponding quantities. Since $\mathbf{Q}$ is an orthogonal tensor, the tensor $\mathbf{Q}^\top \cdot \delta\mathbf{Q}$ is a skew-symmetric tensor and can be represented as follows

$$\mathbf{Q}^\top \cdot \delta\mathbf{Q} = -\mathbf{I} \times \boldsymbol{\psi},$$

where $\boldsymbol{\psi}$ is the infinitesimal rotation vector. It can be expressed by the increment of the finite rotation vector as follows

$$\boldsymbol{\psi} = \frac{4}{4+\theta^2}\left(\delta\boldsymbol{\theta} + \frac{1}{2}\boldsymbol{\theta} \times \delta\boldsymbol{\theta}\right).$$

The increments of the strain measures are given by the formulae [31]

$$\delta\mathbf{E} = (\boldsymbol{\nabla}_\varkappa \delta\boldsymbol{\rho}) \cdot \mathbf{Q}_0^\top + \mathbf{F}_0 \cdot \delta\mathbf{Q}^\top = \mathbf{F}_0 \cdot \boldsymbol{\varepsilon} \cdot \mathbf{Q}_0^\top, \tag{24}$$

$$\delta\mathbf{K} = (\boldsymbol{\nabla}_\varkappa \boldsymbol{\psi}) \cdot \mathbf{Q}^\top = \mathbf{F}_0 \cdot \boldsymbol{\varkappa} \cdot \mathbf{Q}_0^\top, \tag{25}$$

where $\boldsymbol{\varepsilon}$ and $\boldsymbol{\varkappa}$ are the linear strain measures given by

$$\boldsymbol{\varepsilon} = \boldsymbol{\nabla}_\chi \mathbf{w} + \mathbf{A} \times \boldsymbol{\psi}, \quad \boldsymbol{\varkappa} = \boldsymbol{\nabla}_\chi \boldsymbol{\psi}, \tag{26}$$

$\mathbf{w} = \delta\boldsymbol{\rho}$ and $\mathbf{F}_0 = \boldsymbol{\nabla}_\varkappa \boldsymbol{\rho}_0$.

Assuming that $\delta\mathbf{f} = \mathbf{0}$ and $\delta\mathbf{m} = \mathbf{0}$ the linearization of Eqs. (13) and (14) leads to the Lagrangian linearized equations of motion

$$\boldsymbol{\nabla}_{\varkappa} \cdot \delta \mathbf{T}_{\varkappa} = \rho_{\varkappa} \frac{\mathrm{d}^2 \mathbf{w}}{\mathrm{d}t^2}, \tag{27}$$

$$\boldsymbol{\nabla}_{\varkappa} \cdot \delta \mathbf{M}_{\varkappa} + \left[(\boldsymbol{\nabla}_{\varkappa} \mathbf{w})^{\top} \cdot \mathbf{T}_{\varkappa} + \mathbf{F}_0^{\top} \cdot \delta \mathbf{T}_{\varkappa} \right]_{\times} = \rho_{\varkappa}\, \gamma\, \frac{\mathrm{d}^2 \boldsymbol{\psi}}{\mathrm{d}t^2}. \tag{28}$$

The increments of the stress and couple stress tensors are calculated by the relations

$$\delta \mathbf{T}_{\varkappa} = \delta \mathbf{S}_1 \cdot \mathbf{Q}_0 + \mathbf{S}_1 \cdot \delta \mathbf{Q} = \delta \mathbf{S}_1 \cdot \mathbf{Q}_0 - \mathbf{T}_{\varkappa} \times \boldsymbol{\psi}, \tag{29}$$

$$\delta \mathbf{M}_{\varkappa} = \delta \mathbf{S}_2 \cdot \mathbf{Q}_0 + \mathbf{S}_2 \cdot \delta \mathbf{Q} = \delta \mathbf{S}_2 \cdot \mathbf{Q}_0 - \mathbf{M}_{\varkappa} \times \boldsymbol{\psi}, \tag{30}$$

$$\delta \mathbf{S}_1 = \frac{\partial W}{\partial \mathbf{E} \partial \mathbf{E}} \,:\, \delta \mathbf{E} + \frac{\partial W}{\partial \mathbf{E} \partial \mathbf{K}} \,:\, \delta \mathbf{K}, \tag{31}$$

$$\delta \mathbf{S}_2 = \frac{\partial W}{\partial \mathbf{K} \partial \mathbf{E}} \,:\, \delta \mathbf{E} + \frac{\partial W}{\partial \mathbf{K} \partial \mathbf{K}} \,:\, \delta \mathbf{K}. \tag{32}$$

Using (20) for the physically linear shell we have

$$\delta \mathbf{S}_1 = \mathbf{C}_1 \,:\, \delta \mathbf{E} = \mathbf{D}_1 \,:\, \boldsymbol{\varepsilon}, \quad \delta \mathbf{S}_2 = \mathbf{C}_2 \,:\, \delta \mathbf{K} = \mathbf{D}_2 \,:\, \boldsymbol{\varkappa},$$

where $\mathbf{D}_1$ and $\mathbf{D}_2$ are fourth-order tensors given by

$$\begin{aligned}
\mathbf{D}_1 &= \alpha_1 \mathbf{A} \otimes \mathbf{F}_0^{\top} \cdot \mathbf{P}_{\alpha} \otimes \mathbf{Q}_0^{\top} \cdot \mathbf{P}^{\alpha} + \alpha_2 \mathbf{P}_{\alpha} \otimes \mathbf{P}_{\beta} \otimes \mathbf{F}_0^{\top} \cdot \mathbf{P}^{\beta} \otimes \mathbf{Q}_0^{\top} \cdot \mathbf{P}^{\alpha} \\
&\quad + \alpha_3 \mathbf{P}_{\alpha} \otimes \mathbf{P}_{\beta} \otimes \mathbf{F}_0^{\top} \cdot \mathbf{P}^{\alpha} \otimes \mathbf{Q}_0^{\top} \cdot \mathbf{P}^{\beta} + \alpha_4 \mathbf{P}_{\alpha} \otimes \mathbf{N} \otimes \mathbf{F}_0^{\top} \cdot \mathbf{P}^{\alpha} \otimes \mathbf{Q}_0^{\top} \cdot \mathbf{N}, \\
\mathbf{D}_2 &= \beta_1 \mathbf{A} \otimes \mathbf{F}_0^{\top} \cdot \mathbf{P}_{\alpha} \otimes \mathbf{Q}_0^{\top} \cdot \mathbf{P}^{\alpha} + \beta_2 \mathbf{P}_{\alpha} \otimes \mathbf{P}_{\beta} \otimes \mathbf{F}_0^{\top} \cdot \mathbf{P}^{\beta} \otimes \mathbf{Q}_0^{\top} \cdot \mathbf{P}^{\alpha} \\
&\quad + \beta_3 \mathbf{P}_{\alpha} \otimes \mathbf{P}_{\beta} \otimes \mathbf{F}_0^{\top} \cdot \mathbf{P}^{\alpha} \otimes \mathbf{Q}_0^{\top} \cdot \mathbf{P}^{\beta} + \beta_4 \mathbf{P}_{\alpha} \otimes \mathbf{N} \otimes \mathbf{F}_0^{\top} \cdot \mathbf{P}^{\alpha} \otimes \mathbf{Q}_0^{\top} \cdot \mathbf{N}.
\end{aligned}$$

Assuming that $\delta \mathbf{t} = \mathbf{0}$, $\delta \boldsymbol{\mu} = \mathbf{0}$, $\delta \mathbf{r}_0 = \mathbf{0}$, and $\delta \mathbf{h} = \mathbf{0}$, we obtain the linearized boundary conditions

$$\begin{aligned}
&\text{on } \omega_1 \,:\, \mathbf{w} = \mathbf{0}, \quad \text{on } \omega_2 \,:\, \boldsymbol{\nu} \cdot \delta \mathbf{T}_{\varkappa} = \mathbf{0}, \\
&\text{on } \omega_3 \,:\, \boldsymbol{\psi} = \mathbf{0}, \quad \text{on } \omega_4 \,:\, \boldsymbol{\nu} \cdot \delta \mathbf{M}_{\varkappa} = \mathbf{0}.
\end{aligned} \tag{33}$$

Introducing the tensors

$$\boldsymbol{\Phi}_1 = \mathrm{J}_0^{-1} \mathbf{F}_0^{\top} \cdot \delta \mathbf{T}_{\varkappa}, \quad \boldsymbol{\Phi}_2 = \mathrm{J}_0^{-1} \mathbf{F}_0^{\top} \cdot \delta \mathbf{M}_{\varkappa}, \tag{34}$$

where $\mathrm{J}_0 = \mathrm{J}(\mathbf{F}_0)$, we transform Eqs. (27) and (28) into the linearized equations of motion in the actual configuration $\varkappa_0$

$$\boldsymbol{\nabla}_{\chi} \cdot \boldsymbol{\Phi}_1 = \rho \frac{\mathrm{d}^2 \mathbf{w}}{\mathrm{d}t^2}, \tag{35}$$

$$\boldsymbol{\nabla}_{\chi} \cdot \boldsymbol{\Phi}_2 + \left[(\boldsymbol{\nabla}_{\chi} \mathbf{w})^{\top} \cdot \mathbf{T} + \boldsymbol{\Phi}_1 \right]_{\times} = \rho\, \gamma\, \frac{\mathrm{d}^2 \boldsymbol{\psi}}{\mathrm{d}t^2}. \tag{36}$$

For the physically linear isotropic micropolar shell $\mathbf{\Phi}_1$ and $\mathbf{\Phi}_2$ are given by relations

$$\mathbf{\Phi}_1 = \mathbf{H}_1 \,:\, \boldsymbol{\varepsilon} - \mathbf{T} \times \boldsymbol{\psi}, \quad \mathbf{\Phi}_1 = \mathbf{H}_2 \,:\, \boldsymbol{\varkappa} - \mathbf{M} \times \boldsymbol{\psi},$$
$$\mathbf{H}_1 = \mathrm{J}_0^{-1}\mathbf{F}_0^{\top} \cdot \widetilde{\mathbf{D}}_1, \quad \mathbf{H}_2 = \mathrm{J}_0^{-1}\mathbf{F}_0^{\top} \cdot \widetilde{\mathbf{D}}_2,$$

where

$$\begin{aligned}
\widetilde{\mathbf{D}}_1 &= \alpha_1 \mathbf{P}_\alpha \otimes \mathbf{Q}_0^{\top} \cdot \mathbf{P}^\alpha \otimes \mathbf{F}_0^{\top} \cdot \mathbf{P}_\beta \otimes \mathbf{Q}_0^{\top} \cdot \mathbf{P}^\beta + \alpha_2 \mathbf{P}_\alpha \otimes \mathbf{Q}_0^{\top} \cdot \mathbf{P}_\beta \otimes \mathbf{F}_0^{\top} \cdot \mathbf{P}^\beta \otimes \mathbf{Q}_0^{\top} \cdot \mathbf{P}^\alpha \\
&\quad + \alpha_3 \mathbf{P}_\alpha \otimes \mathbf{Q}_0^{\top} \cdot \mathbf{P}_\beta \otimes \mathbf{F}_0^{\top} \cdot \mathbf{P}^\alpha \otimes \mathbf{Q}_0^{\top} \cdot \mathbf{P}^\beta + \alpha_4 \mathbf{P}_\alpha \otimes \mathbf{Q}_0^{\top} \cdot \mathbf{N} \otimes \mathbf{F}_0^{\top} \cdot \mathbf{P}^\alpha \otimes \mathbf{Q}_0^{\top} \cdot \mathbf{N}, \\
\widetilde{\mathbf{D}}_2 &= \beta_1 \mathbf{P}_\alpha \otimes \mathbf{Q}_0^{\top} \cdot \mathbf{P}^\alpha \otimes \mathbf{F}_0^{\top} \cdot \mathbf{P}_\beta \otimes \mathbf{Q}_0^{\top} \cdot \mathbf{P}^\beta + \beta_2 \mathbf{P}_\alpha \otimes \mathbf{Q}_0^{\top} \cdot \mathbf{P}_\beta \otimes \mathbf{F}_0^{\top} \cdot \mathbf{P}^\beta \otimes \mathbf{Q}_0^{\top} \cdot \mathbf{P}^\alpha \\
&\quad + \beta_3 \mathbf{P}_\alpha \otimes \mathbf{Q}_0^{\top} \cdot \mathbf{P}_\beta \otimes \mathbf{F}_0^{\top} \cdot \mathbf{P}^\alpha \otimes \mathbf{Q}_0^{\top} \cdot \mathbf{P}^\beta + \beta_4 \mathbf{P}_\alpha \otimes \mathbf{Q}_0^{\top} \cdot \mathbf{N} \otimes \mathbf{F}_0^{\top} \cdot \mathbf{P}^\alpha \otimes \mathbf{Q}_0^{\top} \cdot \mathbf{N}.
\end{aligned}$$

The fourth-order tensors $\mathbf{H}_1$ and $\mathbf{H}_2$ are tangent stiffness tensors in the non-linear theory of shells which have the same properties as in the three-dimensional non-linear elasticity [35, 36, 48, 55], see also [2]. The components of $\mathbf{H}_1$ and $\mathbf{H}_2$ depend on initial deformations and, as a result, have symmetry properties which are different from ones of $\mathbf{C}_1$ and $\mathbf{C}_2$, in general.

The linearized Eulerian boundary conditions are

$$\text{on } \ell_1 \,:\, \mathbf{w} = \mathbf{0}, \quad \text{on } \ell_2 \,:\, \boldsymbol{\eta} \cdot \mathbf{\Phi}_1 = \mathbf{0}, \quad \text{on } \ell_3 \,:\, \boldsymbol{\psi} = \mathbf{0}, \quad \text{on } \ell_4 \,:\, \boldsymbol{\eta} \cdot \mathbf{\Phi}_2 = \mathbf{0}. \tag{37}$$

Here $\boldsymbol{\eta}$ is the unit vector normal to the shell contour

$$\ell = \partial\sigma, \quad \boldsymbol{\eta} \cdot \mathbf{n} = 0, \quad \ell = \ell_1 \cup \ell_2 = \ell_3 \cup \ell_4,$$

ℓ_1, ℓ_2, ℓ_3, and ℓ_4 are the parts of the shell contour in the actual configuration corresponding to ω_1, ω_2, ω_3, and ω_4, respectively.

The boundary-value problems (27), (28), (33), and (35)–(37) describe the motion of the prestressed micropolar shell. For $\chi_0 = \varkappa$ we have

$$\mathbf{F}_0 = \mathbf{A}, \quad \mathbf{Q}_0 = \mathbf{I}.$$

Assuming in addition the absence of initial stresses

$$\mathbf{T} = \mathbf{M} = \mathbf{0}$$

the linearized boundary-value problems coincide with the equations of motion of linear isotropic micropolar shells discussed in [18, 26, 31, 45].

4 Eigen-Vibrations of Prestressed Micropolar Shells

Let us consider eigen-vibrations of a prestressed shell. By linearity, eigen-solutions are proportional to $e^{i\Omega t}$:

$$\mathbf{w} = \mathbf{W}(q^1, q^2)e^{i\Omega t}, \quad \boldsymbol{\psi} = \boldsymbol{\Xi}(q^1, q^2)e^{i\Omega t}.$$

Substituting the latter relations into (35) and (37) we obtain the boundary-value problem for the physically linear isotropic prestressed micropolar shell

$$\boldsymbol{\nabla}_\chi \cdot \boldsymbol{\Phi}_1 = -\rho\,\Omega^2 \mathbf{W}, \tag{38}$$

$$\boldsymbol{\nabla}_\chi \cdot \boldsymbol{\Phi}_2 + \left[(\boldsymbol{\nabla}_\chi \mathbf{w})^\top \cdot \mathbf{T} + \boldsymbol{\Phi}_1\right]_\times = -\rho\,\gamma\,\Omega^2 \boldsymbol{\Xi}, \tag{39}$$

$$\text{on } \ell_1 : \mathbf{W} = \mathbf{0}, \quad \text{on } \ell_2 : \boldsymbol{\eta} \cdot \boldsymbol{\Phi}_1 = \mathbf{0}, \quad \text{on } \ell_3 : \boldsymbol{\Xi} = \mathbf{0}, \quad \text{on } \ell_4 : \boldsymbol{\eta} \cdot \boldsymbol{\Phi}_2 = \mathbf{0}, \tag{40}$$

where

$$\begin{gathered}\boldsymbol{\Phi}_1 = \mathbf{H}_1 : \boldsymbol{\varepsilon} - \mathbf{T} \times \boldsymbol{\Xi}, \quad \boldsymbol{\Phi}_2 = \mathbf{H}_2 : \boldsymbol{\varkappa} - \mathbf{M} \times \boldsymbol{\Xi}, \\ \boldsymbol{\varepsilon} = \boldsymbol{\nabla}_\chi \mathbf{W} + \mathbf{A} \times \boldsymbol{\Xi}, \quad \boldsymbol{\varkappa} = \boldsymbol{\nabla}_\chi \boldsymbol{\Xi}.\end{gathered} \tag{41}$$

Additionally we consider the linear boundary-value problem of the micropolar shell without initial deformation, that is when $\chi_0 = \varkappa$, which is given by

$$\boldsymbol{\nabla}_\chi \cdot \boldsymbol{\Phi}_1^0 = -\rho\,\Omega^2 \mathbf{W}, \quad \boldsymbol{\nabla}_\chi \cdot \boldsymbol{\Phi}_2^0 + \boldsymbol{\Phi}_{1\times}^0 = -\rho\,\gamma\,\Omega^2 \boldsymbol{\Xi}, \tag{42}$$

$$\text{on } \ell_1 : \mathbf{W} = \mathbf{0}, \quad \text{on } \ell_2 : \boldsymbol{\eta} \cdot \boldsymbol{\Phi}_1^0 = \mathbf{0}, \quad \text{on } \ell_3 : \boldsymbol{\Xi} = \mathbf{0}, \quad \text{on } \ell_4 : \boldsymbol{\eta} \cdot \boldsymbol{\Phi}_2^0 = \mathbf{0}, \tag{43}$$

$$\boldsymbol{\Phi}_1^0 = \mathbf{C}_1 : \boldsymbol{\varepsilon}, \quad \boldsymbol{\Phi}_2^0 = \mathbf{C}_2 : \boldsymbol{\varkappa}. \tag{44}$$

The comparison of $\boldsymbol{\Phi}_1^0$ and $\boldsymbol{\Phi}_1$, $\boldsymbol{\Phi}_2^0$ and $\boldsymbol{\Phi}_2$ shows that difference between these boundary-value problems consists of

1. the difference between the elastic moduli tensors $\mathbf{C}_\alpha$ and $\mathbf{H}_\alpha$, $\alpha = 1, 2$, and
2. the existence of initial stress tensors $\mathbf{T}$ and $\mathbf{M}$ in $\boldsymbol{\Phi}_1$ and $\boldsymbol{\Phi}_2$.

In what follows we show the influence on eigen-frequencies of the prestressed shell using the variational approach.

5 Rayleigh Principle

In the linear and linearized shell theories presented above there is a variational principle for eigen-vibrations called the Rayleigh variational principle. To formulate it

we consider the second variation of the functional of the total energy of the micropolar shell. Suppose that $\mathbf{m} = \boldsymbol{\mu} = \mathbf{0}$ and the external forces are "dead". This means that $\mathbf{f}$ and $\mathbf{t}$ do not depend on $\mathbf{u}$ and $\mathbf{Q}$. Thus the functional of the total potential energy of the shell is

$$\Pi = \iint\limits_{\Sigma} W \, \mathrm{d}\Sigma - \iint\limits_{\Sigma} \mathbf{f} \cdot \mathbf{u} \, \mathrm{d}\Sigma - \int\limits_{\omega_2} \mathbf{t} \cdot \mathbf{u} \, \mathrm{ds}.$$

The first variation of Π is given by

$$\begin{aligned} \delta\Pi = & \iint\limits_{\Sigma} \left[\mathrm{tr} \left(\mathbf{T}_{\varkappa}^{\top} \cdot \boldsymbol{\nabla}_{\varkappa} \mathbf{w} \right) + \mathrm{tr} \left(\mathbf{T}_{\varkappa}^{\top} \cdot \mathbf{F}_0 \times \boldsymbol{\psi} \right) + \mathrm{tr} \left(\mathbf{M}_{\varkappa}^{\top} \cdot \boldsymbol{\nabla}_{\varkappa} \boldsymbol{\psi} \right) \right] \mathrm{d}\Sigma \\ & - \iint\limits_{\Sigma} \mathbf{f} \cdot \mathbf{w} \, \mathrm{d}\Sigma - \int\limits_{\omega_2} \mathbf{t} \cdot \mathbf{w} \, \mathrm{ds}. \end{aligned} \tag{45}$$

Since $\boldsymbol{\rho}_0$ and $\mathbf{Q}_0$ are assumed to satisfy equilibrium equations and boundary conditions (15), the first variation of the energy vanishes

$$\delta\Pi = 0.$$

The second variation of the energy takes the form

$$\begin{aligned} \delta^2\Pi = & \iint\limits_{\Sigma} \left\{ \mathrm{tr} \left(\delta \mathbf{T}_{\varkappa}{}^{\top} \cdot \boldsymbol{\nabla}_{\varkappa} \mathbf{w} \right) + \mathrm{tr} \left(\delta \mathbf{T}_{\varkappa}{}^{\top} \cdot \mathbf{F}_0 \times \boldsymbol{\psi} \right) + \mathrm{tr} \left[\mathbf{T}_{\varkappa}^{\top} \cdot (\boldsymbol{\nabla}_{\varkappa} \mathbf{w}) \times \boldsymbol{\psi} \right] \right. \\ & \left. + \mathrm{tr} \left(\delta \mathbf{M}_{\varkappa}{}^{\top} \cdot \boldsymbol{\nabla}_{\varkappa} \boldsymbol{\psi} \right) \right\} \mathrm{d}\Sigma. \end{aligned}$$

Using identities $\boldsymbol{\nabla}_{\chi} = \mathbf{F} \cdot \boldsymbol{\nabla}_{\varkappa}$, $\mathrm{d}\sigma = J \, \mathrm{d}\Sigma$, and Eq. (34), we transform $\delta^2\Pi$ to

$$\begin{aligned} \delta^2\Pi = & \iint\limits_{\sigma} \left\{ \boldsymbol{\Phi}_1 : \left(\boldsymbol{\nabla}_{\chi} \mathbf{w} + \mathbf{A} \times \boldsymbol{\psi} \right) + \boldsymbol{\Phi}_1 : \boldsymbol{\nabla}_{\chi} \boldsymbol{\psi} + \mathrm{tr} \left[\mathbf{T}^{\top} \cdot (\boldsymbol{\nabla}_{\chi} \mathbf{w}) \times \boldsymbol{\psi} \right] \right\} \mathrm{d}\sigma \\ = & \iint\limits_{\sigma} \left\{ \boldsymbol{\Phi}_1 : \boldsymbol{\varepsilon} + \boldsymbol{\Phi}_2 : \boldsymbol{\varkappa} + \mathrm{tr} \left[\mathbf{T}^{\top} \cdot (\boldsymbol{\nabla}_{\chi} \mathbf{w}) \times \boldsymbol{\psi} \right] \right\} \mathrm{d}\sigma \, . \end{aligned}$$

Finally, with Eqs. (41), the second energy variation takes the form

$$\delta^2\Pi = 2 \iint\limits_{\sigma} w \, \mathrm{d}\sigma, \quad w = w_1 + w_2, \tag{46}$$

where

$$
\begin{aligned}
w_1(\boldsymbol{\varepsilon},\boldsymbol{\varkappa}) &= \frac{1}{2}\boldsymbol{\varepsilon} : \mathbf{H}_1 : \boldsymbol{\varepsilon} + \frac{1}{2}\boldsymbol{\varkappa} : \mathbf{H}_2 : \boldsymbol{\varkappa}, \\
w_2(\boldsymbol{\psi},\boldsymbol{\varepsilon},\boldsymbol{\varkappa}) &= \operatorname{tr}\left(\boldsymbol{\psi}\times\mathbf{T}^{\top}\cdot\boldsymbol{\varepsilon}\right) - \frac{1}{2}\operatorname{tr}\left(\boldsymbol{\psi}\times\mathbf{T}^{\top}\times\boldsymbol{\psi}\right) + \frac{1}{2}\operatorname{tr}\left(\boldsymbol{\psi}\times\mathbf{M}^{\top}\cdot\boldsymbol{\varkappa}\right).
\end{aligned}
\tag{47}
$$

Let us note that w is the increment of the elastic energy density of the initially prestressed shell under additional infinitesimal deformations. By Eqs. (46) and (47), w splits into two terms. The first term, w_1, is similar to the strain energy density of the linear shell. w_1 is the quadratic form of $\boldsymbol{\varepsilon}$ and $\boldsymbol{\varkappa}$ with the elastic moduli tensors $\mathbf{H}_1$ and $\mathbf{H}_2$. w_2 is also a quadratic form but depending on $\boldsymbol{\psi}$, $\boldsymbol{\varepsilon}$ and $\boldsymbol{\varkappa}$. The coefficients in the quadratic form w_2 are expressed in terms of the initial stress and couple stress tensors only, they do not depend on the properties of shell material.

If $\boldsymbol{\chi}_0 = \boldsymbol{\varkappa}$, that is $\mathbf{T} = \mathbf{M} = \mathbf{0}$, then the energy density w is a quadratic form of tensors $\boldsymbol{\varepsilon}$ and $\boldsymbol{\varkappa}$ having the form

$$
w = w_0 \equiv \frac{1}{2}\boldsymbol{\varepsilon} : \mathbf{C}_1 : \boldsymbol{\varepsilon} + \frac{1}{2}\boldsymbol{\varkappa} : \mathbf{C}_2 : \boldsymbol{\varkappa}.
$$

Here w_0 is the strain energy density of an isotropic linear micropolar shell under infinitesimal deformations, see [18, 26, 31, 32].

Now the Rayleigh variational principle can be formulated as follows. The modes of shell eigen-oscillations are stationary points of the energy functional

$$
\mathcal{E}[\mathbf{W},\boldsymbol{\Xi}] = \iint\limits_{\sigma} \left[w_1(\boldsymbol{\varepsilon},\boldsymbol{\varkappa}) + w_2(\boldsymbol{\Xi},\boldsymbol{\varepsilon},\boldsymbol{\varkappa})\right] \mathrm{d}\sigma,
\tag{48}
$$

where

$$
\boldsymbol{\varepsilon} = \boldsymbol{\nabla}_{\chi}\mathbf{W} + \mathbf{A}\times\boldsymbol{\Xi}, \qquad \boldsymbol{\varkappa} = \boldsymbol{\nabla}_{\chi}\boldsymbol{\Xi},
$$

on the set of functions that satisfy the kinematic boundary conditions

$$
\text{on } \ell_1 : \mathbf{W} = \mathbf{0} \quad \text{and on } \ell_3 : \boldsymbol{\Xi} = \mathbf{0}
\tag{49}
$$

and the restriction

$$
\mathcal{K}(\mathbf{W},\boldsymbol{\Xi}) \equiv \frac{1}{2}\iint\limits_{\sigma} \rho\left(\mathbf{W}\cdot\mathbf{W} + \gamma\,\boldsymbol{\Xi}\cdot\boldsymbol{\Xi}\right) \mathrm{d}\sigma = 1.
\tag{50}
$$

Here the functions $\mathbf{W}$, $\boldsymbol{\Xi}$ are the oscillation amplitudes for the translations and rotations, respectively.

The Rayleigh variational principle is equivalent to the stationary principle for the Rayleigh quotient

$$
\mathcal{R}[\mathbf{W},\boldsymbol{\Xi}] = \frac{\mathcal{E}[\mathbf{W},\boldsymbol{\Xi}]}{\mathcal{K}(\mathbf{W},\boldsymbol{\Xi})},
\tag{51}
$$

that is defined on kinematically admissible functions $\mathbf{W}, \boldsymbol{\Xi}$.

The proof of the principle in the case of a prestressed shell is standard and mimics one which can be found, for example, in [9] or in the case of the micropolar shell theory in [26]. For comparison purposes we introduce the Rayleigh quotient of the shell without initial stresses

$$\mathcal{R}_0[\mathbf{W}, \boldsymbol{\Xi}] = \frac{\mathcal{E}_0[\mathbf{W}, \boldsymbol{\Xi}]}{\mathcal{K}(\mathbf{W}, \boldsymbol{\Xi})}, \qquad \mathcal{E}_0[\mathbf{W}, \boldsymbol{\Xi}] = \iint\limits_{\sigma} w_0(\boldsymbol{\varepsilon}, \boldsymbol{\varkappa}) \, \mathrm{d}\sigma \,. \tag{52}$$

Note that the least squared eigenfrequencies of the shell correspond to the minimal values of $\mathcal{R}$ and $\mathcal{R}_0$

$$\Omega^2_{\min} = \inf \mathcal{R}[\mathbf{W}, \boldsymbol{\Xi}], \quad \Omega^{\,2}_{0\min} = \inf \mathcal{R}_0[\mathbf{W}, \boldsymbol{\Xi}]$$

on $\mathbf{W}, \boldsymbol{\Xi}$ that satisfy (49). By the Courant minimax principle [21], the Rayleigh quotient (51) allows us to estimate the values of higher eigen-frequencies. For this we should consider $\mathcal{R}$ on the set of functions that are orthogonal to the previous modes of eigen-oscillations in some functional energy space.

To analyze the influence of initial (residual) stresses we compare the functionals $\mathcal{R}$ and $\mathcal{R}_0$ that is equivalent to comparison of $\mathcal{E}$ and $\mathcal{E}_0$. It is obvious that the difference between $\mathcal{E}$ and $\mathcal{E}_0$ consist of two terms: the difference in elastic moduli, that is the difference between $\mathbf{C}_1$ and $\mathbf{H}_1$, $\mathbf{C}_2$ and $\mathbf{H}_2$, and the term w_2 depending on initial stress and couple stress tensors.

Let us consider first w_1 and w_0. In the linear theory of shell it is assumed that w_0 is a positive definite quadratic form of $\boldsymbol{\varepsilon}$ and $\boldsymbol{\varkappa}$. We also assume that $w_1(\boldsymbol{\varepsilon}, \boldsymbol{\varkappa})$ is a positive definite quadratic form. This means that w_1 satisfies the following inequality

$$w_1(\boldsymbol{\varepsilon}, \boldsymbol{\varkappa}) \geq c_1 \|\boldsymbol{\varepsilon}\|^2 + c_2 \|\boldsymbol{\varkappa}\|^2$$

with positive constants c_1 and c_2 depending on the shell geometry. This restriction plays the same role as the generalized Coleman-Noll inequality used in the non-linear elasticity, see [30]. This case is similar to the dependence of the eigen-frequency of a spring on its stiffness: the increase of stiffness leads to the increase of eigen-frequency.

To analyze the influence of w_2 let us assume that $\mathbf{C}_1 = \mathbf{H}_1$, $\mathbf{C}_2 = \mathbf{H}_2$. This means that we neglect the influence of initial strains on the elastic moduli of the shell. Here we have $w - w_0 = w_2$. It is obvious that w_2 is not a positive definite function, in general. Indeed, let us consider as an example the uniform stretching of the shell with $\mathbf{T} = \top\mathbf{A}$, $\mathbf{M} = \mathbf{0}$, $\top$ is the uniform tension. We have

$$
\begin{aligned}
w_2(\boldsymbol{\Xi}, \boldsymbol{\varepsilon}, \boldsymbol{\varkappa}) &= \mathsf{T}\,\mathrm{tr}\,(\boldsymbol{\Xi} \times \mathbf{A} \cdot \boldsymbol{\varepsilon}) - \frac{\mathsf{T}}{2}\mathrm{tr}\,(\boldsymbol{\Xi} \times \mathbf{A} \times \boldsymbol{\Xi}) \\
&= \mathsf{T}\,\mathrm{tr}\,\left(\boldsymbol{\Xi} \times \boldsymbol{\nabla}_{\chi}\mathbf{W}\right) + \frac{\mathsf{T}}{2}\mathrm{tr}\,(\boldsymbol{\Xi} \times \mathbf{A} \times \boldsymbol{\Xi}) \\
&= \mathsf{T}\,\mathrm{tr}\,\left(\boldsymbol{\Xi} \times \boldsymbol{\nabla}_{\chi}\mathbf{W}\right) + \frac{\mathsf{T}}{2}\left[\boldsymbol{\Xi} \cdot \boldsymbol{\Xi} + (\boldsymbol{\Xi} \cdot \mathbf{N})^2\right].
\end{aligned}
$$

Assuming $\boldsymbol{\nabla}_{\chi}\mathbf{W} = \mathbf{0}$ we obtain

$$
w_2 = \frac{\mathsf{T}}{2}\left[\boldsymbol{\Xi} \cdot \boldsymbol{\Xi} + (\boldsymbol{\Xi} \cdot \mathbf{N})^2\right].
$$

Thus, the sign of w_2 coincides with the sign of T. As a result we have

$$
\mathcal{E}[\mathbf{0}, \boldsymbol{\Xi}] - \mathcal{E}_0[\mathbf{0}, \boldsymbol{\Xi}] = \frac{\mathsf{T}}{2}\iint\limits_{\sigma}\left[\boldsymbol{\Xi} \cdot \boldsymbol{\Xi} + (\boldsymbol{\Xi} \cdot \mathbf{N})^2\right] \mathrm{d}\sigma\,.
$$

Positive values of T leads to an increase of Ω. This case is similar to the dependence of eigen-frequency of a string on tension [21]: stretching ($\mathsf{T} > 0$) leads to the increase while compression ($\mathsf{T} < 0$) leads to the decrease of the eigen-frequencies in comparison with the unstressed shell. Moreover, since initial stresses and couple stresses may lead to instability of the shell that is when $\delta^2\Pi$ becomes non-positive their influence on eigen-oscillations is more important than the change of elastic moduli tensors.

Few examples showing the influence of initial stresses on the least eigenfrequencies of a prestressed six-parameter shell are given in [3].

6 Conclusions

We presented the variational formulation of boundary-value problems described eigen-oscillations of the prestressed six-parameter shells. The Rayleigh quotient is introduced and the Rayleigh variational principle is formulated. Using the Rayleigh variational principle we analyzed the influence of initial stresses on eigen-frequencies. It is determined by changes of elastic moduli tensors due to deformations and by terms depending on initial stress and couple stress tensors only which may play more important role in the case of flexible thin shells with initial stresses.

References

1. Akay, A., Xu, Z., Carcaterra, A., Koç, I.M.: Experiments on vibration absorption using energy sinks. J. Acoust. Soc. Am. **118**(5), 3043–3049 (2005)

2. Altenbach, H., Eremeyev, V.A.: On the effective stiffness of plates made of hyperelastic materials with initial stresses. Int. J. Non-Linear Mech. **45**(10), 976–981 (2010)
3. Altenbach, H., Eremeyev, V.A.: Vibration analysis of non-linear 6-parameter prestressed shells. Meccanica **49**(8), 1751–1761 (2014). doi:10.1007/s11012-013-9845-1
4. Altenbach, H., Eremeyev, V.A.: Actual developments in the nonlinear shell theory—state of the art and new applications of the six-parameter shell theory. In: Pietraszkiewicz, W., Górski, J. (eds.) Shell Structures: Theory and Applications, vol. 3, pp. 3–12. Taylor & Francis, London (2014)
5. Altenbach, J., Altenbach, H., Eremeyev, V.A.: On generalized Cosserat-type theories of plates and shells: a short review and bibliography. Arch. Appl. Mech. **80**(1), 73–92 (2010)
6. Andreaus, U., dell'Isola, F., Porfiri, M.: Piezoelectric passive distributed controllers for beam flexural vibrations. J. Vib. Control **10**(5), 625–659 (2004)
7. Bailie, J.: Review and application of prestressed shell theories to blood vessel wave propagation. AIAA J. **10**(9), 1143–1144 (1972)
8. Banichuk, N.V.: Introduction to Optimization of Structures. Springer, New York (1990)
9. Berdichevsky, V.L.: Variational Principles of Continuum Mechanics: I. Fundamentals. Springer, Heidelberg (2009)
10. Bespalova, E., Urusova, G.: Vibrations of highly inhomogeneous shells of revolution under static loading. J. Mech. Mater. Struct. **3**(7), 1299–1313 (2008)
11. Bîrsan, M., Neff, P.: Existence of minimizers in the geometrically non-linear 6-parameter resultant shell theory with drilling rotations. Math. Mech. Solids **19**(4), 376–397 (2014). doi:10.1177/1081286512466659
12. Bîrsan, M., Neff, P.: Existence theorems in the geometrically non-linear 6-parameter theory of elastic plates. J. Elast. **112**(2), 185–198 (2013a)
13. Bîrsan, M., Neff, P.: On the characterization of drilling rotation in the 6-parameter resultant shell theory. Shell structures: Theory and applications, Vol. 3, pp. 61–64 (2013b). arXiv:1303.1979:1–9
14. Carcaterra, A., Akay, A.: Vibration damping device. US Patent App. 13/910,752 (2014)
15. Carcaterra, A., Akay, A., Bernardini, C.: Trapping of vibration energy into a set of resonators: theory and application to aerospace structures. Mech. Syst. Signal Process. **26**, 1–14 (2012)
16. Chróścielewski, J., Witkowski, W.: On some constitutive equations for micropolar plates. ZAMM—J. Appl. Math. Mech. **90**(1), 53–64 (2010)
17. Chróścielewski, J., Witkowski, W.: FEM analysis of Cosserat plates and shells based on some constitutive relations. ZAMM—J. Appl. Math. Mech. **91**(5), 400–412 (2011)
18. Chróścielewski, J., Makowski, J., Pietraszkiewicz, W.: Statics and Dynamics of Multifolded Shells. Nonlinear Theory and Finite Element Method (in Polish). Wydawnictwo IPPT PAN, Warszawa (2004)
19. Chróścielewski, J., Pietraszkiewicz, W., Witkowski, W.: On shear correction factors in the nonlinear theory of elastic shells. Int. J. Solids Struct. **47**(25–26), 3537–3545 (2010)
20. Chróścielewski, J., Kreja, I., Sabik, A., Witkowski, W.: Modeling of composite shells in 6-parameter nonlinear theory with drilling degree of freedom. Mech. Adv. Mater. Struct. **18**(6), 403–419 (2011)
21. Courant, R., Hilbert, D.: Methods of Mathematical Physics, vol. 1. Wiley, New York (1991)
22. dell'Isola, F., Vidoli, S.: Damping of bending waves in trussbeams byelectrical transmission lines with PZT actuators. Arch. Appl. Mech. **68**(9), 626–636 (1998)
23. dell'Isola, F., Porfiri, M., Vidoli, S.: Piezo-ElectroMechanical (PEM) structures: passive vibration control using distributed piezoelectric transducers. Comptes Rendus Mécanique **331**(1), 69–76 (2003)
24. Eremeyev, V.A.: Nonlinear micropolar shells: theory and applications. In: Pietraszkiewicz, W., Szymczak, C. (eds.) Shell Structures: Theory and Applications, pp. 11–18. Taylor & Francis, London (2005)
25. Eremeyev, V.A., Altenbach, H.: Rayleigh variational principle and vibrations of prestressed shells. In: Pietraszkiewicz, W., Górski, J. (eds.) Shell Structures: Theory and Applications, vol. 3, pp. 285–288. Taylor & Francis, London (2014)

26. Eremeyev, V.A., Lebedev, L.P.: Existence theorems in the linear theory of micropolar shells. ZAMM—J. Appl. Math. Mech. **91**(6), 468–476 (2011)
27. Eremeyev, V.A., Pietraszkiewicz, W.: The non-linear theory of elastic shells with phase transitions. J. Elast. **74**(1), 67–86 (2004)
28. Eremeyev, V.A., Pietraszkiewicz, W.: Local symmetry group in the general theory of elastic shells. J. Elast. **85**(2), 125–152 (2006)
29. Eremeyev, V.A., Pietraszkiewicz, W.: Thermomechanics of shells undergoing phase transition. J. Mech. Phys. Solids **59**(7), 1395–1412 (2011)
30. Eremeyev, V.A., Zubov, L.M.: On constitutive inequalities in nonlinear theory of elastic shells. ZAMM—J. Appl. Math. Mech. **87**(2), 94–101 (2007)
31. Eremeyev, V.A., Zubov, L.M.: Mechanics of Elastic Shells. Nauka, Moscow (2008) (in Russian)
32. Eremeyev, V.A., Lebedev, L.P., Altenbach, H.: Foundations of Micropolar Mechanics. Springer, Berlin (2013)
33. Eremeyev, V.A., Ivanova, E.A., Morozov, N.F.: On free oscillations of an elastic solids with ordered arrays of nano-sized objects. Continuum Mech. Thermodyn. **27**(4–5), 583–607 (2015). doi:10.1007/s00161-014-0343-z
34. Eringen, A.C., Maugin, G.A.: Electrodynamics of Continua. Springer, New York (1990)
35. Federico, S.: Covariant formulation of the tensor algebra of non-linear elasticity. Int. J. Non-Linear Mech. **47**(2), 273–284 (2012)
36. Fu, Y.B., Ogden, R.W.: Nonlinear stability analysis of pre-stressed elastic bodies. Continuum Mech. Thermodyn. **11**, 141–172 (1999)
37. Green, A.E., Adkins, J.E.: Large Elastic Deformations and Non-Linear Continuum Mechanics. Clarendon Press, Oxford (1960)
38. Harari, A.: Generalized non-linear free vibrations of prestressed plates and shells. Int. J. Non-Linear Mech. **11**(3), 169–181 (1976)
39. Ieşan, D.: Prestressed Bodies, Pitman Research Notes in Mathematics Series, vol. 195. Longman Scientific and Technical, London (1989)
40. Kalnins, A.: Vibration and stability of prestressed shells. Nucl. Eng. Des. **20**(1), 131–147 (1972)
41. Kebadze, E., Guest, S.D., Pellegrino, S.: Bistable prestressed shell structures. Int. J. Solids Struct. **41**(11–12), 2801–2820 (2004)
42. Koç, I.M., Carcaterra, A., Xu, Z., Akay, A.: Energy sinks: vibration absorption by an optimal set of undamped oscillators. J. Acoust. Soc. Am. **118**(5), 3031–3042 (2005)
43. Konopińska, V., Pietraszkiewicz, W.: Exact resultant equilibrium conditions in the non-linear theory of branching and self-intersecting shells. Int. J. Solids Struct. **44**(1), 352–369 (2007)
44. Kulikov, G.M.: Analysis of initially stressed multilayered shells. Int. J. Solids Struct. **38**(26–27), 4535–4555 (2001)
45. Lebedev, L.P., Cloud, M.J., Eremeyev, V.A.: Tensor Analysis with Applications in Mechanics. World Scientific, New Jersey (2010)
46. Libai, A., Simmonds, J.G.: Nonlinear elastic shell theory. Adv. Appl. Mech. **23**, 271–371 (1983)
47. Libai, A., Simmonds, J.G.: The Nonlinear Theory of Elastic Shells, 2nd edn. Cambridge University Press, Cambridge (1998)
48. Lurie, A.I.: Nonlinear Theory of Elasticity. North-Holland, Amsterdam (1990)
49. Maugin, G.A.: Continuum Mechanics of Electromagnetic Solids. Elsevier, Oxford (1988)
50. Maurini, C., dell'Isola, F., Vescovo, D.D.: Comparison of piezoelectronic networks acting as distributed vibration absorbers. Mech. Syst. Signal Process. **18**(5), 1243–1271 (2004)
51. Mindlin, R.D.: Influence of rotatory inertia and shear on flexural motions of isotropic elastic plates. Trans. ASME J. Appl. Mech. **18**, 31–38 (1951)
52. Neff, P.: A geometrically exact Cosserat shell-model including size effects, avoiding degeneracy in the thin shell limit. Part I: formal dimensional reduction for elastic plates and existence of minimizers for positive Cosserat couple modulus. Continuum Mech. Thermodyn. **16**(6), 577–628 (2004)

53. Neff, P.: A geometrically exact planar Cosserat shell-model with microstructure: existence of minimizers for zero Cosserat couple modulus. Math. Models Methods Appl. Sci. **17**(03), 363–392 (2007)
54. Neff, P., Chełminski, K.: A geometrically exact Cosserat shell model for defective elastic crystals. Justification via Γ-convergence. Interfaces Free Boundaries **9**(4), 455 (2007)
55. Ogden, R.W.: Non-Linear Elastic Deformations. Dover, Mineola (1997)
56. Pietraszkiewicz, W.: Consistent second approximation to the elastic strain energy of a shell. ZAMM **59**, 206–208 (1979a)
57. Pietraszkiewicz, W.: Finite Rotations and Langrangian Description in the Non-Linear Theory of Shells. Polish Scientific Publishers, Warszawa-Poznań (1979b)
58. Pietraszkiewicz, W.: Refined resultant thermomechanics of shells. Int. J. Eng. Sci. **49**(10), 1112–1124 (2011)
59. Pietraszkiewicz, W., Eremeyev, V.A.: On vectorially parameterized natural strain measures of the non-linear Cosserat continuum. Int. J. Solids Struct. **46**(11–12), 2477–2480 (2009)
60. Pietraszkiewicz, W., Konopińska, V.: On unique kinematics for the branching shells. Int. J. Solids Struct. **48**(14–15), 2238–2244 (2011)
61. Pietraszkiewicz, W., Konopińska, V.: Singular curves in the resultant thermomechanics of shells. Int. J. Eng. Sci. **80**, 21–31 (2014)
62. Placidi, L., dell'Isola, F., Ianiro, N., Sciarra, G.: Variational formulation of pre-stressed solid-fluid mixture theory, with an application to wave phenomena. Eur. J. Mech. A. Solids **27**(4), 582–606 (2008)
63. Rao, G.V., Sundararamaiah, V., Raju, I.: Finite element analysis of vibrations of initially stressed thin shells of revolution. J. Sound Vib. **37**(1), 57–64 (1974)
64. Reissner, E.: On the theory of bending of elastic plates. J. Math.Phys. **23**, 184–194 (1944)
65. Reissner, E.: The effect of transverse shear deformation on the bending of elastic plates. Trans. ASME J. Appl. Mech. **12**(11), A69–A77 (1945)
66. Truesdell, C., Noll, W.: The nonlinear field theories of mechanics. In: Flügge, S. (ed.) Handbuch der Physik, vol. III/3, pp. 1–602. Springer, Berlin (1965)
67. Vidoli, S., dell'Isola, F.: Vibration control in plates by uniformly distributed PZT actuators interconnected via electric networks. Eur. J. Mech. A. Solids **20**(3), 435–456 (2001)
68. Zubov, L.M.: Theory of small deformations of prestressed thin shells. J. Appl. Math. Mech. **40**(1), 73–82 (1976)
69. Zubov, L.M.: Compatibility equations, stress functions, and variational principles in the theory of prestressed shells. J. Appl. Math. Mech. **49**(1), 95–100 (1985)
70. Zubov, L.M.: Micropolar shell equilibrium equations. Dokl. Phys. **54**(6), 290–293 (2009)

Multi-objective Topology Optimization Design of Micro-structures

Sebastián Miguel Giusti and Antonio André Novotny

Abstract This contribution proposes a methodology for the multi-objective synthesis and/or topology optimization of microstructures based on the topological derivative concept. The macroscopic properties are estimated by a standard multi-scale constitutive theory where the macroscopic responses are volume averages of their microscopic counterparts over a Representative Volume Element (RVE). We introduce a macroscopic cost functional that combines the mechanical and thermal effects in a single expression, allowing to design an RVE satisfying a specific thermo-mechanical macroscopic behavior. The algorithm is of simple computational implementation and relies in a level-set domain representation method. The effectiveness of the proposed methodology is illustrated by a set of finite element-based numerical examples.

1 Introduction

The accurate prediction of macroscopic thermal and mechanical properties of materials from the knowledge of their underlying microstructures has long been a subject of great interest in applied mechanics. The increasing understanding of the microscopic mechanisms responsible for the macroscopic response, allied to the industrial demand for more accurate predictive tools, led to the development and use of so-called *multiscale constitutive theories*. Such theories are currently a subject

S.M. Giusti (✉)
Departamento de Ingeniería Civil, Facultad Regional
Córdoba UTN/FRC - CONICET, Universidad Tecnológica Nacional,
Maestro M. López esq. Cruz Roja Argentina, X5016ZAA Córdoba, Argentina
e-mail: sgiusti@frc.utn.edu.ar

A.A. Novotny
Laboratório Nacional de Computação Científica LNCC/MCT,
Coordenação de Matemática Aplicada e Computacional, Av. Getúlio Vargas 333,
Petrópolis, RJ 25651-075, Brazil
e-mail: novotny@lncc.br

P.A. Muñoz-Rojas (ed.), *Computational Modeling, Optimization and Manufacturing Simulation of Advanced Engineering Materials*,
Advanced Structured Materials 49, DOI 10.1007/978-3-319-04265-7_2

of intensive research in applied mathematics and computational mechanics, whose mathematical roots can be traced back to the pioneers works [8, 13, 19, 20, 32].

Early applications were concerned with the description of relatively simple microscale phenomena often treated by analytical or semi-analytical methods [6, 7, 18, 27, 30]. More recent applications rely often on finite element-based computational simulations and are frequently applied to more complex material behavior [9, 25, 26, 31, 34].

One interesting branching of such developments is the study of the sensitivity of the macroscopic response to changes in the underlying microstructure. The sensitivity information becomes essential in the analysis and potential purpose-design and optimization of heterogeneous media. In the present work we adopt an approach that relies on exact formulae for the sensitivities of the macroscopic elastic and thermal responses to topological changes of the microscopic domain. These formulae have been derived in [16, 17]; and rely on the concepts of topological asymptotic analysis and topological derivative [33]—which provide the correct mathematical framework for the calculation of sensitivities under singular topological changes typical of microstructural optimization problems. The obtained sensitivities are given by a symmetric tensor field, of the same order that the constitutive operator, over the Representative Volume Element (RVE) that measures how the macroscopic constitutive parameters estimated within the multiscale framework changes when a small disk is introduced at the microscale. The final format of the proposed analytical formulae are strikingly simple and has been successfully applied to synthesis and optimization of elastic microstructures in [4, 10, 15].

In this work we introduce a macroscopic cost functional that combines the mechanical and thermal effects in a single expression. The associated topological derivative of each term of the cost functional has been respectively derived in [16, 17]. These results are used together with a level-set domain representation method in the synthesis and/or topology optimization of the RVE to achieve a specific thermo-mechanical macroscopic behavior. We claim however that the thermal-expansion effect is neglected, so that the resulting thermo-mechanical model is uncoupled.

The work is organized as follows. The multi-scale constitutive theories used in the estimation of the elastic and thermal macroscopic constitutive response is briefly described in Sect. 2. In Sect. 3 an overview of the topological derivative concept is given and the formulae for the topological derivatives of the macroscopic elasticity and thermal constitutive tensors relevant to the present context are presented. The topology optimization algorithm together with the numerical examples are presented in Sect. 4. Finally, some concluding remarks are made in Sect. 5.

2 Multi-objective Problem Formulation

Let $\Omega_\mu \subset \mathfrak{R}^2$ be an open and bounded domain defining a local Representative Volume Element (RVE) of the material. The domain of the sought optimal structure will be a subset of the hold-all domain Ω_μ. Therefore, given a RVE domain Ω_μ,

a general procedure for the topological design of multifunctional micro-structures consists in finding a subdomain $\omega_\mu \subset \Omega_\mu$ (the optimal structure domain) that solves the following constrained minimization problem:

$$\begin{cases} \underset{\omega_\mu \subset \Omega_\mu}{\text{Minimize}} & \mathscr{J}(\Omega_\mu) = \beta\, z(\mathbb{C}) + (1-\beta) h(\mathbf{K}), \\ \text{Subjected to} & |\omega_\mu| = V^*, \end{cases} \tag{1}$$

where the functional $\mathscr{J}(\Omega_\mu)$ is defined in the domain Ω_μ of the RVE. In the above definition, $h(\mathbf{K})$ and $z(\mathbb{C})$ are scalar functions depending on the constitutive thermal $\mathbf{K}$ and elastic $\mathbb{C}$ response tensors; and $\beta \in [0, 1]$ is the weighting coefficient for the multi-objective cost functional, which allows to control the contributions between the functions $h(\mathbf{K})$ and $z(\mathbb{C})$ on the objective function. By changing the weighting coefficient value from 0 through 1, we obtain a Pareto optimal set if it is convex. Finally, the required volume of the optimal domain at the end of the optimization process is denoted as V^*. The constitutive responses $\mathbf{K}$ and $\mathbb{C}$ are obtained from a variational approach in a constitutive multi-scale model. In the following sections, we briefly describe the adopted model to obtain these constitutive responses by a standard homogenization procedure.

2.1 Preliminaries in the Multi-scale Modeling

In this section we briefly describe the main concepts for a multi-scale constitutive analysis which allows to estimate the macroscopic constitutive tensors by using a homogenization-based variational framework with the complete description of a local RVE of the material. This constitutive modeling approach follows closely the strategy presented by [13, 25, 26], and whose variational structure is described in detail in the works [11, 12]. In this context, the main concept is the assumption that any point x of the macroscopic continuum $\Omega \subset \mathfrak{R}^2$ (refer to Fig. 1) is associated to a local RVE whose domain Ω_μ, with boundary $\partial\Omega_\mu$, has characteristic length L_μ, much smaller than the characteristic length L of the macro-continuum domain. For

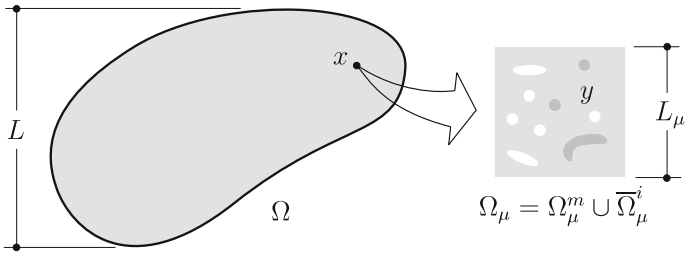

Fig. 1 Macroscopic continuum with a locally attached microstructure

simplicity, we consider that the RVE domain consist of a matrix Ω_μ^m, containing inclusions of different materials occupying a domain Ω_μ^i (see Fig. 1), but the formulation is completely analogous to the one presented here if the RVE contains voids instead. The total volume of the RVE is denoted as V_μ and contains the volume of all elements presented in the RVE, such as, solids phases and voids. Hereafter, symbols $(\cdot)_\mu$ denote quantities associated to the microscale.

2.2 The Homogenized Conductivity Tensor

In the context of the previous section we consider that at any arbitrary point $x \in \Omega$ the macroscopic temperature gradient $\nabla\theta$ is the volume average of the microscopic temperature gradient $\nabla\theta_\mu$:

$$\nabla\theta = \frac{1}{V_\mu}\int_{\Omega_\mu} \nabla\theta_\mu \tag{2}$$

where θ and θ_μ denote, respectively, the macroscopic and microscopic absolute temperature fields. As stated before, since we are in a thermomechanics setting in which the temperature itself has a physical relevance for the mechanical problem, we also consider the following homogenization formula for the temperature

$$\theta = \frac{1}{V_\mu}\int_{\Omega_\mu} \theta_\mu. \tag{3}$$

By making use of Green's theorem, we can promptly establish that the averaging relation (2) is equivalent to the following constraint on the temperature fields of the RVE:

$$\int_{\partial\Omega_\mu} \theta_\mu\, n \;=\; V_\mu\, \nabla\theta\,, \tag{4}$$

where n is the unit outward vector to $\partial\Omega_\mu$. Now, without loss of generality, the microscopic temperature field θ_μ can be split into a sum

$$\theta_\mu(y) = \theta + \overline{\theta}_\mu(y) + \widetilde{\theta}_\mu(y), \tag{5}$$

of a constant temperature field (coinciding with the macrosopic temperature $\theta(x)$), a homogeneous gradient temperature field, $\overline{\theta}_\mu(y) := \nabla\theta \cdot (y - y_o)$, and a temperature fluctuation field, $\widetilde{\theta}_\mu(y)$. In the definition of the field $\overline{\theta}_\mu(y)$, y_o is given by:

$$y_o = \frac{1}{V_\mu}\int_{\Omega_\mu} y\,. \tag{6}$$

Introducing the above splitting in (3) we obtain the following constraint for the microscopic temperature fluctuation field:

$$\int_{\Omega_\mu} \widetilde{\theta}_\mu = 0\,. \tag{7}$$

In view of the splitting (5), and taking into account constraints (2) and (3) we define the minimally constrained space of the admissible microscopic temperature fluctuation fields at the RVE as:

$$\Theta_\mu := \left\{ v \in H^1(\Omega_\mu) \,:\, \int_{\Omega_\mu} v = 0,\ \int_{\partial\Omega_\mu} v\, n = 0 \right\}. \tag{8}$$

Therefore, the resulting space of admissible variations of the microscopic temperature field at the RVE is also Θ_μ.

Following the split (5), the microscopic temperature gradient can be expressed as a sum

$$\nabla\theta_\mu = \nabla\theta + \nabla\widetilde{\theta}_\mu, \tag{9}$$

of a homogeneous gradient (uniform over the RVE) coinciding with the macroscopic temperature gradient and a field $\nabla\widetilde{\theta}_\mu$ corresponding to a fluctuation of the microscopic temperature gradient about the homogenized value.

Another fundamental concept underlying multiscale models of the present type is the *Hill-Mandel Principle of Macro-homogeneity*. Here, we shall assume the analogous relation for the thermal case [13, 17]

$$q \cdot \nabla\hat{\theta} = \frac{1}{V_\mu} \int_{\Omega_\mu} q_\mu(\theta_\mu) \cdot \nabla\hat{\theta}_\mu \quad \forall(\nabla\hat{\theta}, \hat{\theta}_\mu) \text{ kinematically admissible} \tag{10}$$

where $q_\mu(\theta_\mu)$ denotes the microscopic heat flux associated to the microscopic temperature θ_μ and q is its macroscopic counterpart.

Equation (10) plays a crucial role in the formulation of thermal constitutive models within the present framework since it provides the variational principle that governs the scale bridging for the thermal problem. The main consequences of the application of that principles are:

- Micro-thermal equilibrium problem: given the macroscopic temperature θ and the macroscopic temperature gradient $\nabla\theta$, find the temperature fluctuation field $\widetilde{\theta}_\mu \in \Theta_\mu$ such that

$$\int_{\Omega_\mu} q_\mu(\theta_\mu) \cdot \nabla\eta = 0 \quad \forall\eta \in \Theta_\mu. \tag{11}$$

- Characterization of the macroscopic heat flux: given the macroscopic temperature θ, its gradient $\nabla\theta$, and θ_μ—the solution of problem (11), compute q as

$$q = \frac{1}{V_\mu} \int_{\Omega_\mu} q_\mu(\theta_\mu). \tag{12}$$

In the present analysis, we shall assume the materials of the RVE matrix and inclusions to satisfy the classical Fourier constitutive law:

$$q_\mu(\xi) = -\mathbf{K}_\mu \nabla \xi \,, \tag{13}$$

where $\mathbf{K}_\mu$ is the thermal conductivity tensor defined at the RVE level. The isotropic representation of this tensor is given by

$$\mathbf{K}_\mu = k_\mu \mathrm{I} \,, \tag{14}$$

being I used to denote the second order identity tensors and k_μ the thermal conductivity parameter (scalar value). The linearity of (13) together with the additive decomposition (5), allows the microscopic thermal flux field to be split as

$$q_\mu(\theta_\mu) = -\mathbf{K}_\mu \nabla \theta - \mathbf{K}_\mu \nabla \widetilde{\theta}_\mu \,. \tag{15}$$

By introducing decomposition (15) into the thermal equilibrium equation (11), we obtain the closed form of the microscopic thermal equilibrium problem: given $\nabla\theta$, find $\widetilde{\theta}_\mu \in \Theta_\mu$ such that

$$\int_{\Omega_\mu} \mathbf{K}_\mu \nabla \widetilde{\theta}_\mu \cdot \nabla \eta = -\int_{\Omega_\mu} \mathbf{K}_\mu \nabla \theta \cdot \nabla \eta \quad \forall \eta \in \Theta_\mu. \tag{16}$$

Crucial to the developments of the multi-scale model for the thermal problem, is the derivation of formulae for the macroscopic thermal conductivity tensor. This is addressed in the following.

From the additive split of the microscopic temperature field (5) and by using the homogenization procedure, we have that the macroscopic thermal conductivity tensor can be obtained as a sum

$$\mathbf{K} = \overline{\mathbf{K}} + \widetilde{\mathbf{K}}, \tag{17}$$

of a homogenized (volume average) macroscopic thermal conductivity tensor $\overline{\mathbf{K}}$, given by,

$$\overline{\mathbf{K}} = \frac{1}{V_\mu} \int_{\Omega_\mu} \mathbf{K}_\mu \,, \tag{18}$$

and a contribution $\widetilde{\mathbf{K}}$ associated to the solution of the problem (16), defined as:

$$\widetilde{\mathbf{K}} := \left[\frac{1}{V_\mu} \int_{\Omega_\mu} (q_\mu(\widetilde{\theta}_{\mu_j}))_i \right] e_i \otimes e_j \,, \tag{19}$$

where $(q_\mu(\widetilde{\theta}_{\mu_j}))_i$ is the ith component of the microscopic fluctuation flux field associated with the temperature fluctuation field $\widetilde{\theta}_{\mu_j}$; being the scalar fields $\widetilde{\theta}_{\mu_j} \in \mathscr{V}_\mu$ the solutions of the linear variational equations

$$\int_{\Omega_\mu} q_\mu(\widetilde{\theta}_{\mu_j}) \cdot \nabla\eta = -\int_{\Omega_\mu} \mathbf{K}_\mu e_j \cdot \nabla\eta \quad \forall\eta \in \mathscr{V}_\mu. \tag{20}$$

for $j = 1, 2$ (in the two-dimensional case). For a more detailed description on the derivation of the above expressions, we refer the reader to [17, 25].

2.3 The Homogenized Elasticity Tensor

Using the concept of *homogenization* we define the macroscopic strain tensor ε at a point x of the macroscopic continuum as the volume average of its microscopic counterpart ε_μ over the domain of the RVE. For this work, we consider that the microscopic strain field ε_μ is given by the symmetric part of the gradient of the microscopic displacement field u_μ. Then, the macroscopic strain tensor is written as:

$$\varepsilon := \frac{1}{V_\mu} \int_{\Omega_\mu} \nabla^s u_\mu \, . \tag{21}$$

Tacking into account the Green formula in the above definition we obtain the following equivalent expression for the homogenized (macroscopic) strain tensor ε

$$\varepsilon = \frac{1}{V_\mu} \int_{\partial\Omega_\mu} u_\mu \otimes_s n \, , \tag{22}$$

where n is the outward unit normal to the boundary $\partial\Omega_\mu$ and $\otimes_s$ denotes the symmetric tensor product of vectors. Note that, the above expression imposes a kinematical constraint over the admissible displacement fields over the RVE such that the kinematical homogenization principle (21) is satisfied. Now, without loss of generality, it is possible split u_μ into a sum

$$u_\mu(y) = u + \overline{u}_\mu(y) + \widetilde{u}_\mu(y) \, , \tag{23}$$

of a constant (rigid) RVE displacement coinciding with the macro displacement $u(x)$, a field $\overline{u}_\mu(y) := \varepsilon(y - y_o)$ and a fluctuation displacement field $\widetilde{u}_\mu(y)$ (See Fig. 2). With the above split, the microscopic strain field can be written as a sum

$$\nabla^s u_\mu = \varepsilon + \nabla^s \widetilde{u}_\mu \, , \tag{24}$$

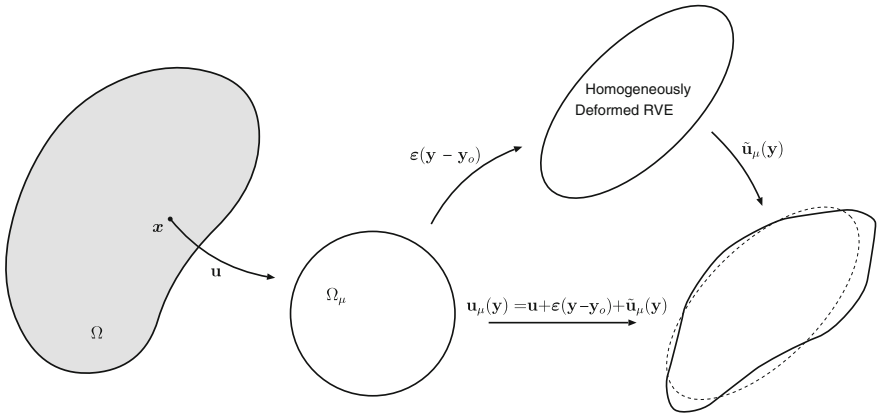

Fig. 2 Additive splitting of the microscopic displacement field

of a homogeneous strain (uniform over the RVE) coinciding with the macroscopic strain and a field $\nabla^s \widetilde{u}_\mu$ corresponding to a fluctuation of the microscopic strain about the homogenized (average) value. We also assume the following constraint on the microscopic displacement field u_μ

$$u = \frac{1}{V_\mu} \int_{\partial\Omega_\mu} u_\mu \, . \tag{25}$$

By introducing the additive splitting for the microscopic displacement field u_μ into the above constraint, we obtain the following expression for the microscopic displacement fluctuation field

$$\int_{\partial\Omega_\mu} \widetilde{u}_\mu = 0 \, . \tag{26}$$

In this sense, the kinematical homogenization procedure introduced in (21) induces the *minimally constrained space of admissible microscopic displacement fluctuation fields* at the RVE

$$\mathscr{U}_\mu := \left\{ v \in H^1(\Omega_\mu, \mathfrak{R}^n) \, : \, \int_{\Omega_\mu} v = 0, \int_{\partial\Omega_\mu} v \otimes_s n = 0 \right\} . \tag{27}$$

Hence, the space of kinematically admissible variations of the microscopic displacement field at the RVE is $\mathscr{U}_\mu$ as well.

As in the thermal case, the physical bridging between macro and micro scales is provided by the Hill-Mandel Principle of Macro-homogeneity [20, 24], which is

$$\sigma \cdot \hat{\varepsilon} := \frac{1}{V_\mu} \int_{\Omega_\mu} \sigma_\mu(u_\mu) \cdot \nabla^s \hat{u}_\mu \ , \quad \forall (\hat{u}_\mu, \hat{\varepsilon}) \text{ kinematically admissible.} \tag{28}$$

where $\sigma_\mu(u_\mu)$ denotes the microscopic stress associated to the microscopic displacement u_μ and σ is its macroscopic counterpart.

As before, using standard variational arguments, the Hill-Mandel principle provides two consequences: the microscopic mechanical equilibrium problem and the homogenization formula for the Cauchy stress.

- Micro-mechanical equilibrium problem: given the macroscopic strain ε, find the microscopic displacement fluctuation field $\widetilde{u}_\mu \in \mathscr{U}_\mu$ such that

$$\int_{\Omega_\mu} \sigma_\mu(u_\mu) \cdot \nabla^s \eta = 0 \quad \forall \eta \in \mathscr{U}_\mu \ . \tag{29}$$

- Characterization of the macroscopic stress: given the macroscopic strain ε, and $\widetilde{u}_\mu$—the solution of problem (29)—, compute σ as

$$\sigma := \frac{1}{V_\mu} \int_{\Omega_\mu} \sigma_\mu(u_\mu) \ . \tag{30}$$

For this work, materials that satisfy the classical linear elastic constitutive law will be used to describe the behavior of the RVE matrix and inclusions. That is, the microscopic stress tensor field $\sigma_\mu(\xi)$ satisfies

$$\sigma_\mu(\xi) = \mathbb{C}_\mu \nabla^s \xi \ , \tag{31}$$

where $\mathbb{C}_\mu$ is the classical fourth order elasticity tensor. In addition, we assume that the matrix and the inclusion are isotropic and homogeneous materials, thus $\mathbb{C}_\mu$ is defined as:

$$\mathbb{C}_\mu = \frac{E_\mu}{1 - \nu_\mu^2} \left[\left(1 - \nu_\mu\right) \mathbb{I} + \nu_\mu \left(\mathrm{I} \otimes \mathrm{I}\right) \right] \ , \tag{32}$$

with E_μ and ν_μ denoting, respectively, the Young's moduli and the Poisson's ratio of the domain Ω_μ. Moreover, in (32) we use $\mathbb{I}$ to denote the fourth order identity tensor.

The linearity of (31) together with the additive decomposition (24), allows the microscopic stress field to be split as

$$\sigma_\mu(u_\mu) = \sigma_\mu(\overline{u}_\mu) + \sigma_\mu(\widetilde{u}_\mu) \ , \tag{33}$$

where $\sigma_\mu(\overline{u}_\mu)$ is the stress field associated with the uniform strain induced by $\overline{u}\,(y)$ and $\sigma_\mu(\widetilde{u}_\mu)$ is the stress fluctuation field associated with $\widetilde{u}_\mu\,(y)$.

In view of expressions (29)–(33), we have that the *RVE mechanical equilibrium problem* consists of finding, for a given macroscopic strain ε, an admissible microscopic displacement fluctuation field $\widetilde{u}_\mu \in \mathscr{U}_\mu$, such that

$$\int_{\Omega_\mu} \sigma_\mu(\widetilde{u}_\mu) \cdot \nabla^s \eta = -\int_{\Omega_\mu} \sigma_\mu(\overline{u}_\mu) \cdot \nabla^s \eta \quad \forall \eta \in \mathscr{U}_\mu \,. \tag{34}$$

In the constitutive multi-scale model previously introduced, was presented how to use the macroscopic information (strain tensor ε) to obtain the microscopic displacement field u_μ. In this context, by using the same concepts it is possible to obtain a closed form of the macroscopic constitutive response, in our case, the homogenized elasticity tensor $\mathbb{C}$. This methodology, suggested by [25], is based on re-writing the problem (34) as a superposition of linear problems associated with the individual Cartesian components of the macroscopic strain tensor. Then, the macroscopic (homogenized) tensor $\mathbb{C}$ can be written as a sum

$$\mathbb{C} = \overline{\mathbb{C}} + \widetilde{\mathbb{C}} \,, \tag{35}$$

of an homogenized (volume average) macroscopic elasticity tensor $\overline{\mathbb{C}}$, given by

$$\overline{\mathbb{C}} = \frac{1}{V_\mu} \int_{\Omega_\mu} \mathbb{C}_\mu \,, \tag{36}$$

and a contribution $\widetilde{\mathbb{C}}$ associated to the choice of space $\mathscr{U}_\mu$, defined as:

$$\widetilde{\mathbb{C}} := \left[\frac{1}{V_\mu} \int_{\Omega_\mu} (\sigma_\mu(\widetilde{u}_{\mu_{kl}}))_{ij} \right] \left(e_i \otimes e_j \otimes e_k \otimes e_l \right) \,, \tag{37}$$

where $(\sigma_\mu(\widetilde{u}_{\mu_{kl}}))_{ij}$ is the ijth component of the fluctuation stress field associated with the fluctuation displacement field $\widetilde{u}_{\mu_{kl}}$; being the vector fields $\widetilde{u}_{\mu_{kl}} \in \mathscr{U}_\mu$ the solutions of the linear variational equations

$$\int_{\Omega_\mu} \sigma_\mu(\widetilde{u}_{\mu_{kl}}) \cdot \nabla^s \eta = -\int_{\Omega_\mu} \mathbb{C}_\mu(e_k \otimes e_l) \cdot \nabla^s \eta \quad \forall \eta \in \mathscr{U}_\mu \,, \tag{38}$$

for $k, l = 1, 2$ (in the two-dimensional case). After solving the set of variational problems (38), the full microscopic displacement field $u_{\mu_{kl}}$ can be obtained using the eq. (23) for each canonical direction $\{e_k, e_l\}$. For a more detailed description on the derivation of expressions (35)–(38) we refer the reader to [12, 16, 25].

3 Topological Derivative

In this section we present the topological derivative concept used to devise a topology design algorithm of micro-structures, within the multi-scale framework introduced in the previous section. The concept of topological sensitivity analysis, rigorously

introduced by Sokołowski and Żochowsky in 1999 [33], allows to obtain asymptotic expansions of shape functionals defined over a given domain, when a singular perturbation is introduced in an arbitrary point changing the topology of the (original) domain. The notion of topological derivative has proved extremely useful in the treatment of a wide range of problems in mechanics, optimization, inverse analysis and image processing and has become a subject of intensive research in the last years, see for instance, the works [1, 5, 15, 16, 21, 22, 35] and the book [29].

Now, let ψ be a functional that depends on a given domain and let it have sufficient regularity so that the following expansion is possible

$$\psi(\rho) = \psi(0) + f(\rho)\, T_D\psi + o(f(\rho)) \ , \tag{39}$$

where $\psi(0)$ is the functional evaluated in the original domain and $\psi(\rho)$ denotes the functional for the topologically perturbed domain. The parameter ρ defines the size of the topological perturbation, so that the original domain is retrieved when $\rho = 0$. In addition, $f(\rho)$ is a *function* such that $f(\rho) \to 0$ with $\rho \to 0^+$ and $o(f(\rho))$ contains all terms of higher order in $f(\rho)$. The term $T_D\psi$ of (39) is defined as the *topological derivative* of ψ at the unperturbed (original) RVE domain. Thus, the topological derivative can be seen as a first order correction factor over $\psi(0)$ to approximate $\psi(\rho)$. In fact, rearranging (39) and taking the limit $\rho \to 0^+$, we have the definition of the topological derivative

$$T_D\psi(\hat{x}) = \lim_{\rho \to 0^+} \frac{\psi(\rho(\hat{x})) - \psi(0)}{f(\rho)} \ . \tag{40}$$

In this work we will use a closed formula for the sensitivity of the homogenized constitutive response (17) and (35) to the introduction of a circular inclusion centered at an arbitrary point of the RVE domain. To present this formula it is appropriate to define the topologically perturbed RVE by a small inclusion of radius ρ represented by $\mathscr{B}_\rho$. More precisely, the perturbed domain is obtained when a circular hole $\mathscr{B}_\rho$ of radius ρ is introduced at an arbitrary point $\hat{y} \in \Omega_\mu$. Next, this region is replaced with the circular inclusion with different material property (refer to Fig. 3). In the presence of the perturbation described above, the microscopic constitutive tensors are given by

$$\mathbb{C}_\mu^\rho = \begin{cases} \mathbb{C}_\mu \ in \ \Omega_\mu \backslash \overline{\mathscr{B}_\rho} \\ \gamma \mathbb{C}_\mu \ in \ \mathscr{B}_\rho \end{cases} \quad \text{and} \quad \mathbf{K}_\mu^\rho = \begin{cases} \mathbf{K}_\mu \ in \ \Omega_\mu \backslash \overline{\mathscr{B}_\rho} \\ \gamma \mathbf{K}_\mu \ in \ \mathscr{B}_\rho \end{cases} \ , \tag{41}$$

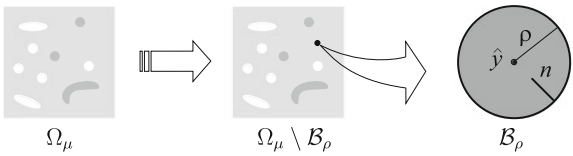

Fig. 3 Topological perturbation at the microscopic level

where the scalar parameter $\gamma \in \Re^+$ is defined as the contrast parameter between the constitutive responses of the domains $\Omega_\mu \backslash \overline{\mathscr{B}_\rho}$ and $\mathscr{B}_\rho$.

In view of the previous description of the topologically perturbed RVE domain, we can state the following results:

Theorem 1 *The topological asymptotic expansion of the macroscopic elasticity tensor associated to the topologically perturbed RVE domain, namely $\mathbb{C}^\rho$, is written as*

$$\mathbb{C}^\rho = \mathbb{C} + \frac{\pi\rho^2}{V_\mu} T_D\mathbb{C} + o(\rho^2)\,, \tag{42}$$

where the fourth order topological derivative tensor $T_D\mathbb{C}$ is given by

$$T_D\mathbb{C} = \mathbb{H}_\mu \sigma_\mu(u_{\mu_{ij}}) \cdot \sigma_\mu(u_{\mu_{kl}})\,(e_i \otimes e_j \otimes e_k \otimes e_l)\,. \tag{43}$$

Some terms in the above formula require explanation. The canonical stress tensors $\sigma_\mu(u_{\mu_{ij}})$ are given by

$$\sigma_\mu(u_{\mu_{ij}}) = \mathbb{C}_\mu(e_i \otimes e_j) + \sigma_\mu(\widetilde{u}_{\mu_{ij}}) \tag{44}$$

where $\widetilde{u}_{\mu_{ij}}$ are the solutions to the set of canonical variational problems presented in (38)*. In addition, the isotropic fourth order tensor $\mathbb{H}_\mu$ is defined as*

$$\mathbb{H}_\mu = -\frac{1}{E_\mu}\left(\frac{1-\gamma}{1+a\gamma}\right)\left[4\mathbb{I} - \frac{1-\gamma(a-2b)}{1+b\gamma}\,(\mathrm{I}\otimes\mathrm{I})\right], \tag{45}$$

with the parameters a and b given by

$$a = \frac{1+\nu_\mu}{1-\nu_\mu} \quad \textit{and} \quad b = \frac{3-\nu_\mu}{1+\nu_\mu}\,. \tag{46}$$

Proof The reader interested in the proof of this theorem may refer to [4, 16].

Theorem 2 *The topological asymptotic expansion of the macroscopic thermal conductivity tensor associated to the topologically perturbed RVE domain, namely $\mathbf{K}^\rho$, is written as*

$$\mathbf{K}^\rho = \mathbf{K} + \frac{\pi\rho^2}{V_\mu} T_D\mathbf{K} + o(\rho^2)\,, \tag{47}$$

where the second order topological derivative tensor $T_D\mathbf{K}$ is given by

$$T_D\mathbf{K} = -2k_\mu \frac{1-\gamma}{1+\gamma} \nabla\theta_{\mu_i} \cdot \nabla\theta_{\mu_j}\,(e_i \otimes e_j)\,, \tag{48}$$

being $\nabla\theta_{\mu_i}$ *the canonical microscopic temperature gradient fields given by*

$$\nabla\theta_{\mu_i} = \nabla\theta \cdot e_i + \widetilde{\theta}_{\mu_i}, \tag{49}$$

with the scalars $\widetilde{\theta}_{\mu_i}$ *representing the solutions of the set of canonical variational problems* (20).

Proof The reader interested in the proof of this theorem may refer to [17].

Remark 1 The topological derivatives $T_D\mathbb{C}$ and $T_D\mathbf{K}$, presented in Eqs. (43) and (48), exactly measures the sensitivity of the constitutive operators $\mathbb{C}$ and $\mathbf{K}$ when a new material (characterized by a singular perturbation) is introduced at an arbitrary point of the RVE domain. This information is of paramount importance for the designer in order to produce a material-by-design for an specific application.

The optimization procedure presented in (1) can be alternatively written as the following unconstrained minimization problem:

$$\underset{\omega_\mu \subset \Omega_\mu}{\text{Minimize}} \;\; J(\Omega_\mu) = \beta\, z(\mathbb{C}) + (1-\beta) h(\mathbf{K}) + \lambda \frac{\left|\omega_\mu\right|}{V_\mu}\,, \tag{50}$$

where λ is a fixed Lagrange multiplier associated to a volume constraint over ω_μ. Since the topological sensitivity is a derivative with respect to the volume fraction of the perturbation, then, we can apply directly the rules of differential calculus. Thus, according to the topological asymptotic expansion of the homogenized constitutive response given by Eqs. (42) and (47), the topological derivative of the cost function $J(\Omega_\mu)$ can be obtained by using the chain rule. Therefore, it comes

$$T_D J = \beta \left\langle Dz(\mathbb{C}), T_D(\mathbb{C}) \right\rangle + (1-\beta) \left\langle Dh(\mathbf{K}), T_D(\mathbf{K}) \right\rangle + \lambda\,. \tag{51}$$

where the term $\langle Dh(\mathbf{K}), T_D(\mathbf{K})\rangle$ and $\langle Dz(\mathbb{C}), T_D(\mathbb{C})\rangle$ should be understood as the derivatives of the functions $h(\mathbf{K})$ and $z(\mathbb{C})$ with respect to the tensor $\mathbf{K}$ or $\mathbb{C}$ in the direction of $T_D\mathbf{K}$ or $T_D\mathbb{C}$, respectively. Also, note that the brackets $\langle\cdot,\cdot\rangle$ denotes the appropriate product between the derivatives of any function $h(\mathbf{K})$ or $z(\mathbb{C})$ and the corresponding topological derivative $T_D\mathbf{K}$ or $T_D\mathbb{C}$.

We use this simple idea to devise a topology algorithm for the synthesis and optimization of multi-purpose micro-structures based on the minimization/maximization of cost functions defined in terms of homogenized properties. In order to fix theses ideas, let us present four examples concerning the topological derivatives of given functions $h(\mathbf{K})$ and $z(\mathbb{C})$. For Let $\varphi_1, \varphi_2 \in \mathbb{R}^n \times \mathbb{R}^n$ be any pair of second order tensors, and $\phi_1, \phi_2 \in \mathbb{R}^n$ be any pair of vectors. Then we obtain the following results:

Example 1 We consider a function $h(\mathbf{K})$ of the form

$$h(\mathbf{K}) := \mathbf{K}\phi_1 \cdot \phi_2\,. \tag{52}$$

Therefore, by performing the derivation as indicated previously, its topological derivative is given by

$$\langle Dh(\mathbf{K}), T_D(\mathbf{K})\rangle = T_D(\mathbf{K})\phi_1 \cdot \phi_2 \, . \tag{53}$$

If we set $\phi_1 = e_i$ and $\phi_2 = e_j$, for instance, we get $h(\mathbf{K}) = (\mathbf{K})_{ij}$ and its topological derivative is given by $(T_D(\mathbf{K}))_{ij}$. It means that the product $\langle Dh(\mathbf{K}), T_D(\mathbf{K})\rangle$ actually represents the topological derivative of the component $(\mathbf{K})_{ij}$ of the homogenized thermal conductivity tensor $\mathbf{K}$.

Example 2 Now, we consider an objective function $h(\mathbf{K})$ of the form

$$h(\mathbf{K}) := \mathbf{K}^{-1}\phi_1 \cdot \phi_2 \, . \tag{54}$$

In order to perform the derivative, note that we can differentiate the relation $\mathbf{K}\mathbf{K}^{-1} = \mathbf{I}$ with respect to the volume fraction of the perturbation in the RVE, namely

$$T_D(\mathbf{K})\mathbf{K}^{-1} + \mathbf{K}T_D(\mathbf{K}^{-1}) = 0 \, . \tag{55}$$

After multiplying to the left by $\mathbf{K}^{-1}$ we get

$$\mathbf{K}^{-1}T_D(\mathbf{K})\mathbf{K}^{-1} + T_D(\mathbf{K}^{-1}) = 0 \, , \tag{56}$$

which leads to

$$T_D(\mathbf{K}^{-1}) = -\mathbf{K}^{-1}T_D(\mathbf{K})\mathbf{K}^{-1} \, . \tag{57}$$

Thus, the topological derivative of $h(\mathbf{K})$ is given by

$$\langle Dh(\mathbf{K}), T_D(\mathbf{K})\rangle = -(\mathbf{K}^{-1}T_D(\mathbf{K})\mathbf{K}^{-1})\phi_1 \cdot \phi_2 \, . \tag{58}$$

Note that by setting tensors ϕ_1 and ϕ_2 properly, we can obtain the topological derivative in its explicit form of any component of the inverse of the homogenized elasticity tensor $\mathbf{K}^{-1}$.

Example 3 Let us consider an objective function $h(\mathbf{K})$ of the form

$$h(\mathbf{K}) := \frac{1}{2}\mathbf{K}^{-1} \cdot \mathbf{I} \, . \tag{59}$$

By taking into account the result previously obtained, the topological derivative of $h(\mathbf{K})$ is given by

$$\langle Dh(\mathbf{K}), T_D(\mathbf{K})\rangle = -\frac{1}{2}(\mathbf{K}^{-1}T_D(\mathbf{K})\mathbf{K}^{-1}) \cdot \mathbf{I} \, . \tag{60}$$

Example 4 Finally, we consider a function $z(\mathbb{C})$ of the form

$$z(\mathbb{C}) := \mathbb{C}^{-1}\varphi_1 \cdot \varphi_2 \,. \tag{61}$$

By using the same methodology as the previous example, the corresponding topological derivative can be written as

$$\langle Dz(\mathbb{C}), T_D(\mathbb{C})\rangle = -(\mathbb{C}^{-1}T_D(\mathbb{C})\mathbb{C}^{-1})\varphi_1 \cdot \varphi_2 \,. \tag{62}$$

Again, note that by setting tensors φ_1 and φ_2 properly, we can obtain the topological derivative in its explicit form of any component of the inverse of the homogenized elasticity tensor $\mathbb{C}^{-1}$.

In the next section, the optimization problem stated in (50) is solved by using the level-set-based algorithm devised in [3], which was also successfully applied in the context of microstructure topology optimization in the works [4, 10]. It relies on a level-set domain representation and the topological derivative (51) is used as a feasible descent direction. As cost functions for the multi-objective optimization problem will be used a combinations of the functions presented above. For other type of cost function in this context see the works [4, 10, 28].

4 Numerical Results

The numerical solution of the minimization problem (50) is undertaken here by the algorithm proposed in [3] in conjunction with the finite element approximation of the multiscale boundary value problems (20) and (38) proposed in [14]. The algorithm relies essentially on an optimality criterion based on the topological derivative of the objective function and on a level-set representation of the structure domain. For completeness, the algorithm is outlined in the following. For further details we refer to the works [3, 5].

With the level-set representation, the current optimized domain ω_μ is characterized by a level-set function $\psi \in L^2(\Omega_\mu)$ as

$$\omega_\mu = \{x \in \Omega_\mu, \psi(x) < 0\} \,, \tag{63}$$

and its complement as

$$\Omega_\mu \backslash \overline{\omega}_\mu = \{x \in \Omega_\mu, \psi(x) > 0\} \,. \tag{64}$$

To devise a level-set-based algorithm whose aim is to produce a optimal topology that satisfies (50) it is convenient to define the function

$$g(x) = \begin{cases} -T_D J(x) \text{ if } \psi(x) < 0 \\ T_D J(x) \text{ if } \psi(x) > 0 \end{cases} . \tag{65}$$

Here it should be noted that a negative (positive) value of the topological derivative $T_D J(x)$ at a point $x \in \Omega_\mu$ indicates that the introduction of an infinitesimal inclusion centered at that point of the RVE produces a perturbed domain whose objective functional value is smaller (greater) than that of the original domain. Then, according to [3], a sufficient condition of local optimality in this context is that

$$T_D J(x) > 0 \quad \forall x \in \Omega_\mu . \tag{66}$$

That is, no infinitesimal inclusion in Ω_μ can cause a reduction in the value of the objective functional.

The present algorithm relies on the fact that, in view of definition (65), a sufficient condition for (66) to holds is

$$\exists\, \tau > 0 \quad \text{s.t} \quad g = \tau\, \psi , \tag{67}$$

or, equivalently,

$$\theta := \arccos \left[\frac{\langle g, \psi \rangle_{L^2(\Omega_\mu)}}{\|g\|_{L^2(\Omega_\mu)} \, \|\psi\|_{L^2(\Omega_\mu)}} \right] = 0 , \tag{68}$$

where θ is the angle between the vectors g and ψ in $L^2(\Omega_\mu)$. The algorithm itself aims to generate a sequence $\{\psi_i\}$ of level set functions (a sequence of microstructural domains $\{\omega_{\mu_i}\}$) that will produce for some iteration n a domain ω_{μ_n} such that (68) is satisfied to within a given small numerical tolerance $\varepsilon_\theta > 0$:

$$\theta_n = \arccos \left[\frac{\langle g_n, \psi_n \rangle_{L^2(\Omega_\mu)}}{\|g_n\|_{L^2(\Omega_\mu)} \, \|\psi_n\|_{L^2(\Omega_\mu)}} \right] \leq \varepsilon_\theta . \tag{69}$$

The procedure starts with the choice of an initial guess for the optimal domain, i.e. with the choice of a starting level-set function $\psi_0 \in L^2(\Omega_\mu)$. With $\mathscr{S}$ denoting the unit sphere in $L^2(\Omega_\mu)$, the algorithm is explicitly given by

$$\begin{aligned} &\psi_0 \in \mathscr{S} , \\ &\psi_{i+1} = \frac{1}{\sin\theta_i} \left[\sin((1-\kappa_i)\theta_i)\Psi_i + \sin(\kappa_i \theta_i) \frac{g_i}{\|g_i\|_{L^2(\Omega_\mu)}} \right] , \end{aligned} \tag{70}$$

where i denotes a generic iteration number and $\kappa_i \in [0, 1]$ is a step size determined by a line-search in order to decrease the value of the objective function $T_D J$. The iterative process is stopped when for some iteration the step size κ_i is smaller than a given numerical tolerance $\varepsilon_\kappa > 0$:

$$\kappa_i < \varepsilon_\kappa \ . \tag{71}$$

That is, when the topology is effectively no longer changing with the iterations. If, at this stage, the optimality condition (69) is not satisfied to the desired degree of accuracy, i.e. if

$$\theta_i > \varepsilon_\theta \ , \tag{72}$$

then a uniform mesh refinement of the hold-all RVE domain Ω_μ is carried out and the iterative procedure is continued.

In the computation of $T_D J$ according to expression (50) the topological derivatives are first computed within the finite elements (at Gauss points) and then extrapolated to nodes. The final discretized version of the field $T_D J$ used in the iterations is generated by the finite element shape functions with smoothed nodal values obtained in a standard fashion. The level-set functions ψ and the discretized field $T_D J$ are generated by the same shape functions used in the finite element approximation of the boundary value problems (20) and (38). The material properties are assigned to nodes of the mesh depending on whether they are at points with $\psi < 0$ or $\psi > 0$. In this way, elements crossed by the interface (defined by $\psi = 0$) will have material properties obtained by a standard interpolation of the nodal values of these properties using the element shape functions. Obviously, according to the above procedure, the resolution of the optimal RVE domain depends directly on the fineness of the adopted mesh.

The effectiveness of the algorithm described above is demonstrated in the next numerical examples. These examples are related to the synthesis of microstructures in order to meet a specified macroscopic behavior. The optimization procedure is conducted by considering the RVE constituted in a bi-material fashion, i.e. the matrix part and the voids.

We start by fixing the RVE geometry, which is represented by the unity square $\Omega_\mu = (0, 1) \times (0, 1)$. The level-set initialization is given by a circular disc, with radius $r = 0.25$, centered in the RVE at point (0.5, 0.5)—with the origin of the Cartesian coordinate system located at the bottom left hand corner of the RVE, see Fig. 4.

For the conduction cases, the thermal conductivity associated to the microstructure is given by $k_\mu = 1$. The constitutive properties for the elasticity case are Young's modulus $E_\mu = 1$ and Poisson ratio $\nu_\mu = 0.3$. For both cases, the parameter γ is the same and equal to 0.01. The inclusion with constitutive properties given by γk_μ and γE_μ is used in the topology design to mimic the void part of the RVE. To solve the multi-scale variational problems (20) and (38) we consider periodic boundary condition [32].

In all cases, the initial mesh is structured as shown in Fig. 4, with 3281 nodes and 6400 three-noded triangular elements. Although the algorithm converges on the initial mesh in each case to the prescribed accuracy of $\varepsilon_\theta = 1°$, we perform some uniform refinements in order to improve the final result. The final mesh contains 205441 nodes and 409600 elements. In all figures presented in this section, the black color represent the matrix part of the RVE optimal domain ω_μ and the white color is used to mimic the void part of the domain.

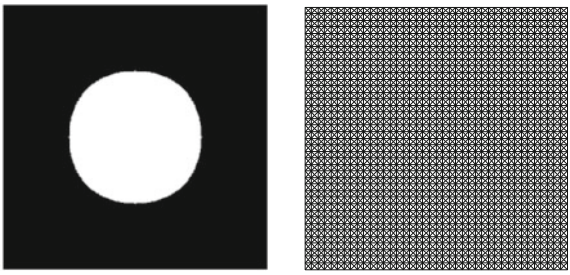

Fig. 4 Initial guess (*left*) and initial mesh (*right*)

4.1 Example 1. Bulk Modulus and Horizontal Conductivity Maximization

In this first example, we wish to maximize the macroscopic thermal conductivity in the direction e_1 (horizontal direction) and the bulk modulus simultaneously. Accordingly we use the objective function $h(\mathbf{K})$ and $z(\mathbb{C})$ defined by Eqs. (54) and (61), respectively. For this case we choose $\phi_1 = \phi_2 = e_1$ and $\varphi_1 = \varphi_2 = \mathbf{I}$. The Lagrange multiplier is taken as $\lambda = 10.0$. The resulting optimized topologies for three values of parameter β are shown in Fig. 5. The obtained RVEs have a volume of 40 % of the initial volume. The macroscopic constitutive properties of the results are presented in Table 1.

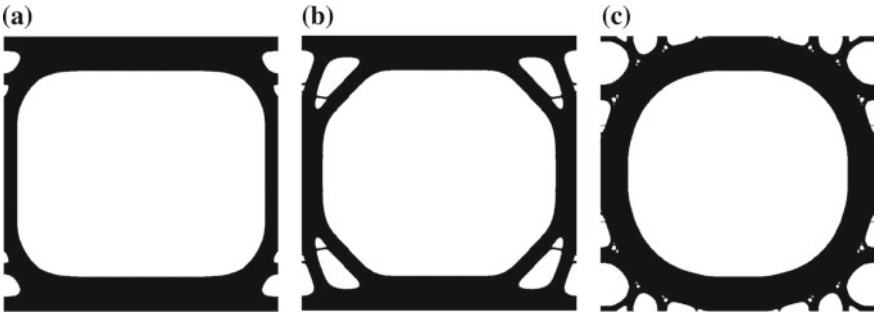

Fig. 5 Example 1. Bulk modulus and horizontal conductivity maximization. **a** $\beta = 0.25$, **b** $\beta = 0.50$, **c** $\beta = 0.75$

Table 1 Example 1

β	0.25	0.50	0.75
Bulk modulus (K)	0.115	0.131	0.140
Conductivity k_{11}	0.273	0.273	0.268
Conductivity k_{22}	0.143	0.204	0.242

Effective properties

From the previous results, the influence of the weighting parameter β is evident. When this parameter decreases, the microstructure tends to promote the thermal conductivity in the direction of e_1 maintaining the bulk modulus in a low value. Moreover, for low values of β the differences between the conductivities k_{11} and k_{22} increases. The topology obtained for the higher values of β are very similar to the one analyzed by Hashin and Shtrikman [19]. These authors obtained microstructures known as *coated spheres assemblages* or *Hashin-Shtrikman micro-structures* that provide lower and upper bounds for the elastic properties of bi-material composites.

4.2 Example 2. Bulk Modulus and Orthogonal Conductivity Maximization

The aim of this example is to show the topology of the RVE that maximize the bulk modulus and the conductivity in two orthogonal directions (coinciding with e_1 and e_2). Therefore, we define the objective function $J(\Omega_\mu)$ by using the functions $h(\mathbf{K})$ and $z(\mathbb{C})$ defined by Eqs. (59) and (61), respectively. For this case we choose again $\varphi_1 = \varphi_2 = \mathbf{I}$. For a Lagrange multiplier $\lambda = 10.0$, the resulting optimized topologies for three value of parameter β are shown in Fig. 6. The effective (or macroscopic) properties are presented in Table 2.

The obtained RVEs have a volume of 40 % of the initial volume. Due to the definition of the objective functional $h(\mathbf{K})$, the RVEs are completely symmetric with

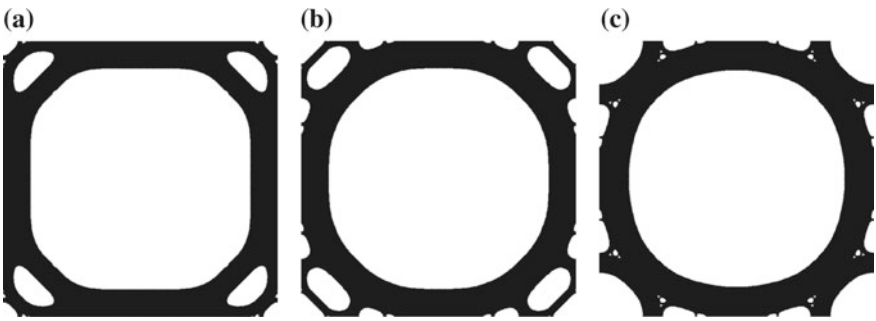

Fig. 6 Example 2. Bulk modulus and orthogonal conductivity maximization. **a** $\beta = 0.25$, **b** $\beta = 0.50$, **c** $\beta = 0.75$

Table 2 Example 2

β	0.25	0.50	0.75
Bulk modulus (K)	0.129	0.131	0.137
Conductivity k_{11}	0.236	0.239	0.250
Conductivity k_{22}	0.236	0.239	0.250

Effective properties

respect the two axis parallel to e_1 and e_2; and the conductivities in these directions have the same value (for each β). As in the previous example, the Bulk modulus of the microstructure increases with the values of the parameter β. The conductivities shown the same trend as the bulk modulus K. This behavior can be explained as following. The maximization of the bulk modulus implies in obtaining of a microstructure whose internal structure is aligned in two orthogonal directions. On the other hand, the maximization of the conductivity implies in the same kind of RVE. Therefore, these two goals of the optimization procedure involve the same type of internal arrangement of the microstructural elements in the RVE. Similar to the previous examples, the topology obtained for $\beta = 0.75$ are very similar to the one analyzed by Hashin and Shtrikman [19]. They consist of disks of the most compliant material coated with rings of stiffer material (bi-material composites).

4.3 Example 3. Poisson's Ratio and Horizontal Conductivity Maximization

The goal of the optimization procedure for this example is obtain a microstructure whose macroscopic the Poisson's ratio and conductivity in the direction of e_1 are maximums. To this ends, we use the objective function $h(\mathbf{K})$ and $z(\mathbb{C})$ defined by Eqs. (54) and (61), respectively. Here, we choose $\phi_1 = \phi_2 = e_1$ and $\varphi_1 = e_1 \otimes e_1$ and $\varphi_2 = e_2 \otimes e_2$. The Lagrange multiplier is taken as $\lambda = 1.0$. The results of the optimization procedure for three value of parameter β are shown in Fig. 7, and the macroscopic constitutive properties are presented in Table 3.

The obtained RVEs have a volume of around of the 20 % of the initial volume. The higher value of Poisson's ratio was obtained for the lower value of parameter β and in the same direction as the higher conductivity. This effect is due to the contribution of the function $h(\mathbf{K})$ to the mechanical part in the objective function $J(\Omega_\mu)$. We observe here that for the three value of the weighting coefficient β, the synthesized microstructure exhibit at the end of the optimization procedure has a *pantograph-like*

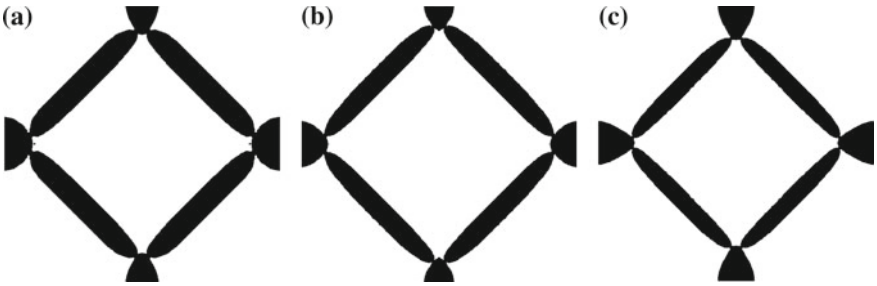

Fig. 7 Example 3. Poisson ratio and horizontal conductivity maximization. **a** $\beta = 0.25$, **b** $\beta = 0.50$, **c** $\beta = 0.75$

Table 3 Example 3

β	0.25	0.50	0.75
Poisson ratio ν_{12}	0.803	0.810	0.789
Poisson ratio ν_{21}	0.841	0.811	0.787
Conductivity k_{11}	0.112	0.095	0.082
Conductivity k_{22}	0.104	0.092	0.081

Effective properties

topology. This type of microstructure allows a maximum transfer of strain energy from one direction to the direction orthogonal to it.

4.4 *Example 4. Poisson's Ratio Minimization and Horizontal Conductivity Maximization*

In this example, we wish to promote the macroscopic conductivity in the direction of e_1 and minimize the Poisson's ratio. Accordingly we use the objective function $h(\mathbf{K})$ and $z(\mathbb{C})$ defined by Eqs. (54) and (61), respectively. For this case where we choose $\phi_1 = \phi_2 = e_1$ and $\varphi_1 = e_1 \otimes e_1$ and $\varphi_2 = -e_2 \otimes e_2$. The Lagrange multiplier is taken as $\lambda = 1.0$ and the resulting optimized topologies for three value of parameter β are shown in Fig. 8. The macroscopic constitutive properties are presented in Table 4.

The obtained final volume of the topologies presented in Fig. 8 are of around of the 45 % of the initial volume. For all cases, and as consequence of the optimization procedure, the obtained microstructures exhibit negative values for the macroscopic Poisson's ratio. In the following we present the homogenized fourth-order elasticity tensors for the topologies of Fig. 8.

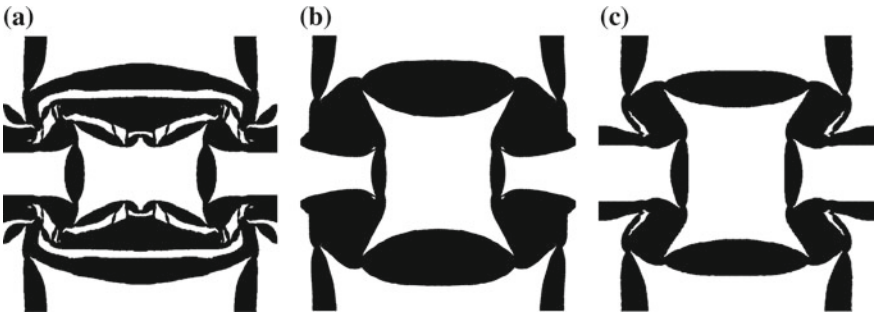

Fig. 8 Example 4. Poisson ratio minimization and horizontal conductivity maximization. **a** $\beta = 0.25$, **b** $\beta = 0.50$, **c** $\beta = 0.75$

Table 4 Example 4

β	0.25	0.50	0.75
Poisson ratio ν_{12}	−0.289	−0.376	−0.439
Poisson ratio ν_{21}	−0.511	−0.482	−0.475
Conductivity k_{11}	0.265	0.214	0.139
Conductivity k_{22}	0.111	0.141	0.128

Effective properties

$$\begin{aligned}
\mathbb{C}|_{\beta=0.25} &= \begin{pmatrix} 0.1256 & -0.0364 & 0.0 \\ -0.0364 & 0.0713 & 0.0 \\ 0.0 & 0.0 & 0.0096 \end{pmatrix}, \\
\mathbb{C}|_{\beta=0.50} &= \begin{pmatrix} 0.1064 & -0.0401 & 0.0 \\ -0.0401 & 0.0830 & 0.0 \\ 0.0 & 0.0 & 0.0105 \end{pmatrix}, \\
\mathbb{C}|_{\beta=0.75} &= \begin{pmatrix} 0.0788 & -0.0346 & 0.0 \\ -0.0346 & 0.0728 & 0.0 \\ 0.0 & 0.0 & 0.0075 \end{pmatrix}.
\end{aligned} \tag{73}$$

When the value of β decreases the differences in the behavior in the two orthogonal direction are more evident. This effect as been analyzed in the previous examples and the conclusion presented there remain valid here as well.

The best value for a negative Poisson's ratio was obtained for a parameter $\beta = 0.25$ for the same direction where the conductivity is maximized. Also, for the same value of β the internal arrangement of the microstructure is more complex than higher values of the parameter. The results show that, regardless of the particular values of β used in the objective functional $J(\Omega_\mu)$, the optimized microstructure features the auxetic behavior of the star-shaped encapsulated inclusions analyzed, among others, in [2, 23]. This type of micro-cell is known as *nonconvex-shaped* or *re-entrant corner* microstructures.

4.5 Example 5. Poisson Ratio Minimization and Orthogonal Conductivity Maximization

Similar to the previous example, here the goal is to minimize the macroscopic Poisson's ratio and the conductivity in two orthogonal directions (coinciding with e_1 and e_2). Therefore, in the definition of the objective function $J(\Omega_\mu)$ we consider the functions $h(\mathbf{K})$ and $z(\mathbb{C})$ given by Eqs. (59) and (61), respectively. Again we choose $\varphi_1 = e_1 \otimes e_1$ and $\varphi_2 = -e_2 \otimes e_2$. For the optimization procedure, a Lagrange multiplier $\lambda = 1.0$ is used. The resulting optimized topologies for several values of

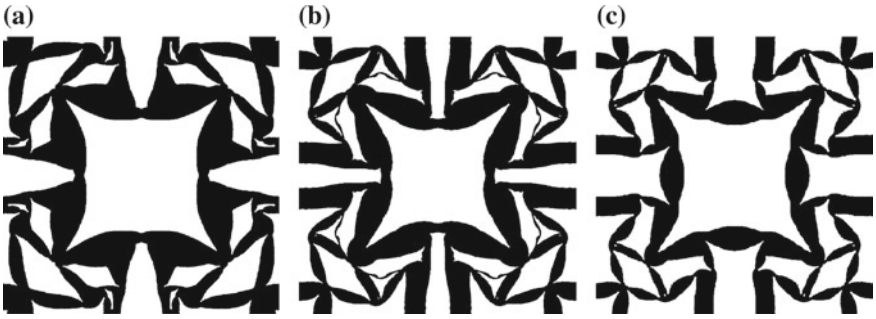

Fig. 9 Example 5. Poisson ratio minimization and orthogonal conductivity maximization. **a** $\beta = 0.25$, **b** $\beta = 0.50$, **c** $\beta = 0.75$

Table 5 Example 5

β	0.25	0.50	0.75
Poisson ratio ν_{12}	−0.403	−0.421	−0.425
Poisson ratio ν_{21}	−0.403	−0.421	−0.425
Conductivity k_{11}	0.195	0.169	0.138
Conductivity k_{22}	0.195	0.169	0.138

Effective properties

parameter β are shown in Fig. 9 and the effective constitutive properties are presented in Table 5.

The obtained final volume of the topologies presented in Fig. 9 are of around of the 50 % of the initial volume. As in the previous example, the obtained microstructures exhibit negative values for the macroscopic Poisson's ratio. For this case, the value of the Poisson's ratio in the two orthogonal directions are the same. This behavior is due to the symmetry imposed to the results by the objective functional $h(\mathbf{K})$. In the following we present the homogenized fourth-order elasticity tensors for the topologies of Fig. 9.

$$\begin{aligned}
\mathbb{C}|_{\beta=0.25} &= \begin{pmatrix} 0.0983 & -0.0397 & 0.0 \\ -0.0397 & 0.0983 & 0.0 \\ 0.0 & 0.0 & 0.0215 \end{pmatrix}, \\
\mathbb{C}|_{\beta=0.50} &= \begin{pmatrix} 0.0939 & -0.0396 & 0.0 \\ -0.0396 & 0.0939 & 0.0 \\ 0.0 & 0.0 & 0.0163 \end{pmatrix}, \\
\mathbb{C}|_{\beta=0.75} &= \begin{pmatrix} 0.0795 & -0.0338 & 0.0 \\ -0.0338 & 0.0795 & 0.0 \\ 0.0 & 0.0 & 0.0099 \end{pmatrix}.
\end{aligned} \tag{74}$$

The value of the Poisson's ratios decreases (more negative) when the weighting coefficient β is higher. In fact, when the contribution of the functional $z(\mathbb{C})$ is higher, the objective functional $J(\Omega_\mu)$ tends to promote a mechanical response instead of a conductivity. Here, the results also show that the optimized microstructure features the auxetic behavior analyzed, among others, in [2, 23]. This type of micro-cell is known as *nonconvex-shaped* or *re-entrant corner* microstructures.

4.6 Example 6. Shear Modulus and Horizontal Conductivity Maximization

For this last example, the aim is to show the topology of the RVE that maximize the macroscopic conductivity in the direction e_1 and the Shear modulus simultaneously. Therefore, the definition of the objective functions $h(\mathbf{K})$ and $z(\mathbb{C})$ given by Eqs. (54) and (61), respectively, will be used. For the complete definition of the functions $h(\mathbf{K})$ and $z(\mathbb{C})$, we choose $\phi_1 = \phi_2 = e_1$ and $\varphi_1 = \varphi_2 = e_1 \otimes e_2 + e_2 \otimes e_1$. The minimization of the present function $z(\mathbb{C})$ corresponds to the maximization of the effective shear modulus G. The Lagrange multiplier is taken as $\lambda = 5.0$. The resulting optimized topologies for three value of parameter β are shown in Fig. 10 and the effective constitutive properties are presented in Table 6.

The obtained final volume of the topologies presented in Fig. 10 are of around of the 40 % of the initial volume. Notice that the highest values of the macroscopic

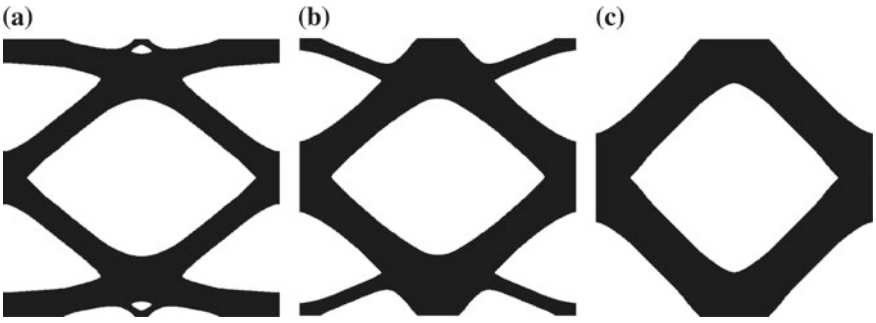

Fig. 10 Example 6. Shear modulus and horizontal conductivity maximization. **a** $\beta = 0.25$, **b** $\beta = 0.50$, **c** $\beta = 0.75$

Table 6 Example 6

β	0.25	0.50	0.75
Shear modulus G	0.084	0.109	0.117
Conductivity k_{11}	0.362	0.339	0.280
Conductivity k_{22}	0.160	0.227	0.262

Effective properties

shear modulus G is obtained when the parameter β increases. Independently of the parameter β, the main structure of the RVE is composed by four bars in a rhomboidal arrangement. To promote the conductivity in the direction e_1, for lower values of β, the microstructure develop bars in that direction, see Fig. 10a, b. With this arrangement the conductivity in the direction of e_1 increases.

5 Concluding Remarks

A multi-objective topology design of periodic microstructures procedure has been proposed. This procedure is based on the concept of topological derivative and a level-set domain representation method. For the optimization problem, a cost functional was constructed in order to archive simultaneously a specific macroscopic elastic and thermal behavior. The homogenized elasticity and conductivity tensors are estimated by a well-established multi-scale constitutive theory in which the macroscopic response are obtained as the volume averages of their microscopic counterparts over a RVE. The analytical topological derivatives of the constitutive responses are tensor fields of the same order that the constitutive tensors. To deal with a specific macroscopic behavior, scalar functions depending on the elasticity and thermal tensors were defined. The topological derivative of these functions are obtained through the direct application of conventional rules of differential calculus. These features have been explored in the minimization/maximization of cost functions defined in terms of homogenized properties. The proposed procedure was successfully and efficiently used in several numerical examples of optimum topology design of microstructures. We remark that the methodology presented here is of simple implementation in a material-by-design engineering or industrial application.

References

1. Allaire, G., Jouve, F., Van Goethem, N.: Damage and fracture evolution in brittle materials by shape optimization methods. J. Comput. Phys. **230**(12), 5010–5044 (2011)
2. Almgreen, R.F.: An isotropic three-dimensional structure with Poisson's ratio–1. J. Elast. **15**(4), 427–430 (1985)
3. Amstutz, S., Andrä, H.: A new algorithm for topology optimization using a level-set method. J. Comput. Phys. **216**(2), 573–588 (2006)
4. Amstutz, S., Giusti, S.M., Novotny, A.A., de Souza Neto, E.A.: Topological derivative for multi-scale linear elasticity models applied to the synthesis of microstructures. Int. J. Numer. Methods Eng. **84**, 733–756 (2010)
5. Amstutz, S., Novotny, A.A., de Souza Neto, E.A.: Topological derivative-based topology optimization of structures subject to Drucker-Prager stress constraints. Comput. Methods Appl. Mech. Eng. **233–236**, 123–136 (2012)
6. Auriault, J.L.: Effective macroscopic description for heat conduction in periodic composites. Int. J. Heat Mass Transf. **26**(6), 861–869 (1983)
7. Auriault, J.L., Royer, P.: Double conductivity media: a comparison between phenomenological and homogenization approaches. Int. J. Heat Mass Transf. **36**(10), 2613–2621 (1993)

8. Bensoussan, A., Lions, J.L., Papanicolau, G.: Asymptotic Analysis for Periodic Microstructures. North Holland, Amsterdam (1978)
9. Celentano, D.J., Dardati, P.M., Godoy, L.A., Boeri, R.E.: Computational simulation of microstructure evolution during solidification of ductile cast iron. Int. J. Cast Met. Res. **21**(6), 416–426 (2008)
10. de Souza Neto, E.A., Amstutz, S., Giusti, S.M., Novotny, A.A.: Topology optimization design of micro-structures considering different multi-scale models. Comput. Model. Eng. Sci. **62**(1), 23–56 (2010)
11. de Souza Neto, E.A., Feijóo, R.A.: On the equivalence between spatial and material volume averaging of stress in large strain multi-scale solid constitutive models. Mech. Mater. **40**(10), 803–811 (2008)
12. de Souza Neto, E.A., Feijóo, R.A.: Variational foundations of large strain multiscale solid constitutive models: kinematical formulation. In: Advanced Computational Materials Modeling: From Classical to Multi-Scale Techniques. Wiley-VCH Verlag GmbH & Co. KGaA, Weinheim, Germany (2011)
13. Germain, P., Nguyen, Q.S., Suquet, P.: Continuum thermodynamics. J. Appl. Mech. Trans. ASME **50**(4), 1010–1020 (1983)
14. Giusti, S.M., Blanco, P.J., de Souza Neto, E.A., Feijóo, R.A.: An assessment of the Gurson yield criterion by a computational multi-scale approach. Eng. Comput. **26**(3), 281–301 (2009)
15. Giusti, S.M., Novotny, A.A., de Souza Neto, E.A.: Sensitivity of the macroscopic response of elastic microstructures to the insertion of inclusions. In: Proceeding of the Royal Society A: Mathematical, Physical and Engineering Sciences, vol. 466, pp. 1703–1723 (2010)
16. Giusti, S.M., Novotny, A.A., de Souza Neto, E.A., Feijóo, R.A.: Sensitivity of the macroscopic elasticity tensor to topological microstructural changes. J. Mech. Phys. Solids **57**(3), 555–570 (2009)
17. Giusti, S.M., Novotny, A.A., de Souza Neto, E.A., Feijóo, R.A.: Sensitivity of the macroscopic thermal conductivity tensor to topological microstructural changes. Comput. Methods Appl. Mech. Eng. **198**(5–8), 727–739 (2009)
18. Gurson, A.L.: Continuum theory of ductile rupture by void nucleation and growth: part I—yield criteria and flow rule for porous ductile media. J. Eng. Mater. Technol. Trans. ASME **99**(1), 2–15 (1977)
19. Hashin, Z., Shtrikman, S.: A variational approach to the theory of the elastic behaviour of multiphase materials. J. Mech. Phys. Solids **11**(2), 127–140 (1963)
20. Hill, R.: A self-consistent mechanics of composite materials. J. Mech. Phys. Solids **13**(4), 213–222 (1965)
21. Hintermüller, M., Laurain, A.: Multiphase image segmentation and modulation recovery based on shape and topological sensitivity. J. Math. Imaging Vis. **35**, 1–22 (2009)
22. Hintermüller, M., Laurain, A., Novotny, A.A.: Second-order topological expansion for electrical impedance tomography. Adv. Comput. Math. **36**(2), 235–265 (2012)
23. Lakes, R.: Foam structures with negative Poisson's ratio. Sci. AAAS **235**(4792), 1038–1040 (1987)
24. Mandel, J.: Plasticité Classique et Viscoplasticité. CISM Lecture Notes. Springer, Udine (1971)
25. Michel, J.C., Moulinec, H., Suquet, P.: Effective properties of composite materials with periodic microstructure: a computational approach. Comput. Methods Appl. Mech. Eng. **172**(1–4), 109–143 (1999)
26. Miehe, C., Schotte, J., Schröder, J.: Computational micro-macro transitions and overall moduli in the analysis of polycrystals at large strains. Comput. Mater. Sci. **16**(1–4), 372–382 (1999)
27. Nemat-Nasser, S., Hori, M.: Micromechanics: Overall Properties of Heterogeneous Materials. North-Holland, Amsterdam (1993)
28. Novotny, A.A.: Topological derivative for multi-scale linear elasticity models in three spatial dimensions. Optimization of Structures and Components. Advanced Structured Materials, vol. 43. Springer, Switzerland (2013)
29. Novotny, A.A., Sokołowski, J.: Topological Derivatives in Shape Optimization. Interaction of Mechanics and Mathematics. Springer, Berlin (2013)

30. Ostoja-Starzewski, M., Schulte, J.: Bounding of effective thermal conductivities of multiscale materials by essential and natural boundary conditions. Phys. Rev. B **54**(1), 278–285 (1996)
31. Oyen, M.L., Ferguson, V.L., Bembey, A.K., Bushby, A.J., Boyde, A.: Composite bounds on the elastic modulus of bone. J. Biomech. **41**(11), 2585–2588 (2008)
32. Sanchez-Palencia, E.: Non-homogeneous Media and Vibration Theory. Lecture Notes in Physics, vol. 127. Springer, Berlin (1980)
33. Sokołowski, J., Żochowski, A.: On the topological derivative in shape optimization. SIAM J. Control Optim. **37**(4), 1251–1272 (1999)
34. Speirs, D.C.D., de Souza Neto, E.A., Perić, D.: An approach to the mechanical constitutive modelling of arterial tissue based on homogenization and optimization. J. Biomech. **41**(12), 2673–2680 (2008)
35. Van Goethem, N., Novotny, A.A.: Crack nucleation sensitivity analysis. Math. Methods Appl. Sci. **33**(16), 197–1994 (2010)

Sensitivity Analysis of Micro Models for Solidification of Pure Metals

B. Mochnacki and R. Szopa

Abstract Theoretical aspects and examples of the application of sensitivity analysis in the thermal theory of foundry processes are presented. In particular, the so-called second generation models of solidification (micro models) are considered. The sensitivity information can be applied for different purposes, among which it is possible to use the results obtained for a given set of input data to obtain the solution for different input data. The sensitivity coefficients are also necessary for the numerical solution of inverse problems using gradient methods. The application examples concern the sensitivity of the temperature field of a casting-mould system with respect to perturbations of parameters appearing in the micro/macro model of solidification. Numerical computations are performed using the finite difference method.

1 Introduction

In this chapter, micro/macro models for the solidification of pure metals are discussed. According to the classification proposed by Stefanescu [1] the approach presented belongs to the family of the so-called second generation models.

The first generation models include problems connected with the analysis of metals and alloys solidification at the macro-scale. In this group, two of the most popular and most frequently used models are the ones that solve the Stefan problem (e.g. [2]) or the one domain method (e.g. [3]). The classical Stefan model is based on a system of two parabolic equations (molten metal and solid body) supplemented by

B. Mochnacki (✉)
Higher School of Labour Safety Management, Katowice, Poland
e-mail: bmochnacki@wszop.edu.pl

R. Szopa
Czestochowa University of Technology, Częstochowa, Poland

P.A. Muñoz-Rojas (ed.), *Computational Modeling, Optimization and Manufacturing Simulation of Advanced Engineering Materials*, Advanced Structured Materials 49, DOI 10.1007/978-3-319-04265-7_3

the condition given on the moving boundary (the Stefan boundary condition), the boundary conditions given on the external surface of the system and the initial conditions. The model of solidification and cooling processes based on the one domain method is created by the energy equation concerning the whole, conventionally homogeneous, metal domain, while the evolution of latent heat is taken into account by the introduction of a parameter called *substitute thermal capacity* [4, 5]. It is also possible to rebuild the basic mathematical model using the enthalpy convention or the Kirchhoff transformation [3].

The second generation models including the one presented in this paper, allow to determine the transient temperature field in the macro domain of solidifying and cooling metals, but the crystallization process is considered at the micro scale. For example, changes of the local values of solid state fraction result from the course of nucleation and nuclei growth [6–9].

The third generation models concern the modeling of heat transfer processes proceeding at the micro-scale (for example heating and melting of a thin metal film subjected to a strong laser pulse). In such a case an other approach should be used for modeling the micro-scale heat transfer. Because of extremely short duration, extreme temperature gradients and very small geometrical dimensions of the domain considered, the generalized form of the Fourier law should be taken into account. The generalized forms of the Fourier law result from the introduction of a lag time (with respect to temperature gradient) for the heat flux. This is called the relaxation or the lag time concerning both the heat flux and the temperature gradient (relaxation and thermalization times). The first generalization leads to the governing equation called the Cattaneo-Vernotte equation [10], while the second generalization leads to the dual phase lag model [11, 12]. This equation contains a second order time derivative and higher order mixed derivatives in both time and space. Additionally, the boundary conditions supplementing the basic equation should be adequately reconstructed. The micro-scale heat transfer problems can be also described using the two temperature parabolic or hyperbolic models, e.g. [13, 14].

The sensitivity model determining the changes of transient temperature field due to perturbations of parameters appearing in the energy equations and boundary-initial conditions can be found by the differentiation of successive equations and conditions with respect to the parameter considered (direct approach) [15, 16]. In the case of micro models (mainly due to the complicated form of source function) the equations creating the sensitivity model are very complex for mathematical manipulations and also for numerical modeling. A very detailed description of these problems can be found in [17, 18].

In the present study a simpler approach to obtain the sensitivity functions is proposed. The local and temporary values of the sensitivity expressions defined as partial derivatives of the temperature with respect to the parameter considered (for example the volumetric latent heat), are found using an approximation based on the differential quotients. So, the boundary initial problem describing the process discussed should be solved twice, the first solution corresponds to the basic input data (set of parameters p_1, p_2, … p_k, … p_n), while the second one corresponds to the input data containing the disturbed parameter $p_k \pm \Delta p_k$. Next the temporary local

values of sensitivity function ($\Delta T/\Delta p_k$) can be found. The testing computations show that this method gives results very close to the ones obtained using the numerical solution corresponding to the direct variant of sensitivity analysis [18].

2 Governing Equations

The following energy equation is considered

$$c(T)\frac{\partial T(x,t)}{\partial t} = \nabla[\lambda(T)\nabla T(x,t)] + L\frac{\partial f_S(x,t)}{\partial t} \tag{1}$$

where $c(T)$ is the volumetric specific heat of the material, $\lambda(T)$ is the thermal conductivity, L is the volumetric latent heat, $T = T(x, t)$ and $f_S = f_S(x, t)$ denote the temperature and the local volumetric solid state fraction, $\boldsymbol{x} = \{x_1, x_2, x_3\}$ and t are the geometrical co-ordinates and time. One can see, that only heat conduction in a casting domain is considered. According to [3, 5] Eq. (1) can be applied in both macro and the micro/macro modeling. The differences appear at the stage of computing the solidification rate $\partial f_S/\partial t$ and when the micro/macro approach is considered. Then the changes of f_S result from the crystallization laws at the micro-scale (nucleation and nuclei growth).

In literature one can find two basic models determining the mutual connections between f_S and temporary density and volume of grains. In particular, the following function is introduced

$$\omega\ (x,\ t) = N(x,\ t)\ V(x,\ t) \tag{2}$$

where N is a nuclei density [nuclei/m^3], V is a single grain volume. Equation (2) becomes more complicated when the volumes of different grains are considered. Then the integral form for determining $\omega(\boldsymbol{x}, t)$ should be introduced.

The acceptance of the assumption

$$f_S(x,t) = \omega(x,t) \tag{3}$$

leads to the so-called linear model of crystallization, which yields

$$\frac{\partial f_S(x,t)}{\partial t} = \frac{\partial \omega(x,t)}{\partial t} \tag{4}$$

The linear model determines the geometrical volume (volume fraction) and is the correct assumption at the first stages of crystallization [19].

To take into account the geometrical limitations of growth in the final stages of the process (collisions between growing grains) the following modification of Eq. (4) is introduced [20, 21]

$$\frac{\partial f_S(x,t)}{\partial t} = \frac{\partial \omega(x,t)}{\partial t}\left[1 - f_S(x,t)\right] \tag{5}$$

and then

$$\frac{\mathrm{d}f_S(\omega)}{1 - f_S(\omega)} = \mathrm{d}\omega \tag{6}$$

The solution of this simple differential equation is of the form

$$f_S(\omega) = 1 + C\ \exp(-\omega) \tag{7}$$

Because for $\omega = 0 \Rightarrow f_S = 0$, it comes out that $C = -1$, and finally

$$f_S(\omega) = 1 - \ \exp(-\omega) \tag{8}$$

The last equation corresponds to the exponential model (the Kolmogoroff formula).

The following modification of Eq. (5) can be also taken into account [22]

$$\frac{\partial f_S(x,t)}{\partial t} = \frac{\partial \omega(x,t)}{\partial t}\left[1 - f_S(x,t)\right]^n \tag{9}$$

where $n \geq 0$.

Then

$$\frac{\mathrm{d}f_S(\omega)}{\left[1 - f_S(\omega)\right]^n} = \mathrm{d}\omega \tag{10}$$

The solution fulfilling the condition $\omega = 0$: $f_S = 0$ is of the form

$$f_S(\omega) = 1 - \left[(n-1)\omega + 1\right]^{\frac{1}{1-n}} \tag{11}$$

One can see that the last power-type formula constitutes the generalization of linear and exponential models. For $n = 0$ one obtains the linear model, while for $n = 1$ one has

$$\lim_{n \to 1}\ 1 - \left[(n-1)\omega + 1\right]^{\frac{1}{1-n}} = 1 - \exp(-\omega) \tag{12}$$

At the end of this part of considerations one can see that for small values of ω, the linear and exponential models lead to the same results. This comes from the fact that $\exp(-\omega) \Rightarrow 1 - \omega$ and $1 - \exp(-\omega) \Rightarrow \omega$. During the final stages of solidification the linear and exponential models give different results.

Summing up, the source term in the energy equation results from the equation

$$L\frac{\partial f_S(x,t)}{\partial t} = L\frac{\mathrm{d}f_S(\omega)}{\mathrm{d}\,\omega}\frac{\partial \omega(x,t)}{\partial t} \tag{13}$$

The external derivative in Eq. (13) can be determined analytically, the internal one can be found using numerical methods. For example, if Eq. (11) is accepted, then

$$L\frac{\partial f_S(x,\ t)}{\partial\, t} \approx L\left[(n-1)\,\omega + 1\right]^{\frac{n}{1-n}}\frac{\Delta\,\omega}{\Delta\, t} \tag{14}$$

Equation (1) concerning the casting domain, must be supplemented by a similar equation determining the course of thermal processes in a mould sub-domain, namely

$$c_m(T)\frac{\partial T_m(x,t)}{\partial t} = \nabla\left[\lambda_m\,(T)\nabla T_m(x,t)\right] \tag{15}$$

where c_m and λ_m denote the mould volumetric specific heat and mould thermal conductivity.

On the external surface of the mould, the boundary condition in a general form

$$\Phi\left[T_m(x,t),\ \frac{\partial T_m(x,t)}{\partial n}\right] = 0 \tag{16}$$

is accepted ($\partial/\partial n$ denotes a normal derivative). As a rule, the condition (16) is assumed in the form of a Robin boundary condition.

On the contact surface between casting and mould the continuity condition is given by

$$-\lambda\frac{\partial T(x,t)}{\partial n} = \frac{T(x,t)-T_m(x,t)}{R(x,t)} = -\lambda_m\frac{\partial T_m(x,t)}{\partial n} \tag{17}$$

where R is the thermal resistance. The value of R depends primarily on the radiative heat transfer through the air gap between casting and mould. The condition (17) is used in the case of casting production in the metal mould. Considering the system casting—sand mix mould (as in this work) one can assume $R = 0$ (an ideal contact) and then

$$\begin{cases} -\lambda\frac{\partial T(x,t)}{\partial n} = -\lambda_m\frac{\partial T_m(x,t)}{\partial n} \\ T(x,t) = T_m(x,t) \end{cases} \tag{18}$$

The initial temperature for $t = 0$ is also known.

3 Nucleation and Nuclei Growth

The driving force for nucleation and nuclei growth is an undercooling below solidification point T^*, defined as $\Delta T(x,t) = T^* - T(x,t)$, where $T(\boldsymbol{x}, t)$ is the temporary temperature at the point x. According to literature, e.g. [23] one can assume that a local and temporary number of nuclei (nuclei density) is proportional to the second power of undercooling below the temperature T^*

$$N(x,t) = \eta \Delta T(x,t)^2 = \eta \left[T^* - T(x,t)\right]^2 \tag{19}$$

where η is the nucleation coefficient. The nucleation stops when $\Delta T(x, t + \Delta t) < \Delta T(x, t)$. Additionally for $T(\boldsymbol{x}, t) > T^*$ one has that: $N(\boldsymbol{x}, t) = 0$. This is illustrated in Fig. 1.

The rate of solid phase growth (equiaxial grains) is determined by

$$\frac{\mathrm{d}R(x,t)}{\mathrm{d}t} = \mu \Delta T(x,t)^m \tag{20}$$

where μ is the growth coefficient, R is grain radius and $m \in [1, 2]$. In literature one can also find the following equation

$$\frac{\mathrm{d}R(x,t)}{\mathrm{d}t} = \mu_1 \Delta T(x,t)^2 + \mu_2 \Delta T(x,t)^3 \tag{21}$$

where μ_1, μ_2 are growth coefficients. It should be pointed out that the coefficients η, μ, μ_1, μ_2 are assumed to be constant values. Modeling of a solidification process can be done in several ways. So, because the problem considered is non-steady, a time grid defined as follows

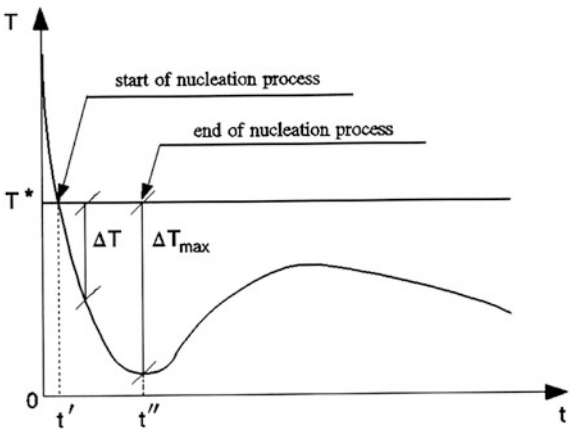

Fig. 1 Temperature history at the point $\boldsymbol{x}$ from casting domain

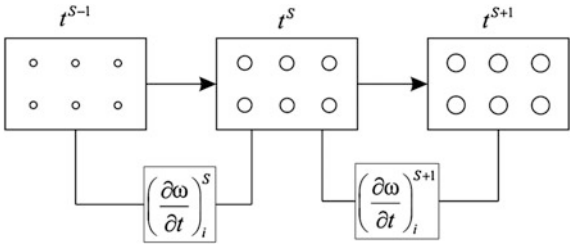

Fig. 2 Constant number of nuclei

$$0 = t^0 < t^1 < t^1 < \cdots < t^{s-1} < t^s < \cdots < t^S, \quad \Delta t = t^s - t^{s-1} \tag{23}$$

should be introduced. At the same time the casting domain is divided into m control volumes.

Let us consider a control volume ΔV_i from the domain considered. During a certain interval of time the temperature at the central point of ΔV_i decreases below the solidification point and the crystallization process starts.

In this place, different numerical procedures can be taken into account. The first procedure considered is based on the assumption that the nuclei density is a constant value, e.g. $N = 10^{10}$ [nuclei/m^3]. In other words, Eq. (19) is neglected and changes in the function ω result only from the nuclei growth, given by Eq. (20) (see Fig. 2). The second (more complex) procedure considered consists in the averaging of nuclei dimensions at each time step, as shown in Fig. 3. The most complicated model studied corresponds to the observation of the growth of successive grain families (see Fig. 4). The first value of ω in the domain of a control volume ΔV_i for which $T_i^{s-1} > T^*$, $T_i^S < T^*$ equals

$$\omega_i^{(1)} = \frac{4}{3}\pi v N_i^{(1)} \Delta R_i^{(1)}. \tag{24}$$

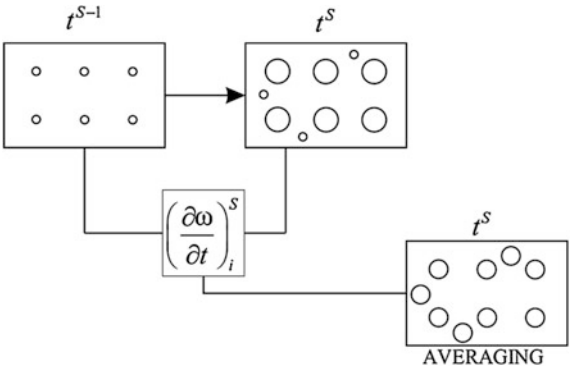

Fig. 3 Averaging procedure

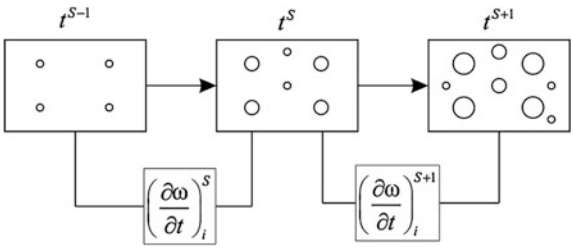

Fig. 4 Grains families

At the same time, for spherical grains $v = 1$, while for the other types of crystallization (e.g. dendritic growth) $v < 1$. A very clear geometrical interpretation of coefficient v can be found in [7]. The value resulting from (24) is introduced into the source function for the transition corresponding to the next time interval.

For modeling the second stage of the crystallization process one can find the quantity N_i using Eq. (19), which is employed to estimate the size of the second generation (this means $N_i^{(2)} = N_i - N_i^{(1)}$). It is also possible to find the new increment of the grains radii $\Delta R_i^{(2)}$, now employing Eq. (20). It should be pointed out that the current radii of the first generation are equal to $\Delta R_i^{(1)} + \Delta R_i^{(2)}$, while for the second generation the radii are $\Delta R_i^{(2)}$ (see Fig. 4). The new value of the function ω is determined by

$$\omega_i^{(2)} = \frac{4}{3}\pi v \left[N_i^{(1)} \left(\Delta R_i^{(1)} + \Delta R_i^{(2)} \right)^3 + N_i^{(2)} \Delta R_i^{(2)3} \right]. \tag{25}$$

On the basis of Eqs. (24) and (25) one can find the approximate value of the derivative $\frac{\partial \omega(x,t)}{\partial t}$ in the control volume ΔV_i for time t^{s+1} using the differential quotients. The next stages of algorithm result from the simple generalization of the step described above.

In Figs. 2, 3 and 4 the different versions of nucleation and nuclei growth modeling are presented.

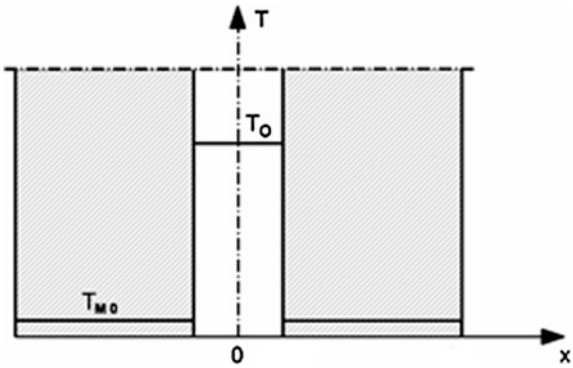

Fig. 5 Domain considered

As a numerical example consider an aluminum 1D plate ($G = 0.02$ [m]) produced in a typical sand mould, as shown in Fig. 5 [9]. Taking into account the mould dimensions, the non-flux condition on its outer surface has been taken into account. Some additional properties are: growth coefficient $\mu = 3 \times 10^{-6}$ [m/sK^2], nucleation coefficient $\eta = 10^{10}$ [m^{-3}K^{-2}] (this parameter is redundant in the case of the model concerning the constant number of nuclei). The Kolmogoroff model has been adopted and the grains shape coefficient has been considered as $v = 1$ (spherical grains). Initial temperature of metal equals $T_0 = 700$ °C, solidification point: $T^* = 660$ °C, initial mould temperature: $T_{M0} = 20$ °C. The values of casting thermophysical parameters can be found in Mochnacki and Suchy [3]. Additionally $\lambda_M = 0.5$ [W/mK], $c_M = 1.75$ [MJ/m^{3}K].

Hence, the following boundary-initial problem has been considered

$$\begin{aligned} &0 < x < G/2: \quad \frac{\partial T(x,t)}{\partial t} = a\frac{\partial^2 T(x,t)}{\partial x^2} + \frac{L}{c}\left[(n-1)\omega(x,t)+1\right]^{\frac{n}{1-n}}\frac{\partial \omega(x,t)}{\partial t} \\ &G/2 < x < 2G: \quad \frac{\partial T_M(x,t)}{\partial t} = a_M\frac{\partial^2 T_M(x,t)}{\partial x^2} \end{aligned} \tag{26}$$

where $a = \lambda/c$, $a_M = \lambda_M/c_M$, λ_M is the mould thermal conductivity and c_M is the volumetric specific heat of the mould. Equation (26) are supplemented by the boundary conditions.

In particular:

- axis of symmetry

$$x = 0: \quad q(x,t) = -\lambda\frac{\partial T(x,t)}{\partial x} = 0 \tag{27}$$

- external surface of mould

$$x = 2G: \quad q_M(x,t) = -\lambda_M\frac{\partial T_M(x,t)}{\partial x} = 0 \tag{28}$$

- casting-mould contact surface

$$x = G/2: \quad \begin{cases} -\lambda\dfrac{\partial T(x,t)}{\partial x} = -\lambda_M\dfrac{\partial T_M(x,t)}{\partial x} \\ T(x,t) = T_M(x,t) \end{cases} \tag{29}$$

The initial conditions are also given

$$t = 0: \quad T(x,t) = T_0 > T^*, \quad T_M(x,t) = T_{M0} \tag{30}$$

At the stage of numerical simulation, the explicit scheme of the finite difference method (FDM) detailed in [3] has been used.

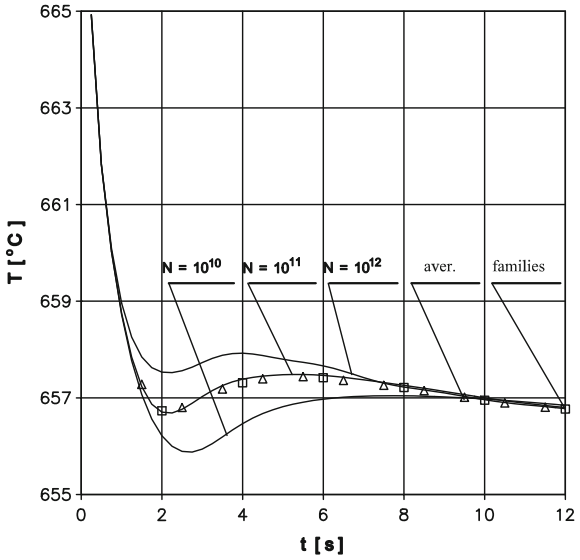

Fig. 6 Temperature history

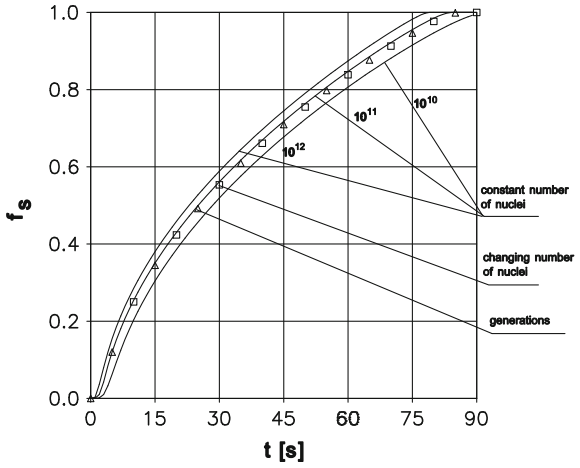

Fig. 7 Solid state fraction in the casting domain

The computations have been performed both for the case of a constant number of nuclei and also taking into account the nucleation process. In Fig. 6 the cooling curves at the points corresponding to the axis of symmetry ($x = 0$) are shown. The triangular and square symbols correspond to the averaging procedure and grains families, respectively. A very essential conclusion results from the observation of the results obtained, namely the solution found using the averaging of grains dimensions is practically the same as the solution concerning the grains generations. Noteworthy, the first model is clearly simpler for computational implementation. Figure 7 shows the changes of global solid stage fraction in the casting domain.

4 Sensitivity Analysis

The changes of the transient temperature field due to the perturbations of process parameters are defined in the following way

$$U_k(x,t) = \lim_{\Delta p_k \to 0} \frac{T(x,t,p_1 \ldots p_k + \Delta p_k, \ldots p_n) - T(x,t,p_1 \ldots p_k, \ldots p_n)}{\Delta p_k} = \frac{\partial T(x,\ t)}{\partial p_k} \quad (31)$$

where U_k $(\boldsymbol{x},\ t)$ is the sensitivity function. So, the sensitivity model can be created by the differentiation of energy equations and boundary-initial conditions with respect to the parameter considered (a direct approach—e.g. [15, 16]). The knowledge of the sensitivity distribution can be used for a variety of aims. In particular, the basic solution can be rebuilt into another solution corresponding to perturbed parameters (it results from the Taylor formula—e.g. [24]), the sensitivity methods can be used for finding the optimal location for measurement sensors—e.g. [25] and finally for the solution of inverse problems using gradient methods—e.g. [17].

The source term (13) under the assumption that the nuclei density N is a constant value and when the exponential crystallization model is taken into account has the form

$$q_V = L\frac{\partial f_S}{\partial t} = 4\pi NL\nu\mu T^m \left(\int_0^t \mu T^m \mathrm{d}\tau \right)^2 \exp\left[-\frac{4}{3}\pi\nu N \left(\int_0^t \mu T^m \mathrm{d}\tau \right)^3 \right] = F_1 F_2 F_3 \quad (32)$$

As previously, for spherical grains $\nu = 1$, while for other types of crystallization (e.g. dendritic growth) $\nu < 1$. The sensitivity model with respect to the parameter ν is discussed below.

The source function (32) is the product of three factors

$$F_1 = 4NL\nu\mu T^m \quad (33)$$

$$F_2 = \left(\int_0^t \mu T^m \mathrm{d}\tau \right)^2 \quad (34)$$

$$F_3 = \exp\left[-\frac{4}{3}\pi\nu N \left(\int_0^t \mu T^m \mathrm{d}\tau \right)^3 \right] \quad (35)$$

Functions (33), (34) and (35) should be differentiated with respect to the parameter ν

$$\frac{\partial F_1}{\partial \nu}_1 = 4\pi NL\mu\left(\Delta T^m - \nu m \Delta T^{m-1} U\right) \tag{36}$$

$$\frac{\partial F_2}{\partial \nu} = -2\int_0^t \mu T^m \mathrm{d}\tau \int_0^t \mu\, m \Delta T^{m-1} U \mathrm{d}\tau \tag{37}$$

$$\begin{aligned}\frac{\partial F_3}{\partial \nu} = \exp\left[-\frac{4}{3}\pi\nu N\left(\int_0^t \mu T^m \mathrm{d}\tau\right)^3\right] \cdot \\ \left[-\frac{4}{3}\pi N\left(\int_0^t \mu T^m \mathrm{d}\tau\right)^3\right] + 4\pi\nu N\left(\int_0^t \mu T^m \mathrm{d}\tau\right)^2 \int_0^t \mu\, m \Delta T^{m-1} U \mathrm{d}\tau\end{aligned} \tag{38}$$

where $U = \frac{\partial T}{\partial \nu}$ is the sensitivity function. Denoting

$$r_S = \int_0^t \mu\, T^m \mathrm{d}\tau, \qquad \rho_S = \int_0^t \mu\, m T^{m-1} U \mathrm{d}\tau \tag{39}$$

and after some mathematical manipulations, one obtains

$$\begin{aligned}q_{VU} = \frac{\partial q_V}{\partial \nu} = 4\pi LN\mu\, r_S \exp\left(-\frac{4}{3}\pi\nu N r_S^3\right) \cdot \\ \left[\Delta T^m\left(r_S - 2\nu\rho_S - \frac{4}{3}\pi N\nu r_S^4 + 4\pi N\nu^2 r_S^3 \rho_S\right) - \nu m \Delta T^{m-1} r_S U\right]\end{aligned} \tag{40}$$

Summing up, the sensitivity model corresponding to Eqs. (1) and (15), boundary condition (18) on the contact surface and the well known Robin condition on the external surface of the system, supplemented by the initial conditions (30) (under the assumption that the volumetric specific heats and the thermal conductivities of sub-domains are constant values), takes the form

$$\begin{cases} x \in \Omega & : \quad c\dfrac{\partial U(x,t)}{\partial t} = \lambda \nabla^2 U(x,t) + q_{VU} \\ x \in \Omega_M & : \quad c_M \dfrac{\partial U_M(x,t)}{\partial t} = \lambda_M \nabla^2 U_M(x,t) \\ x \in \Gamma_M & : \quad \begin{cases} -\lambda \dfrac{\partial U(x,t)}{\partial x} = -\lambda_M \dfrac{\partial U_M(x,t)}{\partial x} \\ U(x,t) = U_M(x,t) \end{cases} \\ x \in \Gamma & : \quad -\lambda \dfrac{\partial U(x,t)}{\partial x} = \alpha\, U(x,t) \\ t = 0 & : \quad U(x,0) = U_M(x,0) = 0 \end{cases} \tag{41}$$

From the mathematical point of view, the basic model and the sensitivity one are very similar, but the source function q_{VU} is more complicated than q_V. For numerical modeling, the same procedures can be used both in the case of the basic problem and the sensitivity one. Additionally, the sensitivity model is coupled with the basic one (see the equation determining the source function) and the knowledge of the basic solution is necessary.

In the paper presented by Mochnacki and Szopa [9], an aluminum plate of thickness $L = 0.01$ [m] has been considered (1D problem), the influence of the mould has been taken into account by the introduction of an *artificial* Robin condition on the external surface of the plate. The following input data are assumed: thermal conductivity $\lambda = 150$ W/mK, volumetric specific heat $c = 2.875$ MJ/m^{3}K, volumetric latent heat $L = 975$ MJ/m^3, solidification point $T^* = 660$ °C, exponent $m = 2$ (Eq. (20)), number of nuclei $N = 10^{10}$ nucl/m^3, growth coefficient $\mu = 3 \times 10^{-6}$ m/sK^2, initial temperature $T_0 = 670$ °C, substitute heat transfer coefficient $\alpha = 100$ W/m^{2}K, ambient temperature $T_a = 30$ °C, shape coefficient $v = 0.8$. The crystallization process is described by the exponential model.

As previously mentioned, one of the advantages of modeling the sensitivity problems is the possibility of reconstruction of the basic solution for a practically infinite number of different solutions corresponding to other values of the process parameters. This results from the application of Taylor's expansion truncated at first order terms

$$T(x,t,p_1 \ldots p_k \pm \Delta p_k, \ldots p_n) \approx T(x,t,p_1 \ldots p_k, \ldots p_n) \pm U_k(x,t)\Delta p_k. \tag{42}$$

In Fig. 8 the cooling curves at the axis of symmetry and at the boundary are shown. In particular, the region of undercooling process is presented. The successive curves correspond to the basic solution (central lines) and the solutions obtained on the basis of sensitivity analysis under the assumption that $\Delta v = \pm 0.2$. One can see, that the differences appear at the stage of crystallization process.

Figure 9 shows the change of temperature at the axis and on the boundary due to a change in the parameter v ($\Delta v = \pm 0.2$). In other words, the differences between the basic and border solutions are marked. The assumed change of the shape parameter (the border values determine the spherical grains and dendritic ones) causes the change of the local temperature less than 1 K. So, from the numerical point of view the value of v is not very essential for the course of thermal processes in the solidifying metal domain.

The examples presented have been solved using the direct variant of sensitivity analysis. For the present chapter the authors carried out the computations of sensitivity functions using differential quotients (in particular the central differential quotients have been used). Such an approach requires the solution of two basic problems with parameters analyzed equal to $p_k - 0.5\Delta p_k, p_k + 0.5\Delta p_k$. A disadvantage of this approach is the lack of knowledge of the sensitivity model and the numerical algorithm operates on the principle of the 'black box'.

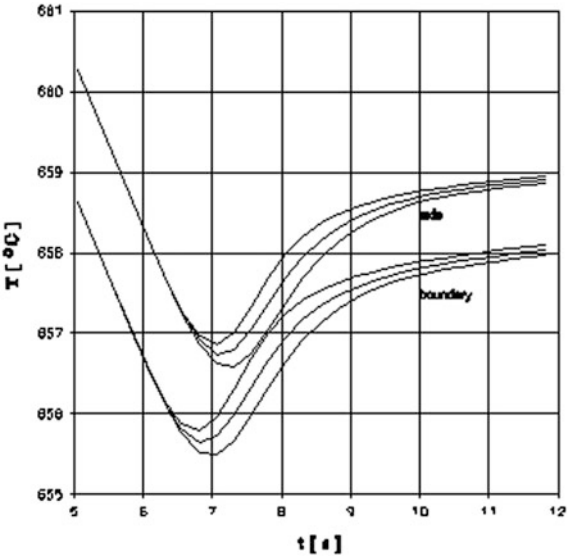

Fig. 8 Cooling/heating curves close to the undercooling region

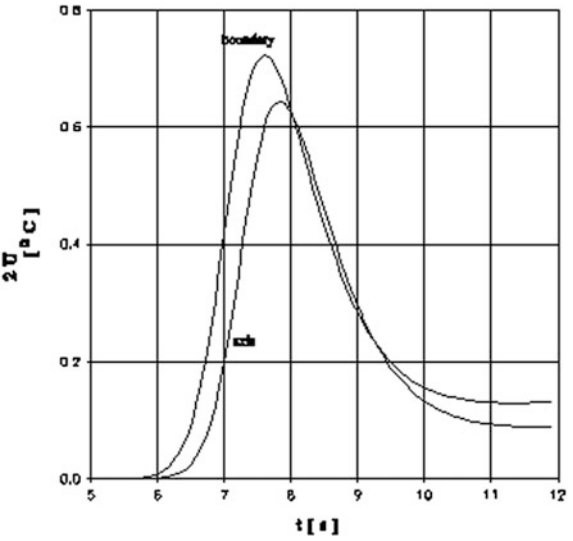

Fig. 9 Temperature differences

Comparison of the results presented above with the results obtained using differential quotients confirms that the application of differential quotients can give very good effects. The differences between numerical solutions are negligible and the results shown in Figs. 8 and 9 are practically the same both in the case of *exact* and *approximate* approaches. Nevertheless, caution must be taken with issues such as the size of the perturbation and computational costs.

5 Final Remarks

This Chapter presents a review work and includes mainly the results of own research. The first part is devoted to the mathematical description of pure metal solidification using the micro/macro approach. Among others, the generalization of the well known linear and exponential models of crystallization is presented. From the mathematical point of view, the crystallization model is correct but the proper choice of the exponent n requires additional experimental investigations. Its value is likely to be dependent on the technological process conditions and also on the type of material. In Sect. 3 the numerical procedures concerning the numerical modeling of nucleation and nuclei growth are discussed. The nucleation (nuclei density) is the effect of undercooling below the solidification point, but the position of nuclei in the control volume domain ΔV_i is unknown, of course. It seems that the procedure of averaging of nuclei dimensions at each time step is sufficiently exact and rather simple in numerical execution. The sensitivity analysis of the changes of the transient temperature field due to perturbations of process parameters is presented in Sect. 4. At the same time, the direct approach is taken into account. In spite that the sensitivity model discussed concerns the shape coefficient v, any other parameters can be considered. The crystallization model has a very complicated form for the source function, which is present in the equation concerning the casting domain. Thus, numerical rather than analytical procedures are preferred to solve the associated direct and sensitivity problems. A more effective algorithm can be constructed using a differential approximation of the sensitivity function $U_k(x, t)$. The example presented in this chapter shows the applications of the sensitivity analysis to estimate changes of a transient temperature field due to assumed changes of a given parameter.

Acknowledgments The work was done as a part of Project 2012/05/B/ST8/01477.

References

1. Stefanescu D.M.: Critical review of the second generation of solidification models for casting. In: Pivonka, T.S., Voller, V., Katgerman, L. (eds.) Modeling of Casting, Welding and Advanced Solidification Processes VI. The Minerals, Metals & Material s Society, pp. 3–20 (1993)
2. Rubinstein, L.I.: The Stefan problem, Translations of Mathematical Monographs 27. American Mathematical Society, Providence, R.I. (1971)
3. Mochnacki, B., Suchy, J.S.: Numerical Methods in Computations of Foundry Processes. PFTA, Cracow (1995)
4. Majchrzak, E., Mochnacki, B., Suchy, J.S.: Identification of substitute thermal capacity of solidifying alloy. J. Theor. Appl. Mech. **46**(2), 257–268 (2008)
5. Mochnacki, B.: Numerical modeling of solidification process (Chapter 24). In: Zhu, J. (ed.) Computational Simulations and Applications, pp. 513–542. INTECH (2011)
6. Fraś, E., Kapturkiewicz, W., Lopez, H.F.: Macro and micro modelling of the solidification kinetics of casting. AFS Trans. **92–48**, 583–591 (1993)

7. Majchrzak, E., Piasecka, A.: Numerical micro/macro model of solidification process. J. Mater. Process. Technol. **64**, 267–276 (1997)
8. Mochnacki, B., Szopa, R.: Model of pure metal solidification using the power-type function. J. Achiev. Mater. Manuf. Eng. **22**, 65–71 (2007)
9. Mochnacki, B., Szopa, R.: Application of sensitivity analysis in numerical simulation of solidification process. In: Szajnar, J. (ed.) Progress of Foundry Theory and Practice, pp. 271–286. Polish Ac. of Sciences, Foundry Commission (2009)
10. Cattaneo, C.: A form of heat conduction equation which eliminates the paradox of instantaneous propagation. Comput. Rend. **247**, 431–433 (1958)
11. Chen, J.K., Beraun, J.E.: Numerical study of ultrashort laser pulse interactions with metal films. Numer. Heat Transf. Part A **40**, 1–20 (2001)
12. Mochnacki, B., Majchrzak, E.: Modelling of microscale heat transfer in cylindrical domains. Comput. Methods Mater. Sci. **11**(2), 337–342 (2011)
13. Majchrzak, E.: Parabolic and hyperbolic two-temperature models. Comparison of numerical solutions. Mater. Sci. Forum **706–709**, 1454–1459 (2012)
14. Chen, J.K., Tzou, D.Y., Beraun, J.E.: A semiclassical two-temperature model for ultrafast laser heating. Int. J. Heat Mass Transf. **49**, 307–316 (2006)
15. Kleiber, M.: Parameter sensitivity in nonlinear mechanics. Wiley, Chichester, England (1997)
16. Dems, K.: Sensitivity analysis in thermal problems, 1: variation of material parameters within fixed domain. J. Therm. Stresses **9**, 303–324 (1996)
17. Mochnacki, B., Majchrzak, E.: Identification of macro and micro parameters in solidification model. Bull. Polish Acad. Sci. Tech. Sci. **55**(1), 107–113 (2007)
18. Szopa, R.: Sensitivity Analysis and Inverse Problems in the Thermal Theory of Foundry Processes. Czestochowa University of Technology, Czestochowa (2006)
19. Majchrzak, E., Suchy, J.S., Szopa, R.: Linear model of crystallization. Identification of nuclei density, Giessereiforschung. Int. Foundry Res. **2**, 29–32 (2006)
20. Kapturkiewicz, W.: Modeling of Cast Iron Solidification. AKAPIT, Cracow (2003)
21. Szopa, R.: Modelling of solidification using the combined variant of the BEM, Metallurgy. Publication of the Silesian University of Technology, Gliwice (1999)
22. Mochnacki, B., Szopa, R.: Generalized micro/macro model of crystallization and its numerical realization. Int. J. Multiscale Comput. Eng. **8**(3), 259–266 (2010)
23. Fraś, E.: Crystallization of Metals and Alloys. PWN, Warsaw (1992)
24. Majchrzak, E., Mochnacki, B.: Sensitivity analysis of transient temperature field in microdomains with respect to the dual lag phase model parameters. Int. J. Multiscale Comput. Eng. **12**(1), 65–77 (2014)
25. Majchrzak, E., Mendakiewicz, J.: Sensitivity analysis as a tool of optimal sensors location for solidification parameters estimation. Mater. Sci. Forum **638–642**, 2640–2645 (2010)

Part II
Biological Tissues

Variational Constituive Models for Soft Biological Tissues

Jakson Manfredini Vassoler and Eduardo Alberto Fancello

Abstract Biological soft tissues are heterogeneous composite materials made of cells and molecules of the extracellular matrix. These tissues are frequently classified into four basic categories: muscle, epithelial, nervous and connective, each one with its own mechanical and functional properties. Their mechanical response to external forces (excluding those mechanisms associated with time scales typical of tissue remodeling), are characterized by anisotropy, high nonlinearity, strain rate dependency, permanent deformation and eventually, damage. Despite a wide set of constitutive models that have already been proposed in the specialized literature to represent the macroscopic behavior of these materials, this work focuses attention on a particular group, coined as variational in the sense that the incremental internal variable updates are found as minimizers of a pseudo strain-energy potential, called Incremental Potential evaluated at each time-step. General cases of models for viscoelastic, viscoplastic and fiber reinforced soft materials are discussed with the aid of numerical examples exploring the features of the corresponding approach.

1 Background

Biological tissues are heterogeneous composite materials made of cells and molecules of the extracellular matrix. These tissues are frequently classified into four basic categories: muscle, epithelial, nervous and connective, each one with its own characteristic and functional importance [1]. Muscle tissue is composed of elongated cells responsible for movement with a moderate amount of extracellular matrix. Epithelial tissue is composed of polyhedral cells that have strong adhesion and form

J.M. Vassoler (✉)
Department of Mechanical Engineering,
Universidade Federal do Rio Grande do Sul, Porto Alegre, RS, Brazil
e-mail: vassoler@mecanica.ufrgs.br

E.A. Fancello
Department of Mechanical Engineering,
Universidade Federal de Santa Catarina, Florianópolis, SC, Brazil
e-mail: fancello@ufsc.br

P.A. Muñoz-Rojas (ed.), *Computational Modeling, Optimization and Manufacturing Simulation of Advanced Engineering Materials*,
Advanced Structured Materials 49, DOI 10.1007/978-3-319-04265-7_4

cellular sheets that cover the surface of body organs and have a small amount of extracellular matrix. Nervous tissue is composed mostly by cells with few extracellular matrix and it is responsible for transmission of nervous impulses. Connective tissues have the main function of providing mechanical support and protection to the body. They are composed mainly by extracelullar matrix (cells, fibers and ground substance), forming a wide variety of structures with remarkable mechanical performance. Fibers, such as elastin and collagen, are extracellular material produced by their tissue cells, which polymerize into highly organized structures providing the main structural characteristics of the tissue. Elastin is comprised of long flexible molecules that form three-dimensional networks by cross-linking and is responsible for the elasticity of the tissues. Collagen is the most important structural element of soft and hard tissues. These molecules can be aggregated to form different structures depending on the tissue. The particular arrangement of the collagen proteins—three left-handed helices twisted together into a right-handed triple helix—provides this structure with a high stretch resistance to traction [2].

Connective tissues such as ligaments and tendons have a pronounced anisotropic mechanical behavior due to their regular parallel arrangement of collagen fibers [2]. Arteries are organized mainly in biaxial layers of fibers and cartilages into complex triaxial structures. The skin presents a three-dimensional network of collagen, but due to its internal structure, it allows large strains without stretching of the individual fibers that are in a wavy form when undeformed.

Important mechanical responses are experimentally observed on most (soft fibered) biological tissues: nonlinear stress-strain relationship, large deformation, viscous phenomena, anisotropy and mechanical damage of fibers [3–5]. The numerical characterization of the mechanical behavior of such materials have attracted much attention of the scientific community due to the possibility to perform realistic mechanical simulations of biological systems. As example, surgical robot control systems [6], prediction of the mechanical response of a human Anterior Cruciate Ligament (ACL) under multiaxial loading [7], vascular surgery and design of endoprostheses [8], among others applications.

Different constitutive models have been proposed to perform this task, e.g. [9–14]. In this chapter a particular unified mathematical framework for the development of constitutive equations of nonlinear dissipative materials is presented. This framework, based on variational principles, is specialized to account for different dissipative phenomena observed in the mechanical response of soft biological tissues.

2 Variational Framework

A general framework for a set of inelastic materials is proposed in [15, 16]. Based on variational (extremization) principles, it is able to accommodate a wide set of constitutive models, depending on the choice of certain potential functions.

This approach was specialized in [17] to the case of nonlinear finite strain viscous behavior applicable, for example, to the case of soft brain tissue [18]. The same approach was extended in [19] to include permanent viscous deformations coupled with arbitrary hyperelastic behaviors. Typical anisotropy introduced by fibers was taken into account in [20]. These applications demonstrate the capability of this variational constitutive family to incorporate inelastic mechanical behaviors, such as those observed experimentally in biological tissues.

The principles that form the basis of variational models used here are founded on the laws of continuum thermodynamics with internal variables. The first and second principles of thermodynamics may be expressed by the Clausius-Planck inequality [21]. If the thermal effects are ignored, the inequality is reduced to

$$\mathscr{D}_{int} = \mathbf{P} : \dot{\mathbf{F}} - \dot{W} \geq 0 \tag{1}$$

where $\mathbf{P}$ is the first Piola Kirchhoff stress tensor, $\mathbf{F}$ is the deformation gradient and W is the free energy function. The inequality (1) represents the non-negativeness of the internal dissipation $\mathscr{D}_{int}$, where the first term is the rate of internal mechanical work ($w_{int} = \mathbf{P} : \dot{\mathbf{F}}$) per unit reference volume and the second term is the material time derivative of the free energy.

The thermodynamics approach with internal variables postulates that the state of a material point p at instant t of a thermodynamical process is defined by the value of a finite set of state variables, disregarding their rates or history [22]. This set of state variables is usually composed of external (observable) and internal variables. The latter associated, in general, with internal irreversible mechanisms.

Let $\xi = \{\mathbf{F}, \mathbf{Q}\}$ be a set of state variables necessary to define the thermodynamical state of a material point, where $\mathbf{F}$ represents the total deformation gradient, and $\mathbf{Q}$ a subset of (scalar, vector, tensor) internal state variables. With this choice, the free energy W (other state variable) is given as a function of the set ξ

$$W = W(\mathbf{F}, \mathbf{Q}) \tag{2}$$

By using the well known procedure of Coleman-Noll it is possible to obtain the set $\xi^* = \{\mathbf{P^c}, \mathbf{Y}\}$ of state variables energetically conjugate to the corresponding variables of ξ

$$\mathbf{P^c} = W_{,\mathbf{F}}(\mathbf{F}, \mathbf{Q}), \qquad \mathbf{Y} = -W_{,\mathbf{Q}}(\mathbf{F}, \mathbf{Q}) \tag{3}$$

where, $\mathbf{P^c}$ is the conservative part of the first Piola Kirchhoff stress tensor and $\mathbf{Y}$ is the conjugate force of $\mathbf{Q}$. In order to account for irreversible mechanisms, laws for the evolution of the internal variables are needed. This is frequently accomplished by assuming the existence of a dissipative pseudo-potential $\psi(\xi^*)$, convex and null at the origin such that

$$\dot{\mathbf{Q}} = \psi_{,\mathbf{Y}}(\xi^*) \tag{4}$$

which ensures automatically the satisfaction of inequality (1). Convexity properties of ψ guarantees the existence of a dual pseudo-potential $\psi^*\left(\dot{\mathbf{Q}}; \xi\right)$ such that

$$\mathbf{Y} = \psi^*_{,\dot{\mathbf{Q}}}(\dot{\mathbf{Q}}; \xi) \tag{5}$$

In this way the evolution of the internal variables is defined by the equation

$$W_{,\mathbf{Q}}(\xi) + \psi^*_{,\dot{\mathbf{Q}}}(\dot{\mathbf{Q}}; \xi) = \mathbf{0} \tag{6}$$

It is shown in [15, 16] that this equation can be alternatively obtained as the extremization condition of a rate potential

$$\Xi_{eff}\left(\dot{\mathbf{F}}\right) = \min_{\dot{\mathbf{Q}}} \left\{ \dot{W} + \psi^*\left(\dot{\mathbf{Q}}\right) \right\} \tag{7}$$

Moreover, this extremization defines a rate potential Ξ_{eff} for $\mathbf{P}^c$

$$\mathbf{P}^c = \frac{\partial \Xi_{eff}\left(\dot{\mathbf{F}}\right)}{\partial \dot{\mathbf{F}}} \tag{8}$$

Aiming for discrete temporal expressions (time integration) an equivalent incremental potential consistent with (7) is also proposed with the form

$$\Psi = \min_{\mathbf{Q}_{n+1}} \left\{ W_{n+1} - W_n + \Delta t \psi^* \left(\frac{\mathbf{Q}_{n+1} - \mathbf{Q}_n}{\Delta t}; \mathbf{Q}_{n+\alpha} \right) \right\} \tag{9}$$

where $\mathbf{Q}_{n+\alpha}$ is the value of the internal variables at an intermediate time between n and $n+1$. It also shown that this expression provides a potential for the updated value of the First Piola Kirchhoff stress, that is analogous to the case of an hyperelastic material

$$\mathbf{P}^c_{n+1} = \frac{\partial \Psi\left(\mathbf{F}_{n+1}; \xi_n\right)}{\partial \mathbf{F}_{n+1}}, \tag{10}$$

If in addition to conservative part of the stress, the material behaves producing a dissipative (out of equilibrium) term, a new dissipative pseudo-potential may be defined as a function of the rate $\dot{\mathbf{F}}$ such that

$$\mathbf{P}_{n+1} = \mathbf{P}^c_{n+1} + \mathbf{P}^d_{n+1} = \frac{\partial \Psi\left(\mathbf{F}_{n+1}; \xi_n\right)}{\partial \mathbf{F}_{n+1}} + \Delta t \frac{\partial \Phi\left((\mathbf{F}_{n+1} - \mathbf{F}_n)/\Delta t; \xi_n\right)}{\partial \mathbf{F}_{n+1}} \tag{11}$$

This mathematical structure allows the mechanical representation of different dissipative materials by tailoring the appropriate mathematical expressions for the free energy and dissipation potentials. In the next section, a set of variational models that make use of the advantages of this mathematical framework is presented.

3 A Set of Variational Inelastic Models

The set of models described here share the common decomposition of the strain energy into volumetric and isochoric contributions. To this aim, the total gradient of deformation $\mathbf{F}$ is multiplicatively decomposed into isochoric and volumetric parts:

$$\hat{\mathbf{F}} = J^{-\frac{1}{3}}\mathbf{F}; \quad J = \det(\mathbf{F}) \tag{12}$$

The isochoric tensor $\hat{\mathbf{F}}$ is also multiplicatively decomposed into elastic $\hat{\mathbf{F}}^e$ and inelastic $\hat{\mathbf{F}}^i$ contributions

$$\hat{\mathbf{F}} = \hat{\mathbf{F}}^e\hat{\mathbf{F}}^i; \quad \hat{\mathbf{C}} = \hat{\mathbf{F}}^\top\hat{\mathbf{F}}; \quad \hat{\mathbf{C}}^e = \hat{\mathbf{F}}^{e\top}\hat{\mathbf{F}}^e \tag{13}$$

where $\hat{\mathbf{C}}$ and $\hat{\mathbf{C}}^e$ are, respectively, the total and elastic isochoric right Cauchy-Green strain tensors. Moreover, these deformation tensors can be decomposed in terms of spectral quantities

$$\hat{\mathbf{C}} = \sum_{i=1}^{3} c_i\mathbf{E}_i; \quad \hat{\mathbf{C}}^e = \sum_{i=1}^{3} c_i^e\mathbf{E}_i^e; \tag{14}$$

where c_i , c_i^e are eigenvalues and $\mathbf{E}_i$, $\mathbf{E}_i^e$ the corresponding eigenprojections.

The free energy W is assumed to have a separable dependence of the already defined kinematical variables

$$W(\mathbf{F}, \hat{\mathbf{F}}^i, \mathbf{Q}) = \varphi(\hat{\mathbf{C}}) + \varphi^e(\hat{\mathbf{C}}^e) + \varphi^i(\hat{\mathbf{F}}^i, \mathbf{Q}) + U(J) \tag{15}$$

Elastic potentials φ and φ^e are functions of the total deformation $\hat{\mathbf{C}}$ and elastic deformation $\hat{\mathbf{C}}^e$ respectively. The inelastic potential φ^i is a function of the internal variables and it accounts for internal inelastic phenomena such as hardening or softening. Assuming that the volumetric behavior of the modeled materials is reversible (elastic), the same common expression for the volumetric strain energy U is used in all models presented here

$$U(J) = \frac{K}{2}(J-1)^2 \tag{16}$$

This expression may be used to emulate incompressibility in finite element analyses when the material parameter K is taken as a penalty factor ($K \to \infty$).

Finally, the dissipative pseudo-potential ψ^* is now explicitly dependent on the new internal variable rate $\dot{\hat{\mathbf{F}}}^i$, i.e., $\psi^*(\dot{\hat{\mathbf{F}}}^i, \dot{\mathbf{Q}})$.

This general framework is schematically represented by the rheological mechanical model of Fig. 1.

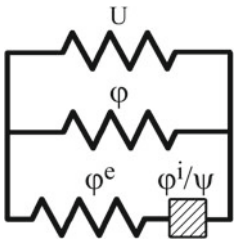

Fig. 1 Generalized mechanical rheological model with three nonlinear elastic springs and one inelastic mechanical component, to be defined depending on the inelastic mechanical behavior of the material

3.1 A Viscoelastic Model for Isotropic Soft Materials

Some soft biological tissues, like brain matter, are considered isotropic viscoelastic materials that can be subject to finite strains [18]. Let the nonlinear viscoelastic model be as proposed in [17], phenomenologically based on the rheological representation of Fig. 2.

In this model, the free energy W given by (15) specializes to

$$W(\mathbf{F}, \mathbf{F}^v, \mathbf{Q}) = U(J) + \varphi(\hat{\mathbf{C}}) + \varphi^e(\hat{\mathbf{C}}^e) \tag{17}$$

The elastic potential φ is the isochoric contribution of elastic energy. It may be expressed by the eigenvalues c_i of $\hat{\mathbf{C}}$

$$\varphi(\hat{\mathbf{C}}) = \varphi(c_1, c_2, c_3) \tag{18}$$

The Maxwell branch in the Fig. 2 is based on a multiplicative split of the total isochoric gradient of deformation $\hat{\mathbf{F}}$ into an isochoric elastic $\hat{\mathbf{F}}^e$ and an isochoric viscous part $\hat{\mathbf{F}}^v$ (inelastic part), such as

$$\hat{\mathbf{F}} = \hat{\mathbf{F}}^e\hat{\mathbf{F}}^v \quad \Rightarrow \quad \hat{\mathbf{F}}^e = \hat{\mathbf{F}}\hat{\mathbf{F}}^{v-1}; \quad \hat{\mathbf{F}}^v = \hat{\mathbf{F}}^{e-1}\hat{\mathbf{F}} \tag{19}$$

$$\hat{\mathbf{C}}^v = \hat{\mathbf{F}}^{v\mathsf{T}}\hat{\mathbf{F}}^v \tag{20}$$

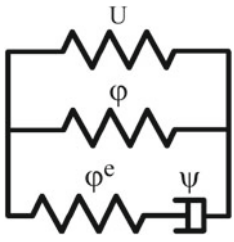

Fig. 2 Generalized Maxwell model for isotropic viscoelastic response

where $\hat{\mathbf{C}}^v$ is the viscous isochoric right Cauchy-Green tensor. The evolution of the internal variable $\hat{\mathbf{F}}^v$ depends on the viscous stretching tensor $\mathbf{D}^v$

$$\mathbf{D}^v = \text{sym}\left(\dot{\hat{\mathbf{F}}}^v \hat{\mathbf{F}}^{v-1}\right) = \sum_{i=1}^{3} d_i^v \mathbf{M}_i^v \tag{21}$$

being d_i^v and $\mathbf{M}_i^v$ the eigenvalues and eigenprojections of $\mathbf{D}^v$. Since the viscous flow is assumed to be isochoric, the spectral decomposition of $\mathbf{D}^v$ is subject to the constrains

$$d_j^v \in K_Q^v = \{p_j \in \mathbb{R} \Rightarrow p_1 + p_2 + p_3 = 0\} \tag{22}$$

$$\mathbf{M}_j^v \in K_M = \{\mathbf{N}_j \in \text{sym} \Rightarrow \mathbf{N}_j \cdot \mathbf{N}_j = 1, \mathbf{N}_i \cdot \mathbf{N}_j = 0, i \neq j\} \tag{23}$$

where the set K_Q^v enforces the traceless form of the tensor and K_M the orthonormal properties.

Potentials φ^e and ψ of the Maxwell branch are isotropic functions of the elastic tensor $\hat{\mathbf{C}}^e$ and viscous stretching $\mathbf{D}^v$ and thus dependent on their respective eigenvalues

$$\varphi^e(\hat{\mathbf{C}}^e) = \varphi(c_1^e, c_2^e, c_3^e) \tag{24}$$

$$\psi(\hat{\mathbf{D}}^v) = \psi(d_1^v, d_2^v, d_3^v) \tag{25}$$

Using the classical exponential mapping [23], the viscous deformations $\mathbf{D}^v$ is approximated by an incremental expression of $\Delta\mathbf{C}^v$

$$\mathbf{F}_{n+1}^v \mathbf{F}_n^{v^{-1}} = \exp[\Delta t \mathbf{D}^v] \Rightarrow \mathbf{D}^v = \frac{1}{2\Delta t} \ln(\Delta \mathbf{C}^v) \tag{26}$$

Finally, with these definitions, the minimizing variables $\mathbf{Q}$ and $\hat{\mathbf{F}}^i$ in (9) are replaced by new internal variables d_i^v and $\mathbf{M}_i^v$, and the incremental potential is given by

$$\Psi_{iso} = \Delta U(J_{n+1}) + \Delta\varphi(\hat{\mathbf{C}}_{n+1}) + \min_{d_i^v, \mathbf{M}_i^v} \left\{ \Delta\varphi^e(\hat{\mathbf{C}}_{n+1}^e) + \Delta t \psi^*(\mathbf{D}^v) \right\} \tag{27}$$

where

$$\begin{aligned} \Delta\varphi(\hat{\mathbf{C}}_{n+1}) &= \varphi(\hat{\mathbf{C}}_{n+1}) - \varphi(\hat{\mathbf{C}}_n) \\ \Delta\varphi^e(\hat{\mathbf{C}}_{n+1}^e) &= \varphi^e(\hat{\mathbf{C}}_{n+1}^e) - \varphi^e(\hat{\mathbf{C}}_n^e) \\ \Delta U(J_{n+1}) &= U(J_{n+1}) - U(J_n) \end{aligned} \tag{28}$$

such that

$$d_j^v \in K_Q = \{p_j \in \mathbb{R} \Rightarrow p_1 + p_2 + p_3 = 0\} \tag{29}$$

$$\mathbf{M}_j^v \in K_M = \{\mathbf{N}_j \in \text{sym} \Rightarrow \mathbf{N}_j \cdot \mathbf{N}_j = 1, \mathbf{N}_i \cdot \mathbf{N}_j = 0, i \neq j\} \tag{30}$$

The optimality condition of (27) with respect to $\mathbf{M}_i^v$ results in $\hat{\mathbf{C}}_{n+1}^e$ and $\mathbf{D}^v$ sharing the same eigenprojections $\mathbf{E}_i^e = \mathbf{M}_i^v$ respectively. The minimization with respect to d_i^v results in the following set of nonlinear equations [17]

$$\begin{aligned} \frac{\partial \varphi^e}{\partial \varepsilon_j^e} - \frac{\partial \psi}{\partial d_i^v} + \lambda = 0 \qquad i = 1, 2, 3 \\ d_1^v + d_2^v + d_3^v = 0 \end{aligned} \tag{31}$$

where λ is the Lagrangian multiplier associated with the constraint (29) and $\varepsilon_j^e = \frac{1}{2}\ln(c_j^e)$. The four nonlinear equations (31) can be solved by the Newton method. Once the minimizers Δq_j^v are obtained, the first Piola-Kirchhoff stress tensor is calculated from (10)

$$\begin{aligned} \mathbf{P}_{n+1} &= 2\mathbf{F}_{n+1} \frac{\partial \Psi_{iso}(\mathbf{C}_{n+1}; \xi_n)}{\partial \mathbf{C}_{n+1}} \\ &= \mathbf{F}_{n+1} \left[2J_{n+1}^{-2/3} \text{DEV}\left(\frac{\partial (\varphi + \varphi^e)}{\partial \hat{\mathbf{C}}_{n+1}} \right) + \frac{\partial U}{\partial J_{n+1}} J_{n+1} \mathbf{C}_{n+1}^{-1} \right] \end{aligned} \tag{32}$$

where $\text{DEV}(\cdot) = (\cdot) - 1/3[(\cdot) : \mathbf{C}]\mathbf{C}^{-1}$. Detailed information regarding these operations is found in [17].

3.2 A Viscoelastic Model for Fiber-Reinforced Soft Materials

Biological tissues, like tendons, ligaments and arterial walls, are strongly anisotropic materials due to the presence of fibers. Usually referred to as a fiber-reinforced material [20], these biological tissues are modeled as composites formed by fibers embedded in a isotropic matrix represented by the ground substance.

In the present case the same variational structure of the isotropic case is used to incorporate the mechanical behavior of fibers. This inclusion is performed in the simplest way of adding the (uncoupled) contribution of the fibers Ψ_f on the isotropic incremental potential Ψ_{iso} (27) to obtain the incremental potential of the composite material

$$\Psi_{ani} = \Psi_{iso} + \Psi_f \tag{33}$$

The rheological model that represent this approach is shown in Fig. 3.

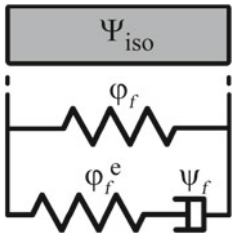

Fig. 3 Rheological mechanical model of the fiber contribution

Since fibers introduce anisotropy related to their directions, the incremental potential depends explicitly on both, the right Cauchy-Green tensor $\hat{\mathbf{C}}$ and the structural tensor $\mathbf{A}_f = \mathbf{a}_f \otimes \mathbf{a}_f$, being $\mathbf{a}_f$ the fiber direction

$$\Psi_f = \Psi_f \left(\hat{\mathbf{C}}, \mathbf{A}_f \right) \tag{34}$$

This dependence can be related to the pseudo-invariant I_4 [21]

$$I_4 \left(\hat{\mathbf{C}}, \mathbf{A}_f \right) = \mathbf{A}_f : \hat{\mathbf{C}} = \lambda_f^2 \tag{35}$$

that allows to obtain a simpler expression dependent only on the fiber stretch λ_f obtained from projection (35).

The free energy associated with both springs of the rheological scheme in Fig. 3 depends on the elastic stretch values λ_f and λ_f^e, the latter obtained from the multiplicative decomposition of λ_f into a elastic and a viscous stretch λ^v

$$\lambda_f = \lambda_f^e \lambda_f^v \tag{36}$$

$$W_f \left(\hat{\mathbf{C}}, \mathbf{A}_f \right) = \varphi_f(\lambda_f) + \varphi_f^e(\lambda_f^e) \tag{37}$$

The dissipative potential $\psi_f = \psi(d_f^v)$ depends on the viscous stretching d_f^v

$$\lambda_f^v = \lambda_f \lambda_f^{e-1} \qquad d_f^v = \dot{\lambda}_f^v \lambda_f^{v-1} \tag{38}$$

Using the exponential mapping [23], it is possible to write

$$\lambda_{fn+1}^v {\lambda_{fn}^v}^{-1} = \exp[\Delta t d_f^v] \quad \Rightarrow \quad d_f^v = \frac{1}{\Delta t} \ln \left(\frac{\lambda_{f_{n+1}}^v}{\lambda_{f_n}^v} \right) \tag{39}$$

Finally, the fiber incremental potential is defined as

$$\Psi_f = \Delta \varphi_f(\lambda_{fn+1}) + \min_{d_f^v} \left\{ \Delta \varphi^e(\lambda_{fn+1}^e) + \Delta t \psi_f(d_f^v) \right\} \tag{40}$$

where

$$\begin{aligned}\Delta\varphi(\lambda_{fn+1}) &= \varphi(\lambda_{fn+1}) - \varphi(\lambda_{fn})\\ \Delta\varphi^e(\lambda^e_{fn+1}) &= \varphi^e(\lambda^e_{fn+1}) - \varphi^e(\lambda^e_{fn})\end{aligned}$$

The optimality condition of (40) with respect to d^v_i results in the following equations

$$\begin{aligned} r &= \frac{\partial\varphi^e_f(\lambda^e_{f_{n+1}})}{\partial\lambda^v_{f_{n+1}}} + \Delta t\frac{\psi_f\left(d^v_{f_{n+1}}\right)}{\partial\lambda^v_{f_{n+1}}}\\ &= \frac{\partial\varphi^e_f}{\partial\lambda^e_{f_{n+1}}}\left(-\frac{\lambda_{f_{n+1}}}{{\lambda^v_{f_{n+1}}}^2}\right) + \frac{\psi_f}{\partial d^v_{f_{n+1}}}\frac{1}{\lambda^v_{f_{n+1}}} = 0 \end{aligned} \tag{41}$$

that can be solved by the Newton method. Once the internal variable $d^v_{f_{n+1}}$ is found, the first Piola-Kirchhoff stress tensor of the viscoelastic model for fiber-reinforced materials is calculated by the *hyperelastic-like* expression

$$\begin{aligned}\mathbf{P}_{n+1} &= 2\mathbf{F}_{n+1}\frac{\partial\Psi_{ani}(\mathbf{C}_{n+1};\xi_n)}{\partial\mathbf{C}_{n+1}}\\ &= 2\mathbf{F}_{n+1}\left[J^{-2/3}_{n+1}\mathrm{DEV}\left(\frac{\partial\left(\varphi+\varphi^e+\varphi_f+\varphi^e_f\right)}{\partial\hat{\mathbf{C}}_{n+1}}\right) + \frac{1}{2}\frac{\partial U}{\partial J_{n+1}}J_{n+1}\mathbf{C}^{-1}_{n+1}\right]\\ &= 2\mathbf{F}_{n+1}\left[J^{-2/3}_{n+1}\mathrm{DEV}\left(\frac{\partial\left(\varphi+\varphi^e\right)}{\partial\hat{\mathbf{C}}_{n+1}}\right) + \frac{1}{2}\frac{\partial U}{\partial J_{n+1}}J_{n+1}\mathbf{C}^{-1}_{n+1}\right] +\\ &+ 2\mathbf{F}_{n+1}\left[J^{-2/3}_{n+1}\mathrm{DEV}\left(\frac{\partial\left(\varphi_f+\varphi^e_f\right)}{\partial\hat{\mathbf{C}}_{n+1}}\right)\right]\\ &= 2\mathbf{F}_{n+1}\frac{\partial\Psi_{iso}(\mathbf{C}_{n+1};\xi_n)}{\partial\mathbf{C}_{n+1}} + 2\mathbf{F}_{n+1}\frac{\partial\Psi_f(\mathbf{C}_{n+1};\xi_n)}{\partial\mathbf{C}_{n+1}}\\ &= \mathbf{P}_{iso} + \mathbf{P}_f\end{aligned} \tag{42}$$

where $\mathbf{P}_{iso}$ is the first Piola-Kirchhoff stress tensor of the isotropic viscoelastic model (32) and $\mathbf{P}_f$ is the first Piola-Kirchhoff stress contribution due to the existence of the fiber-reinforcement. Further details regarding these operations are found in [20].

3.3 A Viscoplastic Model for Isotropic Soft Materials Undergoing Permanent Deformations

In order to include the presence of permanent deformations it is possible to use a internal variable with the same features of plasticity models. Thus, new restrictions and laws related to the evolution of this internal variable should be introduced. In this framework, it is achieved by means of the construction of the inelastic and dissipative potentials [19]. The rheological mechanical model that represent such behavior is shown in Fig. 4.

The free energy W is now composed of the following terms

$$W(\mathbf{F}, \mathbf{F}^p, \mathbf{Q}) = U(J) + \varphi^e(\hat{\mathbf{C}}^e) + \varphi^p(\hat{\mathbf{C}}^p, \mathbf{Q}) \tag{43}$$

To account for the behavior of the Maxwell branch, the gradient of deformation $\hat{\mathbf{F}}$ is decomposed multiplicatively into elastic and inelastic (viscoplastic) terms

$$\hat{\mathbf{F}} = \hat{\mathbf{F}}^e\hat{\mathbf{F}}^p \quad \Rightarrow \quad \hat{\mathbf{F}}^e = \hat{\mathbf{F}}\hat{\mathbf{F}}^{p-1}; \quad \hat{\mathbf{F}}^p = \hat{\mathbf{F}}^{e-1}\hat{\mathbf{F}} \tag{44}$$

where $\hat{\mathbf{F}}^p$ is the permanent isochoric right Cauchy-Green tensor. The evolution of the internal variable $\hat{\mathbf{F}}^p$ is related to the plastic stretching tensor $\mathbf{D}^p$

$$\dot{\hat{\mathbf{F}}}^p = \mathbf{L}^p\hat{\mathbf{F}}^p = \mathbf{D}^p\hat{\mathbf{F}}^p \tag{45}$$

expression obtained by assuming null plastic spin ($\mathbf{W}^p = \text{skew}(\mathbf{L}^p) = 0$).

This plastic spin is conveniently parameterized as [19]

$$\mathbf{D}^p = \dot{q}\sum_{i=1}^{3} q_i\mathbf{M}_i^p \tag{46}$$

$$\dot{q} \in \mathbb{R}; \qquad q_i \in K_Q^p = \left\{ p_i \in \mathbb{R} \Rightarrow \sum_{i=1}^{3} p_i = 0; \quad \sum_{i=1}^{3} p_i^2 = \frac{3}{2}; \right\} \tag{47}$$

$$\mathbf{M}_j^p \in K_M = \{\mathbf{N}_j \in \text{sym} \Rightarrow \mathbf{N}_j \cdot \mathbf{N}_j = 1, \mathbf{N}_i \cdot \mathbf{N}_j = 0, i \neq j\} \tag{48}$$

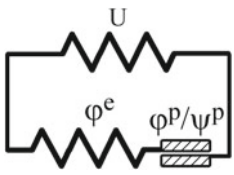

Fig. 4 Generalized Maxwell model for isotropic viscoelastic response

where the set K_Q^p enforces traceless property and limited norm to the tensor. In this parametrization, $\dot{q}$ accounts for the amplitude of $\mathbf{D}^p$ while q_i and $\mathbf{M}_j^p$ for its direction. Using the exponential mapping [23], the update value of $\mathbf{F}^p$ is approximated by

$$\mathbf{F}_{n+1}^p = \exp[\Delta t \mathbf{D}^p]\mathbf{F}_n^p = \exp[\Delta q \sum_{i=1}^{3} q_i \mathbf{M}_i^p]\mathbf{F}_n^p \tag{49}$$

The free energy associated to hardening/softening effects was here simplified to be isotropic and consequently depending on the accumulated plastic amplitude q

$$\varphi^p(\hat{\mathbf{C}}^p, \mathbf{Q}) \;\; = \varphi^p(q) \tag{50}$$

$$q(t) = \int_0^t \dot{q} dt = q_n + \Delta q \tag{51}$$

The dissipative potential ψ^p is defined to be function of $\dot{q}$ and provides penalization for negative values

$$\psi^p(\mathbf{D}^p) = \psi^p(\dot{q}) = \psi^p\left(\frac{\Delta q}{\Delta t}\right) = \begin{cases} \bar{\psi}^p(\dot{q}) & if \quad \dot{q} \geq 0 \\ 0 & if \quad \dot{q} < 0 \end{cases} \tag{52}$$

where $\bar{\psi}^p(\dot{q})$ can be defined by different expressions.

The minimizing variables $\mathbf{Q}$ and $\mathbf{F}_i$ in (9) are replaced by the set of internal variables Δq, q_i and $\mathbf{M}_i^p$, and the incremental potential is represented by

$$\Psi_{ep} = \Delta U(J_{n+1}) + \min_{\Delta q, q_i, \mathbf{M}_i^p} \left\{ \Delta\varphi^e(\hat{\mathbf{C}}_{n+1}^e) + \Delta\varphi^p(\hat{\mathbf{F}}_{n+1}^p, \mathbf{Q}_{n+1}) + \Delta t \psi^*(\mathbf{D}^v) \right\} \tag{53}$$

$$= \Delta U(J_{n+1}) + \min_{\Delta q, q_i, \mathbf{M}_i^p} \left\{ \Delta\varphi^e(\hat{\mathbf{C}}_{n+1}^e) + \Delta\varphi^p(\Delta q) + \Delta t \psi^* \left(\frac{\Delta q}{\Delta t}\right) \right\} \tag{54}$$

where

$$\Delta\varphi^e(\hat{\mathbf{C}}_{n+1}^e) = \varphi^e(\hat{\mathbf{C}}_{n+1}^e) - \varphi^e(\hat{\mathbf{C}}_n^e) \tag{55}$$

$$\Delta\varphi^p(\Delta q) \;\; = \varphi^p(\Delta q) - \varphi^p(q_n) \tag{56}$$

such that

$$q_i \in K_Q^p = \left\{ p_i \in \mathbb{R} \Rightarrow \sum_{i=1}^{3} p_i = 0; \quad \sum_{i=1}^{3} p_i^2 = \frac{3}{2}; \right\} \tag{57}$$

$$\mathbf{M}_j^p \in K_M = \{ \mathbf{N}_j \in \text{sym} \Rightarrow \mathbf{N}_j \cdot \mathbf{N}_j = 1, \mathbf{N}_i \cdot \mathbf{N}_j = 0, i \neq j \} \tag{58}$$

$$\Delta q \geq 0 \tag{59}$$

The first order optimality condition of the incremental potential (54) with respect to $\mathbf{M}_i^p$ results in $\hat{\mathbf{C}}_{n+1}^e$ and $\mathbf{D}^p$ sharing the same eigenvectors $\mathbf{E}_i^e = \mathbf{M}_i^v$ respectively. The minimization with respect to the other internal variables Δq, q_i results in six nonlinear equations [19]

$$\begin{gathered}
-\frac{\partial \varphi^e}{\partial \varepsilon_1^e}\Delta q + \lambda + 2\beta q_1 = 0 \\
-\frac{\partial \varphi^e}{\partial \varepsilon_2^e}\Delta q + \lambda + 2\beta q_2 = 0 \\
-\frac{\partial \varphi^e}{\partial \varepsilon_3^e}\Delta q + \lambda + 2\beta q_3 = 0 \\
-\left(\frac{\partial \varphi^e}{\partial \varepsilon_1^e}q_1 + \frac{\partial \varphi^e}{\partial \varepsilon_2^e}q_2 + \frac{\partial \varphi^e}{\partial \varepsilon_3^e}q_3\right) + \frac{\partial \varphi^p}{\partial \Delta q} + \frac{\partial \psi^p}{\partial \dot{q}} = 0 \\
q_1 + q_2 + q_3 = 0 \\
q_1^2 + q_2^2 + q_3^2 = \frac{3}{2}
\end{gathered} \tag{60}$$

where λ and β are Lagrange multipliers used to introduce the restrictions (58).

The nonlinear equations (60) can be solved by the Newton method. The first Piola-Kirchhoff stress tensor is calculated by (10)

$$\begin{aligned}
\mathbf{P}_{n+1} &= 2\mathbf{F}_{n+1}\frac{\partial \Psi_{ep}(\mathbf{C}_{n+1}; \xi_n)}{\partial \mathbf{C}_{n+1}} \\
&= \mathbf{F}_{n+1}\left[2J_{n+1}^{-2/3}\mathrm{DEV}\left(\frac{\partial \varphi^e}{\partial \hat{\mathbf{C}}_{n+1}}\right) + \frac{\partial U}{\partial J_{n+1}}J_{n+1}\mathbf{C}_{n+1}^{-1}\right]
\end{aligned} \tag{61}$$

where $\mathrm{DEV}(\cdot) = (\cdot) - 1/3[(\cdot) : \mathbf{C}]\mathbf{C}^{-1}$.

Detailed information regarding this model and the minimizing strategy used to identify the begin of the plastic flow are found in [19].

3.4 Material Models

A consequence of the provided mathematical structure is that different functions describing specific materials may be combined to obtain a desired behavior. The spectral decomposition considered in the representation of tensorial quantities allows the use of classical expressions commonly used by hyperelastic models.

3.4.1 Hencky Model

The Hencky-type strain energy is a quadratic expression of the logarithmic strain ϵ. In the present context, a similar structure can be used for the other defined potentials

$$\varphi = \sum_{j=1}^{3} \mu(\epsilon_j)^2 \qquad \varphi^e = \sum_{j=1}^{3} \mu^e(\epsilon_j^e)^2 \qquad \psi^* = \sum_{j=1}^{3} \eta^v(d_j^v)^2 \tag{62}$$

where μ, μ^e and η are material parameters.

3.4.2 Ogden Model

The Ogden model is usually chosen due to its flexibility to represent polymeric materials. Originally based on the principal stretches representation, this strain-energy function can be written as a function of the logarithmic strains using the relation $\lambda_j = \left(\exp(\epsilon_j^e) - 1\right)$

$$\varphi = \sum_{j=1}^{3} \sum_{p=1}^{N} \frac{\mu_p}{\alpha_p} \left(\left[\exp(\epsilon_j)\right]^{\alpha_p} - 1 \right) \tag{63}$$

where α_p and μ_p are material parameters. The following expressions can be used for the elastic strain-energy function and the dissipative potential

$$\varphi^e = \sum_{j=1}^{3} \sum_{p=1}^{N} \frac{\mu_p^e}{\alpha_p^e} \left(\left[\exp(\epsilon_j^e)\right]^{\alpha_p^e} - 1 \right) \tag{64}$$

$$\psi^* = \sum_{j=1}^{3} \sum_{p=1}^{N} \frac{\eta_p^v}{\alpha_p^v} \left(\left[\exp(d_j^v)\right]^{\alpha_p^v} - 1 \right) \tag{65}$$

where α_p^e, μ_p^e, α_p^v and η_p^v are material parameters.

3.4.3 Holzapfel Model

The strain-energy function of the Holzapfel model is based on the scalar pseudo-invariant I_4. It was proposed in [24] to model the fiber contribution of fibrous medium (collagen/elastine) and it is suitable to be used on the fiber contribution of the fiber-reinforced model. Its general form is given by

$$\varphi_f = \frac{k_1}{2k_2} \exp\{[k_2(I_4 - 1)^2] - 1\} \tag{66}$$

where k_1 and k_2 are material parameters. The same expression can be used for the elastic potential

$$\varphi_f^e = \frac{k_1^e}{2k_2^e} \exp\{[k_2(I_4^e - 1)^2] - 1\} \tag{67}$$

where k_1^e and k_2^e are material parameters.

3.4.4 Hardening Model

A simple but effective expression used for metallic hardening, that results in a linear hardening, is given by

$$\varphi^p = \sigma_0 q + \frac{1}{2} H q^2 \tag{68}$$

where σ_0 and H are material parameters. The parameter σ_0 represents the equivalent permanent flow stress (yield stress in plasticity problems). If the tissue is loaded at stress levels higher than σ_0, then evolution of permanent strains takes place. The parameter H is related with the stiffness of the material during the evolution of the permanent strain. Other more flexible functions can be used. For instance, it is possible to obtain a saturating hardening behavior at stress σ_u by considering the expression

$$\varphi^p = \sigma_0 q + (\sigma_u - \sigma_0)\left(q + \frac{1}{\beta_p}\exp(-\beta_p q)\right) \tag{69}$$

where σ_u and β_p are material parameters.

3.4.5 Perzina Model

The Perzina rate-dependent law, commonly used to model viscoplastic metallic materials, can be written explicitly as a function of $\dot{q}$ by

$$\psi^p = \frac{m\sigma_p \dot{q}_0}{m+1}\left(\frac{\dot{q}}{\dot{q}_0}\right)^{\frac{m+1}{m}} \tag{70}$$

where m, σ_p and $\dot{q}_0$ are material parameters.

3.5 Tangent Moduli

The numerical implementation of material models depends on the determination of the exact expressions for the tangent tensor, consistent with the constitutive incremental update algorithm. The contribution to the tangent moduli from geometric terms is similar to any strain-energy-based model and follows the same procedure

applied to hyperelastic models. The presented models are based on an additive decomposition of energy into volumetric and isochoric contributions (15), in which the internal mechanical aspects are related to the isochoric contribution ($\hat{\mathbf{C}}$) alone. Thus, the focus here is on the expression

$$\mathscr{C} = \frac{d}{d\hat{\mathbf{C}}_{n+1}}\left(\frac{d\Psi}{d\hat{\mathbf{C}}_{n+1}}\right) \tag{71}$$

The tangent matrix for each model is obtained analytically according to the definition of the incremental potential Ψ, which depends on W. Since W is decomposed additively in terms of energy potentials, the tangent matrix can be obtained likewise.

3.5.1 Isotropic Viscoelastic Model

Isotropic contribution on the isochoric part

$$\mathscr{C}_{iso} = \frac{d}{d\hat{\mathbf{C}}_{n+1}}\left(\frac{d\Psi_{iso}}{d\hat{\mathbf{C}}_{n+1}}\right) = \frac{d}{d\hat{\mathbf{C}}_{n+1}}\left(\frac{\partial\varphi}{\partial\hat{\mathbf{C}}_{n+1}}\right) + \frac{d}{d\hat{\mathbf{C}}_{n+1}}\left(\frac{\partial\varphi^{e}}{\partial\hat{\mathbf{C}}_{n+1}}\right) \tag{72}$$

3.5.2 Viscoelastic Fiber-Reinforced Model

Fiber contribution on the isochoric part

$$\mathscr{C}_{f} = \frac{d}{d\hat{\mathbf{C}}_{n+1}}\left(\frac{d\Psi_{f}}{d\hat{\mathbf{C}}_{n+1}}\right) = \frac{d}{d\hat{\mathbf{C}}_{n+1}}\left(\frac{\partial\varphi_{f}}{\partial\hat{\mathbf{C}}_{n+1}}\right) + \frac{d}{d\hat{\mathbf{C}}_{n+1}}\left(\frac{\partial\varphi_{f}^{e}}{\partial\hat{\mathbf{C}}_{n+1}}\right) \tag{73}$$

3.5.3 Elasto-Plastic Model

Elasto-plastic contribution on the isochoric part

$$\mathscr{C}_{ep} = \frac{d}{d\hat{\mathbf{C}}_{n+1}}\left(\frac{d\Psi_{ep}}{d\hat{\mathbf{C}}_{n+1}}\right) = \frac{d}{d\hat{\mathbf{C}}_{n+1}}\left(\frac{\partial\varphi^{e}}{\partial\hat{\mathbf{C}}_{n+1}}\right) \tag{74}$$

4 Numerical Examples

In this section a set of numerical examples were selected in order to illustrate the capability of these models to reproduce some of the typical inelastic behaviors observed in soft biological tissues.

Table 1 Combinations of material models

Case	φ	φ^e	ψ
1	Ogden	Ogden	Ogden
2	Hencky	Hencky	Hencky

Table 2 Material parameters for cyclic shear test

Potential	Ogden			Hencky
φ	$\mu_1 = 10$	$\mu_2 = -4$	$\mu_3 = 2$	$\mu = 22.5$
φ^e	$\mu_1^e = 40$	$\mu_2^e = -16$	$\mu_3^e = 8$	$\mu^e = 90$
ψ	$\eta_1^v = 240$	$\eta_2^v = -96$	$\eta_3^v = 48$	$\eta^v = 540$

4.1 Isotropic Viscoelastic Case

Two cyclic simple shear cases are presented for a incompressible element of unitary dimensions. The element is subject to lateral displacement following a sinusoidal function $u_x = U_x \sin(t)$ and tested for the material model combinations shown in Table 1. Ogden and Hencky models were used for φ, φ^e and ψ for two different amplitudes: $U_x = 0.001$ and $U_x = 1$, during three load cycles.

The parameters considered in these tests are presented in the Table 2. For Ogden models is used three terms ($N = 3$). Also, the Ogden exponents $\alpha_1 = 2$; $\alpha_2 = -2$; $\alpha_3 = 7$ are the same for the potentials φ, φ^e and ψ.

The results for the amplitude that correspond to small strains ($U_x = 0.001$) are shown in Fig. 5. Both cases give identical results. The results for a larger amplitude ($U_x = 1$) are presented in Fig. 6 and are quite different. This behavior is due to the fact that the Hencky model used in the Maxwell branch provides a contribution in stress much lower than a corresponding Ogden model for large strains. Also, the viscous potential modifies the minimization condition and, thus, the amount of viscous deformation [17].

4.2 Viscoelastic Fiber-Reinforced Case

Two uniaxial tests are presented here, where controlled stretching cycles are applied in the fiber direction. The parameters of the fiber potential used in these examples are presented in Table 3. The applied stretching history and the results are shown in Figs. 7 and 8. Both figures show the mechanical behavior expected from a fiber, where the material presents stiffness only for positive strains.

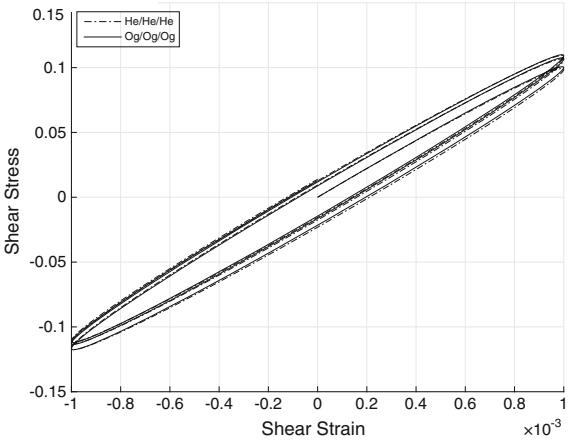

Fig. 5 Cyclic shear test. Shear amplitude $U_x = 0.001$

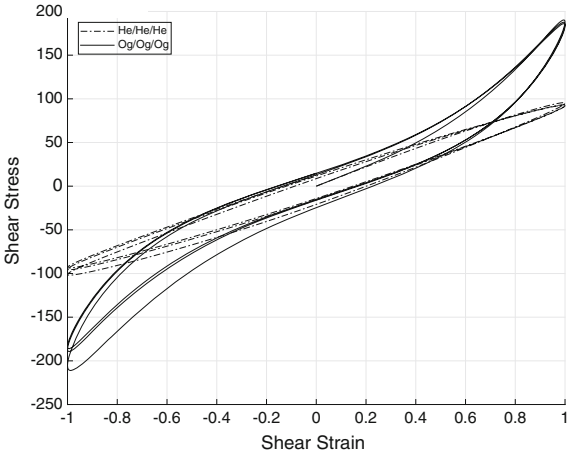

Fig. 6 Cyclic shear test. Shear amplitude $U_x = 1$

Table 3 Material parameters the fiber contribution

Potential	Fiber	
	Model	Parameters
φ	Holzapfel	$k_1 = 1; k_2 = 5$
φ^e	Holzapfel	$k_1 = 1; k_2 = 20$
ψ	Hencky	$\eta^v = 100$

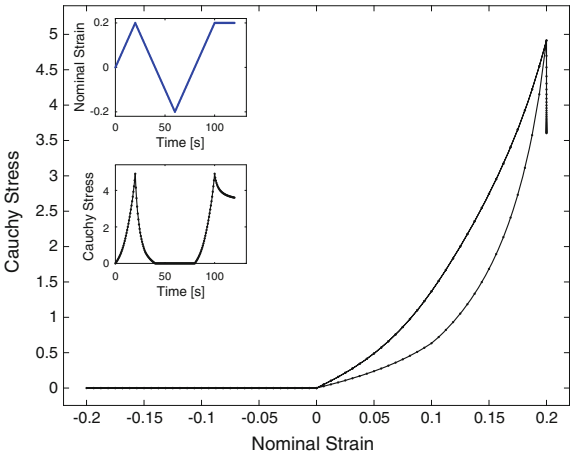

Fig. 7 Stress response for the first tensile loading

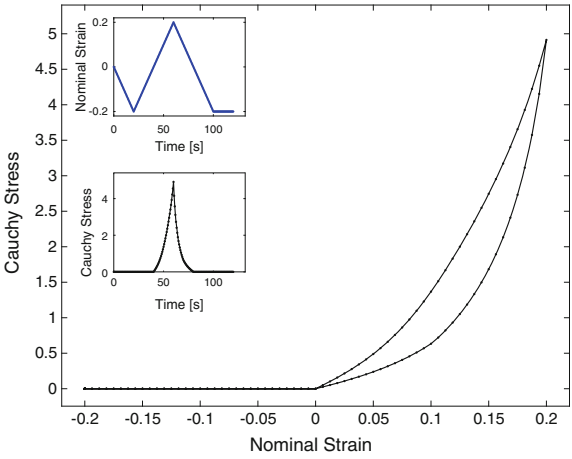

Fig. 8 Stress response for the first compressive loading

4.3 Elasto-Vicoplastic Model

This section focuses on a simple numerical test illustrating the mechanical behavior obtained in a case of a traction test of a element of unitary dimensions, submitted to a constant natural strain rate. Two material models were tested with different elastic strain energy φ^e: Hencky and Ogden models. The parameters used in these tests are shown in Table 4. For both cases, the functions of linear hardening (68) and the Perzina (70) were used, respectively, for the plastic potential φ^p and the dissipative potential ψ^p. The material parameters are the same: $\sigma_p = 2, H = 10, m = 1, \sigma_0 = 40$ and $\dot{q}_0 = 0.1$. Both specimens were elongated up to $\varepsilon = \ln \lambda = 1.2$ with constant strain rates of $1s^{-1}, 0.5s^{-1}$ and $0.1s^{-1}$ and unloaded at the same strain rate. The results for the Hencky model are shown in Fig. 9 where the expected linear dependence

Table 4 Material parameters of the elastic strain-energy φ^e

Potential	Ogden			Hencky
μ_i	-120	156	42	$\mu = 50$
α_i	3.0	1.4	4.0	

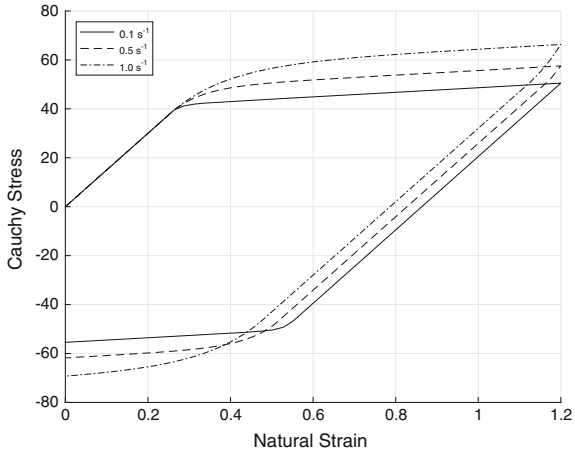

Fig. 9 Uniaxial traction test. Hencky model

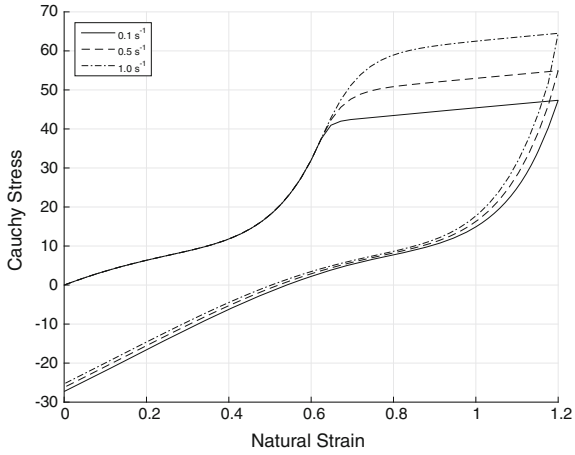

Fig. 10 Uniaxial traction test. Ogden model

of the natural strain (logarithm strain) in the elastic region is obtained. The results for the Ogden model are shown in Fig. 10, where the classical Ogden-type elastic response is obtained. In both cases, the expected dependence of the strain rate in the plastic region is observed.

5 Concluding Remarks

Biological tissues show a complex, history dependent, mechanical response to finite strains. The ability of reproducing these macroscopic behaviors in numerical simulations certainly provide improved support for implant design as well as for surgical decisions. The variational framework presented here provides a consistent unified basis to design a number of specific material models appropriate for the representation of soft biological tissues. Due to its sound thermodynamical basis, all proposed models satisfy a priori the positive dissipation inequality. The main task is reduced to choose the appropriate free energy and dissipative potential expressions to tailor a specific material phenomenon. From a numerical point of view, the constitutive procedure recasts into a convex minimization problem that in most cases has a numerical cost equivalent to that of classical predictor/corrector schemes.

References

1. Junqueira, L.C., Carneiro, J.: Histologia Basica, 10th edn. Guanabara Koogan S.A, Rio de Janeiro (2004)
2. Fung, Y.: Biomechanics—Mechanical Properties of Living Tissues. Springer, New York (1993)
3. Shergold, O.A., Fleck, N.A., Radford, D.: The uniaxial stress versus strain response of pig skin and silicone rubber at low and high strain rates. Int. J. Impact Eng. **32**, 1384–1402 (2006)
4. Giles, J.M., Black, A.E., Bischoff, J.E.: Anomalous rate dependence of the preconditioned response of soft tissue during load controlled deformation. J. Biomech. **40**, 777–785 (2007)
5. Munõz, M.J., Bea, J.A., Rodríguez, J.F., Ochoa, I., Grasa, J., Pérez Del Palomar, A., Zaragoza, P., Osta, R., Doblaré, M.: An experimental study of the mouse skin behaviour: damage and inelastic aspects. J. Biomech. **41**(1), 93–99 (2008)
6. Miller, K.: Constitutive model of brain tissue suitable for finite element analysis of surgical procedures. J. Biomech. **32**(5), 531537 (1999)
7. Limbert, G., Taylor, M., Middleton, J.: Three-dimensional finite element modelling of the human ACL: simulation of passive knee flexion with a stressed and stress-free ACL. J. Biomech. **11**(41), 1723–1731 (2004)
8. Holzapfel, G.A., Weizscker, H.W.: Biomechanical behavior of the arterial wall and its numerical characterization. Comput. Biol. Med. **28**(4), 37792 (1998)
9. Lanir, Y.: Constitutive equations for fibrous connective tissues. J. Biomech. **16**(1), 1–12 (1983)
10. Pioletti, D.P., Rakotomanana, L.R.: Viscoelastic constitutive law in large deformations: application to human knee ligaments and tendons. J. Biomech. **31**(8), 753–757 (1998)
11. Pioletti, D.P., Rakotomanana, L.R.: Non-linear viscoelastic laws for soft biological tissues. Eur. J. Mech. A/Solids **19**, 749–759 (2000)
12. Limbert, G., Taylor, M.: On the constitutive modeling of biological soft connective tissues: a general theoretical framework and explicit forms of the tensors of elasticity for strongly anisotropic continuum fiber-reinforced composites at finite strain. Int. J. Solids Struct. **39**(8), 2343–2358 (2002)
13. El Sayed, T., Mota, A., Fraternali, F., Ortiz, M.: A variational constitutive model for soft biological tissues. J. Biomech. **41**, 1458–1466 (2008)
14. Ehret, A.E., Itskov, M.: Modeling of anisotropic softening phenomena: application to soft biological tissues. Int. J. Plast. **25**(5), 901–919 (2009)

15. Ortiz, M., Stainier, L.: The variational formulation of viscoplastic constitutive updates. Comput. Methods Appl. Mech. Eng. **171**(31), 419–444 (1999)
16. Radovitzky, R., Ortiz, M.: Error estimation and adaptive meshing in strongly nonlinear dynamic problems. Comput. Methods Appl. Mech. Eng. **172**, 203–240 (1999)
17. Fancello, E., Ponthot, J.P., Stainier, L.: A variational formulation of constitutive models and updates in nonlinear finite viscoelasticity. Int. J. Numer. Methods Eng. **65**(13), 1831–1864 (2006)
18. Fancello, E.A., Vigneron, L., Ponthot, J., Stainier, L.: A viscoelastic formulation for finite strains: application to brain soft tissues. In: XXVII CILAMCE—Iberian Latin American Congress on Computational Methods in Engineering (2006)
19. Fancello, E., Vassoler, J., Stainier, L.: Comput. Methods Appl. Mech. Eng. A variational constitutive update algorithm for a set of isotropic hyperelastic viscoplastic material models **197**, 4132–4148 (2008)
20. Vassoler, J.M., Reips, L., Fancello, E.A.: A variational framework for fiber-reinforced viscoelastic soft tissues. Int. J. Numer. Methods Eng. **89**(13), 16911706 (2012)
21. Holzapfel, G.A.: Nonlinear Solid Mechanics: A Continuum Approach for Engineering. Wiley, New York (2000)
22. Neto, E.D.S., Peric, D., Owen, D.R.J.: Computational Methods for Plasticity. Wiley, Chichester (2008)
23. Anand, L., Weber, G.: Finite deformations constitutive equations and a time integration procedure for isotropic hyperelastic-viscoplastic solids. Comput. Methods Appl. Mech. Eng. **79**(14), 173–202 (1990)
24. Holzapfel, G., Gasser, T.C.: A viscoelastic model for fiber-reinforced composites at finite strains: continuum basis, computational aspects and applications. Comput. Methods Appl. Mech. Eng. **190**(21), 4379–4403 (2001)

Sensitivity Analysis of Temperature Field and Parameter Identification in Burned and Healthy Skin Tissue

E. Majchrzak, M. Paruch, M. Dziewoński, S. Freus and K. Freus

Abstract In the chapter, problems connected with the numerical modeling of bioheat transfer processes are presented. In particular the non-homogeneous system of a burn wound and healthy tissue is considered. The heat exchange between sub-domains and environment is described by a system of partial differential equations (the Pennes equations) supplemented by adequate boundary conditions. The first goal of the research is the estimation of the changes of temperature fields due to perturbations in thermal parameters using the direct method of sensitivity analysis. Both the basic problem and additional ones concerning the sensitivity with respect to selected parameters are solved using the boundary element method. The second goal is the problem of burn wound shape identification. The additional information necessary to solve such a task results from the knowledge of temperature distribution on the external surface of skin tissue. At the stage of solving the inverse problem, a gradient method has been used. In the final part of the chapter the results of computations are shown.

Keywords Bioheat transfer · Sensitivity analysis · Boundary element method · Burn wounds · Parameter identification · Gradient method

E. Majchrzak (✉) · M. Paruch · M. Dziewoński
Institute of Computational Mechanics and Engineering, Silesian University of Technology, Gliwice, Poland
e-mail: ewa.majchrzak@polsl.pl

S. Freus · K. Freus
Institute of Mathematics, Czestochowa University of Technology, Częstochowa, Poland

P.A. Muñoz-Rojas (ed.), *Computational Modeling, Optimization and Manufacturing Simulation of Advanced Engineering Materials*, Advanced Structured Materials 49, DOI 10.1007/978-3-319-04265-7_5

1 Introduction

A very important problem in burn therapy is the estimation of the temperature field in the injured and surrounding healthy tissue [1–4]. The information concerning the skin surface temperature allows one to observe the process of burn wounds healing.

In the chapter the heterogeneous domain, constituted of the composition of burned and healthy layers of skin tissue, is considered. The temperature distribution in the domains is described by a system of two Pennes equations [5–7] with different thermophysical parameters. In the healthy layer, the metabolic and perfusion heat sources are taken into account, while the burned layer is dead and the blood perfusion and metabolic do not occur in this region. On the surface between burned and healthy layers, ideal contact is assumed (continuity of heat flux and temperature field), whereas on the internal surface limiting the system, the body temperature is known. Heat transfer between skin surface and environment is described by the well known Robin boundary condition (ambient temperature and heat transfer coefficient are given).

Thermophysical parameters occurring in the presented mathematical model differ significantly because they are individual features of each person. Thus, the aim of the research presented is to estimate the temperature changes due to changes in these parameters. Here the direct approach of sensitivity analysis [8–11] is used. So, the governing equations are differentiated with respect to the parameters considered. In this way, additional problems are formulated, whose number corresponds to the number of the parameters analyzed.

To solve the basic problem and additional ones the classical boundary element method for burned sub-domain [12, 13] and multiple reciprocity boundary element method [14, 15] for healthy tissue sub-domain are used. These methods are coupled by the boundary condition given on the contact surface between sub-domains considered. This approach allows one to avoid the discretization of the domain interior (inside the healthy tissue sub-domain, the volumetric internal heat sources must be taken into account).

Another aim of the study is to identify the depth of burn on the basis of the temperature distribution on the skin surface [1, 4]. Formulated in this way the inverse problem is solved using a gradient method [16]. The inverse problem is defined by the minimization of an objective function that measures the norm of the error between a numerical solution and experimental data. The sensitivity coefficients are necessary to evaluate the gradients of the objective function. To determine these coefficients the implicit differentiation method is applied [17].

In the final part of the chapter the results of computations are shown.

2 Governing Equations

The domain of healthy tissue and burn wound is considered. In the case of 2D problem it is a rectangular domain of dimensions $2L \times L$ (Fig. 1), while in the case of 3D problem it is a cuboid of dimensions $2L \times L \times 2L$ (Fig. 2).

The steady temperature field in domain of healthy tissue is described by the Pennes equation [5–7]

$$x \in \Omega_1: \quad \lambda_1 \nabla^2 T_1(x) + G_B c_B [T_B - T_1(x)] + Q_{met} = 0 \tag{1}$$

where $T_1(x)$ is the tissue temperature, λ_1 is the tissue thermal conductivity, G_B is the blood perfusion rate, c_B is the specific heat of blood, T_B is the arterial blood temperature, Q_{met} is the metabolic heat source, $x = \{x_1, x_2, x_3\}$ for 3D problems and $x = \{x_1, x_2\}$ for 2D problems.

In the domain of burned tissue, blood perfusion and metabolic heat generation are equal to zero, because the tissue is dead. So, the Pennes equation takes the form

$$x \in \Omega_2: \quad \lambda_2 \nabla^2 T_2(x) = 0 \tag{2}$$

where λ_2 is the thermal conductivity of burned tissue.

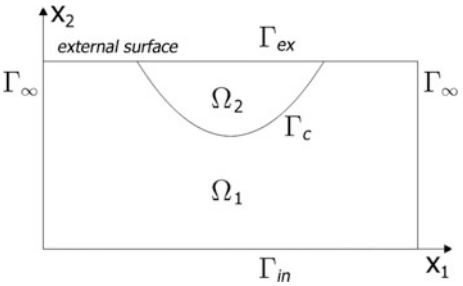

Fig. 1 Domain considered (2D problem)

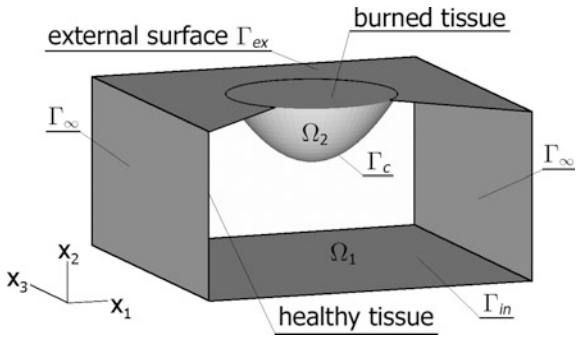

Fig. 2 Domain considered (3D problem)

On the surface between sub-domains the continuity condition is assumed

$$x \in \Gamma_c: \quad \begin{cases} -\lambda_1 \frac{\partial T_1(x)}{\partial n} = -\lambda_2 \frac{\partial T_2(x)}{\partial n} \\ T_1(x) = T_2(x) \end{cases} \tag{3}$$

where $\partial T_e/\partial n$, $e = 1, 2$, denotes the normal derivative and $n = [\cos\alpha_1, \cos\alpha_2, \cos\alpha_3]$ for 3D problems or $n = [\cos\alpha_1, \cos\alpha_2]$ for 2D problems is the normal outward vector.

In the contact between the skin surface and the environment, the Robin condition is taken into account; it reads

$$x \in \Gamma_{ex_e}: \quad -\lambda_e \frac{\partial T_e(x)}{\partial n} = \alpha[T_e(x) - T_a], \quad e = 1, 2 \tag{4}$$

where α is the heat transfer coefficient, T_a is the ambient temperature and $\Gamma_{ex} = \Gamma_{ex_1} \cup \Gamma_{ex_2}$, Γ_{ex_1} is the healthy skin surface, Γ_{ex_2} is the burned skin surface.

On the internal surface the body core temperature is known

$$x \in \Gamma_{in}: \quad T_1(x) = T_b \tag{5}$$

For the other boundaries zero heat flux is assumed

$$x \in \Gamma_\infty: \quad q_1(x) = -\lambda_1 \frac{\partial T_1(x)}{\partial n} = 0 \tag{6}$$

3 Sensitivity Analysis

In this chapter the sensitivity analysis of the process discussed with respect to the thermophysical parameters appearing in the mathematical model described by Eqs. (1)–(6), is presented. The direct approach [8–11], which depends on the differentiation of Pennes equations and boundary conditions with respect to the parameter considered, is applied. In this way, additional problems connected with these parameters are formulated.

Let $p_1 = \lambda_1$, $p_2 = \lambda_2$, $p_3 = G_B$ and $p_4 = Q_{met}$. Equations (1), (2) are differentiated with respect to the parameter p_s, $s = 1, 2, 3, 4$. So

$$\frac{\partial \lambda_1}{\partial p_s} \nabla^2 T_1(x) + \lambda_1 \nabla^2 \left[\frac{\partial T_1(x)}{\partial p_s} \right] + \frac{\partial G_B}{\partial p_s} c_B [T_B - T_1(x)] - G_B c_B \frac{\partial T_1(x)}{\partial p_s} + \frac{\partial Q_{met}}{\partial p_s} = 0 \tag{7}$$

and

$$\frac{\partial \lambda_2(x)}{\partial p_s}\nabla^2 T_2(x) + \lambda_2 \nabla^2\left[\frac{\partial T_2(x)}{\partial p_s}\right] = 0 \tag{8}$$

Information resulting from Eqs. (1), (2) is of the form

$$\nabla^2 T_1(x) = -\frac{1}{\lambda_1}\left[G_B c_B[T_B - T_1(x)] + Q_{met}\right] \tag{9}$$

and

$$\nabla^2 T_2(x) = 0 \tag{10}$$

After introducing (9) into Eq. (7) and (10) into Eq. (8) one has

$$\lambda_1 \nabla^2 U_{1s}(x) - G_B c_B U_{1s}(x) + R_{1s}(x) = 0 \tag{11}$$

and

$$\lambda_2 \nabla^2 U_{2s}(x) = 0 \tag{12}$$

where $U_{es}(x) = \partial T_e(x)/\partial p_s$, $e = 1, 2$, are the sensitivity functions, and

$$R_{1s}(x) = -\frac{\partial \lambda_1}{\partial p_s}\frac{1}{\lambda_1}\left[G_B c_B[T_B - T_1(x)] + Q_{met}\right] + \frac{\partial G_B}{\partial p_s} c_B[T_B - T_1(x)] + \frac{\partial Q_{met}}{\partial p_s} \tag{13}$$

Next, the boundary condition (3) is differentiated with respect to p_s

$$x \in \Gamma_c: \quad \begin{cases} -\frac{\partial \lambda_1}{\partial p_s}\frac{\partial T_1(x)}{\partial n} - \lambda_1 \frac{\partial}{\partial n}\left[\frac{\partial T_1(x)}{\partial p_s}\right] = \frac{\partial \lambda_2}{\partial p_s}\frac{\partial T_2(x)}{\partial n} + \lambda_2 \frac{\partial}{\partial n}\left[\frac{\partial T_2(x)}{\partial p_s}\right] \\ \frac{\partial T_1(x)}{\partial p_s} = \frac{\partial T_2(x)}{\partial p_s} \end{cases} \tag{14}$$

or

$$x \in \Gamma_c: \quad \begin{cases} -\frac{\partial \lambda_1}{\partial p_s}\frac{\partial T_1(x)}{\partial n} - \lambda_1 \frac{\partial U_{1s}(x)}{\partial n} = \frac{\partial \lambda_2}{\partial p_s}\frac{\partial T_2(x)}{\partial n} + \lambda_2 \frac{\partial U_{2s}(x)}{\partial n} \\ U_{1s}(x) = U_{2s}(x) \end{cases} \tag{15}$$

Boundary conditions (4), (5) and (6) are also differentiated, namely

$$x \in \Gamma_{in}: \quad U_{1s}(x) = \frac{\partial T_b}{\partial p_s} = 0 \tag{16}$$

$$x \in \Gamma_{ex_e}: \quad -\frac{\partial \lambda_e}{\partial p_s}\frac{\partial T_e(x)}{\partial n} - \lambda_e \frac{\partial U_{es}(x)}{\partial n} = \alpha U_{es}(x), \quad e = 1, 2 \tag{17}$$

$$x \in \Gamma_\infty: \quad -\frac{\partial \lambda_1}{\partial p_s}\frac{\partial T_1(x)}{\partial n} - \lambda_1 \frac{\partial U_{1s}(x)}{\partial n} = 0 \tag{18}$$

Equations (15), (17), (18) can be written in the form

$$x \in \Gamma_c: \quad \begin{cases} \frac{1}{\lambda_1}\frac{\partial \lambda_1}{\partial p_s} q_1(x) + W_{1s}(x) = -\frac{1}{\lambda_2}\frac{\partial \lambda_2}{\partial p_s} q_2(x) - W_{2s}(x) \\ U_{1s}(x) = U_{2s}(x) \end{cases} \tag{19}$$

$$x \in \Gamma_{ex_e}: \quad W_{es}(x) = \alpha U_{es}(x) - \frac{1}{\lambda_e}\frac{\partial \lambda_e}{\partial p_s} q_e(x) \tag{20}$$

$$x \in \Gamma_\infty: \quad W_{1s}(x) = -\frac{1}{\lambda_1}\frac{\partial \lambda_1}{\partial p_s} q_1(x) \tag{21}$$

where $W_{es}(x) = -\lambda_e \partial U_{es}(x)/\partial n$, $e = 1, 2$.

In this way, the Eqs. (11), (12) supplemented by boundary conditions (16), (19), (20), (21) create additional problems associated with sensitivity analysis with respect to the successive parameters p_s. It should be pointed out that the number of additional problems is equal to the number of analyzed parameters. To solve the additional problems the temperature distribution in the domain considered should be known because the sensitivity problems are coupled with the basic task.

4 Boundary Element Method

The basic problem and additional ones connected with the sensitivity analysis have been solved using the boundary element method [12, 13].

From a mathematical point of view, Eq. (1) is the Poisson equation in which the source function is the sum of the temperature-dependent component and a constant value

$$x \in \Omega_1: \quad \lambda_1 \nabla^2 T_1(x) - G_B c_B T_1(x) + Q = 0 \tag{22}$$

while $Q = G_B c_B T_B + Q_{met}$.

The boundary integral equation corresponding to the Eq. (22) can be expressed as follows [13]

$$B(\xi)T_1(\xi) + \int_{\Gamma_1} q_1(x) T_1^*(\xi, x)\mathrm{d}\Gamma_1 = \int_{\Gamma_1} T_1(x) q_1^*(\xi, x)\mathrm{d}\Gamma_1 + \int_{\Omega_1} T_1^*(\xi, x) Q(x)\mathrm{d}\Omega_1 \tag{23}$$

where $q_1(x) = -\lambda_1 \partial T_1(x)/\partial n$ and $\Gamma_1 = \Gamma_{ex_1} \cup \Gamma_\infty \cup \Gamma_{in} \cup \Gamma_c$. In Eq. (23) ξ is the observation point, the coefficient $B(\xi)$ depends on the location of source point ξ, $T_1^*(\xi, x)$ is the fundamental solution, $q_1^*(\xi, x) = -\lambda_1 \partial T_1^*(\xi, x)/\partial n$.

The fundamental solution is of the form

$$T_1^*(\xi,x)=\begin{cases}\frac{1}{2\pi\lambda_1}\mathrm{K}_0\left(r\sqrt{\frac{G_B c_B}{\lambda_1}}\right) & \text{for 2D problem}\\ \frac{1}{4\pi\lambda_1 r}\exp\left(-r\sqrt{\frac{G_B c_B}{\lambda_1}}\right) & \text{for 3D problem}\end{cases} \tag{24}$$

where $\mathrm{K}_0(\cdot)$ is the modified Bessel's function of second kind, zero order [13], r is the distance between the source point ξ and the field point x

$$r=\sqrt{\sum_{i=1}^{m}(x_i-\xi_i)^2} \tag{25}$$

while m is the dimension of the problem.

To solve the Eq. (23), not only the boundary but also the interior of the domain considered must be discretized. This variant of the BEM has been used, among others, in [6].

It should be pointed out that in the case of solving the inverse problem connected with the burn depth identification (Sect. 5), it is more convenient to use such a method which does not require the interior domain discretization. One of them is the multiple reciprocity boundary element method (MRBEM) [14, 15]. In this case, the following integral equation is considered [15]

$$\begin{aligned}&B(\xi)T_1(\xi)+\sum_{l=0}^{\infty}\left(\frac{G_B c_B}{\lambda_1}\right)^l\int_{\Gamma_\mathrm{I}} q_1(x)V_l^*(\xi,x)\mathrm{d}\Gamma_\mathrm{I}\\ &=\sum_{l=0}^{\infty}\left(\frac{G_B c_B}{\lambda_1}\right)^l\int_{\Gamma_\mathrm{I}} T_1(x)Z_l^*(\xi,x)\,\mathrm{d}\Gamma_\mathrm{I}-\frac{Q}{\lambda_1}\sum_{l=1}^{\infty}\left(\frac{G_B c_B}{\lambda_1}\right)^{l-1}\int_{\Gamma_\mathrm{I}} Z_l^*(\xi,x)\mathrm{d}\Gamma_\mathrm{I}\end{aligned} \tag{26}$$

where the functions $V_l^*(\xi,x)$ for 2D and 3D problems are defined as follows [14, 15]

$$V_l^*(\xi,x)=\begin{cases}\frac{1}{2\pi\lambda_1}r^{2l}\left(A_l\ln\frac{1}{r}+B_l\right) & \text{for 2D problem}\\ \frac{1}{4\pi\lambda_1}r^{2l-1}C_l & \text{for 3D problem}\end{cases} \tag{27}$$

while

$$\begin{aligned}&A_0=1, \quad A_l=\tfrac{A_{l-1}}{4l^2}, && l=1,2,3,\ldots\\ &B_0=0, \quad B_l=\tfrac{1}{4l^2}\left(\tfrac{A_{l-1}}{l}+B_{l-1}\right), && l=1,2,3,\ldots\end{aligned} \tag{28}$$

and

$$C_0=1, \quad C_1=\tfrac{1}{2}, \quad C_2=\tfrac{1}{24}, \quad C_l=\tfrac{1}{(2l-1)(2l-3)}C_{l-1}, \quad l=3,4,5,\ldots \tag{29}$$

The heat fluxes $Z_l^*(\xi, x) = -\lambda_1 \partial V_l^*(\xi, x)/\partial n$ resulting from the fundamental solutions (27) can be calculated analytically and then

$$Z_l^*(\xi, x) = \begin{cases} \frac{d}{2\pi} r^{2l-2}\left[A_l - 2l\left(A_l \ln\frac{1}{r} + B_l\right)\right] & \text{for 2D problem} \\ -\frac{d}{4\pi}(2l-1)r^{2l-3}C_l & \text{for 3D problem} \end{cases} \tag{30}$$

where

$$d = \sum_{i=1}^{m} (x_i - \xi_i)\cos\alpha_i \tag{31}$$

The boundary integral equation corresponding to the Eq. (2) is the following

$$B(\xi)T_2(\xi) + \int_{\Gamma_{II}} q_2(x)T_2^*(\xi, x)\mathrm{d}\Gamma_{II} = \int_{\Gamma_{II}} T_2(x)q_2^*(\xi, x)\mathrm{d}\Gamma_{II} \tag{32}$$

where ξ is the observation point, the coefficient $B(\xi)$ depends on the location of source point ξ, $T_2^*(\xi, x)$ is the fundamental solution, $q_2^*(\xi, x) = -\lambda_2 \partial T_2^*(\xi, x)/\partial n$ is the heat flux resulting from fundamental solution, $q_2(x) = -\lambda_2 \partial T_2(x)/\partial n$ is the heat flux and $\Gamma_{II} = \Gamma_c \cup \Gamma_{ex_2}$.

Fundamental solution of the problem discussed is of the form

$$T_2^*(\xi, x) = \begin{cases} \frac{1}{2\pi\lambda_2}\ln\frac{1}{r} & \text{for 2D problem} \\ \frac{1}{4\pi\lambda_2 r} & \text{for 3D problem} \end{cases} \tag{33}$$

and then

$$q_2^*(\xi, x) = \begin{cases} \frac{d}{2\pi r^2} & \text{for 2D problem} \\ \frac{d}{4\pi r^3} & \text{for 3D problem} \end{cases} \tag{34}$$

To solve the Eqs. (26) and (32) the boundary is divided into N elements $\Gamma_j = 1, 2, \ldots, N$ and the integrals in the Eqs. (26), (32) can be replaced by the sums of integrals over these elements. So

$$\begin{aligned} &B(\xi)T_1(\xi) + \sum_{l=0}^{\infty}\left(\frac{G_B c_B}{\lambda_1}\right)^l \sum_{j=1}^{N_1}\int_{\Gamma_j} q_1(x)V_l^*(\xi, x)\mathrm{d}\Gamma_j \\ &= \sum_{l=0}^{\infty}\left(\frac{G_B c_B}{\lambda_1}\right)^l \sum_{j=1}^{N_1}\int_{\Gamma_j} T_1(x)Z_l^*(\xi, x)\,\mathrm{d}\Gamma_j - \frac{Q}{\lambda_1}\sum_{l=1}^{\infty}\left(\frac{G_B c_B}{\lambda_1}\right)^{l-1} \sum_{j=1}^{N_1}\int_{\Gamma_j} Z_l^*(\xi, x)\,\mathrm{d}\Gamma_j \end{aligned} \tag{35}$$

and

$$B(\xi)T_2(\xi) + \sum_{j=N_1+1}^{N} \int_{\Gamma_j} q_2(x)T_2^*(\xi,x)\mathrm{d}\Gamma_j = \sum_{j=N_1+1}^{N} \int_{\Gamma_j} T_2(x)q_2^*(\xi,x)\mathrm{d}\Gamma_j \tag{36}$$

where N_1 is the number of elements on the boundary limiting domain Ω_1.

It should be pointed out that different types of boundary elements can be used, namely constant elements, linear or parabolic ones [12, 13]. Here the linear boundary elements are applied. The singular and weakly singular integrals occurring in the BEM Eqs. (35), (36) are calculated analytically using the expressions presented, among others, in [13].

After the mathematical manipulations one obtains the following system of algebraic equations corresponding to the healthy tissue

$$\sum_{k=1}^{K_1} G_{ik}^1 q_k^1 = \sum_{k=1}^{K_1} H_{ik}^1 T_k^1 + P_i, \quad i = 1, 2, \ldots, K_1 \tag{37}$$

and the system of equations corresponding to the burned tissue

$$\sum_{k=K_1+1}^{K} G_{ik}^2 q_k^2 = \sum_{k=K_1+1}^{K} H_{ik}^2 T_k^2, \quad i = K_1+1, K_1+2, \ldots, K \tag{38}$$

where K_1 is the number of boundary nodes located on the boundary limiting sub-domain Ω_1, $K - K_1$ is the number of boundary nodes located on the boundary limiting sub-domain Ω_2.

It should be pointed out that taking into account the boundary conditions, on the contact surface between sub-domains Ω_1 and Ω_2 (Fig. 2) the double numbering of boundary nodes should be introduced.

The systems of Eqs. (37), (38) can be written in the matrix form

$$\mathbf{G}_1\,\mathbf{q}_1 = \mathbf{H}_1\,\mathbf{T}_1 + \mathbf{P} \tag{39}$$

and

$$\mathbf{G}_2\,\mathbf{q}_2 = \mathbf{H}_2\,\mathbf{T}_2 \tag{40}$$

The way of calculation of matrices $\mathbf{G}_1$, $\mathbf{H}_1$, $\mathbf{G}_2$, $\mathbf{H}_2$, $\mathbf{P}$ elements is described in details in [14, 15].

For the needs of further considerations concerning the temperature field modeling, the following denotations are introduced (c.f. Figs. 1 and 2)

- $\mathbf{T}_1^{ex_1}$, $\mathbf{T}_1^{\infty}$, $\mathbf{T}_1^{in}$, $\mathbf{q}_1^{ex_1}$, $\mathbf{q}_1^{\infty}$, $\mathbf{q}_1^{in}$ are the vectors of functions T and q at the boundary $\Gamma_{ex_1} \cup \Gamma_{\infty} \cup \Gamma_{in}$ of domain Ω_1,
- $\mathbf{T}_{c1}$, $\mathbf{T}_{c2}$, $\mathbf{q}_{c1}$, $\mathbf{q}_{c2}$ are the vectors of functions T and q on the contact surface Γ_c between sub-domains Ω_1 and Ω_2,
- $\mathbf{T}_2^{ex_2}$, $\mathbf{q}_2^{ex_2}$ are the vectors of functions T and q at the boundary Γ_{ex_2} of domain Ω_2.

Using above designations one obtains the following systems of equations

- for the healthy tissue domain

$$\begin{bmatrix} \mathbf{G}_1^{ex_1} & \mathbf{G}_1^{\infty} & \mathbf{G}_1^{in} & \mathbf{G}_{c1} \end{bmatrix} \begin{bmatrix} \mathbf{q}_1^{ex_1} \\ \mathbf{q}_1^{\infty} \\ \mathbf{q}_1^{in} \\ \mathbf{q}_{c1} \end{bmatrix} = \begin{bmatrix} \mathbf{H}_1^{ex_1} & \mathbf{H}_1^{\infty} & \mathbf{H}_1^{in} & \mathbf{H}_{c1} \end{bmatrix} \begin{bmatrix} \mathbf{T}_1^{ex_1} \\ \mathbf{T}_1^{\infty} \\ \mathbf{T}_1^{in} \\ \mathbf{T}_{c1} \end{bmatrix} + \mathbf{P} \tag{41}$$

- for the burned region

$$\begin{bmatrix} \mathbf{G}_{c2} & \mathbf{G}_2^{ex_2} \end{bmatrix} \begin{bmatrix} \mathbf{q}_{c2} \\ \mathbf{q}_2^{ex_2} \end{bmatrix} = \begin{bmatrix} \mathbf{H}_{c2} & \mathbf{H}_2^{ex_2} \end{bmatrix} \begin{bmatrix} \mathbf{T}_{c2} \\ \mathbf{T}_2^{ex_2} \end{bmatrix} \tag{42}$$

The condition (3) written in the form

$$\begin{cases} \mathbf{q}_{c1} = -\mathbf{q}_{c2} = \mathbf{q} \\ \mathbf{T}_{c1} = \mathbf{T}_{c2} = \mathbf{T} \end{cases} \tag{43}$$

should be introduced to the Eqs. (41), (42). Therefore

$$\begin{bmatrix} \mathbf{G}_1^{ex_1} & \mathbf{G}_1^{\infty} & \mathbf{G}_1^{in} & -\mathbf{H}_{c1} & \mathbf{G}_{c1} \end{bmatrix} \begin{bmatrix} \mathbf{q}_1^{ex_1} \\ \mathbf{q}_1^{\infty} \\ \mathbf{q}_1^{in} \\ \mathbf{T} \\ \mathbf{q} \end{bmatrix} = \begin{bmatrix} \mathbf{H}_1^{ex_1} & \mathbf{H}_1^{\infty} & \mathbf{H}_1^{in} \end{bmatrix} \begin{bmatrix} \mathbf{T}_1^{ex_1} \\ \mathbf{T}_1^{\infty} \\ \mathbf{T}_1^{in} \end{bmatrix} + \mathbf{P} \tag{44}$$

and

$$\begin{bmatrix} -\mathbf{H}_{c2} & -\mathbf{G}_{c2} & \mathbf{G}_2^{ex_2} \end{bmatrix} \begin{bmatrix} \mathbf{T} \\ \mathbf{q} \\ \mathbf{q}_2^{ex_2} \end{bmatrix} = \mathbf{H}_2^{ex_2} \mathbf{T}_2^{ex_2} \tag{45}$$

Coupling of these systems of equations gives

$$\begin{bmatrix} \mathbf{G}_1^{ex_1} & \mathbf{G}_1^{\infty} & \mathbf{G}_1^{in} & -\mathbf{H}_{c1} & \mathbf{G}_{c1} & \mathbf{0} \\ \mathbf{0} & \mathbf{0} & \mathbf{0} & -\mathbf{H}_{c2} & -\mathbf{G}_{c2} & \mathbf{G}_2^{ex_2} \end{bmatrix} \begin{bmatrix} \mathbf{q}_1^{ex_1} \\ \mathbf{q}_1^{\infty} \\ \mathbf{q}_1^{in} \\ \mathbf{T} \\ \mathbf{q} \\ \mathbf{q}_2^{ex_2} \end{bmatrix} = \begin{bmatrix} \mathbf{H}_1^{ex_1} & \mathbf{H}_1^{\infty} & \mathbf{H}_1^{in} & \mathbf{0} \\ \mathbf{0} & \mathbf{0} & \mathbf{0} & \mathbf{H}_2^{ex_2} \end{bmatrix} \begin{bmatrix} \mathbf{T}_1^{ex_1} \\ \mathbf{T}_1^{\infty} \\ \mathbf{T}_1^{in} \\ \mathbf{T}_2^{ex_2} \end{bmatrix} + \begin{bmatrix} \mathbf{P} \\ \mathbf{0} \end{bmatrix} \tag{46}$$

The remaining boundary conditions (4), (5), (6) should be also taken into account and then

$$\begin{bmatrix} \alpha\mathbf{G}_1^{ex_1} - \mathbf{H}_1^{ex_1} & -\mathbf{H}_1^{\infty} & \mathbf{G}_1^{in} & -\mathbf{H}_{c1} & \mathbf{G}_{c1} & \mathbf{0} \\ \mathbf{0} & \mathbf{0} & \mathbf{0} & -\mathbf{H}_{c2} & -\mathbf{G}_{c2} & \alpha\mathbf{G}_2^{ex_2} - \mathbf{H}_2^{ex_2} \end{bmatrix} \begin{bmatrix} \mathbf{T}_1^{ex_1} \\ \mathbf{T}_1^{\infty} \\ \mathbf{q}_1^{in} \\ \mathbf{T} \\ \mathbf{q} \\ \mathbf{T}_2^{ex_2} \end{bmatrix} = \begin{bmatrix} \alpha\mathbf{G}_1^{ex_1} & \mathbf{G}_1^{in} & \mathbf{0} \\ \mathbf{0} & \mathbf{0} & \alpha\mathbf{G}_2^{ex_2} \end{bmatrix} \begin{bmatrix} \mathbf{T}_a \\ \mathbf{T}_b \\ \mathbf{T}_a \end{bmatrix} + \begin{bmatrix} \mathbf{P} \\ \mathbf{0} \end{bmatrix} \tag{47}$$

or

$$\mathbf{AY} = \mathbf{B} \tag{48}$$

where **A** is the main matrix of the system of Eq. (47), **Y** is the vector of unknowns and **B** is the free terms vector.

The system of Eq. (48) allows one to find the "missing" boundary values. Knowledge of boundary temperatures and heat fluxes at all nodes constitutes a basis for computations of internal temperatures at the optional points selected from the domain of burned region and at the internal points distinguished in the healthy tissue [14, 15].

In the case of additional problems solution (associated with the sensitivity analysis) the procedure is similar but slightly more difficult. Boundary integral equations corresponding to Eqs. (11), (12) have the following form

$$
\begin{aligned}
B(\xi)U_{1s}(\xi)+\int_{\Gamma_I} W_{1s}(x)\sum_{l=0}^{\infty}\left(\frac{G_B c_B}{\lambda_1}\right)^l V_l^*(\xi,x)\,\mathrm{d}\Gamma &= \int_{\Gamma_I} U_{1s}(x)\sum_{l=0}^{\infty}\left(\frac{G_B c_B}{\lambda_1}\right)^l Z_l^*(\xi,x)\,\mathrm{d}\Gamma \\
&-\left(\frac{\partial\lambda_1}{\partial p_s}\frac{G_B c_B}{\lambda_1}-\frac{\partial G_B}{\partial p_s}c_B\right)\frac{1}{\lambda_1}\int_{\Gamma_I} T_1(x)\sum_{l=1}^{\infty} l\left(\frac{G_B c_B}{\lambda_1}\right)^{l-1} Z_l^*(\xi,x)\,\mathrm{d}\Gamma \\
&+\left(\frac{\partial\lambda_1}{\partial p_s}\frac{G_B c_B}{\lambda_1}-\frac{\partial G_B}{\partial p_s}c_B\right)\frac{1}{\lambda_1}\int_{\Gamma_I} q_1(x)\sum_{l=1}^{\infty} l\left(\frac{G_B c_B}{\lambda_1}\right)^{l-1} V_l^*(\xi,x)\mathrm{d}\Gamma \\
&-\left(-\frac{\partial\lambda_1}{\partial p_s}\frac{1}{\lambda_1}Q+\frac{\partial G_B}{\partial p_s}c_B T_B+\frac{\partial Q_{met}}{\partial p_s}\right)\frac{1}{\lambda_1}\int_{\Gamma_I}\sum_{l=1}^{\infty}\left(\frac{G_B c_B}{\lambda_1}\right)^{l-1} Z_l^*(\xi,x)\mathrm{d}\Gamma \\
&+\left(\frac{\partial\lambda_1}{\partial p_s}\frac{G_B c_B}{\lambda_1}-\frac{\partial G_B}{\partial p_s}c_B\right)\frac{Q}{\lambda_1^2}\int_{\Gamma_I}\sum_{l=1}^{\infty}(l-1)\left(\frac{G_B c_B}{\lambda_1}\right)^{l-2} Z_l^*(\xi,x)\,\mathrm{d}\Gamma
\end{aligned}
\tag{49}
$$

and

$$
B(\xi)U_{2s}(\xi)+\int_{\Gamma_{II}} W_{2s}(x)T_2^*(\xi,\ x)\mathrm{d}\Gamma_{II}=\int_{\Gamma_{II}} U_{2s}(x)q_2^*(\xi,\ x)\mathrm{d}\Gamma_{II} \tag{50}
$$

After discretization, the following systems of equations are obtained

- for the healthy tissue domain

$$
\mathbf{G}_1\mathbf{W}_{1s}=\mathbf{H}_1\mathbf{U}_{1s}+\mathbf{Z}_{1s} \tag{51}
$$

- for the burned region

$$
\mathbf{G}_2\mathbf{W}_{2s}=\mathbf{H}_2\mathbf{U}_{2s} \tag{52}
$$

or

$$
\begin{bmatrix}\mathbf{G}_1^{ex_1} & \mathbf{G}_1^{\infty} & \mathbf{G}_1^{in} & \mathbf{G}_{c1}\end{bmatrix}\begin{bmatrix}\mathbf{W}_{1s}^{ex_1}\\ \mathbf{W}_{1s}^{\infty}\\ \mathbf{W}_{1s}^{in}\\ \mathbf{W}_{c1s}\end{bmatrix}=\begin{bmatrix}\mathbf{H}_1^{ex_1} & \mathbf{H}_1^{\infty} & \mathbf{H}_1^{in} & \mathbf{H}_{c1}\end{bmatrix}\begin{bmatrix}\mathbf{U}_{1s}^{ex_1}\\ \mathbf{U}_{1s}^{\infty}\\ \mathbf{U}_{1s}^{in}\\ \mathbf{U}_{c1s}\end{bmatrix}+\mathbf{Z}_{1s} \tag{53}
$$

and

$$
\begin{bmatrix}\mathbf{G}_{c2} & \mathbf{G}_2^{ex_2}\end{bmatrix}\begin{bmatrix}\mathbf{W}_{c2s}\\ \mathbf{W}_{2s}^{ex_2}\end{bmatrix}=\begin{bmatrix}\mathbf{H}_{c2} & \mathbf{H}_2^{ex_2}\end{bmatrix}\begin{bmatrix}\mathbf{U}_{c2s}\\ \mathbf{U}_{2s}^{ex_2}\end{bmatrix} \tag{54}
$$

Taking into account the depencence (43), the boundary condition (19) can be written as follows

$$x \in \Gamma_c: \quad \begin{cases} \mathbf{W}_{c2s} = -\mathbf{W}_{c1s} + \left(\frac{1}{\lambda_2}\frac{\partial \lambda_2}{\partial p_s} - \frac{1}{\lambda_1}\frac{\partial \lambda_1}{\partial p_s}\right)\mathbf{q} \\ \mathbf{U}_{c1s} = \mathbf{U}_{c2s} = \mathbf{U}_s \end{cases} \tag{55}$$

Introducing (55) into the Eqs. (53), (54) one obtains

$$\begin{bmatrix} \mathbf{G}_1^{ex_1} & \mathbf{G}_1^{\infty} & \mathbf{G}_1^{in} & -\mathbf{H}_{c1} & \mathbf{G}_{c1} \end{bmatrix} \begin{bmatrix} \mathbf{W}_{1s}^{ex_1} \\ \mathbf{W}_{1s}^{\infty} \\ \mathbf{W}_{1s}^{in} \\ \mathbf{U}_s \\ \mathbf{W}_{c1s} \end{bmatrix} = \begin{bmatrix} \mathbf{H}_1^{ex_1} & \mathbf{H}_1^{\infty} & \mathbf{H}_1^{in} \end{bmatrix} \begin{bmatrix} \mathbf{U}_{1s}^{ex_1} \\ \mathbf{U}_{1s}^{\infty} \\ \mathbf{U}_{1s}^{in} \end{bmatrix} + \mathbf{Z}_{1s} \tag{56}$$

and

$$\begin{bmatrix} -\mathbf{H}_{c2} & -\mathbf{G}_{c2} & \mathbf{G}_2^{ex_2} \end{bmatrix} \begin{bmatrix} \mathbf{U}_s \\ \mathbf{W}_{c1s} \\ \mathbf{W}_{2s}^{ex_2} \end{bmatrix} = \left(\frac{1}{\lambda_1}\frac{\partial \lambda_1}{\partial p_s} - \frac{1}{\lambda_2}\frac{\partial \lambda_2}{\partial p_s}\right)\mathbf{G}_{c2}\mathbf{q} + \mathbf{H}_2^{ex_2}\mathbf{U}_{2s}^{ex_2} \tag{57}$$

The coupling of Eqs. (56), (57) gives

$$\begin{bmatrix} \mathbf{G}_1^{ex_1} & \mathbf{G}_1^{\infty} & \mathbf{G}_1^{in} & -\mathbf{H}_{c1} & \mathbf{G}_{c1} & \mathbf{0} \\ \mathbf{0} & \mathbf{0} & \mathbf{0} & -\mathbf{H}_{c2} & -\mathbf{G}_{c2} & \mathbf{G}_2^{ex_2} \end{bmatrix} \begin{bmatrix} \mathbf{W}_{1s}^{ex_1} \\ \mathbf{W}_{1s}^{\infty} \\ \mathbf{W}_{1s}^{in} \\ \mathbf{U}_s \\ \mathbf{W}_{c1s} \\ \mathbf{W}_{2s}^{ex_2} \end{bmatrix} = \begin{bmatrix} \mathbf{H}_1^{ex_1} & \mathbf{H}_1^{\infty} & \mathbf{0} \\ \mathbf{0} & \mathbf{0} & \mathbf{H}_2^{ex_2} \end{bmatrix} \begin{bmatrix} \mathbf{U}_{1s}^{ex_1} \\ \mathbf{U}_{1s}^{\infty} \\ \mathbf{U}_{2s}^{ex_2} \end{bmatrix} + \begin{bmatrix} \mathbf{Z}_{1s} \\ \left(\frac{1}{\lambda_1}\frac{\partial \lambda_1}{\partial p_s} - \frac{1}{\lambda_2}\frac{\partial \lambda_2}{\partial p_s}\right)\mathbf{G}_{c2}\mathbf{q} \end{bmatrix} \tag{58}$$

The remaining boundary conditions (16), (20), (21) should be also taken into account and then

$$\begin{bmatrix} \alpha\mathbf{G}_1^{ex_1} - \mathbf{H}_1^{ex_1} & -\mathbf{H}_1^{\infty} & \mathbf{G}_1^{in} & -\mathbf{H}_{c1} & \mathbf{G}_{c1} & \mathbf{0} \\ \mathbf{0} & \mathbf{0} & \mathbf{0} & -\mathbf{H}_{c2} & -\mathbf{G}_{c2} & \alpha\mathbf{G}_2^{ex_2} - \mathbf{H}_2^{ex_2} \end{bmatrix} \begin{bmatrix} \mathbf{U}_{1s}^{ex_1} \\ \mathbf{W}_{1s}^{\infty} \\ \mathbf{U}_{1s}^{\infty} \\ \mathbf{U}_s \\ \mathbf{W}_{c1s} \\ \mathbf{U}_{2s}^{ex_2} \end{bmatrix} \tag{59}$$

$$= \begin{bmatrix} \frac{1}{\lambda_1}\frac{\partial\lambda_1}{\partial p_s}\mathbf{G}_1^{ex_1} & \mathbf{0} & \mathbf{0} \\ \mathbf{0} & \left(\frac{1}{\lambda_1}\frac{\partial\lambda_1}{\partial p_s} - \frac{1}{\lambda_2}\frac{\partial\lambda_2}{\partial p_s}\right)\mathbf{G}_{c2} & \frac{1}{\lambda_2}\frac{\partial\lambda_2}{\partial p_s}\mathbf{G}_2^{ex_2} \end{bmatrix} \begin{bmatrix} \mathbf{q}_1^{ex_1} \\ \mathbf{q} \\ \mathbf{q}_2^{ex_2} \end{bmatrix} + \begin{bmatrix} \mathbf{Z}_{1s} \\ \mathbf{0} \end{bmatrix}$$

It should be pointed out that the main matrix of the system of Eq. (59) associated with the sensitivity functions is the same as in the case of the basic problem solution (c.f. Eq. (47)).

5 Inverse Problem

The inverse problem considered here is based on the assumption that the temperature distribution at the boundary Γ_{ex} is known (e.g. thermograms), while the position of Γ_c is unknown. The 'measured' temperatures on the skin surface are denoted by T_{di}, $i = 1, 2, \ldots M$, where M is the number of sensors.

It is assumed that in the case of a 3D problem the surface Γ_c is defined by the rotational paraboloid ($x_2 \le L$)

$$x_2 = b + \frac{4(L-b)}{L^2}\left[(x_1 - L)^2 + x_3^2\right] \tag{60}$$

where the point (L, b, 0) corresponds to the paraboloid vertex. The section $x_3 = 0$ gives the line (parabolic function) described the boundary Γ_c

$$x_2 = b + \frac{4(L-b)}{L^2}(x_1 - L)^2 \tag{61}$$

where (L, b) is the parabolic vertex.

The inverse problem consists in the identification of value b which determines maximum burn depth in the domain considered.

The criterion which should be minimized is of the form [16]

$$S(b) = \frac{1}{M}\sum_{i=1}^{M}(T_i - T_{di})^2 \tag{62}$$

where T_i are the calculated temperatures. These temperatures are obtained from the direct problem solution with an estimate for unknown value of b.

Using the necessary condition of minimum, one obtains

$$\sum_{i=1}^{M} (T_i - T_{di}) U_i^k = 0 \tag{63}$$

where

$$U_i^k = \left. \frac{\partial T_i}{\partial b} \right|_{b = b^k} \tag{64}$$

are the sensitivity coefficients, k is the number of iterations; for $k = 0$, b^0 is the arbitrary assumed value of parameter b, while b^k for $k > 0$ results from the previous iteration.

Function T_i is expanded in the Taylor series about the known value of b^k, that is:

$$T_i = T_i^k + U_i^k (b^{k+1} - b^k) \tag{65}$$

Introducing (65) into (63) one obtains

$$\sum_{i=1}^{M} \left[T_i^k + U_i^k (b^{k+1} - b^k) - T_{di} \right] U_i^k = 0 \tag{66}$$

or

$$b^{k+1} = b^k + \frac{\sum_{i=1}^{M} \left(T_{di} - T_i^k \right) \left(U_i^k \right)}{\sum_{i=1}^{M} \left(U_i^k \right)^2}, \qquad k = 0, 1, 2, \ldots, K \tag{67}$$

where K is the assumed number of iterations.

It should be pointed out that in order to determine the coefficients (64) the shape sensitivity analysis [17–19] is used.

6 Shape Sensitivity Analysis

In literature one can find two basic approaches to sensitivity analysis using the boundary element method: the continuous approach and the discretized one [17, 20]. In the case of the continuous approach (explicit differentiation method) the mathematical model of sensitivity is formulated and the solution is found numerically using the BEM. The implicit differentiation method, which belongs to the

discretized approach, is based on the differentiation of algebraic boundary element matrix equations.

Here the implicit differentiation method is applied. Let us assume that b is the shape parameter. The system of Eq. (48) should be differentiated with respect to parameter b and then

$$\frac{\partial \mathbf{A}}{\partial b}\mathbf{Y} + \mathbf{A}\frac{\partial \mathbf{Y}}{\partial b} = \frac{\partial \mathbf{B}}{\partial b} \tag{68}$$

or

$$\mathbf{A}\frac{\partial \mathbf{Y}}{\partial b} = \frac{\partial \mathbf{B}}{\partial b} - \frac{\partial \mathbf{A}}{\partial b}\mathbf{Y} \tag{69}$$

It should be pointed out that the derivatives of the boundary element matrices are calculated analytically [17]. The additional problem defined by the system of Eq. (69) has been solved using the BEM (c.f. Sect. 4). The main matrix of the systems of Eqs. (48) and (69) is the same.

7 Results of Computations

At first, the direct problem is considered. In the case of the 2D problem the domain of dimensions $2L \times L$, where $L = 0.02$ m, is analyzed; in the case of the 3D problem the domain of dimensions $2L \times L \times 2L$ is taken into account. The parameter b (c.f. Eqs. (60), (61)) is equal to 0.012 m. The following input data are assumed: thermal conductivity of healthy tissue $\lambda_1 = 0.2$ W/(mK), thermal conductivity of burned tissue $\lambda_2 = 0.1$ W/(mK), blood perfusion rate $G_B = 0.5$ kg/(m^{3}s), specific heat of blood $c_B = 4200$ J/(kgK), arterial blood temperature $T_B = 37$ °C, metabolic heat source $Q_{met} = 200$ W/m^3, heat transfer coefficient $\alpha = 10$ W/(m^{2}K), ambient temperature $T_a = 20$ °C [1]. The discretization of the boundaries of healthy and burned tissue sub-domains using linear boundary elements is shown in Figs. 3 and 4, while Figs. 5 and 6 illustrate the temperature distribution in the domains considered.

In Figs. 7, 8, 9 and 10 the distributions of sensitivity functions with respect to the successive parameters are presented (2D problem).

Knowledge of the sensitivity functions allows one to estimate the changes of temperatures due to the perturbations of the parameters considered. The influence of change of a single parameter on the temperature distribution can be analyzed using the formulas

$$\Delta_1 T = U_1 \Delta\lambda_1, \quad \Delta_2 T = U_2 \Delta\lambda_2, \quad \Delta_3 T = U_3 \Delta G_B, \quad \Delta_4 T = U_4 \Delta Q_{met} \tag{70}$$

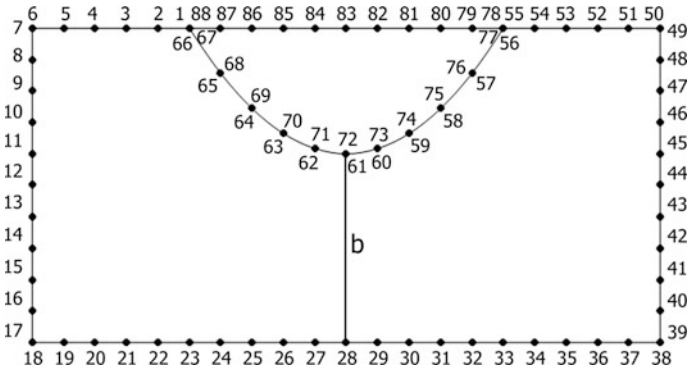

Fig. 3 Discretization of boundaries (2D problem)

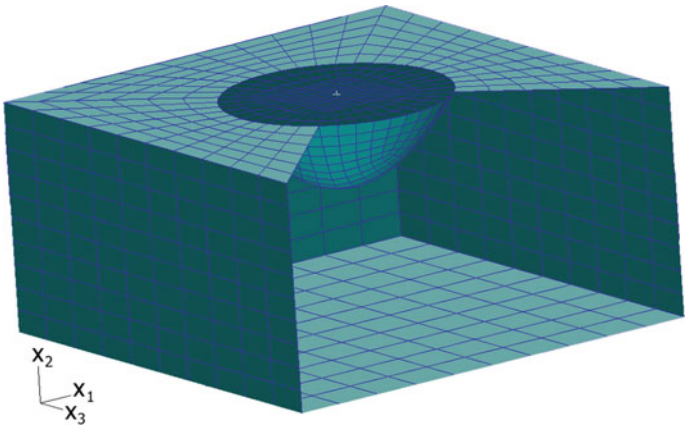

Fig. 4 Discretization of boundaries (3D problem)

Fig. 5 Temperature distribution (2D problem)

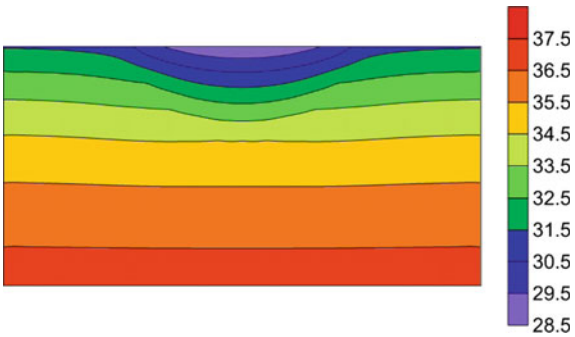

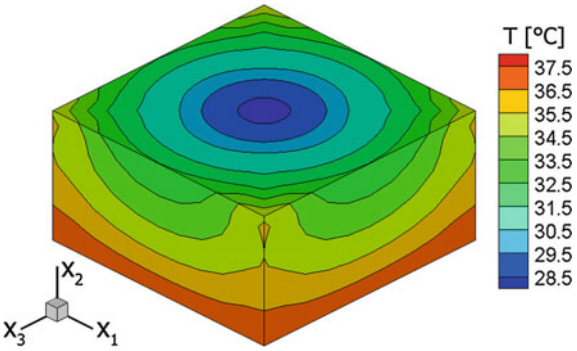

Fig. 6 Temperature distribution (3D problem)

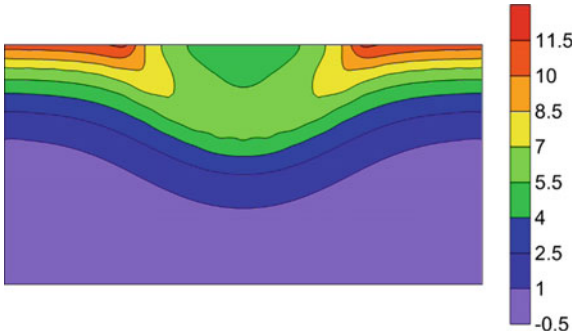

Fig. 7 Distribution of sensitivity function with respect to the parameter $p_1 = \lambda_1$

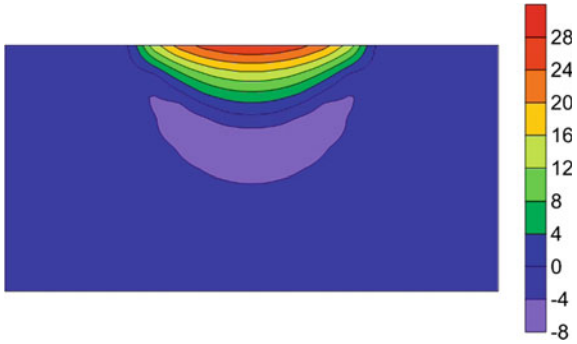

Fig. 8 Distribution of sensitivity function with respect to the parameter $p_2 = \lambda_2$

where $\Delta\lambda_1$, $\Delta\,\lambda_2$, ΔG_B and ΔQ_{met} are the assumed perturbations of parameters (e.g. $\Delta\lambda_1 = 0.1\lambda_1$). In expressions (70) the indexes associated with the sub-domains Ω_1 and Ω_2 are neglected.

In Fig. 11 the changes of temperature on the skin surface corresponding to perturbations equal to 10 % of the adopted values of the parameters are shown.

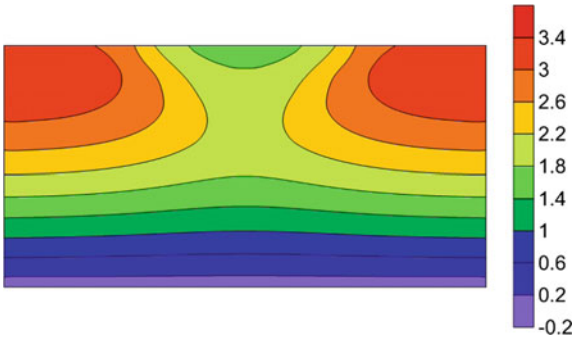

Fig. 9 Distribution of sensitivity function with respect to the parameter $p_3 = G_B$

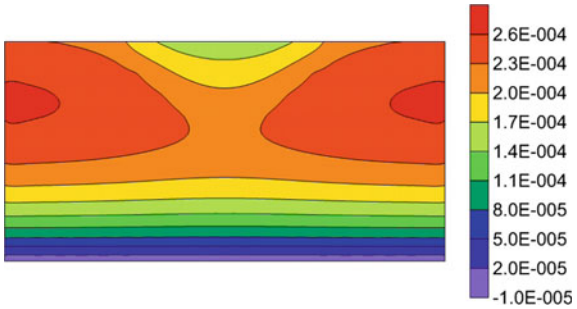

Fig. 10 Distribution of sensitivity function with respect to the parameter $p_4 = Q_{met}$

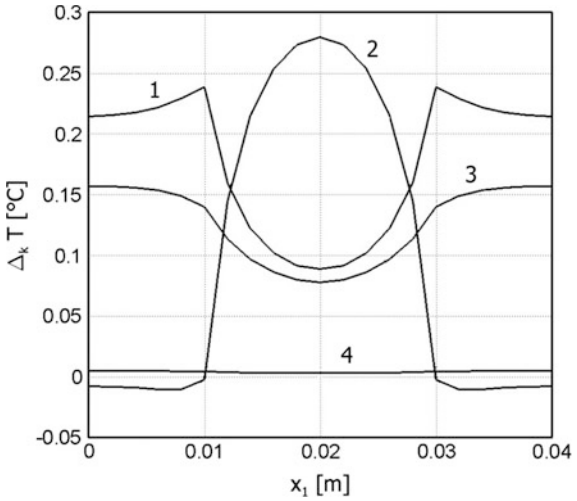

Fig. 11 Changes of temperature on the skin surface due to the 10 % perturbations of successive parameters (1 – λ_1, 2 – λ_2, 3 – G_B, 4 – Q_{met})

It is seen that the metabolic heat source capacity has a little influence in the temperature distribution, while the perturbations in the other parameters induce comparable changes in maximum temperatures of skin surface (0.15−0.28 °C).

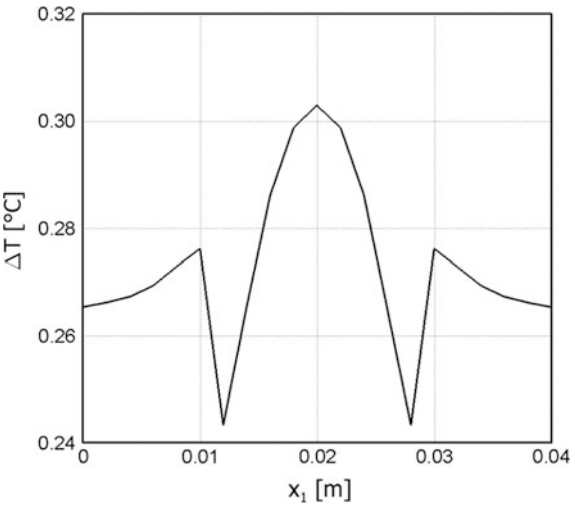

Fig. 12 Change of temperature on the skin surface due to the 10 % perturbations of all parameters

It is also possible to estimate the changes of temperature due to the simultaneous perturbations of all parameters, namely

$$\Delta T = \sqrt{(U_1 \Delta\lambda_1)^2 + (U_2 \Delta\lambda_2)^2 + (U_3 \Delta G_B)^2 + (U_4 \Delta Q_{met})^2} \tag{71}$$

In the above case, the maximum change in temperature of the skin surface caused by perturbations of all parameters is equal to 0.3 °C and corresponds to the maximum depth of burn ($x_1 = 0.02$ m), as shown in Fig. 12.

The next task is the determination of the surface position between the healthy tissue and burned region under the assumption that the temperature distribution on the skin surface is known.

In Fig. 13 the temperature distribution for different values of maximum burn depth (parameter b in Eq. (61), c.f. Fig. 3) is shown (2D problem). Using the values of temperatures at the skin surface (nodes 1–6, 50–55, 78–88) the parameter b has been estimated iteratively (Eq. (67)). In Figs. 14, 15 the results of inverse problems solution are shown. These Figures illustrate the values of parameter b for successive iterations and the curves correspond to the different initial values of parameter b^0. In all cases presented the iteration process was convergent and the exact value of b has been obtained after the several iterations.

In the case of the 3D problem, in order to identify the parameter b (c.f. Eq. (60)), the temperature distribution on the skin surface shown in Fig. 16 is used. The obtained results concerning the burn depth both in the case of the 2D solution and the 3D one are very close.

As mentioned earlier, basing on the knowledge of temperature on the skin surface, the shape of burn wound can be assessed. Using the method presented in this paper, the surface between the healthy tissue and burned region containing the unknown geometrical parameter b has been found (c.f. Eqs. (60) or (61)).

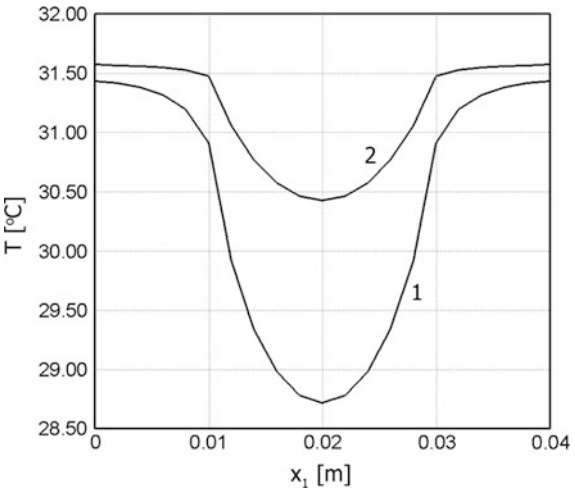

Fig. 13 Temperature distribution on the skin surface: 1 – $b = 0.012$ m, 2 – $b = 0.018$ m

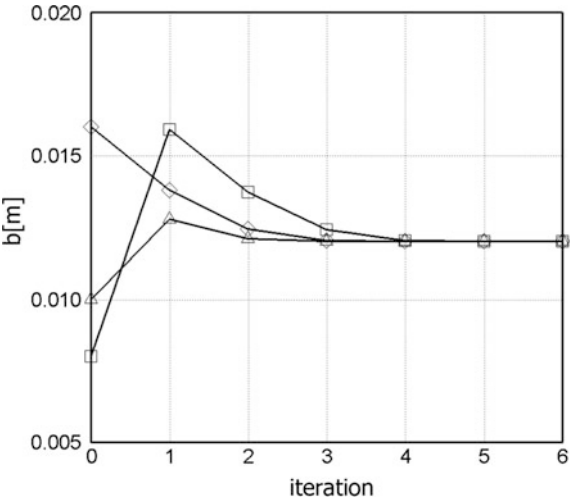

Fig. 14 Results of identification for different initial values of b^0 ($b_{real} = 0.012$ m)

The others forms of equations determining the position of border surface Γ_c can be considered. For example (in the case of 2D problem) the surface Γ_c is defined using the following function

$$x_2 = L - b \exp\left[- \frac{4(x_1 - L)^2}{L^2} \right] \tag{72}$$

On the basis of the temperature distribution on the skin surface (as shown in Fig. 17), the parameter b has been estimated as $b = 0.01$ m. In Fig. 18 the identified shape of burn wound is presented.

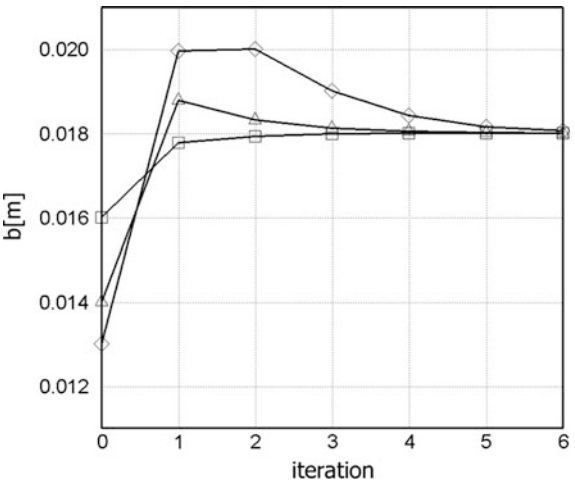

Fig. 15 Results of identification for different initial values of b^0 ($b_{real} = 0.018$ m)

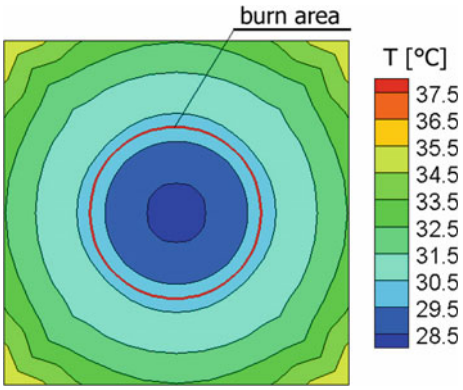

Fig. 16 Temperature distribution on the skin surface (3D problem)

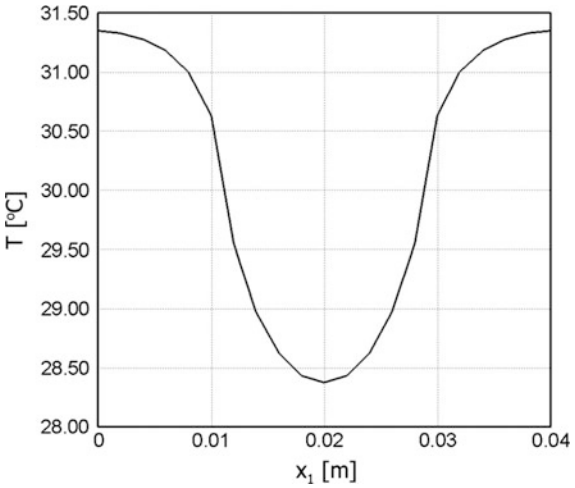

Fig. 17 Temperature distribution on the skin surface (example 2)

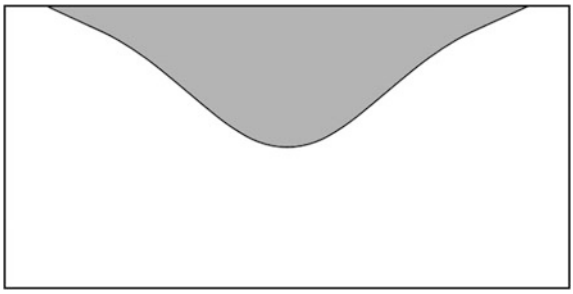

Fig. 18 Identified shape of burn wound

8 Conclusions

The application of sensitivity analysis methods in the scope of bioheat transfer problems gives essential information concerning the influence of thermophysical parameters perturbations on the changes of temperature field in the homogeneous or heterogeneous tissue domain. In this way one can estimate which parameter significantly affects the final result and which one is rather insignificant.

The possibilities of burn shape estimation on the basis of knowledge of skin surface temperature are also shown. To this end the mathematical model based on the system of two Pennes equations for burned and healthy tissue has been formulated and least square criterion has been applied. The inverse problem has been solved using the gradient method coupled with the BEM. In future, the real values of skin temperatures obtained from the experiments (thermograms) [21] will be applied.

Acknowledgements The article and research are financed within the project N R13 0124 10 sponsored by Polish National Centre for Research and Development.

References

1. Romero Mendez, R., Jimenez-Lozano, J.N., Sen, M., Gonzalez, F.J.: Analytical solution of a Pennes equation for burn-depth determination from infrared thermographs. Math. Med. Biol. **27**, 21–38 (2010). doi:10.1093/imammb/dqp010
2. Srinivas, S.M., de Boer, J.F., et al.: Determination of burn depth by polarization-sensitive optical coherence tomography, J. Biomed. Opt. **9**(1), 207–212 (2004)
3. Riordan, C.L., et al.: Noncontact laser doppler imaging in burn depth analysis of the extremities. J. Burn Care Rehabil. 177–186 (2003)
4. Rumiński, J., Kaczmarek, M., Renkielska, A., Nowakowski, A.: Thermal parametric imaging in the evaluation of skin burn depth. IEEE Trans. Biomed. Eng. **54**(2), 303–312 (2007)
5. Pennes, H.H.: Analysis of tissue and arterial blood temperatures in the resting human forearm. J. Appl. Physiol. **1**, 93–122 (1948)
6. Majchrzak, E., Dziatkiewicz, G., Paruch, M.: The modelling of heating a tissue subjected to external electromagnetic field. Acta Bioeng. Biomech. **10**(2), 29–37 (2008)

7. Majchrzak, E., Paruch, M.: Identification of electromagnetic field parameters assuring the cancer destruction during hyperthermia treatment. Inverse Probl. Sci. Eng. **19**(1), 45–58 (2011)
8. Kleiber, M.: Parameter Sensitivity. Wiley, Chichester (1997)
9. Dems, K., Rousselet, B.: Sensitivity analysis for transient heat conduction in a solid body. Struct. Optim. **17**, 36–45 (1999)
10. Jasiński, M.: Sensitivity analysis of transient bioheat transfer with perfusion rate dependent on tissue injury. Comput. Assist. Mech. Eng. Sci. **16**, 267–277 (2009)
11. Jasiński, M.: Investigation of tissue thermal damage process with application of direct sensitivity method. Mol. Cell. Biomech **10**(3), 201–232 (2013)
12. Brebbia, C.A., Dominguez, J.: Boundary Elements, An Introductory Course, CMP, McGraw-Hill Book Company, London (1992)
13. Brebbia, C.A., Telles, J.C.F., Wrobel, L.C.: Boundary Element Techniques. Springer, Berlin (1984)
14. Nowak, A.J.: Chapter 3: Solving linear heat conduction problems by the multiple reciprocity boundary element method. In: Wrobel, L.C., Brebbia, C.A. (eds.) Boundary Element Methods In Heat Transfer, pp. 63–132. Computational Mechanics Publications, Southampton, Boston (1992)
15. Paruch, M., Majchrzak, E.: Identification of tumor region parameters using evolutionary algorithm and multiple reciprocity boundary element method. Eng. Appl. Artif. Intell. **20**, 647–655 (2007)
16. Kurpisz, K., Nowak, A.J.: Inverse Thermal Problems, pp. 259–298. Computational Mechanics Publications, Southampton-Boston (1995)
17. Burczyński, T.: Sensitivity analysis, optimization and inverse problems. In: Beskos, D., Maier, G. (eds.) Boundary Element Advances in Solid Mechanics, pp. 245–307. Springer, New York (2003)
18. Tortorelli, D.A., Zixian, W.: A systematic approach to shape sensitivity analysis. Int. J. Solids Struct. 1181–1212 (1993)
19. Sokołowski, J., Zolesio, J.-P.: Introduction to Shape Optimization. Shape Sensitivity Analysis, Springer Series in Computational Mathematics, Springer (1992)
20. Mochnacki, B., Majchrzak, E.: Application of the shape sensitivity analysis in numerical modelling of solidification process. In: THERMEC'2006, Pts 1–5 Book Series: Materials Science Forum, vol. **539–543**, pp. 2524–2529 (2006)
21. Ciesielski, M., Dziewonski, M., Freus, S.:Scanning method of temperature distribution of human body by device registering encircling images. In: Desing and Computation of Modern Engineering Materials. Advanced Structured Materials, vol. 54, pp. 97–106 (2014)

Application of the hp-FEM for Hyperelastic Problems with Isotropic Damage

Jorge L. Suzuki and Marco L. Bittencourt

Abstract This work presents a damage formulation applied to hyperelastic materials in order to capture the Mullins effect, observed in rubber-like materials and biological tissues. A mixed (u/p) formulation with a pressure projection procedure is used with the *hp*-FEM to overcome the volumetric locking. The isotropic damage model uses a scalar variable that evolves coupled with the maximum attained equivalent strain. This damage variable defines a stress reduction factor, which describes the softening behavior. Cyclic loading tests were performed to reproduce the Mullins effect. Convergence analyses were made for compressible and nearly-incompressible materials imposing smooth solutions. The results presented a spectral convergence rate for the *p*-refinement. In the case of near-incompressibility, the material showed locking-free characteristics.

1 Introduction

A considerable number of engineering applications involve the use of rubber-like materials, which are usually modeled with the use of hyperelastic material models. In this sense, several phenomenological and mechanistic hyperelastic models were established to describe the material response. Among the first ones were the Neo-Hookean and Mooney-Rivlin models, which use strain energy density functions based on the deformation tensor invariants [27]. The Ogden model was developed in the decade of 1980s, and based on the principal strain directions [24]. A more recent contribution is the Fung material [13], developed in the decade of 1990s, and widely used to model biological tissues. Despite the application for engineering rubber materials, the modeling of soft tissues is of increasing interest, and these material models provide a satisfactory mechanical response [4, 25].

J.L. Suzuki · M.L. Bittencourt(✉)
University of Campinas, Cidade Universitária Zeferino Vaz, Rua Mendeleyev, 200, Campinas 13083-860, Brazil
e-mail: mlb@fem.unicamp.br

J.L. Suzuki
e-mail: jlsuzuki@fem.unicamp.br

P.A. Muñoz-Rojas (ed.), *Computational Modeling, Optimization and Manufacturing Simulation of Advanced Engineering Materials*, Advanced Structured Materials 49, DOI 10.1007/978-3-319-04265-7_6

Hyperelastic formulations are not able to predict the Mullins effect, which is characterized by the strain induced loss of stiffness observed in experimental tests [10, 23]. This behavior is achieved with the use of damage models. The first continuum damage formulation developed for hyperelasticity was the one-dimensional Gurtin-Francis model [15]. A generalization of this model for three dimensions was later introduced by [10]. Another model, based on the principle of equivalent stress [26], was developed for hyperelasticity and extended to viscoelastic models in a fully three-dimensional context.

Compressible formulations are of simple implementation and stable. However, they are inaccurate when close to incompressible behavior. For this purpose, nearly-incompressible formulations are used. However, they suffer volumetric locking without proper treatment in the FEM. For Poisson ration $\nu \rightarrow 0.5$, only very small volumetric deformations are allowed [19]. That yields, for conventional low order FEM, small, moderate or very high errors for the displacements. Additionally, due to the high bulk modulus K, the errors for the stresses become very high [2, 16].

Several solution strategies were proposed to overcome the volumetric locking phenomenon. The most known are the Selective Reduced Integration [12], B-bar method [19] and F-bar method [9]. The methodology used in this work is a mixed (u/p) formulation with a pressure projection procedure introduced by [7]. The strain energy density is separated into deviatoric and volumetric parts, the pressure is kinematically coupled to the displacements in a weak sense, and volumetric strains are limited with the enforcement of a high bulk modulus, which acts as a penalty factor. A projection is performed in a least squares sense at the element level onto an appropriate pressure field. The pressure variable is assumed discontinuous between the element boundaries, and thus there is no need to solve it globally [7, 29]. Another advantage relies on the fact that the local treatment for the pressure makes the methodology simpler to implement in a displacement only FE code.

The high-order FEM is a version that uses high-order polynomials to interpolate the variables. In this context, the p-FEM version considers only the increase of polynomial order, keeping the element size. The hp-FEM considers the combination of higher order polynomials with the increase of the number of elements. The high-order FEM provides a locking-free behavior for nearly-incompressible problems [16, 29], and shows spectral convergence rate for smooth solutions [11, 21]. It also permits the use of elements with higher/lower aspect ratio. Some recent applications of the high-order FEM include transient problems [11], fluid dynamics [21], structural analysis [28], powder metallurgy [17], plasticity [14] and contact [22].

In this work we used the hp-version for treating nearly-incompressible hyperelastic problems with damage. The volumetric locking is avoided with the use of high-order polynomials and the mixed method [7]. The damage is introduced as a scalar variable, following the works of [18, 26] to reproduce the Mullins Effect. Then we investigate the coupled effect of near-incompressibility and damage over the approximate solution when increasing the interpolation order.

This work is organized as follows: in Sect. 2 we present the compressible Neo-Hookean and nearly-incompressible hyperelastic Mooney-Rivlin materials with the deviatoric/volumetric separation, followed by the principle of virtual power, pres-

sure projection procedure and discretization [7, 29]. Section 3 presents the damage model, the modified stress and the resulting constitutive relations [18, 26]. The obtained results are reported in Sect. 4, where three convergence tests are analyzed. The first validates the nearly-incompressible formulation for small and large strains. The second focuses the reproduction of the Mullins effect followed by a convergence analysis for the compressible Neo-Hookean material. The third studies the convergence of the nearly-incompressible Mooney-Rivlin material with damage, where we impose a high bulk modulus and analyze the errors for the displacements, stresses and damage.

2 Hyperelasticity

In isotropic hyperelasticity, we can define a strain energy function W, which is dependent on the right Cauchy-Green deformation tensor $\mathbf{C}$ (when using a total Lagrangian description), in terms of its invariants I_1, I_2, I_3. Moreover, considering material homogeneity, W is independent of material points $\mathbf{X}$, and thus [5]

$$W(\mathbf{C}) = W(I_1, I_2, I_3). \tag{1}$$

The second Piola-Kirchhoff stress tensor can be obtained from the following expression

$$\mathbf{S} = 2\frac{\partial W}{\partial \mathbf{C}} = \frac{\partial W}{\partial \mathbf{E}}, \tag{2}$$

where $\mathbf{E}$ is the Green-Lagrange strain tensor. The fourth-order constitutive tensor is defined as

$$\boldsymbol{C} = 2\frac{\partial \mathbf{S}}{\partial \mathbf{C}} = \frac{\partial \mathbf{S}}{\partial \mathbf{E}}. \tag{3}$$

The above equations will be used in the next sections to define the constitutive terms for the compressible and nearly-incompressible formulations, where the latter will have a special treatment for the deviatoric and volumetric parts.

2.1 Compressible Neo-Hookean Material

The Neo-Hookean material is an extension of Hooke's law for large strains [3]. The associated strain energy function for compressible behavior is

$$W(\mathbf{C}) = \frac{\lambda}{2}(\ln J)^2 - \mu \ln J + \frac{1}{2}\mu(\mathrm{tr}\mathbf{C} - 3), \tag{4}$$

where λ and μ are the Lamé parameters and $J = \det \mathbf{F}$, where $\mathbf{F}$ is the deformation gradient tensor. We use Eq. 2 to obtain the second Piola-Kirchhoff stress tensor as [5]

$$\mathbf{S} = \lambda \ln J \mathbf{C}^{-1} + \mu \left(\mathbf{I} - \mathbf{C}^{-1} \right). \tag{5}$$

Using Eq. 3 we obtain the fourth order constitutive tensor

$$\boldsymbol{\mathcal{C}} = \lambda \mathbf{C}^{-1} \otimes \mathbf{C}^{-1} + 2 \left(\mu - \lambda \ln J \right) \boldsymbol{\mathcal{I}}, \tag{6}$$

where $\boldsymbol{\mathcal{I}}$ is the fourth-order tensor given by

$$\boldsymbol{\mathcal{I}} = -\frac{\partial \mathbf{C}^{-1}}{\partial \mathbf{C}} = -\mathbf{C}^{-1} \otimes \mathbf{C}^{-1}. \tag{7}$$

Substituting Eq. 7 into Eq. 6 and rearranging the terms, we obtain

$$\boldsymbol{\mathcal{C}} = \left[2\mu + \lambda \left(1 - \ln J \right) \right] \mathbf{C}^{-1} \otimes \mathbf{C}^{-1}. \tag{8}$$

The constitutive Eq. (8) can be used directly in a pure-displacement nonlinear FEM code to describe compressible behavior. However, unrealistic results are obtained if the Poisson ratio gets close to 0.5. To model materials close to the incompressible limit we need special treatment for the hydrostatic pressure. We define initially the strain energy potential from the purely incompressible state and introduce a small amount of compressibility, making the formulation nearly-incompressible. This procedure will be considered in the next section.

2.2 *Nearly-Incompressible Mooney-Rivlin Material*

For the purely incompressible state ($J = 1$), the strain energy function of the Mooney-Rivlin material is given by [27]

$$W\left(I_1, I_2\right) = A_{10}\left(I_1 - 3\right) + A_{01}\left(I_2 - 3\right), \tag{9}$$

with the material parameters A_{10} and A_{01}, which are related with the shear modulus G for small strain in the following way:

$$G = 2\left(A_{10} + A_{01}\right). \tag{10}$$

A small amount of compressibility can be considered, allowing us to rewrite Eq. 9 in the nearly-incompressible form [27]:

$$W\left(I_1, I_2, J\right) = \bar{W}\left(I_1, I_2\right) + \tilde{W}\left(J\right), \tag{11}$$

where the terms

$$\bar{W}\left(I_1, I_2\right) = A_{10}\left(I_1 J^{-2/3} - 3\right) + A_{01}\left(I_2 J^{-4/3} - 3\right), \tag{12}$$

$$\tilde{W}(J) = \frac{K}{2}(J-1)^2, \tag{13}$$

respectively represent the deviatoric and volumetric strain energy functions. The above regularization introduces the bulk modulus K to the volumetric part, and makes the strain energy dependent on the three invariants of $\mathbf{C}$. Notice that when $J = 1$, there is no volume change and perfect incompressibility is recovered. In linear elasticity, the following relation is valid [19]:

$$\frac{K}{G} = \frac{2(1+\nu)}{3(1-2\nu)}. \tag{14}$$

When $\nu \to 0.5$, we obtain $K/G \to \infty$ (see Fig. 1), which indicates greater tendency to deviatoric rather than volumetric strains. The hydrostatic pressure is kinematically coupled to the displacements as

$$p = \frac{\partial \tilde{W}}{\partial J}, \tag{15}$$

which yields the following linear relationship

$$p = K(J-1). \tag{16}$$

Applying the deviatoric/volumetric split, the second Piola-Kirchhoff stress tensor is represented by

$$\mathbf{S} = \bar{\mathbf{S}} + \tilde{\mathbf{S}}, \tag{17}$$

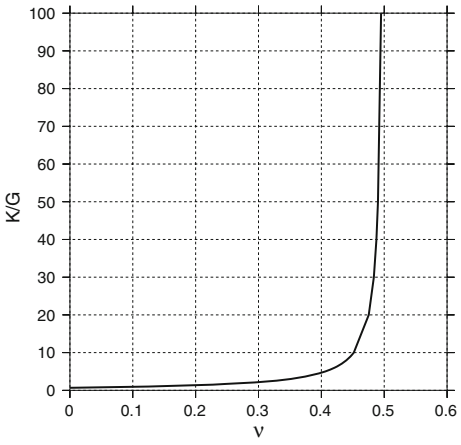

Fig. 1 Ratio K/G in terms of the Poisson ratio. Notice the sudden increase when the Poisson ratio goes to 0.5. This increasing behavior leads to large internal forces due to the enforcement of very small volumetric strains

where the deviatoric $\bar{\mathbf{S}}$ and volumetric $\tilde{\mathbf{S}}$ stress tensors are given by

$$\bar{\mathbf{S}} = 2A_{10}J^{-2/3}\mathbf{I} + 4A_{01}J^{-4/3}\left(I_1\mathbf{I} - \mathbf{C}\right) + \left(-\frac{2}{3}A_{10}I_1J^{-2/3} - \frac{4}{3}A_{01}I_2J^{-4/3}\right)\mathbf{C}^{-1}, \tag{18}$$

$$\tilde{\mathbf{S}} = Jp\mathbf{C}^{-1}. \tag{19}$$

The fourth-order constitutive tensor is obtained from Eq. 3, where we split the deviatoric and volumetric terms in the following way:

$$\boldsymbol{\mathcal{C}} = \bar{\boldsymbol{\mathcal{C}}} + \tilde{\boldsymbol{\mathcal{C}}}. \tag{20}$$

The term $\tilde{\boldsymbol{\mathcal{C}}}$ is obtained by applying the product rule when taking the directional derivative of Eq. 19:

$$\tilde{\boldsymbol{\mathcal{C}}} = \tilde{\boldsymbol{\mathcal{C}}}^{\mathbf{1}} + \tilde{\boldsymbol{\mathcal{C}}}^{\mathbf{2}} = 2\frac{\partial\left(J\mathbf{C}^{-1}\right)}{\partial\mathbf{C}}p + 2J\mathbf{C}^{-1}\otimes\frac{\partial p}{\partial\mathbf{C}}, \tag{21}$$

with

$$\tilde{\boldsymbol{\mathcal{C}}}^{\mathbf{1}} = 2\frac{\partial\left(J\mathbf{C}^{-1}\right)}{\partial\mathbf{C}}p = -pJ\mathbf{C}^{-1}\otimes\mathbf{C}^{-1} \tag{22}$$

$$\tilde{\boldsymbol{\mathcal{C}}}^{\mathbf{2}} = 2J\mathbf{C}^{-1}\otimes\frac{\partial p}{\partial\mathbf{C}} = \left(J\mathbf{C}^{-1}\right)\otimes\left(KJ\mathbf{C}^{-1}\right). \tag{23}$$

In the above equations, we wrote the second volumetric part $\tilde{\boldsymbol{\mathcal{C}}}^{2}$ with the separate Jacobian terms in the tensor product for convenience, as will be presented in the next section, where we apply the Principle of Virtual Power (PVP) and linearize it using directional derivative.

2.3 *Principle of Virtual Power (PVP)*

After the definition of the material constitutive tensors, we write the total power by unit of volume in a total Lagrangian formulation as [7]

$$\dot{W} = \dot{W}_{\text{int}} - \dot{W}_{\text{ext}} = \int_{\Omega}\bar{W}_{int}d\Omega + \int_{\Omega}\tilde{W}_{int}d\Omega - \dot{W}_{\text{ext}}, \tag{24}$$

where $\dot{W}_{ext}$ is the external power. The internal power $\dot{W}_{int}$ is split in the deviatoric and volumetric parts. Applying the Principle of Virtual Power, there is an equilibrium state ϕ with kinematically admissible virtual velocities $\delta\mathbf{v}$, where

$$\delta\dot{W}(\phi, \delta\mathbf{v}) = \delta\dot{W}_{\text{int}} - \delta\dot{W}_{\text{ext}} = 0. \tag{25}$$

The internal power $\delta\dot{W}_{\text{int}}$ is

$$\delta\dot{W}_{\text{int}} = \int_{\Omega} \bar{\mathbf{S}} \,:\, \delta\dot{\mathbf{E}} d\Omega + \int_{\Omega} \tilde{\mathbf{S}} \,:\, \delta\dot{\mathbf{E}} d\Omega, \tag{26}$$

and $\delta\dot{W}_{\text{ext}}$ is given by

$$\delta\dot{W}_{\text{ext}} = \int_{\Omega} \mathbf{f} \cdot \delta\mathbf{v} d\Omega + \int_{\Gamma} \mathbf{t} \cdot \delta\mathbf{v} d\Gamma, \tag{27}$$

with $\mathbf{f}$ and $\mathbf{t}$ respectively the body and surface forces. To treat the near-incompressi bility and define the mixed method, the power functional of Eq. 24 is perturbed in the following way [5]:

$$\dot{W}_1 = \dot{W}_{\text{int}} - \dot{W}_{\text{ext}} - \dot{W}_K = \int_{\Omega} \bar{W}_{int} d\Omega + \int_{\Omega} \tilde{W}_{int} d\Omega - W_{\text{ext}} - \int_{\Omega} \frac{1}{2K} p^2 \, d\Omega, \tag{28}$$

where the bulk modulus K acts as a penalty factor, so that $\dot{W}_1 \to \dot{W}$ when $K \to \infty$. The directional derivative of the perturbed functional relative to the admissible virtual pressures δp is given by [5, 29]

$$\int_{\Omega} (J-1)\delta p d\Omega = \frac{1}{K} \int_{\Omega} p \delta p d\Omega, \quad \forall\, \delta p \in L^2, \tag{29}$$

with L^2 being the Hilbert space with square integrable functions. Notice that in Eq. 29, as K approaches sufficiently high values, the condition $J \approx 1$ is enforced, reducing the volumetric strain as much as possible and thus defining the nearly-incompressible behavior. Therefore, the inclusion of the above constraint completes the mixed formulation.

2.4 Linearization of the Weak Form

In this section, we obtain the linearized form of the PVP, which will be later discretized to obtain the FE stiffness matrices. To linearize the equations, we apply the directional derivative on Eq. 25 for an increment $\boldsymbol{\Delta}\mathbf{u}$ [5], that is,

$$\mathcal{D}\delta\dot{W}(\phi, \delta\mathbf{v})[\boldsymbol{\Delta}\mathbf{u}] = \mathcal{D}\delta\dot{W}_{\text{int}}(\phi, \delta\mathbf{v})[\boldsymbol{\Delta}\mathbf{u}] - \mathcal{D}\delta\dot{W}_{\text{ext}}(\phi, \delta\mathbf{v})[\boldsymbol{\Delta}\mathbf{u}]. \tag{30}$$

As we are not treating follower loads in this formulation, the virtual external power is assumed to be strain-independent, and thus

$$\mathcal{D}\delta\dot{W}_{\text{ext}}\left(\phi,\delta\mathbf{v}\right)\left[\Delta\mathbf{u}\right]=0. \tag{31}$$

The internal power of Eq. 30 is split into deviatoric and volumetric contributions by means of the stress tensor as

$$\mathcal{D}\delta\dot{W}_{\text{int}}\left(\phi,\delta\mathbf{v}\right)\left[\Delta\mathbf{u}\right]=\int_{\Omega}\mathcal{D}\left(\bar{\mathbf{S}}\,:\,\delta\dot{\mathbf{E}}\right)\left[\Delta\mathbf{u}\right]\,\mathrm{d}\Omega+\int_{\Omega}\mathcal{D}\left(\tilde{\mathbf{S}}\,:\,\delta\dot{\mathbf{E}}\right)\left[\Delta\mathbf{u}\right]\,\mathrm{d}\Omega, \tag{32}$$

where $\delta\dot{\mathbf{E}}$ is the Green-Lagrange strain rate tensor, which is a function of the virtual velocities $\delta\mathbf{v}$ and configuration ϕ, and is given by

$$\delta\dot{\mathbf{E}}\left(\phi,\delta\mathbf{v}\right)=\frac{1}{2}\left(\delta\dot{\mathbf{F}}^{T}\mathbf{F}+\mathbf{F}^{T}\delta\dot{\mathbf{F}}\right), \tag{33}$$

with the rate of the deformation gradient

$$\delta\dot{\mathbf{F}}\left(\delta\mathbf{v}\right)=\boldsymbol{\nabla}_{0}\delta\mathbf{v}. \tag{34}$$

Substituting Eq. 34 into Eq. 33, we obtain

$$\delta\dot{\mathbf{E}}\left(\phi,\delta\mathbf{v}\right)=\frac{1}{2}\left[\left(\boldsymbol{\nabla}_{0}\delta\mathbf{v}\right)^{T}\mathbf{F}+\mathbf{F}^{T}\left(\boldsymbol{\nabla}_{0}\delta\mathbf{v}\right)\right], \tag{35}$$

We first focus on the first term of the right-hand side of Eq. 32, which represents the deviatoric part. Using the product rule, we obtain

$$\int_{\Omega}\mathcal{D}\left(\bar{\mathbf{S}}\,:\,\delta\dot{\mathbf{E}}\right)\left[\Delta\mathbf{u}\right]\,\mathrm{d}\Omega=\int_{\Omega}\delta\dot{\mathbf{E}}\,:\,\mathcal{D}\bar{\mathbf{S}}\left[\Delta\mathbf{u}\right]\,\mathrm{d}\Omega+\int_{\Omega}\bar{\mathbf{S}}\,:\,\mathcal{D}\delta\dot{\mathbf{E}}\left[\Delta\mathbf{u}\right]\,\mathrm{d}\Omega. \tag{36}$$

We substitute the derivative $\mathcal{D}\bar{\mathbf{S}}\left[\Delta\mathbf{u}\right]$ in the above equation by the constitutive relation $\bar{\mathbf{S}}=\bar{\boldsymbol{C}}\,:\,\mathbf{E}$ to obtain

$$\int_{\Omega}\mathcal{D}\left(\bar{\mathbf{S}}\,:\,\delta\dot{\mathbf{E}}\right)\left[\Delta\mathbf{u}\right]\,\mathrm{d}\Omega=\int_{\Omega}\delta\dot{\mathbf{E}}\,:\,\bar{\boldsymbol{C}}\,:\,\mathcal{D}\mathbf{E}\left[\Delta\mathbf{u}\right]\,\mathrm{d}\Omega+\int_{\Omega}\bar{\mathbf{S}}\,:\,\mathcal{D}\delta\dot{\mathbf{E}}\left[\Delta\mathbf{u}\right]\,\mathrm{d}\Omega, \tag{37}$$

where the linearized Green-Lagrange strain tensor is given by

$$\mathcal{D}\mathbf{E}\left[\Delta\mathbf{u}\right]=\frac{1}{2}\left(\mathbf{F}^{T}\mathcal{D}\mathbf{F}\left[\Delta\mathbf{u}\right]+\mathcal{D}\mathbf{F}^{T}\left[\Delta\mathbf{u}\right]\mathbf{F}\right). \tag{38}$$

The term $\mathcal{D}\mathbf{F}[\Delta\mathbf{u}]$ is the linearized deformation gradient with respect to the initial configuration [5]:

$$\mathcal{D}\mathbf{F}[\Delta\mathbf{u}] = \nabla_0 \Delta\mathbf{u}. \tag{39}$$

Substituting Eq. 39 into Eq. 38, we obtain

$$\mathcal{D}\mathbf{E}[\Delta\mathbf{u}] = \frac{1}{2}\left[\mathbf{F}^T\left(\nabla_0\Delta\mathbf{u}\right) + \left(\nabla_0\Delta\mathbf{u}\right)^T\mathbf{F}\right]. \tag{40}$$

The linearized Green-Lagrange strain rate $\mathcal{D}\delta\dot{\mathbf{E}}[\Delta\mathbf{u}]$ is obtained by taking the directional derivative of Eq. 35:

$$\mathcal{D}\delta\dot{\mathbf{E}}[\Delta\mathbf{u}] = \frac{1}{2}\left[\left(\nabla_0\delta\mathbf{v}\right)^T\left(\nabla_0\Delta\mathbf{u}\right) + \left(\nabla_0\Delta\mathbf{u}\right)^T\left(\nabla_0\delta\mathbf{v}\right)\right]. \tag{41}$$

Notice that the gradient of the virtual velocities $\nabla_0\delta\mathbf{v}$ is independent of the configuration ϕ, and thus we can rewrite the above equation as [5]

$$\mathcal{D}\delta\dot{\mathbf{E}}[\Delta\mathbf{u}] = \left(\nabla_0\Delta\mathbf{u}\right)^T\left(\nabla_0\delta\mathbf{v}\right). \tag{42}$$

Substituting Eqs. 40 and 42 into Eq. 37, we obtain the linearized form of the deviatoric part of the PVP,

$$\int_\Omega \mathcal{D}\left(\bar{\mathbf{S}} : \delta\dot{\mathbf{E}}\right)[\Delta\mathbf{u}]\,\mathrm{d}\Omega = \int_\Omega \bar{\mathbf{S}} : \left[\left(\nabla_0\Delta\mathbf{u}\right)^T\left(\nabla_0\delta\mathbf{v}\right)\right] d\Omega \tag{43}$$

$$+\int_\Omega \frac{1}{2}\left[\left(\nabla_0\delta\mathbf{v}\right)^T\mathbf{F} + \mathbf{F}^T\left(\nabla_0\delta\mathbf{v}\right)\right] : \bar{\mathbf{C}} : \frac{1}{2}\left[\left(\nabla_0\Delta\mathbf{u}\right)^T\mathbf{F} + \mathbf{F}^T\left(\nabla_0\Delta\mathbf{u}\right)\right] d\Omega.$$

The linearization of the volumetric part can be obtained by just exchanging $\bar{\mathbf{S}}$ by $\tilde{\mathbf{S}}$ and $\bar{\mathbf{C}}$ by $\tilde{\mathbf{C}}$ to obtain

$$\int_\Omega \mathcal{D}\left(\tilde{\mathbf{S}} : \delta\dot{\mathbf{E}}\right)[\Delta\mathbf{u}]\,\mathrm{d}\Omega = \int_\Omega \tilde{\mathbf{S}} : \left[\left(\nabla_0\Delta\mathbf{u}\right)^T\left(\nabla_0\delta\mathbf{v}\right)\right] d\Omega \tag{44}$$

$$+\int_\Omega \frac{1}{2}\left[\left(\nabla_0\delta\mathbf{v}\right)^T\mathbf{F} + \mathbf{F}^T\left(\nabla_0\delta\mathbf{v}\right)\right] : \left(\tilde{\mathbf{C}}^1 + \tilde{\mathbf{C}}^2\right)$$

$$: \frac{1}{2}\left[\left(\nabla_0\Delta\mathbf{u}\right)^T\mathbf{F} + \mathbf{F}^T\left(\nabla_0\Delta\mathbf{u}\right)\right] d\Omega. \tag{45}$$

The total linearized internal work is obtained by substituting Eqs. 43 and 44 into Eq. 32:

$$\mathcal{D}\delta W(\phi, \delta\mathbf{v})[\Delta\mathbf{u}] = \int_\Omega \left(\bar{\mathbf{S}} + \tilde{\mathbf{S}}\right) : \left[\left(\nabla_0\Delta\mathbf{u}\right)^T\nabla_0\delta\mathbf{v}\right] d\Omega \tag{46}$$

$$+\int_{\Omega}\frac{1}{2}\left[\mathbf{F}^{T}\left(\boldsymbol{\nabla}_{0}\delta\mathbf{v}\right)+\mathbf{F}\left(\boldsymbol{\nabla}_{0}\delta\mathbf{v}\right)^{T}\right]\;:\;\left(\bar{\boldsymbol{C}}+\tilde{\boldsymbol{C}}^{1}+\tilde{\boldsymbol{C}}^{2}\right)$$
$$:\frac{1}{2}\left[\mathbf{F}^{T}\left(\boldsymbol{\nabla}_{0}\Delta\mathbf{u}\right)+\mathbf{F}\left(\boldsymbol{\nabla}_{0}\Delta\mathbf{u}\right)^{T}\right]d\Omega. \tag{47}$$

We can substitute the volumetric term $\tilde{\boldsymbol{C}}^{2}$ from Eq. 23 into the above equation and rewrite it in the following way:

$$\mathcal{D}\delta W\left(\boldsymbol{\phi},\delta\mathbf{v}\right)[\Delta\mathbf{u}]=\int_{\Omega}\left(\bar{\mathbf{S}}+\tilde{\mathbf{S}}\right)\;:\;\left[\left(\boldsymbol{\nabla}_{0}\Delta\mathbf{u}\right)^{T}\boldsymbol{\nabla}_{0}\delta\mathbf{v}\right]d\Omega \tag{48}$$
$$+\int_{\Omega}\frac{1}{2}\left[\mathbf{F}^{T}\left(\boldsymbol{\nabla}_{0}\delta\mathbf{v}\right)+\mathbf{F}\left(\boldsymbol{\nabla}_{0}\delta\mathbf{v}\right)^{T}\right]\;:\;\left(\bar{\boldsymbol{C}}+\tilde{\boldsymbol{C}}^{1}\right)\;:\;\frac{1}{2}\left[\mathbf{F}^{T}\left(\boldsymbol{\nabla}_{0}\Delta\mathbf{u}\right)+\mathbf{F}\left(\boldsymbol{\nabla}_{0}\Delta\mathbf{u}\right)^{T}\right]d\Omega$$
$$+\int_{\Omega}\frac{1}{2}\left[\mathbf{F}^{T}\left(\boldsymbol{\nabla}_{0}\delta\mathbf{v}\right)+\mathbf{F}\left(\boldsymbol{\nabla}_{0}\delta\mathbf{v}\right)^{T}\right]\;:\;J\mathbf{C}^{-1}\Delta p\,d\Omega.$$

The term Δp is the pressure increment defined by

$$\Delta p=\frac{1}{2}KJ\mathbf{C}^{-1}\;:\;\left[\mathbf{F}^{T}\left(\boldsymbol{\nabla}_{0}\Delta\mathbf{u}\right)+\mathbf{F}\left(\boldsymbol{\nabla}_{0}\Delta\mathbf{u}\right)^{T}\right]. \tag{49}$$

The above pressure increment will be part of the pressure projection procedure, which will be performed in Sect. 2.7. The third integral in the right-hand side of Eq. 48 will represent, after the pressure projection and FE discretization, the symmetric pressure stiffness matrix.

2.5 High-Order Shape Functions

We use Lagrange polynomials $h_i(\xi)$ to construct the shape functions $N_a(\xi)$ to interpolate the kinematic variables. The pressure interpolation will be presented in Sect. 2.7, and the shape functions for pressure are indicated as $Q_a(\xi)$ for convenience. We use Gauss-Lobatto-Legendre collocation points for the nodal coordinates, which provides an efficient expansion for high-order polynomials, without the oscillations and ill-conditioning observed when using equally-spaced points [21].

Let $-1\leq\xi\leq 1$ be the local coordinate system and P a given polynomial order. Thus we have $n=P+1$ nodal coordinates ξ_b $(0\leq b\leq P)$. The expression for the Lagrange polynomials for a node a is

$$N_a^P(\xi)=h_a^P(\xi)=\frac{\Pi_{b=0,b\neq a}^{n}(\xi-\xi_b)}{\Pi_{b=0,b\neq a}^{n}(\xi_a-\xi_b)}. \tag{50}$$

For instance, the shape functions for $n = (P+1)^3$ nodes of the hexahedrical element are given by the following tensor product

$$N_a(\xi,\eta,\zeta) = h_i^P(\xi)h_j^P(\eta)h_k^P(\zeta), \quad a = 1,\ldots,n. \tag{51}$$

In the next section, we apply the above shape functions to the FE discretization.

2.6 Local Finite Element Discretization

Using isoparametric elements, the discretization of the material coordinates $\mathbf{X}$ representing the undeformed configuration is given by

$$\mathbf{X} = \sum_{a=1}^{n} N_a(\xi,\eta,\zeta)\,\mathbf{X}_a \text{ or } \mathbf{X} = \mathbf{N}_a^T\mathbf{X}_a, \tag{52}$$

where n is the number of element nodes and $\mathbf{X}_a$ are the nodal coordinates in the undeformed state. The nodal displacements $\mathbf{u}_a$ are interpolated analogously

$$\mathbf{u} = \sum_{a=1}^{n} N_a(\xi,\eta,\zeta)\,\mathbf{u}_a \text{ or } \mathbf{u} = \mathbf{N}_a^T\mathbf{u}_a \tag{53}$$

The interpolated nodal virtual velocities are

$$\delta\mathbf{v} = \sum_{a=1}^{n} N_a(\xi,\eta,\zeta)\,\delta\mathbf{v}_a \text{ or } \delta\mathbf{v} = \mathbf{N}_a^T\delta\mathbf{v}_a, \tag{54}$$

where $\delta\mathbf{v}_a$ are the nodal virtual velocities. The interpolated displacement increments are:

$$\Delta\mathbf{u} = \sum_{a=1}^{n} N_a(\xi,\eta,\zeta)\,\Delta\mathbf{u}_a \text{ or } \Delta\mathbf{u} = \mathbf{N}_a^T\Delta\mathbf{u}_a, \tag{55}$$

where $\Delta\mathbf{u}_a$ are the nodal displacement increments. The above discretized variables will be substituted in the linearized equations defined in Sect. 2.4 and in the incremental pressure to be defined in the next section, in order to obtain the element stiffness matrices.

2.7 Local Pressure Projection

The pressure projection procedure is performed at the element level, and thus the variables are accompanied by the subscript ^{e}. The projected variables are represented

by the subscript *. Also, the shape functions used to interpolate the displacements are denoted by $\mathbf{N}$, with interpolation order O_u. In the case of pressure, we denote the shape functions as $\mathbf{Q}$ and the interpolation order as O_p.

Consider the approximation of $p^e(\mathbf{X})$ denoted here in the undeformed configuration, in a least squares sense using a linear combination of functions $\mathbf{Q} = \left\{Q_1(\mathbf{X}), Q_2(\mathbf{X}), \ldots, Q_n(\mathbf{X})\right\}$ in L^2. Hence, we should find the pressure coefficients $\mathbf{p}^e = \left[p_1^e, p_2^e, \ldots, p_n^e\right]$ that minimize [7]:

$$\phi(\mathbf{p}^e) = ||p^e - \mathbf{Q}\mathbf{p}^e||^2_{L_2(\Omega^e)}. \tag{56}$$

The term $p^e - \mathbf{Q}\mathbf{p}^e$ is the pressure residual defined by

$$R = p^e - \mathbf{Q}\mathbf{p}^e. \tag{57}$$

Applying the least squares method, we obtain the following projection problem:

$$\frac{\partial ||R||^2}{\partial \mathbf{p}^e} = \int_{\Omega^e} \frac{\partial R^2}{\partial \mathbf{p}^e} d\Omega^e = 0. \tag{58}$$

Substituting the pressure residual of Eq. 57 into Eq. 58, and taking the derivative, we obtain

$$2\int_{\Omega^e} \left(-\mathbf{Q}^T p^e + \mathbf{Q}^T\mathbf{Q}\mathbf{p}^e\right)\, d\Omega^e = 0, \tag{59}$$

which implies that the integrand must be zero to satisfy the equality. Therefore, we obtain the following linear system:

$$\mathbf{M}^e\mathbf{p}^e = \mathbf{F}^e, \tag{60}$$

where $\mathbf{M}^e$ is a projection matrix and $\mathbf{F}^e$ is the right hand side vector containing the pressure

$$\mathbf{M}^e = \int_{\Omega^e} \mathbf{Q}^T\mathbf{Q}\, d\Omega^e, \tag{61}$$

$$\mathbf{F}^e = \int_{\Omega^e} \mathbf{Q}^T p^e\, d\Omega^e. \tag{62}$$

The element projection matrix $[\mathbf{M}^e]$, also known as the mass matrix [21], has rank $N_p^e \times N_p^e$:

$$\left[\mathbf{M}_p^e\right] = \begin{bmatrix} m_{11} & \cdots & m_{1N_p^e} \\ \vdots & \ddots & \vdots \\ m_{N_p^e 1} & \cdots & m_{N_p^e N_p^e} \end{bmatrix}, \; m_{ij} = \int_{\Omega^e} Q_i Q_j\, d\Omega^e. \tag{63}$$

The force vector $\{\mathbf{F}^e\}$ has dimension N_p^e, and is given by

$$\begin{aligned}\{\mathbf{F}^e\} &= \left[\int_{\Omega^e} Q_1 p^e \, d\Omega^e, \int_{\Omega^e} Q_2 p^e \, d\Omega^e, \ldots, \int_{\Omega^e} Q_{N_p^e} p^e \, d\Omega^e\right]^T \\ &= K\left[\int_{\Omega^e} Q_1 (J-1) \, d\Omega^e, \int_{\Omega^e} Q_2 (J-1) \, d\Omega^e, \ldots, \int_{\Omega^e} Q_{N_p^e} (J-1) \, d\Omega^e\right]^T.\end{aligned} \tag{64}$$

Therefore, the projected hydrostatic pressure at the element level is

$$p^{e*} = \mathbf{Q}\mathbf{p}^e = \mathbf{Q}\left(\mathbf{M}^e\right)^{-1}\mathbf{F}^e. \tag{65}$$

The hydrostatic pressure increment Δp defined in Eq. 49 is also projected for algorithmic consistency. Thus, we should minimize

$$\phi\left(\Delta\mathbf{p}^e\right) = ||\Delta p^e - \mathbf{Q}\Delta\mathbf{p}^e||^2_{L_2(\Omega^e)}. \tag{66}$$

Applying the projection problem of Eq. 58 for $\Delta\mathbf{p}^e$, and recalling Eqs. 49 and 55, we obtain

$$2\int_{\Omega^e}\left(-\frac{1}{2}KJ\mathbf{Q}^T\mathbf{C}^{-1} \;:\; \left[\mathbf{F}^T\left(\boldsymbol{\nabla}_0\mathbf{N}_a^T\right) + \mathbf{F}\left(\boldsymbol{\nabla}_0\mathbf{N}_a^T\right)^T\right]\Delta\mathbf{u}_a + \mathbf{Q}^T\mathbf{Q}\Delta\mathbf{p}^e\right) d\Omega^e = 0, \tag{67}$$

which results in the following matrix system:

$$-K\mathbf{K}_p^e\Delta\mathbf{u}_a + \mathbf{M}^e\Delta\mathbf{p}^e = 0. \tag{68}$$

Equating the above system for $\Delta\mathbf{p}^e$, we obtain

$$\Delta\mathbf{p}^e = K\left(\mathbf{M}^e\right)^{-1}\mathbf{K}_p^e\Delta\mathbf{u}_a, \tag{69}$$

where $\mathbf{K}_p^e$ is the mixed matrix given by

$$\mathbf{K}_p^e = \int_{\Omega^e} J\mathbf{Q}^T\mathbf{g}\mathbf{B}_{\mathrm{NL}}\, d\Omega^e. \tag{70}$$

The term $\mathbf{B}_{\mathrm{NL}}$ is the nonlinear Green deformation tensor given by

$$\mathbf{B}_{\mathrm{NL}} = \frac{1}{2}\left[\mathbf{F}^T\left(\boldsymbol{\nabla}_0\Delta\mathbf{u}\right) + \mathbf{F}\left(\boldsymbol{\nabla}_0\Delta\mathbf{u}\right)^T\right]. \tag{71}$$

For a general stress state, the term $\mathbf{B}_{NL}$ written in Voigt notation has 6 rows and $3 \times N_u^e$ columns, according to the number of shape functions for the displacement interpolation. For a given shape function a, we have the following matrix form

$$\left[\mathbf{B}^e_{NL}\right]_a = \begin{bmatrix} N_{a,X_1}F_{11} & N_{a,X_1}F_{21} & N_{a,X_1}F_{31} \\ N_{a,X_2}F_{12} & N_{a,X_2}F_{22} & N_{a,X_2}F_{32} \\ N_{a,X_3}F_{13} & N_{a,X_3}F_{23} & N_{a,X_3}F_{33} \\ N_{a,X_2}F_{11}+N_{a,X_1}F_{12} & N_{a,X_2}F_{21}+N_{a,X_1}F_{22} & N_{a,X_2}F_{31}+N_{a,X_1}F_{32} \\ N_{a,X_3}F_{11}+N_{a,X_1}F_{13} & N_{a,X_3}F_{21}+N_{a,X_1}F_{23} & N_{a,X_3}F_{31}+N_{a,X_1}F_{33} \\ N_{a,X_3}F_{12}+N_{a,X_2}F_{13} & N_{a,X_3}F_{22}+N_{a,X_2}F_{23} & N_{a,X_3}F_{32}+N_{a,X_2}F_{33} \end{bmatrix}, \tag{72}$$

where N_{a,X_i} denotes the derivative of N_a in direction X_i. The term $\mathbf{g}$ in Eq. 70 is the inverse of the Cauchy-Green tensor written in the following vector form:

$$\{\mathbf{g}\} = \left[C^{-1}_{11},\, C^{-1}_{22},\, C^{-1}_{33},\, C^{-1}_{12},\, C^{-1}_{13},\, C^{-1}_{23}\right]^T. \tag{73}$$

For a general stress state, the mixed matrix $\left[\mathbf{K}^e_p\right]$ has rank $3N^e_u \times N^e_p$, and is composed of $N^e_u \times N^e_p$ blocks, being each block a 3×1 matrix $(K^e_p)_{ij} (i = 1, \ldots, N^e_u, j = 1, \ldots, N^e_p)$:

$$\left[\mathbf{K}^e_p\right] = \begin{bmatrix} (K^e_p)_{1,1} & \cdots & (K^e_p)_{1,N^e_p} \\ \vdots & \ddots & \vdots \\ (K^e_p)_{3N^e_u,1} & \cdots & (K^e_p)_{3N^e_u,N^e_p} \end{bmatrix}, \tag{74}$$

in index notation,

$$(\mathbf{K}^e_p)_{ij,m} = \sum_{k,l=1}^{3} \int_{\Omega^e} JQ_j \mathbf{C}^{-1}_{kl} \frac{1}{2} \left(N_{i,X_k}\mathbf{F}_{ml} + \mathbf{F}_{mk}N_{i,X_l}\right) d\Omega^e, \quad m = 1, 2, 3. \tag{75}$$

The final expression for the projected pressure increment at the element level is obtained as

$$\Delta p^{e*} = K\mathbf{Q}\left(\mathbf{M}^e\right)^{-1} \left(\mathbf{K}^e_p\right)^T \Delta\mathbf{u}^e. \tag{76}$$

Algorithm 1 describes the pressure projection procedure at the integration points. This procedure is performed before the main loop to integrate the element stiffness matrix.

Algorithm 1 Pressure projection procedure.

1. Calculate the displacement based hydrostatic pressure p^e (16) for all integration points;
2. Calculate the element projection matrix $\mathbf{M}^e$, using the pressure order O_p (store this matrix for later calculation on algorithm 2);
3. Calculate the right-hand side vector $\{\mathbf{F}^e\}$ with order O_p;
4. Solve the linear system (60) to find the pressure coefficients $\mathbf{p}^e$;
5. Compute the product $\mathbf{Qp}^e$ to find the projected pressure p^{e*}.

Notice that the pressure increment Δp^{e*} is not considered in the above algorithm, because in the next section we will substitute it in Eq. 48 after discretization to obtain the pressure stiffness matrix.

2.8 Discretization of the Equilibrium Equation

In this section we apply the discretization to the equilibrium equation, which will result in the final equations for the element internal and external forces. Recalling Eq. 25, which represents the total virtual power done by a residual force $\mathbf{R}$, we have

$$\delta \dot{W}(\phi, \delta \mathbf{v}) = \int_{\Omega} \mathbf{S} \,:\, \delta \dot{\mathbf{E}} \, d\Omega - \int_{\Omega} \mathbf{f} \cdot \delta \mathbf{v} \, d\Omega - \int_{\Gamma} \mathbf{t} \cdot \delta \mathbf{v} \, d\Gamma. \tag{77}$$

Introducing the finite element discretization defined in Sect. 2.6, we can rewrite Eq. 77 for an element e as

$$\delta \dot{W}(\phi, \mathbf{N} \delta \mathbf{v}_a) = \delta \mathbf{v}_a^T \left(\mathbf{f}_{\text{int}}^e - \mathbf{f}_{\text{ext}}^e \right) = 0. \tag{78}$$

As the PVP equation must be satisfied for any nodal virtual velocity $\delta \mathbf{v}_a$, the discretized equilibrium terms are expressed by an element residual force $\mathbf{R}^e$ given by

$$\mathbf{R}^e = \mathbf{f}_{\text{int}}^e - \mathbf{f}_{\text{ext}}^e. \tag{79}$$

where $\mathbf{f}_{int}^e$ and $\mathbf{f}_{ext}^e$ respectively are the discretized internal and external forces at the element,

$$\mathbf{f}_{\text{int}}^e = \int_{\Omega^e} \mathbf{B}_{\text{NL}}^T \left(\bar{\mathbf{S}}_v + \tilde{\mathbf{S}}_v \right) d\Omega^e, \tag{80}$$

$$\mathbf{f}_{\text{ext}}^e = \int_{\Omega^e} \mathbf{N} \mathbf{f} d\Omega^e + \int_{\Gamma^e} \mathbf{N} \mathbf{t} d\Gamma^e. \tag{81}$$

The terms $\bar{\mathbf{S}}_v$ and $\tilde{\mathbf{S}}_v$ are the vector forms of the deviatoric and volumetric stress tensor, respectively given by

$$\{\bar{\mathbf{S}}_v\} = \left[\bar{S}_{11} \; \bar{S}_{22} \; \bar{S}_{33} \; \bar{S}_{12} \; \bar{S}_{13} \; \bar{S}_{23} \right]^T, \tag{82}$$

$$\{\tilde{\mathbf{S}}_v\} = \left[\tilde{S}_{11} \; \tilde{S}_{22} \; \tilde{S}_{33} \; \tilde{S}_{12} \; \tilde{S}_{13} \; \tilde{S}_{23} \right]^T. \tag{83}$$

2.9 Discretization of the Linearized Equilibrium Equation

Having the discretized element residual force, now we apply the same procedure to the linearized equilibrium equation in order to obtain the element tangent stiffness matrix. Therefore, applying the finite element discretization on Eq. 48, we obtain

$$\mathcal{D}\delta\dot{W}^e\left(\phi, \mathbf{N}\delta\mathbf{v}_a\right)\left[\mathbf{N}\Delta\mathbf{u}_a\right] = \delta\mathbf{v}_a^T\mathbf{K}_t^e\Delta\mathbf{u}_a, \tag{84}$$

with $\mathbf{K}_t^e$ as the element tangent stiffness matrix [7], which is given by

$$\mathbf{K}_t^e = \bar{\mathbf{K}}^e + \tilde{\mathbf{K}}^e + \tilde{\mathbf{K}}^{e*}, \tag{85}$$

with

$$\bar{\mathbf{K}}^e = \int_{\Omega^e}\left(\mathbf{B}_\sigma^T\bar{\mathbf{T}}\mathbf{B}_\sigma + \mathbf{B}_{\mathrm{NL}}^T\bar{\mathbf{D}}\mathbf{B}_{\mathrm{NL}}\right)d\Omega^e, \tag{86}$$

$$\tilde{\mathbf{K}}^e = \int_{\Omega^e}\left(\mathbf{B}_\sigma{}^T\tilde{\mathbf{T}}\mathbf{B}_\sigma + \mathbf{B}_{\mathrm{NL}}{}^T\tilde{\mathbf{D}}^1\mathbf{B}_{\mathrm{NL}}\right)d\Omega^e, \tag{87}$$

$$\tilde{\mathbf{K}}^{e*} = K\left(\mathbf{K}_p^e\right)^T\left(\mathbf{M}^e\right)^{-1}\left(\mathbf{K}_p^e\right). \tag{88}$$

Matrix $\tilde{\mathbf{K}}^{e*}$ is symmetric, with rank $3N_u^e \times 3N_u^e$ for general stress. It is obtained by substituting Eq. 76 in the third term of the right-hand side of Eq. 48. The terms $\bar{\mathbf{D}}$ and $\tilde{\mathbf{D}}^1$ represent the matrix forms of $\bar{\boldsymbol{C}}$ and $\tilde{\boldsymbol{C}}^1$, respectively. These matrices represented in Voigt notation for a general stress state are

$$[\mathbf{D}] = \begin{bmatrix} C_{1111} & C_{1122} & C_{1133} & C_{1112} & C_{1113} & C_{1123} \\ C_{1122} & C_{2222} & C_{2233} & C_{2212} & C_{2213} & C_{2223} \\ C_{1133} & C_{2233} & C_{3333} & C_{3312} & C_{3313} & C_{3323} \\ C_{1112} & C_{2212} & C_{3312} & C_{1212} & C_{1213} & C_{1223} \\ C_{1113} & C_{2213} & C_{3313} & C_{1213} & C_{1313} & C_{1323} \\ C_{1123} & C_{2223} & C_{3323} & C_{1223} & C_{1323} & C_{2323} \end{bmatrix}. \tag{89}$$

The term $\mathbf{B}_\sigma$ is the initial stress matrix with rank $9 \times 3N_u^e$, which operates the geometric stiffness contribution. It has the following form for a given node a:

$$\left[\mathbf{B}_\sigma\right]_a = \begin{bmatrix} N_{a,X_1} & N_{a,X_2} & N_{a,X_3} & 0 & 0 & 0 & 0 & 0 & 0 \\ 0 & 0 & 0 & N_{a,X_1} & N_{a,X_2} & N_{a,X_3} & 0 & 0 & 0 \\ 0 & 0 & 0 & 0 & 0 & 0 & N_{a,X_1} & N_{a,X_2} & N_{a,X_3} \end{bmatrix}^T. \tag{90}$$

The terms $\bar{\mathbf{T}}$ and $\tilde{\mathbf{T}}$ are the stress matrices composed by the Kronecker product between the stress and identity matrices as

$$\bar{\mathbf{T}} = \bar{\mathbf{S}} \otimes \mathbf{I}, \tag{91}$$

$$\tilde{\mathbf{T}} = \tilde{\mathbf{S}} \otimes \mathbf{I}, \tag{92}$$

which in general stress have rank 9×9.

2.10 Global Newton-Raphson Equation

After the definition of the element matrices, an assembly procedure is performed to obtain the global matrices. Considering a test solution ϕ_k [5], the global Newton-Raphson equation is given by

$$\mathcal{D}\delta\dot{W}\left(\phi_k, \delta\mathbf{v}\right)[\Delta\mathbf{u}] = -\delta\dot{W}\left(\phi_k, \delta\mathbf{v}\right). \tag{93}$$

The discrete form of the above equation is

$$\delta\mathbf{v}_g^T \mathbf{K}_g^t \Delta\mathbf{u}_g = -\delta\mathbf{v}_g^T \mathbf{R}_g. \tag{94}$$

The global virtual velocities $\delta\mathbf{v}_g$ are arbitrary, and thus we obtain the final incremental form

$$\mathbf{K}_g^t \Delta\mathbf{u}_g = -\mathbf{R}_g, \tag{95}$$

where $\mathbf{K}_g^t$ is the global tangent stiffness matrix, $\mathbf{R}_g$ is the global residual force vector and $\Delta\mathbf{u}_g$ are the global displacement increments.

The Newton-Raphson method is used to solve the incremental form of Eq. 95 for the global displacements. According to [5], it is usually possible to obtain the solution by applying the external load directly, especially when treating near-incompressibility, because the internal forces increase dramatically as we increase the bulk modulus K, leading to a hard convergence of the residual. However, when treating large displacements, there may be some convergence issues. Thus, it is convenient to consider the following incremental external force:

$$\mathbf{f}_{\text{ext}} = \sum_{i=1}^{l} \Delta\mathbf{f}_{\text{ext}}^i, \tag{96}$$

where $\Delta\mathbf{f}_{\text{ext}}$ is an external force increment, and l the total number of load increments. The steps for solving the Newton-Raphson procedure are described by Algorithm 2.

Algorithm 2 Newton Raphson procedure

1. Given $\mathbf{u}$ for iteration k, compute the kinematic variables and perform the pressure projection described by Algorithm 1;
2. *Begin for over the integration points*
   Update the stresses $\tilde{\mathbf{S}}$ and the volumetric part of the elasticity tensor $\tilde{\mathcal{C}}^1$ with the projected pressure $\mathbf{p}^{e*}$;
   Calculate $\bar{\mathbf{K}}^e$ and $\tilde{\mathbf{K}}^e$ (Eqs. 86 and 87), $\mathbf{K}_p^e$ (Eq. 70) and $\mathbf{f}_{int}^e$ (Eq. 80);
   End for
3. Calculate the pressure stiffness matrix $\tilde{\mathbf{K}}^{e*}$ (Eq. 88);
4. Assemble the global matrices and solve Eq. 95 for $\Delta\mathbf{u}_g^k$, using a linear solver;
5. Update the displacements: $\mathbf{u}_g^{k+1} = \mathbf{u}_g^k + \Delta\mathbf{u}_g^k$;
6. Check the convergence criterion. If satisfied, go to the next load step. Or else, go to step 1.

3 Hyperelastic Damage

In this section we introduce the Mullins effect, followed by the hyperelastic damage formulation, where the evolution law is applied to the constitutive relation. The tangent modulus is also presented for consistency. At the end we present the damage equations in algorithmic form for the consistent update of stresses and tangent modulus. The model adopted here is phenomenological based on the work by [26]. Other relevant details about this formulation can be found in [18], and an extensive review of continuum damage models for hyperelastic materials can be found in [6].

3.1 Mullins Effect in Hyperelastic Materials

Some idealized hyperelastic materials, such as elastomers, present a softening behavior when subjected to cyclic loading called Mullins effect [18]. Figure 2 illustrates a stress-strain curve for a uniaxial cyclic test. The process initiates at the undeformed configuration 0, and follows path A, reaching point 1. The body is then unloaded, following path B and returning to point 0.[1] The area between curves A and B represents the dissipated energy. When applying a second loading cycle, the curve follows path B-D, reaching point 2, where more internal material degradation occurs and so on.

Notice from Fig. 2 that the stress levels for curves B and C are lower than the primary loading curve A-D for a constant strain value. The Mullins effect is characterized by the stiffness reduction (or softening) of the material in a strain-driven process, with this reduction being only dependent of the maximum attained strain [18]. After several loading cycles, the increasing softening tends to saturate, and the

[1] In practical cases, there are small residual stresses, characterizing hysteresis. However, idealized models do not account for these stresses, as well as temperature and viscosity effects.

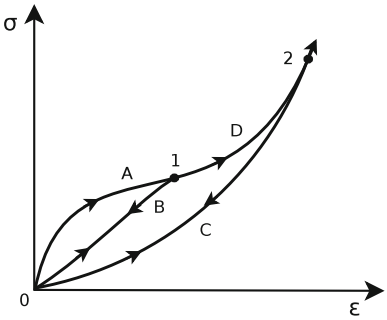

Fig. 2 Stress-strain diagram illustrating the characteristic softening (Mullins effect) observed in hyperelastic materials [18]

material becomes "conditioned" [13], that is, subsequent loading cycles yield stress curves over the same loading path, without further softening.

3.2 Damage Variable and Thermodynamic Aspects

Consider a given material with deviatoric strain energy density $\bar{W}^D(\mathbf{E})$, which is subjected to a strain-driven process with damage. The starting point consists in the definition of a modified strain energy density function [26],

$$\bar{W}^D(\mathbf{E}, D) = (1 - D)\,\bar{W}(\mathbf{E}), \tag{97}$$

applied on $\bar{W}$, because the damage is assumed to be of deviatoric nature.[2] The term $(1 - D)$ is the energy reduction parameter introduced by [20], and the scalar isotropic damage parameter D is defined in the range

$$0 \leq D \leq 1. \tag{98}$$

When $D = 0$ the material is undamaged, and when $D = 1$, the maximum damage value is attained, characterizing an idealized failure. The maximum value for D results in zero strain energy $\bar{W}^D = 0$. Notice that $D = 1$ is not necessarily the critical damage value D_c. Such critical value is an experimental rupture estimation, and is different for several materials and different continuum damage models. This damage model has the following characteristics:

- The damage evolution is isotropic and only function of the maximum attained strain until the current time;
- The damage evolution is an irreversible process and independent of the loading direction (there is no crack-closure effect). Therefore, compressive and tractive loads have the same effect;

[2] For compressible materials with damage, the reduction factor $(1 - D)$ of Eq. 97 is applied to W, rather than $\bar{W}$.

- The evolution function to be presented has an asymptotic behavior, and thus the damage reaches a value characterizing saturation. Close to the saturation threshold a critical value D_c is achieved, characterizing material failure.

Consider the first law of thermodynamics written in the following form

$$\rho \dot{e} = \mathbf{S} \,:\, \dot{\mathbf{E}}, \tag{99}$$

which means that the internal energy rate $\dot{e}$ by unit volume should be equal to the power due to stresses. The second law of thermodynamics postulates the irreversibility of entropy (s), given by the following inequation

$$\rho \dot{s} \geq 0. \tag{100}$$

A Helmholz free energy term ψ is introduced, which relates the internal energy with entropy in the following way:

$$\psi = e - \theta s, \tag{101}$$

where θ is the temperature. The strain energy and the free Helmholz energy are related as

$$\bar{W}^D = \rho \psi, \tag{102}$$

taking the time derivative of Eqs. (101–102), and recalling Eqs. (99–100), we obtain the Clausius-Duhem inequality

$$\dot{\bar{\mathbf{S}}}^D \,:\, \dot{\mathbf{E}} - \dot{W}^D \geq 0, \tag{103}$$

where $\dot{\bar{\mathbf{S}}}^D$ is the damaged deviatoric stress rate. The left-hand side of the above inequality represents the dissipated energy by unit volume. The deviatoric damaged internal strain rate is obtained with the application of the time derivative on Eq. 97:

$$\dot{\bar{W}}^D = \frac{\partial \bar{W}^D (D, \mathbf{E})}{\partial D} \dot{D} + \frac{\partial \bar{W}^D (D, \mathbf{E})}{\partial \mathbf{E}} \,:\, \dot{\mathbf{E}}. \tag{104}$$

Substituting (104) in (103), we obtain

$$- \frac{\partial \bar{W}^D (\mathbf{E}, D)}{\partial D} \dot{D} \equiv \bar{W} (\mathbf{E}) \dot{D} \geq 0, \tag{105}$$

$$\bar{\mathbf{S}}^D = (1 - D) \frac{\partial \bar{W}(\mathbf{E})}{\partial \mathbf{E}}. \tag{106}$$

Eq. 105 defines the dissipative nature of damage, and $\bar{W}(\mathbf{E})$ is thermodinamically conjugate to $\dot{D}$, because $\partial \bar{W}^D / \partial D \equiv -\bar{W}(\mathbf{E})$. Equation 106 is the damaged stress, and is based on the equivalent stress concept, first introduced by [20].

3.3 Damage Criterion

An equivalent strain ζ_s is defined, which is related with the strain energy density in the following way

$$\zeta_s = \sqrt{2\bar{W}\left(\mathbf{E}\left(t\right)\right)}, \tag{107}$$

where $\mathbf{E}\left(t\right)$ is the Green-Lagrange strain tensor for a given pseudo-time interval t of the strain-driven process. We define the maximum equivalent strain ζ_t^m as the maximum value of ζ_s until time t, that is,

$$\zeta_t^m = \max_{t\in(-\infty,t]} \sqrt{2\bar{W}\left(\mathbf{E}\left(t\right)\right)}. \tag{108}$$

The damage is calculated using the following function

$$\chi\left(\mathbf{E}\left(t\right), \zeta_t^m\right) = \sqrt{2\bar{W}\left(\mathbf{E}\left(t\right)\right)} - \zeta_t^m \leq 0, \tag{109}$$

which defines the damage surface in the strain space illustrated in Fig. 3. This surface has an isotropic growth with the strains. The time derivative of the damage surface (109) is

$$\dot{\chi} = \frac{\partial \chi}{\partial \mathbf{E}} \,:\, \dot{\mathbf{E}} = \mathbf{N} \,:\, \dot{\mathbf{E}}, \tag{110}$$

where $\mathbf{N}$ is the normal tensor to the damage surface. For a given strain state, we have four possible situations:

- The strain state is not the maximum attained, and inequality $\chi < 0$ is automatically satisfied (no damage evolution);
- The strain state is the maximum attained ($\chi = 0$) but in an unloading path from a damaged state ($\mathbf{N} \,:\, \dot{\mathbf{E}} < 0$);
- The strain state is maximum ($\chi = 0$) and in a neutral direction ($\mathbf{N} \,:\, \dot{\mathbf{E}} = 0$);
- The strain state is maximum ($\chi = 0$) and the direction points to a new damaged state ($\mathbf{N} \,:\, \dot{\mathbf{E}} > 0$), so that the damage surface grows.

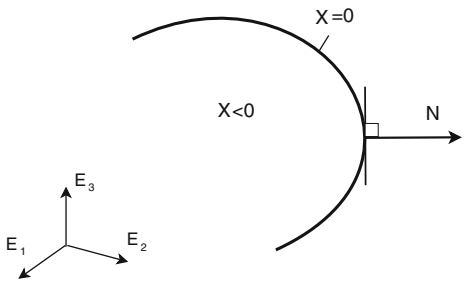

Fig. 3 Damage surface in the strain space [18]

The first three cases correspond to situations with no damage evolution for the given strain state. On the other hand, the last case attains a new maximum strain state, such that the damage parameter must increase. Therefore, if $\chi > 0$, the strain state is out of the damage surface, and is not defined by Eqs. 109 and 110. That means that the damage is evolving and the surface should be updated in a consistent way to satisfy $\chi = 0$ from Eq. 109.

3.4 Damage Evolution Law

Having the criterion for damage evolution defined, the evolution law in terms of the equivalent strain is defined:

$$\dot{D} = \begin{cases} \bar{h}(\zeta)\,\dot{\zeta} & \text{if } \chi = 0 \text{ and } \mathbf{N} : \dot{\mathbf{E}} > 0, \\ 0 & \text{else} \end{cases} \tag{111}$$

where $\bar{h}(\zeta) = -d\bar{g}(\zeta)/d\zeta$ is the derivative of function $\bar{g}(\zeta)$ with exponential behavior, initially introduced by [26] for highly-filled polymers, given by

$$\bar{g}(\zeta) = \beta + (1-\beta)\,\frac{1 - e^{-\zeta/\alpha}}{\zeta/\alpha}, \tag{112}$$

with $\beta \in [0, 1]$ e $\alpha \in [0, \infty)$ being the damage material parameters. The plot of $\bar{g}$ is illustrated in Fig. 4, with the variation of parameters α and β. Notice that lower values for α characterize a faster decrease for the function (left), while parameter β defines the asymptotic value (characterizing a damage saturation limit) for the

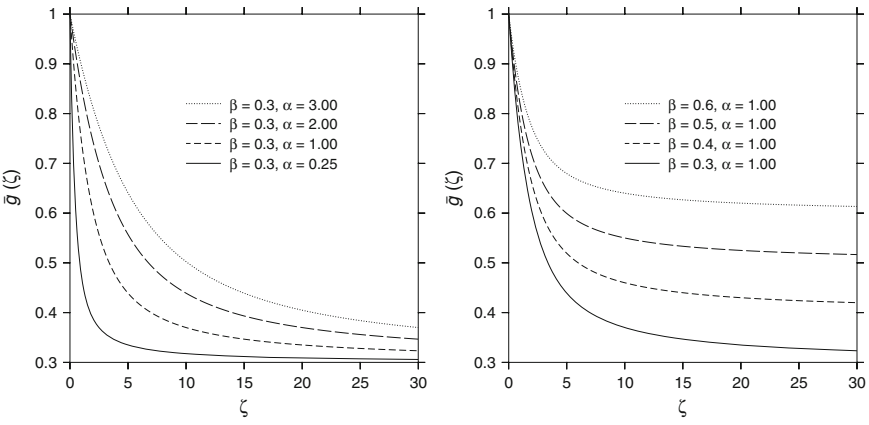

Fig. 4 Function $\bar{g}$ in terms of the equivalent strain for different values of parameters α and β

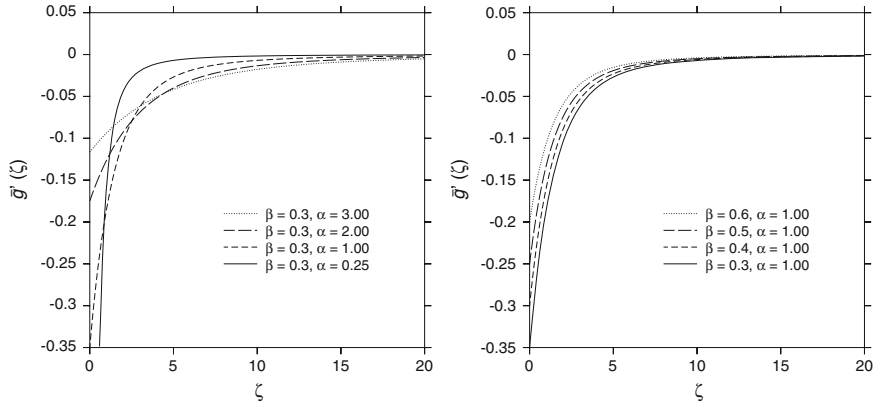

Fig. 5 Derivative of function $\bar{g}$ in terms of the equivalent strain for different values of parameters α and β

function (right). Figure 5 (left) shows that α influences the rate of the function until the asymptotic value. We also see from Fig. 5 (right) that β has a small effect on the derivative. In general, the higher the value of β, the higher the saturation limit value and the greater the softening for the strain range under consideration. The smaller the value of α, the higher the growth rate of $\bar{g}$.

3.5 Constitutive Relations

The evolution function is applied as a reduction factor over the stresses as

$$\bar{\mathbf{S}}^D(t) = \bar{g}(\zeta_t^m)\frac{\partial \bar{W}(\mathbf{E})}{\partial \mathbf{E}}. \tag{113}$$

Considering Eq. 106, we relate the stress reduction factor with the damage evolution function in the following way

$$(1 - D) = \bar{g}(\zeta_t^m). \tag{114}$$

Applying the time derivative to Eq. 113, we obtain

$$\dot{\mathbf{S}}^D = \frac{\partial \bar{\mathbf{S}}^D}{\partial \mathbf{E}} \;:\; \dot{\mathbf{E}}. \tag{115}$$

Applying the product rule in the above equation, we obtain

$$\dot{\mathbf{S}}^D = \left(\bar{g}(\zeta_t^m)\frac{\partial^2 \bar{W}(\mathbf{E})}{\partial \mathbf{E}^2} + \frac{\partial \bar{g}(\zeta_t^m)}{\partial \zeta_t^m}\frac{\partial \zeta_t^m}{\partial \mathbf{E}} \otimes \frac{\partial \bar{W}(\mathbf{E})}{\partial \mathbf{E}}\right) \;:\; \dot{\mathbf{E}}, \tag{116}$$

and therefore we have the constitutive relation for a nearly-incompressible hyperelastic material with damage:

$$\dot{\mathbf{S}}^D(t) = \begin{cases} \left[\bar{g}(\zeta_t^m)\bar{\boldsymbol{C}} + \frac{\bar{g}'(\zeta_t^m)}{(\zeta_t^m)}\bar{\mathbf{S}} \otimes \bar{\mathbf{S}}\right] \;:\; \dot{\mathbf{E}}, \text{ if } \quad \chi = 0 \text{ and } \quad \mathbf{N} \;:\; \dot{\mathbf{E}} > 0 \\ \bar{g}(\zeta_t^m)\bar{\boldsymbol{C}} \;:\; \dot{\mathbf{E}}, \qquad\qquad\qquad\qquad\qquad\qquad \text{else.} \end{cases} \tag{117}$$

with

$$\bar{g}'(\zeta) = (1-\beta)\left[\frac{e^{-\zeta/\alpha}}{\zeta} - \frac{\alpha}{\zeta^2}\left(1 - e^{-\zeta/\alpha}\right)\right]. \tag{118}$$

Notice the following from Eq. 117: If there is no damage evolution, the reduction function $\bar{g}(\zeta_t^m)$ is applied to the deviatoric part of the constitutive tensor $\bar{\boldsymbol{C}}$. Otherwise, an additional contribution of the derivative applied to the Kroenecker product of the stress tensor deviator must be considered for consistency.

3.6 Damage Algorithm

A damage algorithm with the consistent update of equations is necessary to ensure the stress and damage prediction, as well as a consistent tangent modulus for the Newton-Raphson method.

The damage coupled equations are described for a time interval $[t_n, t_{n+1}]$, and we consider a monotonic loading/unloading for this time interval. The equations are also valid for compressible materials. However, the algorithmic terms are not separated in deviatoric/volumetric form, but fully calculated.

- Deviatoric right Cauchy-Green tensor

$$\bar{\mathbf{C}}_{n+1} = \det F_{n+1}^{-2/3}\mathbf{C}_{n+1}. \tag{119}$$

- Invariants of $\bar{\mathbf{C}}_{n+1}$

$$\bar{I}_{1,n+1} = J^{-2/3}I_{1,n+1}, \quad \bar{I}_{2,n+1} = J^{-4/3}I_{2,n+1}. \tag{120}$$

- Equivalent strain

$$\zeta_{n+1} = \sqrt{2\bar{W}_{n+1}}. \tag{121}$$

- Damage surface

$$\chi_{n+1} = \zeta_{n+1} - \zeta_n^m \leq 0. \tag{122}$$

- Damage evolution function and derivative

$$\bar{g}_{n+1}\left(\zeta_{n+1}\right) = \beta + (1-\beta)\,\frac{1 - e^{-\zeta_{n+1}/\alpha}}{\zeta_{n+1}/\alpha}, \tag{123}$$

$$\bar{g}'_{n+1}(\zeta_{n+1}) = (1-\beta)\left[\frac{e^{-\zeta_{n+1}/\alpha}}{\zeta_{n+1}} - \frac{\alpha}{\zeta_{n+1}^2}\left(1 - e^{-\zeta_{n+1}/\alpha}\right)\right]. \tag{124}$$

- Damage variable in terms of the damage evolution function

$$D_{n+1} = 1 - \bar{g}_{n+1}. \tag{125}$$

- Second Piola-Kirchhoff stress tensor

$$\bar{\mathbf{S}}^{D}_{n+1} = \bar{g}_{n+1}\bar{\mathbf{S}}_{n+1}. \tag{126}$$

- Tangent modulus without damage evolution

$$\bar{\mathbf{D}}^{ed}_{n+1} = \bar{g}_{n+1}\bar{\mathbf{D}}_{n+1}. \tag{127}$$

- Tangent modulus with damage evolution

$$\bar{\mathbf{D}}^{ed}_{n+1} = \bar{g}_{n+1}\bar{\mathbf{D}}_{n+1} + \frac{\bar{g}'_{n+1}}{(\zeta_t^m)}\bar{\mathbf{S}}_{n+1} \otimes \bar{\mathbf{S}}_{n+1}. \tag{128}$$

Algorithm 3 presents the steps for the stress and tangent modulus update procedure.

Algorithm 3 Update procedure for the stress tensor and tangent modulus with damage.

1. Given $\mathbf{F}_{n+1}$, ζ_t^m, $\bar{g}_n$ e D_n (initial state or last converged iteration), calculate $\bar{\mathbf{C}}_{n+1}$ and their invariants.
2. Calculate the deviatoric strain energy density $\bar{W}_{n+1}$;
3. Calculate the equivalent strain ζ_{n+1} and damage surface χ_{n+1}.
   If $\chi_{n+1} \leq 0$ then
   Step without damage evolution:
   $\bar{g}_{n+1} = \bar{g}_n$
   $\bar{\mathbf{D}}^{ed}_{n+1} = \bar{g}_{n+1}\bar{\mathbf{D}}_{n+1}$
   Else
   $\zeta^t_{n+1} = \zeta_{n+1}$
   Calculate $\bar{g}_{n+1}$, $\bar{g}'_{n+1}$, $\bar{\mathbf{S}}_{n+1}$ and $\bar{\mathbf{D}}^{ed}_{n+1}$
4. Update the stresses $\bar{\mathbf{S}}^{D}_{n+1}$

4 Convergence Tests

The formulation presented in Sects. 2 and 3 was implemented in the high-order FEM code $(hp)^2$FEM, developed by our research group in C++ using the object-oriented paradigm [8]. We perform three validation tests with the imposition of analytical solutions. These solutions are constructed from the linear momentum equation (without dynamic considerations)

$$\text{div}\,\boldsymbol{\sigma} + \rho\mathbf{f} = 0, \tag{129}$$

where $\boldsymbol{\sigma}$ is the Cauchy stress tensor and ρ is the density. Imposing a displacement field $\mathbf{u}$, it is possible to obtain the strain measures, and making use of the constitutive equation, we calculate the analytical stress. Using Eq. 129, we obtain the body forces $\mathbf{f}$ and traction forces $\mathbf{t}$.

The first test validates the nearly-incompressible behavior for the Mooney-Rivlin material for small and large strains. In tests 2 and 3 we capture the Mullins effect and respectively study the convergence behavior of the compressible Neo-Hookean and the nearly-incompressible Mooney-Rivlin materials with damage. We used Lagrange shape functions, with Gauss-Legendre quadrature and Gauss-Lobatto-Legendre collocation points for all tests.

We used the hexahedrical domain illustrated in Fig. 6, with the face at $X = 0$ clamped. The geometry is discretized with several hexahedrical elements, illustrated in Fig. 7. For the p-refinement, we used a single element mesh. For near-incompressibility, the h-refinement is performed with displacement interpolation orders $O_u = 2$ and 3. In the compressible problems, the h-refinement is performed with $O_u = 1$.

For the tests involving near-incompressibility, we used the following interpolation scheme for the primary variables [29]

$$O_p = O_u - 1, \tag{130}$$

where O_u and O_p respectively are the interpolation orders for the displacements and pressure. The above relation yields more algorithmic stability, independent of the displacement interpolation order [29].

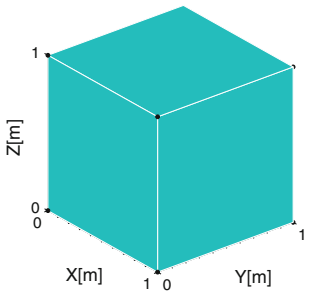

Fig. 6 Hexahedrical geometry used for all convergence tests, defined in $0 < X, Y, Z < 1$ m

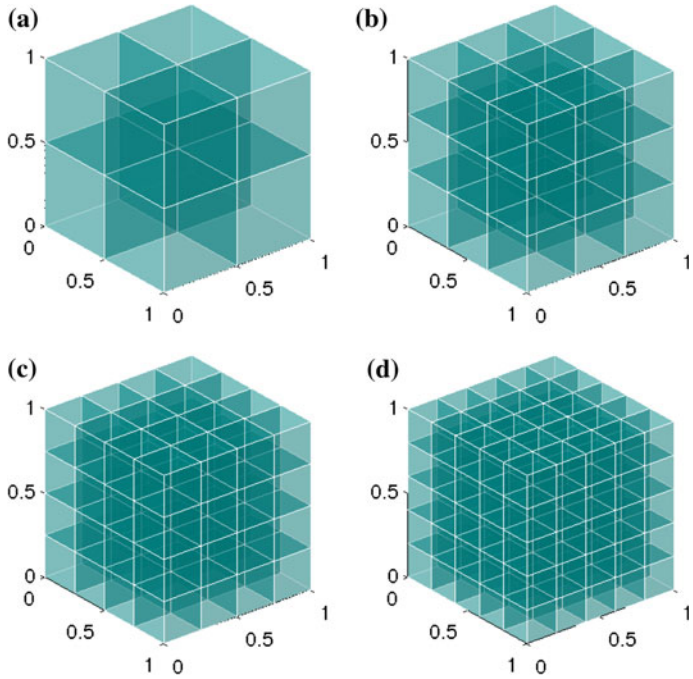

Fig. 7 Hexahedrical element meshes used for the convergence tests. **a** 8 elements, **b** 27 elements, **c** 64 elements, **d** 125 elements

4.1 Test 1—Nearly-Incompressible Mooney-Rivlin Material

For this test, we use the following smooth solution:

$$\begin{aligned} u_1 &= 0, \\ u_2 &= A \sin(BX), \\ u_3 &= 0. \end{aligned} \tag{131}$$

The material properties are $A_{10} = A_{01} = 1.0\,\text{Pa}$ and $K = 1.0 \times 10^3\,\text{Pa}$. The relation between the material properties yields the Poisson's ratio of approximately 0.4996. From the chosen displacement field, we calculate the strain measure, and using the constitutive equation, we determine $\boldsymbol{\sigma}$. Substituting $\boldsymbol{\sigma}$ in Eq. 129, we find the body forces

$$\begin{cases} f_1 = -\frac{2A^2B^3 \sin(2BX)\left(2A_{01}+A_{10}\right)}{3} \\ f_2 = 2AB^2 \sin(BX)\left(A_{01}+A_{10}\right). \\ f_3 = 0 \end{cases} \tag{132}$$

Substituting $\boldsymbol{\sigma}$ in the expression for the boundary conditions in terms of the stress vector $\mathbf{t} = \boldsymbol{\sigma}\mathbf{n}$, we determine the corresponding surface tractions, that is,

$$\begin{cases} t_1 = n_1 \left[\frac{2A^2B^2\cos(BX)^2\left(2A_{01}+A_{10}\right)}{3} \right] - n_2 \left[2AB\cos(BX)\left(A_{01}+A_{10}\right) \right] \\ t_2 = n_2 \left[\frac{2A^2B^2\cos(BX)^2\left(2A_{01}+A_{10}\right)}{3} \right] \\ \quad - n_1 AB\cos(BX)\left[2\left(A_{01}+A_{10}\right) + \left(\frac{2A^2B^2\cos(BX)^2\left(2A_{01}+A_{10}\right)}{3} \right) \right] \\ t_3 = 0, \end{cases} \tag{133}$$

The first step is to validate the formulation for small displacements with the choice $A = 0.0001$ m, $B = 1\,\mathrm{m}^{-1}$, which yields $u_2 \approx 0.000084$ m at $X = 1$ m. To check the convergence with the p refinement, we used interpolation orders $O_u = 2 - 9$ and $O_p = 1 - 8$. We calculate the L^2- and L^∞- error norms for the entire domain as

$$E_{L^2} = \sqrt{\int_\Omega \left(u_{an} - u_{ap}\right)^2 \, d\Omega}, \tag{134}$$

$$E_{L^\infty} = max|u_{an} - u_{ap}|, \tag{135}$$

with u_{an} the analytical solution and u_{ap} the approximate solution for displacements. Figure 8 presents the obtained errors for each direction. Notice the spectral convergence rate, with the error norm practically zero with $O_u = 8$.

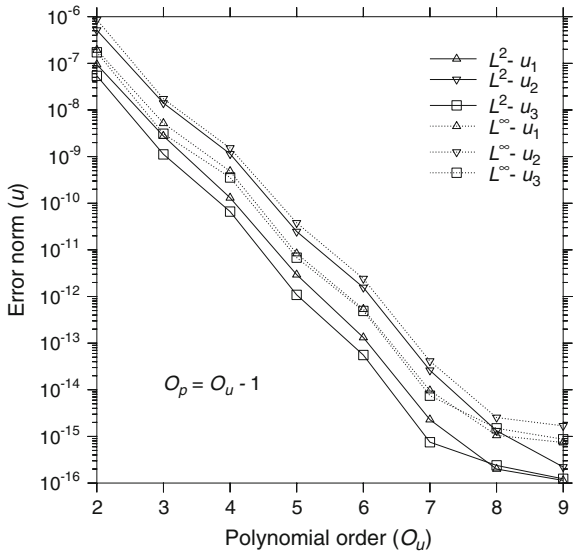

Fig. 8 Error norm in terms of O_u for a nearly-incompressible MR material under small displacements and strains

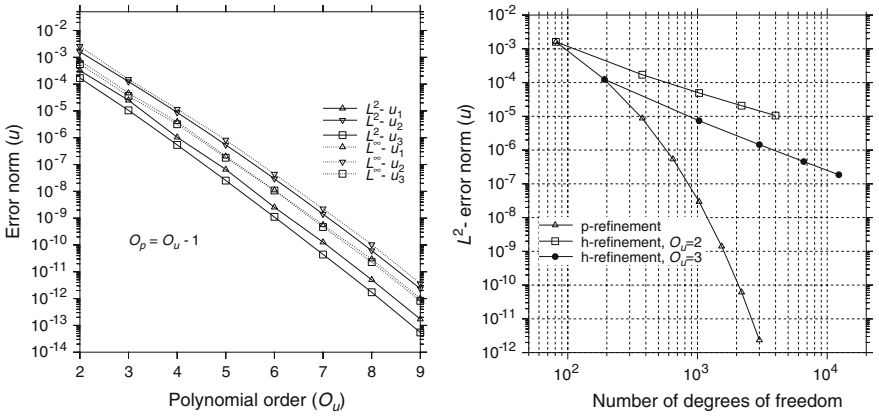

Fig. 9 L^2- and L^∞- error norms for u_1, u_2, u_3 (*left*). L^2- error norm for *h*- and *p*-refinements (*right*) for the nearly-incompressible MR material under large strains

Now we consider the analytical solution for large strains by setting $A = 0.1$ m and $B = \frac{\pi}{2}$ m^{-1} in Eq. 131. This gives $u_2 \approx 0.1$ m at $X = 1$ m. The external load was partitioned in 10 equal steps. We performed an *h*-refinement with meshes of 1, 8, 27, 64 and 125 elements and $O_u = 2, 3$. The *p*-refinement used one element with $O_u = 2 - 9$ and $O_p = 1 - 8$. Figure 9 presents the error in terms of the polynomial order and number of degrees of freedom. Notice that the error is much higher for the *h*-refinement using the same number of degrees of freedom for the problem. Such spectral convergence for the *p*-refinement is expected for problems with smooth solution [1, 21, 29].

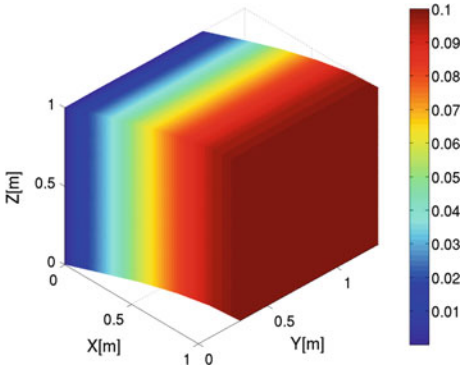

Fig. 10 Deformed geometry with the solution for u_2. Scale 3:1

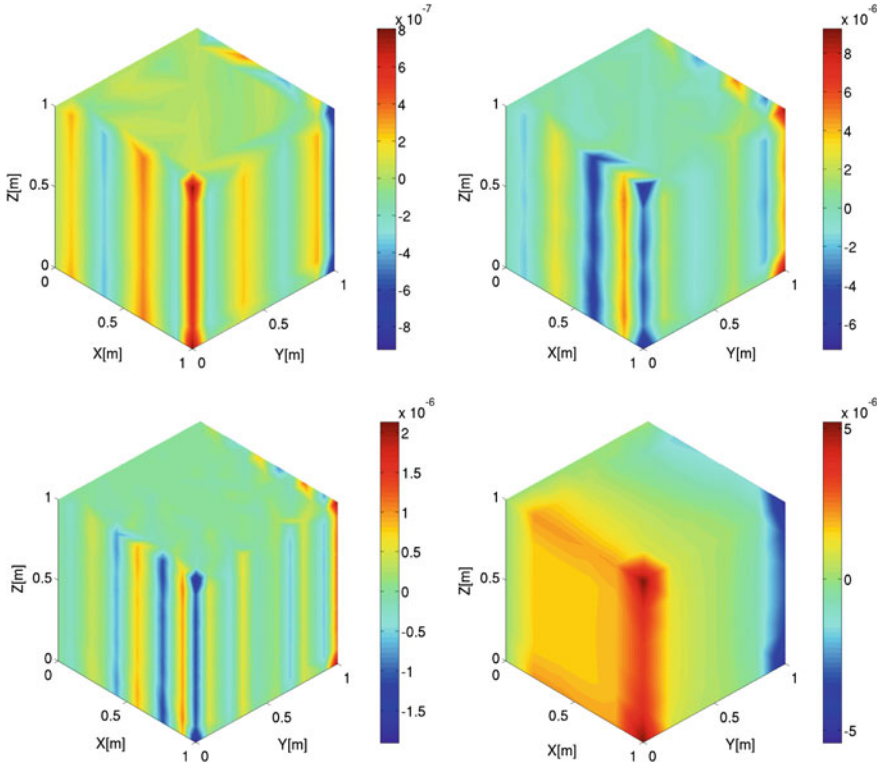

Fig. 11 Solution for displacements u_1 using one element with $O_u = 5$ (*upper left*), 8 elements with $O_u = 3$ (*upper right*), 27 elements with $O_u = 3$ (*lower left*), 125 elements with $O_u = 2$ (*lower right*)

The displacement field u_2 is illustrated in Fig. 10. Recall from Eq. 131 that the imposed analytical solutions for u_1 and u_3 are zero. Thus, the approximate solution for these directions already represent the absolute error for u_1 and u_3 in the entire domain, and is shown in Figs. 11 and 12. There are significant oscillations for a p refinement with a single element (a). The greater variations are present in the edges, where the displacements values are higher. Cases (*b*) and (*c*), respectively with 8 and 27 elements, showed higher variations in the edges and vertices. We obtained smaller oscillations using 125 elements and $O_u = 2$.

The stresses were calculated at the nodes by weighting the neighboring elements. The maximum principal stress σ_1 was calculated and compared to the analytical solution. Figure 13 presents the nodal stresses along X for edge $Y = 0, Z = 0$. In the case of the p-refinement, we obtained a very good approximation with $O_u = 5$. Using 27 elements, we obtained good results starting at $O_u = 3$.

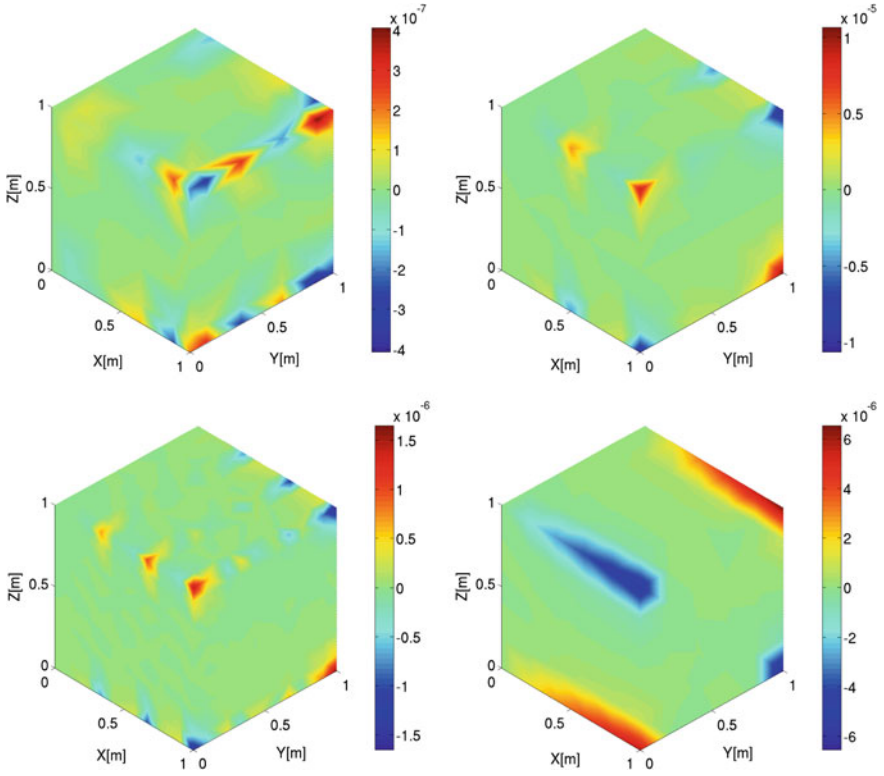

Fig. 12 Solution for displacements u_3 using one element with $O_u = 5$ (*upper left*), 8 elements with $O_u = 3$ (*upper right*), 27 elements with $O_u = 3$ (*lower left*), 125 elements with $O_u = 2$ (*lower right*)

Fig. 13 Maximum principal stress σ_1 at edge $Y = 0$, $Z = 0$

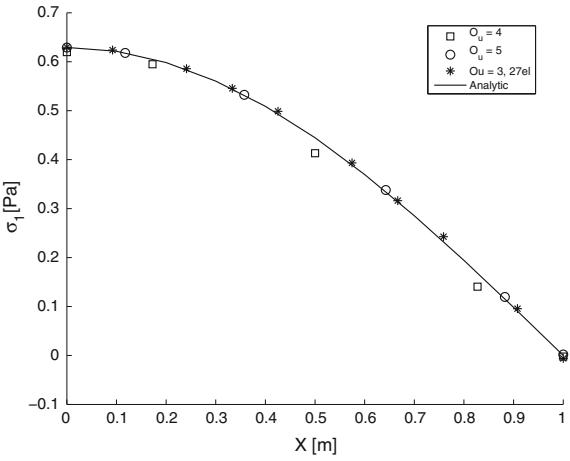

4.2 Test 2—Damaged Neo-Hookean Material

In order to analyze the Mullins effect, we considered a cyclic loading test using the Neo-Hookean material with damage. The material is compressible, without locking behavior. Therefore, we used the pure displacement formulation.

As described in Sect. 3, the Mullins effect is the progressive loss of material stiffness as the loading increases and results in higher strains. For this purpose, we used the single element mesh of Fig. 6 with the face $X = 0$ clamped. Then we applied three loading/unloading cycles at face $X = 1$ with traction forces $t_1 = 35,\ 50,\ 75$ N. The following material properties are considered

$$E = 1000 \text{ Pa},\ \nu = 0.3,\ \alpha = 0.5,\ \beta = 0.3.$$

The interpolation order used is $O_u = 1$, and the maximum principal stress is analyzed for the local integration point $(\xi, \eta, \zeta) = (-1, -1, -1)$. Figure 14 shows the Mullins effect with the progressive reduction of the stresses in the transition of each loading cycle. When in reloading phase, the stresses return to the main loading path (solid line, same for all loading cycles), and a subsequent unloading (dotted lines) depends on the new maximum achieved strain.

Now we perform a convergence test using the same meshes as Test 1. The analytic solution imposed in this case is

$$\begin{aligned} u_1 &= \sin(X), \\ u_2 &= 0, \\ u_3 &= 0, \end{aligned} \tag{136}$$

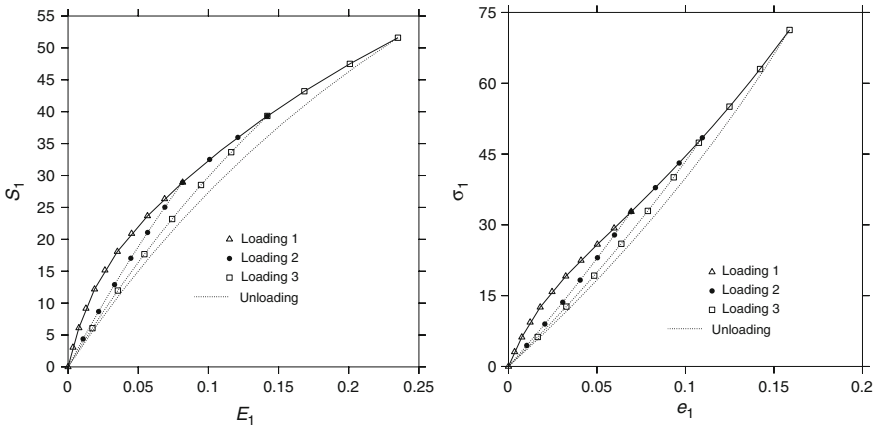

Fig. 14 Mullins effect for the damaged Neo-Hookean material. Maximum principal second Piola-Kirchhoff stress versus the maximum principal Green-Lagrange strain (*left*). Maximum principal Cauchy stress versus the maximum principal Almansi strain (*right*)

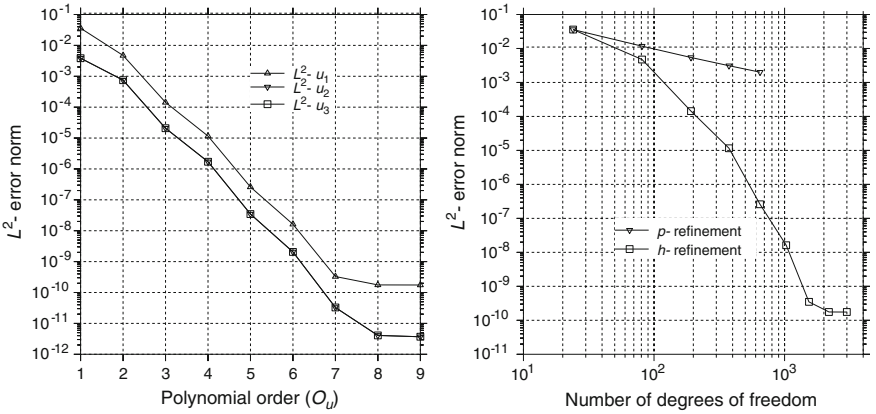

Fig. 15 L^2- error norm in terms of the polynomial order O_u (*left*), and in terms of the total number of degrees of freedom (*right*)

which is smooth and yields a displacement $u_1 \approx 0.84$ m at face $X = 1$ m. The body forces and traction fields are also obtained from Eq. 129, inserting the damage in the stress tensor. This is only valid if the load is monotonically applied, because the derived analytical solution does not account for unloading behavior. We do not show the expressions of the body and traction forces because the damage equations increase the size of the force expressions dramatically. Recall that we know a priori that for smooth solutions, the *p*-refinement leads to an exponential error reduction, which is algebraic for the *h*-refinement. We used the damage parameters $\alpha = 1.0,\ \beta = 0.3$. Figure 15 (left) illustrates the results for the L^2 error norm for the displacements. Notice that the insertion of damage to the analytical solution (136) did not change the spectral convergence with the increase of the polynomial order. The error stagnated at 10^{-10} for $O_u > 7$. Figure 15 (right) shows a comparison between both refinements.

We performed a *p* refinement with a single element and analyzed the stress and damage along edge $Y = 0,\ Z = 0$. The obtained results are illustrated in Figs. 16 and 17 comparing the analytical solution and approximate solutions with $O_u = 3, 4, 5$. Notice the very good approximation for both variables.

4.3 Test 3—Damaged Nearly-Incompressible Mooney-Rivlin Material

The first part of this test consists on reproducing the Mullins effect, using the same procedure as test 2. In this case, we used loading cycles with $t_1 = 1, 2, 3$ Pa applied at face $X = 1$ of Fig. 6. The material and damage properties are

$$A_{10} = A_{01} = 1.0 \text{ Pa},\ K = 1.0 \times 10^3 \text{ Pa},\ \alpha = 1.0,\ \beta = 0.3. \tag{137}$$

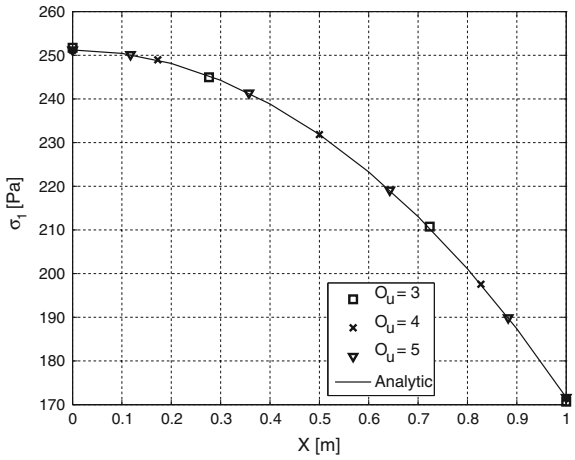

Fig. 16 Approximate solution for σ_1 at the nodal points along the edge $Y = 0$, $Z = 0$

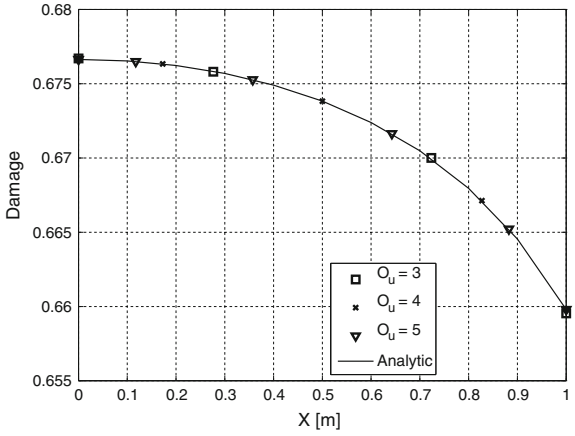

Fig. 17 Approximate solution for damage at the nodal points along edge $Y = 0, Z = 0$

We used the displacement interpolation order $O_u = 3$, and analyzed the maximum principal stress σ_1 for local integration point $(\xi, \eta, \zeta) = (-1, -1, -1)$. Figure 18 (left) presents the maximum principal stress for the second Piola-Kirchhoff stress tensor in terms of the Green-Lagrange strain. Figure 18 (right) presents the maximum principal Cauchy stress in terms of the Almansi strain. Notice that the softening behavior is similar to observed on test 2.

Now we test the convergence when coupling near-incompressibility and damage. The analytical solution is defined by Eq. 131, with $A = 0.25$ m and $B = 1.0\,\mathrm{m}^{-1}$, yielding a displacement $u_2 \approx 0.21$ m at $X = 1$ m. As with the damaged compressible Neo-Hooke material, the applied loads are not shown due to the excessive size of the expressions. We divided the external load into 10 load steps. The material properties are the same as Eq. 137.

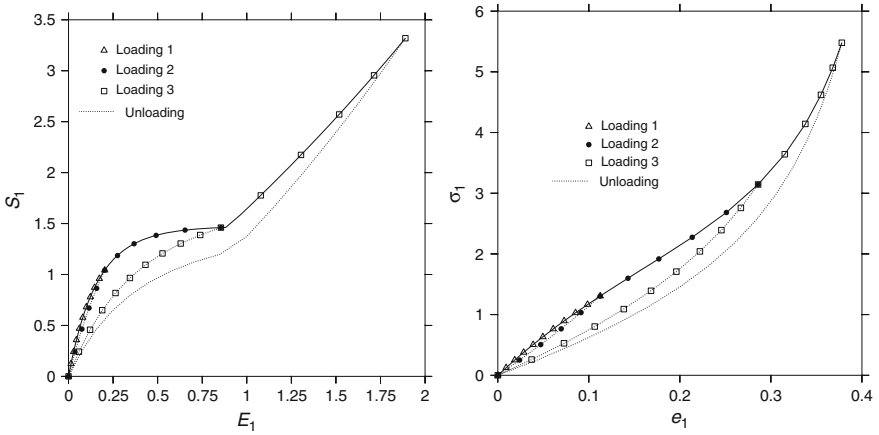

Fig. 18 Mullins effect for the maximum principal stress for an integration point. Second Piola-Kirchhoff stress (*left*), Cauchy stress (*right*)

We performed the *h*-refinement with $O_u = 2$. Two types of *p*-refinements were performed. The first one used a single element mesh, by varying the displacement order from 2 to 9. The second used 8 elements, increasing the displacement order from 2 to 6. Figure 19 shows the results for the L^2- error norm. Notice that for this problem, the inclusion of damage did not make the convergence of displacements harder, when comparing with the undamaged material. The error norm stagnated at 10^{-10} for the *p*-refinements. Figures 20 and 21 present the maximum principal stresses and damage distributions along edge $Y = 0$, $Z = 0$. The increase of the

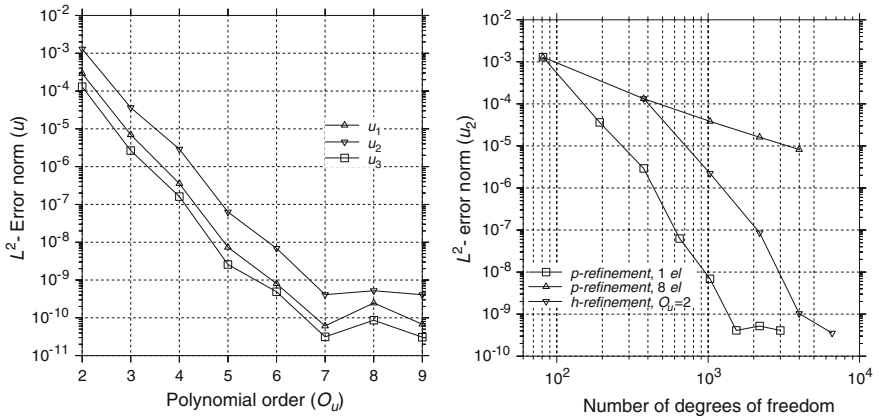

Fig. 19 L^2 error norm in terms of the displacement order (*left*), in terms of the total number of degrees of freedom (*right*)

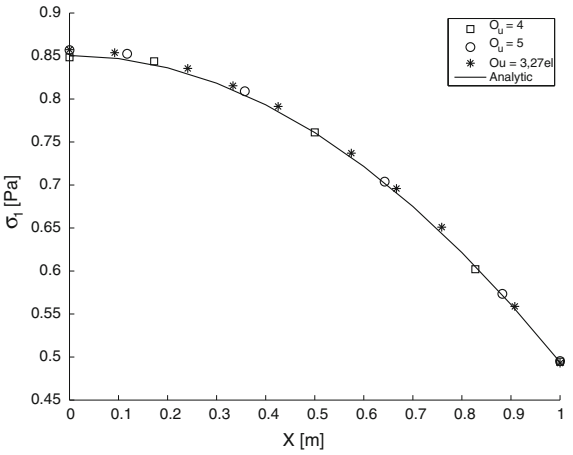

Fig. 20 Approximate solution for the maximum principal stress σ_1 along the edge $Y = 0, Z = 0$

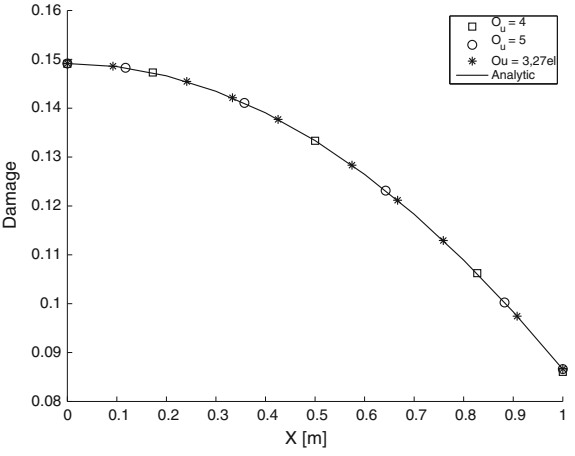

Fig. 21 Approximate solution for damage along the edge $Y = 0, Z = 0$

interpolation order and number of elements provided better results, and generally, for both variables, the difference is similar to the undamaged material. However, the results for stress are worse when compared to the compressible case.

5 Conclusion

The coupling of a compressible hyperelastic material with damage led to a very good convergence for the *p*-refinement, as expected since a smooth solution was considered. The errors for the stress are greater in magnitude compared to damage. The Mullins effect could be reproduced with the application of a cyclic loading test,

and showed a reduction of the material stiffness, depending on the maximum attained equivalent strain.

We also reproduced the Mullins effect for nearly-incompressible behavior with damage. We obtained a good convergence of the displacements without locking. There was a good approximation for the damage variable, but the errors for the stresses are still higher due to the effect of near-incompressibility.

For the performed tests, the reduction on element size had no significant effect on the approximated solution for the damage variable when sufficiently high interpolation orders were applied.

The convergence difficulties related to large displacements can be avoided by partitioning the external load in incremental smaller values. It should be observed that this partitioning must consider sufficiently small values to obtain a reasonable number of Newton-Raphson iterations, mainly when treating nearly-incompressible behavior.

References

1. Babuška, I.: The p and h-p versions of the finite element method: the state of the art. In: Dwoyer, D.L., Hussaini, M.Y., Voigt, R.G. (eds.) Finite Elements, ICASE/NASA LaRC Series, pp. 199–239. Springer, New York (1988)
2. Bathe, K.J.: Finite Element Procedures. Prentice Hall (1996)
3. Belytschko, T., Liu, W.K., Moran, B.: Nonlinear Finite Elements for Continua and Structures. Wiley (2000)
4. Bendre, A.A.: Finite element analysis and preliminary experiments to study the effects of high myopia in macular degeneration. Master's thesis, Northeastern University (2009)
5. Bonet, J., Wood, R.D.: Nonlinear Continuum Mechanics for Finite Element Analysis. Cambridge (1997)
6. Chagnon, G., Verron, E., Gornet, L., Marckmann, G., Charrier, P.: On the relevance of continuum damage mechanics as applied to the mullins effect in elastomers. J. Mech. Phys. Solids **52**, 1627–1650 (2004)
7. Chen, J.S., Pan, C.: A pressure projection method for nearly incompressible rubber hyperelasticity, part i: theory. J. Appl. Mech. **63**(4), 862–868 (1996)
8. Costa, G.L.V.: hp2fem—a p non-uniform software architecture to the high order finite element method. Master's thesis, State University of Campinas (2012)
9. de Souza Neto, E.A., Perić, D., Dutko, M., Owen, D.R.J.: Design of simple low order finite elements for large strain analysis of nearly incompressible solids. Int. J. Solids and Struct. **33**(20–22), 3277–3296 (1994)
10. de Souza Neto, E.A., Perić, D., Dutko, M., Owen, D.R.J.: A phenomenological three-dimensional rate-independent continuum damage model for highly filled polymers: formulation and computational aspects. J. Mech. Phys. Solids, **42**(10), 1533– 1550 (1994)
11. Dong, S., Yosibashi, Z.: A parallel spectral element method for dynamic three-dimensional nonlinear elasticity problems. Comput. Struct. **87**(1–2), 59–72 (2009)
12. Fried, I.: Finite element analysis of incompressible material by residual energy balance. Int. J. Solids Struct. **10**, 993–1002 (1974)
13. Fung, Y-C.: Biomechanics: Mechanical Properties of Living Tissues, 2nd edn. Springer, New York (1993)
14. Gharti, H.N., Komatitsch, D., Oye, V., Martin, R., Tromp, J.: Application of an elastoplastic spectral-element method to 3d slope stability analysis. Int. J. Numer. Meth. Eng. **91**(1), 1–26 (2012)

15. Gurtin, M.E., Francis, E.C.: Simple rate-independent model for damage. J. Spacecr. **18**(3), 285–286 (1981)
16. Heisserer, U., Hartmann, S., Düster, A., Yosibash, Z.: On volumetric locking-free behaviour of p-version finite elements under finite deformations. Commun. Numer. Meth. Eng. **24**(11) (2007)
17. Heisserer, U., Hartmann, S., Düster, A., Yosibash, Z., Bier, W., Rank, E.: p-fem for finite deformation powder compaction. Comput. Meth. Appl. Mech. Eng. **197**(6–8), 727–740 (2008)
18. Holzapfel, G.A.: Nonlinear Solid Mechanics: A Continuum Approach for Engineering. Wiley (2000)
19. Hughes, T.J.R.: The Finite Element Method: Linear Static and Dynamic Finite Element Analysis. Dover Civil and Mechanical Engineering Series. Dover Publications (2000)
20. Kachanov, L.M.: Time rupture process under creep conditions. Izv Akad Nauk SSR **8**, 26–31 (1958)
21. Karniadakis, G.E., Sherwin, S.J.: Spectral/hp Element Methods for Computational Fluid Dynamics. Numerical Mathematics and Scientific Computation. Oxford University Press, Oxford (2005)
22. Konyukhov, A., Schweizerhof, K.: Incorporation of contact for high-order finite elements in covariant form. Comput. Meth. Appl. Mech. Eng. **198**(13–14), 1213–1223 (2009)
23. Mullins, L.: Softening of rubber by deformation. Rubb. Chem. Technol. **42**(1), 339–351 (1969)
24. Ogden, R.W.: Non-Linear Elastic Deformations. Dover Civil and Mechanical Engineering Series. Dover Publications (1997)
25. Power, E.D.: A nonlinear finite element model of the human eye to investigate ocular injuries from night vision goggles. Master's thesis, Virginia tech, USA (2001)
26. Simo, J.C.: On a fully 3-dimensional finite strain viscoelastic damage model—formulation and computational aspects. Comput. Meth. Appl. Mech. Eng. **60**(2), 153–173 (1987)
27. Souza Neto, E.A., Perić, D., Owen, D.R.J.: Computational Methods for Plasticity: Theory and Applications. Wiley (2008)
28. Yosibash, Z., Hartmann, S., Heisser, U., Dster, A., Rank, E., Szanto, M.: Axisymmetric preassure boundary loading for finite deformation analysis using p-fem. Comput. Meth. Appl. Mech. Eng. **196**(7), 1261–1277 (2007)
29. Yu, Y., Baek, H., Bittencourt, M.L., Karniadakis, G.E.: Mixed spectral/hp element formulation for nonlinear elasticity. Comput. Meth. Appl. Mech. Eng. **213–216**, 42–57 (2012)

Mechanical Characterization of the Human Aorta: Experiments, Modeling and Simulation

Claudio M. García-Herrera, Diego J. Celentano, Marcela A. Cruchaga and Gustavo V. Guinea

Abstract This chapter presents an overview of recent works aimed at characterizing the mechanical behaviour of the human aorta via experiments, modeling and simulation. The application of these techniques are in particular detailed in the analysis of the following cases: ascending aorta, aortic arch and thoracic descending aorta under in-vitro and in-vivo conditions. The experimental procedure encompasses uniaxial tension and pressurization tests on healthy and pathological tissues of different ages. The tensile measurements are used to calibrate the material parameters of isotropic or anisotropic quasi-static elastic constitutive models which are intended to predict the material response in a wide deformation range. Although this task is usually carried out analytically, numerical simulations (using a discretized formulation defined in the context of the finite element method) are also performed for problems in which more complex geometry, boundary conditions and loads are considered. Overall, the reported material characterization was found to provide a realistic description of the mechanical behaviour of the aorta subjected to various deformation and stress scenarios. Finally, the implication of these studies is the possibility to predict the mechanical response of the human aorta under generalized loading states like those that can occur in physiological conditions and/or in medical device applications.

C.M. García-Herrera (✉) · M.A. Cruchaga
Departamento de Ingeniería Mecánica, Universidad de Santiago de Chile, USACH,
Av. Bernardo O'Higgins 3363, Santiago de Chile, Chile
e-mail: claudio.garcia@usach.cl

D.J. Celentano
Departamento de Ingeniería Mecánica y Metalúrgica,
Pontificia Universidad Católica de Chile,
Av. Vicuña Mackenna 4860, Santiago de Chile, Chile

G.V. Guinea
E.T.S.I. Caminos, Canales y Puertos, Universidad Politécnica de Madrid,
C/ Profesor Aranguren s/n, Madrid, Spain

P.A. Muñoz-Rojas (ed.), *Computational Modeling, Optimization and Manufacturing Simulation of Advanced Engineering Materials*,
Advanced Structured Materials 49, DOI 10.1007/978-3-319-04265-7_7

1 Introduction

The aim of this chapter is to present an overview of recent developments devoted to the characterization of the mechanical behaviour of the human aorta considering experiments, modeling and simulation. In particular, this methodology is applied to the study of the ascending aorta, aortic arch and thoracic descending aorta under in-vitro and in-vivo conditions. Important features related to this topic are discussed in what follows.

The aorta is the paradigm of major arteries, which not only serve as conduits for the bloodstreams but they also play a key role in modulating pressure and flow in the entire circulatory system by means of their mechanical response. Major vascular diseases alter and degrade the structure and composition of the aortic wall, and have an effect on its mechanical behaviour. Consequently, a better understanding of the mechanical performance of the vessel wall and its connection with pathologies should be warranted in order to prevent circulatory accidents, as well as for the development of effective and reliable treatments and surgical procedures [10, 89].

Aneurysms are placed among the severe, potentially life-threatening abnormalities of the aorta. They are caused by a pathological expansion of the aortic diameter, which may lead to dissection and rupture. Interventional criteria balance the risks associated with surgical repair with the risk of complications due to the development of the disease. The risk of growth and rupture is commonly related to aortic diameter, with this being the most used criterion for intervention [9, 30]. Although there is considerable evidence that the risk of rupture, dissection or death is dramatically increased in thoracic aortic aneurysms with diameters in excess of 60 or 70 mm for ascending or descending aorta, respectively [17, 22], the fraction of aneurysms that rupture before reaching that size it is not negligible [21, 49, 102]. Rupture of aneurysms occurs when the mechanical stresses acting on that zone of the vessel exceed the strength of the wall tissue. It seems that a particular patient-specific criterion is therefore necessary. However, all the size-based criteria, either considering absolute [9] or relative aortic diameters [23], do not take into account explicitly the actual mechanical behaviour of the arterial wall. Enhanced and more reliable criteria accounting for the particular characteristics of every patient, and more closely related to the mechanical performance and strength of the arterial wall, are still needed.

Customarily associated to aortic disease and aneurysm development, bicuspid aortic valve is an anomaly probably due to the presence of a genetic defect that, in addition to valve leaflets, affects the medial layer of aorta [32]. The high risk of dilatation and aortic dissection up to nine times higher favours that many asymptomatic patients are operated on prophylactically for aortic replacement [9]. Nevertheless, recent studies have questioned such a practice on the basis that surgical guidelines are not based on objective evidence [47].

The accumulated experience with aneurysmal and bicuspid aortic valve patients two prevalent aortic pathologies demonstrates the relevance of obtaining experimental information on the mechanical behaviour and strength of the pathological aorta, in order to develop accurate and dependable diagnostic and interventional criteria.

Nevertheless, data on the mechanical strength of human ascending aorta are still limited and somehow controversial. It is generally agreed that healthy tissue is stronger than aneurysmal in both longitudinal and circumferential directions. Control and aneurysmal ascending aorta in both such orientations have been compared, with findings supporting this contention [101]. Pathologic tissue was 30 % weaker and appreciably stiffer than control. However, other authors presented the unexpected finding of aneurysmal aorta as being as equally resistant as normal aortic tissue, and pointed out the importance of considering age-matched subject groups before drawing conclusions [57]. In particular, these authors tested aneurysm tissue from four regions and reported an increased stiffness and reduction in extensibility compared to control tissue and anisotropy of both aneurysm and control tissue. The influence of age on the rupture of pathological ascending aorta and aneurismal strengths in between the other two studies have been analysed and reported [79]. The fact that most of the few available studies on the tensile properties of the ascending aortic wall [79, 101] have been performed at a non-physiological temperature (around 20 °C), and the variable nature of most control vessels, that were taken from autopsies, might be at the root of these differences. It was demonstrated that peak stretch at failure is lower for samples from older patients [99]. It should be noted that no significant anisotropy was reported in these last three works.

The human aortic arch is an elastic artery whose mechanical properties play a crucial role in damping the pressure wave that occurs inside the vessel and, besides, to influence the blood flow coming from the heart [74]. Moreover, the knowledge of the rupture stress and strain in this artery under normal, hypertension and severe (e.g., automobile accidents or cardiovascular problems) physiological conditions is also a relevant area of current interest [24, 33, 87]. The aortic arch motion is linked to that of the heart left ventricle through the aortic root. This motion generates axial stresses in the ascending aorta. Beller et al. [6] consider that the motion of the aortic root induces high stress levels in the aortic arch that, in turn, may cause an aortic dissection even in patients without other risk factors. The surgical operation aimed at preventing the rupture of the aortic arch is still nowadays a risky procedure [31] that is only recommended when the risk of failure of the artery wall is greater than that associated to the operation itself. Such decision is mainly based on the dimensions of the vessel without taking into account its mechanical strength. Although the maximum artery diameter of 50 mm is usually taken as the criterion leading to surgery, 23 % of the arteries fail, however, before reaching this threshold [30, 80]. Clinical reports on complex anomalies of the human aortic arch have been extensively published in the past (e.g., double aortic arch and right aortic arch with left ductus/ligamentum arteriosus; see Kocis et al. [59] for a complete review on this subject). Other relevant anomalies closely related to the human aortic arch have been recently studied, e.g., the so-called bovine aortic arch [7] and the aberrant right subclavian artery [98]. On the other hand, some of the genetical pathologies usually deriving in aneurysms that affect the mechanical response of the aortic arch are the Marfan [75], DiGeorge [73] and MAGIC [12] syndromes. Surgical repairs for aortic arch aneurysms have been carried out in different ways: complete replacement [4] or reconstruction consisting of an off-pump distal or proximal reimplantation of

the aortic arch vessels combined with an endovascular large stent graft to exclude the entire aortic arch [2, 20]. These surgical techniques are not only associated with considerable mortality and morbidity but also have undoubtedly mechanical consequences since they involve the application of loading (typically pressure) and the generation of strain during the repairing or replacement of sick vessels.

The aortic arch may be subjected to extreme loading conditions in situations such as automobile crashes. In this context, traumatic aortic arch false aneurysms after blunt chest trauma can be developed [8]. Three types of mechanical actions causing the blunt traumatic aortic rupture have been identified: stretching, intravascular pressure and water-hammer effect [34, 87]. In particular, hypertension at rest or during effort in patients with aortic arch coarctation has been studied in cases with successful repair or mild degree of obstruction [24]. Moreover, impact-sled tests with human cadaver thoraces have been carried out to investigate the aortic injury mechanism caused by the effect of acceleration that induces a differential motion of the aortic arch relative to the heart and its neighboring vessels [35].

All the preceding facts clearly justify the need of achieving a better understanding of the mechanical response of the human aortic arch. One possible way to achieve this goal is by using numerical simulations that predict the mechanical response of the artery in order to quantify its risk of failure under different loading conditions and, thus, may provide useful information for medical therapies of the related pathologies. In this context, one of the major challenges is the definition of realistic and reliable stress-strain relationships of the vessel [25, 26, 28, 29, 54].

Numerical simulations have been recently performed to predict the mechanical response of the human aortic arch. Beller et al. [5] and [6] studied aortic arches under physiological conditions (in patients with and without aortic insufficiency) by means of a linear elastic isotropic constitutive model (i.e., the tissue stiffness variation with increasing strain was not taken into account) and boundary conditions that accounted for experimentally-measured aortic root displacements during the cardiac cycle. However, the effect of the ligamentum arteriosum was not included in the analysis. Both aortic root displacement and hypertension were found to significantly increase the longitudinal stress in the ascending aorta. Gao et al. [37] performed a study of the stress distribution in a layered aortic arch model (also using a linear elastic isotropic law) with interaction between a pulsatile flow and the wall of the blood vessel. This work indicates that the circumferential stress in the aortic wall is directly associated with blood pressure, supporting the clinical importance of blood pressure control. Moreover, another relevant aspect that should be addressed in the numerical simulation under in-vivo conditions is the definition of a representative initial configuration of the aortic arch. This can be firstly achieved by means of clinical techniques, e.g. computed tomography (CT) and angiography, that afterwards allow the application of geometric reconstruction methods which finally give a real model of the vessel [71, 95]. This geometry is obtained at a specific blood pressure and, consequently, unknown initial stresses in equilibrium with this internal load have to develop at the artery wall. It is seen, therefore, that an accurate estimation of the initial stresses is needed to correctly describe the material response. A method to account for this stress computation is the inverse analysis in which the effect of the

residual strain is neglected [43, 66]. This assumption is not always valid in arteries [54]. It should be noted that the numerical simulation and experimental validation of the mechanical response of the human aortic arch under in-vivo conditions including all the aspects mentioned above is nowadays a research subject to be explored.

Another important aspect closely related to the mechanical behaviour of the artery is the development of surgical treatments and techniques. Some of these treatments (e.g., angioplasty, stent, bypass, aortic valve surgery) involve mechanical features such as the application of loading (usually pressure) and the generation of strain during the repairing or replacement of sick vessels [58]. Moreover, the knowledge of rupture stress and strain in arteries under both normal (physiological) and severe (e.g., automobile accidents or cardiovascular problems) conditions is also a relevant area of current interest [33, 87].

Experiments in aortic samples have been carried out in animals [36] and in addition, in human tissues (healthy and with aneurisms) for the ascending [38, 60, 79], the thoracic [96] and the abdominal [54, 68, 84, 86, 100, 103] aortas. These last three groups have been also mathematically characterized. However, reported in-vitro experimental data and constitutive modeling for healthy human descending aortas in youngs and newborns is, in particular, rather scarce.

The most common procedure aimed at characterizing the passive mechanical behaviour of the human aortic wall is the tensile test. Mohan and Melvin [72] have used this test to analyze failure properties, anisotropic degree and rate-dependent effects in human descending aortic samples. Later, Raghavan et al. [86] have carried out uniaxial tests in human abdominal aortic aneurisms to assess the tissue degradation as well as the thickness distribution in the aneurism wall.

An alternative approach used to analyze the passive mechanical response of the human aorta is the pressurization test. In particular, Roy [93] assessed via this test the non-linearity of the stress-strain relationship in animal and human aortic tissues. Further studies [90] demonstrated that the aortic stiffness is relatively small for low pressure levels (i.e., less than those corresponding to the physiological conditions that range from 80 to 120 mmHg) and very large for higher pressure values. Later, Wolinsky and Glagov [104] analyzed the structural changes experienced by the aortic tissue during this test concluding that the collagen is mainly involved at high pressure levels (this is due to the observed alignment of the collagen fibers at such stress state) whereas the elastin plays an important role at low pressure levels. More recently, Atienza et al. [3] used this test to study the combined effects of pressure and temperature on the mechanical response of the human thoracic descending aorta. Experimental measurements obtained with this test have been also employed to fit material parameters of different constitutive models applied to coronary arteries in animals [36, 91].

The objectives of the present study are fourfold. First, to provide researchers with basic mechanical data on healthy and pathological (aneurysmal and bicuspid aortic valve arterial tissues) ascending aortic wall measured in vitro at physiological temperature. Second, to evaluate the effect of the two pathologies on the mechanical deterioration and mechanical performance of the ascending aortic wall. The assessment of data of young healthy tissues (i.e., 16–35 years old) and the analysis of the

anisotropic response of control and pathological tissues are both original contributions of this research. Third, to analyze the mechanical response of the human aortic arch both during the bending and pressurization test through in-vitro experiments and under in-vivo physiological conditions by means of constitutive modeling and numerical simulation. Fourth, to characterize the passive mechanical response of the human thoracic descending aorta. The Materials and Methods considered in this study are presented in Sect. 2 while the obtained experimental, analytical and numerical results included in Sect. 3 are discussed in Sect. 4 where, finally, the corresponding numerical results are satisfactorily validated with the available experimental measurements also carried out in this research.

2 Materials and Methods

2.1 Experimental Procedure

2.1.1 Materials

The human aortic tissues considered in this work, i.e., ascending aorta, aortic arch and thoracic descending aorta, have been provided by the Hospital Puerta de Hierro de Madrid. In all cases, the tissues were obtained according to a protocol approved by the Hospital Ethics Committee [42], which included the informed consent from either the patients or the next of kin. The specific analysis carried out on each of them is separately described below.

Ascending Aortas

Healthy ascending aortic segments were obtained from patients who had died from non-cardiovascular-related causes. Aortic wall samples were obtained from 23 brain-dead heart donors, previously deemed acceptable for transplantation, aged between 16 and 57. Despite their origin, histological analyses were performed on samples from all segments to corroborate the absence of vascular pathologies. For the study, healthy specimens were divided into two groups depending on age: Group 0A (<35 years old, nine patients, 25 ± 3 years) and Group 0B (>35 years old, 14 patients, 51 ± 2 years). Donor information (sex, age and body surface area) is summarised in Table 1.

Pathologic tissue was obtained from patients undergoing ascending aorta surgery with or without aortic valve replacement. Ascending aortic samples were classified into two groups according to the presence/absence of a bicuspid aortic valve (BAV). Group I enclosed segments coming from 12 patients diagnosed with BAV, aged between 36 and 80 years (57 ± 5 years).

Group II was made up of 14 patients aged between 44 and 81 (60 ± 4 years) with normal (tricuspid) aortic valve and diagnosed with ascending aortic aneurysm. Five patients were operated due to ascending aortic thoracic aneurysm (AATA) and four had aortic insufficiency (AI) together with AATA. Three patients underwent surgery

Table 1 Ascending aortas: donor's data

Sex (F or M)	Age (Years)	BSA (m^2)
Control group 0A (<35 years, 9 donors, 25 ± 3 years)		
F	31	1.78
M	16	1.88
M	35	1.82
M	20	2.05
M	18	1.98
M	25	2.12
M	20	1.54
M	29	1.99
M	32	1.95
Control group 0B (>35 years, 12 donors, 52 ± 2 years)		
M	45	1.97
M	49	1.93
M	52	1.82
F	50	1.78
F	45	1.60
M	50	1.81
F	48	1.44
M	57	2.06
M	57	1.68
F	46	1.66
F	64	1.78
M	62	1.86

having aortic valve (AoVR) and ascending aorta replacement and two patients were heart receptors due to dilated cardiomiopathy (DCM) in conjunction with AATA. Patients in group II had neither Marfan's nor Loeys-Dietz's syndromes and only one case presented few atheroma plaques (Ather). Nevertheless, in that case the testing samples were taken far (at least 2 cm) from the plaques and no significant differences were observed between the specimens excised closer or further from the plaques nor with the other patients from group II. Patient information of groups I and II is shown in Table 2.

All aortic samples were obtained at least 5 mm above the sinotubular junction and preserved in saline solution at 4 °C until testing within 24 h from excision. The average dimensions of the vessels studied in this work are summarised in Table 3.

Aortic Arch

This sample came from a cardiac transplant donor without previous arterial risk factors (i.e., tissue with low cholesterol levels, normal physiological pressure and absence of arterial pathologies of a donor with neither smoking nor diabetes records) whose death was not related to cardiovascular problems. The aortic arch consid-

Table 2 Ascending aortas: patient's data

Sex (F or M)	Age (Years)	BSA (m^2)
Bicuspid aortic valve group I (11 patients, 55 ± 4 years)		
F	36	1.72
M	49	2.04
M	63	1.76
F	58	1.80
M	48	1.80
M	43	2.12
M	75	1.79
M	65	1.90
F	63	1.68
M	42	1.94
F	66	1.87
Aneurysm group II (11 patients, 56 ± 2 years)		
F	57	1.71
M	60	1.83
F	45	1.81
M	62	1.94
M	44	1.95
M	51	1.68
M	58	1.97
M	53	1.80
M	71	2.12
M	65	1.90
M	51	1.94

Table 3 Ascending aortas: average dimensions for different groups

	Diameter (mm)	Thickness (mm)
Control group 0A	22.0 ± 2.2	1.9 ± 0.3
Control group 0B	23.7 ± 4.4	2.2 ± 0.3
Bicuspid aortic valve group I	38.0 ± 2.0	1.9 ± 0.2
Aneurysm group I	38.5 ± 7.7	2.0 ± 0.3

ered in this study is shown in Fig. 1. This arch configuration, which corresponds to approximately 70 % of the population [1], belonged to to a 44 years-old woman of 65 kg in weight and 1.60 m tall. All the in-vitro mechanical tests described in this work have been performed in the same day using samples obtained immediately after excision (i.e., one day from the time of death to testing). Although for experimental purposes the use of more samples would have been desirable, it should be

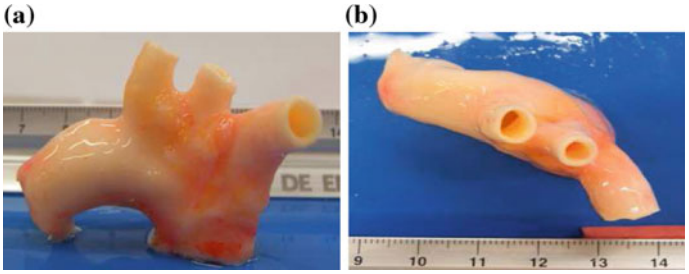

Fig. 1 Human aortic arch considered in the analysis: **a** *frontal view* and **b** *top view*

noted that healthy and young aortic arches are not easily available. However, taking into account the low dispersion observed in the mechanical response of healthy and young human thoracic descending aortas in tensile and pressurization tests [38], the mechanical characterization described below can be assumed to provide a representative behaviour of aortic arches belonging to young donors without cardiovascular pathologies.

The present study is focused on two groups selected according to the age of the donors: 16–36 (12 patients) and 65–90 (8 patients). The experimentally measured average diameter and thickness values at different locations of the sample are summarised in Table 4. Moreover, the average radius of the arch directrix for both groups was 37 mm ±4.5 (a similar value was reported by Beller et al. [5]).

Descending Aortas

All these samples came from cardiac transplant young and adult donors without previous arterial risk factors (i.e., tissues with low cholesterol levels and absence of arterial pathologies of donors with neither smoking nor diabetes records) whose deaths were not related to cardiovascular problems (e.g., automobile accidents, suicide, etc.) and, in addition, from autopsies of newborns that presented cerebral death. Aorta segments with an approximate length of 50 mm were considered in this study. All the in-vitro mechanical tests described in this work have been performed in the same day using samples obtained immediately after their excision (the time between the death of the donors and the moment of excision was around 20 h in all cases). After harvesting, the aortic tissue specimens were stored in refrigerated saline at 4 °C.

Table 4 Average external diameter and thickness of different parts of the aortic arch

	Vessel			
	Brachyocephalic trunk	Carotid artery	Subclavian artery	Aorta
Diameter (mm)	12.0 ± 0.34	10.1 ± 0.25	11.2 ± 0.31	24.4 ± 0.45
Thickness (mm)	2.06 ± 0.11	1.89 ± 0.21	2.10 ± 0.08	1.95 ± 0.15

Table 5 Descending aortas: data of Group A (newborns)

Vessel	Sex	Weight (kg)	Height (m)
A1	F	2.8	0.49
A2	M	3.5	0.53

Table 6 Descending aortas: data of Group B (youngs)

Vessel	Sex	Age (Years)	Weight (kg)	Height (m)
B1	F	32	63	1.64
B2	F	21	75	1.75
B3	F	36	49	1.65
B4	F	20	52	1.60
B5	M	35	75	1.65

Table 7 Descending aortas: data of Group C (adults)

Vessel	Sex	Age (Years)	Weight (kg)	Height (m)
C1	F	60	65	1.60
C2	M	45	85	1.70
C3	M	53	73	1.66
C4	M	57	60	1.70
C5	F	46	75	1.68

The analyzed vessels consisted of thoracic descending aortas that were classified in three groups, named as A, B and C, whose data is respectively shown in Tables 5, 6 and 7. Group A corresponds to newborns while the respective age intervals for the samples of Groups B and C are 20–36 and 45–60. Although for experimental purposes the use of more human newborn samples would have been desirable, it should be noted that this kind of arteries are difficult to get due to the low mortality rate of newborns and, in addition, to the social dramatic conditions involved in such cases.

The composition and structure of the tissues to be mechanically tested were firstly studied via a histological analysis performed by specialist of the Hospital Puerta de Hierro at Madrid. Images of the vessels were taken in order to quantify the fractions of nuclei, elastin and collagen, to study the distribution of elastin and collagen fibers. This analysis ratified the absence of damaged tissue.

2.1.2 Tensile Test

One of the most common procedures to characterize the passive mechanical behaviour of the human aortic wall is the tensile test. Specifically, the aim of this test is to

obtain a stress-strain relationship of the material under a uniform deformation pattern. This test also provides other important material data as its maximum strength and rupture elongation. In this study, the strip samples were obtained from the different parts (i.e., ascending, arch and descending) of the aortic tissue wall.

The tensile test assembly together with the clamp used to fix the sample to the jaws is shown in Fig. 2. The tests were carried out with the specimens fixed to the grips of an electromechanical tensile testing machine (Instron 5866) and permanently submerged in physiological serum (standard Phosphate Buffered Saline, PBS) at a temperature of 37 ± 0.5 °C controlled by a K-type thermocouple located in the chamber and close to the artery (<4 mm). The axial force was measured by means of a 10 N load cell (Instron 2519-101, accuracy better than 5 mN) and the crosshead displacement was taken as a direct measurement of the elongation of the sample, as the compliance of the aortic specimen had been estimated as being 100 times greater than that of the equipment (it should be noted that this strain measure was found to be practically the same as that obtained via video-extensometer measurements of the axial displacement between two markers drawn on the sample [38]; for simplicity, the first procedure was adopted in the present study). The machine internal LVDT sensor (accuracy better than 10 m) was used to measure the displacement of the crosshead.

The tests were performed in the passive state, without electrical or chemical activation of the vascular wall. In order to achieve uniform conditions for each sample, a time interval of 10 min was considered between the end of the assembly and the beginning of the test. To precondition the samples, ten successive loading-unloading cycles between 0 and 30 % of the maximum load were executed to remove the initial stress relaxation effect and to yield a stable response. The load cell velocity considered in the tests up to the rupture of the sample was 0.03 mm/s (which results in a deformation rate of 15 %/min approximately).

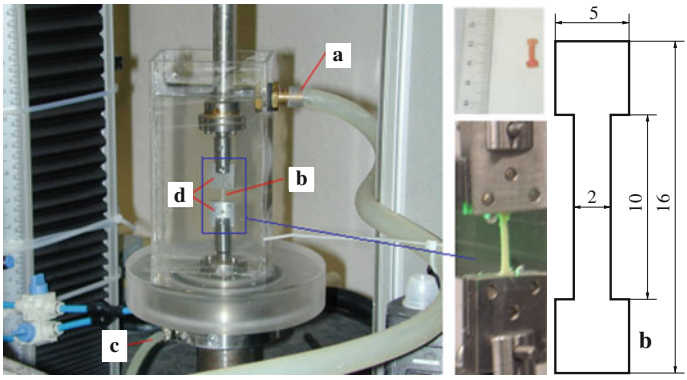

Fig. 2 Tensile test assembly; **a** Physiological serum exit, **b** Sample (dimensions in mm), **c** Physiological serum entry, **d** Supporting jaws

In this study, the strip samples were obtained from the artery wall. The sample dimensions were selected on the basis of balancing the larger number of specimens with the ease in their manipulation during the experiment (in average, ten samples were obtained for each available vessel). The chosen sample length and width are plotted in Fig. 2. As usual, the samples were cut along the longitudinal and circumferential directions in order to characterize the degree of anisotropy in the material response [38, 72, 79]. These directions are respectively denoted by the angles 0° and 90°. At least six samples of the different parts of the aorta were tested for each direction. Only tests exhibiting rupture at approximately the center of the sample have been considered. Since the artery wall is composed of three different layers [36], valid results are assumed up to the rupture instant of any of such layers. The specimen thickness was measured on each sample by means of a Mitutoyo 7301 thickness gage with 10 m accuracy (e.g., initial thicknesses ranged from 1.6 to 2.1 mm and 1.5 mm to 2.4 mm for ascending and thoracic descending aortic samples, respectively).

Axial load and axial jaws displacement were recorded during the whole test. The Cauchy axial stress σ_1 was computed as F/A, where F is the axial load and A is the current transversal area. The axial stretch λ_1 was calculated as L/L_0, with L and L_0 being the current and initial sample lengths, respectively. The current transversal area A is evaluated through the incompressibility condition that leads to $A = A_0/\lambda_1$, where A_0 is the initial transversal area of the sample. Moreover, assuming a uniform strain distribution along the sample, the stresses associated with two orthogonal directions perpendicular to the loading direction 1 vanish, i.e., $\sigma_2 = \sigma_3 = 0$.

2.1.3 Pressurization Test

This test is intended to mimic the in-vivo loading conditions that exist in the vessel at the interior of the human body. In this test, the vessel is subjected to an axial deformation in the tensile machine followed by the application of internal pressure by means of a external compressor [46]. To this end, both ends of the specimen are clamped to the jaws. These boundary conditions together with some particular features of the vessel (e.g., relatively low wall thickness to diameter and diameter to length ratios, material heterogeneity and cylindrical asymmetry) typically cause a complex stress pattern in the sample. However, a nearly uniform stress distribution at least at the central region of the sample may develop when large length to diameter and diameter to thickness ratios are used; e.g., length/diameter ≥ 5 and diameter/thickness ≥ 10 [76].

In this study, the following initial ratios were considered: length/diameter = 6.5 and diameter/thickness = 10. As mentioned above, these sample dimensions guarantee the development of approximately uniform stress patterns in the wall. The adopted setup of the pressurization test was that already described in [46]. Figure 3 shows the experimental assembly used in this work. The tissue response in both the physiological and high pressure ranges is specifically analyzed.

Internal pressure, axial jaws displacement and external diameter of the vessel were recorded during the whole test. An optical extensometer was used to record the

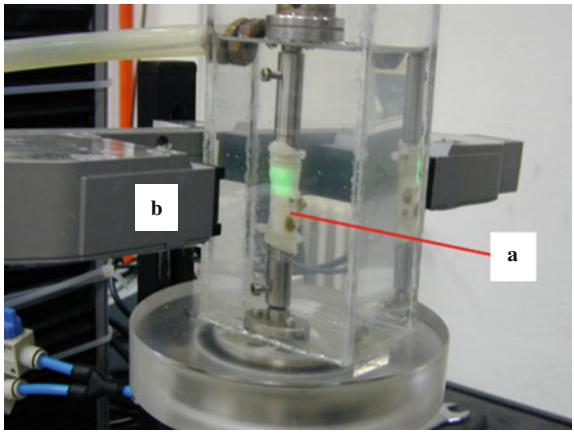

Fig. 3 Experimental assembly of the pressurization test. **a** Artery, **b** Optical extensometer

external diameter evolution. Curves of internal pressure P_i versus circumferential stretch λ_θ for different levels of longitudinal stretch λ_z were obtained. The circumferential stretch was defined as D/D_0, where D and D_0 denote the current and initial diameters of the tube, respectively. As in the previous test, the longitudinal stretch was calculated as the ratio between the current and initial lengths of the tube. Moreover, in order to improve the accuracy of the measurements of D, small pieces of tissue located at the outer surface of the sample were removed before its assembly for the test. Once again, ten successive loading cycles up to an axial stretch value of 1.2 followed by a pressure value of 200 mmHg were executed to precondition the samples.

2.1.4 Bending and Pressurization Test of the Aortic Arch

This test is aimed at assessing the mechanical response of the human aortic arch when it is subjected to large quasi-static deformations given by severe bending, axial stretching and internal pressurization. The initial configuration of the artery (shown in Fig. 1) is approximately a 90° circular arch with medium radius of 28.5 mm where the average internal diameter and thickness of the transversal section of the arch are 18 mm and 1.3 mm, respectively.

The test was carried out with the specimen permanently submerged in physiological serum (PBS) at a temperature of 37 ± 0.5 °C. In order to achieve uniform temperature conditions in the sample, a time interval of 10 min was considered between the end of the assembly and the beginning of the test.

In this test, the bending stage is performed to place the specimen in the tensile machine jaws as shown in Fig. 4. The self-contact wrinkles that can be seen in the front view are due to the local buckling that develops in this zone during the bending. In contrast, the tissue observed in the back view exhibits a tensile axial stress state.

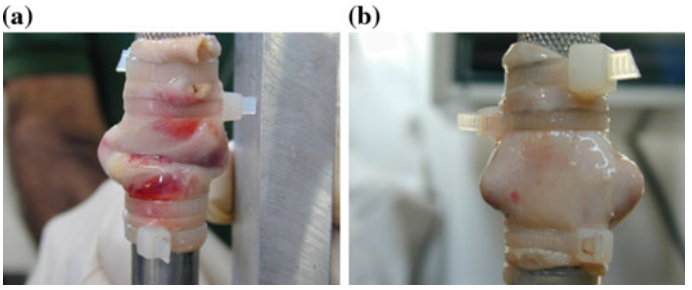

Fig. 4 Aortic arch sample mounted and clampled in the tensile machine jaws (end of bending stage); **a** *front view* and **b** *back view*

The next loading stage is achieved by axially deforming the arch whereas the subsequent pressurization stage consists in the application of internal pressure by means of an external compressor that injects PBS into the artery (further details of the experimental setup can be found in Guinea et al. [46]). The full loading sequence is schematically depicted in Fig. 5.

The axial stretching stage is accomplished via a prescribed displacement that corresponds to an average longitudinal stretch, defined as the ratio between the final and initial lengths of the artery axis, of 1.7. The initial length of the artery axis is considered as the average of the internal and external arc lengths (measured via image postprocessing with an error of ± 2.0 mm) while the final length of the artery axis corresponds to the final distance between the jaws. This displacement value was selected to remove the wrinkles and, thus, to allow more accurate measurements of the external diameter of the artery during the pressurization stage. Moreover, the load cell velocity considered in the tests up to the rupture of the sample was 0.03 mm/s.

Internal pressure and external diameter of the sample were recorded during the pressurization stage. An optical extensometer was used to acquire the external

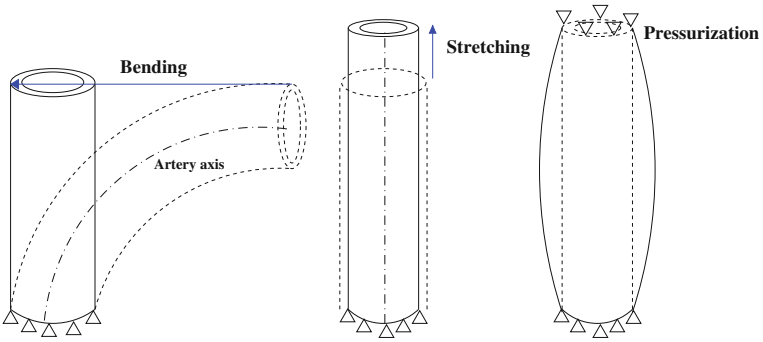

Fig. 5 Loading sequence applied to an aortic arch sample: bending, axial stretching and internal pressurization

diameter evolution (with a precision of 0.001 mm) along the height of the sample. Although the deformed cross-sections were no longer circular, the diameter values measured from the optical extensometer located at different angular positions varied around 10 % with respect to the maximum diameter. Moreover, ten successive loading cycles up to a pressure value of 200 mmHg were executed to precondition the samples. This pressure level is beyond the normal physiological range (i.e., 80–120 mmHg). The pressure rate considered in this stage was 1 mmHg/s.

2.2 Constitutive Modeling

According to the measurements to be presented in Sect. 3, an elastic (either isotropic or anisotropic) and rate-independent material response is considered for the artery analyzed in the present work. Moreover, its behaviour is taken as incompressible due to the large amount of water present in it [78]. To this end, hyperelastic constitutive models can be used to describe its mechanical response [36, 51, 61, 69, 76, 82, 85]. In this context, a deformation energy function W, assumed to describe the isothermal material behaviour under any loading conditions, is usually defined in terms of the right Cauchy deformation tensor $\boldsymbol{C} = \boldsymbol{F}^{\mathrm{T}} \cdot \boldsymbol{F}$, where $\boldsymbol{F}$ is the deformation gradient tensor and T is the transpose symbol (note that $\det \boldsymbol{F} = 1$ in this case). Invoking classical arguments of continuum mechanics, the Cauchy stress tensor $\boldsymbol{\sigma}$ is defined as $\boldsymbol{\sigma} = 2\boldsymbol{F} \cdot \frac{\partial W}{\partial \boldsymbol{C}} \cdot \boldsymbol{F}^{\mathrm{T}}$. The isotropic and anisotropic constitutive models considered in this work are separately described below. Both constitutive models are implemented in an in-house finite element code extensively validated in many engineering applications where isoparametric elements including a *B-bar* technique are used to avoid numerical locking due to material incompressibility (see Celentano [14] and references therein).

2.2.1 Demiray Model

The isotropic energy function proposed by Demiray [26] is expressed as:

$$W = \frac{a}{b}\left[\exp\left(\frac{b}{2}\left(I_1 - 3\right)\right) - 1\right] \tag{1}$$

where I_1 is the first invariant of $\boldsymbol{C}$ ($I_1 = \mathrm{tr}(\boldsymbol{C})$, tr being the trace symbol). Although this isotropic model is relatively simple (i.e., only depends on I_1), reasonably good responses at high levels of deformation can be predicted with it [25]. Only two constants, a and b, are needed for the material characterization where the parameter a has a clear physical meaning given by the slope at the origin of the Cauchy stress versus stretch tensile test curve.

The constitutive model expressed by Eq. 1 is adopted in this work to assess its capabilities in the prediction of the material responses to be presented in Sect. 3

by using the material parameters obtained from the mechanical characterization described below. Although the Demiray model is used in the present study to assess the risk of rupture, it should be noted that it cannot predict the risk of dissection since it does not take into account the layered nature of the tissue.

2.2.2 Holzapfel Model

The Holzapfel model adopted in this work aims at consistently characterizing the material anisotropy present in the internal structure of artery tissues [51]. To this end, it assumes that the colagen fibers, which are strongly involved in the mechanical response at moderate-to-high levels of deformation, are helically oriented by means of an approximately constant angle with the artery axis. This model, formulated within the pseudo-invariants framework developed by Spencer [97], considers the orientations of two symmetric family of fibers defined in the reference (initial) configuration through two unit vectors $\boldsymbol{a}$ and $\boldsymbol{a}'$ disposed with an angle $\pm\varphi$ with the vessel axis; see Fig. 6 (it should be noted that, for simplicity, neither fiber dispersion nor layer-specific responses have been considered; see e.g., Holzapfel et al. [52] and Gasser et al. [41]). The following two invariants can be accordingly defined: $I_4 = \boldsymbol{a} \cdot \boldsymbol{C} \cdot \boldsymbol{a}$ and $I_6 = \boldsymbol{a}' \cdot \boldsymbol{C} \cdot \boldsymbol{a}'$. In this context, the energy function proposed by Holzapfel and Gasser [51] is written as:

$$W = \frac{\mu}{2}(I_1 - 3) + \frac{k_1}{2k_2} \sum_{i=4,6} \left[\exp\left(k_2(I_i - 1)^2\right) - 1\right] \tag{2}$$

where I_1 is the first invariant of $\boldsymbol{C}$ ($I_1 = \mathrm{tr}(\boldsymbol{C})$, tr being the trace symbol) and μ, k_1, k_2, φ are material parameters (all with positive values). In Eq. 2, the first term expressed by a classical Neo-Hookean isotropic model is intended to describe the

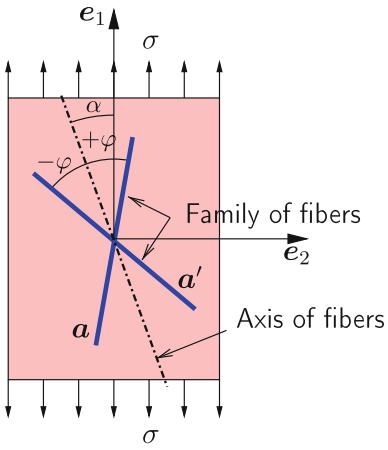

Fig. 6 Holzapfel-type material tensile sample

elastin response while the goal of the other terms is to predict the anisotropic behaviour of the artery given by the directions of the colagen fibers defined, in turn, by the invariants I_4 and I_6. Since this model only accounts for macroscopic response, the collagen fraction quantified in the histological analysis is not explicitly considered in this context. Its capabilities in the predictions of the material response are illustrated in Sect. 3.

2.3 Material Characterization via the Tensile Test

2.3.1 Determination of Characteristic Stress and Strain Values

True stress (σ) versus stretch (λ) relationships for all the tests were derived from experimental load-displacement curves. When tensile tested, aortic wall specimens either circumferential or longitudinal typically display the characteristic J-shape curve depicted in Fig. 7. For small values of applied stress, the aortic tissue exhibits a compliant behaviour that turns into a much stiffer response when stresses exceed the elbow of the curve. To simplify the analysis and allow comparison among different specimens, the stress-stretch curve was condensed into three parameters that summarised the main mechanical response of the arterial wall: the stretch and stress at the breaking point (λ_R, σ_R), and the stress at the transition point, or elbow, between the compliant and the stiff regions (σ_e).

The breaking point of the sample was defined as the first point where one of its layers fails, easily identified in the tensile curve by a sudden drop of the load. Although in the vascular biomechanics literature the ultimate tensile strength is usu-

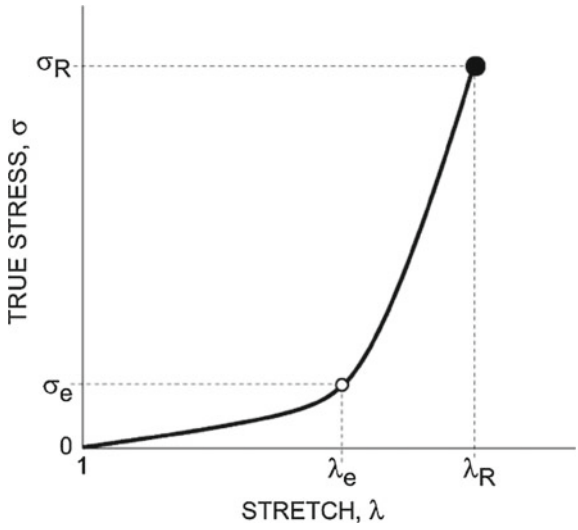

Fig. 7 Stress-stretch curve of an aortic tissue and mechanical parameters

ally taken as the stress at the rupture stage, in the measurements reported in this work the difference between these two definitions was less than 5 %. Therefore, the values presented in this study are comparable to other published data. Moreover, the elbow stress was determined by the change in the first derivative of stress with respect to stretch, according to the procedure given in the appendix.

Data processing and statistics At least six specimens were tensile tested per individual, three in each of two directions (longitudinal and circumferential). All in all, 355 tests on ascending aortic tissue were carried out. Values of the three parameters defined above were averaged for each individual and orientation, and individual means averaged again for each study group and orientation. Data are presented as mean ± standard error. An unpaired 2-tailed Student's t test was performed to compare mechanical parameters. Significance was assumed for p as less than 0.05.

2.3.2 Fitting of Model Material Parameters

The aim of this section is to determine the material parameters of the Demiray and Holzapfel constitutive model briefly presented in Sect. 2.2 from the uniaxial test measurements to be reported in Sect. 3.

Demiray Model

For the Demiray constitutive model, the Cauchy stress associated to the loading direction 1 can be exclusively written in terms of the related stretch λ_1 since the incompressibility constraint for an isotropic behaviour reads as $\lambda_2 = \lambda_3 = \frac{1}{\sqrt{\lambda_1}}$ [76]. Thus:

$$\sigma_1 = a\left(\lambda_1^2 - \frac{1}{\lambda_1}\right)\exp\left[\frac{b}{2}\left(\lambda_1^2 + \frac{2}{\lambda_1} - 3\right)\right] \tag{3}$$

In this case, the logarithmic version of Eq. 3 results in a linear least-squares fitting procedure of the material parameters a and b [40]. Moreover, equal weights for both the longitudinal and circumferential responses were simultaneously considered. The resulting material parameters for some vessels studied in this work are presented in Sect. 3.

Holzapfel Model

For the Holzapfel constitutive model it is not possible to obtain a closed expression for the Cauchy stress σ_1 (stress associated with the loading direction 1) and the related stretch λ_1. Therefore, this aspect precludes in this case a straightforward derivation of the related material parameters. According to the procedure described in Ogden [77], the material response during the tensile test predicted by this model is governed by:

$$\sigma_1 = \mu\left(\lambda_1^2 - \frac{1}{\lambda_1^2\lambda_2^2}\right) + 2W_4\lambda_1^2\cos^2(\varphi - \alpha) + 2W_6\lambda_1^2\cos^2(\varphi + \alpha) \tag{4}$$

$$\sigma_2 = \mu\left(\lambda_2^2 - \frac{1}{\lambda_1^2\lambda_2^2}\right) + 2W_4\lambda_2^2\sin^2(\varphi-\alpha) + 2W_6\lambda_2^2\sin^2(\varphi+\alpha) = 0 \quad (5)$$

where $W_i = \partial W/\partial I_i$ $(i = 4, 6)$ and α denotes the sample orientation (i.e., $\alpha = 0°$ and $\alpha = 90°$ for longitudinal and circumferential samples, respectively; see Fig. 6). In this case, the $\sigma_1(\lambda_1)$ expression can be obtained by previously solving λ_2 from Eq. 5 for an estimated set of material parameters (i.e., μ, k_1, k_2, φ) and a given value of λ_1. This last operation is performed through the application of the Newton-Raphson method due to the non-linear nature of Eq. 5.

The fitting procedure to determine the material parameters for the Holzapfel model is inherently non-linear. Robust and optimal identification procedures have been developed by Sacks [94], Vande Geest et al. [99, 100]. However, a simpler alternative approach is considered in the present work. It basically consists in two steps respectively associated with the two elongation zones defined in Sect. 2.3.1 [13, 53]:

(1) Estimation of parameter μ through a linear least-squares computation aimed at exclusively characterizing the isotropic response (i.e., the anisotropic terms of the energy function (2) are neglected at this stage) at low stretching levels.
(2) Derivation, at high levels of elongation, of the anisotropic parameters k_1, k_2, φ (with a fixed μ value) via a non-linear least-squares expression solved with the Levenberg-Marquardt algorithm [67]. In this step, the constraint $\lambda_2 < 1$ is additionally considered in order to obtain a more realistic material response.

Finally, the fitting procedure simultaneously considers both the longitudinal and circumferential responses where equal weights are adopted for the two sample directions.

2.4 Analysis of the Pressurization Test

Although some authors have used this test to derive material parameters for different constitutive models [91, 96], the aim of the present analysis is to assess the ability of the material characterization previously described in Sect. 2.3 via tensile tests to properly model the behaviour of the vessel when it is subjected to axial load and internal pressure.

The mechanical response of the pressurized artery is analyzed in this work by using the constitutive models presented in Sect. 2.2. The effects of both residual stresses and instabilities due to buckling are neglected. It is further assumed here that the artery is a homogeneous thin-walled cylinder with a large length to diameter ratio in order to neglect edge effects. At what extent this relatively simple approach is able to realistically describe the average material response during the pressurization test is another objective of this study. For the loading conditions carried out in

the experiments shown in Sect. 2.1.3, the material response provided by the Demiray and Holzapfel constitutive models are presented below.

Demiray Model

$$P_i = \frac{2aB_0}{D_0\,\lambda_\theta\,\lambda_z}\left(\lambda_\theta - \frac{1}{\lambda_\theta^3\,\lambda_z^2}\right)\exp\left[\frac{b}{2}\left(\lambda_\theta^2 + \lambda_z^2 - 1\right)^2\right] \tag{6}$$

Holzapfel Model

$$P_i = \frac{2\mu B_0}{D_0\,\lambda_\theta\,\lambda_z}\left(\lambda_\theta - \frac{1}{\lambda_\theta^3\,\lambda_z^2}\right) + 8k_1\frac{B_0}{D_0\,\lambda_\theta\,\lambda_z}\exp\left[k_2\left(\lambda_\theta^2\sin^2\varphi + \lambda_z^2\cos^2\varphi - 1\right)^2\right] \left(\lambda_\theta^2\sin^2\varphi + \lambda_z^2\cos^2\varphi - 1\right)\lambda_\theta\sin^2\varphi \tag{7}$$

where P_i is the pressure, λ_θ is the circumferential stretch, λ_z is the axial stretch, D_0 is the initial diameter and B_0 is the initial thickness of the vessel wall.

3 Results

3.1 Ascending Aorta

3.1.1 Tensile Stretches

Tensile stretches at failure are shown in Fig. 8. To evaluate the anisotropy of the arterial wall, circumferential and longitudinal values are displayed for every group in both figures. No distinction has been made between male and female specimens, as no significant differences between the two sexes have been found in the experiments.

Directional differences in mechanical behaviour were found for healthy specimens, groups 0 A and 0B, where the circumferential failure stresses were greater than the longitudinal ones (2.18 ± 0.24 vs. 1.14 ± 0.10 MPa, p = 0.001 for group 0A and 1.20 ± 0.20 vs. 0.66 ± 0.07 MPa, p = 0.02 for group 0B). A similar trend was observed for BAV and aneurismal groups, although only in the BAV group the difference was statistically significant (1.23 ± 0.15 MPa circumferential vs. 0.84 ± 0.10 MPa longitudinal, p = 0.04 for group I (BAV), and 1.19 ± 0.13 MPa circumferential vs. 0.88 ± 0.12 MPa longitudinal, p = 0.09 for group II).

Values of stretch at failure, shown in Fig. 9, confirm the anisotropy of the young healthy specimens, group 0A, (2.35 ± 0.10 circumferential vs. 2.00 ± 0.10 longitudinal, p = 0.03) and BAV aortic wall tissues, group I (1.80 ± 0.08 circumferential vs. 1.58 ± 0.06 longitudinal, p = 0.04), with the differences being non significant for the other groups, either healthy (0B) or diseased (II).

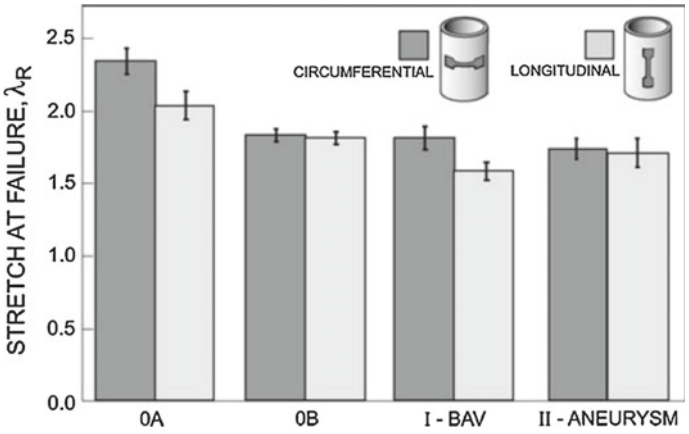

Fig. 8 Stretch at failure (mean ± standard error) of ascending aortic wall samples for healthy and pathologic groups

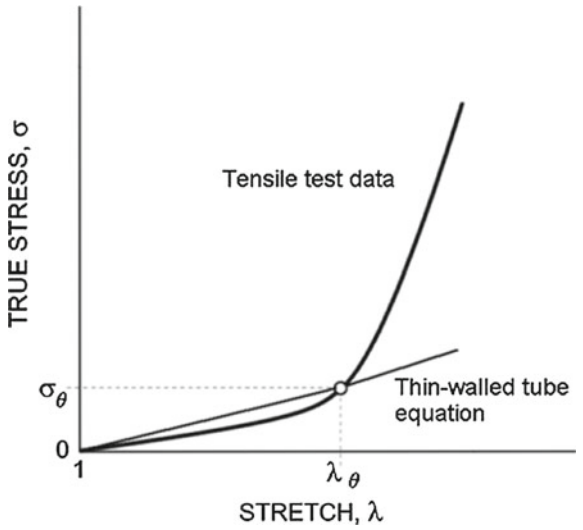

Fig. 9 Procedure to obtain the circumferential stretch for in-vivo conditions

3.1.2 Tensile Strengths

The tensile strengths of the ascending aortic wall for the two control groups 0A and 0B (young and old specimens, respectively) and the two groups of pathologies considered in the study. To assess the risk of rupture of aortic ascending wall, tensile strengths have to be compared with the circumferential stresses exerted on the aortic wall by blood pressure, which can be readily evaluated to a good approximation by means of the thin-walled tube equation: $\sigma_\theta = \frac{p}{2t}\,\lambda_\theta\,\lambda_z(\lambda_\theta\,D - \frac{t}{\lambda_\theta\,\lambda_z})$, where σ_θ is the circumferential stress, p is the blood pressure, λ_θ is the circumferential stretch, λ_z

is the longitudinal stretch, t the wall thickness and D the aortic diameter. Note that $\sigma_\theta, p, \lambda_\theta, \lambda_z$ are in-vivo variables while D, t are in-vitro variables (see Table 3).

This equation allows the computation of the in vivo circumferential stress considering the following assumptions: (1) the longitudinal stretch under in vivo conditions is $\lambda_z = 1.2$ [56] and (2) the circumferential stretch λ_θ is estimated from the tensile test measurements, as depicted in Fig. 10, resulting the values 1.52, 1.47, 1.44 and 1.38 for groups 0A, 0B, I and II, respectively. Figure 10 shows the mean circumferential wall stresses computed for every group of study under the assumption of normotensive pressure levels (100 mmHg). The in-vivo ascending aortic diameters agree well with those reported in the literature for healthy specimens of corresponding age (around 30 ± 0.5 mm) [48] and for bicuspid aortic valve group (50 ± 4 mm) [79]. For aneurysm group (II), the computed in vivo circumferential wall stresses is similar to that measured elsewhere from a group of age-matched patients (65 ± 5 years) [60].

Stress at the elbow of the tensile curve Tensile curves of aortic wall specimens display an initial compliant zone for small and medium strains followed by a region of higher stiffness. Elastin fibres contribute mostly to the first part of the curve, while progressive recruitment and extension of collagen fibres are responsible for the second region [90]. The transition zone, or elbow point, is usually well marked and can be characterised by its corresponding stress. Figure 11 plots the circumferential elbow stresses for the four groups of aortic specimens considered in this work. Elbow stresses were computed from stress-strain curves, as explained in the appendix. Figure 11 also shows the mean circumferential wall stresses produced by blood pressure (100 mmHg) that were estimated earlier in this section.

The elbow stress decreases markedly with age, with it being more than halved in healthy specimens from 0.31 ± 0.02 MPa for group 0A (25 ± 3 years) to 0.14 ±

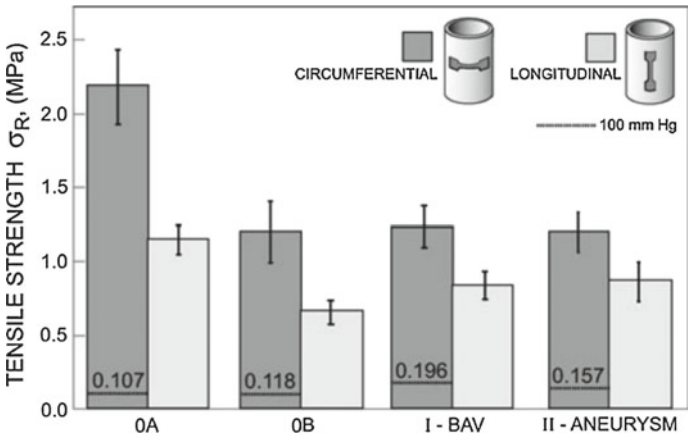

Fig. 10 Tensile strength (mean ± standard error) of ascending aortic wall samples for healthy and pathologic groups. The mean physiological stress level in the aortic wall at 100 mmHg is shown for each group

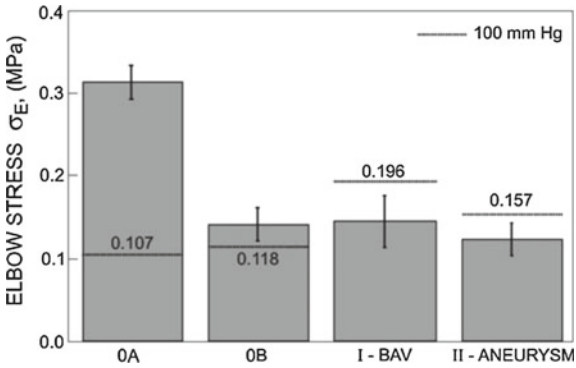

Fig. 11 Elbow stress (mean ± standard error) of ascending aortic wall samples for healthy and pathologic groups. The mean physiological stress level in the aortic wall at 100 mmHg is shown for each group

0.02 MPa for group 0B (51 ± 2 years). Pathologies do not show a subsequent reduction of elbow stress, as their values do not show significant differences with respect to group 0B (0.15 ± 0.02 for group I, bicuspid aortic valve, and 0.13 ± 0.02 MPa for group II, aneurysm).

3.2 Aortic Arch

3.2.1 Tensile Test

The average stress-stretch curves corresponding to an adult group (see Table 8) for both the longitudinal and circumferential directions are plotted in Fig. 12 (the vertical bars denote the standard error, i.e., the ratio between the standard deviation and the square root of the number of specimens). It should be noted that similar material responses were observed at different positions around the circumference and along the length of the artery. Therefore, the good repeatability achieved in the experiments justifies the assumption of homogeneity in the constitutive models described in Sect. 2.2. Moreover, the high rupture stress value obtained for this aortic arch can be attributable to the fact that this tissue was relatively young and healthy.

The stress-stretch curve obtained by applying a least-squares fitting of the resulting $\sigma_1(\lambda_1)$ relationship (3) to the corresponding experimental data for both the longi-

Table 8 Aortic arch groups considered in the study: age interval and material parameters

		Material parameters	
Group	Age	a (kPa)	b
Young	16–36	104.0	0.844
Adult	36–65	107.0	1.400
Aged	65–90	69.2	5.792

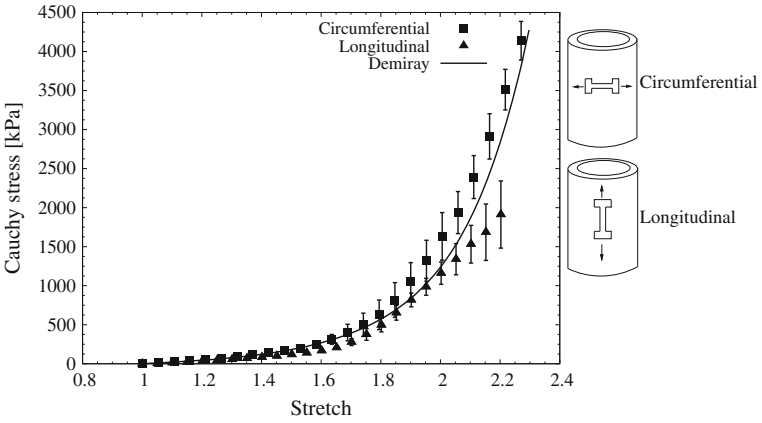

Fig. 12 Experimental and computed results of Cauchy stress versus stretch for the aortic arch adult group

tudinal and circumferential directions is plotted in Fig. 12. According to the measurements reported above, the whole stretch range (1.0–2.3) was chosen for the present material characterization. The resulting material parameters derived with this procedure are shown in Table 8. These parameters are used in the simulations presented in Sect. 3.2.2.

The average experimental stress-stretch curves obtained up to the rupture stage along the circumferential direction for both young and aged groups (see Table 8) are plotted in Fig. 13 where a good repeatability of the measurements can clearly be observed. Although not shown, the stress-stretch curves along the axial direction exhibited no significant differences with those along the circumferential direction in a wide stretch range ([1.0–2.1] and [1.0–1.6] for the young and aged samples, respectively). Thus, the behaviour can be assumed as practically isotropic since its stiffness is mainly provided by the elastin component of the tissue. Moreover, it should be noted that similar material responses were observed at different positions around the circumference and along the length of the artery. Therefore, these two aspects (i.e., material isotropy and homogeneity) justify the assumption that an adequate description of the material behaviour can be simply tackled by means of the constitutive model expressed by Eq. 1. In addition, the tensile response of arteries belonging to healthy patients with ages between 37 and 51 years old (not shown here) exhibits an intermediate response between those presented in Fig. 13.

The stress-stretch curves obtained by applying a least-squares fitting of Eq. 3 to the corresponding experimental data are also plotted in Fig. 13. The material parameters derived with this methodology are included in Table 8. A detailed description of this material characterisation procedure is reported in García-Herrera et al. [40]. These parameters are used in the simulations presented in Sect. 3.2.3.

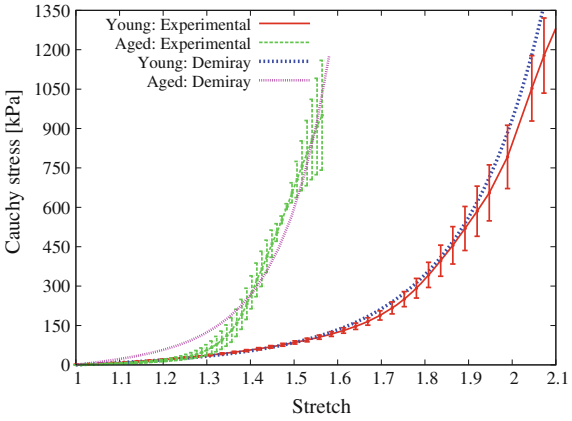

Fig. 13 Experimental measurements and computed results of Cauchy stress versus stretch along the circumferential direction for the aortic arch young and aged groups ($r^2_{Young} = 0.996$ and $r^2_{Aged} = 0.961$)

3.2.2 Bending and Pressurisation Test

The experimentally measured evolution of the internal pressure (during the loading and unloading phases) in terms of the maximum external diameter for the axial stretch achieved in the previous loading stage of an artery belonging to the adult group (see Table 8) is shown in Fig. 14. In this case, the external diameter rate was found to be 0.05 mm/s approximately (which results in a circumferential deformation rate of 45 %/min approximately). The average circumferential stretch at the end of the test, defined as the ratio between the final and initial external diameters of the artery, was approximately 1.5.

The mechanical response of the human aortic arch during the bending and pressurization test already described in Sect. 2.1.4 is analyzed in this work by using the non-linear constitutive model and the corresponding material parameters respec-

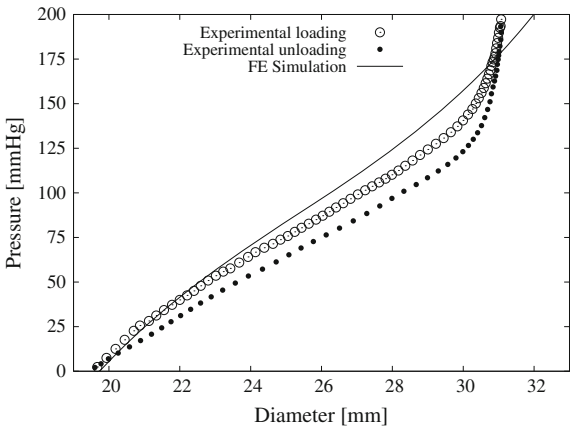

Fig. 14 Experimental and computed results of internal pressure versus external diameter of the adult aortic arch

tively presented in Sects. 2.2 and 3.2.1. To this end, a numerical simulation of the stages involved in such test (i.e., bending including axial stretching and pressurization) is carried out. The aortic arch was geometrically discretized as a 90° elbow with constant internal diameter and thickness (18 mm and 1.3 mm, respectively). A convergence study of the numerical response to different discretizations was performed. The resulting finite element mesh shown in Fig. 15a is composed of 1280 eight-noded isoparametric elements. It is seen that only one half of the arch was considered in the computations owing to the symmetry of the problem. A finer discretization was chosen for both ends since large strain and stress gradients are expected in those zones.

The boundary conditions adopted in the simulation, which are essentially the same as those imposed in the experiment, are schematically depicted in Fig. 5. The lower end was clamped during the whole test. The bending stage (which also involves axial stretching in the present analysis) was carried out by applying a prescribed displacement at the upper end of the arch (as in the experiment, with an average longitudinal stretch of 1.7) in order to straighten it. In this way, the numerical simulation of local buckling and self-contact developed during the purely bending phase shown in Fig. 4 was avoided. As the mechanical behaviour of the arch is considered elastic,

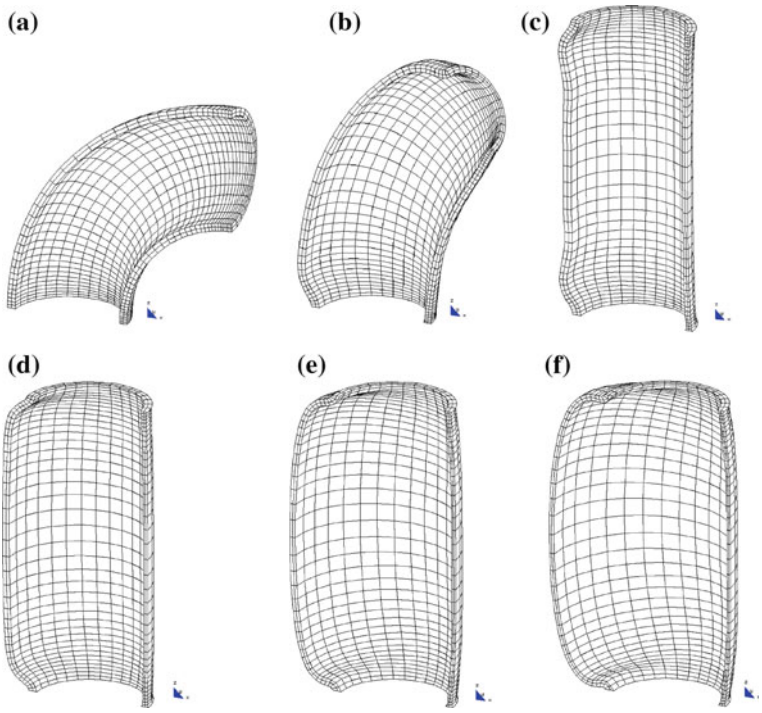

Fig. 15 Deformed configurations of the adult aortic arch for different steps of the numerical simulation: initial (**a**), bending and axial stretching (**b**, **c**) and pressurization (**d**–**f**)

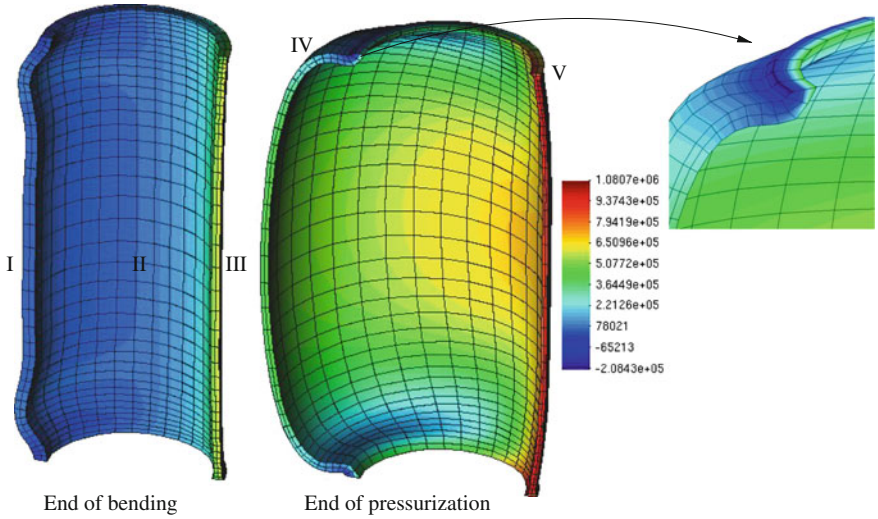

Fig. 16 Maximum principal stress contours (Pa) of the adult aortic arch

it can be assumed that the simplified boundary conditions adopted in the simulation do not affect the predictions of the material response (this load-history independent response was verified by performing an additional simulation with exactly the same boundary conditions as those of the experiment where, in this case, self-contact is developed at the end of the bending stage). Then, the upper end was clamped to subsequently perform the pressurization stage up to a final pressure value of 200 mmHg (it should be mentioned that the additional non-linearity that resulted from this follower load was taken into account in the simulation). Moreover, due to the large deformations considered in this test, the effect of the residual stress is neglected in the present analysis (according to [38], the residual stresses can be estimated as 20 % of the stresses in an artery loaded within the physiological range).

Figure 15 depicts the computed deformed configurations of the adult aortic arch during the whole loading sequence: bending (b, c) and pressurization (d–f). Figure 16 plots maximum principal stress contours at the end of the bending and pressurization stages.

The computed curve of the internal pressure versus the maximum external diameter of the adult aortic arch is plotted in Fig. 14. Moreover, qualitative and quantitative experimental-numerical comparisons of the final deformed configuration of this artery are respectively shown in Figs. 17 and 18.

3.2.3 Simulation Under In-Vivo Conditions

This section presents the numerical simulation of the mechanical response of young and aged human aortic archs (see Table 8) under in-vivo normal and hypertension

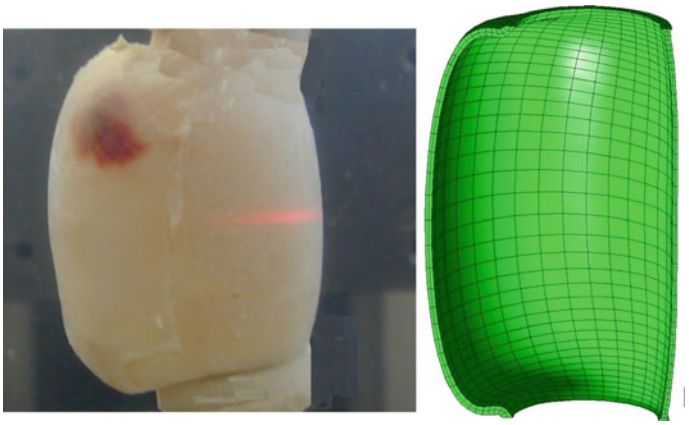

Fig. 17 Final deformed configuration of the adult aortic arch: experiment (*left*) and simulation (*right*)

Fig. 18 Maximum external diameter distribution along the length of the adult aortic arch

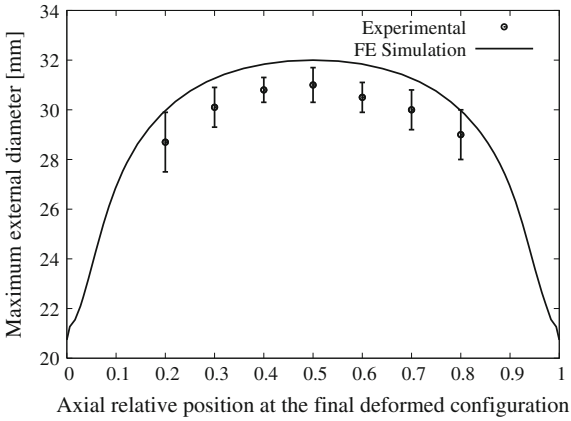

physiological conditions, i.e., systolic pressure of 120 and 160 mmHg, respectively. To this end, important aspects related to this analysis are separately presented below.

Geometry and Boundary Conditions

The geometry of the human aortic arch used in the numerical simulation carried out in this work was obtained from anatomical data of adults [6, 83] and from the samples considered in Sect. 2.1.1. The geometric configuration corresponds to the arch subjected to the diastolic pressure (80 mmHg). It should be noted that the initial stresses resulting from this condition must be taken into account in the simulation, otherwise the response is fictitiously flexible. This aspect is described in below. Figure 19 depicts the geometry of the human aortic arch considered in the present analysis.

In-vivo measurements on healthy patients during their cardiac cycle reported by Beller et al. [5] are adopted here in order to define appropriate boundary conditions.

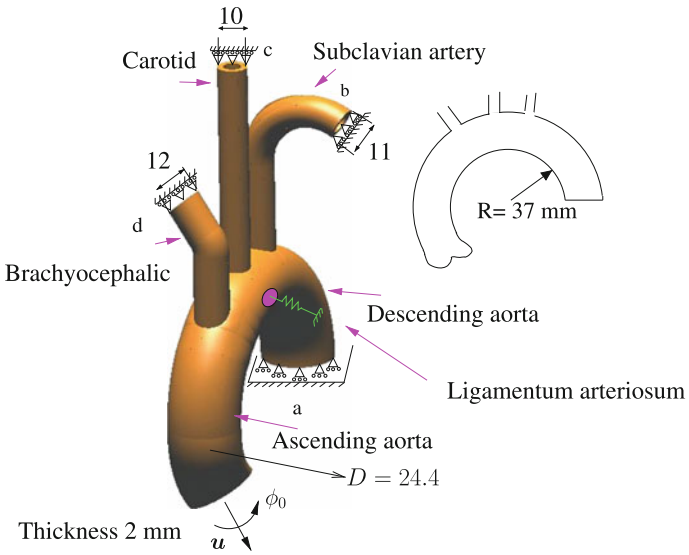

Fig. 19 Geometry and boundary conditions of the human aortic arch considered in the analysis for young and aged groups (dimensions in mm)

They encompass three types of kinematic constraints. Firstly, the axial motion of the aortic root, caused by its connection to the left ventricle, consisting in an axial displacement of $u = 8.9$ mm and a rotation of $\phi_0 = 6°$; see Fig. 19. Secondly, the other four edges of the aortic arch are assumed to be axially fixed and unconstrained along the radial direction. Thirdly, the effect of the ligamentum arteriosum is taken into account by means of a spring element with a stiffness ten times higher than that of the aortic arch tissue. The influence of this ligamentum on the mechanical response of the aortic arch under extreme scenarios was described by Richens et al. [87, 88]. All these boundary conditions are shown in Fig. 19.

Estimation of Initial Stresses

The in-vivo initial stresses present in the different arteries of the aortic arch are estimated in this work for the diastolic pressure (80 mmHg) together with and axial stretch of 1.2 according to the measurements reported by Chuong and Fung [16]. Both the circumferential σ_θ and axial σ_z components of the stress tensor are firstly computed with the thin-walled equation for cylinders [39]. The assumption of constant stress along the wall thickness is justified by the long recognized fact that the main purpose of the initial hoop stress radial distribution that develops along the artery wall is the achievement of a nearly uniform stress pattern in the vessel when it is subjected to standard physiological loading states [36, 79]. The obtained values for the initial circumferential and axial stress components are summarised in Table 9. However, this computed initial stress field does not strictly fulfill, in general, the equilibrium with the internal pressure (80 mmHg). This drawback is overcome via the numerical procedure described below.

Table 9 First estimation for the initial stress components of young and aged arteries at a pressure of 80 mmHg

Vessel	σ_θ (kPa)	σ_z (kPa)
Aortic arch	65.1	32.6
Brachyocephalic trunk	32.0	16.0
Carotid artery	26.7	13.4
Subclavian artery	26.7	13.4

The approach to obtain a compatible initial stress field is iteratively tackled by solving the equilibrium equations together with the Demiray constitutive model using the finite element method [40] until the condition of a nearly zero displacement field for the whole aortic arch is fulfilled. For this problem, a maximum admissible diameter variation of 2 % was chosen. The converged initial maximum principal stress field obtained with this procedure, which is considered in the simulations presented below, is shown in Fig. 20. It is seen that the stresses are mainly concentrated at the vicinity of the bifurcations and ligamentum arteriosum. Although the stress distribution is not uniform along the thickness, the corresponding average values nearly agree with those summarised in Table 10. It should be noted the stress concentrations located around these zones were found to not be strongly affected by the curvature radii of the junctions of the branches from the aorta.

Stress and Stretch Contours

As mentioned above, the mechanical response of a human aortic arch is simulated under in-vivo normal and hypertension physiological conditions. In the first case, the systolic pressure of 120 mmHg is applied to the young aortic arch. In the second case, the effect of the hypertension pressure of 160 mmHg on young and aged vessels is analysed.

The simulations were carried out using the non-linear constitutive model and the corresponding material parameters respectively presented in Sects. 2.2 and 3.2.1.

The finite element mesh used in the simulations was composed of 28,437 nodes and 22,176 isoparametric hexahedra. Four elements were considered along the wall thickness in order to properly capture the stress radial gradients that may develop in the different regions of the aortic arch. It should be noted that this mesh is the result of a previous convergence study of the numerical response to different discretisations.

Table 10 Material parameters of the constitutive model for newborn, young and adult thoracic descending aortas

Group	μ (kPa)	k_1 (kPa)	k_2 (kPa)	φ (°)	R^2
A	21.972	3.011	0.7667	63.67	0.98
B	37.202	14.085	3.4752	43.88	0.95
C	24.655	45.055	5.3279	42.19	0.88

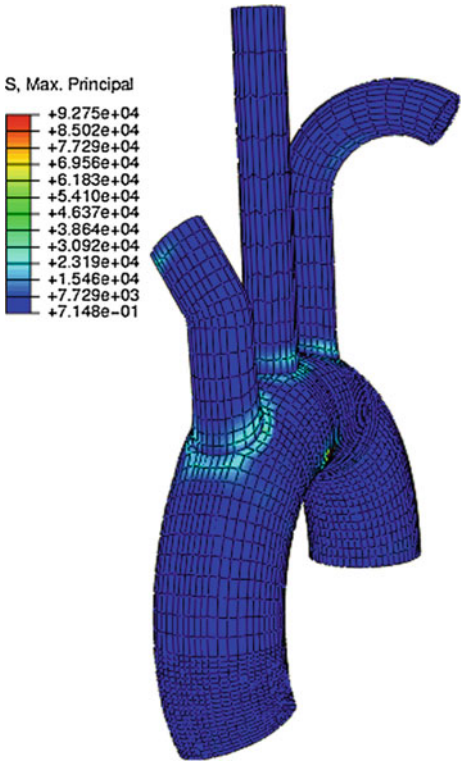

Fig. 20 Computed initial maximum principal stress at 80 mmHg for young and aged groups

The maximum principal stress and stretch contours at the deformed configuration for the young aortic arch subjected to 120 mmHg are plotted in Fig. 21. The same results at 160 mmHg for the young and aged aortic archs are respectively shown in Figs. 22 and 23. In addition, the radial, circumferential and longitudinal stress components computed for the hypertension conditions for both groups are respectively depicted in Figs. 24 and 25.

3.3 Descending Aorta

3.3.1 Tensile Test

The experimental average stress-stretch curves corresponding to the thoracic descending aorta Groups A, B and C (see Tables 5, 6 and 7, respectively) for both the longitudinal and circumferential directions are plotted in Fig. 26 (the vertical bars

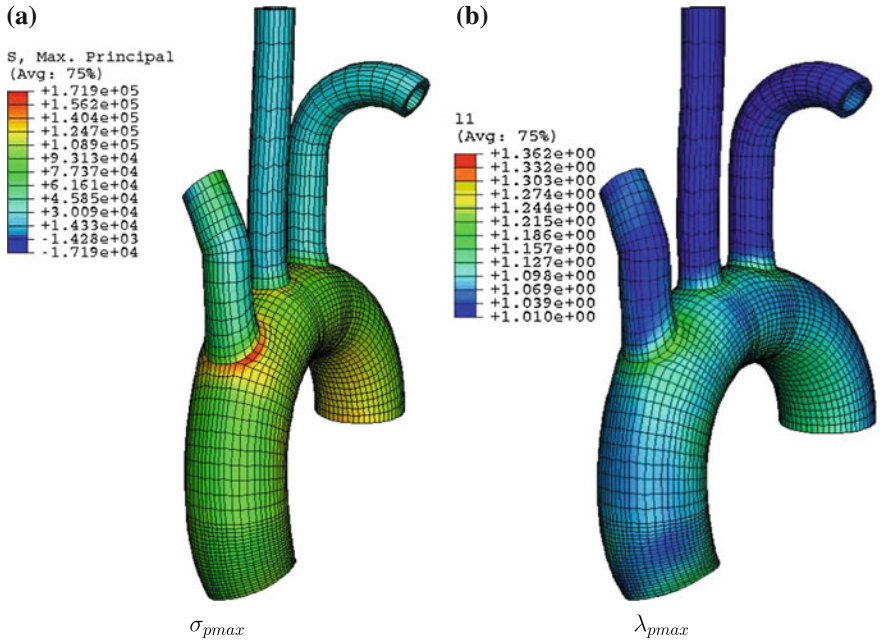

Fig. 21 Deformed configuration for the young aortic arch at 120 mmHg: **a** maximum principal stress (Pa) and **b** maximum principal stretch

denote the standard error, i.e., the ratio between the standard deviation and the square root of the number of specimens).

The stress-stretch curves obtained by applying the least-squares fitting described in Sect. 2.3 to the corresponding experimental data of Groups A, B and C for both the longitudinal and circumferential directions are plotted in Fig. 27 whereas Table 10 summarizes the derived material parameters for the Holzapfel constitutive model and the normalized mean square root error (R^2). According to the measurements reported above, the stretch range (1.0–1.8) was chosen for the present material characterization since it encompasses a larger deformation interval than that occurring the pressurization test presented below. Moreover, the computed R^2 values show that a good fitting was achieved for all groups.

3.3.2 Pressurisation Test

Figure 28 shows pressure versus circumferential stretch experimental data corresponding to the thoracic descending aorta Groups B and C for two different values of λ_z (1.0 and 1.2), where the two horizontal lines denote the physiological range of diastole and sistole of the cardiac cycle. The value $\lambda_z = 1.2$ was chosen since it

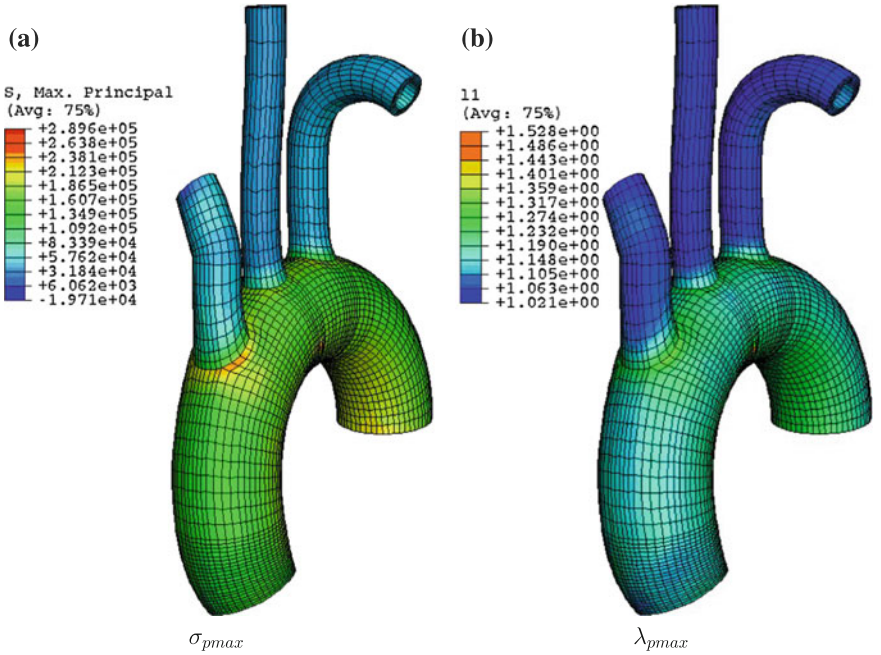

Fig. 22 Deformed configuration for the young aortic arch at 160 mmHg: **a** maximum principal stress (Pa) and **b** maximum principal stretch

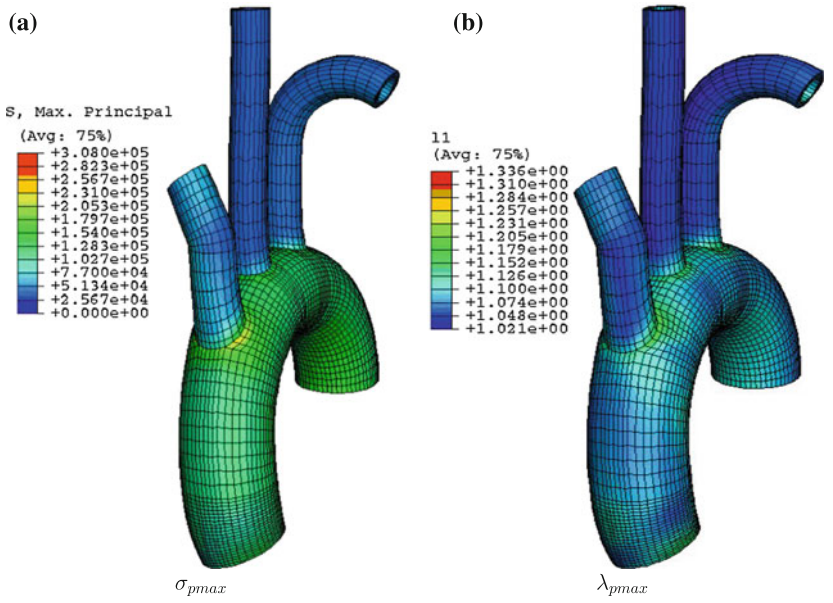

Fig. 23 Deformed configuration for the aged aortic arch at 160 mmHg: **a** maximum principal stress (Pa) and **b** maximum principal stretch

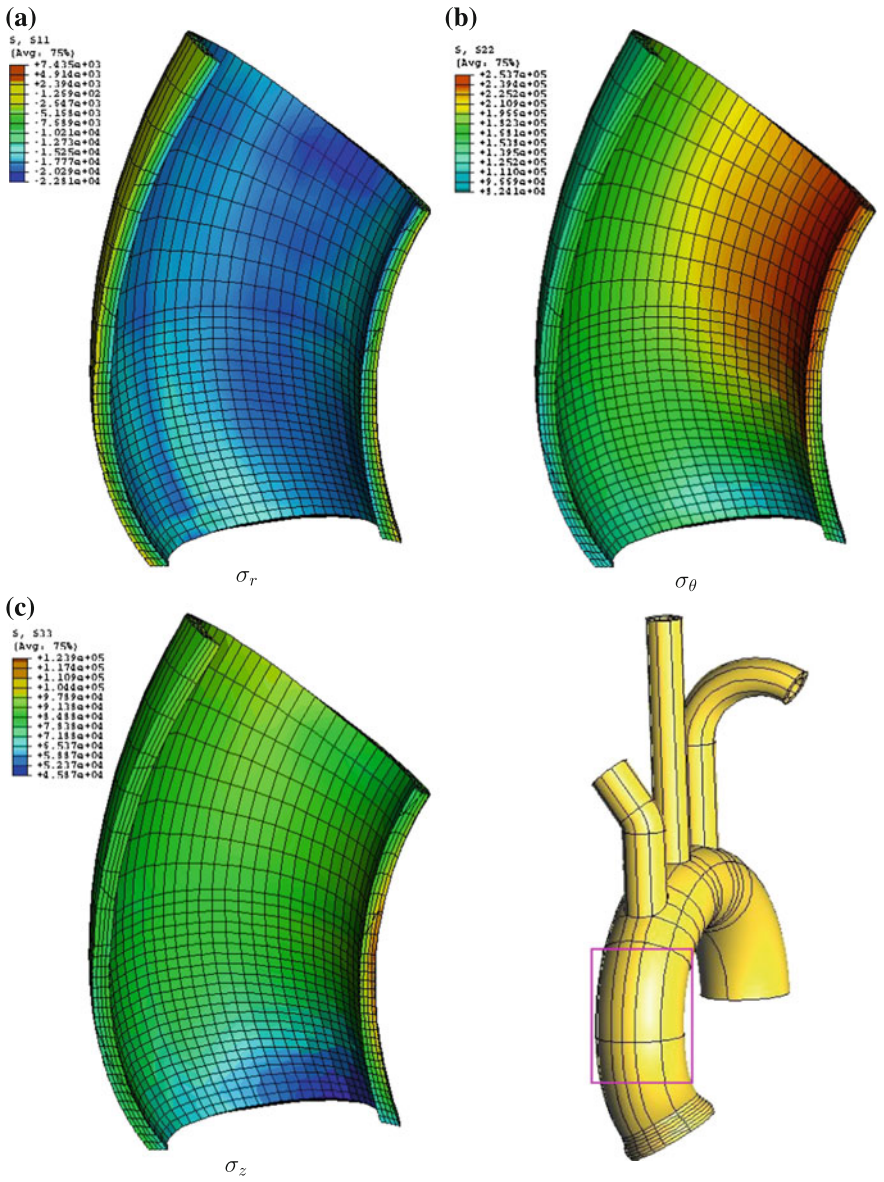

Fig. 24 Deformed configuration for the young aortic arch at 160 mmHg: **a** radial, **b** circumferential and **c** longitudinal stress components (Pa)

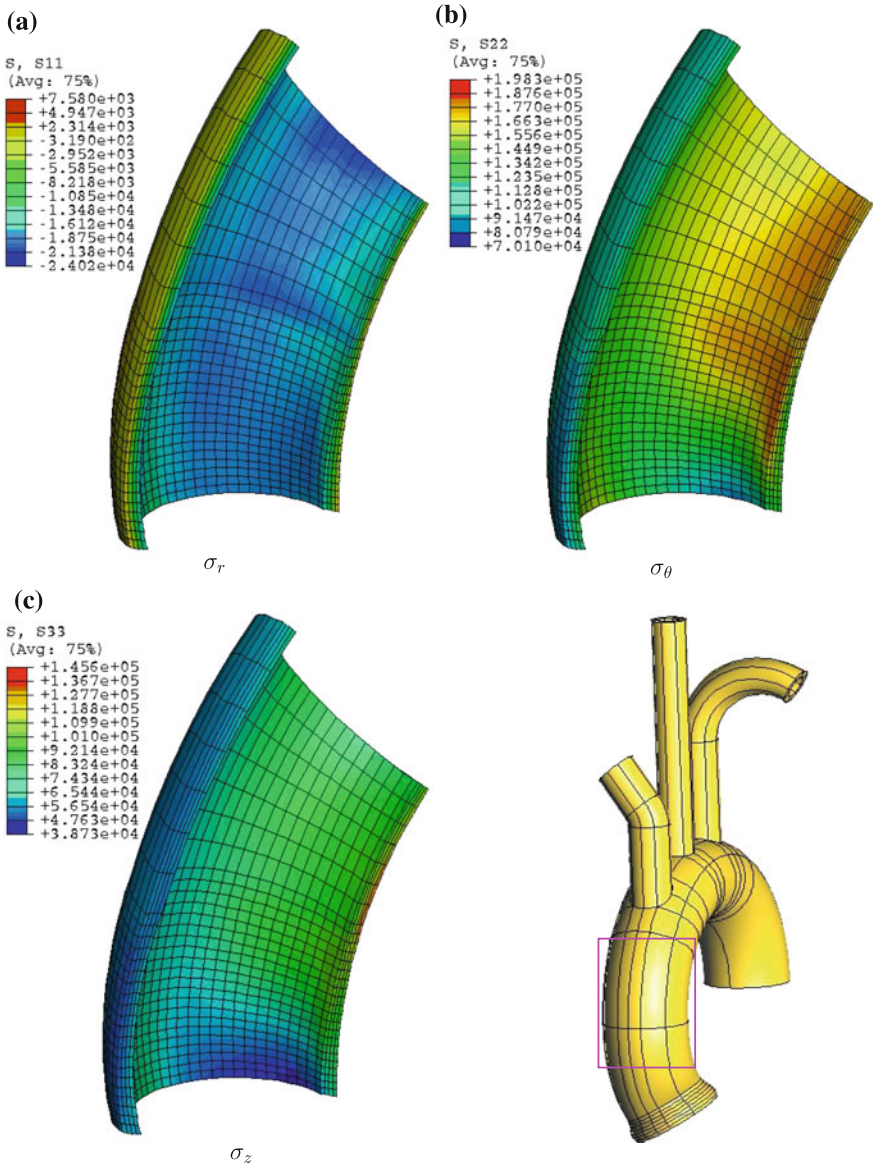

Fig. 25 Deformed configuration for the aged aortic arch at 160 mmHg: **a** radial, **b** circumferential and **c** longitudinal stress components (Pa)

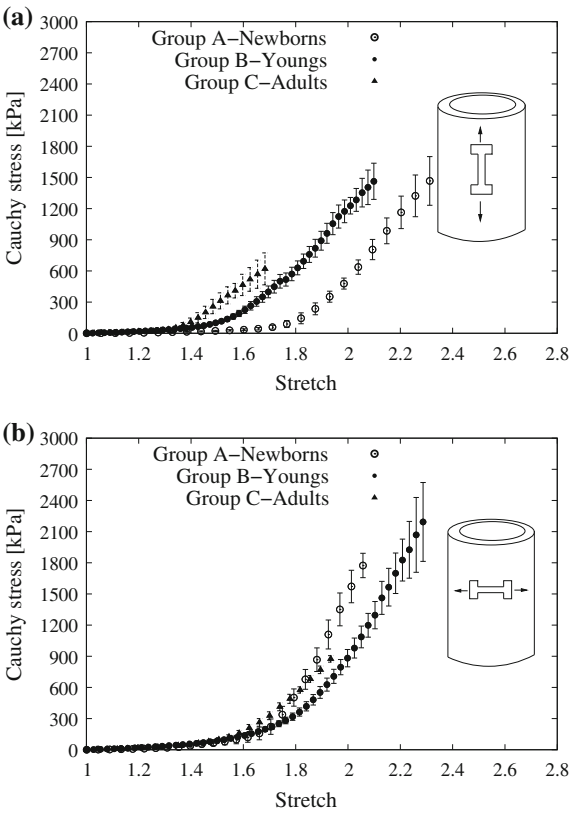

Fig. 26 Experimental data of Cauchy stress versus stretch for newborn, young and adult thoracic descending aortas. **a** Specimens oriented in longitudinal direction (0°). **b** Specimens oriented in circumferential direction (90°)

approximately corresponds to the average stretch measured in the vessel before the excision.

The internal pressure versus circumferential stretch curves obtained with the Holzapfel model (i.e., Eq. 7) are also presented in Fig. 28. The material response of Groups B and C is analyzed under the two axial stretch conditions described above.

4 Discussion

4.1 Ascending Aorta

Although our results are partially in agreement with previous data reported elsewhere [101], which did not find significant difference between circumferential and longitudinal specimens of either control or aneurismal tissue of aged patients, the trend

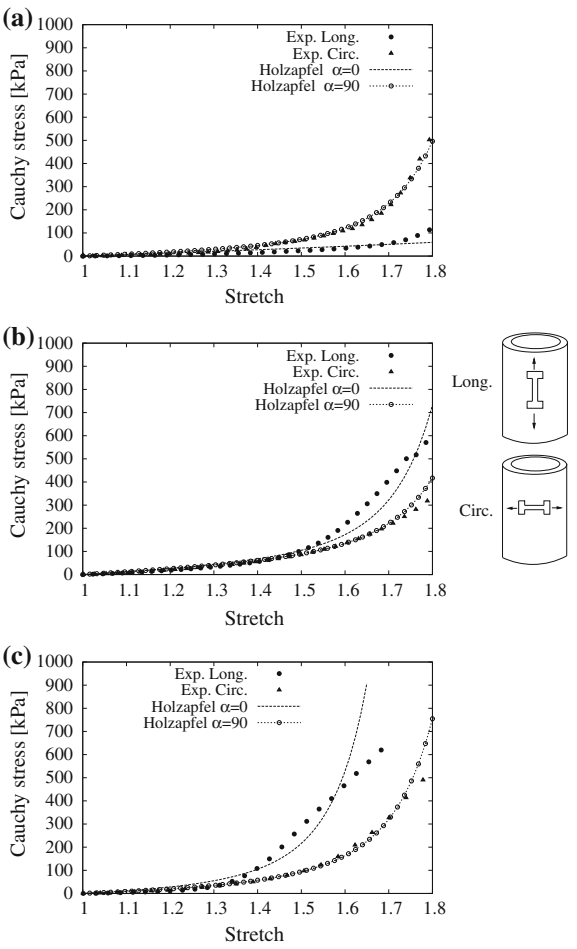

Fig. 27 Material characterization via Cauchy stress versus stretch curves for newborn, young and adult thoracic descending aortas. **a** Group A. **b** Group B. **c** Group C

noted in Fig. 10 suggests that a small anisotropy could be present in both diseased and healthy aortic walls, as has also been recently reported [57].

While the effect of age on the aortic wall strength had been noticed in dilated ascending aorta [79], such a phenomenon had not been demonstrated yet in healthy specimens. Figures 8 and 10 show that age has a predominant role in the mechanical behaviour of the healthy ascending aortic wall, as tensile mechanical resistance decreases markedly when age is doubled from group 0A to 0B. This effect is more pronounced in tensile strength, that reduces in group 0B in circumferential direction up to 55 % of value corresponding to group 0A. In contrast, circumferential stretch at failure falls only by 22 % from the young to the older specimens. In longitudinal direction, older specimens retain up to 58 and 89 % of the tensile strength and stretch at failure of younger ones, respectively, with these differences being statistically significant.

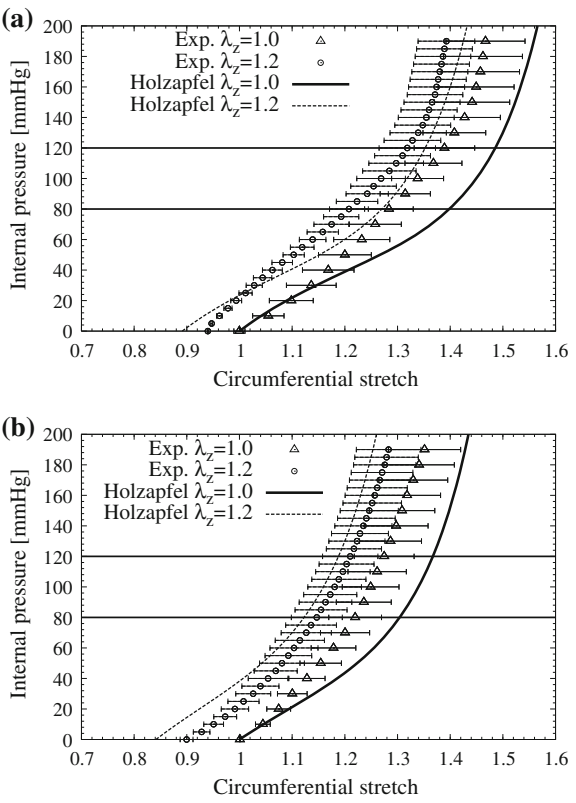

Fig. 28 Internal pressure versus circumferential stretch curves for newborn, young and adult thoracic descending aortas. **a** Group B. **b** Group C

The effect of age is even more remarkable if, as noted in Figs. 8 and 10, the reduction of stress and stretch at failure due to aging places the mechanical parameters of healthy old specimens either measured in circumferential or longitudinal directions at a level statistically undistinguishable from pathologic aortas, with the only exception being the failure stretch of specimens from group I (BAV), which is significantly lower than the longitudinal stretch of group 0B. Other values of stretch at failure or tensile strength from group 0B are statistically similar to bicuspid aortic valve (I) or aneurysm (I) pathologic groups, even though the mean age of group 0B is a little younger. Our results confirm recently published data on tensile strength of healthy and aneurysmal ascending aortic tissues [57] and stress the importance of comparison of age-matched specimens to avoid biased conclusions.

Another interesting result deduced from Figs. 8 and 10 is that the effect of pathology makes no significant differences in rupture parameters, as tensile strengths and stretches at failure measured on tissues from patients of comparable ages were found statistically undistinguishable. The measured circumferential tensile strengths and stretches for groups I (bicuspid aortic valve) and II (aneurysm) are concordant with

the values reported elsewhere on dilated ascending aortas of age-matching patients [79].

Tensile strengths of ascending aortic tissues are much higher than wall stresses for all conditions, with factors of safety (defined as the ratio of tensile strength to the mean wall stress) about 20 for group 0A. Interestingly, while circumferential tensile strength seems to reduce to approximately the same stress levels for groups 0B (old healthy), I (bicuspid aortic valve) and II (aneurysm), the factor of safety shows noticeable differences between healthy and pathologic groups (10.2 for 0B, and 6.3 and 7.6 for I and II, respectively), thus reflecting the different working stress at the vessel wall.

Mechanical performance of the ascending aortic wall. The determination of the tensile strength is of unquestionable interest in evaluating the deterioration and risk of rupture of aortic wall. Nevertheless, the results shown previously from pathologic samples that were obtained from patients undergoing aortic replacement demonstrate that wall stresses due to the cardiac cycle lie fairly below the rupture level of aortic wall. In contrast, degeneration and dilatation of the aortic wall seems to be a continuous process caused, among other factors, by the permanent effect of alternating stresses due to blood pressure. From this perspective, the evaluation of the mechanical performance of the aortic tissue at the working point and its variation with age and pathology is of primary interest to cardiovascular research.

The circumferential stress level set off by blood pressure causes the aortic wall to work during the cardiac cycle, either in the compliant elastin-dominated part before the elbow or in the stiff collagen-dominated zone beyond it. Consequently, it is expected that variations in the mechanical behaviour of the aortic wall produced by age or pathologies lead to a change in the position of the elbow point and have a direct effect on the arterial compliance throughout the cardiac cycle.

When compared to the wall stresses produced by blood pressure, only the elbow stress of healthy specimens lies above, meaning that these aortas work in the initial compliant zone. The ratio between the circumferential wall stress and elbow stress is 0.34 for group 0 A and 0.83 for group 0B, with the older group being close to the upturning zone. For the pathologic groups the ratio grows to 1.33 and 1.26 (I and II, respectively), meaning that during physiological operation the aorta works in the stiffer part of its response curve, losing part of its function of damping the pressure waves from the cardiac beat. The reduction in distensibility is present in most pathologies, and connected to deterioration and destructive remodeling of the aortic wall [44, 57]. Although altered distensibility alone cannot account for a higher risk of rupture, increases of in vivo stiffness overload collagen fibres and promote a loss of elastic fibres [57], enlarging aortic diameter and thereby raising the wall stress and indirectly influencing the risk of rupture. Moreover, reduced aortic elasticity and aortic root dilatation in nonstenotic BAV patients were previously in in vivo measurements [45].

4.2 Aortic Arch

Two zones with different stiffnesses can clearly be identified in the experimental curves of Fig. 12. At low deformations, the curves show a flexible response with a nearly constant slope. The first zone ranges up to $\lambda_1 \simeq 1.4$ for both the longitudinal and circumferential samples. In this first zone the material behaviour is clearly isotropic, i.e., its stiffness is mainly provided by the elastin component of the tissue. For larger deformations, on the other hand, the slopes of the curves start to increase up to the rupture stage. The material anisotropy in this second elongation zone, reflected in the largest differences between the responses corresponding to both sample directions, is apparent at the very end of the test. This is due to the significant action of the collagen fibers that occurs at high elongation levels. However, in the stretching range (1.0–1.8) the behaviour can be assumed as practically isotropic. Thus, an adequate description of the material behaviour in this deformation range (which in turn exhibits a low stress dispersion) can be simply tackled by means of isotropic constitutive models.

It is also seen in Fig. 12 that the Demiray model provides, due to its isotropic nature, an average response that lies between those of the two analyzed sample orientations. An excellent adjustment is clearly seen within the stretching range (1.0–1.8). Although an approximate fitting is achieved at high deformations, the stiffness increase in these stretching levels is reasonably well captured.

The experimental tensile curves shown in Fig. 13 exhibit two zones with different stiffnesses. For low stretching, the curves show a flexible response with a nearly constant slope. This first zone ranges up to $\lambda_1 \simeq 1.35$ and $\lambda_1 \simeq 1.20$ for the young and aged samples, respectively. For larger stretches, the slope continuously increases up to the rupture stage. Although some experimental-numerical discrepancies are noticed (e.g., at high and low levels of deformation for the young and aged samples, respectively), an overall good adjustment is clearly seen within the full stretching range for both groups. Moreover, additional experimental tensile tests (not shown) using samples extracted from regions located near the arterial bifurcations showed a similar response to that corresponding to the aortic arch (e.g., within the stretch range [1.0–1.6], the responses are practically the same while a difference of 40 % is observed for a stretch value of 2.0). The discrepancy at high stretch levels can be attributable to the action of the complexly oriented collagen fibers. This effect has been also reported by Hariton et al. [50]. The assumption of homogeneous mechanical properties along the whole arch is clearly a limitation of the present analysis.

The experimental pressure-diameter curves shown in Fig. 14 exhibit a nearly linear response for pressure values less than 130 mmHg. This is presumably due to the fact that mainly the elastin is active in this deformation interval. The effect of the collagen fibers is apparent for pressure values higher than 150 mmHg where the material becomes stiffer. This late elastin-collagen transition can be attributable to the fact that, due to the complex pattern that develops after the two first deformation stages (i.e., bending and axial stretching), the collagen fibers play a relevant role at the very end of the pressurization stage. Finally, it should be noted that the loading-

unloading sequences for both the axial stretching and pressurization stages exhibited nearly elastic and rate-independent material responses in this case. In particular, this effect is apparent in the loading-unloading curves corresponding to the pressurization stage shown in Fig. 14 (note that the maximum difference between the diameters resulting from these two curves is, for a given pressure, less than 5 %).

It is seen in Fig. 16 that the unfolding of the vessel causes a bending stress pattern, i.e., axial compression in zone I (that exhibits, in addition, local buckling at the ends of the arch), axial tension in zone III and a neutral axis in the vicinity of zone II. As shown in Fig. 15c, this last zone experiences large rotations with low stretching levels. Once the final pressure value is applied, tensile stresses with lower values than that recorded at the rupture stage in the tensile test (see Fig. 12) develop in region V. Owing to the previous bending and axial deformation, the stress distribution at the central region of the sample (zones I, II and III) is not uniform. It can also be observed that the severe deformation developed at zone II of the artery is mainly due to the effect of the internal pressure (the ratios of the final to initial average external diameter and thickness values are 1.55 and 0.55, respectively) where the circumferential stress reaches 590 kPa. Using the average dimensions resulting from the simulation (i.e., external diameter of 32 mm and thickness of 0.71 mm), the analytical expression corresponding to thin-walled tubes gives a stress value of 600 kPa. These similar stress values confirms that the bending effect does not substantially affect the circumferential response in zone II. Moreover, the barrelling formation in zone IV is due to the compression stress state promoted by the initial bending of the vessel.

As already mentioned, the residual stresses can be estimated as 20 % of the stresses in an artery loaded within the physiological range (80–120 mmHg), i.e., their values are bounded to 30 kPa [38]. The stresses developed in the bending and pressurization test reached 1000 kPa, hence the effect of the residual stresses is practically negligible.

The numerical results shown in Fig. 14 reasonably adjust the experimental measurements (the maximum experimental-numerical discrepancy in the diameter is, for a given pressure level, lower than 4 %). The nearly linear response predicted by the model is due to the low levels of circumferential stretching developed during the pressurization stage. This is consistent with the material behaviour shown in Fig. 12. In addition, it is seen that the numerical results do not properly capture the very different stiffness regime observed in the experiments at the end of the test. However, the material characterization performed in Sect. 3.1 was found to provide an overall realistic response of the aortic arch when it is subjected to internal pressure.

An overall good agreement between the experimental and computed final deformed configuration of the aortic arch can be clearly appreciated in Fig. 17. In particular, the unsymmetric deformation pattern observed in the experiments is adequately captured by the simulation. The experimental observation that the deformed cross-sections were no longer circular was also confirmed by the numerical predictions. Finally, a reasonable good agreement between experimental and computed values for the maximum external diameter distribution along the artery length at the final deformed configuration can be appreciated in Fig. 18.

The Demiray model is known to be ill-posed for experimental characterization of the material response (see Criscione [18]). This drawback could be tackled, as proposed by Criscione [19], by using an alternative set of invariants such that the resulting energy function minimizes the experimental error. It should be noted, however, that the methodology used in this work was found to provide an overall good fitting between the experimental and numerical results.

The use of the maximum principal stress and stretch values that develop in loaded aortas have been proposed in the literature to predict the failure of the vessel. In particular, this problem has been studied by Di Martino and Vorp [27], Li and Kleinstreuer [63] and Vorp [103] defining a maximum principal stress-based criterion for descending aortas with aneurysms. Moreover, other authors, such as Mohan and Melvin [72] and Lonescu et al. [65], proposed failure criteria for soft tissues in terms of maximum stretchs. In these approaches, the maximum principal stress and stretch values are respectively compared to those measured in the tensile test. In the present work, these two variables are also adopted to assess the failure degree of young and aged aortic archs under normal and hypertension loading conditions.

As depicted in Fig. 21a, the maximum stress values for the young group at the normal physiological condition occur at the intersection of the brachyocephalic trunk with the arch. For the ascending aorta, the maximum stress value is 143 kPa which is well below the tensile rupture stress for the young group (i.e., 1270 kPa, see Fig. 13). Moreover, relevant stress levels are developed at the internal region of the arch. As depicted in Fig. 21b, the maximum stretch value of 1.36 is located at the inner wall of the brachyocephalic trunk—arch union. This value corresponds to 65 % of the rupture stretch (i.e., 2.1, see Fig. 13). Both failure criteria clearly show that the zones with higher risk levels are situated at the root of the three aortic arch bifurcations and at the vicinity of the ligamentum arteriosum. From the clinical point of view, the most important zone is that located near the ligamentum arteriosum due the high stress concentration that takes place there [11, 15, 34, 70, 81, 88]. The stress level in this area is more critical than those developed at the junctions where arteries branch off from the aortic arch. However, relevant stresses can occur in all these regions under extreme loading conditions (e.g., hypertension, automobile accidents, etc.).

Although the systolic pressure P_s does not significantly affect the stress level compared to the diastolic one P_d (see Figs. 20 and 21a), relatively large strains are developed in the ascending aorta due to the kinematic boundary conditions. The external diameter and average thickness of the ascending aorta at 120 mmHg are 26.1 mm and 1.61 mm, respectively. The external diameters of the ascending aorta at the diastolic and systolic conditions (D_d and D_s, respectively) allow the estimation of its stretching capacity. This feature is usually quantified by means of the distensibility DC [62]:

$$DC = \frac{D_s^2 - D_d^2}{D_s^2(P_s - P_d)} \tag{8}$$

where, in this case, the distensibility gives 2.7×10^{-3} mmHg^{-1} which is very close to the in-vivo measured value of 2.5×10^{-3} mmHg^{-1} in healthy young patients [60].

Figure 22 shows that the maximum stress and stretch values for the young group at the hypertension condition (290 kPa and 1.6, respectively) are, as in the former case, also mainly located near the root of the three aortic arch bifurcations and at the vicinity of the ligamentum arteriosum. Considering these values in the stress-stretch curve of Fig. 13, it is seen that the material behaves within the so-called elbow zone (defined approximately by the interval $1.55 < \lambda_1 < 1.85$), which exhibits a moderate stiffness that allows the damping of the pressure wave with stretch levels smaller than that of the rupture stage (the ratio between these two values is 0.73).

The maximum stress and stretch values for the aged aortic arch at the hypertension condition are, as plotted in Fig. 23, 300 kPa and 1.33, respectively. The aged aortic arch exhibits, compared to that of the young group, a stiffer material response with lower stretching levels. This stress-stretch level is beyond the elbow zone of this material (defined approximately in this case by the interval $1.25 < \lambda_1 < 1.40$) which consequently leads to a deterioration of the pressure wave damping capacity of the artery reflected in the development of more irregular downstream flows and pressures. It should be noted that the maximum stresses under in-vivo conditions occur for stretch values higher than 1.4 where the tensile fitting is adequate (see Fig. 13). This fact is also appreciated in the drop of the distensibility to a value of 1.3×10^{-3} mmHg^{-1}, which is very close to the in-vivo measured values of aged arteries [64] and nearly 50 % than that of a healthy young patient. This marked decrease in distensibility with age has been also reported by [92]. Moreover, the ratio between the maximum stretch value and that of the tensile rupture stage (see Fig. 13) is 0.85 in this case, i.e., closer to the failure condition than that of the young aortic archs.

The stress distributions in the ascending aorta at 160 mmHg are depicted in detail in Figs. 24 and 25 for the young and aged patients, respectively. For the young tissue, the maximum stress occurs at the inner part of the aortic arch, e.g., the respective values for the circumferential and longitudinal stress components are 250 kPa and 125 kPa. It should be noted that the value of the radial stress component at the internal surface of the aorta evens up the applied pressure (i.e., 160 mmHg = 21.332 kPa). A similar stress pattern is also observed for the aged tissue where in this case the maximum circumferential and longitudinal stress components are 200 kPa and 146 kPa, respectively. Moreover, different circumferential stress values at the inner and outer parts of the aortic arch are clearly observed for both tissues.

Finally, it should be mentioned that additional simulations carried out with different boundary conditions and lengths of the three arteries (i.e., brachyocephalic trunk, carotid artery and subclavian artery) showed that they do not substantially affect the stress contours at the root of those arteries.

4.3 Descending Aorta

For a given stretch value, the experimental tensile measurements plotted in Fig. 26 show that, in general, older vessels present lower rupture deformations with higher stresses. Minimum rupture stretch values of 1.8 were observed in all cases with the exception of the longitudinal samples of Group C for which an average rupture stretch of 1.7 was measured. Two zones with different stiffnesses can clearly be identified. At low deformations, the curves show a flexible response with a nearly constant slope. The response of Group A exhibits a wider interval of very low stiffness bounded by $\lambda_1 \simeq 1.6$. For Groups B and C, the first zone ranges up to $\lambda_1 \simeq 1.3$ and $\lambda_1 \simeq 1.45$ for the longitudinal and circumferential samples, respectively. In this first zone the material behaviour is clearly isotropic, i.e., its strength is mainly provided by the elastin component of the vessels. For larger deformations, on the other hand, the slopes of the curves start to increase up to the rupture stage. The material anisotropy in this second elongation zone, reflected in the largest differences between the responses corresponding to both samples directions, is apparent at the very end of the test. This is due to the significant action of the collagen fibers that occurs at high elongation levels.

Although some results for aortas in adults have been found in the literature, it should be noted that they don't strictly correspond to the tissue studied in this work (i.e., in-vitro healthy human thoracic descending aortas). For instance, Okamoto et al. [79] reported an average tensile (uniaxial) rupture elongation of 1.6 for circumferential samples corresponding to dilated human ascending aortas in adults. In the present work, the measured final stretch for circumferential samples in adults was 2.0; see Fig. 26b.

Figure 27 shows that the Holzapfel model adequately adjusts the overall material response; in particular, the progressive stiffness increase and the anisotropic character provided by the fibers are properly described. Group A exhibits an average orientation angle $\varphi > 45°$ (see Table 10) which can be attributed to the low level of longitudinal residual stress present in this very young tissue. Therefore, the circumferential response is more rigid than the longitudinal one at low stretch values. On the other hand, the contrary trend is observed for Groups B and C, i.e., $\varphi < 45°$, possibly due to the longitudinal residual stress that may act on the aorta during its life [55]. This fact can be also appreciated in the earlier stiffness increase that occurs in the longitudinal direction samples.

In Fig. 28a, the experimental data corresponding to Group B for $\lambda_z = 1.0$ exhibits a nearly linear response for pressure values less than 75 mmHg since the elastin is only active in this deformation interval. The effect of the collagen fibers is apparent for pressure values higher than 150 mmHg where the material becomes stiffer. In the longitudinally prestrained case (i.e., $\lambda_z = 1.2$), the axial stress at which the vessel is initially subjected caused a diameter reduction (note that $\lambda_\theta < 1$ for $P_i = 0$). However, the average mechanical response of both cases is very similar. Moreover, the stiffness of the vessel also increases in the data corresponding to Group C plotted in Fig. 28b but in a more continuous way than that observed for the younger arter-

ies. In general, slightly stiffer responses can be appreciated for the older arteries. In particular, for a pressure value of $P_i = 100$ mmHg, the stretch ranges are 1.27–1.35 and 1.18–1.25 for Groups B and C, respectively. Although local buckling occurred for the tests with $\lambda_z = 1.0$ (due to the compressive load cell force that caused a compressive axial stress in the sample), this undesirable effect practically vanished when a longitudinal prestrain (as the value $\lambda_z = 1.2$ used in this work which induced a tensile resulting load cell force) was applied to the vessel. In addition, it is important to mention that higher dispersion in the diameter measurements were observed for increasing pressure values. These reported experimental data is used below to validate the predictions of the Holzapfel model considered in this work.

Moreover, another parameter that is commonly used to characterize the mechanical response of in-vivo aortas is the distensibility. Some distensibility values (in 10^{-3} mmHg^{-1}) have been determined for in-vivo aortas: 2.5 (for an ascending aorta in adults; see Koullias et al. [60]) and 3.4 (for only one measurement on an thoracic aorta in an adult; see Schulze and Holzapfel [96]). In the present work, a value of 2.7 was obtained from the experimental data of Group C shown in Fig. 28b. Other available results are mainly devoted to aortas with different types of aneurisms; see e.g., Okamoto et al. [79], Raghavan et al. [86], Vorp [103], Martino et al. [68].

The internal pressure versus circumferential stretch curves for the Holzapfel model are also presented in Fig. 28a, b for Groups B and C, respectively. The differences between the predicted and experimental values for $\lambda_z = 1.0$ can be attributable to local instabilities that, as mentioned above, occurred during the experiment without longitudinal prestrain. A better agreement, however, is in general achieved for $\lambda_z = 1.2$ since in this case the buckling effects are practically precluded. Overall, it is seen that the Holzapfel model properly predicts the experimental measurements. The stiffness increase occurring at high pressure levels (i.e., greater than 120 mmHg) is particularly well described. In this case, the maximum error is less than 8.5 % for the whole test.

5 Conclusions

The characterization of the mechanical behaviour of the human ascending aorta, aortic arch and thoracic descending aorta subjected to in-vitro and in-vivo conditions has been presented. The proposed methodology encompassed experiments, modeling and simulation. The concluding remarks and future perspectives related to each of these three parts of the aorta are separately drawn below.

The mechanical behaviour and strength of the human ascending aorta, both in healthy and pathological conditions, have been measured in this work through in-vitro tensile tests. Results show that aging causes a significant decrease of rupture loads and elongations at breaking, comparable to the effect of severe pathologies such as aneurysm and bicuspid aortic valve. While aortic ascending wall strength decreases significantly beyond the age of 35, the mean physiological wall stresses acting on either healthy or pathologic aortas are always far from the rupture point,

displaying factors of safety larger than six. In contrast, the physiological operation of pathologic vessels seems to be differentially affected by the disease since, contrary to the behaviour of healthy control aortas of similar age, patients with aneurysm and bicuspid aortic valve have their ascending aortas working in the stiff part of its response curve, and consequently impairing the aortic elasticity. Finally, the role of biological processes on the mechanical behaviour of the aortic wall has not been considered in the present analysis and, therefore, this is an aspect that needs to be explored in future works.

Experiments, constitutive modeling and numerical simulation have been considered in this work to analyze the in-vitro and in-vivo mechanical responses of the human aortic arch. These two behaviours were respectively studied via the bending and pressurization test of an adult tissue and the application of physiological conditions to young and aged arteries. The experiments carried out in this work were designed to achieve high stretching and pressure levels as those developed in a real-life situation (e.g., an automobile crash or specific surgical treatments such as stents implants). The tissue of these three groups were firstly characterised via in-vitro tensile test measurements that enabled, via a least-squares procedure, the derivation of the material parameters of a hyperelastic isotropic constitutive model adopted in this work to describe the material response. Overall, the material characterization together with the proposed alternative methodology to estimate the initial stress was found to be consistent since it provided a reasonable and realistic description of the mechanical behaviour of the aortic arch under the different studied loading conditions. In particular, a good agreement between the experimental and computed results of the internal pressure versus the external diameter of the artery have been obtained. Moreover, the maximum principal stress and stretch values adopted here as risk of failure criteria allowed the determination of the critical zones of the vessel under in-vivo normal and hypertension pressures. These two failure criteria clearly showed that the zones with higher risk levels are situated at the root of the three aortic arch bifurcations and at the vicinity of the ligamentum arteriosum for both groups of patients. For the healthy young patients, the computed distensibility was very similar to an experimentally measured value reported in the literature. Besides, the predicted distensibility for the aged tissue was very close to the measured value of pathological arteries which approximately corresponds to 50 % lower than that of the young vessel. Future research on this area will be focused on the limitations of the present analysis, i.e., consideration of patient-specific complex geometry and realistic boundary conditions aimed at achieving a better estimation of the stress and strain patterns in the artery, further validation including more results than those considered in this work, assessment of other constitutive models (e.g., those defined within a well-posed theoretical framework for experimental determination of the material response), effects of the presence of aneurysms, influence of residual stresses, characterisation of the mechanical response of the ligamentum arteriosum in order to more accurately compute the stress concentrations, simulation of the influence of the blood flow on the mechanical response of the aortic arch, material inhomogeneity and, in addition, experiments, modeling, inverse material parameter estimation and simulation of arteries subjected to extreme dynamic loading conditions.

On the other hand, the characterization of the passive mechanical response of the human thoracic descending aorta carried out in this work encompassed three different groups of healthy arteries: newborns, youngs and adults. The experimental data measured in the tensile test have been used to determine the material parameters of a Holzapfel constitutive model. In particular, the application of this methodology to newborn and young tissues is an original contribution of this research. Moreover, the constitutive modeling of the pressurization test has been experimentally validated. The predictive capabilities and limitations of this model have been also discussed. Overall, the characterization carried out in this work was found to provide a reasonable and realistic description of the mechanical behaviour of the human thoracic descending aorta under different loading conditions. The limitations of this work that have to be addressed in further research are mainly related to two different aspects: assumptions in the constitutive modeling (e.g., the consideration of layer-based laws, rate-dependent effects and damage evolution has to be explored) and use of simplified analytical solutions in problems with complex stress and strain patterns (e.g., the opening ring test). encompassed three different groups of healthy arteries: newborns, youngs and adults. The experimental data measured in the tensile test have been used to determine the material parameters of a Holzapfel constitutive model. In particular, the application of this methodology to newborn and young tissues is an original contribution of this research. Moreover, the constitutive modeling of the pressurization test has been experimentally validated. The predictive capabilities and limitations of this model have been also discussed. Overall, the characterization carried out in this work was found to provide a reasonable and realistic description of the mechanical behaviour of the human thoracic descending aorta under different loading conditions. The limitations of this work that have to be addressed in further research are mainly related to two different aspects: assumptions in the constitutive modeling (e.g., the consideration of layer-based laws, rate-dependent effects and damage evolution has to be explored) and use of simplified analytical solutions in problems with complex stress and strain patterns (e.g., the opening ring test).

6 Conflicts of Interest

The authors have no conflicting interests regarding this chapter.

Acknowledgments The authors wish to express their appreciation to Dr. R. Burgos and C. García-Montero of the Hospital de Puerta de Hierro at Madrid for the provision of arterial tissues analyzed in this work. The support provided by DICYT Project No. 051415GH of the Universidad de Santiago de Chile (USACH) is gratefully acknowledged.

References

1. Al-Okaili, R., Schwartz, E.D.: Bilateral aortic origins of the vertebral arteries with right vertebral artery arising distal to left subclavian artery: case report. Surg. Neurol. **67**, 174–176 (2007)
2. Al Shammari, M., Taylor, P., Reidy, J.F.: Use of through-and-through guidewire for delivering large stent-grafts into the distal aortic arch. Cardiovasc. Intervent. Radiol. **23**, 237–238 (2000)
3. Atienza, J.M., Guinea, G.V., Rojo, F.J., Burgos, R.J., García-Montero, C., Goicolea, F.J., Argoncillo, P., Elices, M.: The influence of pressure and temperature on the behavior of the human aorta and carotid arteries. Revista Española de Cardiología **60**, 259–267 (2007)
4. Bednarkiewicz, M., Khatchatourian, G., Christenson, J.T., Faidutti, B.: Aortic arch replacement using a four-branched aortic arch graft. Eur. J. Cardiothorac. Surg. **21**, 89–91 (2002)
5. Beller, C.J., Labrosse, M.R., Thubrikar, M.J., Robicsek, F.: Role of aortic root motion in the pathogenesis of aortic dissection. Circulation **109**, 763–769 (2004)
6. Beller, C.J., Labrosse, M.R., Thubrikar, M.J., Szabo, G., Robicsek, F., Hagl, S.: Increased aortic wall stress in aortic insufficiency: clinical data and computer model. Eur. J. Cardiothorac. Surg. **27**, 270–275 (2005)
7. Bizzarri, F., Mattia, C., Di Nardo, M., Di Marzio, E., Ricci, M., Coluzzi, F., Frati, G., Pagliaro, P., Muzzi, L., Petrozza, V.: Antegrade selective cerebral perfusion in patients with "bovine aortic arch": is it easier? J. Cardiothorac. Surg. **3**, 60 (2008a)
8. Bizzarri, F., Mattia, C., Ricci, M., Chirichilli, I., Santo, C., Rose, D., Muzzi, L., Pugliese, G., Frati, G., Sartini, P., Ferrari, R., Della Rocca, C., Laghi, A.: Traumatic aortic arch false aneurysm after blunt chest trauma in a motocross rider. J. Cardiothorac. Surg. **3**, 23 (2008b)
9. Bonow, R.O., Carabello, B.A., Chatterjee, K., de Leon Jr, A.C., Faxon, D.P., Freed, M.D., Gaasch, W.H., Lytle, B.W., Nishimura, R.A., O'Gara, P.T., O'Rourke, R.A., Otto, C.M., Shah, P.M., Shanewise, J.S., Smith Jr., S.C., Jacobs, A.K., Adams, C.D., Anderson, J.L., Antman, E.M., Faxon, D.P., Fuster, V., Halperin, J.L., Hiratzka, L.F., Hunt, S.A., Lytle, B.W., Nishimura, R., Page, R.L., Riegel, B.: ACC/AHA 2006 guidelines for the management of patients with valvular heart disease: a report of the American College of Cardiology/American Heart Association task force on practice guidelines (writing committee to revise the 1998 guidelines for the management of patients with valvular heart disease) developed in collaboration with the society of cardiovascular anesthesiologists endorsed by the society for cardiovascular angiography and interventions and the society of thoracic surgeons. J. Am. Coll. Cardiol. **48**(3), e1–e148 (2006)
10. Boudoulas, H., Toutouzas, P., Wooley, C.: Functional Abnormalities of the Aorta. Futura, Armonk, New York (1996)
11. Braverman, A., Thomson, R., Sanchez, L.: Braunwald's Heart Disease (Chapter 60: Diseases of the aorta), 9th edn. Elsevier, Philadelphia (2010)
12. Caceres, M., Estrera, A.L., Buja, L.M., Safi, H.J.: Transverse aortic arch replacement associated with MAGIC syndrome: case report and literature review. Ann. Vasc. Surg. **20**, 395–398 (2006)
13. Cacho, F.: Constitutive models for soft biological tissues. Ph.D. thesis, Universidad de Zaragoza (2006) (in Spanish)
14. Celentano, D.: A large strain thermoviscoplastic formulation for the solidification of S.G. cast iron in a green sand mould. Int. J. Plast. **17**, 1623–1658 (2001)
15. Chiesa, R., Moura, M., Lucci, C., Castellano, R., Civilini, E., Melissano, G., Tshomba, Y.: Blunt trauma to the thoracic aorta: mechanisms involved, diagnosis and management. J. Vasc. Brasileiro **2**(3), 197–209 (2003)
16. Chuong, C.J., Fung, Y.C.: On residual stresses in arteries. ASME J. Biomech. Eng. **108**, 189–192 (1986)
17. Coady, M.A., Rizzo, J.A., Goldstein, L.J., Elefteriades, J.A.: Natural history, pathogenesis, and etiology of thoracic aortic aneurysms and dissections. Cardiol. Clin. **17**(4), 615–635 (1999)

18. Criscione, J.C.: Rivlin's representation formula is ill-conceived for the determination of response functions via biaxial testing. J. Elast. **70**, 129–147 (2003)
19. Criscione, J.C.: A constitutive framework for tubular structures that enables a semi-inverse solution to extension and inflation. J. Elast. **77**, 57–81 (2004)
20. Dambrin, C., Marcheix, B., Hollington, L., Rousseau, H.: Surgical treatment of an aortic arch aneurysm without cardio-pulmonary bypass: endovascular stent-grafting after extra-anatomic bypass of supra-aortic vessels. Eur. J. Cardiothorac. Surg. **27**, 159–161 (2005)
21. Darling, R.C., Messina, C.R., Brewster, D.C., Ottinger, L.W.: Autopsy study of unoperated abdominal aortic-aneurysms—case for early resection. Circulation **56**(3), 161–164 (1977)
22. Davies, R.R., Goldstein, L.J., Coady, M.A., Tittle, S.L., Rizzo, J.A., Kopf, G.S., Elefteriades, J.A.: Yearly rupture or dissection rates for thoracic aortic aneurysms: simple prediction based on size. Ann. Thorac. Surg. **73**(1), 17–28 (2002)
23. Davies, R.R., Gallo, A., Coady, M.A., Tellides, G., Botta, D.M., Burke, B., Coe, M.P., Kopf, G.S., Elefteriades, J.A.: Novel measurement of relative aortic size predicts rupture of thoracic aortic aneurysms. Ann. Thorac. Surg. **81**(1), 169–177 (2006)
24. De Caro, E., Trocchio, G., Smeraldi, A., Calevo, M.G., Pongiglione, G.: Aortic arch geometry and exercise-induced hypertension in aortic coarctation. Am. J. Cardiol. **99**, 1284–1287 (2007)
25. Delfino, A., Stergiopulos, N., Moore, J., Meister, J.: Residual strain effects on the stress field in a thick wall finite element model of the human carotid bifurcation. J. Biomech. **30**, 777–786 (1997)
26. Demiray, H.: On the elasticity of soft biological tissues. J. Biomech. **5**, 309–311 (1972)
27. Di Martino, E.S., Vorp, D.A.: Effect of variation in intraluminal thrombus constitutive properties on abdominal aortic aneurysm wall stress. Ann. Biomed. Eng. **31**, 804–809 (2003)
28. Doyle, B.J., Cloonan, A.J., Walsh, M.T., Vorp, D.A., McGloughlin, T.M.: Identification of rupture locations in patient-specific abdominal aortic aneurysms using experimental and computational techniques. J. Biomech. **43**, 1406–1408 (2010)
29. Doyle, B.J., Killion, J., Callanan, A.: Use of the photoelastic method and finite element analysis in the assessment of wall strain in abdominal aortic aneurysm models. J. Biomech. **45**, 1759–1768 (2012)
30. Erbel, R., Eggebrecht, H.: Dimensions and the risk of dissection. Heart **92**(1), 137–142 (2006)
31. Ergin, M.A., Spielvogel, D., Apaydin, A., Lansman, S.L., McCullough, J.N., Galla, J.D., Griepp, R.D.: Surgical treatment of the dilated ascending aorta: when and how? Ann. Thorac. Surg. **67**, 1834–1839 (1999)
32. Fedak, P.W.M., Verma, S., David, T.E., Leask, R.L., Weisel, R.D., Butany, J.: Clinical and pathophysiological implications of a bicuspid aortic valve. Circulation **106**(8), 900–904 (2002)
33. Field, M., Richens, D.: Anticipatory valsalva-type response as a contributory factor in low impact blunt traumatic aortic rupture. Med. Hypotheses **67**, 87–92 (2006)
34. Field, M., Sastry, P., Zhao, A., Richens, D.: Small vessel avulsion and acute aortic syndrome: a putative aetiology for initiation and propagation of blunt traumatic aortic injury at the isthmus. Med. Hypotheses **68**, 1392–1398 (2007)
35. Forman, J., Stacey, S., Evans, J., Kent, R.: Posterior acceleration as a mechanism of blunt traumatic injury of the aorta. J. Biomech. **41**, 1359–1364 (2008)
36. Fung, Y.: Biomechanics. Mechanical Properties of Living Tissues. Springer (1993)
37. Gao, F., Watanabe, M., Matusuzawa, T.: Stress analysis in a layered aortic arch model under pulsatile blood flow. Biomed. Eng. OnLine **5**, 25 (2006)
38. García-Herrera, C.M.: Mechanical behaviour of the human ascending aorta: characterization and numerical simulation. Ph.D. thesis, Universidad Politécnica de Madrid (2008) (in Spanish)
39. García-Herrera, C.M., Celentano, D.J., Cruchaga, M.A., Rojo, F.J., Atienza, J.M., Guinea, G.V., Goicolea, J.M.: Mechanical characterisation of the human thoracic descending aorta: experiments and modelling. Comput. Methods Biomech. Biomed. Eng. **15**, 185–193 (2012a)

40. García-Herrera, C.M., Celentano, D.J., Cruchaga, M.A.: Bending and pressurisation test of the human aoritc arch: experiments, modelling and simulation of a patient-specific case. Comput. Methods Biomech. Biomed. Eng. (2012b) (in press)
41. Gasser, C.T., Ogden, R.W., Holzapfel, G.A.: Hyperelastic modelling of arterial layers with distributed collagen fibre orientations. J. R. Soc. Interface **3**, 15–35 (2006)
42. Goicolea, J., Atienza, J.M., Burgos, R., García-Touchard, A., Goicolea, J., Guinea, G., Mingo, S., Montero, C., Salas, C.: Biomecánica aórtica y su correlación in vivo, estudio del comportamiento mecánico y de la rotura de aorta y su correlación ecocardiográfica, histológica y molecular. Hospital Universitario Puerta de Hierro, Protocolo de extracción de muestras (2006)
43. Govindjee, S., Mihalic, P.A.: Computational methods for inverse finite elastostatics. Comput. Methods Appl. Mech. Eng. **136**, 47–57 (1996)
44. Groenink, M., Langerak, S.E., Vanbavel, E., van der Wall, E.E., Mulder, B.J.M., van der Wal, A.C., Spaan, J.A.E.: The influence of aging and aortic stiffness on permanent dilation and breaking stress of the thoracic descending aorta. Cardiovasc. Res. **43**(2), 471–480 (1999)
45. Grotenhuis, H.B., Ottenkamp, J., Westenberg, J.J.M., Bax, J.J., Kroft, L.J.M., Roos, A.: Reduced aortic elasticity and dilatation are associated with aortic regurgitation and left ventricular hyperthrophy in nonstenotic bicuspid aortic valve patients. J. Am. Coll. Cardiol. **49**, 1660–1665 (2007)
46. Guinea, G.V., Atienza, J.M., Elices, M., Argoncillo, P., Hayashi, K.: Thermomechanical beahavior of human carotid arteries in the pasive state. AJP—Heart Circ. Physiol. **288**, 2940–2945 (2005)
47. Guntheroth, W.G.: A critical review of the American College of Cardiology/American Heart Association practice guidelines on bicuspid aortic valve with dilated ascending aorta. Am. J. Cardiol. **102**(1), 107–110 (2008)
48. Hager, A., Kaemmerer, H., Rapp-Bernhardt, U., Blucher, S., Rapp, K., Bernhardt, T.M., Galanski, M., Hess, J.: Diameters of the thoracic aorta throughout life as measured with helical computed tomography. J. Thorac. Cardiovasc. Surg. **123**(6), 1060–1066 (2002)
49. Hall, A.J., Busse, E.F.G., McCarville, D.J., Burgess, J.J.: Aortic wall tension as a predictive factor for abdominal aortic aneurysm rupture: improving the selection of patients for abdominal aortic aneurysm repair. Ann. Vasc. Surg. **14**(2), 152–157 (2000)
50. Hariton, I., deBotton, G., Gasser, T.C., Holzapfel, G.A.: Stress-modulated collagen fiber remodeling in a human carotid bifurcation. J. Theor. Biol. **248**, 460–470 (2007)
51. Holzapfel, G.: Non Linear Solid Mechanics. Wiley, Chichester (2000)
52. Holzapfel, G.A., Sommer, G., Gasser, C.T., Regitnig, P.: Determination of layer-specific mechanical properties of human coronary arteries with nonatherosclerotic intimal thickening and related constitutive modeling. Am. J. Physiol. Heart Circ. Physiol. **289**, H2048–H2058 (2005)
53. Holzapfel, G.: Determination of material models for arterial walls from uniaxial extension tests and histological structure. J. Theor. Biol. **238**, 290–302 (2006)
54. Holzapfel, G.A., Sommer, G., Auer, M., Regitnig, P., Ogden, R.W.: Layer-specific 3D residual deformations of human aortas with non-atherosclerotic intimal thickening. Ann. Biomed. Eng. **35**, 530–545 (2007)
55. Humphrey, J.: Mechanics of the arterial wall: review and directions. Crit. Rev. Biomed. Eng. **23**, 1–162 (1995)
56. Humphrey, J.D.: Cardiovascular Solid Mechanics. Cells, Tissues and Organs. Springer (2001)
57. Iliopoulos, D.C., Kritharis, E.P., Giagini, A.T., Papadodima, S.A., Sokolis, D.P.: Ascending thoracic aortic aneurysms are associated with compositional remodeling and vessel stiffening but not weakening in age-matched subjects. J. Thorac. Cardiovasc. Surg. **137**(1), 101–109 (2009)
58. Kleinstreuer, C., Li, Z., Basciano, C., Seelecke, S., Farber, M.: Computational mechanics of nitinol stent grafts. J. Biomech. **41**, 2370–2378 (2008)
59. Kocis, K.C., Midgley, F.M., Ruckman, R.N.: Aortic arch complex anomalies: 20-year experience with symptoms, diagnosis, associated cardiac deffects, and surgical repair. Pediatr. Cardiol. **18**, 127–132 (1997)

60. Koullias, G., Modak, R., Tranquilli, M.: Mechanical deterioration underlies malignant behavior of aneurysmal human ascending aorta. J. Thorac. Cardiovasc. Surg. **130**, 677.e1–677.e9 (2005)
61. Kroon, M., Holzapfel, G.A.: Elastic properties of anisotropic vascular membranes examined by inverse analysis. Comput. Methods Appl. Mech. Eng. **198**(45–46), 3622–3632 (2009)
62. Laurent, S., Cockcroft, J., Bortel, L.V., Boutouyrie, P., Giannattasio, C., Hayoz, D., Pannier, B., Vlachopoulos, C., Wilkinson, I., Struijker-Boudier, H.: Expert consensus document on arterial stiffness: methodological issued and clinical applications. Eur. Heart J. **27**, 2588–2605 (2006)
63. Li, Z., Kleinstreuer, C.: A new wall stress equation for aneurysm-rupture prediction. Ann. Biomed. Eng. **33**, 209–213 (2005)
64. Liu, C.Y., Chen, D., Teixido-Tura, G., Chugh, A.R., Redheuil, A., Gomes, A.S., Prince, M.R., Hundley, W., Bluemke, D.A., Lima, J.A.: Aortic size, distensibility, and pulse wave velocity changes with aging: longitudinal analysis from Multi-Ethnic Study of Atherosclerosis (MESA). J. Cardiovasc. Magn. Reson. **14**, 126–127 (2012)
65. Lonescu, I., Guilkey, J.E., Berzins, M., Kirby, R.M., Weiss, J.A.: Simulation of soft tissue failure using the material point method. J. Biomech. Eng. **128**, 917–924 (2006)
66. Lu, J., Zhou, X., Raghavan, M.L.: Inverse elastostatic stress analysis in pre-deformed biological structures: demostration using abdominal aortic aneurysms. J. Biomech. **40**, 693–696 (2007)
67. Marquardt, D.: An algorithm for least squares. SIAM J. Appl. Math **11**, 431–441 (1963)
68. Martino, E.S.D., Bohra, A., Geest, J.P.V., Gupta, N., Makaroum, M.S., Vorp, D.A.: Biomechanical properties of ruptured versus electively repaired abdominal aortic aneurysm wall tissue. J. Vasc. Surg. **43**(3), 570–576 (2006)
69. Masson, I., Boutouyrie, P., Laurent, S., Humphrey, J.D., Zidi, M.: Characterization of arterial wall mechanical behavior and stresses from human clinical data. J. Biomech. **41**(12), 2618–2627 (2008)
70. McGillicuddy, D., Rosen, P.: Diagnostic dilemmas and current controversies in blunt chest trauma. Emerg. Med. Clin. North Am. **25**, 695–711 (2007)
71. Medina, F., Wicker, R.B.: Geometric modeling of the human aorta for rapid prototyping using patient data and commercial software packages. In: Summer Bioengineering Conference, Florida, USA (2003)
72. Mohan, D., Melvin, J.: Failure properties of passive human aortic tissue. I uniaxial tension test. J. Biomech. **15**(11), 887–902 (1982)
73. Momma, K., Matsuoka, R., Takao, A.: Aortic arch anomalies associated with chromosome 22q11 deletion (CATCH 22). Pediatr. Cardiol. **20**, 97–102 (1999)
74. Nichols, W., Rourke, M.O.: McDonald's Flow in Arteries Theoretical, Experimental and Clinical Principles, 3rd edn. Oxford University, New York (1990)
75. Nollen, G.J., Groenink, M., Tijssen, J.G.P., van de Wall, E.E., Mulder, B.J.M.: Aortic stiffness and diameter predict progressive aortic dilatation in patients with Marfan sydrome. Eur. Heart J. **25**, 1146–1152 (2004)
76. Ogden, R.W.: Non-linear Elastic Deformations. Dover Publications Inc., New York (1984)
77. Ogden, R.: Nonlinear Elasticity with Application to Material Modelling. Polish Academy of Sciences (2003)
78. Oijen, C.V.: Mechanics and design of fiber-reinforced vascular prostheses. Ph.D. thesis, Technische Universiteit Eindhoiven (2003)
79. Okamoto, R.J., Wagenseil, J.E., DeLong, W.R., Peterson, S.J., Kouchoukos, N.T., Sundt III, T.M.: Mechanical properties of dilated human ascending aorta. Ann. Biomed. Eng. **30**, 624–635 (2002)
80. Pape, L.A., Tsai, T.T., Isselbacher, E.M., Oh, J.K., O'Gara, P.T., Evangelista, A., Fattori, R., Meinhardt, G., Trimarchi, S., Bossone, E., Suzuki, T., Cooper, J.V., Froehlich, J.B., Nienaber, C.A., Eagle, K.A.: Aortic diameter > 5.5 cm is not a good predictor of type A aortic dissection. Observations from the International Registry of Acute Aortic Dissection (IRAD). Circulation 1120–1127 (2007)

81. Pasic, M., Ewert, R., Engel, M., Franz, N., Bergs, P., Kuppe, H., Hetzer, R.: Aortic rupture and concomitant transection of the left bronchus after blunt chest trauma. Chest **117**, 1508–1510 (2000)
82. Prendergast, P.J., Lally, C., Daly, S., Reid, A.J., Lee, T.C., Quinn, D., Dolan, F.: Analysis of prolapse in cardiovascular stents: a constitutive equation for vascular tissue and finite-element modelling. J. Biomech. Eng. **125**, 692–699 (2003)
83. Putz, R., Pabst, R., Weiglein A.: Sobotta Atlas of Human Anatomic Atlas, vol. 2. Lippincott Williams & Wilkins (2001)
84. Raghavan, M.L., Webster, M., Vorp, D.A.: Ex vivo biomechanical behavior of abdominal aortic aneurysm assessment using a new mathematical model. Ann. Biomed. Eng. **24**(5), 573–582 (1996)
85. Raghavan, M.L., Vorp, D.A.: Toward a biomechanical tool to evaluate rupture potential of abdominal aortic aneurysm: identification of a finite strain constitutive model and evaluation of its applicability. J. Biomech. **33**(4), 475–482 (2000)
86. Raghavan, M.L., Kratzberg, J., de Tolosa, E.M.C., Hanaoka, M.M., Walker, P., da Silva, E.S.: Regional distribution of wall thickness and failure properties of human abdominal aortic aneurysm. J. Biomech. **39**, 3010–3016 (2006)
87. Richens, D., Field, M., Neale, M., Oakley, C.: The mechanism of injury in blunt traumatic rupture of the aorta. Eur. J. Cardiothorac. Surg. **21**, 288–293 (2002)
88. Richens, D., Field, M., Hashim, S., Neale, M., Oakley, C.: A finite element model of blunt traumatic aortic rupture. Eur. J. Cardiothorac. Surg. **25**, 1039–1047 (2004)
89. Rizzo, J.A., Coady, M.A., Elefteriades, J.A.: Interpreting data on thoracic aortic aneurysms. Statistical issues. Cardiol Clin. **17**(4), 797–805 (1999)
90. Roach, M.R., Burton, A.C.: The reason for the shape of the distensibility curves of arteries. Can. J. Biochem. Physiol. **35**, 681–690 (1957)
91. Rodríguez, J., Goicolea, J.M., Gabaldón, F.: A volumetric model for growth of arterial walls with arbitrary geometry and loads. J. Biomech. **40**, 961–971 (2007)
92. Rose, J.L., Lalande, A., Bouchot, O., Bourennane, E.B., Walker, P.M., Ugolini, P., Revol-Muller, C., Cartier, R., Brunotte, F.: Magn. Reson. Imag. **28**, 255–263 (2010)
93. Roy, C.S.: The elastic properties of the arterial wall. J. Physiol. **3**, 125–162 (1880)
94. Sacks, M.S.: Biaxial mechanical evaluation of planar biological materials. J. Elast. **61**, 199–246 (2000)
95. Sanmartín, M., Goicolea, J., García, C., García, J., Crespo, A., Rodríguez, J., Goicolea, J.M.: Influencia de la tensión de cizallamiento en la reestenosis intra-stent: Estudio in vivo con reconstrucción 3D y dinámica de fluidos computacional. Revista Española de Cardiología **59**(1), 20–27 (2006)
96. Schulze-Bauer, C., Holzapfel, G.: Determination of constitutive equations for human arteries from clinical data. J. Biomech. **36**, 165–169 (2003)
97. Spencer, A.: Continuum theory of the mechanics of fibre-reinforced composites. CISM **282**, 1–32 (1984)
98. Tochii, M., Ando, M., Takagi, Y., Yamashita, M., Hoshino, R., Akita, K.: Total arch replacement for a distal arch aneurysm with aberrant right subclavian artery. Gen. Thorac. Cardiovasc. Sur. **56**, 22–24 (2008)
99. Vande Geest, J.P., Di Martino, E.S., Vorp, D.A.: An analysis of the complete strain field within Flexcercell^{TM} membranes. J. Biomech. **37**, 1923–1928 (2004)
100. Vande Geest, J.P., Sacks, M.S., Vorp, D.A.: The effects of aneurysm on the biaxial mechanical behavior of human abdominal aorta. J. Biomech. **39**, 1324–1334 (2006)
101. Vorp, D.A., Schiro, B.J., Ehrlich, M.P., Juvonen, T.S., Ergin, M.A., Griffith, B.P.: Effect of aneurysm on the tensile strength and biomechanical behavior of the ascending thoracic aorta. Ann. Thorac. Surg. **75**(4), 1210–1214 (2003)
102. Vorp, D.A., Vande Geest, J.P.: Biomechanical determinants of abdominal aortic aneurysm rupture. Arterioscler. Thromb. Vasc. Biol. **25**(8), 1558–1566 (2005)
103. Vorp, D.A.: Biomechanics of abdominal aortic aneurysm. J. Biomech. **40**, 1887–1902 (2007)
104. Wolinsky, H., Glagov, S.: Structural basis for the static mechanical properties of the aortic media. Circul. Res. **14**, 400–413 (1964)

Part III
Porous and Multiphase Materials

Optimization of Functionally Graded Materials Considering Dynamical Analysis

F.J. Ramírez-Gil, J.E. Murillo-Cardoso, E.C.N. Silva and W. Montealegre-Rubio

Abstract Functionally graded materials (FGMs) are a new class of bio-inspired composite materials made from different material phases, in which their volume fraction changes gradually towards a particular direction. Accordingly, continuous changes in the composition, microstructure and porosity of the graded materials results in material properties gradients; for this reason, the material properties move smoothly and continuously from one surface to another, eliminating the interface problem. Hence, with appropriate design, FGMs can develop better properties than their homogeneous counterpart due to their better designability. One potential employment of FGMs is as damper or energy absorber in dynamic applications, in which optimization techniques such as the topology optimization method (TOM) can contribute to a better performance in relation to a non-optimized design. In this chapter, functionally graded structures are designed with and without the TOM in order to explore the advantages of the FGM concept in low-velocity impact condition, which is a special case in the world of dynamic analysis, and has interest for designing machinery parts and components.

Keywords Structural optimization · Topology optimization · FGM · Composite materials · Low velocity impact · Finite element modeling

F.J. Ramírez-Gil · J.E. Murillo-Cardoso · W. Montealegre-Rubio (✉)
Faculty of Mines, Department of Mechanical Engineering,
Universidad Nacional de Colombia, 050034 Medellín, Colombia
e-mail: wmontealegrer@unal.edu.co

E.C.N. Silva
Department of Mechatronics and Mechanical Systems Engineering,
Escola Politécnica of the University of São Paulo,
Butantã, São Paulo 05508-900, Brazil

P.A. Muñoz-Rojas (ed.), *Computational Modeling, Optimization and Manufacturing Simulation of Advanced Engineering Materials*,
Advanced Structured Materials 49, DOI 10.1007/978-3-319-04265-7_8

1 Introduction

An impact is defined as the collision of two or more solid bodies within a short time (typically, in the order of millisecond and microseconds depending on the velocity of the impacting objects), in which the load generated has high intensity. Situations involving impact have historically received great attention. Traditionally, the prime interest in this area has been for military applications. However, advances in technology have placed such demands on materials and structures on other problem applications such as [1]:

- safety transportation of hazardous materials;
- vehicle crashworthiness;
- safety of nuclear reactor structures;
- protection of military vehicles, structures, and aircraft;
- design of lightweight armor systems;
- erosion and fracture of solids due to liquid and solid particle;
- impact protection of spacecraft from meteoroid impact;
- explosive forming and welding of metals;
- and the design of machinery tools for manufacturing processes.

Impact on structures involves dynamic effects of particular interest, because their effect is potentially catastrophic although their probability of occurrence is generally lower than for other types of loads. Velocity is perhaps the simplest parameter to classify the different types of impacts, even though other variables of geometric type and/or related to material properties are critical. Several classifications have been suggested, but the most common is the following, which summarizes the effects on the material [2]:

- Low-velocity impacts ($v < 50$ m/s). Elastic effects or localized plastic deformation.
- Medium-velocity impacts (50 m/s $< v < 500$ m/s). Generalized plastic deformation.
- High-velocity impacts (500 m/s $< v < 2000$ m/s). The viscous resistance of the material still matters.
- Hypervelocity impacts (2000 m/s $< v$). The material can be considered a hydrodynamic fluid where the density is the main parameter.

Additionally to the above classification, there are some phenomena that can occur in the structure depending on the impact velocity, some of them are:

- Dynamic and structural vibrations: relevant in low-velocity impacts in which the structure geometry is predominant, and it can be studied by implicit or explicit integration methods.
- Stress and shock waves propagation: the effect of stress waves are important in low- and medium-velocity impacts, which become shock waves at hypervelocity impact.

- Nonlinear material behavior: some phenomena such as plasticity, fracture, and dependence on strain rate and temperature can occur. The nonlinearities increase with the impact velocity; even for very high velocities, the material has a fluid behavior where its resistance can be neglected.
- Large displacements and deformations: changes in geometry and finite rotations that influence the loads and their effect.
- Contacts and interface phenomena: contact is the key to any impact model, since loads are transmitted by it.
- Penetration and perforation: when the impacting object has enough velocity, it can penetrate (does not cross the material thickness) or perforate (crossing the material thickness) the impacted object.
- Local phenomena of rupture, such as spalling, scabbing, petalling and plugging.

As shown above, depending on the impact type or impact velocity, the analysis developed is different. For example, at low-velocity impact, the material properties have influence since the behavior is predominantly elastic and eventually occurs local plasticity. In the elastic region, the Young´s modulus, Poisson's ratio, and material's density and damping have the primary influence. Herein, impact forces classified as low-velocity are considered, in which only dynamic phenomena, structural vibrations and stress wave propagation are presented. Therefore, material nonlinearities are avoided, which means that plasticity, penetration, perforation and local rupture are not considered because these phenomena mainly appear above medium-velocity impacts and require more elaborated analysis and pose greater difficulties to simulation. In that sense, the material is modelled as a linear elastic isotropic material; however, geometric nonlinearities are taken into account to include large-deflection effects in the transient analysis. Finally, contact is not considered since an impulsive pressure load is used to represent the impact. More details about simulation considerations are described in subsequent sections.

2 Functionally Graded Materials

The material used for impact depends on the specific application. For example, ceramics are hard, which is an important characteristic in high-velocity impacts to decelerate and to erode the impacting object. However, the lack of ductility in ceramics is a problem because a ductile element is required to absorb, through deformation, whole or part of the kinetic energy of the impacting object. On other hand, metals are good energy absorbers due to their enhanced ductile behavior; however, their high density represents the major problem because the structures built with these materials are heavy. For that reason, polymers appear as an alternative due to their low density, ranging from 1.0 to 1.4 g/cm^3 [3]. The most common polymers for impact applications are polymeric fibers. These fibers have been found to be very efficient due to their improved specific strengths (the strength/density ratios). More efficient materials are based on aramid fibers (e.g. Kevlar6®), ultra-high molecular weight polyethylene fibers (e.g. Spectra® and

Dyneema®) and the PBO fiber (e.g. Zylon®). Despite the advantages of polymers, these materials are not commonly used alone for impact applications due to their low resistance. Thus, materials with different properties need to be assembled in the most advantageous way for impact applications [4].

The discussion above shows that to dissipate the energy of an impact, the material should contain several properties. Composite materials are an adequate option for this kind of application since they can combine different properties. This idea is supported by the pioneering research on ceramic armor, which concluded that the material performance could be significantly enhanced with materials macrostructurally designed for grading from a pure and stiff ceramic to a ductile material on the back surface [5]. In recent years, these types of materials have been referred to as functionally graded materials (FGMs) [6].

FGMs are also frequently found in nature. Bones, teeth and tree stalks are FGMs designed by nature to meet their expected service requirements. For this reason, the human designs based on the FGM concept are considered bioinspired materials/structures. Some examples of biological FGM are shown in Fig. 1; these nature designs combine high strength with lightweight materials, suitable properties for many applications. Using FGMs means to emulate nature to solve structural engineering problems, in the same way as an artificial neural network is used to emulate the human brain.

An example of a human-made FGM (artificial) is shown in Fig. 2 in which a micrograph reveal the spatially varying composition between two materials, where the matrix and inclusions change through thickness following a graded function

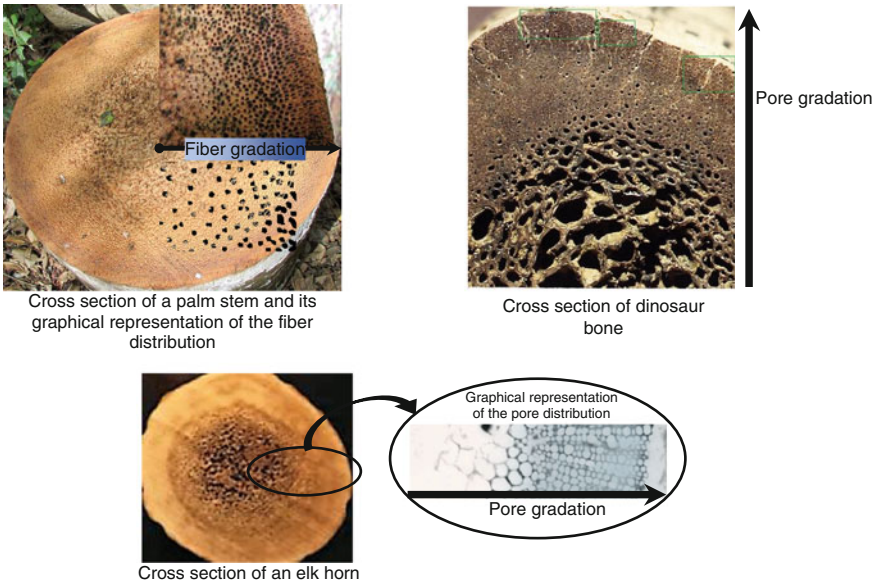

Fig. 1 Natural lightweight FGM examples for impact applications

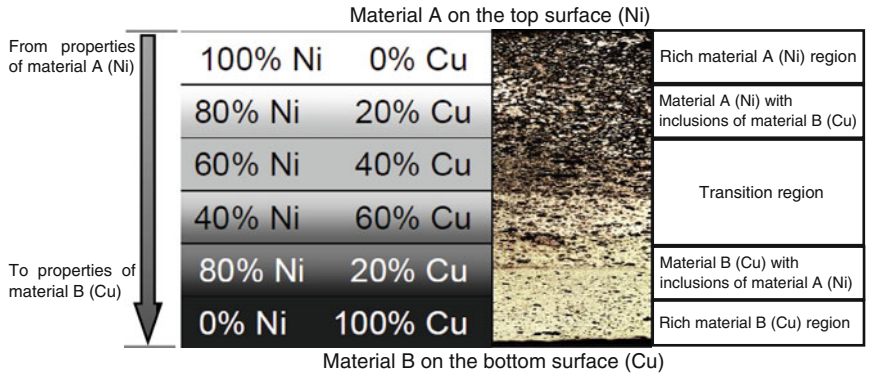

Fig. 2 Microstructure of a FGM graded from material A (Ni) to material B (Cu)

intentionally selected. This gradation provides FGMs with the ability to combine the desired properties of different materials; for example, a metal and a ceramic are used as base materials for taking advantage of the high temperature and corrosion resistance of ceramics, as well as the ductility and toughness of metals.

Functionally graded or gradient materials were first proposed in 1984 aiming to prepare thermal barrier materials exclusively for space application [6]. Functionally graded means that continuous and smooth changes can be obtained in the compositions, microstructure, porosity, etc. in some direction in the material [7]. Hence, the properties of a typical FGM plate change continuously from one surface to another through its thickness direction. This FGM design is intended for taking advantage of certain desirable features of each of the constituent phases [8]. Thus, FGMs have a number of advantages that make them attractive in potential applications, including a possible reduction of in-plane and transverse through-the-thickness stresses, improved residual stress distribution, enhanced thermal properties, higher fracture toughness, and reduced stress intensity factors [9]. Due to its advantages as compared with homogeneous materials, the FGM have found many applications in engineering, not only in the aerospace industry, but also in the nuclear and the automobile industries [10].

Despite the number of FGM advantages, this class of materials has two major drawbacks in their design [7]. The first problem is presented in the materials selection to form the FGM, and the second problem consists in determining the optimal spatial distribution of the material phases (composition profile).

In the context of low-velocity impacts, the first problem lies in the selection of a set of suitable materials to support impact loads and simultaneously get a lightweight structure. As stated before, metals are useful as energy absorbers; however, they are high-density materials. In consequence, herein an artificially graded porosity is introduced in the material, specifically, in a circular steel plate. The steel is selected as a base material due to its popularity, manufacturability and availability, which makes steel less expensive and more usable than other metals. Moreover, the induced porosity is meant to reduce the total weight of the structure

designed with this material, similar to bamboo, bones and horns (see Fig. 1). However, the material is modeled as a linear elastic isotropic material and not as a porous one.

The second problem is the lack of a systematic design approach that allows the selection of the composition profile which best accomplishes the intended purpose of the material application, while maintaining other properties within limits that ensure acceptable performance. Therefore, in this work the topology optimization method (TOM) is proposed for finding the composition profile (gradation function) along the thickness direction to provide an optimal pore distribution in a circular plate under low-velocity impact loads. In addition, since for low-velocity impacts where dynamics and structural vibrations effects mainly occur, the geometry is predominantly as stated before. Thus, the design of mechanical parts subjected to this kind of loads are suitable for TOM since this optimization technique provides novel geometries, apart from other benefits, such as weight reduction.

3 Topology Optimization Method for FGM Design

Currently, there is a need of efficient engineering methodologies to design parts and structures in order to save material, time and costs [11]. Thus, in recent years, there has been increasing interest in methods that automatically obtain optimized structures from performance conditions specified by the designer [12]. Optimization is a field of engineering that can be used to facilitate and to automate the design process. A relatively new method for obtaining optimized designs automatically is the TOM. The next subsections discuss the basis of TOM and its application to FGM design.

3.1 Basics of the Topology Optimization Method

The TOM is a powerful method in which the basic idea is to distribute one or more materials within a predefined design domain containing the geometry and boundary conditions of the problem. In TOM, an objective function is extremized seeking a desired behavior in the structure to meet some designer requests [12]. An additional typical goal in structural optimization is to obtain optimal structures with reduced mass. The TOM commonly produces designs that require some post-processing; TOM is thus considered to produce conceptual designs. These designs are mostly non-intuitive and are usually novel designs [13].

The first work that served as the basis for the TOM was by Michell in 1904 [14], who established the optimality conditions on loaded structures. From this work, many others have contributed to the area. Specifically, in 1988 Bendsøe and Kikuchi developed a computational method for topology optimization [15]. This method consists mainly of two modules, the analysis module and the optimization module [16]. The first is used to calculate the response of the structure against the

physical phenomena considered, for which the finite element method (FEM) is the tool most commonly used. The optimization module is used to update the design variables that improve the designed structure.

The TOM can be applied to design discrete or continuum structures [13]. For inherently discrete structures such as those based on beams and/or trusses, the TOM must determine the optimal number, position and connectivity of structural members. This area of research has been active for several decades and was mainly developed by Prager and Rozvany [13]. Moreover, the TOM in continuum structures must determine the number of holes and the external and internal contour shape. There are several investigations concerning the topology optimization of continuous structures; it can roughly distinguish between two types of approaches: the material or microstructural approach and the geometric or macrostructural approach [13].

The geometric approach consists of an iterative process of positioning new holes or "bubbles" at specific points in the design domain. At each iteration, the holes can appear and disappear, and their contours are subjected to a shape optimization process. This procedure is complicated since the mesh must change every iteration to accurately approximate the new generated contours. Additionally, the "birth" and "death" of the holes require another optimization technique [13].

In the material or microstructural approach, frequently a constant finite element (FE) mesh is used to describe the geometry. Typically, the mesh is uniform, and the design variables are assumed constant for each FE. The method consists in determining if an element in a continuous medium should contain material or not. Then, the design variable is defined for each element with values of 1 to indicate solid elements and 0 for void elements. The result is an approximate description of the outer and inner contours of the continuous structure that represents the optimized topology design.

The microstructural approach is preferred for simplicity. However, the topology optimization problem formulated as 0–1 is a discrete optimization problem, which is an ill-conditioned problem. Then, in order to obtain a well-conditioned problem, an adjustment is required in the problem formulation, which can be achieved by including additional restrictions on the problem formulation and/or by introducing a continuous design variable [13]. Consequently, the microstructural approach uses a basic concept known as material model.

The material model addresses the topology optimization problem by relaxing it by varying design variables continuously between 0 and 1. There are several material models used in the literature to solve topology optimization problems [17]. However, the models most commonly used in topology optimization apply the homogenization method, which was first introduced in 1988 by Kikuchi and Bendsøe [15], and the "power-law" or SIMP (solid isotropic material with penalization) model, proposed a year later by Bendsøe [18].

The material models based on the homogenization method provide a regularization of the optimization problem via relaxation (extension) of the design space, and its periodicity implies that the effective mechanical properties of the microstructures can be determined through homogenization [13]. There are some

variants of this model, such as the hole-in-cell microstructures and layered 2D/3D microstructures. Even though these methods are useful, the number of design variables used in the optimization problem are higher than those used in the SIMP model. Additionally, homogenization models require a dependence model for the material properties with respect to the geometric parameters of the unit cell, which complicates their implementation [11].

The SIMP model is a simple approximation used to relax the space of possible solutions of the optimization problem without increasing the number of design variables [19]. This material model does not regularize the topology optimization problem; however, it can be well-conditioned if an additional constraint on the formulation is used; for example, using a constraint on the perimeter for 2D structures or surfaces in 3D structures or by using a filtered technique [13]. In the SIMP model, the design variables are assigned to each FE and the material properties are assumed constant on it. The general form of SIMP is:

$$A = \rho(x)^p A_0, \quad 0 \leq \rho(x) \leq 1, \quad p > 1, \quad x \in \Omega \tag{1}$$

where A represents the material interpolated property, ρ is the design variable also called pseudo-density, p is the penalization factor and A_0 is the base or reference material property. Vector x represents the position in the design domain Ω. Depending on the dimensionality used in the TOM problem, vector x can be $x = x$ for one-dimension, $x = \{x \quad y\}^T$ for two-dimension or $x = \{x \quad y \quad z\}^T$ for three-dimension problems. With SIMP can appear some gray areas with intermediate pseudo-densities (composite material) that avoid the convergence to a black-and-white design (solid and void—porous material), then, the penalization factor is set to a value higher than 1 [19].

The SIMP model provides good results in topology optimization and is relatively easy to implement in commercial finite element codes contrasted with the homogenization methods [20, 21]. However, this model has disadvantages, such as the topology dependence on input design parameters and mesh discretization; nevertheless, these problems can be solved by using several strategies, such as those presented in [22].

For solving the optimization problems there are several approaches which can be grouped in three main categories: mathematical programming (MP), optimality criteria (OC) and evolutionary programming (EP) methods. The MP techniques are math-based methods for optimization [12]. The OC methods are rules intuitively or rigorously derived if a closed-form formulation is expressed [23]. The EP methods are heuristic or intuition-based approaches that use mechanisms inspired by biological evolution, such as reproduction, mutation and survival for finding an optimal solution to the problem [24]. The MP and OC methods use continuous design variables whereas EP methods typically use discrete representations as design variables. However, the MP methods are preferred over the others due to their generality, allowing the solution of complex and non-linear optimization problems. Additionally, MP methods are more suitable to deal with optimization problems with more than one constraint.

The most common searching technique used in MP is the sequential linear programming (SLP) due to its straightforward implementation. The SLP algorithm searches for the optimum in a nonlinear design space using a sequence of linear approximations for the objective function and constraints. It uses linear programming to solve each linear sub-problem. The linear approximation is calculated with gradient information by using the first-order Taylor expansion series, process commonly known as sensitivity analysis.

Figure 3 shows the flowchart of the SLP-based topology optimization algorithm. The first step of this process defines the design domain with loads and boundary conditions. Next, the optimization iterative process starts with the finite element analysis (FEA) of the structure under some considered phenomena. After this, the

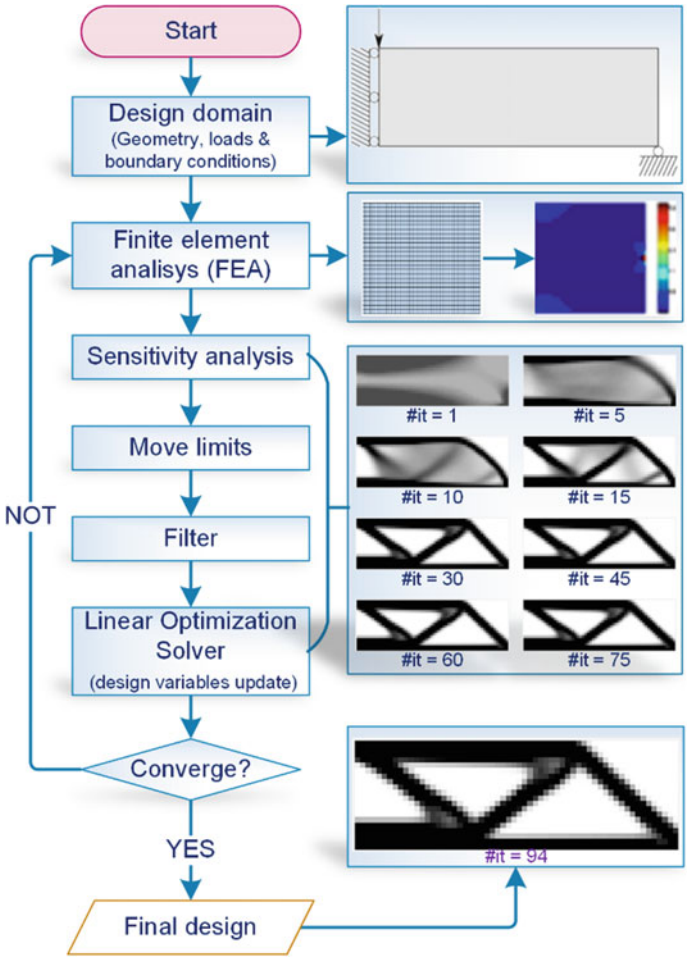

Fig. 3 SLP-based topology optimization flowchart

sensitivity analysis, which determines the change in the structural response of small changes in the design variables, is carried out. The move limits are calculated in the next step. The move limits are additional side constraints on the optimization problems that define a region of the design space where the solution of the linearized sub-problem will lie [25]. Next, in order to avoid some numerical instabilities, such as mesh dependence and grey areas, a filter on the design variables, sensitivities or move limits is computed [22]. After the above steps are finalized, a linear optimization solver optimizes the linearized objective function. Some typical linear optimization solvers are based on the simplex or Karmarkar algorithms. Finally, a convergence criterion is evaluated to verify if the optimization process can finish. When the iterative process ends, the optimal topology of the structure is obtained.

3.2 Topology Optimization of FGMs

From the designer viewpoint, the introduction of gradient distribution in a material provides a larger design domain, therefore providing a better designability. Consequently, the graded material will outperform (or perform just as) its uniform counterpart [26]. Optimization techniques are hence required in order to find an optimal gradation for this type of materials.

The optimum topology optimization result is known to consist of a structure with gray-scale areas, which means intermediate or composite material. In a typical topology optimized structure, the gray areas are undesirable since they avoid a precise definition of the boundaries. However, these gray-scale results given by the TOM are strongly related to the concept of FGM materials, which essentially considers a continuous transition of material properties [27].

The design of FGM materials using topology optimization has two approaches. The first consists in finding the optimal property variation of the FGM in the domain for achieving the design requirements. The second approach consists of a predefined functionally graded design domain, where the properties change in a particular direction according to a specified model. These FGM approaches differ in that in the first case, all the elements are in the final design, i.e., they fill the whole design domain; however, their material properties are not known a priori, and the TOM finds them. In the second case, each FE has a specified property; however, this varies from one element to the other continuously following a predefined graded function. Hence, the elements that occupy the final design are not known and the TOM has to find them.

Depending on the FGM optimization approach, a material model is used. For the first approach, a layered FGM material model is used. This is because current FGM manufacturing techniques emphasize layered systems, and a layered material constraint is adopted. In this case, two-phase material systems are considered. Thus,

the FGMs represent the transition between two base materials, and the objective is to find the optimal FGM property variation such that the material model allows local distribution of the two materials in the domain. The material model used is based on a density method approach, defined for the Lame constants [27].

The material model for the second FGM optimization approach is the FGM-SIMP material model. This new material model is similar to the traditional SIMP; the difference is that in the FGM-SIMP, a design domain known as FGM domain is used. The FGM domain presents a continuous variation in the material properties, defined by the designer. The TOM must find the elements that satisfy the objective function and constraints, as in a traditional TOM problem. Thus, in the FGM-SIMP material model, property A_0 considered in Eq. (1) for the traditional SIMP is not constant along the design domain, but it depends on position x as:

$$A = \rho(x)^p A_0(x), \quad x \in \Omega \tag{2}$$

In traditional topology optimization formulations, the design variable is defined in a piecewise fashion in the discretized domain, which means that the continuity of the material distribution does not occur between FEs (see Fig. 4a). However, considering the topology optimization results as an FGM-type, a more natural way of representing the material distribution emerges by using the concept of the graded finite elements (GFE) [27]. The GFE leads to a continuous representation of material properties that are interpolated within the finite element using the FE shape functions (see Fig. 4b) [28]. Some works have suggested the continuum distribution of the design variable within the FE in the topology optimization formulation [29].

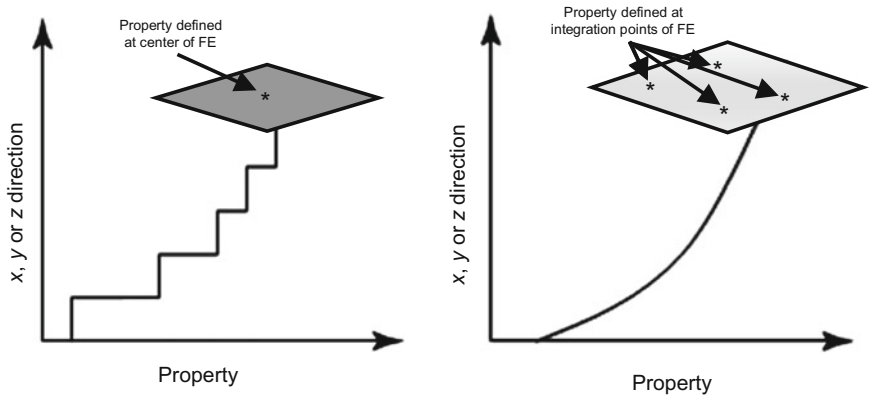

Fig. 4 Finite element modeling of FGMs: **a** Homogeneous finite element and, **b** graded finite element

This formulation is known as CAMD (continuous approximation of material distribution) which is a variation of the SIMP model. By means of the continuum model approach, the design of FGM structures can be fully achieved by applying topology optimization because a continuous change in material properties is considered within the design domain.

4 Topology Optimization of Dynamically Loaded Structures

In this section, the TOM for solving dynamic optimization problems is described. Since a TOM problem requires two modules (the analysis and optimization modules) to be solved, some methods for solving the dynamic analysis problem are first introduced; after this, the addressed methodology to solve the optimization problem is exposed.

4.1 Dynamic Finite Element Analysis

The structures under low-velocity impacts can be analyzed as an elastic dynamic phenomenon as previously stated. However, there are three main dynamics analysis types: modal, harmonic and transient analysis [31]:

- The modal analysis is used to calculate the natural frequencies and mode shapes of a structure or a machine component. It can also serve as a starting point for another, more detailed, dynamic analysis, such as a transient dynamic analysis, a harmonic analysis, or a spectrum analysis.
- The harmonic analysis is used to determine the response of a structure to harmonically time-varying loads (cyclic loads). This type of analysis is useful to analyze structures subjected to resonance, fatigue, and other harmful effects of forced vibrations.
- The transient analysis is used to evaluate structures under loads that are arbitrarily time-varying. In an interval of time, the loads can change their magnitude, direction and/or position. Within this analysis, the inertial and damping effects are considered important.

Consequently, since for low-velocity impacts the structure is under the action of a general time-dependent load, thus the transient analysis is preferred over the others. However, there are two solution methods for the transit analysis, which are mode-superposition and full transient. The mode-superposition method is commonly used in analysis where nonlinearities are not included for being less computationally expensive that the full method. Nevertheless, the full method is a more general method allowing any kind of nonlinearity and any type of load. Therefore,

since geometric nonlinearities are considered herein in order to allow large-deflection effects in the transient analysis, the full method is selected.

The most generic approach for solving the dynamic response in structures is the direct numerical integration of the dynamic equilibrium equation [31]:

$$\mathbf{M}\ddot{\mathbf{U}} + \mathbf{C}\dot{\mathbf{U}} + \mathbf{R}^{\text{int}} = \mathbf{R}^{\text{ext}} \tag{3}$$

where $\mathbf{M}$ is the mass matrix, $\mathbf{C}$ is the damping matrix, and $\mathbf{R}^{\text{int}}$ and $\mathbf{R}^{\text{ext}}$ are the internal and external loads, respectively. Eq. (3) is valid for both linear and nonlinear material properties. If the material is linearly elastic, then internal loads are $\mathbf{R}^{\text{int}} = \mathbf{K}\mathbf{U}$, where $\mathbf{K}$ is the stiffness matrix, and Eq. (3) becomes:

$$\mathbf{M}\ddot{\mathbf{U}} + \mathbf{C}\dot{\mathbf{U}} + \mathbf{K}\mathbf{U} = \mathbf{R}^{\text{ext}} \tag{4}$$

being $\mathbf{U}$, $\dot{\mathbf{U}}$, $\ddot{\mathbf{U}}$ the displacements, velocities, and accelerations of the structure, respectively. Matrices $\mathbf{M}$, $\mathbf{C}$ and $\mathbf{K}$ are obtained as a sum (assembly) of local matrices:

$$\mathbf{M} = \sum_{e=1}^{nel} \mathbf{m}, \quad \mathbf{C} = \sum_{e=1}^{nel} \mathbf{c}, \quad \mathbf{K} = \sum_{e=1}^{nel} \mathbf{k} \tag{5}$$

where the symbol $\sum$ represent the assembly operation, *nel* is the number of FEs in the mesh (discretized design domain) and the local matrices can be obtained as:

$$\mathbf{m} = \int \rho \mathbf{N}^{\mathrm{T}}\mathbf{N} dV, \quad \mathbf{c} = \int c_d \mathbf{N}^{\mathrm{T}}\mathbf{N} dV, \quad \mathbf{k} = \int \mathbf{B}^{\mathrm{T}}\mathbf{D}\mathbf{B} dV \tag{6}$$

with shape functions matrix $\mathbf{N}$, gradient matrix $\mathbf{B}$ and material properties matrix $\mathbf{D}$, ρ represents mass density and c_d is a damping parameter analogous to viscosity. In Eq. (6), $\mathbf{m}$ and $\mathbf{c}$ are identified as "consistent" element mass and damping matrices, which emphasizes that these forms follow directly from the FE discretization, and use the same shape functions as the element stiffness matrix [31]. However, non-consistent forms of these matrices are also used.

The consistent mass matrix $\mathbf{m}$ is symmetric, full, and positive definite. However, there is a simpler formulation for the mass matrix known as "lumped". This approach consists in placing concentrated masses at nodes, which produce a diagonal mass matrix. Although the lumped formulation has computational advantages, such as less storage space and processing time, this formulation can require especial solution algorithms once the lumped matrices are positive semidefinite or, indeed, indefinite. Additionally, for implicit integration methods, a diagonal mass matrix provides little computational economy and a consistent formulation provides more accuracy [31]. Thus, the consistent formulation is chosen for this work.

The damping matrix can be generated from Eq. (6) or by using other formulations. Damping dissipates energy by limiting the amplitude of vibration produced by the loads and produces a decay of these vibrations over time. Several types of damping can be included in a dynamic analysis; some of them are the viscous or Rayleigh damping, hysteresis or solid damping, Coulomb or friction damping, and numerical damping. Here, the numerical damping is considered, which is further discussed in section "implicit integration".

Finally, Eq. (4) is discretized in time and solved by some direct integration method, which makes Eq. (4) be held for all t and then it is also valid at time $t + \Delta t$:

$$\mathbf{M}\ddot{\mathbf{U}}_{t+\Delta t} + \mathbf{C}\dot{\mathbf{U}}_{t+\Delta t} + \mathbf{K}\mathbf{U}_{t+\Delta t} = \mathbf{F}_{t+\Delta t} \tag{7}$$

Various numerical techniques have been developed in direct numerical integration for solving the system of Eq. (7). However, the next subsections describe the most common methods: explicit and implicit direct time integration methods.

Explicit Integration

Explicit methods only require information on time step t to predict the structural response at time $t + \Delta t$, e.g.:

$$\mathbf{U}_{t+\Delta t} = f\left(\mathbf{U}_t, \dot{\mathbf{U}}_t, \ddot{\mathbf{U}}_t, \mathbf{U}_{t-\Delta t}, \ \ldots\right) \tag{8}$$

These methods are conditionally stable, i.e., the time step size (Δt) has to be smaller than a critical value Δt_{cr}; otherwise, the solution is not stable, that is, the solution diverges [31]. With time step Δt, the velocity and acceleration at time step t are approximated through conventional central differential equation (in the notation, time t is equivalent to n, e.g. $\mathbf{U}_t \equiv \mathbf{U}_n$):

$$\begin{gathered}\dot{\mathbf{U}}_n = \frac{1}{2\Delta t}\left(\mathbf{U}_{n+1} - \mathbf{U}_{n-1}\right) \rightarrow \mathbf{U}_{n+1} = \mathbf{U}_{n-1} + 2\Delta t\dot{\mathbf{U}}_n \\ \ddot{\mathbf{U}}_n = \frac{1}{\Delta t^2}\left(\mathbf{U}_{n+1} - 2\mathbf{U}_n + \mathbf{U}_{n-1}\right)\end{gathered} \tag{9}$$

Substituting Eq. (9) into Eq. (3), and reorganizing it:

$$\left[\frac{1}{\Delta t^2}\mathbf{M} + \frac{1}{2\Delta t}\mathbf{C}\right]\mathbf{U}_{n+1} = \mathbf{R}_n^{\mathrm{ext}} - \mathbf{R}_n^{\mathrm{int}} + \frac{2}{\Delta t^2}\mathbf{M}\mathbf{U}_n - \left[\frac{1}{\Delta t^2}\mathbf{M} - \frac{1}{2\Delta t}\mathbf{C}\right]\mathbf{U}_{n-1} \tag{10}$$

Equation (10) is conditionally stable with the condition [31]:

$$\Delta t \leq \frac{2}{\omega_{\max}}\left(\sqrt{1-\xi^2} - \xi\right) \tag{11}$$

with ξ as the rate of damping and ω_{max} as largest contributing frequency to the dynamic response. Thus, the critical time step (time discretization) can be expressed by the so-called Courant–Friedrichs–Lewy (CFL) condition [31]:

$$\Delta t_{cr} \leq \frac{L_{mesh}}{c} \tag{12}$$

where c is the velocity of sound in the material. In practice, the spatial discretization is obtained as:

$$\Delta x = \Delta y = \frac{\lambda}{20} \quad \text{with} \quad \lambda = \frac{c}{f_0}; \quad c = \sqrt{E/\rho} \tag{13}$$

Term λ is the wavelength, f_0 is the fundamental frequency, E is the Young modulus and ρ is the density.

Implicit Integration

The most common implicit integration method is the Newmark method, which computes the structural response at time $t + \Delta t$ based on the solution at current and previous times as follows:

$$\mathbf{U}_{t+\Delta t} = f\left(\mathbf{U}_{t+\Delta t}, \dot{\mathbf{U}}_{t+\Delta t}, \ddot{\mathbf{U}}_{t+\Delta t}, \mathbf{U}_t, \dot{\mathbf{U}}_t, \ddot{\mathbf{U}}_t, \ldots\right) \tag{14}$$

Specifically, Newmark relations are (as above, the time $t + \Delta t$ is equivalent to $n + 1$, e.g. $\mathbf{U}_{t+\Delta t} \equiv \mathbf{U}_{n+1}$):

$$\begin{aligned} \dot{\mathbf{U}}_{n+1} &= \dot{\mathbf{U}}_n + \Delta t\left(\gamma \ddot{\mathbf{U}}_{n+1} + (1-\gamma)\ddot{\mathbf{U}}_n\right) \\ \mathbf{U}_{n+1} &= \mathbf{U}_n + \Delta t \dot{\mathbf{U}}_n + \frac{1}{2}\Delta t^2\left(2\beta \ddot{\mathbf{U}}_{n+1} + (1-2\beta)\ddot{\mathbf{U}}_n\right) \end{aligned} \tag{15}$$

Manipulating Eqs. (4) and (11), and reorganizing:

$$\begin{aligned} \mathbf{K}^{eff}\mathbf{U}_{n+1} = \mathrm{R}^{ext}_{n+1} &+ \mathbf{M}\left\{\frac{1}{\beta\Delta t^2}\mathbf{U}_n + \frac{1}{\beta\Delta t}\dot{\mathbf{U}}_n + \left(\frac{1}{2\beta} - 1\right)\ddot{\mathbf{U}}_n\right\} \\ &+ \mathbf{C}\left\{\frac{\gamma}{\beta\Delta t}\mathbf{U}_n + \left(\frac{\gamma}{\beta} - 1\right)\dot{\mathbf{U}}_n + \Delta t\left(\frac{\gamma}{2\beta} - 1\right)\ddot{\mathbf{U}}_n\right\} \end{aligned} \tag{16}$$

with:

$$\mathbf{K}^{eff} = \frac{1}{\beta\Delta t^2}\mathbf{M} + \frac{\gamma}{\beta\Delta t}\mathbf{C} + \mathbf{K} \tag{17}$$

where γ and β are constant terms that determine the algorithm characteristics, such as accuracy, numerical stability and the amount of algorithmic damping.

When $\gamma > 1/2$, Newmark methods display algorithmic damping and, in order to retain unconditional stability, the following choice of β is appropriate:

$$\gamma \geq \frac{1}{2}, \quad \beta = \frac{1}{4}\left(\gamma + \frac{1}{2}\right)^2 \tag{18}$$

For $\gamma = 0.5$ and $\beta = 0.25$, Eq. (15) produces the average acceleration method, while for $\gamma = 0.5$ and $\beta = 1/6$, Eq. (15) is the linear acceleration method. Moreover, an amplitude decay factor δ can be introduced and Eq. (18) is rewritten as:

$$\gamma = \frac{1}{2} + \delta, \quad \beta = \frac{1}{4}(1+\delta)^2, \quad \delta \geq 0 \tag{19}$$

Although Eqs. (18) and (19) impose a condition in order to get an unconditionally stable solution, i.e., the convergence is independent of the time integration step Δt, this value must be appropriately selected for accuracy purposes.

At this point, a choice must be made between these two direct integration methods: explicit or implicit. The explicit integration methods require many, but low computational cost, integration sub-steps and are useful for short time impact problems. Conversely, the implicit methods require less, but computational-intense, integration sub-steps and are useful for structural dynamic problems. Hence, since a low-velocity impact with material linear effects is considered herein, the Newmark implicit integration method is suitable. Finally, since only numerical damping is considered, the Newmark method presented in Eqs. (16) and (17) becomes:

$$\left\{\frac{1}{\beta\Delta t^2}\mathbf{M} + \mathbf{K}\right\}\mathbf{U}_{n+1} = \mathrm{R}^{\mathrm{ext}}_{n+1} + \mathbf{M}\left\{\frac{1}{\beta\Delta t^2}\mathbf{U}_n + \frac{1}{\beta\Delta t}\dot{\mathbf{U}}_n + \left(\frac{1}{2\beta} - 1\right)\ddot{\mathbf{U}}_n\right\} \tag{20}$$

which will be used for the simulation later in this chapter with $\mathbf{K} = \mathbf{K}(\mathbf{U})$ since geometric nonlinearities are considered. Consequently, the Newmark integration scheme may be used in association with the Newton-Raphson iterative algorithm.

4.2 Topology Optimized Structures Under Impact Loads

The TOM has been applied successfully to many fields [12]. However, most attention has been paid to structural optimization, especially under static loading condition. As optimization techniques and computers have increased their power, new major complex problems can be solved by TOM. One example is the optimization of structures under dynamic loading conditions. These kinds of problems are complex since they require dynamic finite element and sensitivity analysis. Topology optimized structures under transient loads are of primary interest to automotive safety, specifically regarding crashworthiness [32].

In a dynamic problem, such as impacts involving two or more bodies, the loads are applied over a short period and transient effects must be considered. Dynamic FEA is required to obtain the numerical dynamic response of the system. Dynamic FEA commonly requires geometric and/or materials and/or contact nonlinearities. Even though the dynamic FEA does not consider any nonlinearities and is evaluated as an elastic analysis, large simulation times are needed.

The complexity of dynamics TOM problems is increased due to the dynamics sensitivity analysis, which is computational expensive and due to nonlinearities, the gradient calculation is usually a difficult task or maybe impossible for the most complex problems. Consequently, these difficulties have hindered research in the structure optimization for impact loading conditions. To overcome these problems, surrogate models or non-gradient methodologies are often employed [32].

Surrogate methodologies use design variables in the range of 10–50, while the topology optimization problems typically need from thousands to millions of design variables, which increase the problem complexity and the computational time required for finding the solution. Then, fewer methods using topology optimization for dynamical analysis exist due to the large number of design variables involved. Surrogate models reduce the cost of expensive analysis methods as well as alleviate issues with sensitivities. Additionally, they are good alternatives when dealing with the highly nonlinear and noisy design spaces. Examples of surrogates methods are RSM (response surface method), Kriging, artificial neural networks, and RBF (radial basis functions) [32].

TOM based on non-gradients have populated the dynamic problems avoiding the complexity imposed by the dynamics sensitivity analysis. An often used, but inefficient approach, is to utilize genetic algorithms (GAs) or semi-stochastic techniques. These methods may be more likely to find global solutions, but they require thousands of function calls. Another non-gradient based methodology developed by Xie and Stevens is called evolutionary structural optimization (ESO) [33]. It is based on the concept of progressively removing inefficient material from a structure so that it evolves into an optimal design. Another approach that requires non-gradient information is the hybrid cellular automaton (HCA) method [34].

Although the design of energy absorption structures has been studied for many years, the implementation of TOM in this kind of problems is still relatively new [32]. Since most applications under impact events aim at maximizing the energy absorption by the structure during the collision, other structures that have shown a good performance as energy absorbers under impact loads are cellular materials.

Cellular materials, including honeycombs and foams, have been widely applied to various engineering fields and, among these applications, their employment as structural materials of dampers or energy dissipation devices has been the most focused application [35]. These materials with periodic cells are typically configured as cores of panels, tubes and shells, which produce a sandwich-type structure. The properties in these materials that appear most attractive for impact applications are energy absorption, vibration control and reduced weight. Additionally, cellular

materials are topology-sensitive; that is, relevant properties are sensitive to the micro-architecture of the cells [35]. Two kinds of predominant topologies are distinguished in cellular materials: stochastic and periodic microstructures. The second configuration offers structures with superior performance than those constructed with the analogous stochastic configuration. Cellular materials, particularly porous materials are closely related to natural structures and the FGM concept (see Fig. 1).

4.3 Equivalent Static Loads

Dynamic loads are forces that change in the time domain, while static loads are forces that are constant, regardless of the time, and the inertial effects are not considered. Accordingly, structures under dynamic loads cannot be represented by static loads, although at any given time t, Eqs. (3) and (7) can be thought of as a set of "static" equilibrium equations that also take into account inertia forces ($\mathbf{M}\ddot{\mathbf{U}}$) and damping forces ($\mathbf{C}\dot{\mathbf{U}}$). Thus, there are several methods to transform dynamic loads into static loads. One transformation method is the equivalent static load (ESL) method [36]. An ESL is defined as a static load that produces the same displacement field as a dynamic load at an arbitrary time t. A static analysis is expressed as [37]:

$$\mathbf{KX} = \mathbf{S} \tag{21}$$

where $\mathbf{X}$ is the static displacement vector and $\mathbf{S}$ is the vector of external static loads. The dynamic displacement vector $\mathbf{U}(t_d)$ at an arbitrary time t_d can be obtained from Eq. (3), and substituting $\mathbf{X}$ for $\mathbf{U}(t_d)$ in Eq. (21), the ESLs are obtained as follows:

$$\mathbf{S} = \mathbf{K}\,\mathbf{U}(t_d) \tag{22}$$

Then, a set of ESLs vectors are obtained, and its number depends on the time discretization used. This set of ESLs vectors are used as multiple load conditions in the optimization process [37].

4.4 The Optimization Process with ESLs

For a structural optimization problem subjected to an impact load, the objective function is to minimize the compliance (or maximize the stiffness) of the structure. This is a classic objective function in structural optimization, the convexity of which has been mathematically proved. Additionally, this objective function is

usually accompanied by a volume constraint. Thus, the formulation for a linear static optimization problem is:

$$\begin{aligned} \underset{\boldsymbol{\rho}}{\mathbf{Min}} \quad & \boldsymbol{F_o} = \boldsymbol{U}^{\mathrm{T}}\boldsymbol{F} = \boldsymbol{U}^{\mathrm{T}}\boldsymbol{K}\boldsymbol{U} \\ \text{Such that :} \quad & \mathrm{V} - \mathrm{V}_{\max} \leq 0 \\ & \boldsymbol{\rho} - \boldsymbol{\rho}_{\min} \geq 0 \\ & \text{With: } \boldsymbol{K}\boldsymbol{U} = \boldsymbol{F} \end{aligned} \tag{23}$$

where the structural stiffness is represented as $\boldsymbol{U}^{\mathrm{T}}\boldsymbol{F}$, V is the maximum allowed volume in the final optimal design, which is commonly a fraction of the design domain volume $\mathrm{V}_{\max}$, $\boldsymbol{\rho}$ is the design variables vector and $\boldsymbol{\rho}_{\mathbf{min}}$ is a minimum value used to avoid numerical singularities. Furthermore, the equilibrium equation must be satisfied. The sensitivities of the objective function F_o with respect to the design variable ρ_{e} are given by:

$$\frac{\partial F_o}{\partial \rho_{\mathrm{e}}} = -\mathrm{p}\rho_{\mathrm{e}}^{\mathrm{p}-1} E\left(\boldsymbol{u}_{\mathrm{e}}^{\mathrm{T}}\boldsymbol{k}_{\mathbf{0}}\boldsymbol{u}_{\mathrm{e}}\right) \tag{24}$$

where $\boldsymbol{u}_{\mathrm{e}}$ and $\boldsymbol{k}_0$ are the element displacement vector and local stiffness matrix, respectively. The k_0 matrix is computed with a Young's module $E = 1$ and based on isotropic material and axisymmetric modeling. Once the optimization problem has been formulated, their solution is the next phase. The optimization process with ESL method consists of two parts [37]: the analysis and the design domains. Based on the results of the analysis domain, ESLs are calculated for the design domain. In the design domain, static response optimization is conducted with the ESL. The modified design domain is incorporated to the analysis domain. The entire optimization process iterates between the two domains until the convergence criteria are satisfied. Figure 5 shows the optimization process using the ESL method where the algorithm steps are [37]:

- Step 1: initial setting of parameters and design variables (number of iterations $k = 0$, design variables $\rho_k = \rho_0$, convergence parameters: ε a small value)
- Step 2: performs dynamic analysis with ρ_k (domain analysis)
- Step 3: calculates the ESLs at all-time intervals
- Step 4: solves the optimization problem with linear static response set of the equivalent load (in the design domain), as shown in Fig. 3.
- Step 5: evaluates the convergence criteria
- Step 6: updates the design variables if the problem does not reach the convergence and repeats the process.

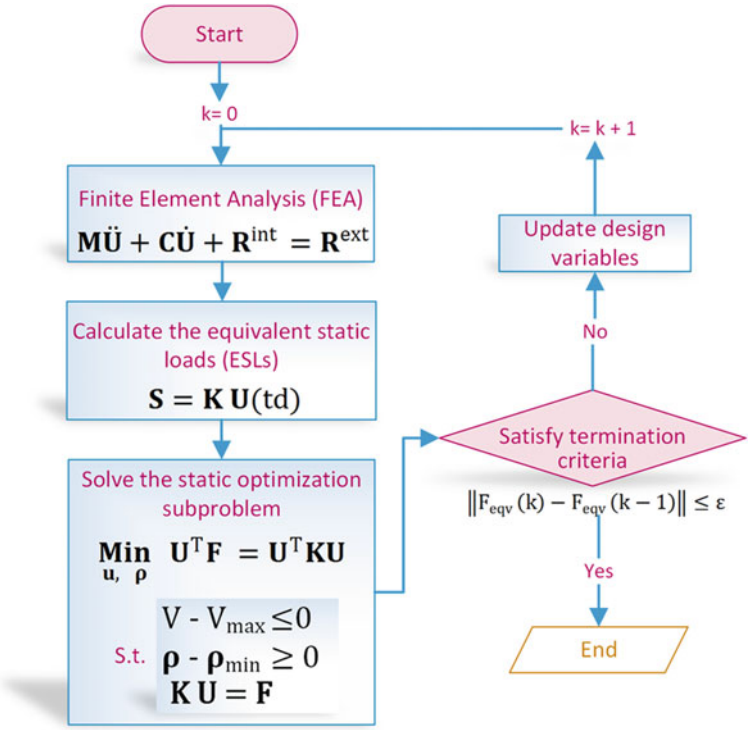

Fig. 5 Optimization process using equivalent static loads [37]

5 TOM-Based Design of FGMs Under Impact Loads

In this work, the design of FGMs under low-velocity impacts by the TOM is conducted by using the ESL method [37]. In this section, cylindrical plates with holes heuristically located are presented first, and next, the behavior of the same cylindrical plate after an optimization procedure that introduces pores (or holes) in the material by using the TOM is shown.

5.1 Heuristic Approach

In this section, functionally graded porous structures subjected to low-velocity impact loads are analyzed. The graded function controls the holes diameter, which is selected heuristically in this first part. Cylindrical steel plates with 10 cm in diameter and 3 cm in thickness are used, as shown in Fig. 6. The plate is supported at the ends; therefore, movements in X and Y are restricted. At the center, an impulsive pressure load is applied, which simulates the impact of an element of

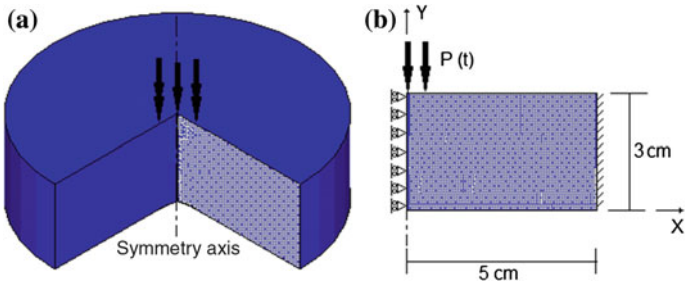

Fig. 6 Steel plate geometry used in the simulation. **a** 3D model and. **b** Axisymmetric model

0.6 cm of diameter. Taking advantage of the geometry, a planar axisymmetric FEM model is used, which reduces the solution time as compared to an equivalent model made in a three-dimensional (3D) domain and produces approximated results.

The gradation in the plate is performed by circular holes,[1] where their diameters and distribution change in the same direction as the stress wave goes through the plate (thickness direction). Figure 7 shows the functionally graded plates with their respective graded function used in the simulations. Holes distribution 1 has relatively small holes through the thickness of the plate with a constant function of gradation (there is no variation in the distribution or diameter size of the holes). Holes distribution 2 has similar characteristics as those of distribution 1, yet with larger hole diameters. Holes distribution 3 begins with a larger diameter on the surface near the impact area, reducing it as the holes approach the opposite surface. Holes distribution 4 is opposed to distribution 3. Finally, holes distribution 5 begins with relatively small holes on the surface near the impact area, then increases in size in the middle and is reduced again on the opposite surface. These distributions are arbitrarily selected for verifying the role of the holes, their distribution and their diameters in the structural behavior subjected to impact loads, and their influence in the stress wave propagation and weight reduction.

The simulations are performed by using the finite element software ANSYS with the Newmark implicit integration method using interpolation parameters $\delta = 0.005$, $\gamma = 0.5050$ and $\beta = 0.2525$, which is an unconditionally stable scheme. Four types of steel are used: a low carbon steel (AISI 1020), an alloy steel (AISI 4140), a tool steel (AISI S2), and a ballistic steel (Mars 300). The material properties needed in the transient simulation are presented in Table 1 for the different steels used. The applied pressure is 350 MPa in 6.12×10^{-6} s (see Fig. 8), which represents the low-velocity impact (an impulsive load applied over one integration time step). The mesh size and the time step for the simulation is calculated by using the Courant condition, obtaining $\Delta t = 6.12 \times 10^{-6}$ s and $\Delta x = \Delta y = 25 \times 10^{-5}$ m. Additionally, a convergence test is performed to adjust the size of the mesh. The axisymmetric FE type used by

[1]Since we use 2D domains, the holes seem circular; however, the model is asymmetric and thus the holes are toroidal. We hereafter refer to them simply as holes.

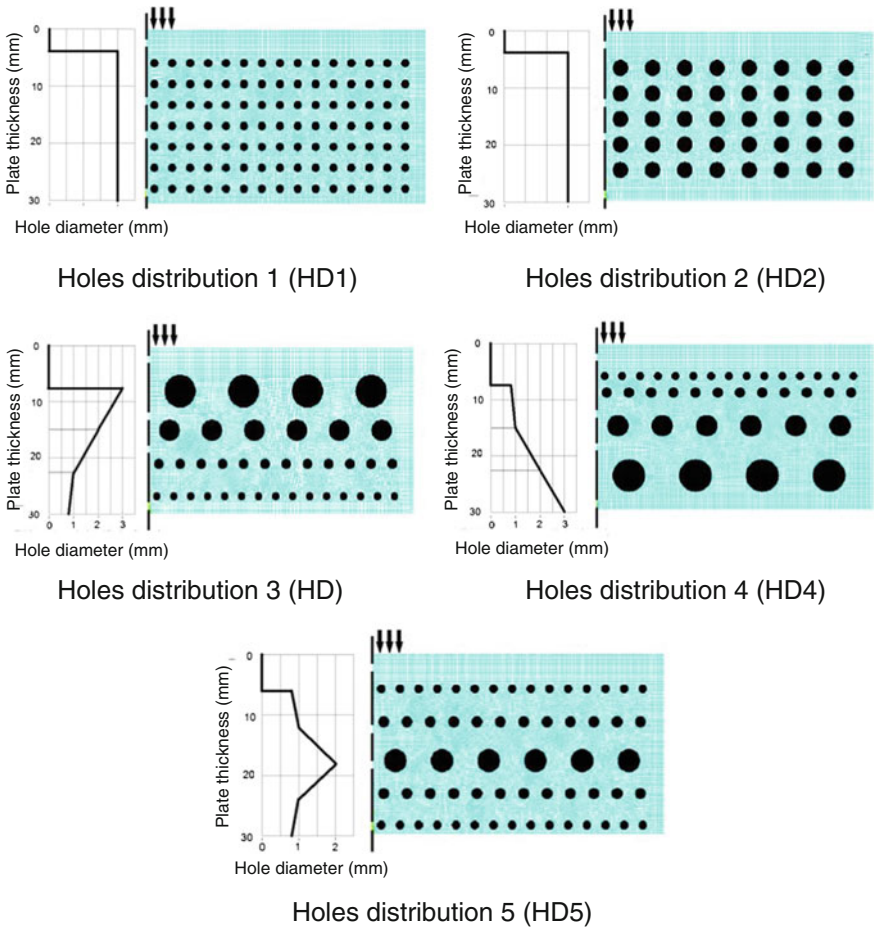

Fig. 7 Arbitrary hole distributions used in the plate

Table 1 Material properties used in the simulations

Material	Density (kg/m^3)	Young's modulus (GPa)	Poisson's ratio
AISI 1020	7500	200	0.29
AISI 4140	7850	205	0.29
AISI S2	7750	207	0.29
Mars 300	8100	210	0.32

ANSYS is the so-called Plane182, which is defined by four nodes having two degrees of freedom at each node: translation in the X and Y directions.

For determining the structural behavior of the arbitrary cylindrical graded plates, they are compared with a solid plate. By simulation, the stresses are obtained in five

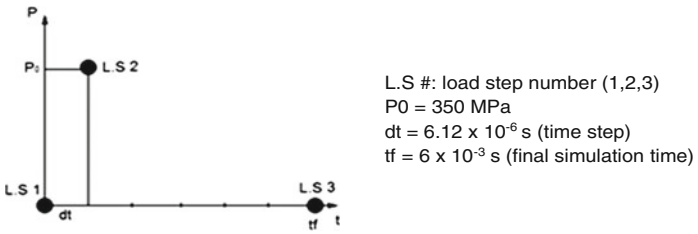

Fig. 8 Load steps used in the simulations (unscaled)

points on the opposite surface where the impact load is applied, as shown in Fig. 9, for the plate with holes distribution 1. Graphs from 1 to 5 show the value of the equivalent von Mises stress versus time. As expected, the impact energy is attenuated by the structure over time. The stresses at point 1 are higher than those at point 5.

Figure 10 shows the stress wave propagation at different times for a graded plate. It can be seen that the stress wave propagates concentrically from the load application point to the ends, across the entire plate. So as to know the stress wave energy that crosses the plate, the von Mises stresses at each discretized point along the entire opposite side where the load is applied are measured (line A–A in Fig. 11). Figure 11 shows, for the graded plate with holes distribution 5, the von Mises stresses at the load application time (6.12×10^{-6} s) and at the end of the simulation time (6×10^{-3} s), when the load has been attenuated. However, the total stress energy[2] per unit volume is obtained as the area under the curve of the stresses versus time. Thus, the von Mises equivalent stress for all points along line A–A are summed and plotted against time as shown in Fig. 12 for the four materials and for the five gradation configurations considered.

The gradation effect in the energy dissipation through the plate is compared with the energy going through the solid plate. For this purpose, the area under the curves in Fig. 12 is computed and a ratio between solid and graded plates are obtained. Table 2 shows the comparison of the energy dissipated by the solid plate against each graded plate and the percentage of weight reduction (relative to the solid plate). It shows that the graded plates present a weight reduction of at least 14 % as a consequence of the porosity introduced. Additionally, the energy going through the graded plates increases in all cases as compared with the solid plate. It is observed that as the material is more resistant to impact, the amount of energy going through the plate is lower, as expected. The best result is for the Mars 300 with graded distribution 1. The worst result is for graded distribution 2, which has the largest weight reduction (18.9 %); however, the energy going through the plate presents the largest values. Accordingly, the results show that the gradation in the

[2]The area under the curve indicates strictly power per unit volume, which is directly related to the elastic deformation energy per unit volume.

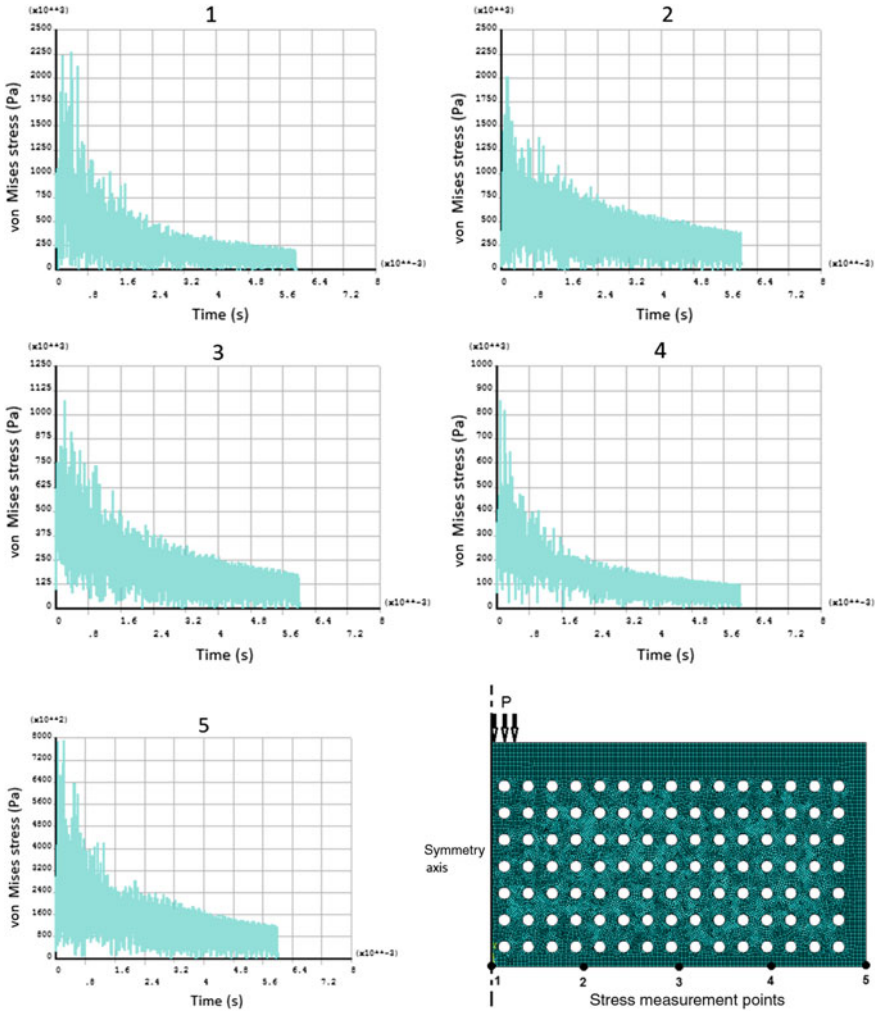

Fig. 9 von Mises stress (*left*) at points 1–5 of the plate (*right*) with holes distribution 1 (AISI 1020)

plates does not reduce the amount of energy going through them; depending on the application, this increase may be relatively less critical as compared with the advantages provided by the weight reduction. Additionally, the graded functions are arbitrarily obtained, making it is important to seek for an optimum graded function obtained by using optimization techniques, which is the subject of the subsequent section.

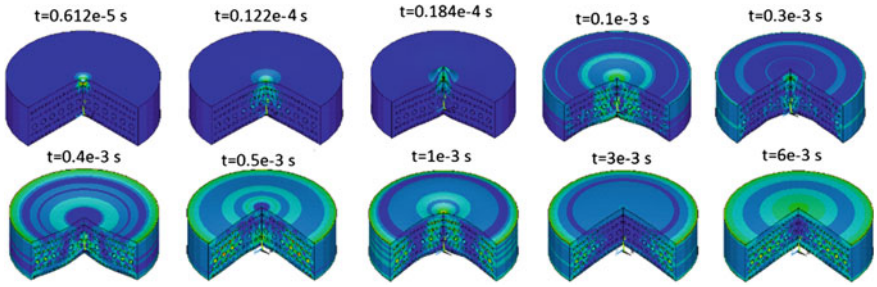

Fig. 10 Propagation of the von Mises stress waves through time (AISI 1020, Holes distribution 5)

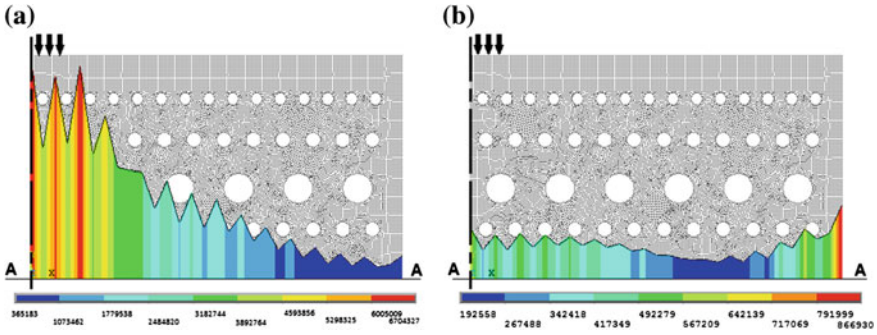

Fig. 11 von Mises stresses along the opposite side where the load is applied. **a** At the time the impact load is applied and, **b** at the end of the simulation (AISI 1020, holes distribution 5)

5.2 Optimized Approach

The optimized approach is carried out in ANSYS APDL by adapting its optimization module with the ESL method, which requires four principal steps:

- Problem definition. In this step, the analysis type and the material properties required by the analysis are defined.
- Active and passive regions definition. The active region corresponds to the domain to be optimized with the objective function, while the passive region is that area in which no optimization occurs. This design domain is defined similarly to a sandwich-like structure: two solid panels enclosing a porous structure (see Fig. 13).
- Loads and boundary conditions definition. The optimization problem requires a FEA analysis at each iteration, which requires the use of loads and boundary conditions. However, in this study, we use the ESL method to convert the dynamic loads into equivalent static loads.
- Optimization process definition. Here, the objective function and constraints are defined.

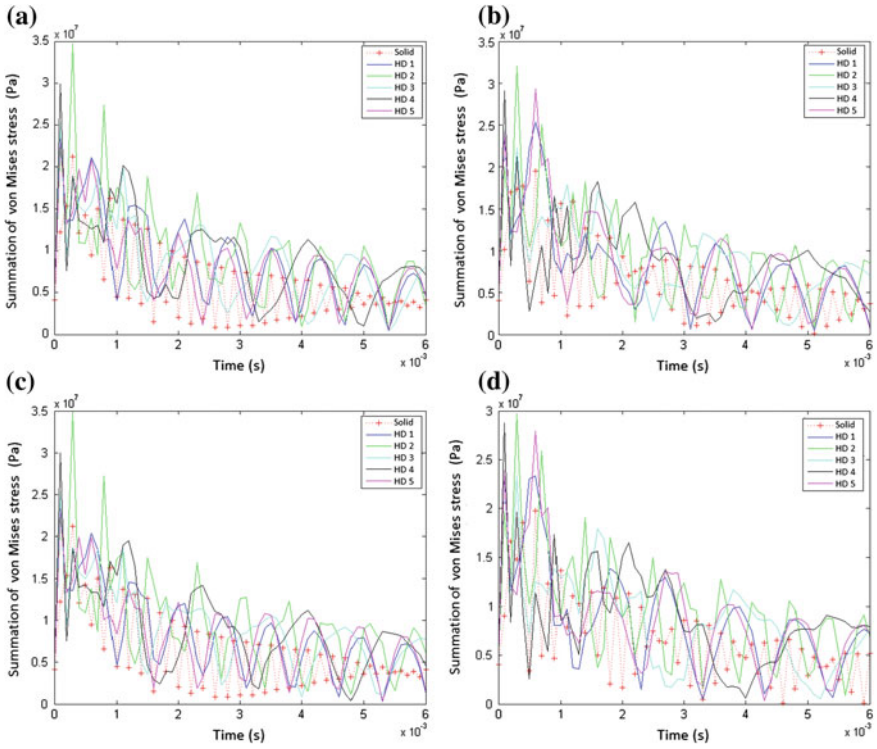

Fig. 12 Summation of von Mises stress for all points along the line A–A against time simulation for different materials. **a** AISI 1020, **b** AISI 4140, **c** AISI S2 and, **d** Mars 300

Table 2 Solid and graded plates comparison for the four materials

Ratio	Weight reduction (%)	Energy increment			
		AISI 1020 (%)	AISI 4140 (%)	AISI S2 (%)	Mars 300 (%)
Solid/gradation 1	14.1	38.8	31.3	30.9	29.2
Solid/gradation 2	18.9	52.8	45.2	53.6	44.9
Solid/gradation 3	17.1	40.2	37.0	43.3	31.5
Solid/gradation 4	17.1	44.2	36.1	43.5	34.7
Solid/gradation 5	14.1	33.2	34.8	33.6	34.0

The material properties used for the optimization process are shown in Table 1. The design domain is shown in Fig. 13a, which consists of active (the TOM can modify it) and passive regions (the TOM cannot modify it). The FE type used in the study is known as *Plane82* in ANSYS. The objective function is the maximization of the stiffness (minimum compliance problem) under low-velocity impact loads. Since the set of ESLs are obtained from dynamic displacements at a particular time, there is an ESL per node; however, for simplifying the study, the areas where the

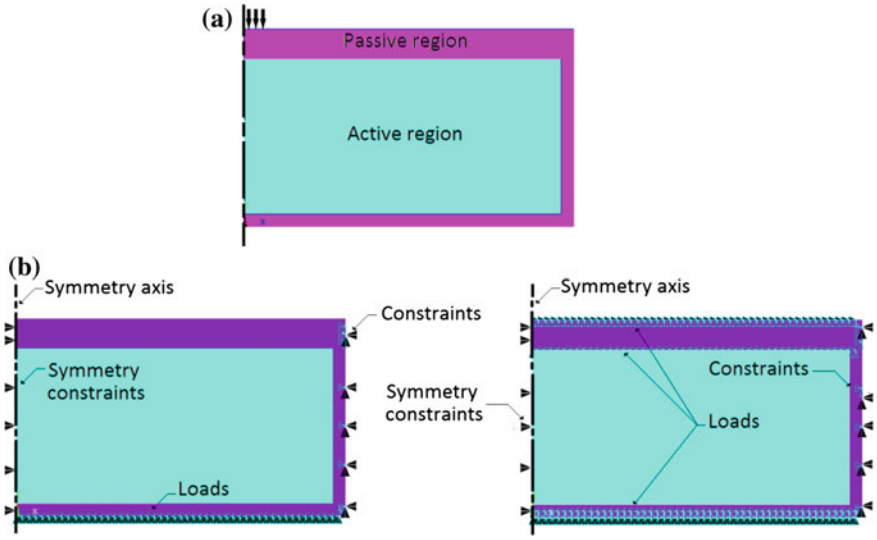

Fig. 13 **a** Two-dimensional design domain with active and passive regions, and **b** loads and boundary conditions for two cases (OTi & OTii, respectively)

largest displacements are presented are used, as shown in Fig. 13b. Case I (abbreviated as OTi – optimized topology for case I) obtains the displacements at the opposite face where the impact load is applied. Case II (abbreviated as OTii - optimized topology for case II) obtains the displacements in three lines: at the top (where the impact load is applied), in the middle (where there is an interface between the passive and the active regions) and at the bottom (similarly to Case I).

Figure 14 shows the optimization process evolution for the AISI 1020 (the worst material for impact application as demonstrated in the previous section). The blue

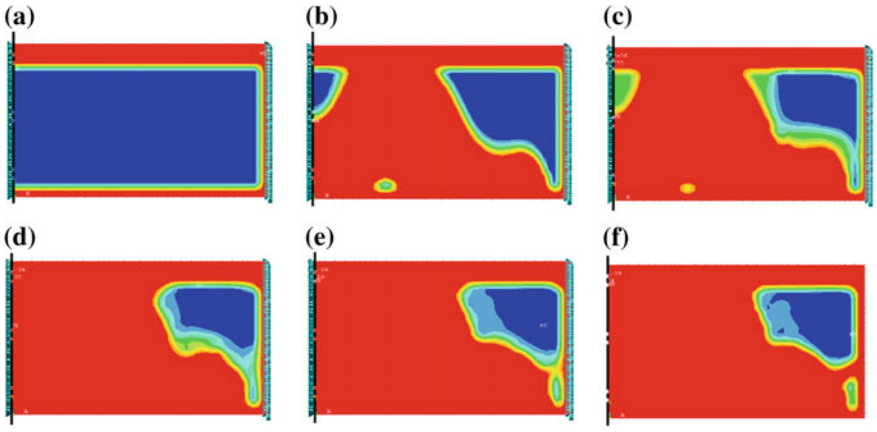

Fig. 14 Topology optimization process at different times (AISI 1020, Case I)

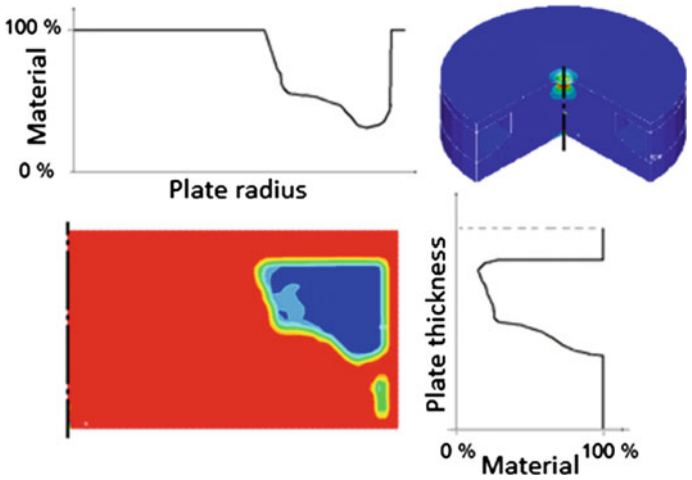

Fig. 15 Topology optimized circular plate with his graded function (AISI 1020, Case I)

color represents voids zones, while the red color indicates zones with base material. For this optimization process, a constraint in volume is imposed, and the convergence is achieved when this constraint is reached. The volume constraint is equivalent to a weight constraint since the density is constant. The final topology obtained by the TOM is given in Fig. 15. The comparison in terms of energy dissipation between the solid plate, the heuristic graded plate (hole distribution 2—HD2–) and optimized version are shown in Fig. 16.

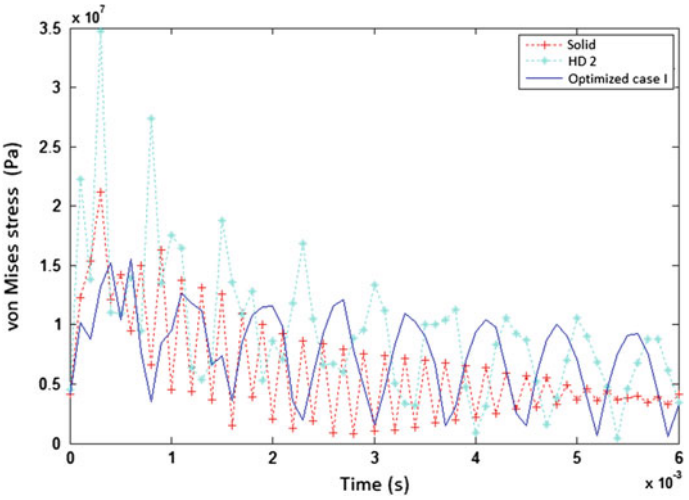

Fig. 16 Energy dissipation between solid, heuristic graded and optimized graded plates (AISI 1020, Case I)

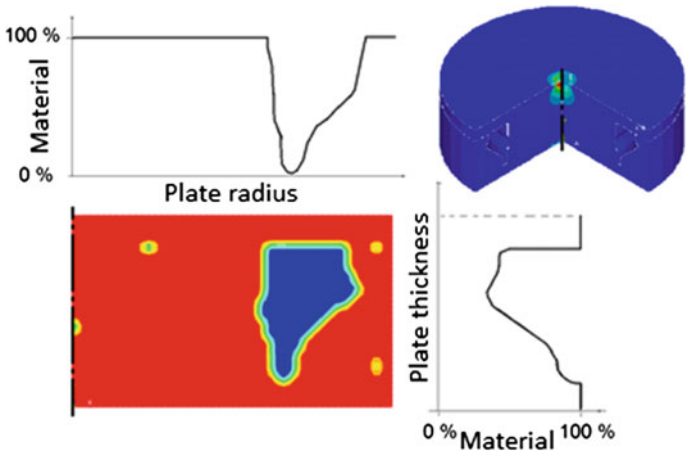

Fig. 17 Topology optimized circular plate with his graded function (AISI 1020, Case II)

However, the optimization results are different if Case II (see Fig. 13b) for the ESLs are considered as shown in Fig. 17. Figure 18 presents the comparison in terms of dissipated energy between solid, heuristic graded and topology optimized plate. Table 3 shows the numerical comparison for the Cases I and II with respect to solid and heuristic graded plate by using the AISI 1020 steel. It can be seen that with optimization approach, the graded plates outperform (Case I) or equally

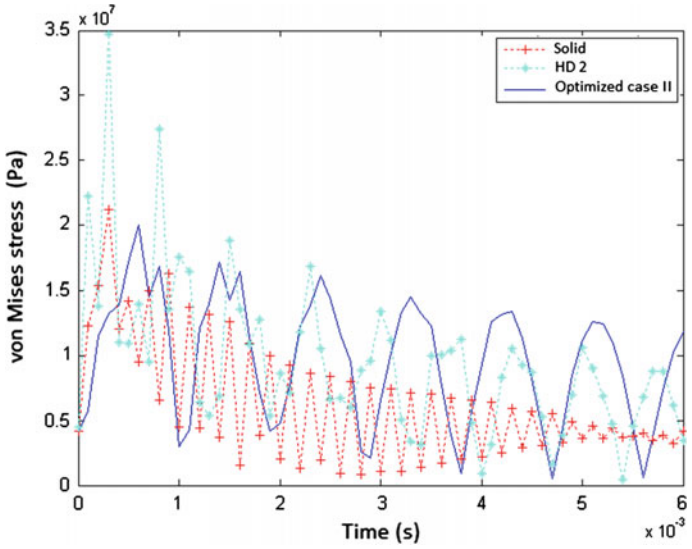

Fig. 18 Energy dissipation between solid, heuristic graded and optimized graded plates (AISI 1020, case II)

Table 3 Dissipated energy comparison for three topology cases by using AISI 1020

Material ratio	Weight reduction (%)	Energy increase (%)
Solid/heuristic hole distribution 2 (HD2)	18.8	52.8
Solid/optimized topology case I (OTi)	18.8	22.0
Solid/optimized topology case II (OTii)	18.8	52.8
HD2/OTi	0	−20.2
HD2/OTii	0	−0.013

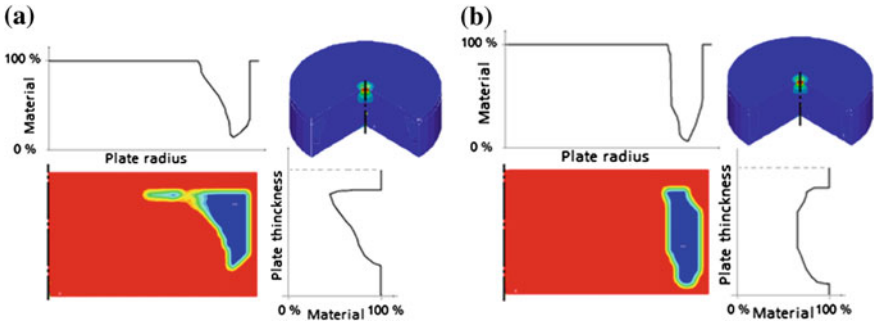

Fig. 19 Topology optimized circular plate with his graded function for Mars 300. **a** Case I and, **b** Case II of loads application

perform (Case II) when compared against the plate with heuristic holes distribution 2; however, both types of graded plates have a poor performance compared with solid plate.

The same study as that conducted above is followed; however, changing the material. In this case, Mars 300 steel is considered. The optimized topologies for cases I and II are given in Fig. 19. The numerical comparison between solid, heuristic graded and optimized graded plates are shown in Table 4. Since, in the non-optimized approach, holes distribution 1 (HD1) gives the best results for Mars 300 steel, this hole distribution is considered here for the comparisons. The optimized topology obtained for Case I improves the energy absorption, indeed, outperforming the solid and heuristic graded plate (HD1). However, the OTii case only

Table 4 Dissipated energy comparison for three topology cases by using Mars 300

Material ratio	Weight reduction (%)	Energy increase (%)
Solid/HD1	14	29.2
Solid/OTi	14	−4.9
Solid/OTii	14	25.4
HD1/OTi	0	−26.4
HD1/OTii	0	−3.0

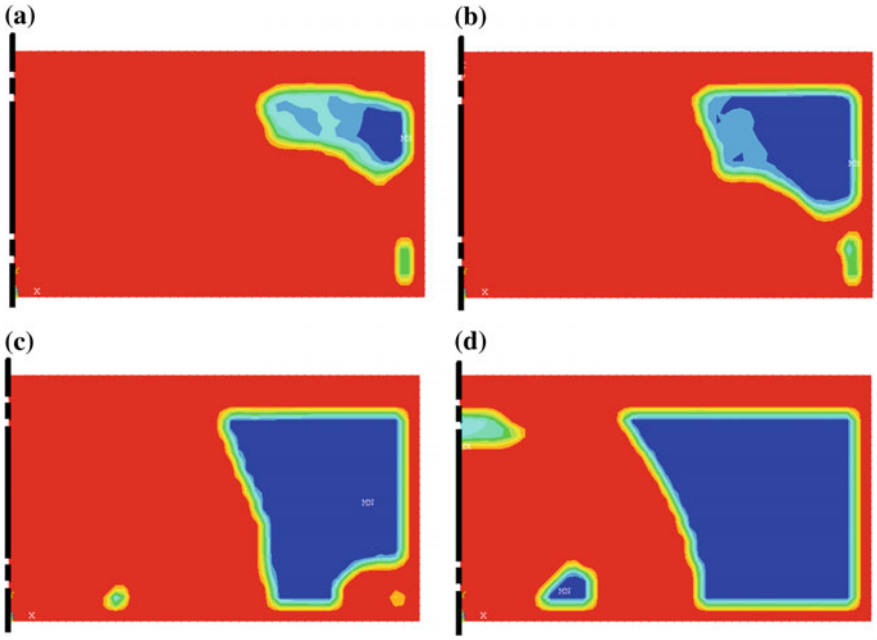

Fig. 20 Topology optimized circular plate for AISI 1020 by reducing. **a** 10 %, **b** 20 %, **c** 35 % and, **d** 50 % of total weight

outperforms the plate with HD1 with a small percentage of difference; and it performs poorly against the solid plate.

Finally, an experiment is conducted by varying the total volume to be removed from the optimized graded plate. The topologies obtained for several percentage of weight reduction are shown in Fig. 20 by using AISI 1020 steel. It is observed that the dissipated energy through the plate decrease when the material removed is increased in a non-linear relation as shown in Table 5.

Table 5 Dissipated energy comparison between solid and optimized plate considering four weight constraints by using AISI 1020

Material ratio	Energy increase (%)
Solid/optimized plate (weight reduction: 10 %)	5.9
Solid/optimized plate (weight reduction: 20 %)	17.6
Solid/optimized plate (weight reduction: 35 %)	113.5
Solid/optimized plate (weight reduction: 50 %)	132.6

6 Conclusions of the Chapter

This chapter presents the concept of functionally graded materials and topology optimization methods. Both concepts are combined to produce lightweight structures for low-velocity impact applications. The form that we use to reduce the weight in the structures considered (circular plates) is by inserting holes into the material. The addition of holes to circular plates under low-velocity impacts is evaluated in two ways, by using heuristic and systematic approaches. However, the introduction of holes to the plate tends to reduce its capacity for absorbing the impact energy. Nevertheless, the porous material outperforms the solid plate once: by using the topology optimization method and a high quality steel for impact applications (Mars 300). Additionally, the optimized approach minimizes the impact energy that crosses the plate when compared with the heuristic holes distributions. These results are promising for getting lightweight structures with improvements in their performance against impact loads.

Acknowledgments The first author acknowledges financial support from COLCIENCIAS by the scholarship "*Becas de Colciencias, Doctorado en Colombia, 567—2012"*. The third author acknowledges the financial support of CNPq (National Council for Research and Development), under grants 304121/2013-4.

References

1. Zukas, J.A.: High Velocity Impact Dynamics. Wiley, New York (1990)
2. Goicolea, J.M.: Estructuras sometidas a impacto. In: Car, E., López, F., y Oller, S. (eds.) Estructuras sometidas a acciones dinámicas, pp. 535–567. Centro Internacional de Métodos Numéricos en Ingeniería (CIMNE), Barcelona (2000)
3. Rosenberg, Z., Dekel, E.: Terminal Ballistics. Springer, Berlin (2012)
4. Anderson, C.E.: A review of computational ceramic armor modeling. In: Prokurat, L., Wereszczak, A., Lara-Curzio, E. (eds.) Advances in Ceramic Armor II: Ceramic Engineering and Science Proceedings, vol. 27, no. 7, pp. 1–18. Wiley, Hoboken, NJ, USA (2008)
5. McCauley, J.W., D'Andrea, G., Cho, K., Burkins, M.S., Dowding, R.J., Gooch, W.A.: Status Report on SPS TiB_2/TiB/Ti Functionally Graded Materials (FGMs) for Armor, U.S. Army Research Laboratory (2006)
6. Koizumi, M.: FGM activities in Japan. Compos. B Eng. **28**(1–2), 1–4 (1997)
7. Markworth, A.J., Ramesh, K.S., Parks, W.P.: Modelling studies applied to functionally graded materials. J. Mater. Sci. **30**(9), 2183–2193 (1995)
8. Huang, J., Fadel, G.M., Blouin, V.Y., Grujicic, M.: Bi-objective optimization design of functionally gradient materials. Mater. Des. **23**(7), 657–666 (2002)
9. Birman, V., Byrd, L.W.: Modeling and analysis of functionally graded materials and structures. Appl. Mech. Rev. **60**(5), 195 (2007)
10. Obata, Y., Noda, N.: Optimum material design for functionally gradient material plate. Arch. Appl. Mech. **66**(8), 581–589 (1996)
11. Cardoso, E.L., Fonseca, J.S.O.: Complexity control in the topology optimization of continuum structures. J. Braz. Soc. Mech. Sci. Eng. **25**(3), 293–301 (2003)
12. Bendsøe, M.P., Sigmund, O.: Topology Optimization: Theory, Methods, and Applications. Springer, Berlin (2003)

13. Eschenauer, H.A.: Topology optimization of continuum structures: a review. Appl. Mech. Rev. **54**(4), 331–389 (2001)
14. Michell, A.G.M.: LVIII. The limits of economy of material in frame-structures. Philos. Mag. Ser. *6* **8**(47), 589–597 (1904)
15. Bendsøe, M.P., Kikuchi, N.: Generating optimal topologies in structural design using a homogenization method. Comput. Methods Appl. Mech. Eng. **71**(2), 197–224 (1988)
16. Sigmund, O.: Topology optimization: a tool for the tailoring of structures and materials. Philos. Trans. Roy. Soc. Lond. Ser. A Math. Phys. Eng. Sci. **358**(1765), 211–227 (2000)
17. Sigmund, O.: A 99 line topology optimization code written in Matlab. Struct. Multi. Optim. **21**(2), 120–127 (2001)
18. Bendsøe, M.P.: Optimal shape design as a material distribution problem. Struct. Optim. **1**(4), 193–202 (1989)
19. Bendsøe, M.P., Sigmund, O.: Material interpolation schemes in topology optimization. Arch. Appl. Mech. **69**(9), 635–654 (1999)
20. Rozvany, G.I.N.: A critical review of established methods of structural topology optimization. Struct. Multi. Optim. **37**(3), 217–237 (2008)
21. Dadalau, A., Hafla, A., Verl, A.: A new adaptive penalization scheme for topology optimization. Prod. Eng. Res. Devel. **3**(4–5), 427–434 (2009)
22. Sigmund, O., Petersson, J.: Numerical instabilities in topology optimization: a survey on procedures dealing with checkerboards, mesh-dependencies and local minima. Struct. Multi. Optim. **16**(1), 68–75 (1998)
23. Hassani, B., Hinton, E.: A review of homogenization and topology optimization III—topology optimization using optimality criteria. Comput. Struct. **69**(6), 739–756 (1998)
24. Tovar, A., Patel, N.M., Niebur, G.L., Sen, M., Renaud, J.E.: Topology optimization using a hybrid cellular automaton method with local control rules. J. Mech. Des. **128**(6), 1205–1216 (2006)
25. Lamberti, L., Pappalettere, C.: Move limits definition in structural optimization with sequential linear programming. Part I: optimization algorithm. Comput. Struct. **81**(4), 197–213 (2003)
26. Zhang, X., Zhang, H.: Optimal design of functionally graded foam material under impact loading. Int. J. Mech. Sci. **68**, 199–211 (2013)
27. Paulino, G.H., Silva, E.C.N.: Design of functionally graded structures using topology optimization. Mater. Sci. Forum **492**, 435–440 (2005)
28. Kim, J.-H., Paulino, G.H.: Isoparametric graded finite elements for nonhomogeneous isotropic and orthotropic materials. J. Appl. Mech. **69**(4), 502–514 (2002)
29. Matsui, K., Terada, K.: Continuous approximation of material distribution for topology optimization. Int. J. Numer. Meth. Eng. **59**(14), 1925–1944 (2004)
30. Vatanabe, S.L., Rubio, W.M., Silva, E.C.N.: Modeling of functionally graded materials. In: Comprehensive Materials Processing, pp. 261–282. Elsevier (2014)
31. Cook, R.D., Plesha, M.E., Malkus, D.S., Witt, R.J.: Concepts and Applications of Finite Element Analysis, 4th edn. Wiley, New York (2002)
32. Patel, N.M., Tovar, A., Kang, B.-S., Renaud, J.E.: Crashworthiness design using topology optimization. J. Mech. Des. **131**(6), 061013 (2009)
33. Xie, Y.M., Steven, G.P.: Evolutionary Structural Optimization. Springer, London (1997)
34. Tovar, A., Patel, N.M., Kaushik, A.K., Renaud, J.E.: Optimality conditions of the hybrid cellular automata for structural optimization. AIAA J. **45**(3), 673–683 (2007)
35. Evans, A.G., Hutchinson, J.W., Fleck, N.A., Ashby, M.F., Wadley, H.N.G.: The topological design of multifunctional cellular metals. Prog. Mater Sci. **46**(3–4), 309–327 (2001)
36. Choi, W.S., Park, G.J.: Transformation of dynamic loads into equivalent static loads based on modal analysis. Int. J. Numer. Meth. Eng. **46**(1), 29–43 (1999)
37. Kang, B.S., Choi, W.S., Park, G.J.: Structural optimization under equivalent static loads transformed from dynamic loads based on displacement. Comput. Struct. **79**(2), 145–154 (2001)

Complex Variable Semianalytical Method for Sensitivity Evaluation in Nonlinear Path Dependent Problems: Applications to Periodic Truss Materials

Geovane A. Haveroth and Pablo A. Muñoz-Rojas

Abstract The evaluation of structural response derivatives with respect to design parameters, usually known as sensitivity analysis, is an issue of paramount importance in gradient-based optimization and reliability analyses in engineering. In the last 20 years, much research has been devoted to develop efficient strategies for the accurate evaluation of sensitivity information. A relatively new and promising procedure combines the semianalytical (SA) approach with the use of complex variables (CVSA). This method allows the use of diminutive perturbations, circumventing the weakness that the traditional SA approach shows when applied to shape design variables. In spite of the great potential of the CVSA, its formulation and application has been restricted to path independent problems. In this chapter we aim to extend the method to handle path dependent problems, emphasizing the treatment of internal variables, such as accumulated plastic strain and damage. In order to make the concept easy to understand, we use the method to evaluate the sensitivity of particular homogenized properties of a 2D periodic truss material (PTM). Optimization of PTMs has encountered great potential in tissue engineering, as well as in automotive and aeronautical applications. Generally PTMs are designed to operate in the linear geometrical and constitutive range. However, using sensitivity analysis we can obtain an insight about how these designed homogenized properties behave when geometrical and/or material nonlinearities are considered.

1 Introduction

The notion of structural improvement and optimization requires the existence of some freedom to change a given set of parameters, often called design parameters or design variables. The evaluation of structural response derivatives with respect to

G.A. Haveroth · P.A. Muñoz-Rojas (✉)
Department of Mechanical Engineering, Center for Technological Sciences,
Santa Catarina State University - UDESC, Campus Avelino Marcante,
Joinville, SC 89223-100, Brazil
e-mail: pablo@joinville.udesc.br

P.A. Muñoz-Rojas (ed.), *Computational Modeling, Optimization and Manufacturing Simulation of Advanced Engineering Materials*,
Advanced Structured Materials 49, DOI 10.1007/978-3-319-04265-7_9

design parameters, known in the literature as sensitivity analysis, is a kernel issue in reliability studies, modeling of control systems, among others. The large and growing number of publications regarding this subject reflects the current interest for this type of analysis [1–4]. Several methodologies to obtain sensitivity exist, and they can be classified into three major groups: overall (global) finite differences (OFD), the semianalytical method (SA) and the analytical method. Among these, the SA method is held as the most attractive alternative because it combines the computational efficiency of the analytical method with the generality and simple implementation of the OFD method [3, 5]. However, many authors have reported severe inaccuracies when the traditional SA method based on real variables (RVSA) is applied to problems dominated by rigid body rotations [6–9]. Due to this limitation, several corrective methods have been developed for both linear and geometrically nonlinear problems [10–13].

In nonlinear structural analyses, two different situations may occur. The first one concerns problems said "path independent" such as hyperelasticity, in which the strain path does not affect the equilibrium points. The second one deals with problems said "path dependent" such as elastoplasticity, which depend on the loading history. The implementation of the sensitivity methods for path dependent problems is slightly more evolved than the independent counterpart.

The analytical sensitivity procedure for nonlinear path dependent problems is described by Tsay et al. [14], among others. The application of this theory to truss and beam elements and the difficulties associated to the evaluation of sensitivity coefficients are widely discussed by Tsay et al. [15]. Some incremental algorithms, based on the analytical method to structural sensitivity analyses of nonlinear systems are presented in the works of Chen [16], Ohsaki and Arora [17], as well as Lee and Arora [18]. The sensitivity analysis considering 2D elastoplasticity and elastoviscoplasticity is also discussed by several authors [2, 19–22]. In the work of Bugeda and Gil [23], damage is introduced in the sensitivity study. Two incremental algorithms based on the analytical method are shown by Wisniewski et al. [24] and Conte et al. [25]. In the study made by Chen et al. [26], the RVSA method is used to perform sensitivity evaluations in creep and thermal stress problems.

The SA method using complex variables (CVSA), has recently been successfully applied for the evaluation of structural responses sensitivity with respect to shape parameters in path independent problems dominated by rigid body rotation [27]. This method consists in the simple concept of improving the OFD accuracy, reducing or eliminating the errors made by rounding. Since this is a promising method, such concept of improvement by using of complex variables is extended to path dependent problems in the present Chapter.

The Chapter is organized in four different and complementary sections: Sect. 2 presents the finite element formulation for truss elements including geometric and material nonlinearities. The tangent stiffness matrix is obtained via exact linearization of the internal force, which is necessary to obtain the correct displacement sensitivities. The formulation is developed using an isoparametric approach, which is

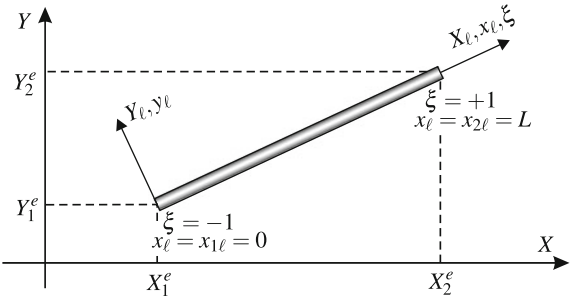

Fig. 1 Truss finite element and its associated global XY and corrotational local $x_\ell y_\ell$ reference systems

intended to ease its extension to continuum finite elements.[1] Section 3 introduces the sensitivity methods studied in this research and their implementation into a finite element code. Special emphasis is devoted to the treatment of internal variables. Section 4 applies the sensitivity methods studied to evaluate the sensitivity of material coefficients of homogenized materials made of periodic truss cells. The sensitivity methods are compared and the superiority of CVSA method is verified for different types of nonlinearities. Finally, Sect. 5 highlights the conclusions of the work.

2 Nonlinear Truss Finite Element Formulation

In order to set the formulation used in this work, consider Fig. 1 which shows a typical two noded truss element and two reference systems associated: a global system XY and a corrotational local system $x_\ell y_\ell$. A parametric coordinate ξ is also defined along the length of the bar, where $\xi = \pm 1$ are related to the extremes.[2] Note that, for simplicity, the truss element in Fig. 1 is set in a 2D framework, while all the equations in the text are generalized to the 3D context.

The local coordinates and displacements of any point on an undeformed element, measured in the local corrotational system are obtained by interpolating the nodal values

$$\begin{bmatrix} X_\ell & u_\ell \end{bmatrix} = \begin{bmatrix} N_1(\xi) & 0 & 0 & N_2(\xi) & 0 & 0 \end{bmatrix} \begin{bmatrix} X_1 & Y_1 & Z_1 & X_2 & Y_2 & Z_2 \\ u_{1x} & u_{1y} & u_{1z} & u_{2x} & u_{2y} & u_{2z} \end{bmatrix}_\ell^T \tag{1}$$

$$= \boldsymbol{N}(\xi) \begin{bmatrix} \boldsymbol{X}_\ell & \boldsymbol{u}_\ell \end{bmatrix}. \tag{2}$$

[1] The use of the isoparametric approach presented in this work does not lead to a direct extension to continuum elements, but preserves the traditional integral form of the internal force vector and tangent matrix. The matrices and vectors obtained have an analogous in continuum elements and thus, the expressions obtained give a deeper insight into the analogous modifications that should be performed in the continuum elements case.

[2] Note that X_ℓ with the "ℓ" subscript stands for the initial value of x_ℓ, while X without the "ℓ" subscript describes the global position in the XY system.

Then, at any time, the updated rotated bar geometry can be obtained taking

$$x_\ell = X_\ell + u_\ell \tag{3}$$

$$= \begin{bmatrix} N_1(\xi) & 0 & 0 & N_2(\xi) & 0 & 0 \end{bmatrix} \begin{bmatrix} x_1 & y_1 & z_1 & x_2 & y_2 & z_2 \end{bmatrix}_\ell^T \tag{4}$$

$$= \boldsymbol{N}(\xi)\boldsymbol{x}_\ell, \tag{5}$$

where $\boldsymbol{N}(\xi)$ is the line matrix containing the interpolation functions. For linear interpolation, the components of $\boldsymbol{N}(\xi)$ are

$$N_1(\xi) = \frac{1}{2}(1-\xi) \quad \text{and} \quad N_2(\xi) = \frac{1}{2}(1+\xi). \tag{6-7}$$

Also, from Eqs. (2) and (5–7), the corresponding Jacobians are expressed by

$$J(X_\ell) = \frac{dX_\ell}{d\xi} = \frac{L_o}{2} \quad \text{and} \quad J(x_\ell) = \frac{dx_\ell}{d\xi} = \frac{L}{2}, \tag{8-9}$$

where L_o and L are respectively the undeformed and deformed lengths of the bar.

In a nonlinear finite element formulation, at each nth increment step, equilibrium must be satisfied. Thus, it is sought to minimize the residue $\boldsymbol{r}_n$ composed by the difference between internal and external force vectors

$$\boldsymbol{r}_n(\boldsymbol{u}_n) = \mu_n \boldsymbol{p} - \boldsymbol{f}_n(\boldsymbol{u}_n) \approx \boldsymbol{0}, \tag{10}$$

where $\boldsymbol{f}_n$ is the global internal force vector, μ_n is the load factor which controls the percentage of the total global external load vector $\boldsymbol{p}$, and n stands for the load step. Without loss of generality, suppose that the incremental iterative Newton-Raphson solution method (NR) is employed. The process begins by an arbitrary and prescribed initial point $\tilde{\boldsymbol{u}}_n^0$ for $\boldsymbol{u}_n$, which, in general, does not satisfy equilibrium. To determine the solution, the initial choice is updated by $\tilde{\boldsymbol{u}}_n^i = \tilde{\boldsymbol{u}}_n^{i-1} + \Delta\boldsymbol{u}_n^i$, where $\Delta\boldsymbol{u}_n^i$ is obtained by the linearization of the residue with origin at $\tilde{\boldsymbol{u}}_n^{i-1}$

$$\boldsymbol{r}_n^i(\tilde{\boldsymbol{u}}_n^i) = \boldsymbol{r}_n^i(\tilde{\boldsymbol{u}}_n^{i-1} + \Delta\boldsymbol{u}_n^i) \approx \boldsymbol{r}_n^i(\tilde{\boldsymbol{u}}_n^{i-1}) + \frac{d\boldsymbol{r}_n^i(\tilde{\boldsymbol{u}}_n^{i-1})}{d\tilde{\boldsymbol{u}}_n^{i-1}}\Delta\boldsymbol{u}_n^i \approx \boldsymbol{0}, \tag{11}$$

with i being the iteration number. To determine $\Delta\boldsymbol{u}_n^i$ it is necessary to evaluate the derivative of the residue with respect to $\tilde{\boldsymbol{u}}_n^{i-1}$, which yields the so-called tangent stiffness matrix $\boldsymbol{K}_{T,n}^{i-1}$. Hence,

$$\boldsymbol{K}_{T,n}^{i-1} = -\frac{d\boldsymbol{r}_n^i(\tilde{\boldsymbol{u}}_n^{i-1})}{d\tilde{\boldsymbol{u}}_n^{i-1}} = -\frac{d\left[\mu_n\boldsymbol{p} - \boldsymbol{f}_n(\tilde{\boldsymbol{u}}_n^{i-1})\right]}{d\tilde{\boldsymbol{u}}_n^{i-1}} = \frac{d\boldsymbol{f}_n(\tilde{\boldsymbol{u}}_n^{i-1})}{d\tilde{\boldsymbol{u}}_n^{i-1}}. \tag{12}$$

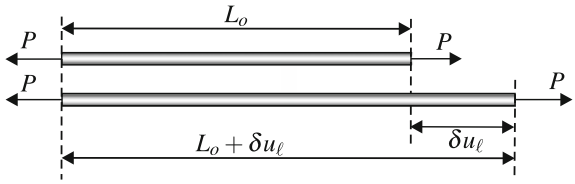

Fig. 2 External virtual work

The last equality holds when the external force does not have any displacement dependence. Furthermore, the tilde is adopted to indicate that the displacement $\boldsymbol{u}_n$ has not converged yet. The absence of the subscript ℓ means that the equations are taken in the global reference system *XYZ*. In order to evaluate Eqs. (10) and (11), the expressions for internal force vector and the tangent stiffness matrix are derived in the next sections.

2.1 Virtual Work

The virtual work principle states that: *The work performed by a real external force applied on a point of the body, over an imaginary (virtual*[3]*) and arbitrary small displacement of the point* (δW_{ext})*, must be equal to the work performed by the internal forces in equilibrium with the real force applied, over the displacement field in equilibrium with the prescribed virtual external displacement* (δW_{int}) [27].

Based on Fig. 2, the resulting virtual work expression from a virtual displacement δu_ℓ on a bar subjected to an axial force P is given by

$$\delta W_{ext} = P\delta u_\ell. \tag{13}$$

The internal virtual work δW_{int} can be expressed using different stress and strain definitions, provided that their joint use leads to the same virtual work δW_{ext}. Stress and strain measures that satisfy this condition are said to be energetically or work conjugate. The rotated[4] engineering stress and strain measures are respectively defined by

$$\sigma_E = \frac{P}{A_o} \quad \text{and} \quad \varepsilon_E = \frac{dx_\ell - dX_\ell}{dX_\ell}. \tag{14-15}$$

It is important to emphasize that in truss structural elements, the scalars σ_E and ε_E are the only nonzero components ($\sigma_{11} = \sigma_{x\ell}$ and $\varepsilon_{11} = \varepsilon_{x\ell}$) in the engineering stress and strain tensors, and therefore, the only components that generate work. The σ_{ij}

[3] A virtual displacement field is defined as an infinitesimal displacement that satisfies the boundary conditions of the original configuration of a given body.

[4] A given entity is said to be rotated if it is described in the corrotational system.

is related to the local system of reference x_1, x_2, x_3. In this case $i, j = 1, 2, 3$, so that $x_1, x_2, x_3 = x_\ell, y_\ell, z_\ell$. Hence,

$$\boldsymbol{\sigma} = \begin{bmatrix} \sigma_{11} & \sigma_{12} & \sigma_{13} \\ \sigma_{21} & \sigma_{22} & \sigma_{23} \\ \sigma_{31} & \sigma_{32} & \sigma_{33} \end{bmatrix}_\ell \approx \begin{bmatrix} \sigma_E & 0 & 0 \\ 0 & 0 & 0 \\ 0 & 0 & 0 \end{bmatrix} \quad \text{and} \quad \boldsymbol{\varepsilon} = \begin{bmatrix} \varepsilon_{11} & \varepsilon_{12} & \varepsilon_{13} \\ \varepsilon_{21} & \varepsilon_{22} & \varepsilon_{23} \\ \varepsilon_{31} & \varepsilon_{32} & \varepsilon_{33} \end{bmatrix}_\ell \approx \begin{bmatrix} \varepsilon_E & 0 & 0 \\ 0 & 0 & 0 \\ 0 & 0 & 0 \end{bmatrix}. \quad (16\text{-}17)$$

From Eqs. (8) and (9), it comes that

$$\varepsilon_E = \frac{J(x_\ell) - J(X_\ell)}{J(X_\ell)} = \frac{L - L_o}{L_o} = \frac{u_\ell}{L_o}, \quad (18)$$

where a linear displacement profile is assumed. Then, the virtual strain resulting from a virtual displacement is given by

$$\delta\varepsilon_E = \frac{d\varepsilon_E}{du_\ell}\delta u_\ell = \frac{\delta u_\ell}{L_o}, \quad (19)$$

satisfying the equality

$$\delta W_{ext} = P\delta u_\ell = \sigma A\delta u_\ell = \frac{P}{A_o}A_o\delta u_\ell = \sigma_E\delta\varepsilon_E A_o L_o = \delta W_{int}, \quad (20)$$

where σ is the rotated Cauchy stress measure, A and A_o are the deformed and undeformed cross-sectional areas, respectively. Equation (20) shows that the rotated stress and strain definitions are work conjugate.

Considering that in a pin-jointed bar the stress and strain values are the same along the length of the bar, and aiming to obtain expressions easily extendable to continuum elements, Eq. (20) can be replaced by

$$\delta W_{int} = \int_{V_o} \sigma_E\delta\varepsilon_E dV_o. \quad (21)$$

2.2 Internal Force Vector

Generalizing the formulation presented for a bar element in Sect. 2.1, the use of Eqs. (2) and (5) lead to the discretized version of virtual work

$$\delta W_{ext} = \underbrace{\sum_{e=1}^{nel} \delta\boldsymbol{u}_\ell^T\boldsymbol{f}_\ell}_{\delta W_{int}} = \underbrace{\sum_{e=1}^{nel}\int_{V_o}\sigma_E\delta\varepsilon_E dV_o}_{\delta W_{int}} = \underbrace{\delta\boldsymbol{u}^T\boldsymbol{p}}_{\delta W_{ext}}, \quad (22)$$

where *nel* corresponds to the total number of elements e which constitute the truss, δW_{ext} stands for the virtual work caused by the virtual displacement $\delta \boldsymbol{u}$, $\boldsymbol{f}_\ell$ is the nodal internal force vector with respect to the local system of reference, and $\boldsymbol{p}$ the external load vector in the global system of reference.

For a given element e, from Eqs. (18) and (19) one gets

$$\delta \varepsilon_E = \frac{1}{J(X_\ell)} \frac{dJ(x_\ell)}{d\boldsymbol{u}_\ell} \delta \boldsymbol{u}_\ell, \tag{23}$$

and nothing that Eq. (23) is valid for an arbitrary $\delta \boldsymbol{u}_\ell$, after some manipulations [28], it results that

$$\boldsymbol{f}_\ell = \int_{-1}^{+1} \boldsymbol{B}_o^T \sigma_E J(X_\ell) A_o d\xi, \tag{24}$$

where

$$\boldsymbol{B}_o = \frac{1}{2J(X_\ell)} \begin{bmatrix} -1 & 0 & 0 & 1 & 0 & 0 \end{bmatrix}. \tag{25}$$

In order to map the internal force vector to the global system of reference, the rotation matrix $\boldsymbol{T}$ is used

$$\boldsymbol{f} = \boldsymbol{T}^T \boldsymbol{f}_\ell, \tag{26}$$

where

$$\boldsymbol{T}(\boldsymbol{u}_n^i) = \begin{bmatrix} \boldsymbol{\theta} & \boldsymbol{0} \\ \boldsymbol{0} & \boldsymbol{\theta} \end{bmatrix} \qquad \text{with} \qquad \theta_{pq} = c_p^q, \quad p, q = 1, 2, 3 \tag{27}$$

and c_p^q is the direction cosine which relates the pth local reference axis of the bar with the qth global reference axis. In practice, from Eqs. (24) and (25), just the first and fourth components of $\boldsymbol{f}_\ell$ are nonzero, then only c_1^q need to be computed.

2.3 Tangent Stiffness Matrix

The global tangent stiffness matrix $\boldsymbol{K}_T$ is obtained by application of an assembly operator Λ which maps local to global degrees of freedom and sums the contribution of each element e to the stiffness of the whole structure [29],

$$\boldsymbol{K}_T = \mathop{\Lambda}_{e=1}^{nel} \boldsymbol{k}_T^e. \tag{28}$$

In turn, the tangent stiffness matrix of each element is obtained by differentiation of the element residue with respect to the element nodal displacement in the global reference system. Considering that the external force its not dependent on the displacement field, it comes out that

$$\boldsymbol{k}_T^e = -\frac{d\boldsymbol{r}^e}{d\boldsymbol{u}^e} = \frac{d\boldsymbol{f}^e}{d\boldsymbol{u}^e} = \frac{d}{d\boldsymbol{u}^e}\left(\boldsymbol{T}^T\boldsymbol{f}_\ell^e\right) = \underbrace{\frac{d\boldsymbol{T}^T}{d\boldsymbol{u}^e}\boldsymbol{f}_\ell^e}_{\boldsymbol{k}_{T1}} + \underbrace{\boldsymbol{T}^T\frac{d\boldsymbol{f}_\ell^e}{d\boldsymbol{u}^e}}_{\boldsymbol{k}_{T2}} = \boldsymbol{k}_{T1} + \boldsymbol{k}_{T2}, \tag{29}$$

Using the engineering stress and strain pair, and after some algebraic manipulations, the term $\boldsymbol{k}_{T1}$ can be expressed as Stahlschimidt [30],

$$\boldsymbol{k}_{T1} = \int_{-1}^{+1} \boldsymbol{B}^T\boldsymbol{H}\boldsymbol{B}J(X_\ell)A_o d\xi, \tag{30}$$

where

$$\boldsymbol{H} = \frac{\sigma_E}{\lambda}\left[\boldsymbol{I} - \left(\frac{1}{\lambda}\right)^2 \boldsymbol{B}\boldsymbol{x}\boldsymbol{x}^T\boldsymbol{B}^T\right], \tag{31}$$

and

$$\boldsymbol{B} = \frac{1}{2J(X_\ell)}\begin{bmatrix} -1 & 0 & 0 & 1 & 0 & 0 \\ 0 & -1 & 0 & 0 & 1 & 0 \\ 0 & 0 & -1 & 0 & 0 & 1 \end{bmatrix}, \tag{32}$$

$\lambda = L/L_o$ is the stretch ratio, $\boldsymbol{I}$ the identity matrix and $\boldsymbol{x}$ the updated coordinate nodal vector with respect to the global reference system. Accordingly, the term $\boldsymbol{k}_{T2}$ can be expressed as

$$\boldsymbol{k}_{T2} = \boldsymbol{T}^T\left[\int_{-1}^{+1} \boldsymbol{B}_o^T\frac{d\sigma_E}{d\varepsilon_E}\boldsymbol{B}_o J(X_\ell)A_o d\xi\right]\boldsymbol{T}, \tag{33}$$

where $d\sigma_E/d\varepsilon_E$ is called tangent modulus and is responsible for introducing the material non-linearity to the formulation. Section 2.6 shows a robust and accurate form to evaluate this expression.

2.4 Geometric Nonlinearity

The geometric nonlinear behavior is introduced into the above formulation through the stretch ratio λ and the updated coordinate vector $\boldsymbol{x}$ into $\boldsymbol{H}$ in $\boldsymbol{k}_{T1}$, and by the rotation matrix $\boldsymbol{T}(\boldsymbol{u}_n^i)$ in $\boldsymbol{k}_{T2}$. It is important to emphasize that the geometric linear

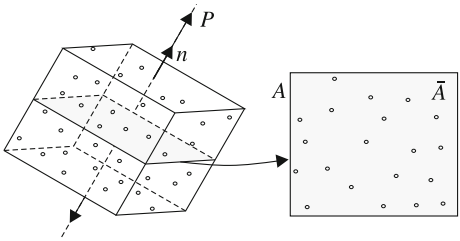

Fig. 3 Damaged representative volume element

formulation can be treated as a particularization of nonlinear formulation. In this case, the $\boldsymbol{k}_{T1}$ vanishes and the linear equation Eq. (11) is exact, so the whole load can be applied in just one step, i.e., $\mu_1 = 1, \tilde{\boldsymbol{u}}_1^0 = \boldsymbol{0}, \boldsymbol{r}_1^1(\tilde{\boldsymbol{u}}_1^1) = \boldsymbol{0}$ and $\boldsymbol{f}(\tilde{\boldsymbol{u}}_1^0) = \boldsymbol{0}$. Then, the discretized equilibrium particularizes to

$$\boldsymbol{r}_1^1(\tilde{\boldsymbol{u}}_1^1 = \boldsymbol{u}) = \boldsymbol{r}_1^1(\tilde{\boldsymbol{u}}_1^0) + \frac{d\boldsymbol{r}_1^1(\tilde{\boldsymbol{u}}_1^0)}{d\tilde{\boldsymbol{u}}_1^0}\boldsymbol{u} \tag{34}$$

$$\boldsymbol{0} = \left[\boldsymbol{p} - \boldsymbol{f}(\tilde{\boldsymbol{u}}_1^0)\right] + \frac{d\boldsymbol{r}_1^1(\tilde{\boldsymbol{u}}_1^0)}{d\tilde{\boldsymbol{u}}_1^0}\boldsymbol{u} \tag{35}$$

$$\Rightarrow \quad -\frac{d\boldsymbol{r}_1^1(\tilde{\boldsymbol{u}}_1^0)}{d\tilde{\boldsymbol{u}}_1^0}\boldsymbol{u} = \boldsymbol{r}_1^1(\tilde{\boldsymbol{u}}_1^0) = \boldsymbol{p} - \boldsymbol{0} \tag{36}$$

or consistently with the Eq. (12),

$$\boldsymbol{K}_T\boldsymbol{u} = \boldsymbol{p}, \tag{37}$$

where

$$\boldsymbol{K}_T = \underset{e=1}{\overset{nel}{\Lambda}}\boldsymbol{k}_{T2}, \quad \boldsymbol{p} = \underset{e=1}{\overset{nel}{\Lambda}}\boldsymbol{p}^e, \quad \text{and} \quad \boldsymbol{f} = \underset{e=1}{\overset{nel}{\Lambda}}\boldsymbol{f}^e. \tag{38-40}$$

2.5 *Material Nonlinearity: A Coupled Elastoplastic Model for Ductile Damage*

A damaged representative volume element (RVE), oriented by the normal vector $\boldsymbol{n}$ and subjected to a load $\boldsymbol{P}$, is shown in Fig. 3. The scalar damage variable is physically defined as the density of micro-cracks and voids inside an overall cross-sectional area A in the RVE[5] [31]. Under isotropic hypothesis, the scalar damage variable D does not dependent on a normal vector and can be defined as

[5]The micro-cracks and voids are small if compared to RVE dimension, but large when compared to the atomic level.

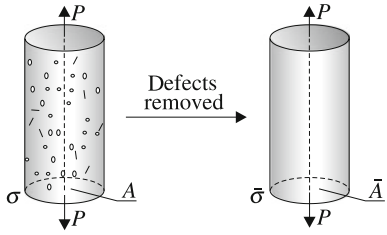

Fig. 4 Bar subjected to uniaxial stress. The micro-cracks and voids are simultaneously removed

$$D = \frac{A - \bar{A}}{A} = \frac{A_D}{A}, \tag{41}$$

where A_D is the damaged area and $\bar{A}$ the effective resisting area. The damage value $D = 0$ corresponds to the undamaged state, $D = 1$ represents the rupture of the material into two parts, and $0 < D < 1$ represents a damaged intermediate state.

Figure 4 shows a bar subjected to uniaxial stress in the damaged and equivalent configuration states. The equivalent configuration state is obtained by removing the micro-cracks and voids. The effective stress $\bar{\sigma}$[6] is related to the equivalent configuration without defects, defined on an RVE plane from Eq. (41) by

$$\bar{\sigma} = \frac{P}{\bar{A}} = \frac{\sigma}{1 - D}. \tag{42}$$

In order to model the damage material behavior, the strain equivalence principle is the most applied. This principle states that the constitutive equations to damaged material are derived in a similar way than for a virgin materials with the sole difference that the effective stress $\bar{\sigma}$ replaces the usual stress σ [32]. Then, from Hooke's law one obtains

$$\varepsilon^e = \frac{\sigma}{\bar{E}} = \frac{\bar{\sigma}}{E} = \frac{\sigma}{E(1 - D)}, \tag{43}$$

with

$$\bar{E} = E(1 - D) \quad \text{and} \quad D = \frac{E - \bar{E}}{E} = 1 - \frac{\bar{E}}{E}, \tag{44-45}$$

where ε^e is the elastic strain, E the initial (undamaged) modulus and $\bar{E}$ the damaged material modulus. This development is based on a phenomenological model using the elastic modulus degradation as a damage macroscopic measure.

Three equations ground the classical continuum theory of plasticity: the yield condition, the flow rule and the hardening law [33]. For a one-dimensional stress state, the yield surface condition can be expressed, considering the effective stress concept [34], as

[6] In favor of neatness, from this point on, the subscript $(.)_E$ is dropped because it is implicit that only the rotated engineering stress and strain tensors will be used throughout the text.

$$f(\sigma, \alpha, D) = \frac{|\sigma|}{1-D} - \left(\sigma_y + H_{iso}\alpha\right) \leq 0, \tag{46}$$

where the scalar variable α is known as accumulated plastic strain and is a parameter associated to isotropic hardening, H_{iso} is the isotropic hardening modulus and σ_y is the initial yield stress. The evolution of the plastic strain and the isotropic hardening laws are respectively given by

$$\dot{\varepsilon}^p = \gamma \frac{\partial f}{\partial \sigma} = \gamma \frac{sign(\sigma)}{1-D} \quad \text{and} \quad \dot{\alpha} = |\dot{\varepsilon}^p| = \gamma, \tag{47-48}$$

where γ is the plastic multiplier and *sign* is the sign function that returns ± 1. Equation (47) evinces the damage plasticity coupling.

Once the damage variable is defined, one can adopt the associate evolution law proposed by Lemaitre [32] which, particularized to the unidimensional case, is given by [34],

$$\dot{D} = \dot{p}\left(\frac{-Y}{r}\right)^S, \tag{49}$$

where $\dot{D}$ is the rate of damage evolution, r and S are material parameters experimentally obtained, Y is the damage energy release rate and $\dot{p}$ is the equivalent plastic strain rate. The last two entities are respectively defined by

$$Y = \frac{\sigma^2}{2E(1-D)^2} \quad \text{and} \quad \dot{p} = \sqrt{\dot{\varepsilon}^p \dot{\varepsilon}^p} = \frac{\gamma}{1-D}. \tag{50-51}$$

Now, the continuous constitutive equations are replaced by their incremental counterparts. Suppose that in the $(n-1)$th incremental step, the plastic strain field, the damage variable and the compatible strain fields are known. For a given strain increment, one wants to update the information for the current step n. The procedure adopted to solve this problem is based in a linear prediction scheme and non-linear correction, schematically shown in Fig. 5.

From the development of Esmaeili and Öchsner [34], based in Fig. 5, the elastic trial strain is obtained by the expressions

$$\varepsilon_n^{e,trial} = \varepsilon_{n-1} - \varepsilon_{n-1}^p + \Delta\varepsilon_{n-1} = \varepsilon_n - \varepsilon_{n-1}^p, \tag{52}$$

$$\varepsilon_n^{e,trial} = \varepsilon_n - \varepsilon_n^p + \Delta\varepsilon_{n-1}^p = \varepsilon_n^e + \Delta\varepsilon_{n-1}^p. \tag{53}$$

Using Hooke's law, the elastic strain in the n state is described as

$$\varepsilon_n^e = \frac{\sigma_n}{(1-D_n)E}, \tag{54}$$

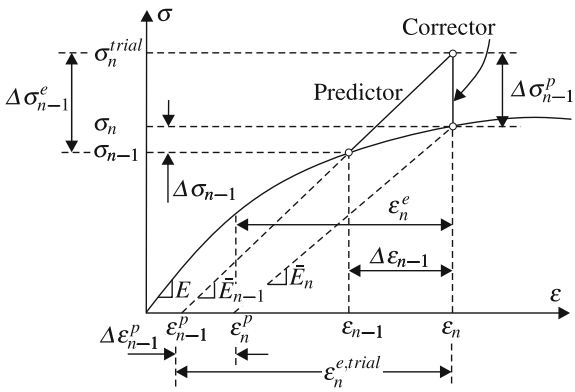

Fig. 5 Scheme integration algorithm considering the damage effects. Linear prediction and nonlinear correction

which together with Eq. (53) returns the final expression for the stress state,

$$\sigma_n = (1 - D_n)E\varepsilon_n^{e,trial} - (1 - D_n)E\Delta\varepsilon_{n-1}^p, \tag{55}$$

where $\varepsilon_n^{e,trial}$ is evaluated by Eq. (52), whereas $\Delta\varepsilon_{n-1}^p$ may be replaced by

$$\Delta\varepsilon_{n-1}^p = \Delta\gamma_n \frac{sign\left(\sigma_n^{trial}\right)}{(1 - D_n)}, \tag{56}$$

obtaining

$$\sigma_n = (1 - D_n)E\varepsilon_n^{e,trial} - \Delta\gamma_n Esign\left(\sigma_n^{trial}\right). \tag{57}$$

The prediction phase consists in evaluating the trial elastic stress, described by

$$\sigma_n^{trial} = \bar{E}_{n-1}\varepsilon_n^{e,trial} = E(1 - D_{n-1})\varepsilon_n^{e,trial}. \tag{58}$$

In order to verify if the trial stress elastic hypothesis is consistent with the assumption of a purely elastic state, one checks the yield function

$$f(\sigma_n^{trial}, \alpha_{n-1}, D_{n-1}) = \frac{|\sigma_n^{trial}|}{(1 - D_{n-1})} - \left(\sigma_y + H_{iso}\alpha_{n-1}\right). \tag{59}$$

If $f \leq 0$, the current step is elastic and the hypothesis that the variables α_{n-1}, D_{n-1} and ε_{n-1}^p are frozen is correct ($\alpha_n = \alpha_{n-1}$, $D_n = D_{n-1}$ and $\varepsilon_n^p = \varepsilon_{n-1}^p$). On the other hand if $f > 0$, the correction phase must be performed. In general, at the end of the nth incremental step, the four Eqs. (60–63) must be satisfied

$$\sigma_n = (1 - D_n)E\varepsilon_n^{e,trial} - \Delta\gamma_n E sign(\sigma_n^{trial}), \tag{60}$$

$$\alpha_n = \alpha_{n-1} + \Delta\gamma, \tag{61}$$

$$f_n = \frac{|\sigma_n|}{1 - D_n} - (\sigma_y + H_{iso}\alpha_{n-1}), \tag{62}$$

$$D_n = D_{n-1} + \frac{\Delta\gamma_n}{1 - D_n}\left(\frac{-Y(\sigma_n, D_n)}{r}\right)^S. \tag{63}$$

Outside this state, one obtains the residue r on each of these equations

$$r_\sigma(\sigma, \Delta\gamma, D) = \frac{\sigma}{E} - (1 - D)\varepsilon_n^{e,trial} + \Delta\gamma sign(\sigma) \neq 0 \tag{64}$$

$$r_\alpha(\alpha, \Delta\gamma) = -\alpha + \alpha_{n-1} + \Delta\gamma \neq 0 \tag{65}$$

$$r_f(\sigma, \alpha, D) = \frac{|\sigma|}{1 - D} - (\sigma_y + H_{iso}\alpha) \neq 0 \tag{66}$$

$$r_D(\sigma, \Delta\gamma, D) = -D + D_{n-1} + \frac{\Delta\gamma}{1 - D}\left(\frac{-Y(\sigma, D)}{r}\right)^S \neq 0. \tag{67}$$

The final stage is the root of the vector function $\boldsymbol{m}$, which consists of the residual functions

$$\boldsymbol{m}(\boldsymbol{v}) = \left[r_\sigma(\boldsymbol{v})\ r_\alpha(\boldsymbol{v})\ r_f(\boldsymbol{v})\ r_D(\boldsymbol{v})\right]^T, \tag{68}$$

where

$$\boldsymbol{v} = \left[\sigma\ \alpha\ \Delta\gamma\ D\right]^T. \tag{69}$$

This root is obtained using any method for the solution of nonlinear equations. In the present work only the full NR is employed

$$\boldsymbol{v}^i = \boldsymbol{v}^{i-1} - \left[\boldsymbol{J}(\boldsymbol{v}^{i-1})\right]^{-1}\boldsymbol{m}(\boldsymbol{v}^{i-1}). \tag{70}$$

At each nth step, the vector

$$\boldsymbol{v}^0 = \begin{bmatrix} \sigma^0 \\ \alpha^0 \\ \Delta\gamma^0 \\ D^0 \end{bmatrix} = \begin{bmatrix} \sigma_n^{trial} \\ \alpha_{n-1} \\ 0 \\ D_{n-1} \end{bmatrix} \tag{71}$$

can be used as the initial value for the argument. The Jacobian matrix of the residue vector function Eq. (68) is obtained from the partial derivatives of Eqs. (64–67), specifically by

$$\boldsymbol{J}(\boldsymbol{v}) = \begin{bmatrix} E^{-1} & 0 & sign(\sigma) & \varepsilon_n^{e,trial} \\ 0 & -1 & 1 & 0 \\ \frac{sign(\sigma)}{1-D} & -H_{iso} & 0 & \frac{|\sigma|}{(1-D)^2} \\ \frac{2sign(\sigma)S\Delta\gamma|\sigma|^{2S-1}}{(1-D)^{2S+1}(2Er)^S} & 0 & \frac{1}{(1-D)^{2S+1}}\left(\frac{\sigma^2}{2Er}\right)^S & -1+\frac{(2S+1)\Delta\gamma}{(1-D)^{2(S+1)}}\left(\frac{\sigma^2}{2Er}\right)^S \end{bmatrix}. \quad (72)$$

The inversion of $\boldsymbol{J}$ must be evaluated in the converged state of the previous NR iteration procedure.

Interestingly, Esmaeili and Öchsner [34] show a simplification of this matrix scheme which results in only one single residual equation to be solved, resulting in a more compact and inexpensive computationally numerical scheme. However, this alternative is not implemented in the present work.

2.6 Tangent Modulus

The tangent modulus depends directly on the constitutive relationship in question. Thus, to generalize its evaluation, a finite difference procedure based on complex derivatives is adopted [35].

The tangent modulus is numerically obtained by a perturbation in the imaginary part of the stress

$$\frac{d\sigma_n}{d\varepsilon_n} \approx \frac{\mathrm{Im}\left[\sigma_n(\varepsilon_n + i\Delta\varepsilon_n)\right]}{\Delta\varepsilon_n}, \quad (73)$$

where

$$\Delta\varepsilon_n = \varphi\varepsilon_n \quad (74)$$

is a perturbation in the strain and φ is the proportionality perturbation factor, which can be given values as low as $\varphi = 10^{-300}$, providing accurate and stable results. In Sect. 3.1.1, the reader will find more details about this procedure based in complex derivatives. Moreover, this procedure presents a low computational and storage cost, because it is set at the element (local) level, at each Gauss point in FE computations.

3 Sensitivity Analysis

This section presents an overview of analytical, SA and OFD methods for the treatment of sensitivity in nonlinear quasi-static problems. Such methods are easily particularized to the linear case simply by considering a single incremental step.

3.1 Sensitivity Analysis for Path Independent Problems

In this type of problem, the sensitivity can be evaluated from calculations based on variables, all of which available in the current incremental step. The residue $\boldsymbol{r}_n$ can be described directly as a function of displacement at the end of the nth incremental step

$$\boldsymbol{r}_n(\boldsymbol{u}_n, \boldsymbol{s}) = \mu_n \boldsymbol{p}(\boldsymbol{s}) - \boldsymbol{f}_n(\boldsymbol{u}_n, \boldsymbol{s}) \approx \boldsymbol{0}, \tag{75}$$

where $\boldsymbol{s} = (s_1, \ldots, s_j, \ldots, s_{ndv})$ is the design variables vector and ndv is the number of design variables. The same equilibrium procedure shown in Sect. 2 is adopted in the present formulation considering the new linearization of the residue around $\tilde{\boldsymbol{u}}_n^{i-1}$

$$\boldsymbol{r}_n(\tilde{\boldsymbol{u}}_n^i, \boldsymbol{s}) = \boldsymbol{r}_n(\tilde{\boldsymbol{u}}_n^{i-1} + \Delta\boldsymbol{u}_n^i, \boldsymbol{s}) \approx \boldsymbol{r}_n(\tilde{\boldsymbol{u}}_n^{i-1}, \boldsymbol{s}) + \frac{\partial \boldsymbol{r}_n(\tilde{\boldsymbol{u}}_n^{i-1}, \boldsymbol{s})}{\partial \tilde{\boldsymbol{u}}_n^{i-1}} \Delta\boldsymbol{u}_n^i. \tag{76}$$

After recursive updating of displacements using Eq. (76), the convergence $\tilde{\boldsymbol{u}}_n^i \rightarrow \boldsymbol{u}_n$ is achieved, that is, $\boldsymbol{r}_n(\boldsymbol{u}_n, \boldsymbol{s}) \approx \boldsymbol{0}$. The residue derivative with respect to $\boldsymbol{u}_n$ refers to the tangent stiffness matrix $\boldsymbol{K}_{T,n}$ shown in Sect. 2.3.

Generally, a given structural constraint can be expressed as

$$\mathsf{G}(\boldsymbol{s}) = G(\boldsymbol{u}_n(\boldsymbol{s}), \boldsymbol{s}) \leq 0. \tag{77}$$

In order to evaluate the constraint sensitivity, Eq. (77) is differentiated with respect to the design parameter $s_j \in \boldsymbol{s}$, resulting in

$$\frac{d\mathsf{G}}{ds_j} = \frac{\partial G}{\partial s_j} + \frac{\partial G}{\partial \boldsymbol{u}_n} \frac{d\boldsymbol{u}_n}{ds_j}. \tag{78}$$

3.1.1 Overall Finite Difference Method

This section shows the OFD methods based on real and complex variables. The details around such formulations are also discussed.

OFD Based on Real Variables

Simplicity and ease of implementation make the traditional (based on real variables) overall finite difference method (RVOFD) widely used in commercial numerical codes. However, this approach suffers from computational inefficiency and numerical errors [36, 37].

In order to apply this method, the iterative procedure expressed by Eq. (76) must be repeatedly used considering each perturbed design variable. To this end, suppose

that the displacement is a differentiable function and consider Δs_j a perturbation in the jth design variable with a vector representation given by

$$\Delta \boldsymbol{s}_j = \left[0 \ \ldots \ \Delta s_j \ \ldots \ 0\right]^T. \tag{79}$$

The design variable can be perturbed positively, negatively or both positively and negatively. Therefore, without loss of generality, considering a positive perturbation in the jth design variable and iteratively solving Eq. (76) one obtains the converged displacement in nth incremental step $\boldsymbol{u}_n(\boldsymbol{s} + \Delta \boldsymbol{s}_j)$. Similarly, making a negative perturbation in the same jth design variable, $\boldsymbol{u}_n(\boldsymbol{s} - \Delta \boldsymbol{s}_j)$ is obtained.

If positive perturbation is used, the approximation obtained is known by forward finite difference (FFD)

$$\frac{d\boldsymbol{u}_n(\boldsymbol{s})}{ds_j} \approx \left[\frac{\Delta \boldsymbol{u}_n(\boldsymbol{s})}{\Delta s_j}\right]_{FFD} = \frac{\boldsymbol{u}_n(\boldsymbol{s} + \Delta \boldsymbol{s}_j) - \boldsymbol{u}_n(\boldsymbol{s})}{\Delta s_j}. \tag{80}$$

On the other hand, if a negative perturbation is used, one obtains the backward finite difference (BFD)

$$\frac{d\boldsymbol{u}_n(\boldsymbol{s})}{ds_j} \approx \left[\frac{\Delta \boldsymbol{u}_n(\boldsymbol{s})}{\Delta s_j}\right]_{BFD} = \frac{\boldsymbol{u}_n(\boldsymbol{s}) - \boldsymbol{u}_n(\boldsymbol{s} - \Delta \boldsymbol{s}_j)}{\Delta s_j}. \tag{81}$$

Finally, using a combination of positive and negative perturbations, one gets the central finite difference (CFD)

$$\frac{d\boldsymbol{u}_n(\boldsymbol{s})}{ds_j} \approx \left[\frac{\Delta \boldsymbol{u}_n(\boldsymbol{s})}{\Delta s_j}\right]_{CFD} = \frac{\boldsymbol{u}_n(\boldsymbol{s} + \Delta \boldsymbol{s}_j) - \boldsymbol{u}_n(\boldsymbol{s} - \Delta \boldsymbol{s}_j)}{2\Delta s_j}. \tag{82}$$

It is important to notice that Eqs. (80) and (81) demand a whole new nonlinear simulation for the perturbed states, while Eq. (82) needs two nonlinear simulations in addition to the solution of the unperturbed state, given by Eq. (76).

OFD Based on Complex Variables

The use of complex variables to estimate approximations of the derivatives was originally introduced in the works of Lyness and Moler [38] and Lyness [39]. Starting from this theory, Squire and Trapp [40] show a procedure based on complex variables that has been largely used in many fields of engineering due to its accuracy, robustness and ease of implementation. Additionally, this procedure demands lower computation cost, although, the storage cost is somewhat higher for complex variables when compared with the real counterpart [41, 42].

Following the work of Lyness and Moler [38] apud Haveroth et al. [27], the first derivative of the displacement vector $\boldsymbol{u}_n$ with respect to $s_j \in \boldsymbol{s}$ can be calculated by

defining all the variables involved as complex entities, applying a small perturbation in the complex part of $\boldsymbol{s}_j$ and evaluating the effect in the complex part of $\boldsymbol{u}_n$. In order to show this, recall that when using real variables one expands $\boldsymbol{u}_n$ using Taylor series with origin at $\boldsymbol{s}$

$$\boldsymbol{u}_n(\boldsymbol{s} + \Delta\boldsymbol{s}_j) = \sum_{k=0}^{\infty} \frac{d\boldsymbol{u}_n{}^k(\boldsymbol{s})}{ds_j^k} \frac{\Delta s_j^k}{k!}, \tag{83}$$

where $\Delta\boldsymbol{s}_j$ is described by Eq. (79). Similarly, it is possible to adopt a perturbation in the imaginary part $i\Delta s_j$ instead of using a real perturbation Δs_j, as usual. In this case,

$$\boldsymbol{u}_n(\boldsymbol{s} + i\Delta\boldsymbol{s}_j) = \sum_{k=0}^{\infty} \frac{d\boldsymbol{u}_n{}^k(\boldsymbol{s})}{ds_j^k} \frac{(i\Delta s_j)^k}{k!}, \tag{84}$$

and using the fact that $i = \sqrt{-1}$, the imaginary part of Eq. (84) is given by

$$\text{Im}\left[\boldsymbol{u}_n(\boldsymbol{s} + i\Delta\boldsymbol{s}_j)\right] = \frac{d\boldsymbol{u}_n(\boldsymbol{s}_j)}{ds_j}\Delta s_j + \sum_{k=1}^{\infty} (-1)^k \frac{d\boldsymbol{u}_n{}^{2k+1}(\boldsymbol{s})}{ds_j^{2k+1}} \frac{\Delta s_j^{2k+1}}{(2k+1)!}. \tag{85}$$

Therefore, the first derivative can be expressed by

$$\frac{d\boldsymbol{u}_n(\boldsymbol{s})}{ds_j} = \frac{\text{Im}\left[\boldsymbol{u}_n(\boldsymbol{s} + i\Delta\boldsymbol{s}_j)\right]}{\Delta s_j} + \mathcal{O}, \tag{86}$$

where $\mathcal{O}$ stands for the high order terms. Assuming a relatively small value Δs_j the Eq. (86) is approximated as follows

$$\frac{d\boldsymbol{u}_n(\boldsymbol{s})}{ds_j} \approx \frac{\text{Im}\left[\boldsymbol{u}_n(\boldsymbol{s} + i\Delta\boldsymbol{s}_j)\right]}{\Delta s_j}, \tag{87}$$

which is known as the overall finite difference expression based on complex variables (CVOFD). This same procedure is used to evaluate the tangent modulus described in Sect. 2.6.

This expression does not involve subtraction between two values in the numerator, a fact that produces errors in traditional finite differences. In addition, it is noteworthy that this approach has accuracy of order two, while the conventional finite difference has accuracy of order one. In other words, the convergence of sensitivity analysis using the complex method has quadratic convergence with decreasing perturbation values [41], whereas in the real case this convergence is linear. These aspects make the complex method remarkable accurate and stable when small perturbations are applied.

3.1.2 Semianalytical Method

To evaluate the displacement sensitivity with respect to the design variable $s_j \in \boldsymbol{s}$, the residue equation is derived using the chain rule

$$\frac{\partial \boldsymbol{r}_n(\boldsymbol{u}_n, \boldsymbol{s})}{\partial s_j} = \frac{\partial \boldsymbol{r}_n(\boldsymbol{u}_n, \boldsymbol{s})}{\partial \boldsymbol{u}_n} \frac{d\boldsymbol{u}_n}{ds_j}, \tag{88}$$

and since the residue derivative with respect to the displacement is expressed by the tangent stiffness matrix, one gets

$$\frac{\partial \boldsymbol{r}_n(\boldsymbol{u}_n, \boldsymbol{s})}{\partial s_j} = -\boldsymbol{K}_{T,n} \frac{d\boldsymbol{u}_n}{ds_j}, \tag{89}$$

resulting in the expression of direct[7] analytical sensitivity

$$\begin{aligned} \frac{d\boldsymbol{u}_n}{ds_j} &= \boldsymbol{K}_{T,n}^{-1} \left[-\frac{\partial \boldsymbol{r}_n(\boldsymbol{u}_n, \boldsymbol{s})}{\partial s_j} \right] \\ &= \boldsymbol{K}_{T,n}^{-1} \left[\frac{\partial \boldsymbol{f}_n(\boldsymbol{u}_n, \boldsymbol{s})}{\partial s_j} - \mu_n \frac{d\boldsymbol{p}(\boldsymbol{s})}{ds_j} \right], \end{aligned} \tag{90}$$

where $\boldsymbol{p}$ and $\boldsymbol{f}$ are explicitly dependent of $\boldsymbol{s}$.

The SA method based on real variables is obtained by evaluating the analytical expression of Eq. (90) using the RVOFD approximation

$$\frac{d\boldsymbol{u}_n}{ds_j} \approx \boldsymbol{K}_{T,n}^{-1} \left[\frac{\Delta \boldsymbol{f}_n(\boldsymbol{u}_n, \boldsymbol{s})}{\Delta s_j} - \mu_n \frac{\Delta \boldsymbol{p}(\boldsymbol{s})}{\Delta s_j} \right]. \tag{91}$$

Similarly, the SA method based on complex variables is obtained evaluating the same expression, now using the CVOFD approximation

$$\frac{d\boldsymbol{u}_n}{ds_j} \approx \boldsymbol{K}_{T,n}^{-1} \left[\frac{\mathrm{Im}\left[\boldsymbol{f}_n(\boldsymbol{u}_n, \boldsymbol{s} + i\Delta \boldsymbol{s}_j)\right]}{\Delta s_j} - \mu_n \frac{\mathrm{Im}\left[\boldsymbol{p}(\boldsymbol{s} + i\Delta \boldsymbol{s}_j)\right]}{\Delta s_j} \right]. \tag{92}$$

The tangent stiffness matrix involved in these systems is the same matrix obtained for the equilibrium of the original (unperturbed problem), after convergence in the nth step. Thus, the exact linearization of the internal force vector is of paramount importance to avoid sensitivity errors, justifying the development presented in Sect. 2. Moreover, Eqs. (91) and (92) represent linear equation systems whose solutions are direct (do not require iterations).

[7] This work focuses on direct analytical sensitivity, since this option offers more advantages than the adjoint approach in path dependent problems even when the number of design variables is smaller than the number of constraints [43].

3.2 Sensitivity Analysis for Path Dependent Problems

Path dependent problems are those that require knowledge of the whole history of the deformed body up to the current configuration, in order to predict the configuration in the next step. If the structural analysis is path dependent, its respective sensitivity analysis also will be. The term path dependent, does not mean only the dependence of the current unperturbed values on the history of deformation, but also the dependence of sensitivity history, namely, the previous stress, displacement and internal variables sensitivities [43]. The sensitivity analysis methods directed for this nature of problems are more complex if compared to their path independent counterparts, because the internal force becomes a function of the current displacement and deformation history. Thus, the internal force differentiation with respect to the particular design parameter, should be performed consistently.

The OFD method used for this type of problem is obtained in analogy to path independent problems, thus will not be discussed in this section. A modification of the OFD method obtaining a significant improvement in computational efficiency is shown by Muñoz-Rojas [37].

3.2.1 Traditional Semianalytical Method

In path independent problems, the vector of internal variables χ is null and the stress σ can be easily evaluated. Conversely, when path dependent problems are considered, internal variables are not null and change according to the load applied. The history of these variables must be considered in the new strain evaluation.

In order to consider the internal variables history, one adopts a slight modification in the approach presented in Sect. 3.1, including an additional update step. Considering that the aim is to calculate the displacement sensitivity with respect to the design variable $s_j \in \boldsymbol{s}$, Eq. (76) is derived using the chain rule. After some manipulations, the direct analytical sensitivity expression is obtained

$$\frac{d\boldsymbol{u}_n}{ds_j} = \boldsymbol{K}_{T,n}^{-1} \left[\left. \frac{\partial \boldsymbol{f}_n(\boldsymbol{u}_n, \boldsymbol{s})}{\partial s_j} \right|_{\boldsymbol{u}} - \mu_n \frac{d\boldsymbol{p}(\boldsymbol{s})}{ds_j} \right] \tag{93}$$

whose solution provides the sensitivity in the current (nth) step. The internal force vector $\boldsymbol{f}_n$ must be described now as dependent on the internal variables vector χ_{n-1}, the stress σ_{n-1}, the displacement $\boldsymbol{u}_n$ and the design variables $\boldsymbol{s}$, as follows

$$\boldsymbol{f}_n = \boldsymbol{f}_n \left(\sigma_{n-1}(\boldsymbol{s}), \chi_{n-1}(\boldsymbol{s}), \boldsymbol{u}_n(\boldsymbol{s}), \boldsymbol{s} \right). \tag{94}$$

The major difficulty to solve Eq. (93) comes from the effective evaluation of the term $\left. \frac{\partial \boldsymbol{f}_n}{\partial s_j} \right|_{\boldsymbol{u}}$, where the notation $(.)|_{\boldsymbol{u}}$ means that the derivative is taken for a fixed value of $\boldsymbol{u}$. Conte et al. [44] refer to this term as conditional derivative. As its analytical

evaluation can be very cumbersome, the SA method represents a general and simple alternative. This method replaces the conditional derivative vector of the internal force by an expression based on finite differences

$$\left.\frac{\partial \boldsymbol{f}_n}{\partial s_j}\right|_{\boldsymbol{u}} \approx \frac{\Delta_s \boldsymbol{f}_n\big|_{\boldsymbol{u}}}{\Delta s_j}. \tag{95}$$

Without loss of generality, FFD method is used to obtain Eq. (95), that is

$$\begin{aligned}\Delta_s \boldsymbol{f}_n = &\boldsymbol{f}_n\left(\sigma_{n-1}(\boldsymbol{s}+\Delta \boldsymbol{s}_j), \chi_{n-1}(\boldsymbol{s}+\Delta \boldsymbol{s}_j), \boldsymbol{u}_n(\boldsymbol{s}+\Delta \boldsymbol{s}_j), \boldsymbol{s}+\Delta \boldsymbol{s}_j\right) + \\ &-\boldsymbol{f}_n\left(\sigma_{n-1}(\boldsymbol{s}), \chi_{n-1}(\boldsymbol{s}), \boldsymbol{u}_n(\boldsymbol{s}), \boldsymbol{s}\right)\end{aligned} \tag{96}$$

and keeping $\boldsymbol{u}$ fixed

$$\begin{aligned}\Delta_s \boldsymbol{f}_n\big|_{\boldsymbol{u}} = &\boldsymbol{f}_n\left(\sigma_{n-1}(\boldsymbol{s}+\Delta \boldsymbol{s}_j), \chi_{n-1}(\boldsymbol{s}+\Delta \boldsymbol{s}_j), \boldsymbol{u}_n(\boldsymbol{s}), \boldsymbol{s}+\Delta \boldsymbol{s}_j\right) + \\ &-\boldsymbol{f}_n\left(\sigma_{n-1}(\boldsymbol{s}), \chi_{n-1}(\boldsymbol{s}), \boldsymbol{u}_n(\boldsymbol{s}), \boldsymbol{s}\right),\end{aligned} \tag{97}$$

where $\sigma_{n-1}(\boldsymbol{s}+\Delta \boldsymbol{s}_j)$ and $\chi_{n-1}(\boldsymbol{s}+\Delta \boldsymbol{s}_j)$ are linearly approximated by

$$\sigma_{n-1}(\boldsymbol{s}+\Delta \boldsymbol{s}_j) \approx \sigma_{n-1}(\boldsymbol{s}) + \frac{d\sigma_{n-1}(\boldsymbol{s})}{ds_j}\Delta \boldsymbol{s}_j, \tag{98}$$

$$\chi_{n-1}(\boldsymbol{s}+\Delta \boldsymbol{s}_j) \approx \chi_{n-1}(\boldsymbol{s}) + \frac{d\chi_{n-1}(\boldsymbol{s})}{ds_j}\Delta \boldsymbol{s}_j. \tag{99}$$

The unconditional derivatives in Eqs. (98) and (99) are obtained from an additional step. This step is performed after obtaining unconditional sensitivity in the nth load step using Eq. (93). The displacement of the perturbed problem at the nth step can be approximated by

$$\boldsymbol{u}_n(\boldsymbol{s}+\Delta \boldsymbol{s}_j) \approx \boldsymbol{u}_n(\boldsymbol{s}) + \frac{d\boldsymbol{u}_n}{ds_j}\Delta \boldsymbol{s}_j \tag{100}$$

(notice that although the approximations in Eqs. (98–100) are linear, for diminutive perturbations they will be nearly exact). From this approximation, the internal variables $\sigma_n(\boldsymbol{s}+\Delta \boldsymbol{s}_j)$ and $\chi_n(\boldsymbol{s}+\Delta \boldsymbol{s}_j)$ are calculated, because they are necessary to evaluate the sensitivity in the next step.

This procedure is represented geometrically in Fig. 6. For illustrative purposes, assume that the external force vector does not have dependence on the design variable. The superscript $(.)^p$ is adopted to indicate that the variable (.) is evaluated in the perturbed structure, while the omission of such symbol, (.) means evaluation in the original structure.

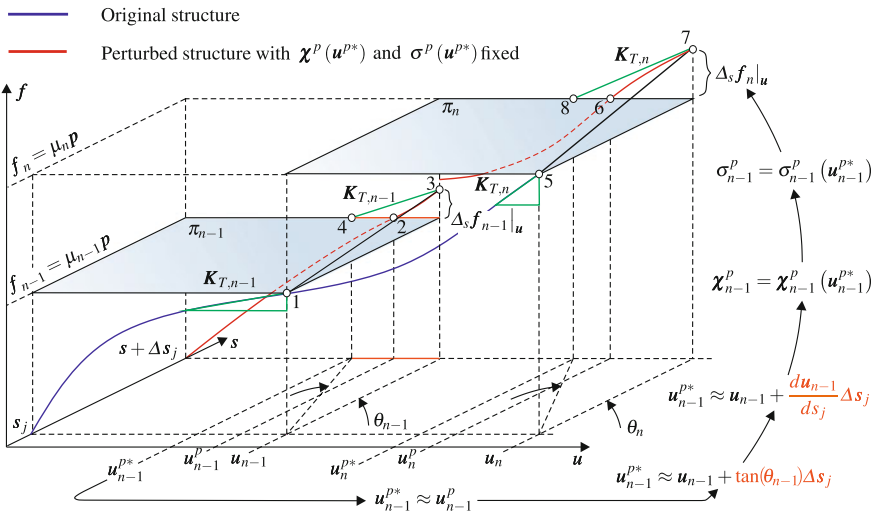

Fig. 6 Structural response with respect to the original and perturbed design parameter. Internal variables update procedure

The equilibrium states of increments $n-1$ and n are represented by the planes π_{n-1} and π_n, respectively. In these states, the structural responses such as displacement, stress and internal force are dependent on the design variables. Applying an external force equivalent to $\mu_{n-1}\boldsymbol{p}$, one can see that the equilibrium state of the original structure is expressed by point 1. This point is obtained from the convergence of the iterative procedure. Therefore, both tangent stiffness matrix $\boldsymbol{K}_{T,n-1}$ and displacement $\boldsymbol{u}_{n-1}$ are known. The objective is to determine equilibrium of the perturbed structure, which is achieved at point 2. As the displacement of the perturbed structure is fixed, the structural response leads to point 3, causing an unbalanced force $\Delta_s \boldsymbol{f}_{n-1}|_{\boldsymbol{u}}$, expressed by Eq. (97). From point 3, the tangent stiffness matrix $\boldsymbol{K}_{T,n-1}$ is used to estimate the $\boldsymbol{u}^p_{n-1}$ value, given by $\boldsymbol{u}^{p*}_{n-1}$, which is located at point 4 rather than point 2. This approach is responsible for an additional source of error due its nature based in approximations, in addition to those already provided in Sect. 3.1. However, if a tiny perturbation can be numerically applied, this source of error will be negligible.

In fact, it is possible to see graphically that this approximation is consistent when the perturbation and increments are small, since the displacement sensitivity is obtained by the tangent of θ_{n-1}. The evaluation of the displacement approximation $\boldsymbol{u}^p_{n-1}$ is of great importance, because from it, the internal variables of the respective step are updated, i.e., (σ^p_{n-1} and χ^p_{n-1}) using Eqs. (98) and (99). This update becomes necessary to evaluate the unbalanced force $\Delta_s \boldsymbol{f}_n|_{\boldsymbol{u}}$ of the next step. The procedure is repeated for each new step.

3.2.2 Complex Variable Semianalytical Method

The CVSA method applied to path dependent problems is obtained replacing the complex derivative approximation Eq. (87) in the analytical expression Eq. (93), that is

$$\frac{d\boldsymbol{u}_n}{ds_j} \approx \boldsymbol{K}_{T,n}^{-1} \left[\frac{\text{Im}\left[\boldsymbol{f}_n(\boldsymbol{s}+i\Delta\boldsymbol{s}_j)\Big|_{\boldsymbol{u}}\right]}{\Delta s_j} - \mu_n \frac{\text{Im}\left[\boldsymbol{p}(\boldsymbol{s}+i\Delta\boldsymbol{s}_j)\right]}{\Delta s_j} \right], \tag{101}$$

where

$$\boldsymbol{f}_n(\boldsymbol{s}+i\Delta\boldsymbol{s}_j)\Big|_{\boldsymbol{u}} = \boldsymbol{f}_n(\sigma_{n-1}(\boldsymbol{s}+i\Delta\boldsymbol{s}_j), \chi_{n-1}(\boldsymbol{s}+i\Delta\boldsymbol{s}_j), \boldsymbol{u}_n(\boldsymbol{s}), \boldsymbol{s}+i\Delta\boldsymbol{s}_j), \tag{102}$$

followed by the same procedure previously presented in Sect. 3.2.1.

The numerical implementation of the semianalytical procedure particularized for complex variables is shown in Fig. 7. To obtain the RVSA procedure, the highlighted blocks must be changed by real finite differences and real perturbations. The semianalytical procedure for path independent problems can be considered a particularization of the path dependent one. Thus, the same flowchart illustrates the procedure for both problems.

This method is very promising because it combines the efficiency and accuracy of the analytical method with the positive considerations related to the CVOFD

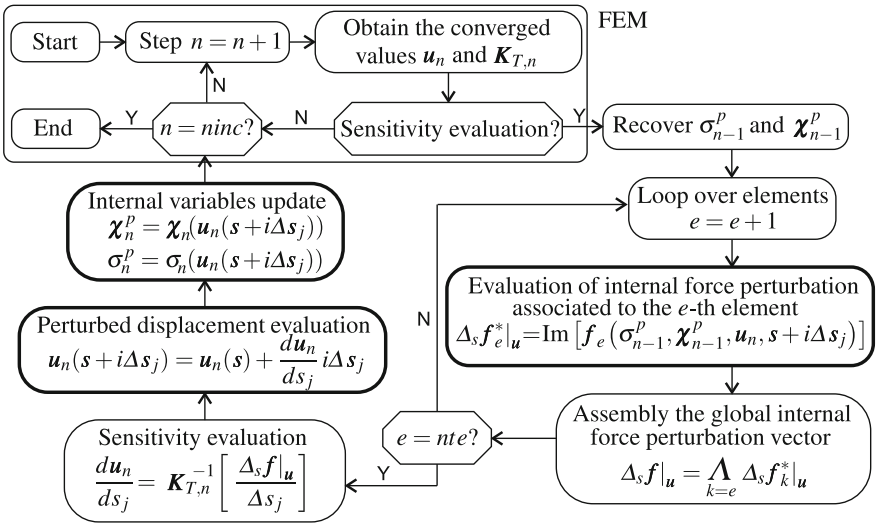

Fig. 7 Displacement sensitivity evaluation via the SA method to path dependent problems. Scheme particularized to CVSA method

method, presented in Sect. 3.1.1. Additionally, the computational and storage cost are drastically reduced when compared to the CVOFD method, because the complex operations are performed at the element level (as seen in Fig. 7). However, it is necessary to allocate a global complex vector for each internal variable in order to save its history.

4 Periodic Truss Material

Periodic truss materials (PTMs) belong to the family of ultralight cellular materials formed by unit cells made of bars, which are spatially distributed in a periodic pattern. These materials have attractive thermophysical and mechanical properties, such as high stiffness/weight ratio and high strain energy absorption capability, properties that can be taylored by modifying the architecture of the unit cell. Due to their periodicity, the PTMs exhibit low dispersion in their physical properties, a fact that can be a great advantage over traditional cellular materials like foams, which feature large dispersion in nominal values of their properties due to a heterogeneous porosity distribution [45–47].

4.1 Sensitivity Analysis of Periodic Truss Materials

In this section, we evaluate the nonlinear behavior of PTMs for which homogenized properties were designed considering that *linear* conditions would apply [45]. The sensitivity of these homogenized properties is evaluated along the nonlinear incremental steps using and comparing the methods previously presented. In this framework, we adopt a 2D PTM designed to maximize the bulk modulus in the linear range keeping mechanical isotropy [45]. To conduct this study, we evaluate the bulk modulus sensitivity with respect to the relative density ρ^* for different types of nonlinearities. Aiming at a fair comparison among the SA procedures studied, all of them are implemented within the same truss finite element code with exactly the same algorithmic operations, such as solvers, time discretization approach, return mapping scheme and so forth.

The linearly optimized unit cell adopted to perform this study is illustrated in Fig. 8a. This material has the following parameters[8]: $E = 210\,\text{GPa}$, $H_{iso} = 150\,\text{GPa}$, $\sigma_y = 1.5\,\text{GPa}$, $S = 1.0$, $r = 80\,\text{MPa}$. The cell is square with both sides length equal to 100 mm.[9] Other information such as cross-sectional areas and coordinates are given in Table 1. Figure 8b shows the periodic material generated from the unit cell,

[8]The material parameters adopted do not necessarily correspond to a real material, being chosen for purely academic purposes.

[9]The dimensions given to the cell are irrelevant provided the relative density is kept unchanged. This is because the cell size must tend to zero when compared to the macroscopic scale [48].

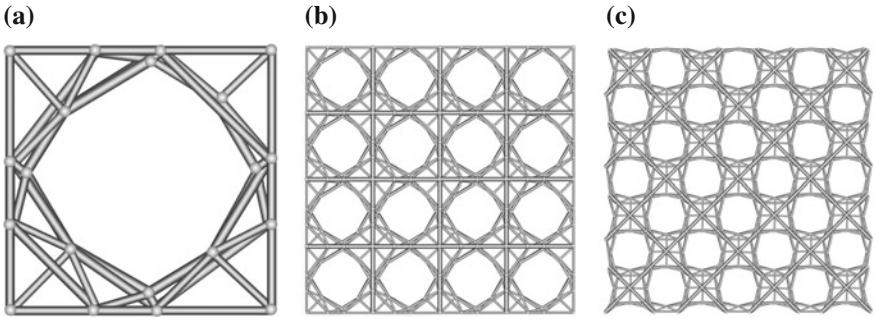

Fig. 8 **a** Basic cell composed of bar elements. **b** Periodic material generated translating the basic cells. **c** Periodic material rotated in 45° evincing symmetry

whereas in Fig. 8c this same material is rotated 45° to evince that the material has geometric symmetry. The periodically repeating process leads to an overlapping of the cell's borders. Hence, in Fig. 8b, c, the area of the bars common to 2 adjacent cells must be summed up.

Consider a membrane Π composed by 10×10 unit cells (an extension of the arrangement illustrated in Fig. 8b) and the subregion Γ formed by 4×4 unit cells located in the center of Π. The loading P and boundary conditions are shown in Fig. 9. In order to minimize the problems associated with the boundary (border distortion effect), the displacement and strains measures are evaluated by their average on the boundary of Γ ($\partial\Gamma$). This choice aims to reduce oscillations that occur when the evaluation is performed pointwise on the boundary of Π ($\partial\Pi$). From this point on, the bar upperscript is used to indicate that the variable is evaluated by average of contributions along the boundary.

The bulk modulus K is a parameter given by the ratio of hydrostatic compressive stress σ_H and volumetric strain ε_V.[10] In the bidimensional case, such measures are respectively defined by

$$\sigma_H = \frac{\sigma_x + \sigma_y}{2} \quad \text{and} \quad \varepsilon_V = \varepsilon_x + \varepsilon_y. \tag{103-104}$$

Particularizing to this problem, one obtains

$$K = \frac{\sigma_H}{\varepsilon_V} = \frac{\sigma_x + \sigma_y}{2\varepsilon_V} = \frac{\sigma_y}{2\varepsilon_V} = \frac{P}{2L\varepsilon_V} = \frac{P}{2\varepsilon_V}, \tag{105}$$

where P is the loading along the unit length L of Π. Note that $\sigma_x = 0$, because there is only axial stress in the bar. In a linear analysis when considering information on $\partial\Gamma$ one obtains $K = 89.9$ MPa corresponding to -2.19 % of error when compared to

[10] In linear analysis the bulk modulus is constant, which does not occur when considering nonlinear behavior [49].

Table 1 Cross-sectional areas, connectivities and node coordinates of the unit cell

Node	Coord. x [mm]	Coord. y [mm]	Node	Coord. x [mm]	Coord. y [mm]
1	0.0	0.0	11	53.3311	97.6912
2	32.3640	0.0	12	97.4020	53.2407
3	0.0	32.3341	13	100.0	0.0
4	21.9762	22.0174	14	0.0	100.0
5	0.0	55.8038	15	100.0	32.3341
6	55.5658	0.0	16	32.3640	100.0
7	52.0023	4.4080	17	79.7751	79.7404
8	4.3940	52.2151	18	100.0	55.8038
9	77.7629	20.1496	19	55.5658	100.0
10	19.9704	77.8184	20	100.0	100.0

Element	Area [mm^2]	Connectivity		Element	Area [mm^2]	Connectivity	
1	9.669613	1	2	29	9.272591	8	5
2	7.722314	2	4	30	8.175303	10	16
3	7.851381	4	3	31	9.669613	16	14
4	9.691293	3	1	32	9.132902	14	5
5	7.652776	1	4	33	10.971773	5	16
6	11.463591	2	3	34	8.329162	10	14
7	10.730236	2	6	35	10.673757	15	18
8	7.723244	6	7	36	8.598719	18	12
9	15.681691	7	4	37	14.323816	12	9
10	9.443370	2	7	38	12.153701	9	18
11	12.153224	6	4	39	10.634020	15	12
12	8.664491	6	9	40	8.876196	18	17
13	14.114726	9	7	41	12.295989	17	12
14	11.518608	6	9	42	9.367847	12	18
15	9.313528	6	7	43	12.041171	18	17
16	9.144346	6	13	44	9.132902	18	20
17	9.691293	13	15	45	9.144346	20	19
18	8.102212	15	9	46	8.840667	19	17
19	10.943938	6	15	47	8.322829	17	20
20	8.304048	13	9	48	10.021312	18	19
21	15.679358	4	8	49	14.203331	10	11
22	7.708146	8	5	50	8.735145	11	19
23	10.673757	5	3	51	10.730236	19	16
24	9.481101	3	8	52	12.132112	10	19
25	12.061977	4	5	53	10.647780	11	16
26	14.104930	8	10	54	12.305260	11	17
27	8.674716	10	5	55	9.439316	11	19
28	11.557651	5	10	56	12.026649	17	19

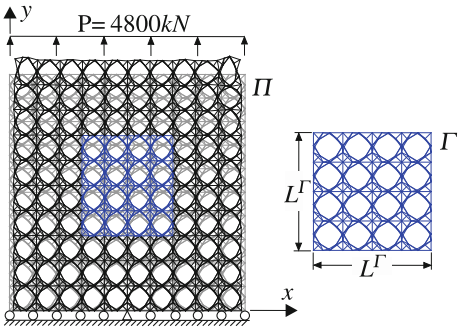

Fig. 9 Periodic material Π composed by 10×10 unit cells. The detail shows the region Γ

the referential homogenized value of 91.8 MPa, taken from the work of Guth [45]. On the other hand, this error becomes $-7.12\,\%$ when evaluated in $\partial\Pi$. This justifies the fact of obtaining the measures in $\partial\Gamma$.

4.2 Bulk Modulus Sensitivity Expression

The relative density ρ^* is defined as the ratio between the volume of the unit cell occupied by the rods V_b and the total volume of the unit cell V, that is

$$\rho^* = \frac{V_b}{V}, \tag{106}$$

where adopting $\rho^* = 49\,\%$, in accordance with Table 1, from the work of Guth [45], one obtains the values

$$V_b = 1.7485281 \times 10^{-5}\mathrm{m}^3 \quad \text{and} \quad V = 3.5684248 \times 10^{-5}\mathrm{m}^3. \tag{107}$$

The bulk modulus variation with respect to the relative density is given by

$$\frac{dK}{d\rho^*} = \frac{dK}{dV_b}\frac{dV_b}{d\rho^*}, \tag{108}$$

where, from Eq. (106),

$$\frac{dV_b}{d\rho^*} = \frac{dV}{d\rho^*}\rho^* + \frac{d\rho^*}{d\rho^*}V = V \quad \text{and} \quad \frac{dK}{dV_b} = \frac{dK}{d\bar{u}_x}\frac{d\bar{u}_x}{dV_b} + \frac{dK}{d\bar{u}_y}\frac{d\bar{u}_y}{dV_b}. \tag{109-110}$$

Since K is given by Eq. (105) and $\bar{\varepsilon}_V$ is evaluated by the average of contributions along $\partial\Gamma$ with $L^\Gamma = 0.4m$, one gets

$$\bar{\varepsilon}_V = \bar{\varepsilon}_x + \bar{\varepsilon}_y = \frac{\bar{u}_x}{L^I} + \frac{\bar{u}_y}{L^I} = 2.5\left(\bar{u}_x + \bar{u}_y\right), \tag{111}$$

and

$$\frac{dK}{dV_b} = \frac{-P}{5(\bar{u}_x + \bar{u}_y)^2}\left[\frac{d\bar{u}_x}{dV_b} + \frac{d\bar{u}_y}{dV_b}\right], \tag{112}$$

where $d\bar{u}_x/dV_b$ and $d\bar{u}_y/dV_b$ are obtained using the methods previously presented in Sect. 3. Finally, the sensitivity of the bulk modulus with respect to the relative density is given by

$$\frac{dK}{d\rho^*} = \frac{-PV}{5(\bar{u}_x + \bar{u}_y)^2}\left[\frac{d\bar{u}_x}{dV_b} + \frac{d\bar{u}_y}{dV_b}\right]. \tag{113}$$

4.3 Numerical Evaluation of the Bulk Modulus Sensitivity

For a given perturbation factor φ, the volume of the unit cell occupied by the bars V_b is updated by

$$\Delta V_b = \varphi V_b = \varphi \sum_{e=1}^{nelem} A_e L_e = \sum_{e=1}^{nelem} \left(\varphi A_e\right) L_e \tag{114}$$

where *nelem* is the total number of bar elements, and A_e and L_e are the area of the cross-section and length of the eth element.[11] For this analysis, φ varies in the interval $[10^{-300}, 10^{-1}]$.

The global measures adopted for the sensitivity and error are defined based on the ℓ_1 norm as

$$\bar{S} = \sum_{i=1}^{ninc} \left|\frac{dK}{d\rho^*}\right|_i \quad \text{and} \quad \bar{E}_{Rel} = 100 \times \frac{\bar{S} - S_{Ref}}{S_{Ref}}. \tag{115-116}$$

The reference value S_{Ref} is obtained via CVSA method using $\varphi = 10^{-300}$ whose values are presented in Table 2 for the various types of analyses considered in this work. The application of this sum along the incremental steps aims to consider the history of the sensitivity as the load application evolves. Recall that for recovering the linear formulation it suffices to apply a single load increment (step). In the case of nonlinear

[11] Note that the formulation of bar elements presented in Sect. 2 keeps the area of the cross-sections unchanged, which does not occur strictly. In fact, the effect of the change of the cross-sections along the deformation of the bars can be very important. An extension to account for this effect can be found in the work of Crisfield [50].

Table 2 Reference values for the 2D periodic truss material

Analysis	Reference value S_{Ref}
Linear	1832272.5310834
Geometric Nonlinearity	91866961.0561386
Elastoplasticity	79334910.8080563
Elastoplasticity and Geometric Nonlinearity	82082439.7992495
Elastoplasticity with Damage and Geometric Nonlinearity	83049902.3622271

Values obtained using the CVSA method and a perturbation factor $\varphi = 10^{-300}$

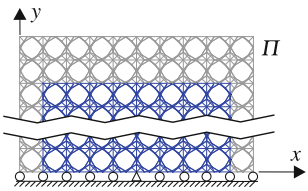

Fig. 10 The damage is considered only in the highlighted region in order to avoid boundary problems (border effect), which results in undesired localized critical damage near the edges

analyses, 50 incremental steps are considered. In this example, only the highlighted bars in Fig. 10 are subject to damage.

Figure 11a depicts the evolution of the bulk modulus along the 50 incremental steps. Figure 11b shows the incremental bulk modulus sensitivity behavior with respect to the relative density for: the linear range, geometric nonlinearity, elastoplasticity, elastoplasticity with geometric nonlinearity, and elastoplasticity coupled to damage and geometric nonlinearity. The sensitivity presented corresponds to Eq. (113) and is obtained using the CVSA method and a perturbation factor $\varphi = 10^{-300}$. It is noted that considering the linear formulation, the sensitivity is constant, as expected. Considering the nonlinear geometric formulation, it is possible to note a small increase of the sensitivity along the increments, which is due to the change of geometry of the periodic bars. The addition of elastoplasticity with or without damage, yields large variations over the increments. The behavior of sensitivity which occurs between steps 6 and 15 in the 10×10 cells arrangement is due to the sequence in which the bars yield.

A summary of the accuracy range of the sensitivity methods, considering the various types of analyses is presented in Fig. 12. In general, all the cases analyzed show that the accuracy range of the SA methods is superior to OFD methods. This is specially true for the CVSA method which resulted in accurate values for all perturbation factors in the domain, that is, for $\varphi \in [10^{-300}, 10^{-1}]$. In this case, for $\varphi \in [10^{-30}, 10^{-1}]$ the error did not surpass $10^{-11}\%$ in the analyses that did not include damage, and $10^{-6}\%$ when damage was considered.

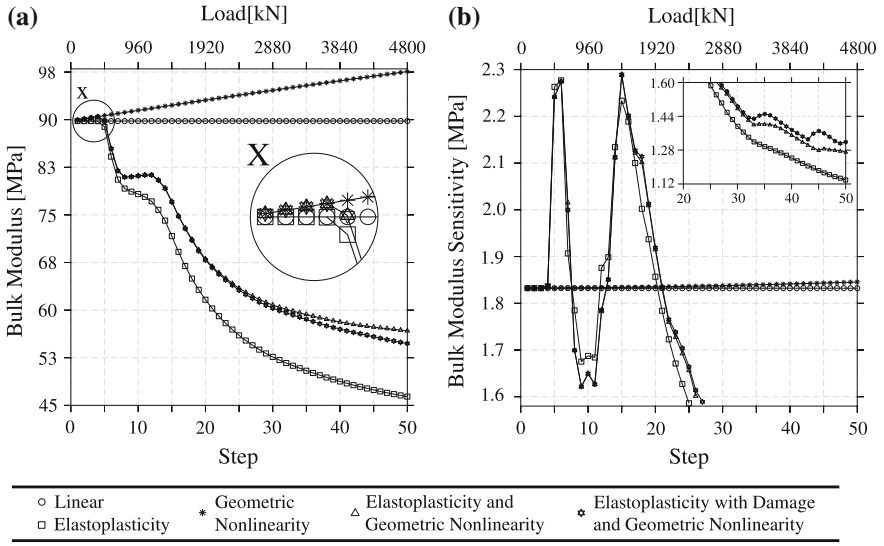

Fig. 11 **a** Bulk modulus over the load increments considering various types of analyses. The detail shows the behavior in the initial incremental steps. **b** Bulk modulus sensitivity with respect to the relative density versus load increments. Reference values obtained via CVSA method considering $\varphi = 10^{-300}$. The detail describes the behavior in the final incremental steps

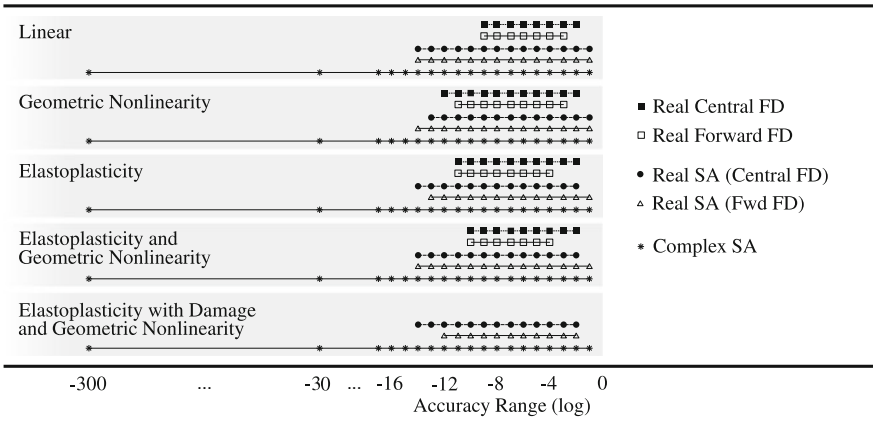

Fig. 12 Accuracy ranges of the SA and OFD methods for different types of analyses

5 Conclusion

A detailed procedure for updating internal variables when using the SA method to perform sensitivity analyses in path dependent problems has been presented. It has been shown that, in this procedure, the use of the CVSA method is an excellent

alternative, since tiny perturbations can be applied and nearly exact sensitivity results obtained.

In fact, the CVSA method shows small errors from moderate perturbation factors to values as low as $\varphi = 10^{-300}$. Although limited to a narrower perturbation range and higher errors, the same behavior was also identified for the RVSA methods.

With respect to computational aspects, a considerable gain in time and storage is verified for the semianalytical methods when compared to global counterparts, because these procedures do not require solving a new global system of equations for each design variable. On the other hand, it is important to remark that in the CVSA method it is necessary to define complex global vectors to store the history of the internal variables. However, the operations involving complex variables are restricted to the element level at the Gauss points.

Due to all the aforementioned advantages, the CVSA procedure is prone to be employed as a black box in simulation softwares. Nonetheless, additional studies using continuum finite elements are recommended.

Acknowledgments The authors wish to express their gratitude to CNPq and CAPES (Brazilian research supporting agencies), and to UDESC for the concession of Master's scholarships associated to this work.

References

1. Barthelemy, B., Haftka, R.T.: Accuracy analysis of the semi-analytical method for shape sensitivity calculation. Mech. Struct. Mach. **18**, 407–432 (1990)
2. Vidal, C.A., Haber, R.B.: Design sensitivity analysis for rate-independent elastoplasticity. Comput. Method Appl. Mech. **107**, 393–431 (1993)
3. Bletzinger, K.U., Firl, M., Daoud, F.: Approximation of derivatives in semi-analytical structural optimization. Comput. Struct. **86**, 1404–1416 (2008)
4. Habibi, A., Moharrami, H.: Nonlinear sensitivity analysis of reinforced concrete frames. Finite Elem. Anal. Des. **46**, 571–584 (2010)
5. Jin, W., Dennis, B.H., Wang, B.P.: Improved sensitivity analysis using a complex variable semi-analytical method. Struct. Multidiscip. Optim. **41**, 433–439 (2010)
6. Barthelemy, B., Chon, C.T., Haftka, R.T.: Accuracy problems associated with semi-analytical derivatives of static response. Finite Elem. Anal. Des. **4**, 249–265 (1988)
7. Cheng, G., Gu, Y., Zhou, Y.: Accuracy of semi-analytic sensitivity analysis. Finite Elem. Anal. Des. **6**, 113–128 (1989)
8. Olhoff, N., Rasmussen, J., Lund, E.: A method of "exact" numerical differentiation for error elimination in finite element based semi-analytical shape sensitivity analysis. Mech. Struct. Mach. **21**, 1–66 (1993)
9. Jin, W., Dennis, B.H., Wang, B.P.: Improved sensitivity and reability analysis of nonlinear Euler-Bernoulli beam using a complex variable semi-analytical method. In: ASME Proceedings (2009). doi:10.1115/DETC2009-87593
10. Cheng, G., Olhoff, N.: New method of error analysis and detection in semi-analytical sensitivity analysis. Report No. 36, Institute of Mechanical Engineering, Aalborg University, Denmark, 34pp (1991)
11. Cheng, G., Gu, Y., Wang, X.: Improvement of semi-analytic sensitivity analysis and MCADS. In: Eschenauer, H.A., Mattheck, C., Olhoff, N. (eds.) Engineering Optimization in Design Processes, vol. 63, pp. 211–223. Springer, Berlin (1991)

12. Mlejnek, H.P.: Accuracy of semi-analytical sensitivities and its improvement by the "natural method". Struct. Optim. **4**, 128–131 (1992)
13. Parente, E., Vaz, L.E.: Improvement of semi-analytical design sensitivities of non-linear structures using equilibrium relations. Int. J. Numer. Methods Eng. **50**, 2127–2142 (2001)
14. Tsay, J.J., Cardoso, J.E.B., Arora, J.S.: Nonlinear structural design sensitivity analysis for path dependent problems. Part 1: General theory. Comput. Method Appl. Mech. **81**, 183–208 (1990)
15. Tsay, J.J., Cardoso, J.E.B., Arora, J.S.: Nonlinear structural design sensitivity analysis for path dependent problems. Part 2: Analytical examples. Comput. Method Appl. Mech. **81**, 209–228 (1990)
16. Chen, X.: Nonlinear finite element sensitivity analysis for large deformation elastoplastic and contact problems, Ph.D. thesis, University of Tokyo, Japan (1994)
17. Ohsaki, M., Arora, J.S.: Design sensitivity analysis of elastoplastic structures. Int. J. Numer. Methods Eng. **37**, 737–762 (1994)
18. Lee, T.H., Arora, J.S.: A computational method for design sensitivty analysis of elastoplastic structures. Comput. Methods Appl. Mech. Eng. **122**, 27–50 (1995)
19. Vidal, C.A., Lee, H.S., Haber, R.B.: The consistent tangent operator for design sensitivity analysis of history-dependent response. Comput. Syst. Eng. **2**, 509–523 (1991)
20. Kleiber, M., Hien, T.D., Postek, E.: Incremental finite element sensitivity analysis for nonlinear mechanics applications. Int. J. Numer. Methods Eng. **37**, 3291–3308 (1994)
21. Kleiber, M., Kowalczyk, P.: Constitutive parameter sensitivity in elasto-plasticity. Comput. Mech. **137**, 36–48 (1995)
22. Kleiber, M., Kowalczyk, P.: Sensitivity analysis in plane stress elasto-plasticity and elasto-viscoplasticity. Comput. Methods Appl. Mech. Eng. **137**, 395–409 (1996)
23. Bugeda, G., Gil, L.: Shape sensitivity analysis for structural problems with non-linear material behaviour. Int. J. Numer. Methods Eng. **46**, 1385–1404 (1999)
24. Wisniewski, K., Kowalczyk, P., Turska, E.: On the computation of design derivatives for Huber-Mises plasticity with non-linear hardening. Int. J. Numer. Methods Eng. **57**, 271–300 (2003)
25. Conte, J.P., Barbato, M., Spacone, E.: Finite element response sensitivity analysis using force-based frame models. Int. J. Numer. Methods Eng. **59**, 1781–1820 (2004)
26. Chen, X., Nakamura, K., Mori, M., et al.: Sensitivity analysis for thermal stress and creep problems. JSME Int. J. **43**, 252–258 (2000)
27. Haveroth, G., Stahlschmidt, J., Muñoz-Rojas, P.A.: Application of the complex variable semi-analytical method for improved sensitivity evaluation in geometrically nonlinear truss problems. Lat. Am. J. Solids Struct. **12**, 980–1005 (2015)
28. Haveroth, G.: Complex semianalytical sensitivity analysis applied to trusses with geometric nonlinearity and coupled elastoplastic behavior, Master thesis (in portuguese), Santa Catarina State University, Brazil (2015)
29. Hughes, T.J.R., Hinton, E.: Finite Element Methods for Plate and Shell Structures: Formulation and Algorithms, vol. 2. Pineridge Press International (1986)
30. Stahlschimidt, J.: Sensitivity analysis for nonlinear problems via complex variables semi-analytical Method: Shape and material parameter application, Master thesis (in portuguese). Santa Catarina State University, Brazil (2013)
31. Lemaitre, J., Desmorat, R.: Engineering Damage Mechanics: Ductile, Creep, Fatigue and Brittle Failures. Springer, Berlin (2005)
32. Lemaitre, J., Chaboche, J.L.: Mechanics of Solid Materials. Cambridge University Press (1990)
33. Simo, J.C., Hughes, T.J.R.: Computational Inelasticity. Springer, New York (1998)
34. Esmaeili, M., Öchsner, A.: A one-dimensional implementation of a coupled elasto-plastic model for ductile damage. Mat. -wiss. u. Werkstofftech **42**, 444–451 (2011)
35. Tanaka, M., Fujikawa, M., Balzani, D., Schröder, J.: Robust numerical calculation of tangent module at finite strains based on complex-step derivative approximation and its application to localization analysis. Comput. Methods Appl. Mech. Eng. **269**, 454–470 (2014)
36. Tortorelli, D.A., Michaleris, P.: Design sensitivity analysis: overview and review. Inverse Probl. Eng. **1**, 71–105 (1994)

37. Muñoz-Rojas, P.A., Fonseca, J.S.O., Creus, G.J.: A modified finite difference sensitivity analysis method allowing remeshing in large strain path-dependent problems. Int. J. Numer. Methods Eng. **61**, 1049–1071 (2004)
38. Lyness, J.N., Moler, C.B.: Numerical differentiation of analytic functions. SIAM J. Numer. Anal. **4**, 202–210 (1967)
39. Lyness, J.N.: Numerical algorithms based on the theory of complex variable. In: ACM Proceedings (1967). doi:10.1145/800196.805983
40. Squire, W., Trapp, G.: Using complex variables to estimate derivatives of real functions. SIAM J. Numer. Anal. **1**, 110–112 (1998)
41. Martins, J., Sturdza, P., Alonso, J.J.: The complex-step derivative approximation. ACM Trans. Math. Softw. **29**, 245–262 (2003)
42. Montoya, A., Fielder, R., Gomez-Farias, A., Millwater, H.: Finite-element sensitivity for plasticity using complex variable methods. J. Eng. Mech. **141**, 04014118 (2015)
43. Kleiber, M., Hien, T.D., Antúnez, H., et al.: Parameter Sensitivity in Nonlinear Mechanics: Theory and Finite Element Computations. Wiley, New York (1997)
44. Conte, J., Vijalapura, P., Meghella, M.: Consistent finite-element response sensitivity analysis. J. Eng. Mech. **129**, 1380–1393 (2003)
45. Guth, D.C.: Optimization of lattice cells materials aiming at thermomechanical applications including isotropy constraints, Master thesis (in portuguese), Santa Catarina State University, Brazil (2012)
46. Guth, D.C., Luersen, M.A., Muñoz-Rojas, P.A.: Optimization of three-dimensional truss-like periodic materials considering isotropy constraints. Multidiscip. Optim. Struct. (2015). doi:10.1007/s00158-015-1282-4
47. Guth, D.C., Luersen, M.A., Muñoz-Rojas, P.A.: Optimization of periodic truss materials including constitutive symmetry constraints. Mat. wiss. u.Werkstofftech. **43**, 447–456 (2012)
48. Hassani, B., Hinton, E.: A review of homogenization and topology optimization I-homogenization theory for media with periodic structure. Comput. Struct. **69**, 707–717 (1998)
49. Penn, R.W.: Volume changes accompanying the extension of rubber. Trans. Soc. Rheol. **14**, 509–517 (1970)
50. Crisfield, M.A.: Non-linear Finite Element Analysis of Solids and Structures. Wiley, New York (1991)

Laser Beam Drilling of Cellular Metals: Numerical Simulation

Manuel Araújo, Markus Merkel and Andreas Öchsner

Abstract Laser drilling is a highly efficient technique to generate holes in almost any material. It offers an alternative manufacturing method to mechanical drilling and water stream cutting. The relatively small amount of heat involved in the process results in a small heat affected zone. This characteristic makes laser processing interesting for several engineering application. Within this chapter the drilling process is applied to cellular materials. A program code was developed and implemented in order to predict the relation between the initial parameters and the final characteristics of the drilling process, such as depth-time behavior for each amount of initial energy. The simulation of the laser drilling process uses the concept of homogenized cellular materials. It is studied the influence of the heat intensity of the laser in the process. Also the influence of material parameters like thermal conductivity, specific heat and enthalpy are studied. The results of the simulations of the drilling process closely match to the experimental results. The thermal conductivity is of paramount importance for the final results of the laser drilling procedures. The program code can be used for example to the optimization of the laser drilling procedures and to determine or confirm the material properties of the materials as well.

Keywords Laser beam drilling · Cellular metals · Finite element method · Temperature analysis

M. Araújo (✉)
Minho University, Campus de Azurém, 4800-058 Guimarães, Portugal
e-mail: m.araujo@dem.uminho.pt

M. Merkel
Aalen University, Beethovenstrasse 1, 73430 Aalen, Germany
e-mail: Markus.Merkel@hs-aalen.de

A. Öchsner
Griffith School of Engineering, Griffith University (Gold Coast Campus), Southport, QLD 4214, Australia
e-mail: andreas.oechsner@gmail.com

P.A. Muñoz-Rojas (ed.), *Computational Modeling, Optimization and Manufacturing Simulation of Advanced Engineering Materials*, Advanced Structured Materials 49, DOI 10.1007/978-3-319-04265-7_10

1 Introduction

Cellular materials cover a large range of different arrangements and forms of cell structures. Metal cellular structures are commonly studied and used in the engineering area because light constructions have more and more importance. Metal cellular structures can be divided in two different types: periodic cellular lattice structures and stochastic porous structures. Honeycomb structures and metallic hollow sphere structures (MHSS) are examples of the different metal cellular structures, respectively. The MHSS represent a relatively new group of cellular metals [1, 2] and they combine the well-known advantages of the cellular metals without major scattering of their material parameters as it is observed at foams. Some of these advantages are good properties for energy adsorption [3, 4], damping behavior [5], specific stiffness [6], sound adsorption [7, 8] and heat insulation [9–11]. These properties provide a wide field of potential multi-functional applications, e.g. in automotive, aviation or space-industry [12], high-speed trains [13] and ships [14].

The application of cellular metals as design parts in any engineering area requires joining as well as separation techniques to process bulk material with a defined geometry. Mechanical processes like milling, drilling, etc. cause burrs and a low life time of the tools. The laser prevents the material from the burrs. Other separation techniques like water stream cutting cannot be applied because of the defocus of the beam [15] and because of the corrosion process involved as well.

Generally, laser beam drilling is a highly efficient technique to generate holes in engineering materials [16]. During the process, the relatively small amount of heat affects only a small zone. This is the reason why the laser beam drilling is an interesting process for composite materials. The process itself has been analyzed in many references for bulk material by experiments [17, 18] and numerical simulation [19, 20].

In order to optimize the laser process, we are going to use numerical simulation on 3D models of cellular materials. There are different types of geometries of cellular materials, and different methods to calculate the temperature as well. There is also an important dichotomy to solve: the more accuracy we need, the more CPU time and data memory is required [21].

The laser technology provides not only a cut but a soldered procedure as well. The simulations are using the concept of a representative volume element (RVE). The final model is based on a homogenized structure and covers the density, heat conductivity and enthalpy as essential material parameters.

2 Fundamentals of Laser Technology

Laser beam drilling is a technique to generate holes in different kinds of materials. Therefore, the laser beam is focused to a small spot to get high power densities. A part of the laser beams energy gets absorbed by the workpiece material and the resulting heat causes it to melt or vaporize. This makes it possible to generate holes of different diameters and large aspect ratios.

2.1 Laser Beam Drilling Technology

Laser beam drilling can be done as single pulse drilling, percussion drilling, trepanning or helical drilling. Single pulse drilling is used for fast processing and high productivity. To achieve higher aspect ratios or a conicity of the drilling hole, percussion drilling can be used. Therefore, the laser performs in short sequential pulses and ablates the material with every pulse. Trepanning is used to generate larger hole diameters. It combines the drilling and cutting process with single pulses on the contour of the hole. Helical drilling works mainly similar to trepanning, but it has short pulses like in percussion drilling.

A jet of process gases like oxygen or nitrogen is used to blow out the molten material and to protect the optics from molten and vaporized material. With the use of oxygen, there is an exothermal reaction that delivers additional heat to the melting or vaporizing process.

There are some advances of laser beam drilling, regarding conventional processing. In laser drilling there is no contact between the tool and workpiece and thus no wear of tools. Further advantages of laser beam drilling are the small heat affected zone (Fig. 1) and forceless machining. This makes the process very suitable for compound materials.

The work developed intents to predict the laser cutting procedure, according to the characteristics of the laser, the material properties and the geometry. Using numerical simulation it is also possible to optimize the process, saving energy and time.

2.2 Laser Beam Behavior

The behavior of a laser beam is generally characterized using different parameters [22]. The radius of the laser is not the same along its axis (z-axis in Fig. 2). The intensity and the direction of the heat flow are not constant. They change over the distance from the z-axis and the radial distance as well [22]. However, there will be different lines of constant intensity, called isophotes (Fig. 2). The volume of each yellow spot in Fig. 2, by rotation over z-axis, is constant. This means that the total

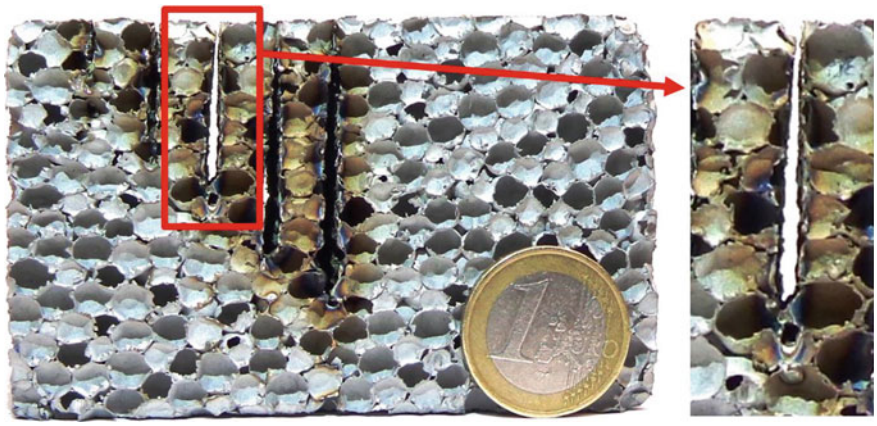

Fig. 1 Experimental laser cutting sample

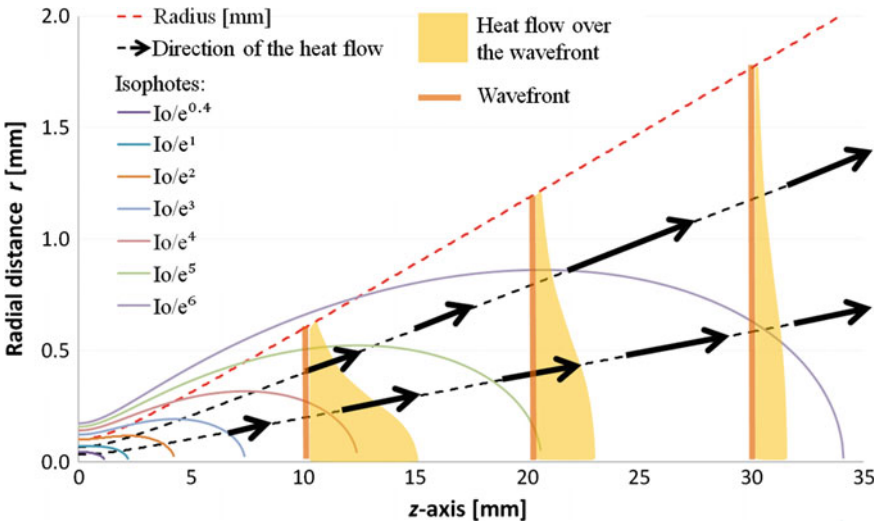

Fig. 2 Frontal/coronal plane of the laser: radius, isophotes, directions and wavefronts of the laser

heat over each wavefront is also constant. The heat distribution is assumed to comply with the Gaussian distribution.

Figure 3 is a detail of Fig. 2, where it is possible to see that the heat flow intercepts perpendicularly each wavefront. In the case of the wavefront represented in Fig. 3, the heat density has a maximum at zero radial distance and a minimum at 1.7645 mm of radial distance. This last value of radial distance corresponds to the double of the standard deviation, $\sigma = 0.882$ (see Fig. 4a). The radius of the laser (w) was printed in Fig. 3 according to Eq. (1) [22]:

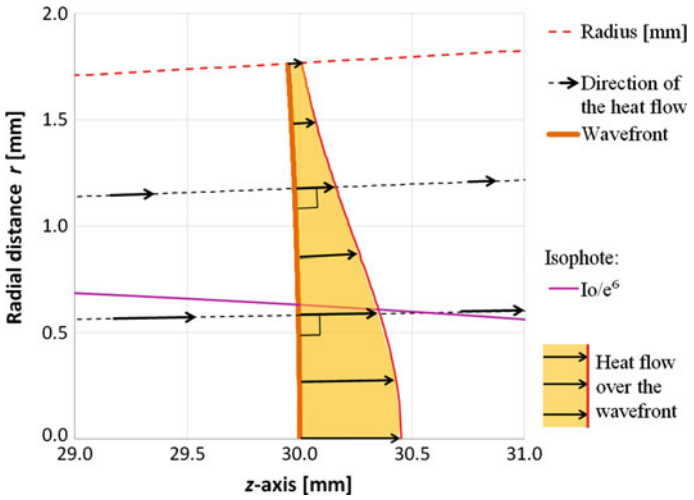

Fig. 3 Interception between the heat flow and the wavefront (detail of Fig. 2)

$$w(z) = w_0 \sqrt{1 + \left(\frac{z}{z_R}\right)^2}, \tag{1}$$

with,

$$z_R = \frac{\pi}{\lambda} K w_0^2, \tag{2}$$

where K and λ, are the dimensionless beam quality parameters and the wavelength, 0.55 and 0.0106 mm respectively; w_o is equal to 0.1 mm, corresponding to a focused beam with a 5''-lens.

The direction of the heat flow, t, on each point of the radial distance and z-axis (r,z), is calculated using the derivative of Eq. (1), where instead of the focal radius, w_o, it was used the correspondent value, w_i, to each point of the radial distance, r. The value of t is not an angle but the tangent between the direction of the heat flow and z-axis. So it comes [22]:

$$\begin{cases} r = w_i \sqrt{1 + \left(\frac{z}{z_R}\right)^2} \\ t(r,z) = \frac{dr}{dz} \end{cases} \Leftrightarrow \begin{cases} w_i = \dfrac{r}{\sqrt{1 + \left(\frac{z}{z_R}\right)^2}} \\ t(r,z) = w_i \dfrac{z}{z_R^2 \sqrt{1 + \left(\frac{z}{z_R}\right)^2}} \end{cases} \Leftrightarrow t(r,z) = \frac{r\,z}{z_R^2 + z^2} \tag{3}$$

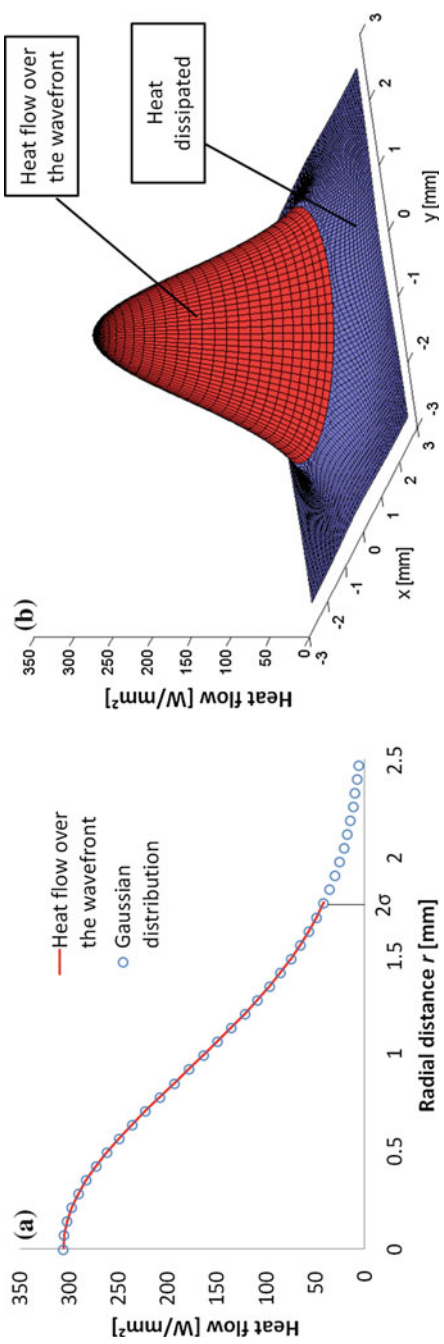

Fig. 4 Representation of heat flow in 2D **a** and 3D **b**

An isophote can be calculated according to [22]:

$$r(z) = \frac{w_0}{\sqrt{2}} \sqrt{\left(1 + \left(\frac{z}{z_R}\right)^2\right) \cdot \ln\left(\frac{e^n}{1 + \left(\frac{z}{z_R}\right)^2}\right)}, \tag{4}$$

where, n is a real number that defines the curve of the isophote.

Figure 2 shows seven different isophotes: $n = \{0.4; 1; 2; 3; 4; 5; 6\}$. The intensity, I_p [W/m^2], of each isophote is determined by [22]:

$$I_P = I_0 \cdot e^{-n}, \tag{5}$$

with,

$$I_0 = \frac{2 P_L}{w_0^2 \pi}, \tag{6}$$

where P_L [W] is the power of the laser.

The heat flow over the wavefront follows a Gaussian distribution (Fig. 4). Figure 4a shows the heat flow over the wavefront represented in Fig. 3 and a Gaussian distribution, G, according to Eq. (7) and assuming a P_L of 1500 W.

$$G(\mu, \sigma) = \frac{M}{\sigma\sqrt{2\pi}} e^{-\frac{(r-\mu)^2}{2\sigma^2}}, \tag{7}$$

with [36],

$$\begin{cases} M = I_0 \cdot \left(1 + \left(\frac{z}{z_R}\right)^2\right) \cdot \sigma\sqrt{2\pi} \\ \sigma = \frac{w_0}{2}\left(1 + \left(\frac{z}{z_R}\right)^2\right) \end{cases}. \tag{8}$$

The heat flow over the wavefront, H, represented in Fig. 4 is calculated according to Eq. (9).

$$H = I_0 \cdot e^{-n}, \tag{9}$$

with,

$$n = 2\left(\frac{r}{w_0}\right)^2 \cdot \left(1 + \left(\frac{z}{z_R}\right)^2\right)^{-1} + \ln\left(1 + \left(\frac{z}{z_R}\right)^2\right). \tag{10}$$

The 3D representation (Fig. 4b) of the heat flow over the wavefront is a revolving feature of the 2D representation (Fig. 4a). The heat flow over the wavefront stops at 2σ (Fig. 4a) and for that reason there will be heat dissipated by the laser (Fig. 4b). Analyzing the power of the laser and the total amount of heat over the wavefront, it is possible to conclude that the laser provides about 86.5 % of the total heat. The simulation results of this topic can be seen in section "Total Heat and Expected Heat".

2.3 Homogenization and RVE

Cellular materials may have a very complex geometry and may be very difficult to model and to simulate with a CAE program because of the computer restrictions. Therefore, it is needed to simplify the geometry of the cellular materials. Furthermore, the aim of this work is the macroscopic analysis of the temperature in the cellular materials during laser procedures. For this reason, a simple geometry is considered.

This objective directs us to the concept of a representative volume element (RVE). Modeling a RVE, results in good agreement with the experiments can be obtained [23]. This approach takes us into a homogenization procedure in order to link the properties of the constituents to the parameters at the macroscopic scale [24–26]. The RVE sample must be selected small enough to be considered as a material point with respect to the size of the domain under analysis, but large enough to be a statistically representative sample of the microstructure [27]. The computational effort is smaller than the direct calculation for the complete problem domain [28]. Specimens of the structure may be tested to validate the results and the material parameters of the RVE. These homogenization procedures have been used with success in other areas of continuum mechanics [29].

In the homogenization, the cellular material is transformed in a cube (Fig. 5). In order to do that, the heat transfer coefficient as well as the density equivalent should be determined. It should not be forgotten that most of the volume of a cellular material is air. However, the heat transfer by the air is quite low, in comparison with the heat transfer by the steel of the sphere. According to some studies [30, 31], when the air is enclosed in volumes within narrow bounds, there is no convection because the Rayleigh number is too low [32]. There is only a small heat transfer by air conduction. The thermal conductivity of the air is also low: 0.03 $Wm^{-1}K^{-1}$ at 80 °C and 0.05 $Wm^{-1}K^{-1}$ at 400 °C [33]. So, we can ignore the heat transfer by the air and consider only the heat conduction through the steel of the sphere. Thus, the thermal conductivity can be calculated by Eq. (11):

$$Q_{\text{basis}} = Q_{\text{hom}} \Leftrightarrow A_1 \lambda_{\text{basis}} \frac{T_2 - T_1}{L} \Leftrightarrow A_3 \lambda_{\text{hom}} \frac{T_4 - T_3}{L}, \tag{11}$$

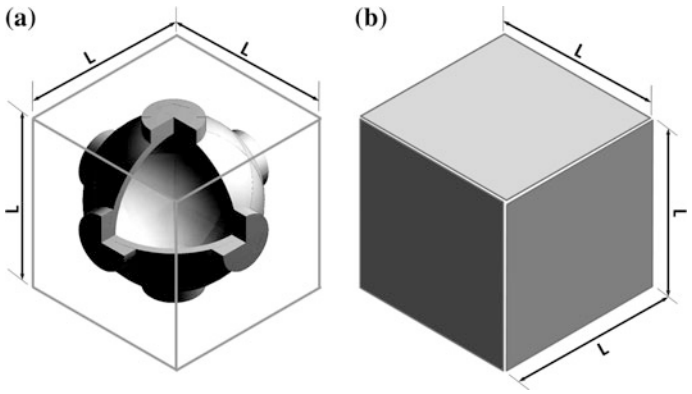

Fig. 5 Homogenization principle: a complex geometry of cellular material **a** becomes a simple geometry **b**

where Q is the heat [W], A_1 is the area [m^2] of a face of the cellular material, A_3 is the area [m^2] of a face of the RVE, T_1 and T_2 are the temperatures [°C] of the cellular material, T_3 and T_4 are the temperatures [°C] of the RVE. The λ_{hom} means the thermal conductivity of the homogenized material and the λ_{basis} means the thermal conductivity of the base material (steel).

The thermal conductivity is a very important parameter in a RVE study. Several simulations of the temperature in a cellular material (Fig. 5a) have been computed in order to analyze the thermal conductivity. It is expected that the value of the thermal conductivity (λ_{hom}) of RVE changes according to the dimensions of the diameter, the thickness of the sphere and also the thermal conductivity of the base material (λ_{basis}). Table 1 shows that the geometrical properties are much more

Table 1 Relation between λ_{hom} and some geometrical and physical parameters

Diameter of the sphere [mm]	Thickness of the wall of sphere [mm]	λ_{basis} [W/(mK)]	λ_{hom} [W/(mK)]
2	0.1	120	4.09
2	0.1	300	4.43
2	0.1	600	4.60
3	0.15	120	3.30
3	0.15	300	3.52
3	0.15	600	3.62
4	0.2	120	2.92
4	0.2	300	3.11
4	0.2	600	3.19
5	0.25	120	2.65
5	0.25	300	2.82
5	0.25	600	2.90

important for the λ_{hom} than the physical properties and the thermal conductivity of the base material. If the λ_{basis} increases 100 %, the λ_{hom} only raises up by 4 %. But, if the geometrical parameters augment twice, the λ_{hom} decreases about 30 %. This effect can be explained by Eq. (11): when the λ_{basis} changes, the final temperature, T_4, will also change inversely.

If the homogenization is correctly done, the general gradient of temperatures has to be the same between the amount of cellular materials and the homogenized geometry. But small variations of the gradient are expected on the cellular materials, because the transversal area is not constant.

If we are dealing with homogenized and non-homogenized cells at the same time, there should be provided a layer between both materials, because of the abrupt variation of the area at the interface between both materials. The heat flux within those materials should be the same. This can be problematic without an interface layer between the geometries. Subsequently, with this layer the gradient of temperature in longitudinal direction can be constant.

3 Program Code

The objective of the program code developed in this work is to study the relation between the power and the depth in a laser drilling process on cellular materials. During a laser drilling process, the geometry is changing along the time according to the power of the laser beam. The commercial CAM programs are able to deal with drilling processes as long as the mechanical procedures or mechanical tools are used. On the other hand, most of the commercial CAE programs are not able to deal with thermal problems when geometry changing is requested. So a program code was written to handle a laser drilling procedure.

3.1 Flow Chart of the Program Code

The program code has a main cycle WHILE that runs until one of the stopping criteria becomes active. The most important stopping criterion is the gradient of the temperature. This criterion compares the gradient of the temperature in the deepest cell at each step (Fig. 6), dividing the rise of temperature by the correspondent step time. If the gradient is lower than a certain limit, then the simulations stops and it is considered that the laser drilling is static. The limit used for the comparison was 10 000 °C/s. This value was chosen because in reality the laser takes around 0.4 s to drill a cellular metal of 40 mm of thickness. Taking into account that the variation of temperature is around 1600 °C, the rough gradient is 4000 °C/s. So, it can be made a rough estimation for 50 mm as 0.5 s, and consequently a gradient of 5000 °C/s is considered. However, a greater gradient criterion can be used because the drilling is

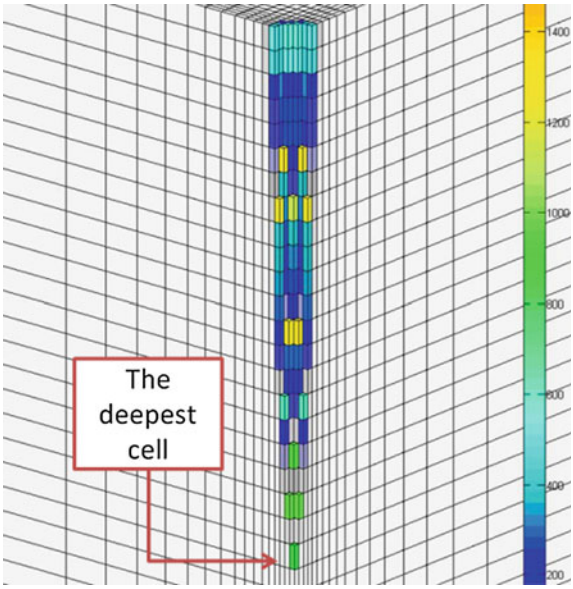

Fig. 6 Cell used to check the gradient of temperature. Detail of a laser drilling simulation (750 W) after 0.02 ms of laser procedure

much slower at the end of the procedure. Moreover, a large amount of CPU time can be saved without losing important accuracy in the final results.

The main program code has two functions (see the flow chart in Fig. 7 left). The first one calculates the temperature in each cell using an explicit methodology (see the flow chart in Fig. 7 right). The second one updates the variables.

The phase change is calculated by the internal energy in the first function. The internal energy has to be enough not only to raise the temperature close to the temperature of phase change but to go over the latent heat thermal energy as well. It is assumed that the phase change happens from solid to vapor.

3.2 Finite Volume Method

The applied approximation strategy was based on the finite volume method. The main Eq. (12) considers conduction, convection and the heat source in the second member. So, all temperatures of the second member are regarded in the previous step ($i-1$). The first member contains the temperature increase in order to calculate the temperature of the new step (i).

$$E = C_d + C_v + S, \tag{12}$$

where E is the internal energy, C_d is the conduction through all of the six faces, C_v is the convection over all of the six faces and S is the heat source of all the six faces. With,

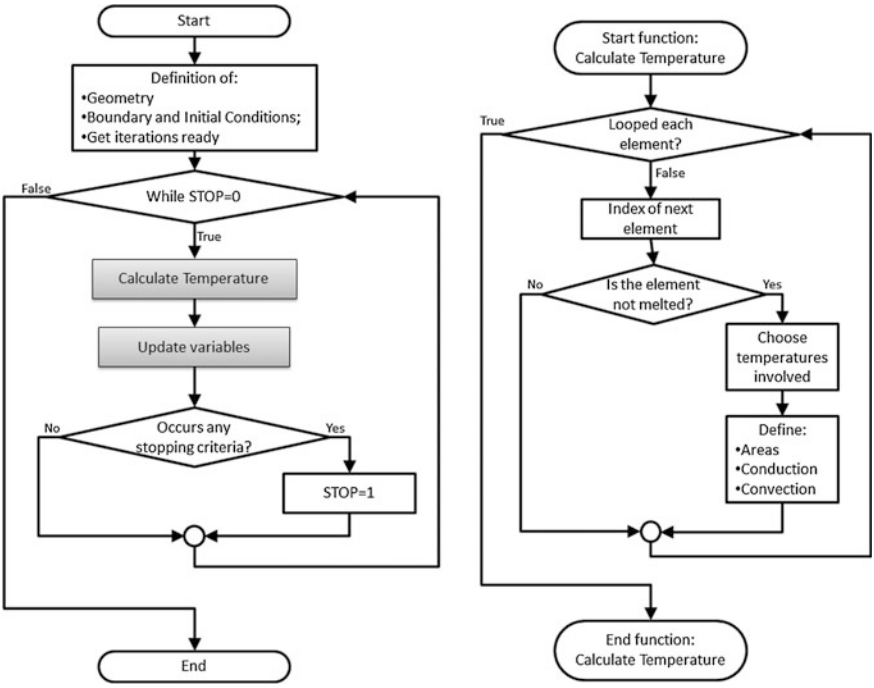

Fig. 7 Flow chart of the main program code (*left*) and of the function that calculates the temperatures (*right*)

$$\begin{cases} E = \rho C\left(T_{\mathrm{E}}^{i} - T_{\mathrm{E}}^{i-1}\right) \\ C_d = \sum_{a=1}^{6}\left(\lambda_{\mathrm{eq}}\frac{A_a}{L_a}\left(T_{\mathrm{E}}^{i-1} - T_a^{i-1}\right)\right) \\ C_v = \sum_{b=1}^{6}\left(\alpha_b A_b\left(T_{\infty}^{i-1} - T_b^{i-1}\right)\right) \\ S = \sum_{c=1}^{6}\left(Q_c\right) \end{cases}, \tag{13}$$

where ρ is the density [kg/m^3], C is the specific heat [Jkg^{-1}K^{-1}], V_{E} is the volume of the element, Δt is the integration time, T_{E} is the temperature of the element. The area [m^2] is represented by A, λ_{eq} is the equivalent thermal conductivity [Wm^{-1}K^{-1}] between the elements. However, the thermal conductivity is considered constant along the temperature and over the elements. The heat source of each face is represented by Q [W] and α [W/m^{2}K] is the convection coefficient at each face. T_{∞} is the room temperature at the correspondent face.

Figure 8 shows a scheme of heat transfer applied in the simulation and represented in Eq. (12). However, there is one type of heat transfer mechanism at each face, and each element only receives the heat source at most from three faces. It is

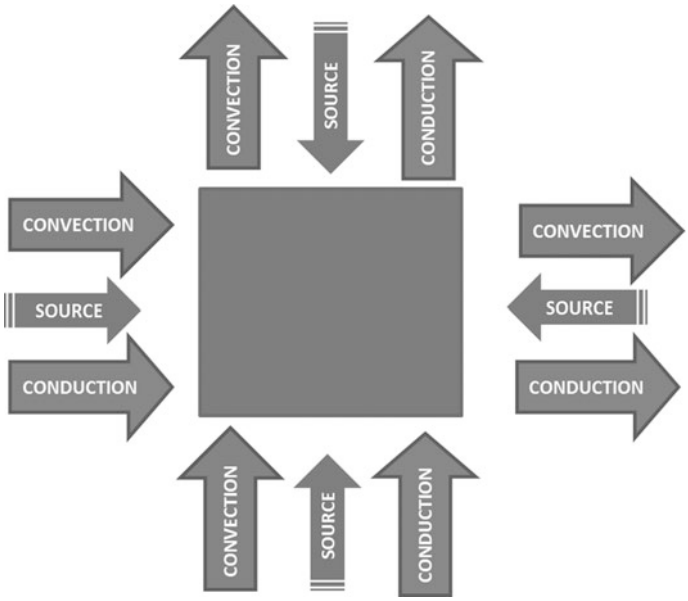

Fig. 8 Scheme of the heat transfer

assumed that if there is heat source applied on a face, the heat transfer by convection is irrelevant when comparing with the source. Moreover, it is also assumed that the heat source is not reflected or redirected to the other faces.

An explicit method is used because the geometry changes when any cell becomes melted, allowing a simpler way to program and to calculate the temperatures than would result from an implicit procedure. On the other hand, the integration time has to be small enough to ensure realistic results, which may result in a larger computation time. That is the common drawback of explicit schemes [34].

The integration time changes along the simulation according to the temperature variation of the previous iteration. Usually the integration time increases faster in the beginning than in the end of the simulation. Nevertheless, each time the deepest cell (see Fig. 6) melts, the integration time decreases.

4 Results

The geometry used was a homogenized full block of $10 \times 10 \times 50$ mm. The results are presented with regards to two different studies:

Soldered and sintered cells with different properties;

Different thermal conductivities.

Two cellular materials, soldered and sintered with a similar geometry (Fig. 9), were taken to compare the results using steel and stainless steel. The difference

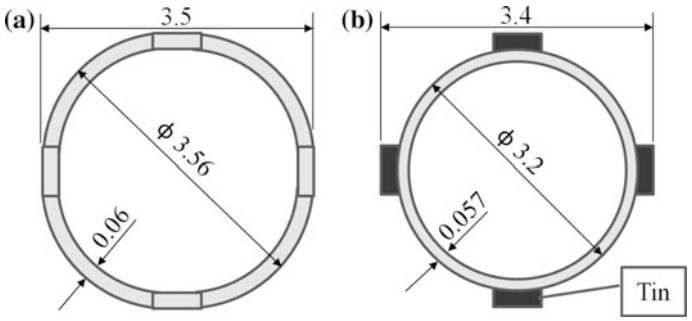

Fig. 9 Geometrical properties [mm] of the cellular materials: sintered **a** and soldered **b**

between these two joining technologies is the connection of the cells. The soldered cells are connected to each other by small parts of tin (Fig. 9b). The sintered cells are spherical shells connected each other by small flat areas. The cellular materials were studied in order to find out the thermal conductivity equivalent for a homogenized geometry using the RVE theory (See the content "Homogenization and RVE"). Volume, mass and the density of the cells are similar (Table 2), but the thermal conductivity (of homogenized geometry) is very different when the different materials are compared.

Other simulations were made to study the influence of the thermal conductivity. The thermal conductivity of the homogenized geometry is the most important property for the heat transfer analysis on drilling procedures. The initial temperature and the room temperature was 20 °C. The heat transfer coefficient was 30 W/(m^{2}K). The properties of homogenized materials (sintered and soldered) and base material are shown in Table 2. It can be seen that the main difference between steel and stainless steel is the thermal conductivity.

Table 2 Material properties used in the simulations

	Homogenized material				Base material		
	Sintered		Soldered				
	Steel	Stain. Steel	Steel	Stain. Steel	Steel	St. Steel	Tin
Volume [mm^3]	42.5	42.5	40.8	40.8	–	–	–
Mass [kg]	1.77e-5	1.75e-5	1.77e-5	1.75e-5	–	–	–
Density [kg/m^3]	417.5	412.2	433.7	429.2	7850	7750	8600
Thermal conductivity [W/(mK)]	1.38	0.34	1.45	0.4	60	15	50
Specific heat [J/(kgK)]	434	480	434	480	434	480	173

4.1 Sintered and Soldered Cells

The power of the laser was 1000 W. The maximal depth of the drilling hole is reached in about 0.1 s. In other words, comparing the models for soldered and sintered, the differences are around 5 %. Furthermore, comparing the materials, the differences are around 8 % for the soldered model and 7 % for sintered model (Table 3).

The drilling process in soldered models is slower than in sintered models. Furthermore, the drilling process in cells of steel is also slower than in cells of stainless steel. This happens not only because the sintered cells of these simulations had a lower density, but particularly because of the thermal conductivity. The thermal conductivity of steel is about four times higher than the coefficient of stainless steel. The influence of the thermal conductivity can be explained using Fig. 10. The numerical simulations of soldered and sintered cells show similar results for the same material properties. However, there are differences between steel and stainless steel. It can be seen that the gradient of the temperature depends principally on the thermal conductivity. The higher the thermal conductivity is, the lower is the gradient. The difference in the results between soldered and sintered models is very small. But when the models with different materials are compared, large differences of temperature gradients show up, because the thermal conductivity is very different.

The numerical simulations that use a higher thermal coefficient have a lower gradient in x and y direction. This means that the energy flows with less difficulty and, consequently, the drilling process needs more time. On the other hand, with a lower thermal coefficient, the laser energy accumulates in the z direction, or rather, in the direction of the heat flow (check Figs. 2 and 3). If the properties of the material are very important during the drilling procedure, we cannot say the same when we compare the results between the different geometry. The results for soldered and sintered cells are very similar when same base materials, steel and stainless steel.

Figure 11 shows a 3D detail of the deepest cells of a drilling procedure. A laser drilling process in a soldered cell looks very close to a process in a sintered cell with the same main material. This can be explained by the similar mechanical properties used in both cells. But it also means that it does not matter which kind of cell we use, but only which thermal properties (specially the thermal coefficient) the cell material has. Another point should be mentioned: the lower the thermal conductivity is, the faster the laser drills and reaches the end of the geometry.

Table 3 Simulation of the performance of drilling process

Heat = 1000 W	Depth [mm]	Time [s]
Soldering-Stainless	50	0.101
Soldering-Steel	50	0.109
Sintering-Stainless	50	0.096
Sintering-Steel	50	0.103

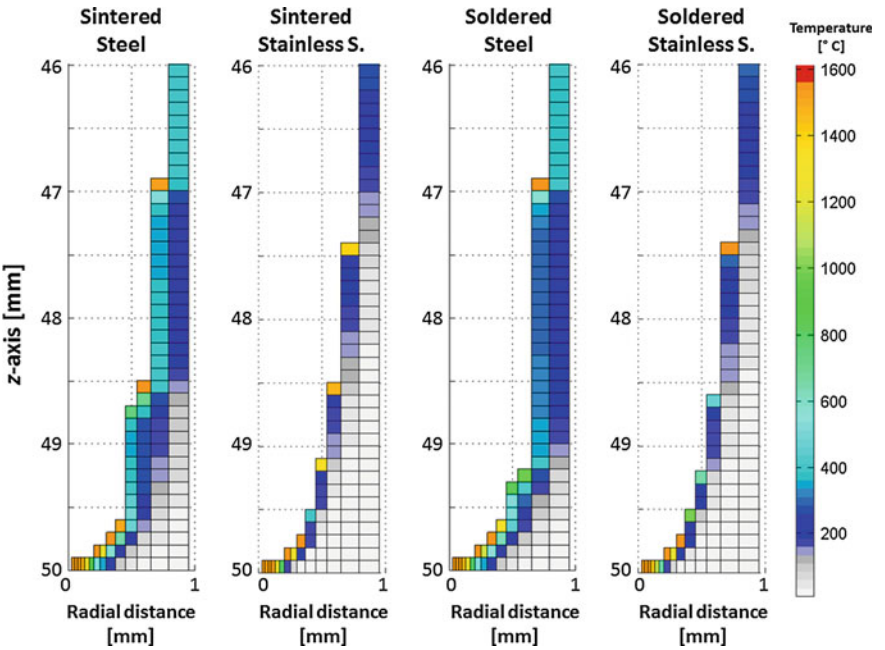

Fig. 10 Detail (2D) of the deepest cells of drilling process

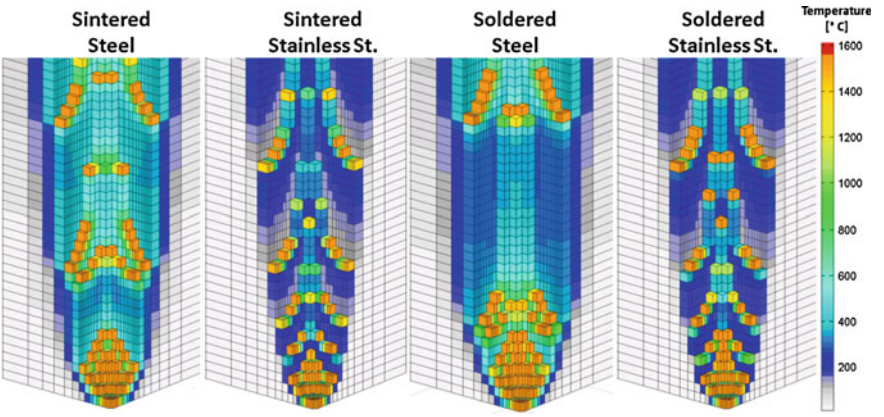

Fig. 11 Detail (3D) of the deepest cells of drilling process

4.2 Thermal Conductivity Influence

In order to study the influence of the thermal conductivity in a laser drilling process, some numerical simulations were made. Those simulations use only different heat sources and two different thermal conductivities.

The results of drilling time and depth over different laser power are shown in Fig. 12. As expected, the drilling process time decreases when the heat increases as well as the laser reaches the end of the geometry (50 mm). Otherwise, if the laser does not reach the end of the geometry, the time of the drilling process will increase if the heat also increases. This fact can be explained by the stopping criteria, namely, the gradient of temperature (check the content "Flow Chart of the Program Code").

The time of the drilling process depends also on the thermal λ coefficient. While the drilling process does not reach the end, it takes more time with a lower λ. On the other hand, if the drilling process reaches the end, a process with a higher λ takes more time than with a lower λ. This can be understood using the value of the depth.

A process with lower λ goes deeper than with a higher λ. The depth reached with lower λ is never inferior to the depth reached with higher λ. In the numerical simulations with lower λ, the energy from the laser is more concentrated on the bottom of the hole. So, it takes more time (and iterations) to activate the stopping criteria of the gradient. Furthermore, the laser drilling has a higher velocity at the beginning but it starts progressively slowing down.

Figure 13 compares the influence of the λ on the gradient of temperatures. As expected, it is possible to see that the gradient of temperatures from the surface of the hole is much smoother with $\lambda = 4\ \mathrm{Wm^{-1}K^{-1}}$ than with a $\lambda = 2\ \mathrm{Wm^{-1}K^{-1}}$. Moreover, with higher heat source the gradient of temperatures is also higher because the drilling velocity is higher as well.

Figure 14 shows the behavior of the laser drilling along time. The behavior is very well defined, comparing with Fig. 15. It is interesting to notice that the behavior of a drilling process with $\lambda = 2\ \mathrm{Wm^{-1}K^{-1}}$ is very similar to the behavior of a drilling with $\lambda = 4\ \mathrm{Wm^{-1}K^{-1}}$ if we add 250 W of laser power. For example, the laser drilling performance using 1250 W and $\lambda = 2\ \mathrm{Wm^{-1}K^{-1}}$ is very similar to the performance using 1500 W and $\lambda = 4\ \mathrm{Wm^{-1}K^{-1}}$. This means that a drilling process with lower λ is more efficient for higher laser power (see also Fig. 16). Moreover, it also means that the difference of heat dissipation between two drilling processes using $\lambda = 2\ \mathrm{Wm^{-1}K^{-1}}$ and $\lambda = 4\ \mathrm{Wm^{-1}K^{-1}}$ is around 250 W.

Figure 15 shows the results for similar numerical simulations but with lower heat. The behavior of these drilling procedures is not so homogeneous as the previous results. This means that the acceleration of the laser drilling through the geometry is not constant.

This particularity can indicate a poor meshing of the geometry for lower heat sources. However, it also can be better explained using the behavior of the gradient stopping criteria (check the content "Gradient of Temperature and Velocity of Drilling"). However, we can take the results as they are, in order to compute the efficiency or the performance of the drilling procedure. The results show that when

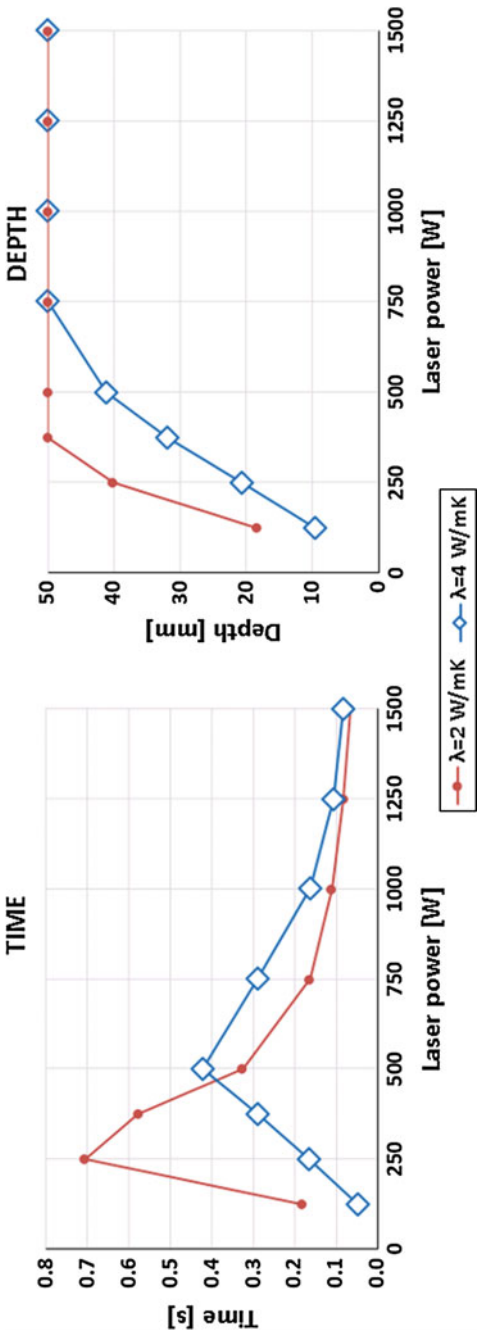

Fig. 12 Results of drilling time and depth over several different laser power

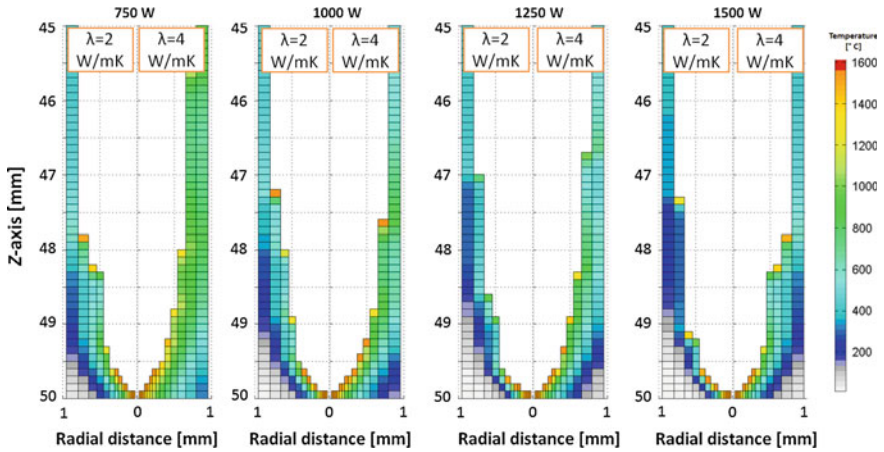

Fig. 13 Detail (2D) of the deepest cells of drilling process with different thermal λ coefficient

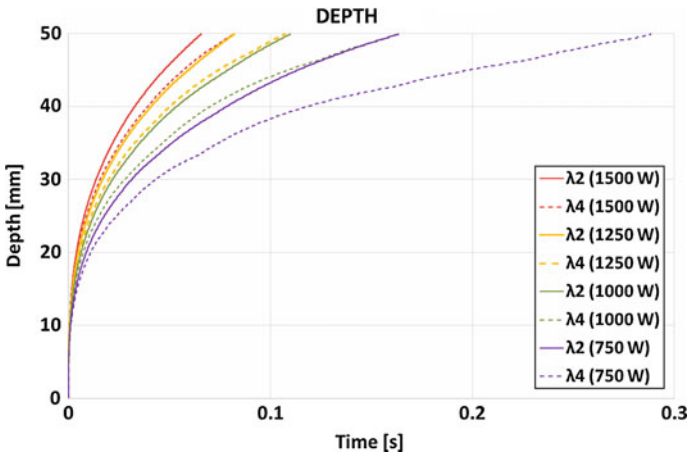

Fig. 14 Depth along the time of drilling process using a laser of 750, 1000, 1250 and 1500 W

the laser power increases, the efficiency of the energy decreases while the laser drilling does not reach the end of the geometry and increases slightly after that (Fig. 16). Nevertheless, the results would be different if we change the stopping criteria.

The results also show that the performance or efficiency of the drilling with λ is higher as long as the laser drilling does not reach the end of the geometry, and lower after that.

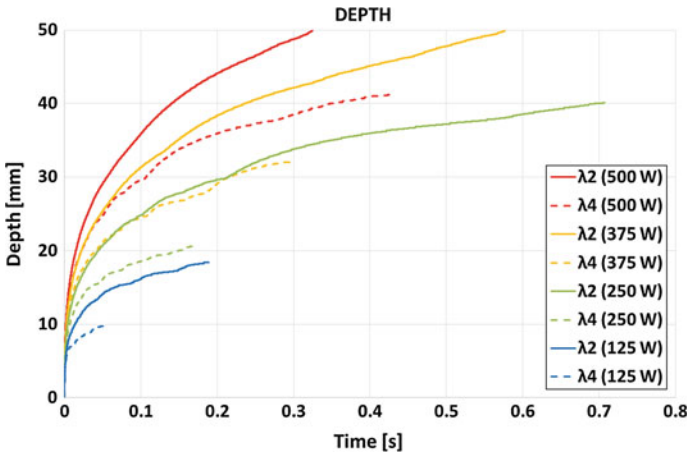

Fig. 15 Depth along the time of drilling process using a laser of 125, 250, 375 and 500 W

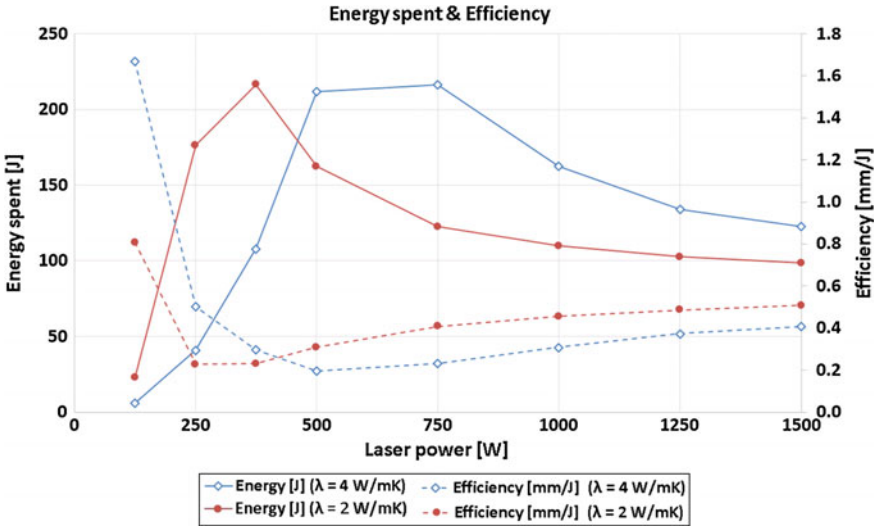

Fig. 16 Energy spent and energy efficiency

4.3 Considerations About the Results

Several interesting aspects about the results should be considered and analyzed. The gradient of temperatures has a huge influence on the integration time and on the stopping criteria. It is closely connected to the velocity of the drilling procedure.

Moreover, the laser does not provide the total amount of heat, because of the characteristics of the laser. Finally, the shape of the laser drilling hole is similar to a drop and it closely matches reality.

5 Gradient of Temperature and Velocity of Drilling

Any production process should be efficient. With this kind of laser, the drilling velocity slows down with the depth because the laser heat flows more and more through the walls of the hole. This means that after a certain depth the process is not efficient any more.

In other words, when the gradient of the temperatures (in z direction) is too low, the process should stop as well as the simulation. However, the gradient of temperatures has not a constant variation.

In a virtual model, the laser warms up and melts the cells one by one. After a cell becomes melted, the next one will abruptly receive heat and increase its temperature. For this reason, the gradient of temperatures has some kind of "chaotic" behavior (Fig. 17).

This characteristic is responsible for the variation of the acceleration of the laser depth. Moreover, this phenomenon is more visible with higher laser power. In order to neutralize this effect, a thinner mesh (z direction) should be chosen and defined. The application of an adaptive remeshing technique could handle properly this issue as well [35].

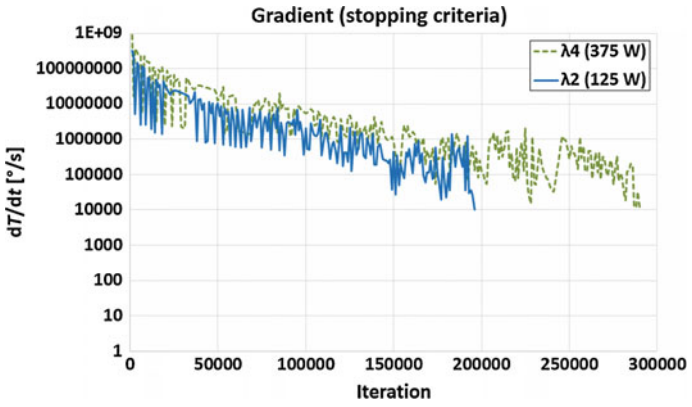

Fig. 17 Gradient stopping criteria

6 Total Heat and Expected Heat

Because we are dealing with a discretization of the problem, there are aspects with less accuracy. One of those aspects is that the total heat at the cells is not constant. For example, if we apply a laser source of 1500 W, we should expect a total heat at the cells of 326 W, according to the double symmetry (25 %) and to the Gaussian distribution of the isophotes (86.5 %) until the radius of the laser (see the content "Laser Beam Behavior").

Figure 18 shows the total heat at the cells along the simulation. As expected, the total heat is not constant, but moreover, the beginning of the simulation is very irregular. However, the average value is about the expected.

The initial jolt at the beginning of the simulation is explained by the interaction of the first melted cells on the total heat (Fig. 19). When the first layer of cells is

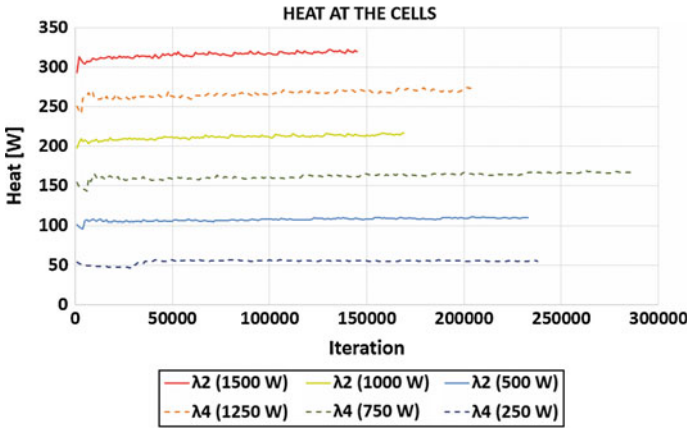

Fig. 18 Total heat at the cells along the simulation

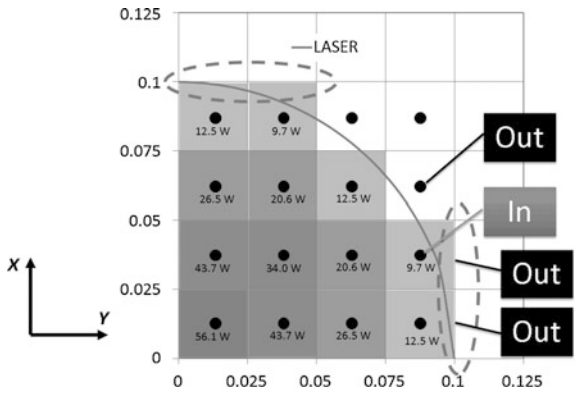

Fig. 19 Interference of the first melted cells on the total heat

melted, the radius of the laser is not enough to capture the surfaces (Fig. 19). Obviously, according to the characteristics of the isophotes (see Fig. 2), the second layer will receive less heat than the first one.

Each surface is captured by the laser when its midpoint has a radial distance above the radius of the laser in the same z coordinate. Because the laser radius is not constant along the z direction (see Fig. 2), the flux of the laser is not as straight as it should be to improve the efficiency of the drilling. This effect is explained in next content.

7 Drilling Width

It is very interesting to analyze the width of a laser drilling hole. Figure 20 shows that the drilling width (at low deepness) increases practically proportional over the deepness, showing a conic profile. On the other hand it is not proportional along the time. The width of the upper part of the hole becomes stable when the drilling process goes deeper.

At the end of the drilling hole, the width decreases significantly and the drilling profile becomes round or spherical. Figure 21 shows the differences of the drilling profile at the beginning (conic profile) and at the end of the hole (spherical profile).

The profile of the drilling hole looks similar to a "drop". The "drop" profile is also related to the isophotes of these laser specifications. This idea can be observed in Fig. 22, which illustrates several sections of the hole over the deepness.

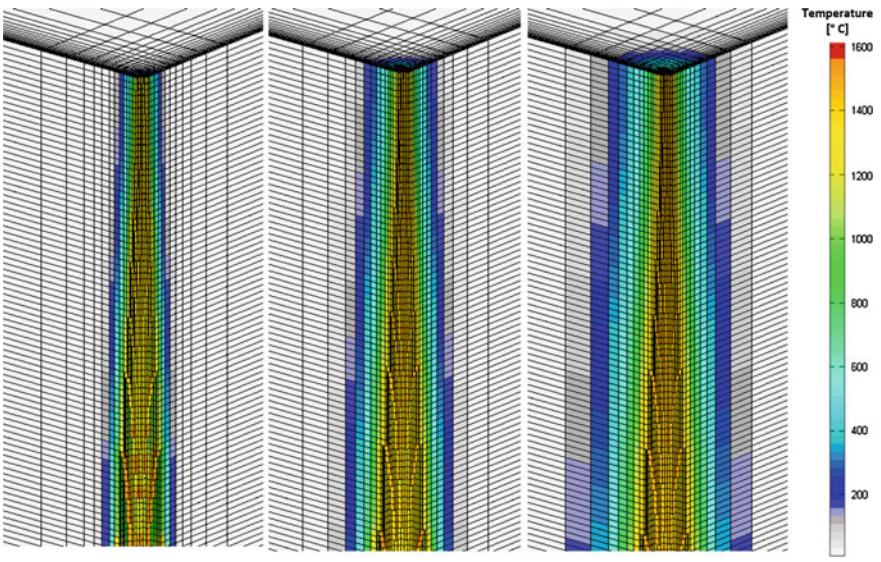

Fig. 20 Sintered steel model (1000 W) along the simulation: 0.0044 s (left), 0.0174 s and 0.0527 s (right)

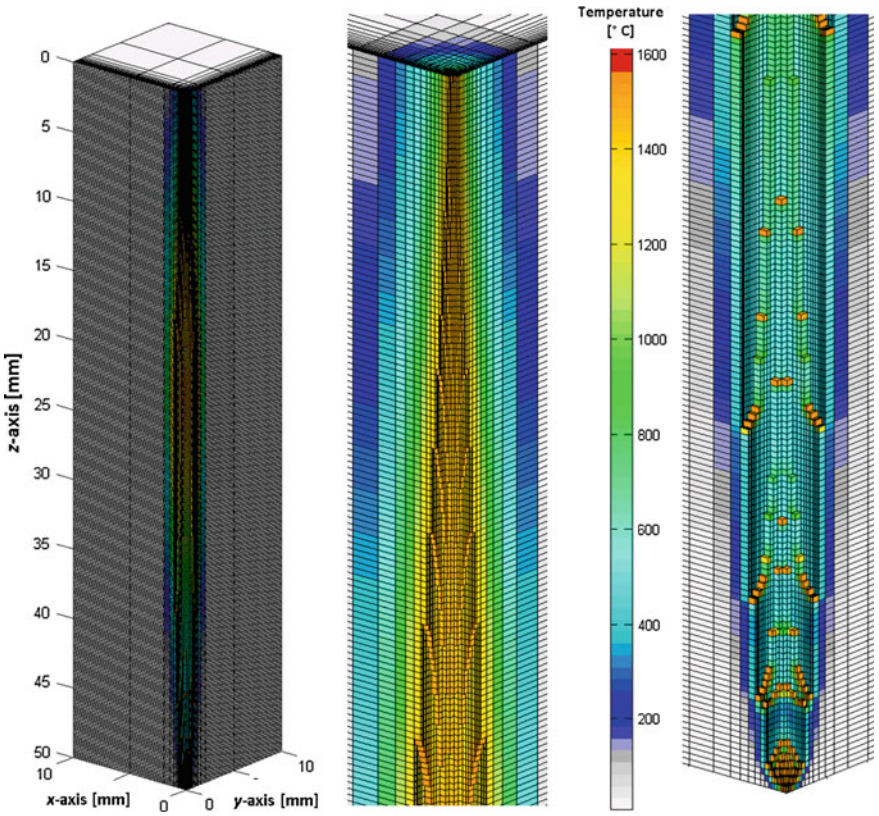

Fig. 21 Sintered steel model (1000 W) at the end of simulation: full model (*left*), beginning and end detail (*right*) of the model

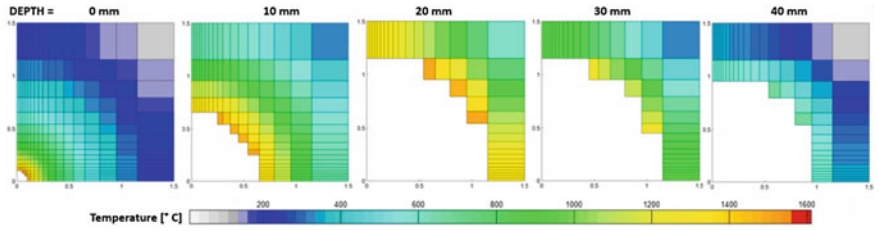

Fig. 22 Width of the drilling using a sintered model with steel and a laser of 1000 W at different section depths: 0 (*left*), 10, 20, 30 and 40 mm (*right*)

Finally, the shape of the drilling profile depends on the thermal properties, specially the thermal conductivity and the heat source. As can be seen in Fig. 23, the drilling profile at the end of the hole is more rounded with a higher heat source. Figure 23 is a 3D detail from the same simulations as Fig. 13.

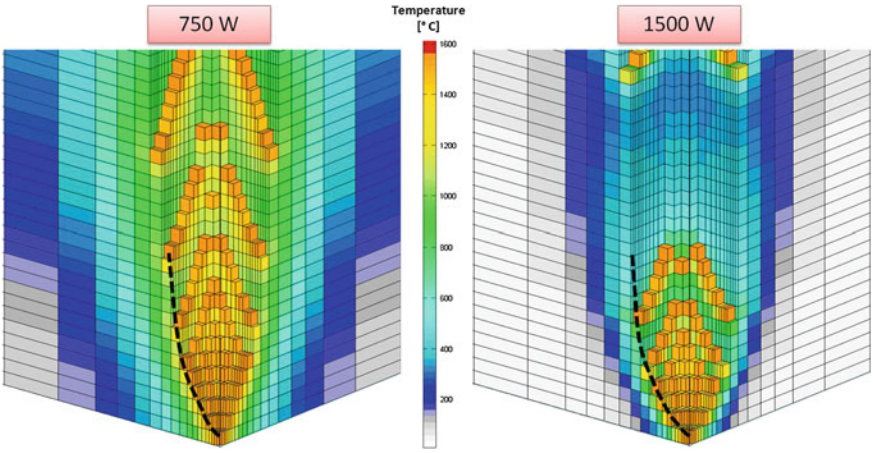

Fig. 23 Detail (3D) of the deepest cells of drilling process with $\lambda = 4\ \mathrm{Wm^{-1}K^{-1}}$

The experimental results of the drilling profile are according to the simulation results of the drilling profile (see Fig. 1). It confirms the profile obtained in the simulations of the drilling process. The "drop profile" can be clearly seen.

8 Conclusions

Laser drilling is a relatively efficient process due to the amount of energy concentrated in a local zone. The results demonstrate that a drilling process in soldered cells is very close to a process in sintered cells. It is not important in which kind of geometry is the laser drilling applied. The thermal properties are the crucial factor, specially the thermal conductivity. With a lower thermal conductivity, the gradient of temperatures inside the geometry is lower, and therefore the efficiency is better. Consequently, the material of the cell is of paramount importance for efficiency of the drilling process.

The laser drilling velocity is not constant. Since the beginning of the process, when the velocity is higher, it decreases until the laser beam reaches the end of the geometry or it stops. The velocity of the laser drilling depends on the thermal properties, not only the heat source but also the thermal conductivity. With a higher thermal conductivity, the gradient of temperatures inside the geometry is also higher, and therefore the velocity of the laser beam is lower because the efficiency decreases. As expected, the velocity of the laser beam drilling also decreases with a lower heat source.

The drilling profile is similar to a "drop" profile. The "drop" profile is also related to the isophotes of this laser. The simulation results are according to the experimental results. This "drop" profile of the hole is dependent to the laser

specifications used. For different laser specifications, different profiles are expected. For example, with a lower focal radius it is expected to obtain different drilling profiles as well as efficiencies. However, these investigations are reserved for our future research work.

References

1. Öchsner, A., Augustin, C.: Multifunctional Metallic Hollow Sphere Structures: Manufacturing, Properties and Application. Springer, Berlin (2009)
2. Araújo, M., Merkel, M., Riegel, H., et al.: On the numerical simulation of laser beam cutting of hollow sphere structures. Materialwiss Werkst **44**, 491–496 (2013)
3. Evans, A.G., Hutchinson, J.W., Ashby, M.F.: Multifunctionality of cellular metal systems. Prog. Mater Sci. **43**, 171–221 (1998)
4. Nemat-Nasser, S., Kang, W.J., McGee, J.D., et al.: Experimental investigation of energy-absorption characteristics of components of sandwich structures. Int. J. Impact Eng. **34**, 1119–1146 (2007)
5. Golovin, I.S., Sinning, H.R.: Damping in some cellular metallic materials. J. Alloy. Compd. **355**, 2–9 (2003)
6. Ashby, M., Fleck, N., Wadley, H., et al.: Metal Foams: A Design Guide. Butterworh-Heinemann, Boston (2000)
7. Pannert, W., Winkler, R., Merkel, M.: On the acoustical properties of metallic hollow sphere structures. Mater. Lett. **63**, 1121–1124 (2009)
8. Winkler, R., Pannert, W., Merkel, M., et al.: Structure borne sound in metallic hollow sphere structures. Materialwiss Werkst **42**, 365–369 (2011)
9. Solórzano, E., Rodríguez-Perez, M.A., Saja, J.A.: Thermal conductivity of metallic hollow sphere structures: an experimental, analytical and comparative study. Mater. Lett. **63–13**, 1128–1130 (2009)
10. Zhao, C.Y., Lu, T.J., Hodson, H.P., et al.: The temperature dependence of effective thermal conductivity of open-celled steel alloy foams. Mater. Sci. Eng. A **367**, 123–131 (2004)
11. Fiedler, T., Öchsner, A.: Influence of the morphology of joining on the heat transfer properties of periodic metal hollow sphere structures. Mater. Sci. Forum **553**, 45–50 (2007)
12. ALM GmbH (2006) Big AFS Test Structure for Ariane Rocket V booster. Cellmet News. http://www.metalfoam.net/cellmet-news_2006-1_net.pdf (2013). Accessed 2 May 2013
13. Kim, J.S., Lee, S.J., Shin, K.B.: Manufacturing and structural safety evaluation of a composite train carbody. Compos. Struct. **78**, 468–476 (2007)
14. Knox, E.M., Cowling, M.J., Winkle, I.E.: Adhesively bonded steel corrugated core sandwich construction for marine applications. Mar. Struct. **11**, 185–204 (1998)
15. Schmid, D.: Industrielle Fertigung. Europa-Lehrmittel, Haan-Gruiten (2011)
16. Apostolos, F., Panagiotis, S., Konstantinos, S., et al.: Energy efficiency assessment of laser drilling process. Phys. procedia **39**, 776–783 (2012)
17. Ramoli, L., Rashed, C.A.A., Fiaschi, M.: Experimental characterization of the inner surface in micro-drilling of spray holes: a comparison between ultrashort pulsed laser and EDM. Opt. Laser Technol. **56**, 35–42 (2014)
18. Tu, J., Paleocrassas, A.G., Reeves, N., et al.: Experimental characterization of a micro-hole drilling process with short micro-second pulses by a CW single-mode fiber laser. Opt. Laser Eng. **55**, 275–283 (2014)
19. Zhang, Y., Li, S., Chen, G., Mazumder, J.: Experimental observation and simulation of keyhole dynamics during laser drilling. Opt. Laser Technol. **48**, 405–414 (2013)
20. Mishra, S., Yadava, V.: Modeling and optimization of laser beam percussion drilling of thin aluminum sheet. Opt. Laser Technol. **48**, 461–474 (2013)

21. Geuzaine, P., Grandmontb, C., Farhata, C.: Design and analysis of ALE schemes with provable second-order time-accuracy for inviscid and viscous flow simulations. J. Comput. Phys. **191**, 206–227 (2003)
22. Riegel, H., Merkel, M., Öchsner, A.: Laser beam cutting of metallic hollow sphere structures. Materialwiss Werkst **43**, 441–446 (2012)
23. Oliveira, B.F., Cunda, L.A.B., Öchsner, A., et al.: Comparison between RVE and full mesh approches for the simulation of compression tests on cellular metals. Materialwiss Werkst **39**, 133–138 (2008)
24. Tanov, R., Tabiei, A.: Finite element implementation of a new sandwich homogenization procedure. Compos. Struct. **50**, 49–58 (2000)
25. Rekik, A., Bornert, M., Auslender, F., et al.: A methodology for an accurate evaluation of the linearization procedures in nonlinear mean field homogenization. C. R. Mec. **333**, 789–795 (2005)
26. Yu, M., Zhu, P., Ma, Y.: Effects of particle clustering on the tensile properties and failure mechanisms of hollow spheres filled syntactic foams. Mater Des. **47**, 80–89 (2013)
27. Dondero, M., Cisilino, A.P., Carella, J.M., et al.: Effective thermal conductivity of functionally graded random micro-heterogeneous materials using representative volume element and BEM. Int. J. Heat Mass Transf. **54**, 3874–3881 (2011)
28. Zohdi, T.I., Wriggers, P.: Introduction to Computational Micromechanics, p. 20. Springer, Berlin (2005)
29. Nakamachi, E., Tam, N.N., Morimoto, H.: Multi-scale finite element analyses of sheet metals by using SEM-EBSD measured crystallographic RVE models. Int. J. Plast. **23**, 450–489 (2007)
30. Poliševski, D.: Steady convection in porous media. Int. J. Eng. Sci. **23**, 741–749 (1985)
31. Vadasz, P.: Equivalent initial conditions for compatibility between analytical and computational solutions of convection in porous media. Int. J. Nonlinear Mech. **36**, 197–208 (2001)
32. Nield, D.A., Bejan, A.: Convection in Porous Media. Spring, New York (1999)
33. Incropera, F.P., DeWitt, D.P.: Introduction to Heat Transfer. Wiley, New York (1996)
34. Bergheau, J.M., Fortunier, R.: Finite Element Simulation of Heat Transfer, p. 119. Wiley, London (2008)
35. Zanger, F., Boev, N., Schulze, V.: Novel approach for 3D simulation of a cutting process with adaptive remeshing technique. Procedia CIRP **31**, 88–93 (2015)
36. Huegel, H., Graf, T.: Laser in der Fertigung. Vieweg und Verlag, Germany (2009)

Metallic Foam Density Distribution Optimization Using Genetic Algorithms and Voronoi Tessellation

Pablo C. Resende, Renato V. Linn and Branca F. de Oliveira

Abstract Metallic foams have a very particular structure due to their high specific stiffness. Density plays an important role on their structural response and is also determinant to the foam's weight. The main goal of this paper is to find an ideal density distribution to open-cell metallic foams in order to achieve optimized structural performance. A density distribution optimization using an irregular description of the foam by a Voronoi tessellation and a genetic algorithm for the numerical optimization is presented in this work. The structural analysis is performed with linear elastic beam finite elements and the foam structure is modeled as a Voronoi tessellation. The density is related to the number of Voronoi seeds, which may configure lighter or denser foams and vary throughout the model. The minimization and maximization of stiffness were analyzed for different structural applications in order to demonstrate the capability of the developed methodology.

Keywords Metallic foam · Density optimization · Voronoi tessellation · Genetic algorithm

P.C. Resende (✉) · B.F. de Oliveira
Graduate Program in Design (PGDesign), Federal University of Rio Grande do Sul (UFRGS), Av. Osvaldo Aranha 99, 4° andar, 90035-190 Porto Alegre, RS, Brazil
e-mail: pblrsnd@gmail.com

B.F. de Oliveira
e-mail: branca@ufrgs.br

R.V. Linn
Graduate Program in Civil Engineering (PPGEC), Federal University of Rio Grande do Sul (UFRGS), Av. Osvaldo Aranha 99, 3° andar, 90035-190 Porto Alegre, RS, Brazil
e-mail: renatolinn@gmail.com

P.A. Muñoz-Rojas (ed.), *Computational Modeling, Optimization and Manufacturing Simulation of Advanced Engineering Materials*, Advanced Structured Materials 49, DOI 10.1007/978-3-319-04265-7_11

1 Introduction

The improvement of production methods allied to advantageous mechanical and thermal characteristics of foam structures, such as high stiffness/density ratio, has increased the interest in structures having foam cores. Practical applications of such structures can be observed in aerospace, automobile, chemical and construction industries and also in orthopedic and clinical applications. Particularly, the present work is concerned with open-cell metallic foam structures. An open-cell foam structure can be considered as an array of composed struts [24], as shown in Fig. 1.

The structural behavior of foam structures is strongly dependent on the density distribution, shape and size of the pores on the media. Many analytical and numerical models describing the foam behavior have been developed and investigated. Regular foam models based on regular cell packing such as the cubic model [9], and the tetrakaidecahedron model [5] for isotropic linear elastic, anisotropic linear elastic and isotropic nonlinear cases are some of the main models investigated. Such models can be used as a repeating cell unit to analytically or numerically (as using the finite element method) estimate the mechanical behavior of the real structure [13, 17–19]. The irregular foam models, however, incorporate the structural disorder present in real foams. One possible approach is the use of a Voronoi tessellation together with finite element analysis, which gives a better representation of the microstructure of real specimens [23]. Another modeling technique is the use of exact geometry using tomographic images, digitized images or X-ray scans of the foam. While being a closer digital reproduction of the structure of real foams, these models are unique for each individual foam sample and may not necessarily be representative [22].

The investigation of the optimization of foam structures in order to improve the mechanical behavior is still a scarcely explored subject. Some investigations on metallic foams include optimization using genetic algorithms [9], stiffness optimization of living bone tissue by density distribution adaptation [3] and optimization of structures with foam core using a regular cubic model and gradient-based optimization algorithm [14]. Apparently, the optimization results strongly depend on the underlying mechanical and foam model assumptions. The related works on

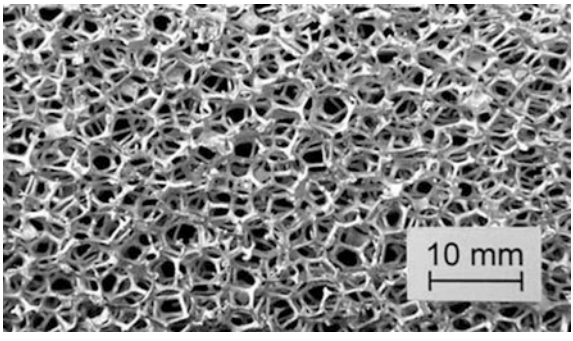

Fig. 1 An aluminum foam with open cell (DUOECEL®) [16]

optimization use a regular model for the foam description. The present work investigates optimization of open-cell metallic foams by density distribution adaptation using an irregular foam model and genetic algorithms. The foam model used is based on an irregular Voronoi tessellation. The mechanical linear elastic model is evaluated using the Finite Element Method.

2 Modeling of Open-Cell Foam Structures

Cellular solids are irregular structures and this irregularity is an important feature to be incorporated on the characterization of the mechanical behavior of such type of structures. In the present work the foam geometry is generated by a Voronoi tessellation in which the cell edges are modeled as beam structures. Particularly, for low-density open-cell foams, beam elements with circular cross section area can be adequately applied with the Voronoi tessellation for a good mechanical characterization [23]. A Voronoi tessellation is generated by the spatial distribution of seed points which uniquely determines the tessellation. The method is closely related to real foam production, where the seed points represent the starting points of growing bubbles with uniform velocity. The resulting geometry has also both angular and connectivity distribution values with good agreement with measured experimental data. The amount of material and disorder in the Voronoi tessellation depends on the spatial distribution of the seed points.

Formally, for a given set of seed points $P = \{p_1, p_2, \ldots, p_n\}$ in the plane, if $d(p, q)$ is the Euclidean distance between two points in space, then the Voronoi diagram of P can be defined as the subdivision of the plane into n sub-domains (or cells), one for each point in P, with the property that some point q lies in the cell corresponding to a point p_i if and only if $d(q, p_i) < d(q, p_j)$ for each $p_j \in P$ and $j \neq i$ [4].

In simple terms, for a set of points a plane is subdivided into Voronoi sub-domains in a way that each sub-domain belongs to a specific point (region) and that every point in that sub-domain is closer to that region than any other. The border lines between sub-domains are bisectors. Every point on one bisector is at an equal distance from the two neighboring sites. Those border lines between sub-domains form the Voronoi diagram, also called Voronoi tessellation [6]. An example of the plane subdivision with the Voronoi tessellation for 8 seed points is depicted in Fig. 2.

When the objective is to predict average mechanical properties of a foam material, a Representative Volume Unit (RVU) cell is usually employed. This RVU can be analyzed using periodic boundary conditions in order to evaluate mechanical properties such as directional elastic modulus, densification and others properties for different applications like compression and tension [22]. In the present work, to optimize structures with foam core, the finite dimensional structure is modeled with

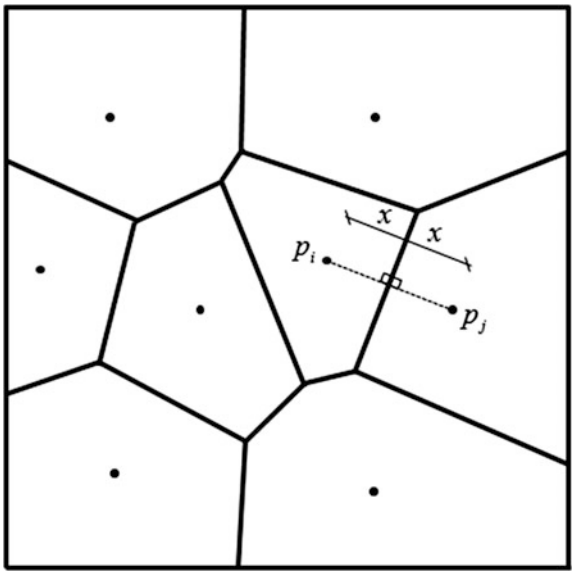

Fig. 2 Voronoi diagram for 8 seed points

real scale using the Voronoi tessellation as the domain distribution. This way, the modeling approach can be viewed as an intermediary situation between the exact representation (such as those obtained with digital scan) and regular models. The amount of geometrical representativeness obtained with the real scale Voronoi model is also accompanied with the drawback of higher computational effort increase when compared with a regular model representation.

The mechanical foam model is evaluated using the Finite Element Method. The cell edges obtained from the Voronoi tessellation are meshed with beam-elements (axial and bending effects are both considered) which have constant circular cross-section. The finite structure is subdivided into regular quadratic sub-domains having edge length L_e. The choice of this edge length should be such that the relation L_e/δ has a value between 2 and 8. The parameter δ is the medium distance between internal seed points contained in the region delimited by the sub-domain. These values give good stiffness representation of the real foam disorder [23]. The seeds of the Voronoi tessellation are randomly distributed into each of these sub-domains and the relation between the amount of material volume on each sub-domain and the total volume of the sub-domain gives the local density of the mesh (Fig. 3). Structural analysis is performed with Karamba software [11], which uses a first order Euler-Bernoulli approach for the beams, considering small displacements and rotations for linear elastic materials in a finite element context.

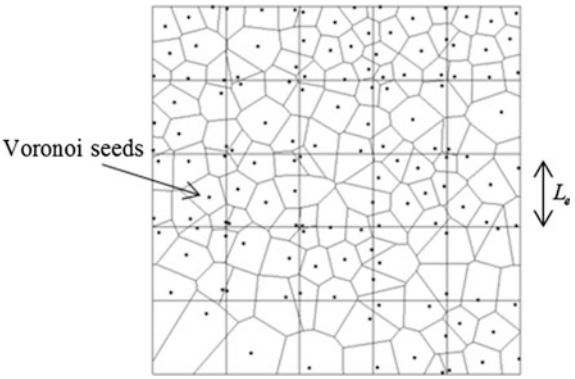

Fig. 3 Foam structure representation using Voronoi tessellation

3 Optimization

The general optimization problem can be stated as:

$$\min \quad f(\mathbf{x}) \quad \text{subjected to} \begin{cases} g_i(\mathbf{x}) \geq 0, & i = 1 \text{ to } \mathbf{p} \\ h_j(\mathbf{x}) = 0, & j = 1 \text{ to } \mathbf{q} \end{cases} \tag{1}$$

where $f(\mathbf{x})$ is the objective function, $g_i(\mathbf{x})$ are the p inequality constraints, $h_j(\mathbf{x})$ are the q equality constraints and $\mathbf{x}$ are n optimization variables. In the present work, the optimization variables employed are positive integer values, i.e., $x \in \mathbb{Z}^*n$.

3.1 Density Modification of Foam

To modify and optimize the density distribution of the foam, the full domain of the structure is divided into m sub-domains. Each sub-domain controls its local density and it is defined as a square region of space. The external edges of these sub-domains have the dimension L_e (Fig. 3). Inside each m sub-domain, there are s^m seed points randomly distributed, which completely define the Voronoi tessellation of the region delimited by this sub-domain. When the number s^m is modified, the Voronoi tessellation also changes, changing both mass and stiffness of the m sub-domain. Note that, formally, a single design vector $\{s^1, s^2, \ldots, s^n\}$ may give rise to an infinite number of Tesselations, since the position of the seeds is not controlled (i.e. inside each rectangular domain the s^m seeds can be positioned anywhere). To ensure uniqueness of the domain representation, a single Voronoi Tessellation is generated for each possible design vector, with randomly positioned seeds. These tessellations are built before the optimization procedure is started and are used whenever the corresponding design vector needs to be evaluated. Thus, increasing s^m does not necessarily increase the total mass or stiffness of the sub-domain, although the number of beams on the region necessarily is increased.

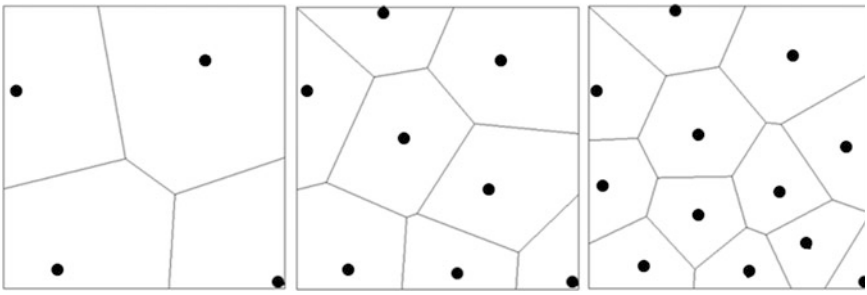

Fig. 4 Increasing the number of seeds inside sub-domain to locally modify density and stiffness

Figure 4 shows an example of this sub-domain modification. Each i optimization variable is thus defined as the number of seeds in each sub-domain, i.e., $x_i = s^i$ in the optimization problem, with $i = 1, 2, \ldots, m$.

3.2 Genetic Algorithms

In the present work, genetic algorithms are employed to solve the general problem stated in Eq. (1). Constraint relations are handled with penalty functions.

In Genetic Algorithms (GA) each individual is represented through a unique chromosome. It is basically an array of numbers that can be used to easily manipulate individuals, combine them, mutate and eventually store them. The chromosome of each individual $\mathbf{y}_i$, $i = 1, n$ is composed by a vector s^m with length j equal to the number of sub-domains m of the foam containing a list of the number of seeds of each of them (Fig. 5). An initial generation is randomly created, containing n individuals

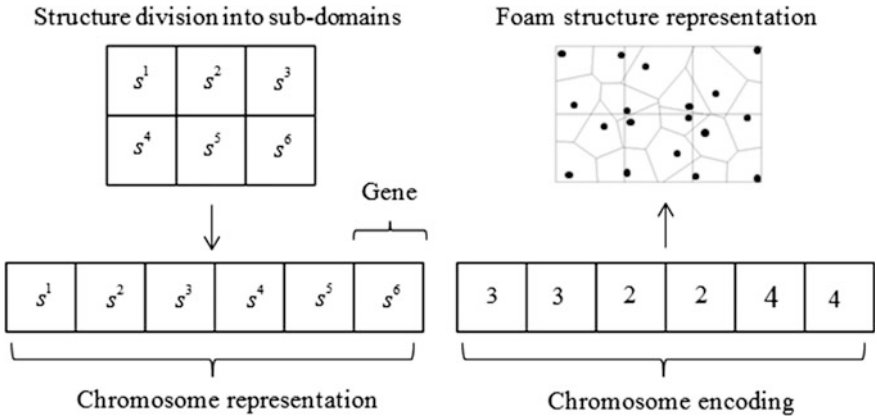

Fig. 5 Chromosome representation and encoding to represent foam structures with Voronoi tessellation

which are evaluated, i.e., their fitness, or objective function is determined. The process enters a loop for a determined number of generations. In this loop, a selection is made to choose the individuals for breeding, based on their fitness. The chosen individuals are then crossed, mutated and evaluated again, thus prepared for the next iteration. The process ends after a predefined number of generations. The genetic algorithm performs standard mutation, uniform crossover and Roulette Wheel selection procedures through the evolutionary process, which are detailed below. Galapagos evolutionary solver is employed in the present work [8].

3.2.1 Selection

The process of selection in Genetic Algorithms chooses individuals of one generation for crossover according to their fitness. In the Roulette Wheel selection, each individual has a chance to survival proportional to their fitness. This method gives a larger variety of solutions and no individuals are neglected as in an elitist selection, where only the best individuals are selected, which is not an efficient method because it usually conducts to only local optimum points. If n individuals are present in one generation, $\mathbf{y}_i$ as the ith individual of that generation and $F(\mathbf{y}_i)$ is the fitness value of that individual, then the probability $p(\mathbf{y}_i)$ of the individual to be chosen for reproduction is:

$$\mathrm{p}(\mathrm{y_i}) = \frac{F(\mathrm{y_i})}{\sum_{j=1}^{n} F(\mathrm{y_i})} \tag{2}$$

This allows the individuals with higher fitness values to have better chances of being selected.

3.2.2 Crossover

The pairs used for breeding are randomly composed using the individuals selected for reproduction at each generation. When the pairs are chosen, they can be crossed generating two individuals or can be just be included into the next generation. The chance of crossover occurrence is called as the crossover probability factor and is set to 0.6, i.e., 60 % of the individuals in a newly created generation are crossed to produce new individuals and 40 % of the individuals are just copied in order to support the survival of the fittest. Here, uniform crossover is used. In this method, each gene (allele) of both parents is swapped with the corresponding allele of the other parent with a probability factor of 0.5. In that way, each parent allele has a 50 % chance of being replaced with the one from the other parent (Fig. 6) [6].

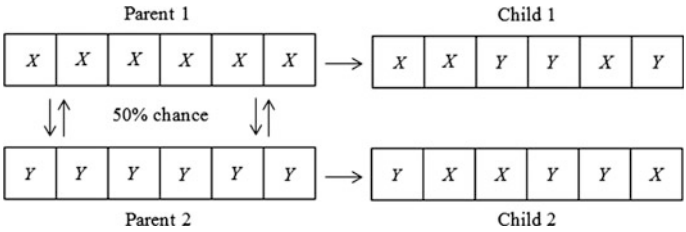

Fig. 6 Uniform crossover

3.2.3 Mutation

Mutation is used to introduce diversity in the current generation. Basically, it introduces a random change on the chromosome of an individual. The chances of mutation happening is regulated by the mutation probability factor, set to 1 % in this work. The mutation process is depicted in Fig. 7, where a gene value in a chromosome is randomly chosen and then switched with a randomly generated value to result in a mutated chromosome.

3.3 Fitness Function Evaluation

The objective function, $f(\mathbf{x})$ is represented as a penalized fitness function $F(\mathbf{x})$ in order to contemplate constraint optimization in Genetic Algorithms. For engineering optimization problems, constraints plays an important role in imposing geometrical, material and other restrictions over the final design. Most gradient-based methods contemplate constraints directly, but in Genetic Algorithms those constraints have to be imposed by some artificial procedure. Different approaches can be adopted to handle constraints with genetic algorithms [7, 12]. An approach is remapping fitness values of both feasible and infeasible individuals in such a way that all feasible solutions have higher fitness than any infeasible solutions [20]. This concept assumes the superiority of the feasible solution. The assumption rarely holds since it always happens that some infeasible individuals

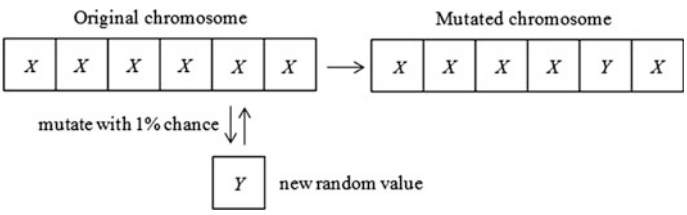

Fig. 7 Mutation

process very good genes that can be very valuable for late generations [6]. That is why these individuals are preferable during the evolution than many low fitness feasible solutions. It is therefore necessary to allow some infeasible individuals to have higher fitness than some feasible solutions [15]. Taking this into consideration the following method [6] which includes a normalized penalty relation over the fitness function is employed in this work:

$$f(\mathbf{x}) = \begin{cases} \frac{f(\mathbf{x}) - f_{\min}(\mathbf{x})}{f_{\max}(\mathbf{x}) - f_{\min}(\mathbf{x})} & \text{if} \quad g_i(\mathbf{x}) \geq 0 \\ \begin{cases} \alpha\left(1 - \left(\frac{e_i(\mathbf{x}) - e_{i_{\min}}(\mathbf{x})}{e_{i_{\max}}(\mathbf{x}) - e_{i_{\min}}(\mathbf{x})}\right)\right) & \text{if} \quad e_i(\mathbf{x}) \neq e_{i_{\min}}(\mathbf{x}) \\ \alpha & \text{else} \end{cases} & \text{if} \quad g_i(\mathbf{x}) < 0 \end{cases} \tag{3}$$

with a feasibility factor $\alpha = 0.6$, the min and max subscripts indicate the minimal and maximal values obtained on the present population and $e_i(\mathbf{x})$ represents a predefined error function for infeasible solutions. The feasible region is delimited by the space where the constraints are satisfied, $g_i(\mathbf{x}) \geq 0$. The infeasible region is delimited by the space where a given constraint is violated, i.e., $g_i(\mathbf{x}) < 0$.

The use of such normalized relations allows a more robust selection procedure. The worst feasible individuals will have fitness equal to 0 and the best one will have fitness 1. The worst has zero chance of being selected for reproduction, and the other individuals are added up for a Roulette selection mechanism. For the infeasible individuals, the function depends on the relative error of the constraint and it is scaled based on the maximum and minimum error obtained for the current population. Since the individual with minimal error is the best infeasible one, the value calculated was subtracted from 1 in order to make the solution with a smaller error have bigger values, thus bigger chances of survival. At the end, the value is multiplied by α, to limit the infeasible solutions and give them a smaller chance of survival than the feasible ones. In the case of $g_i(\mathbf{x}) = g_{i\min}(\mathbf{x})$, we have the best infeasible solution and it is assigned to it the maximal value, defined by feasibility factor α. This calculation is performed for all infeasible solutions. This approach is more robust than simple death penalty where infeasible individuals are eliminated from further reproductions [6]. Infeasible solutions are not eliminated, and the constraints are not necessarily full satisfied, but penalized if violated, leading to converge to a solution where the constraints are almost satisfied. The approach of Eq. (2) is well suited for a maximization optimization. For the case of minimization, the infeasible evaluations are inverted in order that the lower values are the best fitted ones.

Some of the mechanical applications of foam structures are the use as passive safety equipment for energy absorption under compression and sometimes also as a light stiffener inside foam core structures. In this sense, the structure should be more flexible in the first case and more rigid in the second. The fitness function should incorporate a measure of such value, and for this reason the internal energy W is employed, which is a standard approach for such type of structural optimization problem [14]:

$$f(\mathbf{x}) = W = \frac{1}{2}\int_{\Omega} \boldsymbol{\sigma}: \boldsymbol{\varepsilon}\, d\Omega \tag{4}$$

where $\boldsymbol{\sigma}$ is the stress tensor and $\boldsymbol{\varepsilon}$ is the strain tensor. The internal energy W is a measure of stiffness. Its minimization leads to a more rigid structure. On the other hand, its maximization produces a more flexible structure for a given fixed quantity of material.

The constraint employed in the present work is the total mass of the structure M:

$$\mathrm{M} = \int_{\Omega} \rho d\Omega \tag{5}$$

where ρ is the specific mass of the material and Ω is the structural domain. The mass should be controlled for some applications to ensure that the optimization algorithm does not attempt to boundless increase or decrease the mass to achieve the maximization or minimization of the internal energy [1]. In this way, the optimization procedure attempts to distribute a given amount of material to obtain the best structural performance possible. Thus, the error function for infeasible solutions $e_i(\mathbf{x})$ employed is:

$$e_i(\mathbf{x}) = \left(\frac{M_i}{M_0}\right)^2 \frac{W_i}{W_{\mathbf{0}}} \tag{6}$$

which increases when the actual mass M_i of an individual is greater than a reference initial mass of an individual M_0 multiplied by the actual internal strain energy relation between the actual and reference individual W_i/W_0. The mass constraint is required since, otherwise, the optimization procedure would completely fulfil the structural domain with material in order to obtain a stiffer structure (or completely remove all the material in order to obtain a more flexible structure). For maximization, the inverse relation of mass, M_0/M_i, should take place instead of M_i/M_0.

3.4 Algorithm

The coupling of the finite element solver [11] with the genetic algorithm program [8] is performed with Grasshopper tools [10]. Galapagos evolutionary solver is modified to employ Eq. 3 as fitness function and uses the discussed approaches of selection, crossover and mutation. Grasshopper is coupled with the program Rhinoceros [21], allowing the linking of all geometry description with structural analysis and optimization. Thus, the Voronoi tessellation can be modified by changing the number of seeds by the genetic algorithm optimization together with performing structural analysis by the Finite Element Method, which is required for the optimization.

4 Applications

4.1 Example 1

The first example studied consists of a rectangular foam structure with dimensions 10 mm × 5 mm. The material has the following properties: $E = 70{,}000$ N/mm^2 and $\nu = 0.33$, where E is the elastic Young's modulus of and ν is the Poisson's ratio. The foam beams are modeled with constant cross section area $A = 0.0258$ mm^2, which is the average measured value obtained from experimental data for an open cell with average density of $\rho_f = 217$ kg/m^3 [23]. The applied boundary condition is that the structure is simply supported at the bottom corners and load is applied on the middle of the upper border, with $P = 5$ kN, as shown if Fig. 8. Due to the symmetry, only half of the structure is modeled. The rectangular domain of this symmetric part is divided into 25 square sub-domains with a 5 × 5 distribution. Each sub-domain is allowed to have one, five, ten, twenty or thirty seeds randomly positioned inside it. This range of discretization was adopted because it generates a representation of the foam geometry in which the medium distance between internal seed points contained in the region delimited by the sub-domain and the edge length are in agreement with expected values for good representation of the foam (Sect. 2). Larger number of seeds would lead to a not consistent modeling of the foam for the adopted edge length. Only five possibilities of number of seeds are allowed in order to limit the search space of the optimization problem. A representation of the case where all sub-domains exhibits the same number possible number of seeds is displayed in Fig. 9. The average density of each case are 165 kg/m^3, 235 kg/m^3, 380 kg/m^3, 500 kg/m^3 and 615 kg/m^3 for one, five, ten, twelve or thirteen seeds, respectively. The case with all sub-domains with five seeds is used as the reference case because of the better agreement of this case with experimental measured data for which the material properties were evaluated. This reference case is also used to define the reference values of strain energy W_0 and mass M_0.

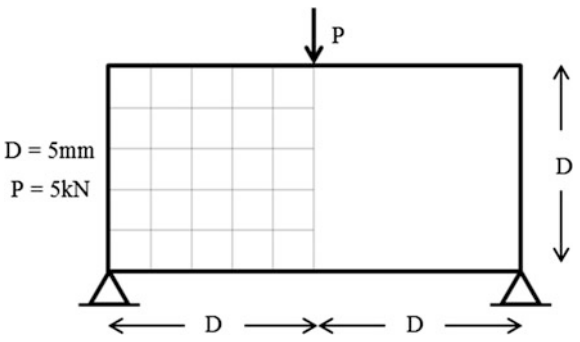

Fig. 8 Geometry, boundary conditions and discretization of example 1

In order to evaluate the convergence of the problem, genetic algorithms are used for three cases of population size: 100, 300 and 500 individuals with all cases evaluated through 100 generations. The relative objective function $f_i = W_i/W_0$ to be minimized is the internal strain energy, evaluated as the relation between the actual internal strain energy W_i of the ith individual and the reference internal strain energy, W_0. The penalty function is employed to control the total mass of the structure using an inequality constraint. Thus, the total mass of the structure must be smaller or equal than M_0, resulting in the constraint $M_i/M_{0-1} \leq 0$, where M_i, is the mass of the ith individual.

The evolution of the best relative fitness function and the average relative fitness along the generations are presented in Fig. 10a and b, respectively. Convergence of the best fitness when 300 and 500 individuals were used is similar. A population of only 100 individuals, on the other hand, seems to be small for the current problem. The case with 500 individuals has more bio-diversity through the generations, as can be observed by the average relative fitness functions of Fig. 10b. This allows a faster convergence compared with the case with 300 individuals (Fig. 10a). The best fitness obtained is $F_{100} = 0.31$, which corresponds to a reduction of about 70 % of the internal strain energy of the homogeneous mass distribution case (Fig. 9 for 5 seeds) with an optimal mass distribution of the total mass of the homogeneous reference.

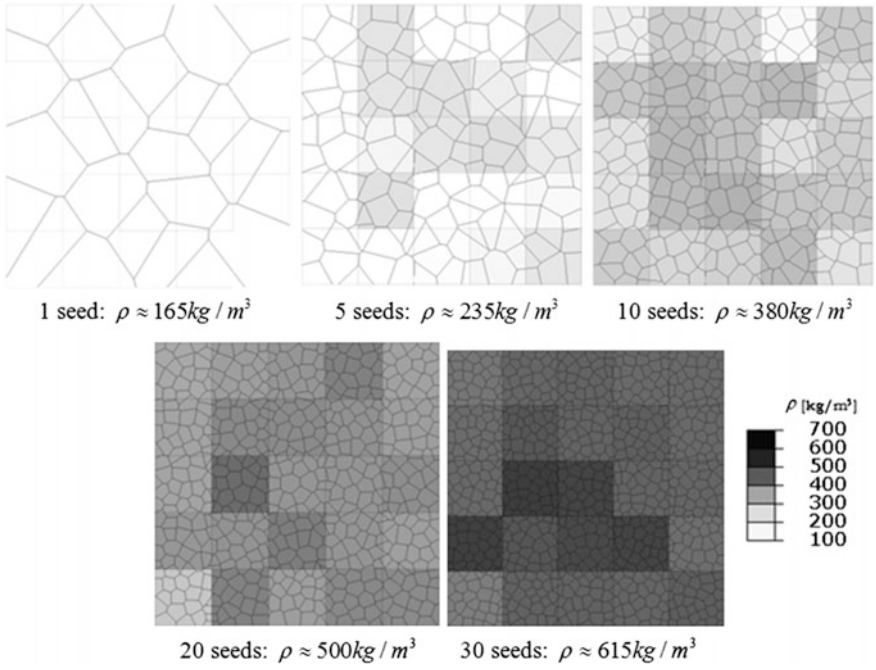

Fig. 9 Average density if all sub-domains have the same number of possible seeds for example 1

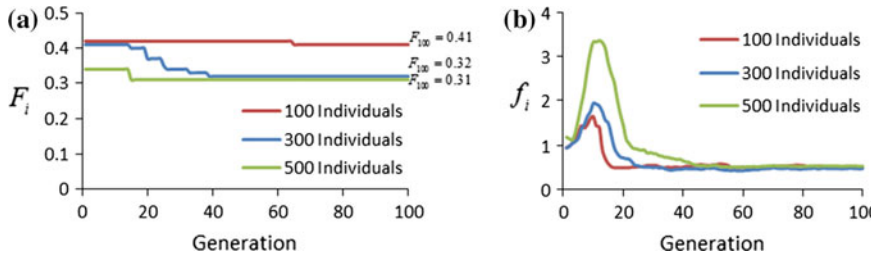

Fig. 10 Convergence of example 1. **a** Best fitness. **b** Average fitness

The best density distribution and the corresponding foam structure of each analyzed case are shown in Fig. 11. A clear linear pattern of mass concentration from the point of load application to the supports becomes more visible for the cases with 300 and 500 individuals. For the case with only 100 individuals some spurious mass concentration at the bottom of the structure appears. With this pattern, the structure has less stress due to bending, with more stress due to axial compression, reducing the internal strain energy, acting like a truss structure (Fig. 12). The material distribution obtained in this example is compatible with the material distribution obtained with topology optimization works [2].

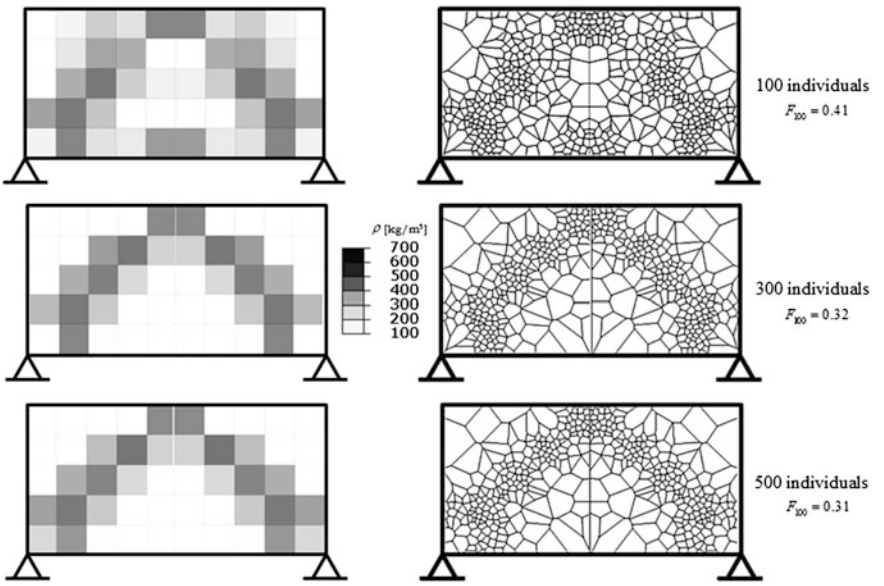

Fig. 11 Density distribution of example 1

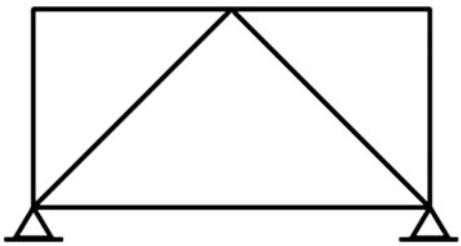

Fig. 12 Truss analogy of density distribution of example 1

4.2 Example 2

The second example studied consists of a quadrangular foam structure with dimensions of 5 mm × 5 mm. All displacements are constrained in the left border. Two vertical forces are applied, as shown in Fig. 13. The same material properties of the first example are employed. The rectangular domain is divided into 25 square sub-domains with a 5 × 5 distribution. Each sub-domain can have one, five, ten, twenty or thirty seeds randomly positioned inside it, like in the first example and the case with five seeds is used as the reference case for mass M_0 and internal strain energy W_0. A population with 300 individuals through 150 generations is employed. Two optimization problems were solved: minimization of the internal strain energy (as in the first example) and maximization of the same quantity.

The evolution of the best relative fitness for minimization and maximization of the strain energy are presented in Fig. 14a and b, respectively. For minimization, the best fitness value obtained is $F_{150} = 0.62$ and for maximization $F_{150} = 1.77$. The optimal density distribution obtained and the corresponding foam structure is shown in Fig. 15. For minimization of the internal strain energy, the density distribution concentrates the mass in the right side and central region of the structure.

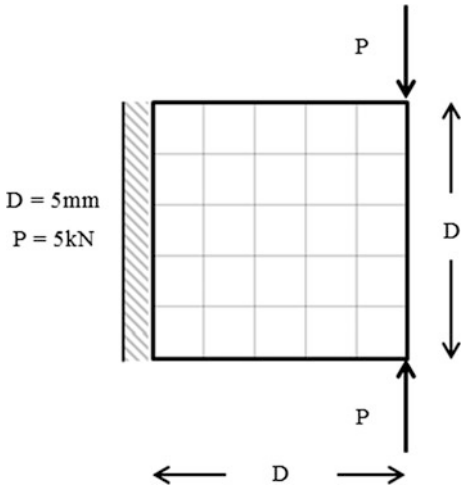

Fig. 13 Geometry, boundary conditions and discretization of example 2

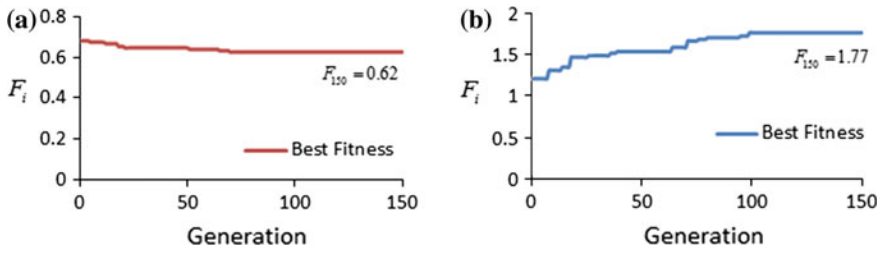

Fig. 14 Convergence of example 2. **a** Minimization. **b** Maximization

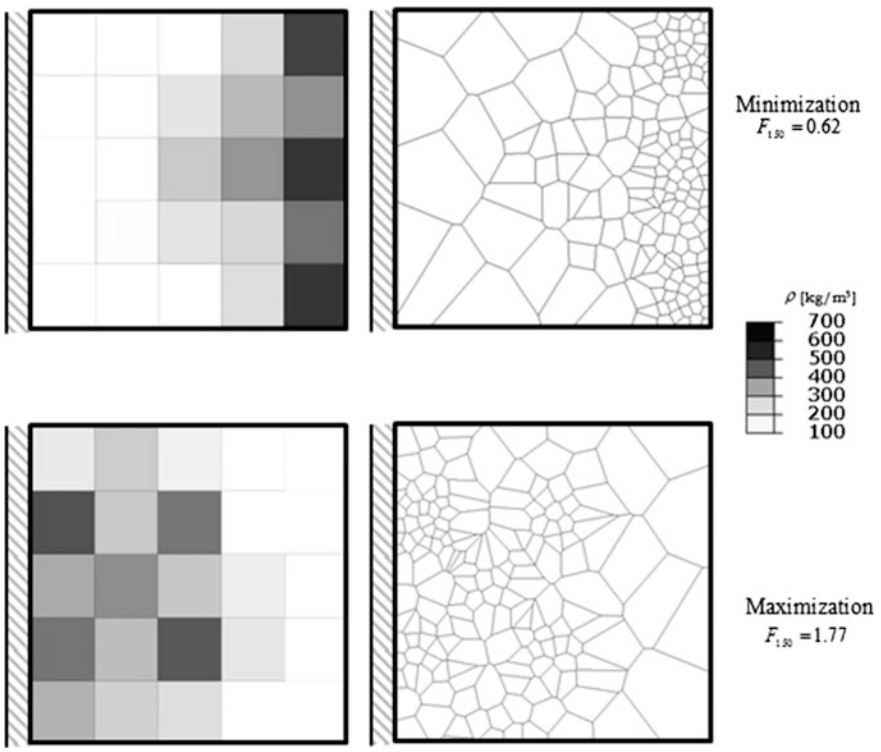

Fig. 15 Density distribution of example 2

The pattern of mass distribution for the maximization case has mass increase in the left and central region, with a more widespread distribution. The region closer to the applied loads has lower density. This example shows that different patterns of mass distribution are developed for the case of maximization and minimization of the strain energy. Thus, optimizing the density distribution it is possible to increase or decrease the stiffness or flexibility of a foam structure.

4.3 Example 3

The last example studied consists of a rectangular foam structure with dimensions of 10 mm × 5 mm. All displacements of the left border are constrained (Fig. 16). The same material properties of the first and second examples are employed. The rectangular domain is divided into 18 square sub-domains with a 3 × 6 distribution. Each sub-domain can have one, five, ten, twenty or thirty seeds randomly positioned inside it, like in the other examples studied and the case with five seeds is used as the reference case for mass M_0 and internal strain energy W_0. A population with 300 individuals through 150 generations is employed. Two optimization problems were solved: minimization of the internal strain energy and maximization of the same quantity.

The evolution of the best relative fitness for minimization and maximization of the strain energy are presented in Fig. 17a and b, respectively. The optimal fitness obtained were $F_{150} = 0.57$ and $F_{150} = 13.90$ for the case of minimization and maximization, respectively. The optimal density distribution obtained and the corresponding foam structure is shown in Fig. 18. For minimization of the internal strain energy, the density distribution concentrates the mass in the upper side and in the region close to the support (left side), in order to reduce the displacements and

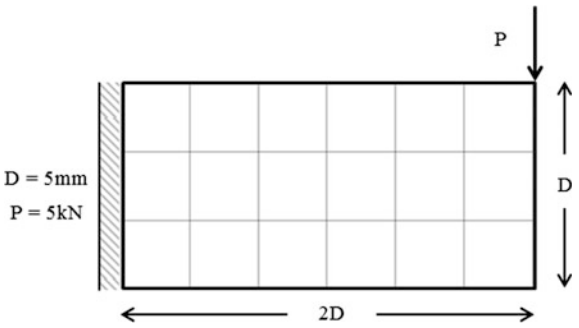

Fig. 16 Geometry, boundary conditions and discretization of example 3

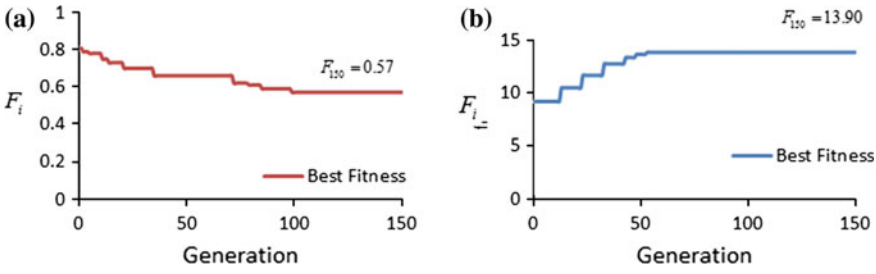

Fig. 17 Convergence of example 3. **a** Minimization. **b** Maximization

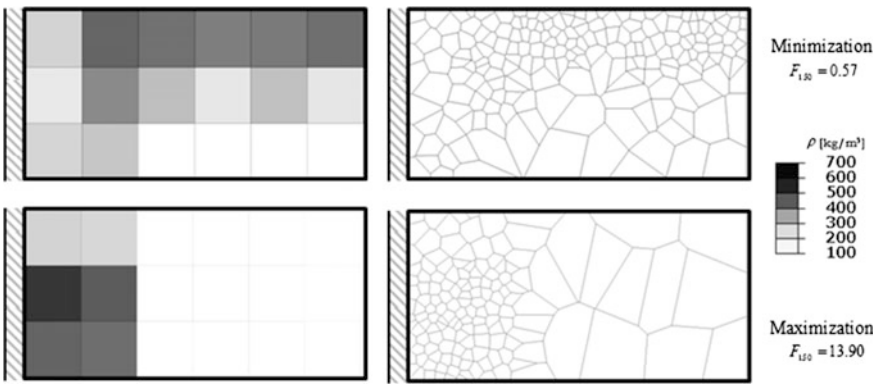

Fig. 18 Density distribution of example 3

deformation of the structure. For the maximization case, the mass distribution pattern becomes concentrated in the region near the supports. With this configuration, high displacements and stress appear in the structure due to bending effects, considerably increasing the internal strain energy up to about 14 times the reference homogeneous cases. The different geometry configuration of the domain and different applied load lead to a different pattern of mass distribution. Thus, an optimal mass distribution has to considerer the specific structural application of the foam structure.

5 Conclusions

The approach developed for foam structures optimization using the Voronoi tessellation has the main difference and advantage of incorporating an irregular representation of foam structure, being a geometrical representation closer to the natural irregularity present on real structures.

For the applications presented, the distribution of density, showing regions of high and low mass concentration were obtained, revealing the mass distribution tendency to achieve the objective function required to be optimized. For the analyzed cases, the flexure and the stiffness were optimized using genetic algorithms. The methodology allows determining the best pattern of mass distribution for structural applications.

When increasing the number of seeds inside a sub-domain, the mass distribution and stiffness of the sub-domain and near sub-domains also changes. As stiffness depends on the direction and the size of the bars, which vary randomly with the position of the Voronoi seeds inside the sub-domains, the optimization problem becomes non-linear in the sense that increasing the mass not always also increases the stiffness of the structure. This is one of the major difficulties found when optimizing structures using a random description.

The use of higher number of optimization variables is the next steps to be investigated, allowing the representation of larger portions of the structure. Higher computational costs are required for such step due to the larger number of optimization variables and larger computational time required to solve the structural analysis. The influence of second order effects and material nonlinearities should also be considered in further investigations.

Acknowledgments We thank CNPq, CAPES, FAPERGS, CESUP, and PROPESQ/UFRGS for continuous support of our research projects.

References

1. Bendsøe, M.P.: Optimization of Structural Topology, Shape and Material. Springer, Berlin (1995)
2. Bendsøe, M.P., Díaz, A.R., Lipton, R., Taylor, J.E.: Optimal design of material properties and material distribution for multiple loading conditions. Int. J. Numer. Meth. Eng. **38**, 1149–1170 (1995)
3. Bruns, T.E., Tortorelli, D.A.: Topology optimization of geometrically nonlinear structures and compliant mechanisms. In: Proceedings of the 7th AIAA/USAF/NASA/ISSMO Symposium on Multidisciplinary Analysis and Optimization. St. Louis, USA, pp. 1874–1882 (1998)
4. de Berg, M., Cheong, O., van Kreveld, M., Overmars, M.: Computational Geometry. Springer 1997
5. Dementjev, A.G., Tarakanov, O.G.: Influence of the cellular structure of foams on their mechanical properties. Mech. Polym. vol. 4, pp. 594–602 (1970a) (in Russian)
6. Dimčić, M.: Structural optimization of grid shells based on genetic algorithms. Ph.D. thesis, Institut für Tragkonstruktionen und Konstruktives Entwerten der Universität Suttgart (2011)
7. Mezura-Montes, E.: Constraint-Handling in Evolutionary Optimization. Springer, Berlin (2009)
8. Galapagos: Evolutionary Solver. http://www.grasshopper3d.com/group/galapagos (2013)
9. Gibson, L.J., Ashby, M.F.: Cellular Solids: Structure and Properties. Pergamon Press, Oxford, UK (1988)
10. Grasshopper: Generative Modeling of Rhino. http://www.grasshopper3d.com/ (2013)
11. Karamba: User Manual: Parametric Structural Modeling. Vienna (2012)
12. Lemonge, A.C.C., Barbosa, H.J.C.: An adaptive penalty scheme for genetic algorithms in structural optimization. Int. J. Numer. Methods Eng. **59**, 703–736 (2004)
13. Linn, R.V., Oliveira, B.F.: Finite element simulation of compression behavior of cellular. In: Proceedings of the CILAMCE 2008—XXIX Iberian-Latin American Congress on Computational Methods in Engineering (2008)
14. Lipka, A., Ramm, A.L.E.: A concept for the optimization of structures with foam core. In: Proceedings of the 6th World Congresses of Structural and Multidisciplinary Optimization. Rio de Janeiro (2005)
15. Nanakorn, P., Meesomklin, K.: An adaptive penalty function in genetic algorithms for structural design optimization. Comput. Struct. **79**(29–30), 2527–2539 (2001)
16. Öchsner, A., Lamprecht, K.: On the uniaxial compression behavior of regular shaped cellular metals. Mech. Res. Commun. **30**, 573–579 (2003)
17. Oliveira, B.F., Cunda, L.A.B., Öchsner, A., Creus, G.J.: Gurson Damage Model: applications to case studies. In: Proceedings of the CILAMCE 2006—XXVII Iberian-Latin American Congress on Computational Methods in Engineering (2006)

18. Oliveira, B.F., Cunda, L.A.B., Öchsner, A., Creus, G.J.: Finite element simulation of compression tests on cellular metals. In: Proceedings of the CILAMCE 2007—XXVIII Iberian-Latin American Congress on Computational Methods in Engineering (2007)
19. Oliveira, B.F., Cunda, L.A.B., Öchsner, A., Creus, G.J.: Comparison between RVE and full mesh approaches for the simulation of compression tests on cellular metals. Materialwiss. Werkstofftech. **39**(2), 133–138 (2008)
20. Powell, D., Skolnick, M.: Using genetic algorithms in engineering design optimization with non-linear constraints. In: Proceeding of the 5th International Conference on Genetic Algorithms. Morgan Kaufmann Publishers (1993)
21. Rhinoceros: *User Manual*, version 5.0 (2013)
22. Ribeiro-Ayeh, S.: Finite element modelling of the mechanics of solid foam materials. Ph.D. thesis, Stockolm, Sweden (2005)
23. Shulmeister, V.: Modelling of the mechanical properties of low-density foams. Ph.D. thesis, Delf University of Technology (1998)
24. Van Der Burg, M.W.D., Shulmeister, V., Van Der Geissen, E., Marissen, R.: On the linear elastic properties of regular and random open-cell foam models. J. Cell. Plast. **33**(1), 31–54 (1997)

Part IV
Polymers

Modeling Material Behavior of Polymers

Maria Anna Polak, Hossein Sepiani and Alexander Penlidis

Abstract Polymers are widely used in the automotive, aerospace and computer industries, building trades and many other applications. Many researchers have worked on the investigation and analysis of polymers' properties and behavior. The present chapter is devoted to polymer material research including testing and modeling. First, an introductory discussion on types of polymers and their tensile and compressive behavior and mechanical properties is provided. Experimental results show a high degree of nonlinearity in polyethylene behavior, which requires modeling based on coupled non-separable formulation. Representations of viscoelastic and viscoplastic models for linear and nonlinear behaviors are presented based on differential formulation. Finally, comparisons are made between the test data and the presented theory for the loading cases of short term, long term and step loadings.

1 Introduction

Polymers are the most widespread materials in nature. Silk, wool, DNA, cellulose, rubber and proteins are typical examples. In contrast, synthetic polymers, like polyethylene, nylon, polyesters, teflon and epoxy, are industrially derived from petroleum oil. They are often formulated for specific applications.

Polymers are widely used in the automotive, aerospace and computer industries, building trades and many other applications. Some important areas of applications of polymers are: fiber reinforced plastics, adhesives, insulation applications, optical applications, fibers and plastic pipes.

M.A. Polak (✉) · H. Sepiani
Department of Civil and Environmental Engineering,
University of Waterloo, Waterloo, Canada
e-mail: polak@uwaterloo.ca

A. Penlidis
Department of Chemical Engineering, Institute for Polymer
Research (IPR), University of Waterloo, Waterloo, Canada

P.A. Muñoz-Rojas (ed.), *Computational Modeling, Optimization and Manufacturing Simulation of Advanced Engineering Materials*,
Advanced Structured Materials 49, DOI 10.1007/978-3-319-04265-7_12

1.1 Micromolecular Background to Viscous and Solid Behavior

There are numerous ways to classify polymers from a micromolecular point of view. Most of the polymers can be classified as either thermoplastics or thermosets. These names are associated with general structural, thermal and processing characteristics. Basic structural differences greatly impact material properties. The fundamental physical difference between the two classes comes from the way the polymer molecules are connected with each other. Thermosets consist of cross-linked molecules, hence they have a network structure. This influences the specific behavior of these materials. In contrast to thermoset polymers, thermoplastic polymers can be made to flow over many processing cycles and they can be melted or molded.

Many polymers are two-phase materials consisting of an amorphous and a crystalline phase. What distinguishes the crystalline phase from the amorphous phase is that in crystals the macromolecules are packed together in an organized fashion as opposed to forming a random shape as in the case of the amorphous phase. When the polymer is subsequently subjected to a load, each phase behaves differently. The crystalline lamellae provide high yield stress, while the amorphous phase provides flexibility and hence a recoverable elastic response. Figure 1 shows a schematic representation of the two phases in polyethylene. The parallel lines at the centre of the figure represent the crystalline phase and the random configuration at the two sides represents the amorphous phase.

What gives most polymers, especially polyethylene, their uniform resistance to load is the existence of covalent bonds between carbon atoms. A covalent bond is a chemical bond in which the electrons are shared between the atoms. The angular relations between atoms in a polymer determine the strength of the covalent bond. To create a polymeric chain each central atom needs to have at least two bonds with other atoms. However, two carbon atoms can have double or triple bonds.

The cohesive properties of a polymer are due to van der Waals forces, which come from interactions between different molecules. There are two mechanisms that are at play when it comes to van Der Waals forces: one is the mass attraction and the other is related to momentary electron fluctuations. The strength of the van Der Waals force

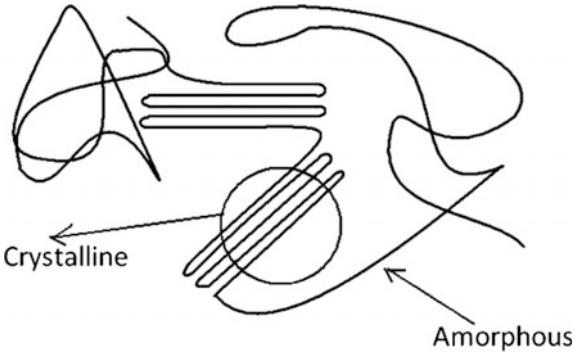

Fig. 1 Amorphous and crystalline phases within the polymer materials

relative to a covalent bond is usually about 1 %. However, there are several factors that can help increase this value to 10 %. Some of these factors are: proximity of molecules, increase in molecule size, and multiple bonds between carbon atoms.

Two general modes of deformation in polymer crystals are described. (1) Within chains of the polymer: This mode of deformation can be caused by stretching of covalent chains (this stretching is strongly resisted and therefore does not account for much of the deformation), change of angle between adjacent covalent bonds (which is more easily accommodated than the previous mode), and rotation of one bond with respect to the next adjacent bond (which is easier than the previous modes). (2) Between chains, which refers to deformations that are perpendicular to the chains. This type of deformation happens with much less resistance than the ones within the chains.

1.2 Types of Polymers and Their Tensile and Compressive Behavior

As mentioned previously, there are two main categories of polymeric material behavior.

Thermoplastic polymers: They can be made to flow and one can melt or mold them during processing. The crystalline phase is denser than the amorphous part. This results in enhancement in some properties like hardness, corrosion resistance or resistance to environmental stress cracking (ESC), friction and wear, and less creep or time-dependent behavior.

Examples include polyethylene, polypropylene, Polyamides (nylon), polytetrafluoroethylene, polyvinyl Chloride (PVC), polystyrene, polycarbonate, and polymethyl Methacrylate.

Thermoset polymers: These are used generally where high thermal and dimensional stability are required. They are suitable for electrical and thermal insulation, high performance composite applications and where high strength and modulus are required. Phenolics, polyurethanes, and epoxy-polymers are typical examples.

Tensile and compressive behavior: Polymers show solid and viscous as well as time-dependent behavior. The induced stress and strain are functions of time. They generally can be thought of as a three-dimensional surface. The stress-strain-time relationship, or time-dependent constitutive law, can be determined by loading a polymer specimen with constant stress (results in creep phase response) or constant strain (results in relaxation or isometric response). These two types of behavior and corresponding experiments will be discussed further in the following sections.

Creep phase: Viscous materials deform continuously when subjected to constant load. The initial strain is produced due to the pure elastic property of a polymer and is predicted by its stress-strain modulus. The elastic region is followed by the viscoelastic or viscoplastic response. The deformation slowly continues until rupture or yielding occurs. As seen in Fig. 2, the primary region is the early stage of loading when the creep rate decreases rapidly with time. Then, the creep rate

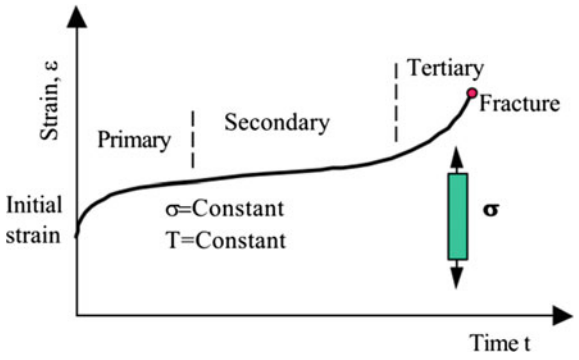

Fig. 2 Creep curve for viscous materials subjected to constant load [9]

reaches a steady-state, which is called the secondary creep stage. The next region is characterized by a rapid increase in strain (tertiary stage) and, finally, fracture.

The creep response depends on material properties and type, magnitude of applied stress, temperature and time. Thermoplastics and thermosets show different behaviors. As seen in Fig. 3, the strain will tend to a constant value after a long time for a thermoset, while the strain will increase without limit for a thermoplastic. Upon removal of the applied load, an immediate elastic recovery equal to the elastic deformation occurs for both types of polymers. It is then followed by a period of slow recovery. For an ideal thermoset material, a decay to zero can be seen, which happens after a long time interval (compared to the loading time).

Relaxation phase: This behavior is defined as a gradual decrease in stress with time under a constant deformation or strain. The resultant response is shown in Fig. 4. After a long period of time, both curves decay to a constant value. This asymptotic value is equal to zero for thermoplastic materials.

The relaxation and creep tests observations reveal both solid and fluid characteristics related to polymeric materials. The relation $E_{(t=0)} = \sigma_0/\varepsilon_c$ shows the instantaneous modulus of elasticity corresponding to the elastic solid behavior in a

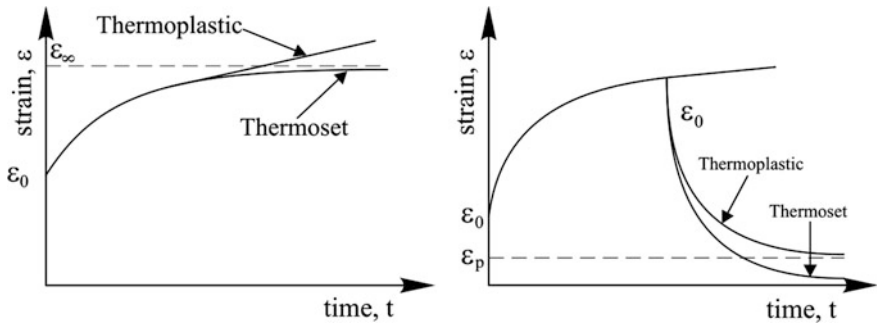

Fig. 3 Strain recovery in both thermoelastic and thermoset polymers [9]

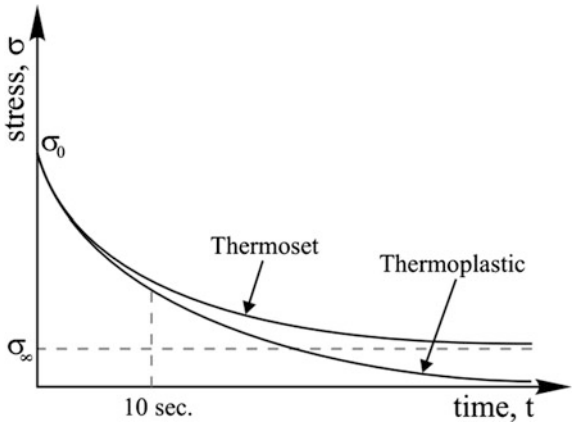

Fig. 4 Relaxation behavior for both thermoelastics and thermosets and the definition of the 10 s relaxation modulus [9]

relaxation test, where index c shows the constant value and index 0 shows the initial one. In similar fashion, the relation $D_{(t=0)} = \varepsilon_0/\sigma_c$ indicates the initial relaxation compliance which is related to the elastic solid portion of the material behavior.

Fluid behavior of polymers is defined by considering a time-dependent relaxation modulus as $E(t) = \sigma(t)/\varepsilon_c$. Plotting this modulus versus log time (Fig. 5) reveals that at short times, the stress is at a high plateau corresponding to a "glassy" modulus E_g, and then falls exponentially to a lower equilibrium "rubbery" modulus E_r.

Modulus versus compliance: Creep and relaxation are both illustrations of the same molecular mechanism, and are related to each other. However, even though $E = 1/D$ in both glassy and rubbery regions, in general $E \neq 1/D$. In particular, the relaxation response moves toward its equilibrium value more quickly than does the creep response. These factors are related by a convolution integral [29]

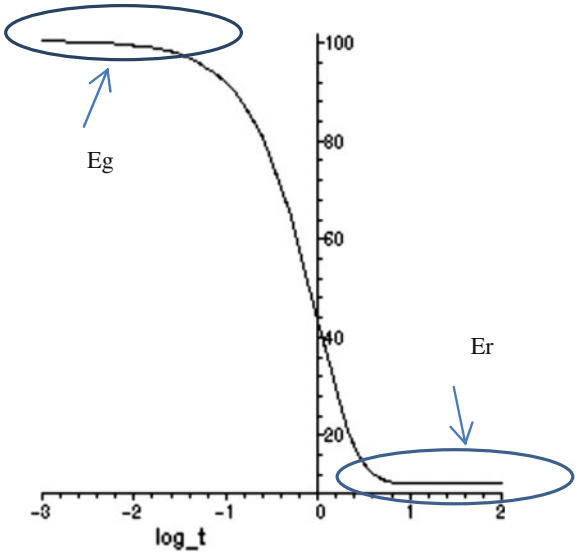

Fig. 5 The stress relaxation modulus E(t) versus log(t) [9]

$$\int_0^t E(t-\tau)D(\tau)d\tau = t \tag{1.1}$$

where t is time and τ is an integration parameter. Several approximation methods of interconversion between transient relaxation modulus, $E(t)$, and creep compliance, $D(t)$, are used in the literature. They are mostly based on adjustment of the elastic-like reciprocal relationship between these two parameters. The simplest interrelationship which is recommended for weakly viscoelastic materials is based on the quasi-elastic interrelationship defined as $E(t)D(t) \approx 1$ [46].

For linear viscoelastic materials in which the relaxation modulus and creep compliance can be represented by simple power laws over their transition zones, Leaderman [37], Christensen [19], Denby [21] and Park [46] presented the following interconversion formulas, respectively.

$$E(t)D(t) = \frac{\sin n\pi}{n\pi} \tag{1.2}$$

$$E(t)D(t) \cong \frac{1}{1 + \frac{n^2\pi^2}{4}} \tag{1.3}$$

$$E(t)D(t) \cong \frac{1}{1 + \frac{n^2\pi^2}{6}} \tag{1.4}$$

$$E(\alpha t)D(t) = E(t)D(t/\alpha) = 1 \tag{1.5}$$

in which $\alpha = \left(\frac{\sin n\pi}{n\pi}\right)^{1/n}$ and n is the local slope of the source function $F(t)(=E(t)$ or $=D(t))$, defined as

$$n = \left|\frac{d\log F(\tau)}{d\log \tau}\right|_{at\,\tau = t} \tag{1.6}$$

Linearity, nonlinearity and the concept of isochronous modulus: Two important definitions of linearity (or nonlinearity) are usually employed: the first is material linearity which deals with Hookean stress-strain behavior or linear relation between stress and strain; and the second is geometric linearity (or nonlinearity).

One of the main points in analysis is to determine if the material behavior under specific conditions is linear or nonlinear. This can be accomplished by determining if the creep compliance (or relaxation modulus) is independent of stress (or strain). This can be performed by plotting the stress-strain curves for different times. It can be seen in Fig. 6 and is called isochronous stress-strain diagram. If this isochronous variation of stress versus strain at any given time, t_i, is linear, the material is linear. In this case the creep compliance (or relaxation modulus) can be determined by $D(t_i) = \varepsilon_i/\sigma_i$ (or $E(t_i) = \sigma_i/\varepsilon_i$). This property is characterized as linear viscoelasticity. In the linear range the compliance (or modulus) is independent of stress

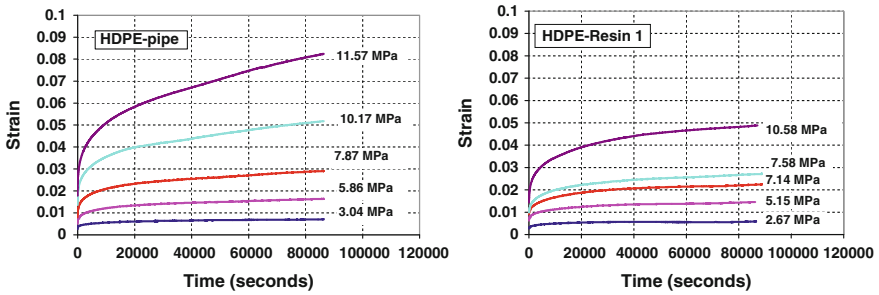

Fig. 6 Strain-time curves for 24-h creep tests on HDPE-pipe (*left*), and HDPE-resin (*right*) [40]

(strain). By increasing the applied stress or strain, a transition from linear to nonlinear viscoelasticity can be observed (Fig. 6). In the nonlinear region, the slope of isochronous stress-strain curve is no longer constant, meaning that the compliance (or modulus) is a function of stress (or strain).

It is worth pointing out that polymers generally exhibit linear behavior at low stresses, while at moderate or higher stress levels, the material is assumed to be nonlinear and will not obey the linear Hookean relationship.

Both the material nonlinearity analysis and geometric nonlinearity analysis are of researchers interest. The linearity corresponds to the small or infinitesimal deformation theory, while the nonlinearity follows the theory of large or finite deformation. Linearity in polymers is the result of the displacements of the material particles assumed to be much smaller than any relevant dimension of the body. With this assumption, the geometry and the constitutive properties of the material such as density and stiffness at each point of space can be assumed to be unchanged by the deformation. This results in simplification of the Lagrangian and Eulerian strain equations. Although a lot of work has been done on large deformation analysis of polymers (see, for instance, [24, 28, 27, 23]), infinitesimal behavior has limited applications in polymers (see [11]).

1.3 Experimental Considerations

The main reason for performing experiments is to determine material characteristics. Creep test involves recording the strain due to application of constant stress, while relaxation test yields the resultant stress when the material is subjected to constant strain. In some cases shear stress or strain experiments are done. Observations which show that deformations in viscoelastic materials such as polymers are more related to changes of shape than changes of volume, suggest that shear tests may be more valuable than the traditional uniaxial tests. The main material classifications which form the basis of mathematical modeling of polymers are as follows:

Viscoelastic and viscoplastic materials: The first level of material classification is determining if the material is described best by a viscoelastic or a viscoplastic model. A viscoelastic material shows a significant amount of delayed recovery upon unloading, whereas there remains a permanent residual 'plastic' strain for viscoplastic materials. Even though either model can be used to describe the time dependent "creep" of materials under uniaxial loading, viscoplastic models are generally used to describe high temperature creep of metals, while viscoelastic models are used to describe creep of ductile polymers [36].

Linear and nonlinear materials: By performing creep tests at several constant stress levels, a series of strain versus time curves are obtained. A plot of the compliance "$X = \varepsilon(t)/\sigma$" versus time can be used to determine if the material response at various stresses is linear or nonlinear. If the compliance is independent of the stress, meaning that a single curve is obtained for the compliance under different levels of constant stress, then the material is said to be 'linear'. Otherwise, the compliance is a function of stress, the material is known as 'nonlinear', and a nonlinear model must be used to represent its creep behavior [36].

Nonlinear materials-separable and non-separable: Nonlinear materials can be categorized taking into account whether the effects of stress (σ) and time (t) on strain (ε) are separable or not. If all compliance curves for nonlinear materials have the same 'shape', the material needs a nonlinear-separable model, i.e., same function for all stresses. ε is given by the following equation [36]

$$\varepsilon = h(\sigma)f(t) \tag{1.7}$$

Otherwise, if the shape of the compliance curves at all stress levels is not similar, then ε must be represented by a different function of time at each stress level. In this case, the material can only be described by a nonlinear non-separable model given by [36]

$$\varepsilon = g(\sigma, t) \tag{1.8}$$

1.4 Polymer Material Testing at the University of Waterloo

Polymer studies have been a major research area at the University of Waterloo. Material testing has included creep and tensile testing of a variety of polyethylenes and polyfluoroethylenes. Mechanical testing was supplemented by detailed analysis of polymer micromolecular properties [14, 48, 47]. This section outlines the testing done and the rationale behind it.

Liu [39] and Liu et al. [40] have done experiments on high density and medium density polyethylene (PE) materials. Testing was done on seven types of PEs and included short term tensile creep (3 and 24 h), long-term creep (7 days and 14 days), creep with step loading, constant stress rate, constant strain rate, and complex load history tests. The specimens were produced from resins by melting

them and machining, and from pipes by cutting out the samples. 24-h creep testing was done at different stress levels to examine time dependent and nonlinear behavior of the materials. The testing showed clear differences in the behavior of different HDPEs; examples of the results of HDPE 24 h creep curves for two different materials are shown in Fig. 6. Based on the measured strain values under different stress levels and observing creep compliance $D(t) = \varepsilon(t)/\sigma$ diagrams versus time [40], it can be inferred that polyethylenes show high degree of material nonlinearity and time dependency. Comparing the compliance curves in terms of similarity reveals that they cannot be separated by two stress dependent and time dependent terms. This leads to the conclusion that the final constitutive equation of polyethylene is a non-linear-non-separable relationship.

The long term, step loading, complex stress and strain history, and tensile tests, were all conducted to provide experimental data for mathematical modeling of the behavior of the materials. Some of the creep tests were later used for parameter estimation, while others served for model verification. Tensile rate tests were conducted with the stress rate equal to 1.0, 0.1, 0.05, and 0.01 (MPa/s), and also with the constant strain rates of 0.05, 0.01 and 0.005 (/s). The step loading tests involved tests where a material first creeps for a period of time under a constant stress and then creeps for a period of time at another (increased or decreased) constant stress level. An example of a strain–time curve for stepped loading creep tests of HDPE-Pipe is shown in Fig. 7. For increasing stress, progressive strain growth can be observed; for decreasing stress, strain reduction under sustained loading can be observed.

Behjat [5] and Behjat et al. [4] performed further experiments on six different HDPEs obtained from various industrial sources and designed for a variety of applications. These PEs had a wide range of environmental stress crack resistance (ESCR) values, determined by prior microstructural analysis testing of the resins performed by Cheng [14]. Two blow-molding resins (PE1 and PE4) had low ESCR

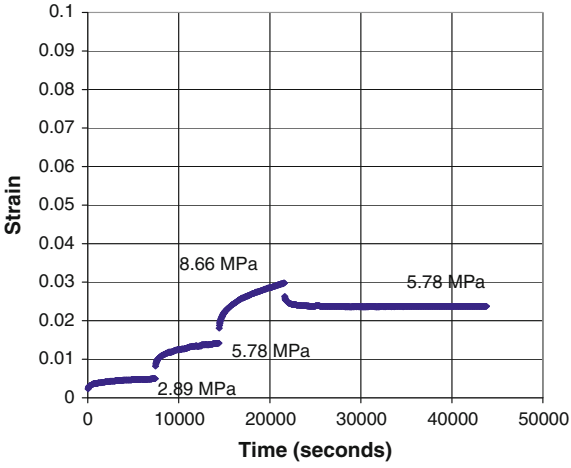

Fig. 7 Strain versus time tests [40]

and unimodal narrow molecular weight distribution (MWD). These were compared to pipe resins (PE 7-10) with high ESCR and broad or bimodal MWD. The differences in the short and long-term behavior of the two groups of resins provided meaningful information on the link between molecular structure and mechanical properties of PEs. The mechanical testing included short and long-term creep tests and strain rate controlled tests at 7 (mm/min) strain rate based on ASTM D638-03 standard recommendation.

ESCR in PE resins occurs through a slow crack growth mechanism under low applied stresses and long periods of time. This property is usually assessed by unreliable and time consuming testing methods, such as the notch constant load test (NCLT) on notched PE specimens in the presence of an aggressive fluid at elevated temperatures. Cheng et al. [18, 15, 16] performed tests on PE resins to determine their average molecular weights (MW), molecular weight distribution (MWD), short chain branching content, crystallinity, crystalline lamella thickness and area, ESCR by notch contact load test (NCLT) and hardening stiffness (HS) from short-term tensile strain hardening tests (i.e., the slope of the stress-strain curve during the strain hardening phase). They found that HS can be related to ESCR of PE. Following this, Behjat et al. [4] investigated the relationship of short term creep strain (8 h at 10 MPa) and ESCR. In Fig. 8 the hardening stiffness (HS) at a 7 mm/min deformation rate is plotted against short-term creep strain at 10 MPa for all resins. The 8-h strain (elastic plus creep strain) was chosen as an indicator of short term creep straining level. The graph indicates a relationship of increasing HS (and thus ESCR) with an increase in short-term creep strain, meaning that short-term creep is inversely related to the long-term creep behavior in environmental stress cracking.

Short chain branches (SCB) are well known to affect ESCR of PE [14]. A general trend of increasing SCB content is associated with an increase in creep strain. SCB interferes with the formation of crystalline lamellae, and hence, makes the PE more malleable.

The long-term mechanical behavior of polyethylene (PE) is of great importance especially in cases where structural integrity is required. In order to predict

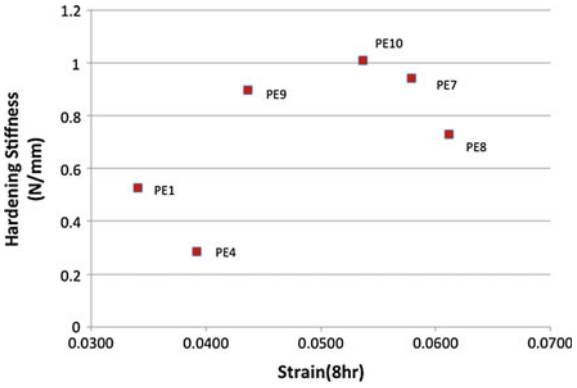

Fig. 8 Strain after 8 h of creep test at 10 MPa versus hardening stiffness [4]

characteristics of the mechanical behavior of PE, it is necessary to fully understand the molecular structure of the employed resins. Sardashti et al. [48] evaluated several micromolecular properties of PE. These properties influence an important performance indicator of PE for structural applications, namely, the environmental stress cracking resistance (ESCR). In [48], relationships between molecular structure and material response characteristics, mainly between molecular weight properties and short chain branching content in relation to strain hardening behavior of PE resins, were investigated based on results from tensile experiments.

Charbonneau [12] and Charbonneau et al. [13] conducted tests on ethylene tetrafluoroethyle (ETFE) films. ETFE is used for producing films used in the construction industry for tensile cushions used for roofs and wall cladding, e.g., China's National Aquatics Centre, commonly known as the Water Cube, which hosted aquatic events during the 2008 summer Olympic Games was built using ETFE. The test program included a series of 24-h uniaxial creep, 7-day creep, and stress-strain tests; all performed in the controlled temperature of 23 °C. Three film grades with varying thicknesses were tested. The 24 h creep tests were done at stress levels of 2, 8, 12 and 14 MPa. All films were tested in both the longitudinal (the direction of extrusion) and transverse directions. A minimum of two independent replications were done on each film type, at each stress level and in each direction.

All of the films were tested at all stress levels in both the longitudinal and transverse directions of the material, and in nearly every case, more strain was observed in the transverse direction than the longitudinal direction. The stress-strain curves in Fig. 9 show the same trend. The extrusion process by which ETFE film is created could be responsible for this anisotropic behavior because it causes the molecules to be stretched in the direction of extrusion such that they are aligned in the longitudinal direction. It could also be due to the crystal structure of the molecule, i.e., the degree of crystallinity, the location of the crystalline regions and the orientation of the crystals, or to thermally activated relaxation processes that occur during film processing.

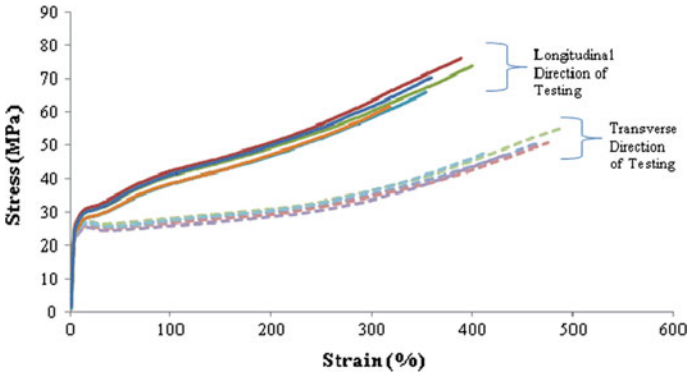

Fig. 9 Sample stress-strain curves for ETFE film tested in tension in both directions

2 Constitutive Modeling

Also known as anelasticity, viscoelasticity is the study of materials that exhibit both viscous and elastic characteristics when undergoing deformation. Viscous materials, like honey, resist shear flow and strain linearly with time when stress is applied. Elastic materials strain instantaneously when stretched and return to their original state once the stress is removed. Viscoelastic materials have elements of both of these properties and, as such, exhibit time-dependent strain. Whereas elasticity is usually the result of bond stretching along crystallographic planes in an ordered solid, viscoelasticity is the result of the diffusion of atoms or molecules inside of an amorphous material.

Another approach is based on viscoplasticity, which is a theory in continuum mechanics that describes the rate-dependent inelastic behavior of solids. Rate-dependence in this context means that the deformation of the material depends on the rate at which loads are applied. The inelastic behavior that is the subject of viscoplasticity is plastic deformation, which means that the material undergoes unrecoverable deformations when a load level is reached. Rate-dependent plasticity is important for transient plasticity calculations. The main difference between rate-independent plastic and viscoplastic material models is that the latter exhibit not only permanent deformations after the application of loads but continue to undergo a creep flow as a function of time under the influence of the applied load. The constitutive equations of these materials may be either linear or nonlinear.

The usefulness of a numerical model depends largely on three features [50]: (1) physically, the constitutive model should be able to predict material response well for a wide range of loading histories; (2) mathematically, the constitutive formulation should be simple and suitable for easy implementation in computer algorithms; and (3) the parameters in the model should be easily evaluated from experimental data.

In this section, different methods are discussed and constitutive models are developed which are useful for implementation in numerical procedures (e.g., finite elements).

2.1 Micro- and Macro-Scale Modeling

Two approaches are usually taken to develop constitutive models for polymeric materials. They are molecular and macroscopic in nature [10]. Micromechanical models emphasize the relation between the macroscopic properties of materials and their microstructure. The mechanical performance of polyethylene materials depends on loading and temperature conditions but also on phenomena occurring at the microscopic level (e.g., [33, 38, 49, 32]). In recent years, there has been a considerable interest in developing reliable experimental and mathematical models to study polymeric materials at different scales. Understanding the nonlinear

behavior of semicrystalline polyethylene by relating microstructure with macroscopic performance under both small [44, 45] and large [38, 20] deformations has been the focus of many studies.

Alvarado-Contreras et al. [2, 1], proposed coupling a damage mechanics formulation for the crystalline phase and its amorphous counterpart in polyethylene. The study involved modeling degradation processes taking place in the microstructure due to loading effects. The mechanical properties were studied considering not only the original microstructure but also the particular mechanisms activated at various deformation steps. The microscopic deterioration was modeled considering an isotropic damage variable. The evolution of this variable was linked to the deformation evolution and the changes in tie-molecule density. This resulted in a damage–coupled model for semicrystalline polyethylene, which effectively incorporated the developed constitutive equations for the crystalline and amorphous phases.

For predicting mechanical response of polymers for structural analysis, the macroscopic approach is usually employed. Examples include the work of Zhang and Moore [50, 51] and Drozdov et al. [26, 25, 22, 24]. The finite element programs developed for simulating viscoelastic or viscoplastic analysis use formulations similar to those of the incremental theory of plasticity, in which the total strain rate is separable into elastic and inelastic components [35, 52, 34].

In viscoelastic theory, constitutive equations are usually formulated using one of the differential or integral forms [42]. In contrast to the differential formulation (simulating the behavior by spring and dash-pot element configurations) which involves only the current values of stress and strain and their current time rates, the integral form takes into account the history of loading and it is more accurate and strict in nonlinear modeling. The viscoplastic formulation is usually an extension of viscoelastic theory which considers permanent residual strain by assuming the rate of total strain as summation of elastic and plastic strain rates. These forms of the constitutive equation in linear viscoelasticity are described in the following sections.

2.2 *Viscoelastic Modeling*

Two explanations can be offered for viscoelastic modeling. The first is defining the material response as a mixture of two simple cases: elastic and viscous. In the elastic behavior, the material acts as a spring in which the length increases by a certain amount u or ε, in proportion to the applied load f or σ. When the force is removed, the spring returns to its original length. Assuming linear-elastic behavior, Hooke's law, $\sigma = E\varepsilon$, is used to describe the stress-strain relation for the spring. In viscous behavior, a piston cylinder (dash-pot) system is used to describe the time-dependent behavior of viscous materials. In this case, the deformation rate is proportional to the applied force. Considering a linear relationship, the applied load is related to the rate of change of displacement by $\sigma = \mu\dot{\varepsilon}$. There are many possible

spring and dash-pot configurations that describe viscoelastic material behavior. *Maxwell Fluid* uses a spring and a dash-pot model in a series configuration and is suitable generally for viscoelastic fluid modeling. *Kelvin Solid* or *Voigt Solid* uses a spring and a dash-pot model in a parallel configuration and is suitable for modeling viscoelastic solid materials.

Direct use of spring and dash-pot elements and their combination in modeling of the material behavior leads to the following constitutive equation and the method is referred as differential formulation,

$$P(D)\sigma(t) = Q(D)\varepsilon(t) \tag{2.1}$$

where the operators P and Q are polynomials in D such that D^n is interpreted as d^n/dt^n. Due to the complicated configurations of these two elements, one of the most useful methods to reach the final governing equation is Laplace Transformation. The second approach to the definition of linear viscoelastic behavior is the hereditary integral form of the constitutive equations which takes into account the history of loading, described as:

$$\varepsilon(t) = \int_{-\infty}^{t} \psi(t-\tau)\dot{\sigma}(\tau)d\tau \tag{2.2}$$

$$\sigma(t) = \int_{-\infty}^{t} \phi(t-\tau)\dot{\varepsilon}(\tau)d\tau \tag{2.3}$$

where $\phi(t)$ is known as the stress relaxation function for the material, and $\psi(t)$ is known as the strain compliance function. They must be determined either by experiments or from the physics of the material structure. It is possible to consider the material to be linear at first and use the rule of linear superposition to calculate the strain produced by the common action of several loads (creep phase) or stress caused by the application of several strain constraints (relaxation phase). This is what makes this method special for non-linear modeling by means of linear superposition. The procedures for both creep and relaxation are the same. For any additional strain (stress), time is measured by a clock that starts at $t = \tau$. The total strain for $t > \tau$ is [31]:

$$\varepsilon(t) = \int_{\tau=-\infty}^{\tau=+\infty} \psi(t-\tau)d\sigma(\tau) \qquad (creep\ phase) \tag{2.4}$$

$$\sigma(t) = \int_{\tau=-\infty}^{\tau=+\infty} \phi(t-\tau)d\varepsilon(\tau) \quad (relaxation\ phase) \tag{2.5}$$

This form plays a significant role in linear and non-linear modeling of viscoelastic and viscoplastic materials. Either Eq. 2.4 or Eq. 2.5 can be used for defining the

material response. Creep functions are easier to obtain from experiments. In the linear modeling case, the stress in the experiment is kept constant and the strain is recorded with time. For a constant applied stress, Eq. 2.4 becomes:

$$\varepsilon(t) = \sigma_c \psi(t) \tag{2.6}$$

The material modeling task is to find an approximation function $\psi(t)$ that best fits test results. This is what one may get from the differential approach to viscoelasticity mentioned before in this section. In linear viscoelastic theory, Christensen [19] introduced the concept of fading memory, which states that the material response depends more on recent history than earlier events. Based on this, an assumption was made for the relaxation modulus and/or creep compliance:

$$A(t) = A_\infty - \sum_{i=1}^{N} A_i e^{-t/\tau_i} \tag{2.7}$$

In order to find the unknown parameters involved in A (assumed ψ and/or ϕ), the Prony series approximation is used. Based on what Christensen [19] stated as fading memory, the best alternative for the Prony series is a multi-Kelvin approach model, since it considers the instantaneous elastic strain, ε^e, and consequently the instantaneous elastic modulus, E_0 (or elastic compliance, ψ_0). The strain growth rate decreases with time and it becomes constant at a certain time. Therefore, the linear viscoelastic material behavior under constant stress can be described as Eq. 2.6, in which [40]:

$$\psi(t) = \psi_e + \psi_v(t) = \psi_0 + \sum_{i=1}^{N} \psi_i \left\{ 1 - exp\left(-\frac{t}{\tau_i} \right) \right\} \tag{2.8}$$

Or, similarly, for constant strain by substituting ψ by ϕ in which $\psi_0 = 1/E_0$ or $\phi_0 = E_0 = 1/\psi_0$. Material constants are E_0 and A_i with corresponding relaxation times τ_i. One can obtain parameter values by fitting the material response (Eq. 2.8) to experimental data.

2.3 Viscoplastic Modeling

The plasticity in semicrystalline polymers like polyethylene starts to develop at small strain and the material behaves with both viscoelastic and viscoplastic characteristics. Yield (the development of permanent deformation) occurs gradually with a steady transition from linear to nonlinear response. Thus, it is difficult to identify exactly where yielding commences. For this reason, classical plastic potential theory [52, 6, 7] which employs a yield surface is unsuitable for

characterizing rate effects. Instead, unified theories, [8, 41, 6, 7], which do not separate creep strains and plastic strains and which consider inelastic deformation to be rate dependent, are a better alternative.

Based on a yield criterion, the total strain rate is considered to be decomposable into elastic and inelastic components:

$$\dot{\varepsilon}_{ij} = \dot{\varepsilon}^{e}_{ij} + \dot{\varepsilon}^{P}_{ij} \tag{2.9}$$

Based on what Krishnaswamy et al. [36] have suggested, a power law function can describe the linear viscoplastic creep behavior. This function is able to model the growing deformation (strain) at decreasing rate, which doesn't approach an asymptotic value and the material remains time-dependent. In this model the compliance is expressed as a power law function [40]

$$\psi(t) = \psi_e + \psi_v(t) = \frac{1}{E_0} + C_0 t^{C_1} \tag{2.10}$$

where ψ_e is the instantaneous elastic component, $\psi_v(t)$ the time-dependent component, and E_0, C_0 and C_1 are material constants. Similar to viscoelastic modeling, the formulation constants are obtained by least squares. Substituting Eq. 2.10 into Eq. 2.6, results in the final constitutive equation for linear viscoplasticity:

$$\varepsilon(t) = \frac{\sigma_n}{E_0} + \sigma_n C_0 t^{C_1} \tag{2.11}$$

3 Parameter Estimation for Linear Modeling

Any configuration of spring and dash-pot obeys the following differential formula:

$$\begin{aligned} \sigma + p_1\dot{\sigma} + p_2\ddot{\sigma} + \ldots \\ = q_0\varepsilon + q_1\dot{\varepsilon} + q_2\ddot{\varepsilon} + \ldots \end{aligned} \tag{3.1}$$

and the material properties are represented by an expression consisting of multiplication of a constant and a time-dependent term. In the development of linear viscoelasticity models it is necessary to perform stress-strain experiments involving time as an independent variable. Thereafter, the experimental results are represented by a constitutive equation obtained by means of theoretical approaches. The relation is fitted to data and an error function has to be minimized.

The other way to construct constitutive equations is approximating a creep compliance or a relaxation modulus using an appropriate function. The function, then, is fitted to experimental data, and unknown parameters associated with the material response are obtained. Researchers use different methods of minimization along with approximation functions. One of the most common functions is called

Prony's series, which uses an exponential basis function. The Prony series is the most used mathematical curve to represent viscoelastic materials properties, which many researches have proved to be a representative and computationally efficient function for such materials. However, the procedure to obtain the Prony series unknown constants from experimental data is not trivial, involving many numerical tasks. Another notable point regarding this method is the complexity of viscoelastic time functions related to material properties, which involves complex mathematical relations that are easy to overcome using Prony's series.

Prony series method: Since the material properties are independent of the testing procedure, Eqs. (2.4)–(2.6) uniquely define the material response. Creep functions are easier to obtain from experiments. The material modeling task is to find an approximation function $\psi(t)$ and/or $\varphi(t)$ that best fits test results (see Eq. 2.7).

The equation representing the viscoelastic material is obtained by a mechanical model consisting of linear springs and dashpots (as discussed in previous sections). The alternative representation of the relation can be of the form of Eq. 2.8, which can be rewritten as:

$$A(t) = A_0 + \sum_{i=1}^{N} A_i(1 - exp(-t/\tau_i)) \tag{3.2}$$

where $A_0 = A_\infty + \sum_{i=1}^{N} A_i$. The terms A_∞ and A_0 are called independent terms. The exponential terms τ_i are known as time constants because they appear in association with the time variable t. The set of terms A_i are the dependent terms of the Prony series and the number of terms N is determined according to the experimental data. Usually, one must use around 8–15 terms in the Prony series in order to have a satisfactory mathematical model based on experimental data.

The objective is to determine the constants A_i and τ_i from measured values of A(t) at fixed moments in time. The problem is particularly difficult in that the τ_i appear non-linearly in the expression. Further the appropriate number N is also unknown. Collocation or least squares approaches are used for obtaining the unknown constants of Prony's series approximation function.

Prony-collocation method: let's say $f(t) = A(t)$. We suppose that experimental values of $f(t)$ are specified on a set of N equally spaced points. Therefore from experimental results we have the values for $f(0), f(\Delta t), f(2\Delta t), \ldots$. For simplicity we set $f_k = f(k\Delta t)$.

In Prony's method we will first find $\alpha_i = exp(-\Delta t/\tau_i)$ (from which $\tau_i = -\Delta t/ln(\alpha_i)$) and then we will find A_i, which are positive values. The procedure is to first note that

$$f_k = f(k\Delta t) = \sum A_i \alpha_i^k \qquad (k = 0, 1, 2, \ldots) \tag{3.3}$$

which is particular for Eq. 2.7, and that the α_j can be considered the roots of the polynomial

$$\begin{aligned} p(\alpha) &= \prod_{i=1}^{N} (\alpha - \alpha_i) \\ &= \alpha^N + c_{N-1}\alpha^{N-1} + \cdots + c_0 \end{aligned} \tag{3.4}$$

With these relations one can observe that

$$\begin{aligned} f_0 c_0 + f_1 c_1 + \cdots + f_{N-1} c_{N-1} + f_N &= 0 \\ f_1 c_0 + f_2 c_1 + \cdots + f_N c_{N-1} + f_{N+1} &= 0 \\ &\cdots \\ f_k c_0 + f_{k+1} c_1 + \cdots + f_{k+N-1} c_{N-1} + f_{k+N} &= 0 \end{aligned} \tag{3.5}$$

The first of these follows easily by expansion and noting that each α_j is a root of $p(\alpha) = 0$; the second follows by introducing $\bar{A}_i = A_i \alpha_i$, expanding, and using the root property again; the third follows by a similar procedure. Rewriting in matrix vector form, we have:

$$\begin{aligned} &\left[\begin{pmatrix} f_0 & f_1 & \cdots & f_{N-1} \\ f_1 & f_2 & & f_N \\ \vdots & & \ddots & \vdots \\ f_{N-1} & f_N & \cdots & f_{2N-2} \end{pmatrix} \right] \begin{pmatrix} c_0 \\ c_1 \\ \vdots \\ c_{N-1} \end{pmatrix} \\ &\qquad = - \begin{pmatrix} f_N \\ f_{N+1} \\ \vdots \\ f_{2N-1} \end{pmatrix} \end{aligned} \tag{3.6}$$

With these equations we have a set of linear equations that we can solve for c_i. One can use only the number of equations needed to uniquely determine c_i (as shown) or one can use more equations and over-determine the system—thus leading to a least squares solution. Once the c_i are known, the roots α_j of $p(\alpha) = 0$ can be determined. Once these are known one can solve the system

$$\left[\begin{pmatrix} 1 & 1 & \cdots & 1 \\ \alpha_1^1 & \alpha_2^1 & & \alpha_N^1 \\ \vdots & & \ddots & \vdots \\ \alpha_1^{N-1} & \alpha_2^{N-1} & \cdots & \alpha_N^{N-1} \end{pmatrix} \right] \begin{pmatrix} A_1 \\ A_2 \\ \vdots \\ A_N \end{pmatrix} = - \begin{pmatrix} f_0 \\ f_1 \\ \vdots \\ f_{N-1} \end{pmatrix} \tag{3.7}$$

for the A_i. These relations are the first N equations from Eq. 3.5. Note that in this procedure one needs to select N ahead of time.

Prony-least squares method: A linear least squares fitting is used by assuming values for the relaxation times τ_j in Eqs. 2.7 and 3.2. We define the squared error as

$$F(t_j) = \sum_{i=1}^{p} \left(f(t_i) - \bar{f}(t_i)\right)^2 \tag{3.8}$$

where p is the number of data (measurements), $\bar{f}(t_i)$ is a data measurement at time t_i, and $f(t_i)$ is the corresponding theoretical value (Eqs. 2.7 and 3.2). By setting $dF/dt_j = 0$ for $j = 1 \ldots N$ (N is the number of terms in Prony series), to minimize $F(t_j)$, a set of linear simultaneous equations with respect to the material parameters t_j is obtained.

$$[T]_{N\times N}\{A\}_{N\times 1} = \{B\}_{N\times 1} \tag{3.9}$$

where for Eq. 2.7

$$\begin{aligned} T_{ij} &= \sum_{k=1}^{p} \left(e^{-t_k/\tau_i}\right)\left(e^{-t_k/\tau_j}\right) \\ B_i &= \sum_{k=1}^{p} \left(\bar{f}(t_k) - A_\infty\right)\left(e^{-t_k/\tau_j}\right) \end{aligned} \tag{3.10}$$

and for Eq. 3.2

$$\begin{aligned} T_{ij} &= \sum_{k=1}^{p} \left(1 - e^{-t_k/\tau_i}\right)\left(1 - e^{-t_k/\tau_j}\right) \\ B_i &= \sum_{k=1}^{p} \left(\bar{f}(t_k) - A_0\right)\left(1 - e^{-t_k/\tau_j}\right) \end{aligned} \tag{3.11}$$

For this approach, see [40, 17].

4 Nonlinear Modeling

This section deals with nonlinear constitutive relations for polymers. Polyethylene is time dependent with a high degree of nonlinearity.

In the linear approach, the compliance is a function of time which means that for a constant applied stress a resultant strain is obtained and the constitutive equation has a separable nature of Eq. 1.7. The nonlinear constitutive equation obeys the non-separable format of Eq. 1.8.

4.1 Methods for 'Nonlinearization' of the Model Parameters

Liu et al. [40] obtained a separate set of material parameters for each stress level. The sets of constants for all creep tests created an array of material constants. The material parameters for stresses other than the tested stresses were obtained by linear interpolation. Thus, piece-wise linear functions were assumed for the material functions. The expressions for the linear interpolation of material parameters for non-linear viscoelatic modeling were the following:

$$\begin{aligned} E_0(\sigma) &= E_0(\sigma_m) + \frac{\sigma - \sigma_m}{\sigma_n - \sigma_m}\left[E_0(\sigma_n) - E_0(\sigma_m)\right] \\ \psi_i(\sigma) &= \psi_i(\sigma_m) + \frac{\sigma - \sigma_m}{\sigma_n - \sigma_m}\left[\psi_i(\sigma_n) - \psi_i(\sigma_m)\right] \end{aligned} \tag{4.1}$$

where σ_m and σ_n are stresses used for model development by considering $\sigma_m < \sigma < \sigma_n$. Similarly, for non-linear viscoplastic modeling:

$$\begin{aligned} C_0(\sigma) &= C_0(\sigma_m) + \frac{\sigma - \sigma_m}{\sigma_n - \sigma_m}\left[C_0(\sigma_n) - C_0(\sigma_m)\right] \\ C_1(\sigma) &= C_1(\sigma_m) + \frac{\sigma - \sigma_m}{\sigma_n - \sigma_m}\left[C_1(\sigma_n) - C_1(\sigma_m)\right] \end{aligned} \tag{4.2}$$

and the interpolation of the instantaneous elastic parameter, $E_0(\sigma)$, is the same as in the viscoelastic case, Eq. 4.1. The presented two-step curve-fitting approach works well at a given stress for a material for which the model is developed. However, since each polyethylene behaves differently under a creep test, the model compliance-stress relationship should theoretically be redefined for each specific material. This means that for each specific material new compliance functions of stress representing material parameters should be created.

In our recent unpublished work, continuous functions for the 'nonlinearizations' of model parameters for the case of viscoelasticity were proposed. The process of developing a non-linear model starts with a linear model for the material under constant stress (separable form) and then it is extended to the nonlinear one by considering effects of stress on the stress dependent part (non-separable form). Thus, the following stress-strain relationship is defined for predicting the response of the material under constant applied stress:

$$\varepsilon(t) = \sigma X(t) \tag{4.3}$$

In this formulation, $X(t)$ describes the creep compliance of the material and is based on the spring and dash-pot method of modeling described previously. According to the concept of fading memory, the material response depends more on recent history than on earlier events. Accordingly, this theory considers the following formulation for creep compliance:

$$X(t) = X_0 + \sum_{i=1}^{N} X_i\left(1 - e^{-t/\tau_i}\right) \tag{4.4}$$

where X_0 is the elastic time-independent compliance at time $t_0 = 0$, and X_i and τ_i are creep compliance and relaxation time, respectively, for the ith Kelvin element. N indicates the number of Kelvin elements in the model.

Most finite element implementations of this form assume that the creep compliance and relaxation modulus have the exponential form of Eq. 4.4, which is a form of a Prony series approximation, with $2 \times N$ unknown material properties (X_i and τ_i). The term $X_0 = 1/E_0$ is called an independent term. One can obtain parameter values by means of least squares estimation by fitting the Prony series to experimental data by fixing a set of τ_i or by pre-setting X_i and τ_i as power law functions of t.

X_i and τ_i can be expressed as power-law functions of stress. To reduce the number of material functions, which is equal to $2 \times N$, all values of X_i and τ_i are obtained using four parameters X_1, τ_1, m and α following the formulation presented by Zhang and Moore [50].

$$X_i = m^{1-i} \times X_1, \quad \tau_i = \alpha^{i-1} \times \tau_1 \tag{4.5}$$

The determination of the material functions proceeds in two steps. In the first step, and for a particular creep stress, Eqs. (4.3)–(4.5) are used to fit the corresponding experimental creep curve and find the specific unknown parameters by means of least squares (linear modeling). Then, in the second step, curve fitting is used to produce stress-dependent parameters $X_1(\sigma_n)$ and $\tau_1(\sigma_n)$ based on the values from linear modeling. This is referred to as 'nonlinearizing the constants' by assuming that they are functions of stress and obey the non-separable form of the kinematic relation [36].

For simplicity, constants m and α are considered to be stress-independent [51]. In recent unpublished work of ours, the curve fitting of the two parameters X_1 and τ_1 showed that the parameter distributions versus applied stress σ_n obeyed the following:

$$\begin{aligned} X_1^{-1} &= b_0 + b_1 exp(b_2 - b_3\sigma_n - b_4/\sigma_n) \\ \tau_1 &= c_0 exp(-c_1 + c_2\sigma_n + c_3\sigma_n^2 - c_4\sigma_n^3) \end{aligned} \tag{4.6}$$

where X_0 is a constant that is obtained from experimental results for each test and it is assumed to vary with respect to stress. The constants b_i, c_i, m and α are obtained via least squares for each examined material. It can be seen that X_0 is approximately constant for all stress levels, and the variation versus stress is trivial and therefore negligible. These material properties are used to plot the response of HDPE resin versus experiments in Fig. 10.

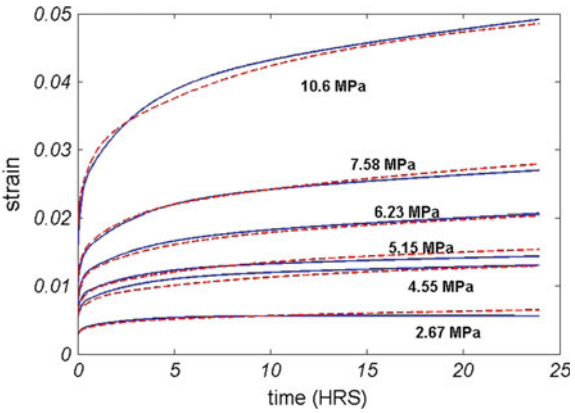

Fig. 10 Experimental (*continuous line*) and non-linear viscoelastic model (*dashed line*) results for 24-h creep tests for an HDPE resin

The nonlinearization for viscoelasticity starts with the assumption that the plastic flow starts to develop when there is a small strain and the material behaves in both viscoelastic and viscoplastic fashion. Since yield occurs gradually with a steady transition from a linear to a nonlinear response, unified theories, which do not separate creep strains and plastic strains, are a better alternative than those that consider creep and plasticity as separate phenomena [50]. Here is the non-separable viscoplastic model that has been discussed in this chapter:

$$\varepsilon = \varepsilon^e + \varepsilon^v = \frac{\sigma}{E_0} + \sigma C_0 \left(\frac{t}{T}\right)^{C_1} \tag{4.7}$$

Similar to viscoelastic modeling, the determination of the material constants proceeds in two steps. In the first step, for a particular constant creep stress, Eq. 4.7 is used to fit the corresponding experimental creep curve and determine the unknown parameters (linear modeling). Then, in the second step, 'nonlinearizing' curve fitting is used to find the distribution of parameters, $C_0(\sigma)$ and $C_1(\sigma)$ with respect to stress. E_0 is also obtained from the experimental data at each stress level.

The first step leads to the material constants, and corresponding plots of model and experiments are shown in Fig. 11 for HDPE resin. Based on the variation of the constants versus stress, the following equations can be fitted:

$$\begin{aligned} C_0 &= \left(b_1 + b_2\sigma_n + b_3\sigma_n^2\right)\sigma_n^{\left(b_4 + b_5\sigma_n + b_6\sigma_n^2\right)} \\ C_1 &= m_1 + m_2\left(1 + \frac{1}{2}atan(sa)\right) \\ T &= T_1\sigma_n^{d_0} \end{aligned} \tag{4.8}$$

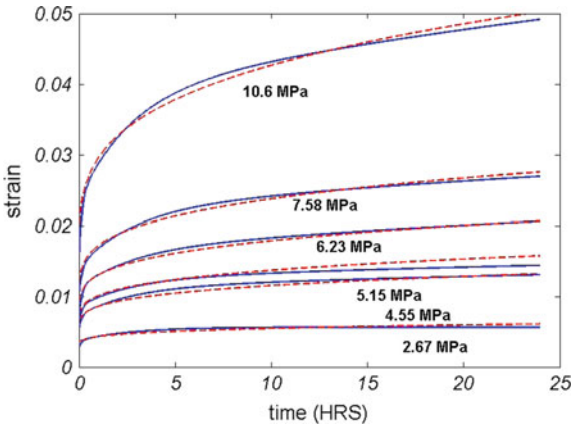

Fig. 11 Experimental (*continuous line*) and non-linear viscoplastic model (*dashed line*) results for 24-h creep tests for an HDPE resin

5 Extending the Material Parameters to Longer Times Frames

In order to realistically model the service life-time for polymeric structures, long-term prediction methods are needed within the developed constitutive law. The constitutive laws are normally formulated based on available short-term tests. One of the most popular methods for predicting long term properties of polymers is 'tme temperature superposition', which is based on short term behavior and uses the information from short duration tests. The method uses the similarity between the variation of relaxation modulus (creep compliance) with time and temperature. The variation of time and temperature of the moduli (compliances) of a polymer is often said to be related or even equivalent [3, 43]. There are also several test methods for evaluating long-term properties of materials, including creep test ASTM-D2990, stress relaxation test D2991, hydrostatic test D1598, D2837, and DMA (Dynamic Mechanical Analysis).

A nonlinear approach has been proposed by recent work of ours and an overview is given in the following section.

5.1 Using Short Term Testing for Predictions at Longer Time Frames

The important point of constructing a mathematical model is predicting the response of creep behavior over extended operating time. Using the material properties and modeling constants, as described in Sect. 4, resulted in good agreement during the test time interval which was 24 h (creep test time, Figs. 10 and 11). To examine the validity of the model for extended times, the method proposed herein is to observe the trend of material constants with respect to test time. First,

the curve fitting is done for all materials in different test times, namely: 10, 14, 18, 20, 22 and 24 h. This allows one to observe how the modeling constants are dependent on test time (λ). It is proposed that the material parameter change over test time can be represented by the following equations for the viscoelastic case:

$$\begin{aligned} b_i(\lambda) &= b_i' \lambda^{d_i} \qquad for \quad i = 0, 1, 2 \\ b_i(\lambda) &= b_i' / \lambda^{d_i} \qquad for \quad i = 3, 4 \\ c_0(\lambda) &= c_0' \times \lambda^{d_5} \end{aligned} \tag{5.1}$$

λ stands for test time and c_0', b_i' and d_i are constants independent of the test time used to develop the model.

Similarly, when the same method is applied to viscoplastic modeling, the following equations for the dependency of constants on λ are obtained:

$$\begin{aligned} b_i(\lambda) &= b_i' \times \lambda^{d_i} \qquad for \quad i = 0 \sim 6 \\ m_i(\lambda) &= m_i' \times \lambda^{n_i} \qquad for \quad i = 1, 2 \\ sa(\lambda) &= sa' \times \lambda^{s} \\ T_1(\lambda) &= T_1' \times \lambda^{T_2} \end{aligned} \tag{5.2}$$

5.2 *Viscoelastic (NVE) and Viscoplastic (NVP) Long Term Responses*

The parameter identification procedure is based on a minimization of the total error between experimental data and model predictions. The models have been developed using the data from 24 h creep testing (using 10, 12, 14… hour time frames). Then the model was verified using experimental data for long-term creep of polyethylene [40]. The model showed the ability to predict well the independent data from long-term testing; it sufficiently describes the variation of strain in time for the loading history. The long-term scheme was validated by tests on PIPE material and other HDPE resins. Creep tests were conducted under three different stress levels of 4.42, 6.08 and 8.15 MPa over 40 h [40]. In addition, creep strain measurements on a pipe material were conducted under 6.89 MPa in a seven-day test [40].

Both NVE and NVP models have been applied to the experimental data. According to the definition, the parameter λ is set to be 40 and 168 for case I and case II, respectively. The theoretical results are depicted in Figs. 12, 13, 14 and 15 and compared with experimental ones.

Looking at Figs. 12, 13, 14 and 15, it can visually be inferred that the NVE model results in smaller fitting error for the long-term strain response prediction compared to the NVP model. The NVE model seems more capable in modeling

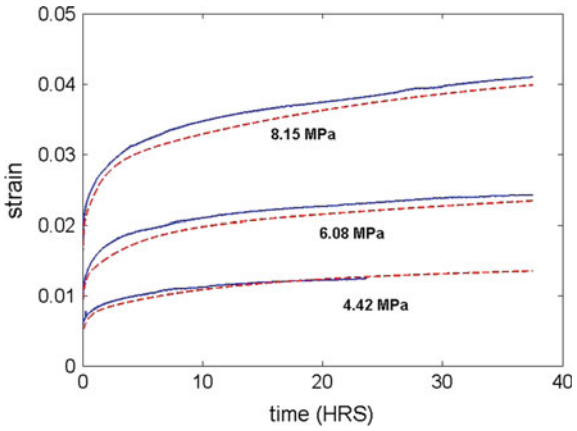

Fig. 12 Experimental (*continuous line*) and NVE model prediction (*dashed line*) in 40 h test time (pipe material)

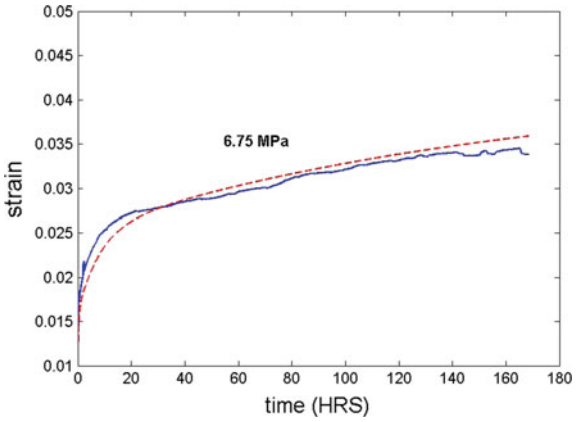

Fig. 13 Experimental (*continuous line*) and NVE model prediction (*dashed line*) in 7 days test time (pipe material)

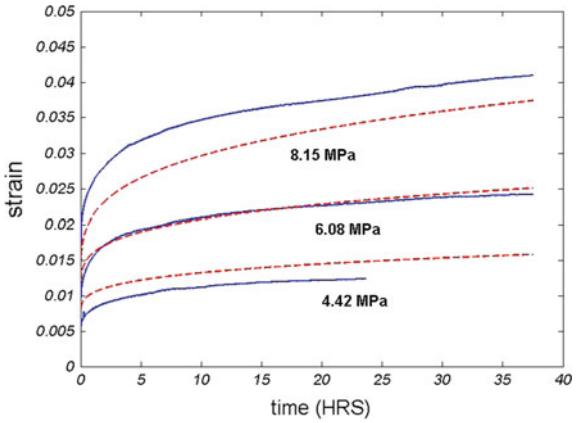

Fig. 14 Experimental (*continuous line*) and NVP model prediction (*dashed line*) in 40 h test time (pipe material)

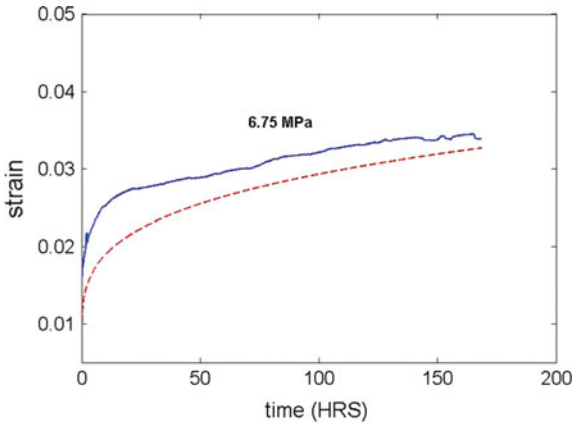

Fig. 15 Experimental (*continuous line*) and NVP model prediction (*dashed line*) in 7 days test time (pipe material)

polymer behavior in extended time. The most important reason for this is that the NVP model has only two parameters to adjust during fitting, while NVE has more, resulting in more accurate curve fitting. The other difference is that based on the nature of the governing equation for each model, viscoplastic materials tend to extend under continuing applied load, while viscoelastic strain reaches an upper limit after a while.

6 Modeling the Response Under Varying Stress

The modified superposition principle [30] employs the assumption that the strain response after any abrupt change of stress is the sum of the strain due to the first loading and the strain response due to each change of stress. This approach makes use of the equations from the multiple functions for constant stress (linear models) to describe the nonlinear yet synergistic characteristics of creep behavior. In this method, the modification of the superposition principle consists of relaxing the requirement of linearity in stress and treating nonlinearity as discussed in this section.

6.1 Modified Superposition Principle (MSP)

The stress-strain equation for viscoelastic and viscoplastic materials consists of time-independent and time-dependent parts:

$$\varepsilon = \varepsilon^e + \varepsilon^v = f^e(\sigma) + f^v(\sigma, t) \tag{6.1}$$

where $f^e(\sigma)$ denotes the elastic strain ε^e, and $f^v(\sigma, t)$ denotes the time dependent strain ε^v, caused by applied constant stress.

The superposition method can be described as follows [30]. When the state of stress is abruptly changed from σ_1 to σ_2 at time t_1, the creep behavior can be considered as if, at this instant, stresses σ_1 are removed and at the same time stresses σ_2 are applied to the specimen, both being considered as independent actions. The recovery strain ε' resulting from removal of σ_1 after loading time t_1 is given by:

$$\begin{aligned} \varepsilon' &= f^e(\sigma_1) - f^e(\sigma_1) + f^v(\sigma_1, t) - f^v(\sigma_1, (t - t_1)) \\ \varepsilon' &= f^v(\sigma_1, t) - f^v(\sigma_1, (t - t_1)) \end{aligned} \tag{6.2}$$

The creep behavior due to σ_2 applied at t_1, denoted by ε'', is

$$\varepsilon'' = f^e(\sigma_2) + f^v(\sigma_2, (t - t_1)) \tag{6.3}$$

The total strain is the sum of ε' and ε'' and equal to

$$\begin{aligned} \varepsilon = {} & f^v(\sigma_1, t) - f^v(\sigma_1, (t - t_1)) + f^e(\sigma_2) \\ & + f^v(\sigma_2, (t - t_1)) \end{aligned} \tag{6.4}$$

In this theory, the time-independent part of the strain response depends only on the final state of stress applied to the specimen. The time-independent part of the strain on loading and unloading follows the same path. Thus, when the stress state changes from σ_1 to σ_n, the total strain response after the nth stress change will be as follows:

$$\begin{aligned} \varepsilon = {} & f^e(\sigma_n) + \sum_{p=1}^{n} \left[f^v\left(\sigma_p, \left(t - t_{p-1}\right)\right) \right. \\ & \left. - f^v\left(\sigma_{p-1}, \left(t - t_{p-1}\right)\right) \right] \end{aligned} \tag{6.5}$$

For example, consider a $2N + 1$-parameter (N Kelvin units) spring and dash-pot model. The stress-strain relationship under constant stress for the kth step is as follows:

$$\begin{aligned} & \varepsilon(t) = f^e(\sigma_i) + f^v(\sigma_i, t) \\ \Rightarrow\ & \varepsilon_k(t) = X_{0,k}(\sigma, \lambda)\sigma_k \\ & \quad + \sum_{j=1}^{k} \left\{ \sum_{i=1}^{N} X_{i,j}(\sigma, \lambda) \left[1 - exp\left(- \frac{t_k - t_{j-1}}{\tau_i(\sigma, \lambda)} \right) \right] \sigma_j \right. \\ & \quad \left. - \sum_{i=1}^{N} X_{i,j-1}(\sigma, \lambda) \left[1 - exp\left(- \frac{t_k - t_{j-1}}{\tau_i(\sigma, \lambda)} \right) \right] \sigma_{j-1} \right\} \end{aligned} \tag{6.6}$$

If the stress state changes from σ_1 to σ_2, the total strain response for each step is:

$$0 \le t < t_1 \qquad \varepsilon_1(t) = X_{0,1}\sigma_1 + \sum_{i=1}^{N} X_{i,1}\left[1 - exp\left(-\frac{t_1 - t_0}{\tau_i}\right)\right]\sigma_1 \tag{6.7}$$

$$\begin{aligned} \varepsilon_2(t) = {} & X_{0,2}\sigma_2 + \left\{\sum_{i=1}^{N} X_{i,1}\left[1 - exp\left(-\frac{t_2 - t_0}{\tau_i}\right)\right]\sigma_1\right\} \\ t_1 \le t < \infty \qquad & + \left\{\sum_{i=1}^{N} X_{i,2}\left[1 - exp\left(-\frac{t_2 - t_1}{\tau_i}\right)\right]\sigma_2 \right. \\ & \left. - \sum_{i=1}^{N} X_{i,1}\left[1 - exp\left(-\frac{t_2 - t_1}{\tau_i}\right)\right]\sigma_1\right\} \end{aligned} \tag{6.8}$$

The theoretical and experimental results for a high density PE resin (HDPE) subjected to various load histories are compared and discussed next. The material was tested subject to multi-stress levels by [39].

Figure 16 shows three steps change in applied stress. The resin was tested under 2.9, 5.8 and 8.7 MPa stresses which lasted 2 h each. Very good correlation can be seen between two data sets. In Fig. 17, the material was tested under five different time step loadings starting from smaller stress values. 1.46, 2.92, 4.38, 5.84 and 7.30 MPa stresses were applied.

MSP can also be applied on viscoplastic formulations. The corresponding relation is:

$$\begin{aligned} \varepsilon_k = {} & X_{0,\sigma_k}\sigma_k + \sum_{j=1}^{k}\left\{\left[C_{0,\sigma_j} \times \left(t_k - t_{j-1}\right)^{C_{1,\sigma_j}}\right]\sigma_j \right. \\ & \left. - \left[C_{0,\sigma_{j-1}} \times \left(t_k - t_{j-1}\right)^{C_{1,\sigma_{j-1}}}\right]\sigma_{j-1}\right\} \end{aligned} \tag{6.9}$$

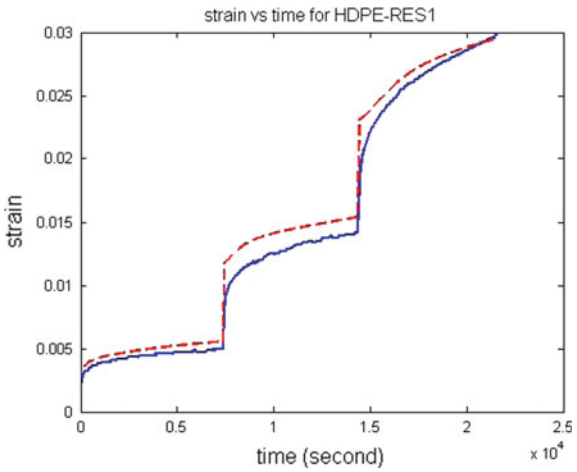

Fig. 16 Strain versus time for HDPE resin. Stress level 1 = 2.90 MPa, stress level 2 = 5.80 MPa, stress level 3 = 8.70 MPa, (*blue continuous line* experimental data, *red dashed line* model)

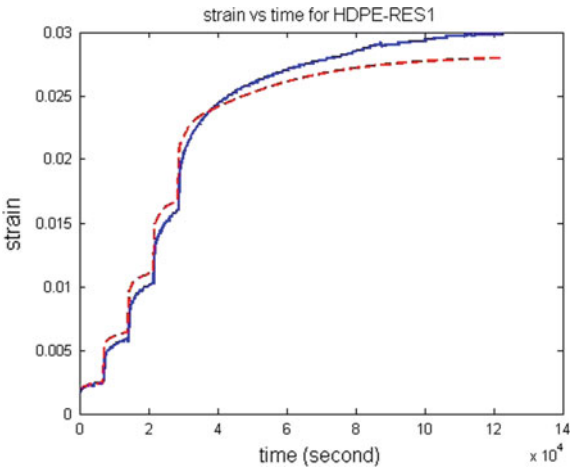

Fig. 17 Strain versus time for HDPE pipe. Stress level 1 = 1.50 MPa, stress level 2 = 2.90 MPa, stress level 3 = 4.38 MPa, stress level 4 = 5.84 MPa, stress level 5 = 7.30 MPa, (*blue continuous line* experimental data, *red dashed line* model)

For the first time-step the stress-strain relationship under constant stress is:

$$\varepsilon_1 = \left\{X_{0,\sigma_1} + C_{0,\sigma_1} \times t^{C_{1,\sigma_1}}\right\}\sigma_1 \tag{6.10}$$

If the stress state changes from σ_1 to σ_2, the total strain response after the second stress change is:

$$\begin{aligned} 0 \le t \le t_1 \qquad & \varepsilon_1 = \left\{X_{0,\sigma_1} + C_{0,\sigma_1} \times t^{C_{1,\sigma_1}}\right\}\sigma_1 \\ & \varepsilon_2 = X_{0,\sigma_1}\sigma_1 + \left\{C_{0,\sigma_1} \times (t_2 - t_0)^{C_{1,\sigma_1}}\right\}\sigma_1 \\ t_1 \le t \le \infty \qquad & + \left\{\left[C_{0,\sigma_2} \times (t_2 - t_1)^{C_{1,\sigma_2}}\right]\sigma_2 \right. \\ & \left. - \left[C_{0,\sigma_1} \times (t_2 - t_1)^{C_{1,\sigma_2}}\right]\sigma_1\right\} \end{aligned} \tag{6.11}$$

7 Conclusion

This chapter presents an overview of polymer material research including testing and modeling. Modeling techniques for short-term, long-term and time-history cases are discussed.

The experimental results show a high degree of nonlinearity in polyethylene behavior which requires simulations based on coupled non-separable formulations. Viscoelastic and viscoplastic models were developed based on differential formulations, suitable for implementation in finite element procedures.

References

1. Alvarado-Contreras, J., Polak, M.A. Penlidis, A.: computational study on a damage-coupled model for crystalline polyethylene. Eng. Comput. **25**, 612–636 (2008)
2. Alvarado-Contreras, J., Polak, M.A., Penlidis, A.: Micromechanical approach to modeling damage in crystalline polyethylene. Polym. Eng. Sci. **47**, 410–420 (2007)
3. Barbero, E.J.: Time–temperature–age superposition principle for predicting long-term response of linear viscoelastic materials. Creep Fatigue Polym. Matrix Compos. 48–69 (2011)
4. Behjat, Y., et al.: Influence of micromolecular structure on environmental stress cracking resistance of high density polyethylene. ASCE J. Mater. Civil Eng. (2014)
5. Behjat, Y.: Relationship between Short-Term and Long-Term Creep, and the Molecular Structure of Polyethylene, p. 73. M.A.Sc. thesis, University of Waterloo, Waterloo, ON (2009)
6. Bodner, S.R., Partom, Y.: A largs deformation elastic-viscoplastic analysis of a thick-walled spherical shell. J. Appl. Mech. 751–757 (1972)
7. Bodner, S.R., Partom, Y.: Constitutive equations for elastic-viscoplastic strain-hardening materials. J. Appl. Mech. 385–389 (1975)
8. Bodner, S.R.: Review of a unifiid elastic-viscoplastic theory. AFOSR-84-004 (1984)
9. Brinson Hall, F., Brinson Catherine, L.: Polymer Engineering Science and Viscoelasticity, An Introduction. Springer Science, New York (2008)
10. Budianski, B.: Micromechanics. Comput. Struct. **16**, 3–12 (1983)
11. Cernocky, E.P., Krempl, E.A.: Theory of viscoplasticity based on infinitesimal total strain. Aeta Meehanica. **36**, 263–289 (1980)
12. Charbonneau, L.: Tensile Time-Dependent Tensile Properties of ETFE Foils. Department of Civil Engineering, University of Waterloo, Waterloo, ON (2011)
13. Charbonneau, L., Polak, M.A., Penlidis, A.: Mechanical properties of ETFE foils, testing and modelling, construction and building materials. Constr. Build. Mater. **60**, 63–72 (2014)
14. Cheng, J.J.: Mechanical and Chemical Properties of High Density Polyethylene: Effects of Microstructure on Creep Characteristics. Ph.D. thesis, University of Waterloo, Waterloo, ON (2008)
15. Cheng, J.J., Polak, M.A., Penlidis, A.: Phase interconnectivity and environmental stress cracking resistance of polyethylene: a crystalline phase investigation. J. Macromol. Sci. Pure Appl. Chem. **46**(6), 572–583 (2009)
16. Cheng, J.J., Polak, M.A., Penlidis, A.: Polymer network mobility and environmental stress cracking resistance of high density polyethylene. Polym. Plast. Technol. Eng. **48**(12), 1252–1261 (2009)
17. Cheng, J.J., Polak, M.A., Penlidis, A.: An alternative approach to estimating parameters in creep models of high-density polyethylene. Polym. Eng. Sci. **51**, 1227–1235 (2011)
18. Cheng J.J., Polak M.A., Penlidis, A.: A tensile strain hardening test indicator of environmental stress cracking resistance. J. Macromol. Sci. Part A: Pure Appl. Chem. **45**, 599–611 (2008)
19. Christensen, R.M.: Theory of Viscoelasticity. Academic Press, [s.l.] (1971)
20. Cowking, A., et al.: A study on the orientation effects in polyethylene in the light of crystalline texture: part 3. J. Mater. Sci. **3**, 646–654 (1968)
21. Denby, E.F.: A note on the interconversion of creep, relaxation and recovery. Rheol. Acta. **14**, 591–593 (1975)
22. Drozdov, A.D., Christansen, J.D.: Constitutive equations for the nonlinear viscoelastic and viscoplastic behavior of thermoplastic elastomers. Int. J. Eng. Sci. **44**, 205–226 (2006)
23. Drozdov, A.D., Christansen, J.D.: Modelling the viscoplastic response of polyethylene in uniaxial loading–unloading tests. Mech. Res. Commun. **30**, 431–442 (2003)
24. Drozdov A.D.: A model for the nonlinear viscoelastic response in polymers at finite strains. lnt. J. Solids Struct. **35**(18), 2315–2347 (1998)
25. Drozdov A.D.: A new model for an aging thermoviscoelastic material. Mech. Res. Commun. **22**(5), 441–446 (1995)

26. Drozdov A.D., Kalamkarov, A.L.: A constitutive model for nonlinear viscoelastic behavior of polymers. Polym. Eng. Sci. **36**(14) (1996)
27. Drozdov A.D.: Constitutive equations in finite elasticity of rubbers. Int. J. Solids Struct. **44**, 272–297 (2007)
28. Drozdov A.D.: Constitutive model of a viscoelastic material at finite strains. Mech. Res. Commun. **19**(6), 535–540 (1992)
29. Ferry, J.D.: Viscoelastic Properties of Polymers. New York, JW (1980)
30. Findley, W.N., Lai, J.S., and Onaran, K.: Creep and Relaxation of Nonlinear Viscoelastic Materials. North-Holland Publishing, **18** (1976)
31. Flugge, W.: Viscoelasticity. Blaisdell Publishing Company, [s.1] (1967)
32. G'Sell, C., Hiver, J.M., Dahoun, A.: Experimental characterization of deformation damage in solid polymers under tension, and its interrelation with necking. Int. J. Solids Struct. **39**, 3857–3872 (2002)
33. G'Sell, C., Dahoun, A.: Evolution of microstructure in semi-crystalline polymer under large plastic deformation. Mater. Sci. Eng. A. **175**, 183–199 (1994)
34. Hughes, T.J.R., Taylor, R.L.: Unconditionally stable algorithms for quasi-static elasto-visco-plastic finite element analysis. Comput. Struct. **8**, 169 (1978)
35. Krishnaswamy, P., Tuttle, M.E., Emery, A.F.: Finite element modelling of crack tip behaviour in viscoelastic materials. Part I: linear behaviour. Int. J. Numer. Methods Eng. **30**, 371–387 (1990)
36. Krishnaswamy, P., Tuttle, M.E., Emery, A.F.: Finite element modeling of the time-dependent behavior of nonlinear ductile polymers. Polym. Eng. Sci. **32**(16), 1086–1096 (1992)
37. Leaderman, H.: Elastic and Creep Properties of Filamentous Materials and Other High Polymers. The Textile Foundation, Washington (1943)
38. Lin, L., Argon, A.S.: Review: structure and plastic deformation of polyethylene. J. Mater. Sci. **29**, 294–323 (1994)
39. Liu, H.: Material Modelling for Structural Analysis of Polyethylene. M.A.Sc thesis, Department of Civil and Environmental Engineering, University of Waterloo, Waterloo, [s.n.] (2007)
40. Liu, H., Polak, M.A., Penlidis, A.: A practical approach to modeling time-dependant nonlinear creep behavior of polyethylene for structural applications. Polym. Eng. Sci. **48**(1), 159–167 (2008)
41. Liu, M.C.M., Krempl, E.: A uniaxial viscoplastic model based on total strain and overstress. J. Mech. Phys. Solids **27**(5), 377–391 (1979)
42. Lockett, F.J.: Nonlinear Viscoelastic Solids. Academic Press, New York (1972)
43. Luo, W., et al.: Long-term creep assessment of viscoelastic polymer by time-temperature-stress superposition. Acta Mechanica Solida Sinica. **25**(6), 571–578 (2012)
44. Nikolov, S., Doghri, I.: A micro/macro constitutive model for the small-deformation behavior of polyethylene. Polymer. **41**, 1883–1891 (2000)
45. Nikolov, S., et al.: Multi-scale constitutive modeling of the small deformations of semi-crystalline polymers. J. Mech. Phys. Solids. **50**, 2275–2302 (2002)
46. Park, S.W., Kim, Y.R.: Interconversion between relaxation modulus and creep compliance for viscoelastic solids. J. Mater. Civil Eng. 76–82 (1999)
47. Sardashti, P., et al.: Effect of temperature on environmental stress cracking resistance and crystal structure of polyethylene. J. Macromol. Sci. Pure Appl. Chem. [s.l.] **51**(3), 1–14, (2014)
48. Sardashti, P., et al.: Improvement of hardening stiffness test as an indicator of environmental stress cracking resistance of polyethylene.J. Macromol. Sci. [s.l.] **49**(9), 689–698, (2012)
49. Schrauwen, B.A.G.: Deformation and Failure of Semicrystalline Polymer Systems: Influence of Micro and Molecular Structure. Ph.D. dissertation, [s.l.], Eindhoven University of Technology, (2003)

50. Zhang, C., Moore, I.D.: Nonlinear mechanical response of high density polyethylene. Part I: experimental investigation and model evaluation. Polym. Eng. Sci. **37**(2), 404–413 (1997)
51. Zhang, C., Moore, I.D.: Nonlinear mechanical response of high density polyethylene. Part II: uniaxial constitutive modeling. Polym. Eng. Sci. **37**(2), 414–420 (1997)
52. Zienkiewicz, O.C.: The Finite Element Method. McGraw Hill, London (1977)

Material Model Based on Response Surfaces of NURBS Applied to Isotropic and Orthotropic Materials

Marianna Coelho, Deane Roehl and Kai-Uwe Bletzinger

Abstract A finite element analysis depends on the material model used to represent the material behavior of a physical phenomenon. Some materials expose a constitutive behavior that cannot be represented by analytical models. Complex material behavior requires the use of appropriate material models able to represent the response under a wide range of load conditions. This contribution uses a response surface based on non-uniform rational B-splines (NURBS) surfaces to define direct biaxial stress–strain relations. For the application in a finite element method, an approach is suggested to compute the matrix of material coefficients from these surfaces. The method was developed for a plane stress condition, which can be used for membranes, beams and thin plates. Two applications of this method are shown: a large strain elastoplastic material behavior with von Mises yield criterion and a linear elastic orthotropic material behavior (Münsch-Reinhardt). The advantage of this material model is that from results of experimental tests, any kind of material can be modeled by fitting the response surface parameters subjected to monotonic load. This approach might be a good alternative to model new fabrics and polymers used in membrane structures.

M. Coelho (✉)
Departamento de Engenharia Civil, Universidade do Estado de Santa Catarina,
Rua Paulo Malschitzki, Joinville, SC 89219-710, Brazil
e-mail: marianna.lorencet@udesc.br

D. Roehl
Instituto Tecgraf, Pontificia Universidade Catolica do Rio de Janeiro,
Rua Marques de Sao Vicente 225, Rio de Janeiro, RJ 22453-900, Brazil
e-mail: droehl@puc-rio.br

K.-U. Bletzinger
Lehrstuhl fuer Statik, Technische Universitaet München,
Arcisstrasse 21, 80333 München, Germany
e-mail: kub@tum.de

P.A. Muñoz-Rojas (ed.), *Computational Modeling, Optimization and Manufacturing Simulation of Advanced Engineering Materials*,
Advanced Structured Materials 49, DOI 10.1007/978-3-319-04265-7_13

1 Introduction

Non–uniform rational basis splines (NURBS) can be used to describe mathematically a 3D geometry using curves and surfaces. This representation is widely used in computer–aided design (CAD) to create and modify designs offering smooth surfaces. Regarding the success in CAD application the use of NURBS has been suggested in other fields as well. An example of this is the isogeometric analysis introduced by Hughes et al. [7], which is a new numerical discretization method to solve problems governed by partial differential equations.

Kiendl et al. [8–10] developed a Kirchhoff-Love shell element on the basis of isogeometric approach. In this isogeometric analysis the functions from the geometry description are used as basis functions for the analysis. This offers a possibility to close the existing gap between design and analysis as both use the same geometry model.

Isogeometric analysis is also used in the contribution of Schmidt et al. [16] for thin-walled structures. This work proposes an integrated design process, which is predicated on a NURBS-based CAD environment as well as on the NURBS-based isogeometric analysis.

Another application of NURBS in numerical analysis is the NURBS–enhanced finite element method (NEFEM). Sevilla et al. [17] has reported that the NEFEM uses NURBS to accurately describe the boundary of the computational domain. The NURBS application proposed in this work aims to state smooth relations between biaxial strains and stresses from which the constitutive material tensor is calculated. This constitutive tensor can be introduced in a finite element application.

Bridgens and Gosling [1] and Gosling and Bridgens [5] have shown another application of splines for response surfaces, in which Bezier functions, B-splines and NURBS are used to represent the biaxial behavior of coated woven fabrics. The validity of the approach is assessed through an extensive fabrics testing program. This approach provides a direct correlation between stresses and strains in the wide range of possible stress paths the material is subject to. As pointed out in Bridgens and Gosling [1] this representation has the additional ability to represent surfaces with rapid changes in gradients and discontinuities in the data. Also, the plane stress constraint, frequently used by the analysis of films and membrane structures is not explicitly imposed.

The response surface approach using NURBS is extended in this contribution to the development of constitutive tensors for easy implementation in finite element method. First results showing this methodology were presented in [2, 3]. Here, the methodology is applied to membrane materials with NURBS surfaces based on two axes of strain and one axis of stress. In order to validate this methodology as an alternative to the use of analytical material models, response surfaces were generated from von Mises material response and from linear elastic orthotropic material behavior (Münsch-Reinhardt).

Aiming at the application of this methodology together with a finite element non–linear analysis program for the investigation of global structural behavior, the

derivation of the NURBS surface for a constitutive matrix has been developed. The implementation was carried out for the structural analysis program CARAT++ (Computer Aided Research Analysis Tool) [4].

It is noteworthy to mention that the present method was developed just for monotonic loading, therefore unloading and cycling loading cannot be considered in the analysis. Further works will improve this limitation.

2 Nonuniform Rational B-Spline Curves and Surfaces

The concept of a NURBS surfaces used in the present study refers to the contribution of Piegl and Tiller [14] and Piegl [13].

The definition of NURBS surface described by Piegl and Tiller [14] and Piegl [13] is the rational generalization of the tensor–product nonrational B–spline surface. Therefore the concepts of tensor–product surface and B–spline surfaces will be introduced.

According to Rogers [15], a NURBS surface is a special case of a general rational B–spline surface that uses a particular form of knot vector. For a NURBS surface, the knot vector has multiplicity of duplicate knot values equal to the order of the basis function at the ends. The knot vector may or may not have uniform internal knot values.

2.1 Tensor Product Surfaces

A surface is defined as a vector-valued function of two parameters, u and v, and represents a mapping of a region of the $u - v$ plane into Euclidean three–dimensional space. Thus, it has the form $S(u, v) = [x(u, v), y(u, v), z(u, v)]$.

The tensor product method is basically a bidirectional curve scheme. It uses basis functions and geometric coefficients. The basis functions are bivariate functions of u and v, which are constructed as products of univariate basis functions. The geometric coefficients are arranged in a bidirectional n X m net. Thus, a tensor product surface has the form:

$$S(u, v) = [x(u, v), y(u, v), z(u, v)] = \sum_{i=0}^{n} \sum_{j=0}^{m} f_i(u) g_j(v) \mathbf{b}_{i,j}, \tag{1}$$

where $\mathbf{b}_{i,j} = (x_{i,j}, y_{i,j}, z_{i,j})$, $0 \leq u, v \leq 1$.

$S(u, v)$ can be rewritten in matrix notation:

$$S(u, v) = [f_i(u)]^T [\mathbf{b}_{i,j}][g_j(v)], \tag{2}$$

where $[f_i(u)]^T$ is a (1) X (n+1) row vector, $[g_j(v)]$ is a (m+1) X (1) column vector, and $[\mathbf{b}_{i,j}]$ is a (n+1) X (m+1) matrix of three–dimensional points.

2.2 Definition of B–Spline Basis Functions

Let $U = \{u_0, \ldots, u_m\}$ be a nondecreasing sequence of real numbers, i.e., $u_i \leq u_{i+1}, i = 0, \ldots, m-1$. The u_i are called knots, and U is the knot vector. The ith B–spline basis functions of p–degree (order p+1), denoted by $N_{i,p}(u)$, are defined as

$$N_{i,0}(u) = \begin{cases} 1 & \text{if } u_i \leq u < u_{i+1} \\ 0 & \text{otherwise,} \end{cases} \tag{3}$$

$$N_{i,p}(u) = \frac{u - u_i}{u_{i+p} - u_i} N_{i,p-1}(u) + \frac{u_{i+p+1} - u}{u_{i+p+1} - u_{i+1}} N_{i+1,p-1}(u), \tag{4}$$

$N_{i,p}$ is written instead of $N_{i,p}(u)$ for brevity.
The derivative of B–spline basis functions with respect to u is given by:

$$N'_{i,p} = \frac{p}{u_{i+p} - u_i} N_{i,p-1}(u) - \frac{p}{u_{i+p+1} - u_{i+1}} N_{i+1,p-1}(u). \tag{5}$$

The proof of Eq. 5 is presented in Piegl and Tiller [14].

2.3 Definition of B–Spline Curves

A pth-degree B-spline is defined by

$$C(u) = \sum_{i=0}^{n} N_{i,p}(u) \mathbf{CP}_i \quad a \leq u \leq b, \tag{6}$$

where the $\mathbf{CP}_i$ are the control points and the $N_{i,p}(u)$ are the pth-degree B-spline basis functions (Eq. 3). These are defined on the nonperiodic and nonuniform knot vector

$$U = \{\underbrace{a, \ldots, a}_{\text{p+1}}, u_{p+1}, \ldots, u_{m-p-1}, \underbrace{b, \ldots, b}_{\text{p+1}}\}, \tag{7}$$

with $n + 1$ number of control points and $m + 1$ number of knots related by:

$$m = n + p + 1. \tag{8}$$

The derivative of the B-spline curve w.r.t. u is given by:

$$C^{'}(u) = \sum_{i=0}^{n} N^{'}_{i,p}(u)\mathbf{CP}_i. \tag{9}$$

Substituting Eq. 5 in Eq. 9, $C^{'}(u)$ can be rewritten as:

$$C^{'}(u) = \sum_{i=0}^{n-1} N_{i+1,p-1}(u)\frac{\mathbf{CP}_{i+1} - \mathbf{CP}_i}{u_{i+p+1} - u_{i+1}} = \sum_{i=0}^{n-1} N_{i+1,p-1}(u)\mathbf{Q}_i, \tag{10}$$

where $\mathbf{Q}_i = \frac{\mathbf{CP}_{i+1} - \mathbf{CP}_i}{u_{i+p+1} - u_{i+1}}$.

Considering $\bar{U}$ the knot vector obtained by dropping the first and last knots from U:

$$\bar{U} = \{\underbrace{a, \ldots, a}_{\text{p}}, u_{p+1}, \ldots, u_{m-p-1}, \underbrace{b, \ldots, b}_{\text{p}}\}, \tag{11}$$

it has $m - 1$ knots. Then it is easy to check that the function $N_{i+1,p-1}(u)$, computed on U, is equal to $N_{i,p-1}(u)$ computed on $\bar{U}$. Thus

$$C^{'}(u) = \sum_{i=0}^{n-1} N_{i,p-1}(u)\mathbf{Q}_i, \tag{12}$$

and $C^{'}(u)$ is a $(p - 1)$th-degree B–spline curve.

2.4 Definition of B–Spline Surfaces

Taking a bidirectional net of control points, two knot vectors and the products of the univariate B–spline functions a B–spline surface is defined as:

$$S(u, v) = \sum_{i=0}^{n}\sum_{j=0}^{m} N_{i,p}(u)N_{j,q}(v)\mathbf{CP}_{i,j}, \tag{13}$$

with

$$U = \{\underbrace{0, \ldots, 0}_{\text{p+1}}, u_{p+1}, \ldots, u_{r-p-1}, \underbrace{1, \ldots, 1}_{\text{p+1}}\},$$

$$V = \{\underbrace{0, \ldots, 0}_{\text{q+1}}, v_{q+1}, \ldots, v_{s-q-1}, \underbrace{1, \ldots, 1}_{\text{q+1}}\}.$$

The knot vector U has $r+1$ knots and knot vector V has $s+1$ knots. Equation 8 takes the form

$$r = n + p + 1 \quad and \quad s = m + q + 1. \tag{14}$$

The derivative of a B–spline surface w.r.t. u is given by

$$\begin{aligned} S_u(u,v) = \frac{\partial S(u,v)}{\partial u} &= \sum_{j=0}^{m} N_{j,q}(v) \frac{\partial \sum_{i=0}^{n} N_{i,p}(u)\mathbf{CP}_{i,j}}{\partial u}, \\ &= \sum_{j=0}^{m} N_{j,q}(v) \frac{\partial C_j(u)}{\partial u}, \end{aligned} \tag{15}$$

where $C_j(u) = \sum_{i=0}^{n} N_{i,p}(u)\mathbf{CP}_{i,j} \;\; j = 0, \ldots, m$ are B-spline curves. Applying Eq. 12 into Eq. 15 gives

$$S_u(u,v) = \sum_{i=0}^{n-1} \sum_{j=0}^{m} N_{i,p-1}(u) N_{j,q}(v) \mathbf{CP}_{i,j}^{(1,0)}, \tag{16}$$

where

$$\mathbf{CP}_{i,j}^{(1,0)} = \frac{\mathbf{CP}_{i+1,j} - \mathbf{CP}_{i,j}}{u_{i+p+1} - u_{i+1}},$$

$$U^{(1)} = \{\underbrace{a, \ldots, a}_{\text{p}}, u_{p+1}, \ldots, u_{r-p-1}, \underbrace{b, \ldots, b}_{\text{p}}\},$$

$$V^{(0)} = V.$$

Analogously $S_v(u,v)$ is determined, similarly as:

$$S_v(u,v) = \sum_{i=0}^{n} \sum_{j=0}^{m-1} N_{i,p}(u) N_{j,q-1}(v) \mathbf{CP}_{i,j}^{(0,1)}, \tag{17}$$

where

$$\mathbf{CP}_{i,j}^{(0,1)} = \frac{\mathbf{CP}_{i,j+1} - \mathbf{CP}_{i,j}}{v_{j+q+1} - v_{j+1}},$$

$$U^{(0)} = U,$$

$$V^{(1)} = \{\underbrace{a, \ldots, a}_{\text{q}}, v_{q+1}, \ldots, v_{s-q-1}, \underbrace{b, \ldots, b}_{\text{q}}\},$$

2.5 Definition of NURBS Surfaces

A NURBS surface is defined as a bivariate vector-valued piecewise rational function of the form

$$S^{NURBS}(u,v) = \frac{\sum_{i=0}^{n}\sum_{j=0}^{m} w_{i,j}\mathbf{CP}_{i,j}N_{i,p}(u)N_{j,q}(v)}{\sum_{i=0}^{n}\sum_{j=0}^{m} w_{i,j}N_{i,p}(u)N_{j,q}(v)}, \qquad 0 \le u, v \le 1, \tag{18}$$

where $w_{i,j}$ are the weights, $\mathbf{CP}_{i,j}$ are control points that form a control net, and $N_{i,p}(u)$ and $N_{i,q}(v)$ are the nonrational B–spline basis functions of degree p and q in the u and v directions, respectively, defined over the knot vectors:

$$U^{NURBS} = [\underbrace{0,\ldots,0}_{\text{p+1}}, u_{p+1},\ldots,u_{r-p-1}, \underbrace{1,\ldots,1}_{\text{p+1}}], \tag{19}$$

$$V^{NURBS} = [\underbrace{0,\ldots,0}_{\text{q+1}}, v_{q+1},\ldots,v_{s-q-1}, \underbrace{1,\ldots,1}_{\text{q+1}}], \tag{20}$$

where $r = n + p + 1$ and $s = m + q + 1$.

Introducing the piecewise rational basis functions as:

$$R_{i,j}(u,v) = \frac{N_{i,p}(u)N_{j,q}(v)w_{i,j}}{\sum_{k=0}^{n}\sum_{l=0}^{m} N_{k,p}(u)N_{l,q}(u)w_{k,l}}. \tag{21}$$

Equation 18 can be rewritten as:

$$S^{NURBS}(u,v) = \sum_{i=0}^{n}\sum_{j=0}^{m} R_{i,j}(u,v)\mathbf{CP}_{i,j}. \tag{22}$$

A NURBS surface example is shown in Fig. 1.

2.6 Derivatives of a NURBS Surface

The derivatives of a NURBS surface are computed analogously to the derivatives of a NURBS curve. Considering $S^{NURBS}(u,v)$ as follows:

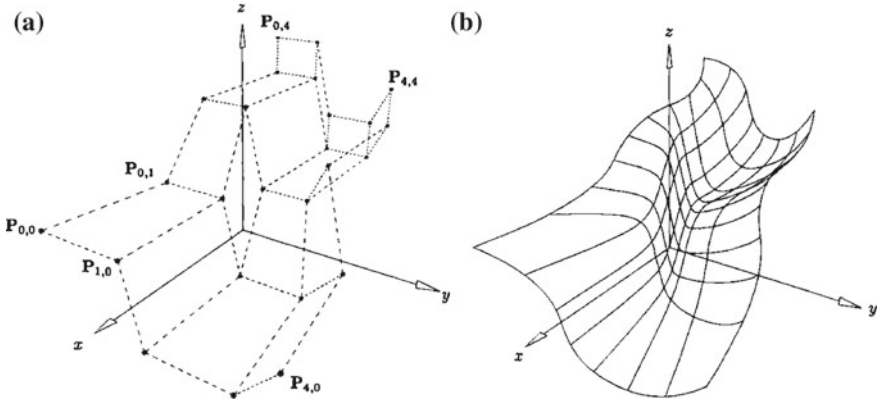

Fig. 1 NURBS surface: (**a**) Control point net (**b**) biquadratic NURBS surface (source: Piegl and Tiller [14])

$$S^{NURBS}(u,v) = \frac{w(u,v)S^{NURBS}(u,v)}{w(u,v)} = \frac{A(u,v)}{w(u,v)}, \tag{23}$$

where $A(u,v)$ is the numerator and $w(u,v)$ is the denominator of Eq. 18, the derivatives of a NURBS surface are calculated:

$$S_{\alpha}^{NURBS}(u,v) = \frac{A_{\alpha}(u,v) - w_{\alpha}(u,v)S^{NURBS}(u,v)}{w(u,v)}, \tag{24}$$

and α denotes either u or v. In the above expression $A_{\alpha}(u,v)$ is defined as:

$$\begin{aligned} A_{\alpha}(u,v) &= w(u,v)\frac{\partial}{\partial\alpha}S^{NURBS}(u,v), \\ &= w(u,v)\left(\frac{\partial}{\partial\alpha}\sum_{j=0}^{m}N_{j,q}(v)\sum_{i=0}^{n}N_{i,p}(u)\mathbf{CP}_{i,j}\right). \end{aligned} \tag{25}$$

The derivatives in direction u of NURBS surface are computed as follow:

$$\frac{\partial}{\partial u}\sum_{i=0}^{n}N_{i,p}(u)\mathbf{CP}_{i,j} = \sum_{i=0}^{n-1}N_{i,p-1}(u)\mathbf{CP}_{i,j}^{(1,0)},$$

$$S_{u}^{NURBS}(u,v) = \sum_{i=0}^{n-1}\sum_{j=0}^{m}N_{i,p-1}(u)N_{j,q}(v)\mathbf{CP}_{i,j}^{(1,0)}, \tag{26}$$

where

$$\mathbf{CP}_{i,j}^{(1,0)} = p\frac{\mathbf{CP}_{i+1,j} - \mathbf{CP}_{i,j}}{u_{i+p+1} - u_{i+1}},$$

$$U^{NURBS^{(1)}} = [\underbrace{0, \ldots, 0}_{\text{p}}, u_{p+1}, \ldots, u_{r-p-1}, \underbrace{1, \ldots, 1}_{\text{p}}],$$

$$V^{NURBS^{(0)}} = V^{NURBS}.$$

Analogously the derivatives in direction v of NURBS surface are also computed:

$$S_v^{NURBS}(u,v) = \sum_{i=0}^{n}\sum_{j=0}^{m-1} N_{i,p}(u)N_{j,q-1}(v)\mathbf{CP}_{i,j}^{(0,1)}, \tag{27}$$

where

$$\mathbf{CP}_{i,j}^{(0,1)} = q\frac{\mathbf{CP}_{i,j+1} - \mathbf{CP}_{i,j}}{v_{j+q+1} - v_{j+1}},$$

$$U^{NURBS^{(0)}} = U^{NURBS},$$

$$V^{NURBS^{(1)}} = [\underbrace{0, \ldots, 0}_{\text{q}}, v_{q+1}, \ldots, v_{s-q-1}, \underbrace{1, \ldots, 1}_{\text{q}}].$$

3 Data Fitting

Data fitting based on least-squares approximation is used to generate NURBS surfaces for the experimental data. This process is briefly described below. For more details the references are the contributions of Piegl and Tiller [13] and Piegl [13].

Equation 22 can be written in matrix notation as:

$$S^{NURBS^f}(u,v) = \mathbf{R}\ \mathbf{CP}, \tag{28}$$

where $S^{NURBS^f}(u,v)$, $\mathbf{CP}$ and $\mathbf{R}$ are $(n+1)\times(n+1)$ matrices. If there are more data points than control points, Eq. 28 is overdetermined and can be solved approximately as follows:

$$S^{NURBS^f}(u,v) = \mathbf{R}[\mathbf{R}_*^T\mathbf{R}_*]^{-1}\mathbf{R}_*^T\mathbf{S}_*^{NURBS}. \tag{29}$$

where $\mathbf{R}_*$ and $\mathbf{S}_*^{NURBS}$ are computed with numeric values corresponding to the experimental surface points.

Assigning initial parameters to the data points, as the p-th degree and the control points, a least-squares fit is generated using Eq. 29.

An alternative approach for the generation of NURBS surfaces is the use of a CAD software. In this case, a surface is generated based on a point cloud.

4 Material Model Based on NURBS for Principal Directions (NURBS–Material)

The formulation of the NURBS–Material model, which is based on principal directions of stress and strain, is presented as follows. Here the special case of membrane state of stress is considered.

The notation used herein follows the contribution of Gruttmann and Taylor [6]. The Green–Lagrange strain tensor is defined as:

$$\mathbf{E}_{\alpha\beta} = \frac{1}{2}\left(\mathbf{x}_{,\alpha} \cdot \mathbf{x}_{,\beta} - \mathbf{X}_{,\alpha} \cdot \mathbf{X}_{,\beta}\right)$$

where $\mathbf{x} = x_i \mathbf{e}_i$ and $\mathbf{X} = X_i \mathbf{e}_i$ are the current and initial configurations with components related to Cartesian basis $\mathbf{e}_i$.

In matrix notation the Green–Lagrange strain tensor is given by:

$$\mathbf{E} = \frac{1}{2}\left(\mathbf{F}^T \cdot \mathbf{F} - \mathbf{I}\right) = \frac{1}{2}\left(\mathbf{C} - \mathbf{I}\right),$$

where the deformation gradient $\mathbf{F}$ transforms the reference configuration into the actual configuration.

$$\mathbf{F} = \frac{\partial \mathbf{x}}{\partial \mathbf{X}}, \tag{30}$$

$\mathbf{x}$ is the position of a point in current configuration and $\mathbf{X}$ is the position of a point in the reference configuration.

$\mathbf{C}$ is the right Cauchy–Green tensor, which can be defined by:

$$\mathbf{C} = \mathbf{F}^T \cdot \mathbf{F}. \tag{31}$$

The right Cauchy–Green tensor in principal direction $\hat{\mathbf{C}}$ is given by:

$$\hat{\mathbf{C}} = \mathbf{T} \cdot \mathbf{C}, \tag{32}$$

$\hat{\mathbf{C}}$ and $\mathbf{C}$ are written in vector form as:

$$\hat{\mathbf{C}} = \left[\hat{C}_{11}\ \hat{C}_{22}\ 2\hat{C}_{12}\right], \tag{33}$$

$$\mathbf{C} = \left[C_{11}\ C_{22}\ 2C_{12}\right], \tag{34}$$

and $\mathbf{T}$ is the rotation matrix:

$$\mathbf{T} = \begin{bmatrix} cos^2\phi & sin^2\phi & cos\phi sin\phi \\ sin^2\phi & cos^2\phi & -cos\phi sin\phi \\ -2cos\phi sin\phi & 2cos\phi sin\phi & cos^2\phi - sin^2\phi \end{bmatrix}. \tag{35}$$

Equation 31 can also be written in spectral representation:

$$\mathbf{C} = \sum_{i=0}^{3} \lambda_i \mathbf{M}_i \qquad i = 1, 2, 3, \tag{36}$$

where λ_i are the principal stretches and $\mathbf{M}_i$ are the eigenprojections.

$$\mathbf{M}_1 = \begin{bmatrix} cos^2\phi & cos\phi sin\phi \\ cos\phi sin\phi & sin^2\phi \end{bmatrix}, \qquad \mathbf{M}_2 = \begin{bmatrix} sin^2\phi & -cos\phi sin\phi \\ -cos\phi sin\phi & cos^2\phi \end{bmatrix}. \tag{37}$$

The value of ϕ is calculated with the spectral decomposition presented in Eqs. 31 and 37. ϕ and it is the rotation angle, which relates the general stress axes to the principal stress axes.

The second Piola–Kirchhoff stresses and the Green–Lagrange strains in principal directions are given, respectively by:

$$\hat{\mathbf{S}} = \left[S_1\ S_2\ 0\right], \tag{38}$$

$$\hat{\mathbf{E}} = \left[E_1\ E_2\ 0\right]. \tag{39}$$

The second Piola–Kirchhoff stresses tensor has the following relation with the rotation matrix:

$$\mathbf{S} = \mathbf{T}^T \cdot \hat{\mathbf{S}}, \qquad \mathbf{S} = [S_{11}\ S_{22}\ S_{12}], \tag{40}$$

The constitutive material tensor is obtained with the rotation matrix calculated as follows:

$$\frac{d\mathbf{S}}{d\mathbf{E}} = \begin{bmatrix} \frac{dS_{11}}{dE_{11}} & \frac{dS_{11}}{dE_{22}} & \frac{dS_{11}}{2dE_{12}} \\ \frac{dS_{22}}{dE_{11}} & \frac{dS_{22}}{dE_{22}} & \frac{dS_{22}}{2dE_{12}} \\ \frac{dS_{12}}{dE_{11}} & \frac{dS_{12}}{dE_{22}} & \frac{dS_{12}}{2dE_{12}} \end{bmatrix} = \mathbf{T}^T \cdot \frac{d\hat{\mathbf{S}}}{d\hat{\mathbf{E}}} \cdot \mathbf{T}, \tag{41}$$

where $\frac{d\hat{\mathbf{S}}}{d\hat{\mathbf{E}}}$ is the constitutive material tensor in principal directions:

$$\frac{d\hat{\mathbf{S}}}{d\hat{\mathbf{E}}} = \begin{bmatrix} \frac{dS_1}{dE_1} & \frac{dS_1}{dE_2} & 0 \\ \frac{dS_2}{dE_1} & \frac{dS_2}{dE_2} & 0 \\ 0 & 0 & \frac{d\hat{S}_{12}}{d\hat{C}_{12}} \end{bmatrix}. \tag{42}$$

The constitutive material tensor in principal directions is computed with the NURBS surface derivatives introduced in Sect. 2.6:

$$\begin{bmatrix} \frac{dS_1}{dE_1} \\ \frac{dS_1}{dE_2} \end{bmatrix} = \left(\begin{bmatrix} \frac{dE_1}{du} & \frac{dE_2}{du} \\ \frac{dE_1}{dv} & \frac{dE_2}{dv} \end{bmatrix} \right)^{-1} \cdot \begin{bmatrix} \frac{dS_1}{du} \\ \frac{dS_1}{dv} \end{bmatrix}, \tag{43}$$

$$\begin{bmatrix} \frac{dS_2}{dE_1} \\ \frac{dS_2}{dE_2} \end{bmatrix} = \left(\begin{bmatrix} \frac{dE_1}{du} & \frac{dE_2}{du} \\ \frac{dE_1}{dv} & \frac{dE_2}{dv} \end{bmatrix} \right)^{-1} \cdot \begin{bmatrix} \frac{dS_2}{du} \\ \frac{dS_2}{dv} \end{bmatrix}. \tag{44}$$

The derivatives of the NURBS surface for direction 1 w.r.t. u and v are given by

$$S_{u_1}^{NURBS}(u,v) = \begin{bmatrix} \frac{dE_1}{du} & \frac{dE2}{du} & \frac{dS_1}{du} \end{bmatrix}, \tag{45}$$

$$S_{v_1}^{NURBS}(u,v) = \begin{bmatrix} \frac{dE_1}{dv} & \frac{dE2}{dv} & \frac{dS_1}{dv} \end{bmatrix}, \tag{46}$$

and analogously for the derivatives of the NURBS surface for direction 2 w.r.t. u and v:

$$S_{u_2}^{NURBS}(u,v) = \begin{bmatrix} \frac{dE_1}{du} & \frac{dE2}{du} & \frac{dS2}{du} \end{bmatrix}, \tag{47}$$

$$S_{v_2}^{NURBS}(u,v) = \begin{bmatrix} \frac{dE1}{dv} & \frac{dE2}{dv} & \frac{dS2}{dv} \end{bmatrix}. \tag{48}$$

The derivative $\frac{d\hat{S}_{12}}{d\hat{C}_{12}}$ is calculated as follows:

$$\frac{d\hat{S}_{12}}{d\hat{C}_{12}} = \frac{d\hat{S}_{12}}{d\phi} \cdot \frac{d\phi}{d\hat{C}_{12}} = \frac{-(S_2 - S_1)cos2\phi}{C_{11} - C_{22}}, \tag{49}$$

where

$$\frac{d\hat{S}_{12}}{d\phi} = sin\phi cos\phi(S_{11} - S_{22}) = S_2 - S_1,$$

$$\frac{d\phi}{d\hat{C}_{12}} = \frac{-cos2\phi}{C_{11} - C_{22}},$$

$$\hat{C}_{12} = \hat{C}_{21} = -\frac{1}{2}\left(C_{11} - C_{22}\right) sin(2\phi) + C_{12}cos(2\phi) = 0.$$

and C_{11} and, C_{22} are the components of the right Cauchy–Green tensor $\mathbf{C}$.

The algorithm of the material model based on NURBS for principal directions is presented in the following box:

1. Update the strain tensor.

$$\mathbf{E}_{n+1} = \frac{1}{2}\left(\mathbf{F}_{n+1}^T \mathbf{F}_{n+1} - \mathbf{I}\right)$$

2. Calculate the rotation matrix $\mathbf{T}$ (Eq. 35)
3. Calculate the strains in principal directions

$$\hat{\mathbf{E}}_{n+1} = \mathbf{T}^T \mathbf{E}_{n+1}$$

4. Calculate the local parameter u and v from the strains (Eq. 22).
5. Obtain the stress values $S_1(u, v)$ and $S_2(u, v)$.
6. Calculate the derivatives $\frac{dS_1}{dE_1}$, $\frac{dS_1}{dE_2}$, $\frac{dS_2}{dE_1}$, $\frac{dS_2}{dE_2}$, and $\frac{d\hat{S}_1}{d\hat{E}_1}$ (Eqs. 43 and 44).
7. The constitutive material tensor is obtained using:

$$\frac{d\mathbf{S}}{d\mathbf{E}} = \mathbf{T}^T \cdot \begin{bmatrix} \frac{dS_1}{dE_1} & \frac{dS_1}{dE_2} & 0 \\ \frac{dS_2}{dE_1} & \frac{dS_2}{dE_2} & 0 \\ 0 & 0 & \frac{d\hat{S}_{12}}{2d\hat{E}_{12}} \end{bmatrix} \cdot \mathbf{T}$$

8. Calculate the stress tensor.

$$\mathbf{S} = \mathbf{T}^T \cdot \hat{\mathbf{S}}$$

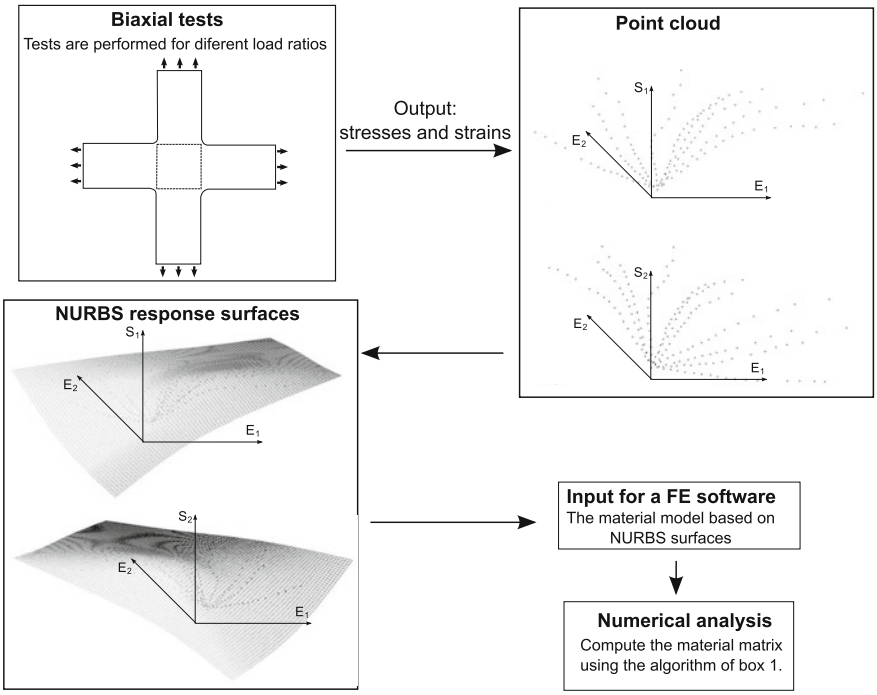

Fig. 2 Schematic representation of the proposed material model

Figure 2 shows the schematic representation of the proposed material model based on NURBS surfaces.

5 Application of NURBS–Material in Membrane Finite Element Modeling

5.1 Comparison with Elastoplastic Material Model

The elastoplastic von Mises material with isotropic hardening is used here to investigate the applicability and accuracy of the NURBS–Material. The example consists in the monotonic stretching of a perforated rectangular membrane with large strains and displacements. This example is taken from Simo and Hughes [18], Simo and Taylor [19], and Souza Neto et al. [20] and is modeled in CARAT++ for plane stress with membrane elements.

The membrane material properties are: $E = 70$ GPa (membrane modulus), $\mu = 0.2$ (Poisson ratio), $K = 0.2$ GPa (hardening modulus), $\sigma_y = 0.243$ GPa (yield stress), and membrane thickness of 1 mm. The dimension and boundary conditions are

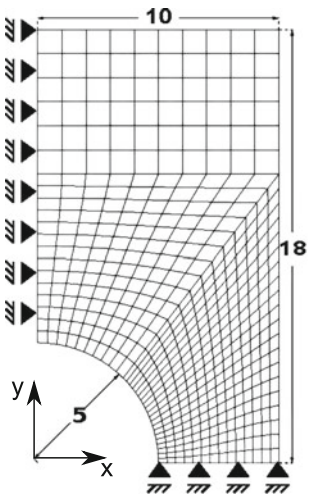

Fig. 3 Mesh, geometry and boundary conditions of a perforated rectangular membrane (dimensions in millimeters)

shown in Fig. 3. The static analysis was carried out with cylindrical arc-length control of the free edge. The mesh is composed of 531 nodes and 480 membrane elements with linear discretization and 2×2 Gauss integration as shown in Fig. 3. Due to symmetry a quarter of the membrane is modeled.

It is worth pointing out that a full elastoplastic stress history can not be obtained with the proposed NURBS–material since unloading/reloading cycles are not represented by the NURBS surfaces herein. The proposed material law is well suited to identify complex materials.

The elastoplastic material properties are used to produce the data points for the generation of the NURBS surfaces in principal directions. These NURBS surfaces are shown in Fig. 4. The control point net has degree 2 ($p = 2$ and $q = 2$) and the number of points are $60(\text{u}) \times 60(\text{v})$ and $100(\text{u}) \times 100(\text{v})$.

The elastic region can be identified in the NURBS surfaces in Fig. 4 as the flat ellipse plane. Outside this region nonlinear behavior is present. Therefore the corresponding axis $S_1(u, v)$ and $S_2(u, v)$ values fall in the elastoplastic range of the plastic model.

5.1.1 Results

The nonlinear analysis was performed in 40 steps. The results obtained with the NURBS–material model are compared with those of the classical von Mises model. Table 1 shows the number of iterations for the von Mises material and NURBS–material with two different control point nets, 60×60 and 100×100. The results for steps 20, 21, 39 and 40 are shown. The plastic behaviour is achieved in step 21. These steps can be visualized in Fig. 5. Step 21 is the first step that presents elastoplastic behavior.

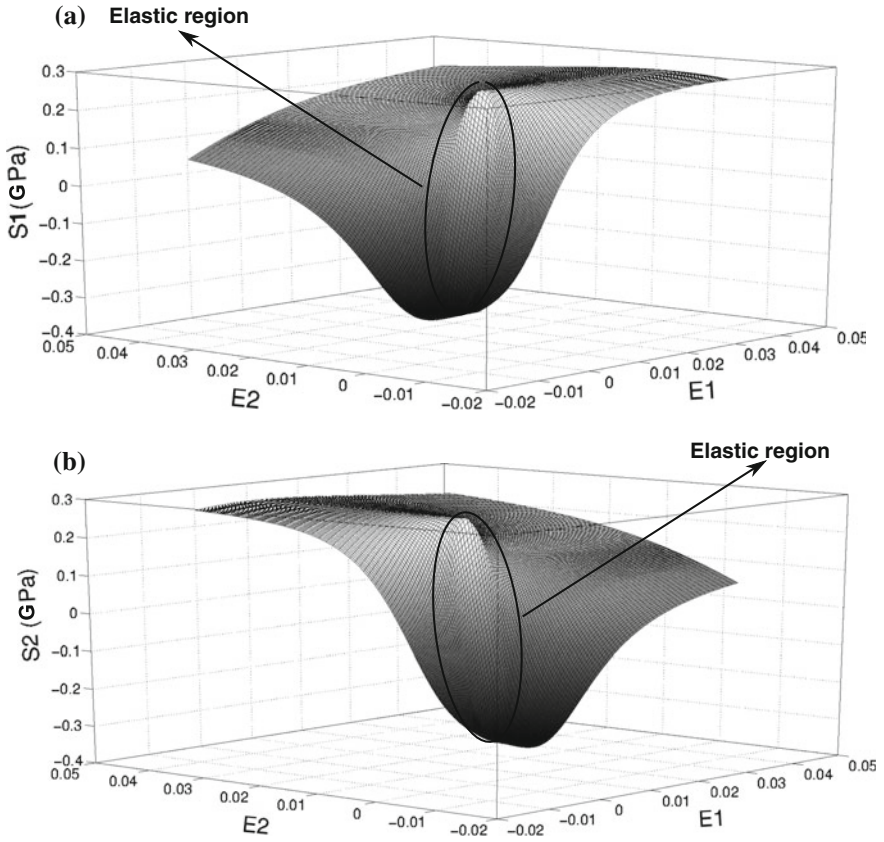

Fig. 4 NURBS surfaces for stresses and strains in principal directions for elastoplastic material: (**a**) stresses in direction 1, and (**b**) stresses in direction 2

For the control point net with 100×100 points (NURBS 100) convergence was achieved for a maximum of 4 iterations. On the other hand, the control point net with 60×60 points (NURBS 60) did not show convergence for step 40 and for step 39 the convergence required 16 iterations.

The convergence depends on the NURBS surface shape, because of the NURBS surface derivatives that are necessary to calculate the material matrix. The linearization of the material matrix was not implemented in the present work. Therefore a quadratic convergence is not guaranteed. Future works will explore and improve this convergence.

The errors for the displacement in y direction for steps 20, 21, 39 and 40 are shown in Table 2. The errors obtained for NURBS 100 and NURBS 60 are quite small for engineering purpose.

Table 1 Displacement residuum and the iteration number for the classical von Mises material and the NURBS–material with 60×60 and 100×100 control points

	Iteration	Classical	NURBS 60	NURBS 100
Step 20	1	3.503109e-04	3.463489e-04	3.327881e-04
	2	4.989924e-10	7.248311e-06	1.655211e-06
Step 21	1	3.197563e-04	3.464462e-04	3.252045e-04
	2	9.020717e-06	1.350109e-05	4.341103e-06
	3		1.603098e-06	
Step 39	1	4.223207e-04	3.978951e-04	4.352328e-04
	2	2.957438e-07	1.307737e-04	1.274219e-05
	3		1.097290e-04	5.325408e-06
	4		8.877458e-05	
	5		7.353401e-05	
	6		6.044716e-05	
	7		4.981207e-05	
	8		4.102275e-05	
	9		3.378555e-05	
	10		2.782875e-05	
	11		2.291854e-05	
	12		1.887753e-05	
	13		1.554703e-05	
	14		1.280550e-05	
	15		1.054647e-05	
	16		8.686593e-06	
Step 40	1	4.719461e-04	no convergence	4.459105e-04
	2	4.185541e-08		2.989403e-05
	3			1.384563e-05
	4			5.056272e-06

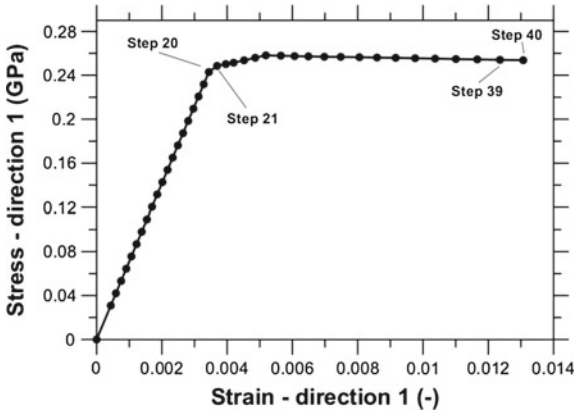

Fig. 5 Stress–strain result for the stretching of a perforated rectangular membrane

Table 2 Results of displacement in y direction for classical von Mises material and NURBS material

	Step	Classical	NURBS 100	Error (%)	NURBS 60	Error (%)
Displac. y (mm)	20	0.0223024	0.0223095	0.03179	0.0223026	0.00087
	21	0.0233277	0.0233360	0.03569	0.0233331	0.02291
	39	0.0418858	0.0419161	0.07243	0.0419490	0.15087
	40	0.0429259	0.0429561	0.07050	no convergence	

5.2 Comparison with an Orthotropic Material Model

The methodology using a NURBS surface as material model was also applied to the Münsch–Reinhardt orthotropic linear elastic material model [12]. The example considers geometric nonlinearity. The stress–strain relation for this model is given by:

$$\mathbf{S} = \mathbf{D}\mathbf{E}, \tag{50}$$

where $\mathbf{D}$ is:

$$\mathbf{D} = \frac{1}{1-\mu\cdot\mu}\cdot\begin{bmatrix} E_k & \mu\cdot E_k & 0 \\ \mu\cdot E_s & E_s & 0 \\ 0 & 0 & (1-\mu\cdot\mu)\cdot G \end{bmatrix}, \tag{51}$$

and the parameters E_k, E_s, μ and G are the Young's modulus in warp and weft direction, Poisson ratio and shear modulus, respectively.

A rectangular membrane was stretched in both in-plane directions. The mesh, geometry and boundary conditions are shown in Fig. 6. The mesh is composed of

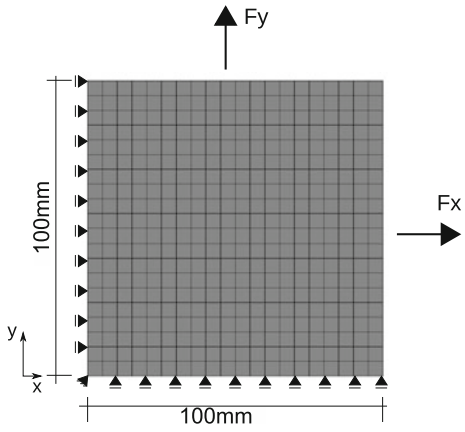

Fig. 6 Mesh, geometry and boundary conditions of a rectangular membrane

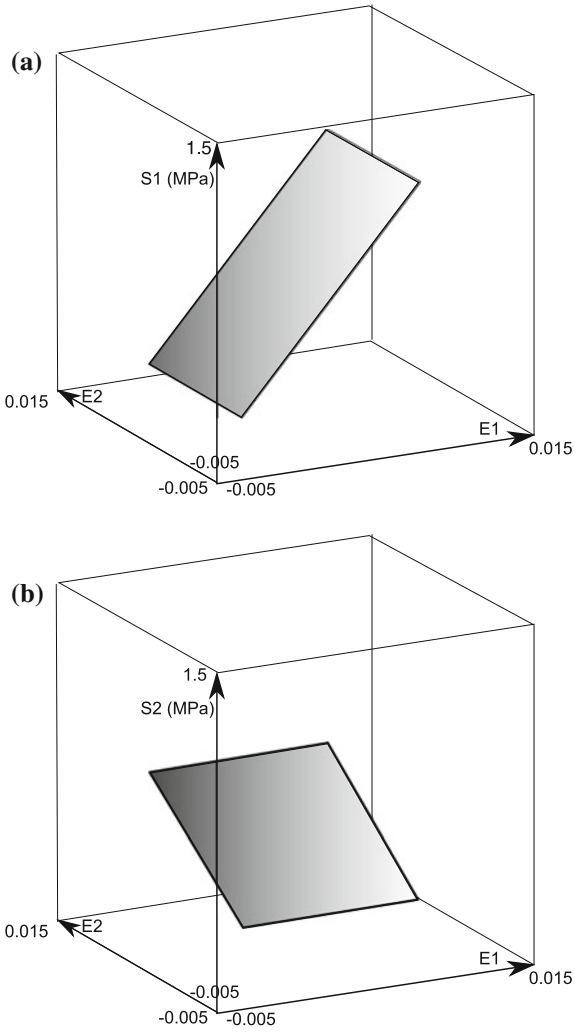

Fig. 7 NURBS surfaces for stresses and strains in principal directions for Münsch–Reinhardt material: (**a**) stresses in direction 1, and (**b**) stresses in direction 2

441 nodes and 400 membrane elements with linear discretization and 2×2 Gauss integration.

The material properties are: $E_k = 100$ kN/m^2, $E_s = 50$ kN/m^2, $\mu = 0.3$ and $G = 10$ kN/m^2. These properties were taken from an example of the contribution of Linhard [11].

The response NURBS surfaces are generated based on a points cloud using a CAD software. The degree of the NURBS surfaces is 1 ($p = 1$ and $q = 1$). A control point net with $2(\text{u}) \times 2(\text{v})$ points was considered in the analyses. The representations of these surfaces are shown in Fig. 7. As the material model is linear elastic, the surfaces

Table 3 Displacement residuum for steps 10 and 20 for Münsch-Reinhardt material and NURBS-material

Step	Iteration	Münsch-Reinhardt	Control points
			2×2
10	1	7.1941e-05	1.4124e-04
	2	2.5250e-07	2.4135e-08
20	1	7.1801e-05	1.4076e-04
	2	2.4622e-07	2.3916e-08

are planar. Due to the orthotropic behavior the surfaces related to S_1 (Fig. 7a) and S_2 (Fig. 7b) have different inclinations.

5.2.1 Results

The analyses were performed in 20 steps using force control up to 100 N. The results obtained with the model based in NURBS surfaces were the same as the classical model.

Table 3 shows the displacement residuum for steps 10 and 20 for conventional and NURBS–material. The analyses obtained the same number of iterations. The convergence rate shows better performance using the NURBS–material.

6 Conclusions

The formulation of a new approach to obtain the constitutive material tensor to be used with finite element analyses was presented. This method is based on NURBS surfaces that act as response surfaces returning stresses from strains. These NURBS surfaces are generated in principal directions and, therefore, the experimental results from biaxial tests can be used. The advantage is that this methodology can directly be applied to orthotropic and nonlinear materials subjected to monotonic loading without further adaptations. This can be a useful tool for the development of new materials, cutting pattern analysis and for complex membrane material behavior. However, the experimental data should provide a point distribution to generate suitable NURBS surfaces.

Two validation examples were presented comparing results of analytical models with those of the NURBS–material: the stretching of a perforated rectangular membrane with classical von Mises material and a biaxial stretching of a square membrane with orthotropic material (Münsch–Reinhardt). The results obtained with

the NURBS–material were in excellent agreement with the classical models. We conclude that this material model is a good alternative for the development of models for new materials.

References

1. Bridgens, B., Gosling, P.: Direct stress-strain representation for coated woven fabrics. Comput. Struct. **82**, 1913–1927 (2004)
2. Coelho, M., Roehl, D., Bletzinger, K.U.: Using NURBS as response surface for membrane material behavior. In: Textile Composites and Inflatable Structures VI, vol. 1, pp. 166–175. Artes Gráficas Torres S.A., Barcelona (2013)
3. Coelho, M.A.O.: Analysis of pneumatic structures considering nonlinear material models and pressure-volume coupling. Ph.D. thesis, Pontificia Universidade Catolica do Rio de Janeiro (2012)
4. Fischer, M.: Carat++ Dokumentation. Lehrstuhl für Statik - Technische Universität München (2008)
5. Gosling, P., Bridgens, B.: Material testing and computational mechanics: a new philosophy for architectural fabrics. Int. J. Space Struct. **23**(4), 215–232 (2008)
6. Gruttmann, F., Taylor, R.: Theory and finite element formulation of rubberlike membrane shells using principal stretches. Int. J. Numer. Methods Eng. **35**(5), 1111–1126 (1992)
7. Hughes, T., Cottrell, J., Bazilevs, Y.: Isogeometric analysis: CAD, finite elements, NURBS, exact geometry and mesh refinement. Comput. Methods Appl. Mech. Eng. **194**, 4135–4195 (2004)
8. Kiendl, J., Bazilevs, Y., Hsu, M.C., Wüchner, R., Bletzinger, K.U.: The bending strip method for isogeometric analysis of Kirchhoff-Love shell structures comprised of multiple patches. Comput. Methods Appl. Mech. Eng. **199**(37–40), 2403–2416 (2010)
9. Kiendl, J., Bletzinger, K.U., Linhard, J., Wüchner, R.: Isogeometric shell analysis with Kirchhoff-Love elements. Comput. Methods Appl. Mech. Eng. **198**, 3902–3914 (2009)
10. Kiendl, J., Schmidt, R., Wüchner, R., Bletzinger, K.U.: Isogeometric shape optimization of shells using semi-analytical sensitivity analysis and sensitivity weighting. Comput. Methods Appl. Mech. Eng. **274**, 148–167 (2014)
11. Linhard, J.: Numerish-mechanische Betrachtung des Entwurfsprozesses von Membrantragwerken. Ph.D. thesis, Technischen Universität München, Fakultät für Bauingenieur- und Vermessungswesen (2009)
12. Münsch, R., Reinhardt, H.W.: Zur Berechnung von Membrantragwerken aus beschichteten Geweben mit Hilfe genäherter elastischer Materialparameter. Bauingenieur **70**(6), 271–275 (1995)
13. Piegl, L.: On NURBS: a survey. IEEE Comput. Graphics Appl. **11**(1), 55–71 (1991)
14. Piegl, L., Tiller, W.: The NURBS Book. Springer (1997)
15. Rogers, D.F.: An Introduction to NURBS: With Historical Perspective, 1st edn. Morgan Kaufmann (2000)
16. Schmidt, R., Kiendl, J., Bletzinger, K.U., Wüchner, R.: Realization of an integrated structural design process: analysis-suitable geometric modelling and isogeometric analysis. Comput. Vis. Sci. **13**(7), 315–330
17. Sevilla, R., Fernández-Méndez, S., Huerta, A.: 3D NURBS-enhanced finite element method (NEFEM) Sonia Fernández-Méndez. Int. J. Numer. Methods Eng. **88**, 103–125 (2011)
18. Simo, J., Hughes, T.: Computational Inelasticity, vol. 7. Springer (1998)
19. Simo, J.C., Taylor, R.L.: Consistent tangent operators for rate-independent elastoplasticity. Comput. Methods Appl. Mech. Eng. **48**, 101–118 (1985)
20. Souza Neto, E., Perić, D., Owen, D.: Computational Methods for Plasticity: Theory and Applications. Wiley (2008)

Characterization of Constitutive Parameters for Hyperelastic Models Considering the Baker-Ericksen Inequalities

Felipe Tempel Stumpf and Rogério José Marczak

Abstract Hyperelastic models are used to simulate the mechanical behavior of rubber-like materials ranging from elastomers, such as natural rubber and silicon, to biologic materials, such as muscles and skin tissue. Once the desired hyperelastic model has its parameters fitted to the available experimental results, these hyperelastic parameters have to fulfill the requirements imposed by the Baker-Ericksen inequalities in order to guarantee a plausible physical behavior to the material, although seldom used. When applied to an incompressible isotropic hyperelastic model, these inequalities state that the first derivative of the strain energy density function with respect to the first strain invariant must be positive and the first derivative of the strain energy density function with respect to the second strain invariant must be non-negative. The aim of this work is to study which improvements the requirement of the Baker-Ericksen inequalities can bring when fitting hyperelastic models to experimental data. This is accomplished through a constrained optimization procedure. Results obtained for natural rubber and silicon samples considering classical and newly developed hyperelastic models are shown and discussed.

Keywords Hyperelasticity · Optimization · Constitutive parameters

1 Introduction

As the applications with rubber-like materials in the industry increased and their mechanical behavior started to be investigated more deeply, several authors have been pointing out about the necessity of imposing mathematical restrictions to the

F.T. Stumpf
School of Engineering, FURG, Av. Itália, km.8, Rio Grande, Brazil

R.J. Marczak (✉)
Mechanical Engineering Department, UFRGS, Rua Sarmento Leite 435, Porto Alegre, Brazil
e-mail: rato@mecanica.ufrgs.br

P.A. Muñoz-Rojas (ed.), *Computational Modeling, Optimization and Manufacturing Simulation of Advanced Engineering Materials*, Advanced Structured Materials 49, DOI 10.1007/978-3-319-04265-7_14

theoretical strain energy density functions used to model these materials, in order to guarantee their positivity, monotonicity, unicity of solutions, numerical stability and ensure that the material will behave in a physically plausible way [3, 14–16] Bilgili [4].

Truesdell and Noll [16] have cited seven different types of conditions to be satisfied by any material model so its mechanical behavior is compatible with the known laws of Physics. Among these conditions are the Baker-Ericksen inequalities [1] which state that, in a compressible isotropic elastic solid body under deformation, the largest principal stress must be aligned with the largest principal strain.

According to Balzani et al. [3] the constitutive equations written as functions of the strain energy density must satisfy general requirements of convexity, in order to ensure numerical stability and a physically plausible behavior of the material. Ball [2] introduced the concept of *polyconvexity*, which was later shown by Ogden [12] and Hartmann and Neff [6] to automatically satisfy the Baker-Ericksen inequalities, when applied to a strain energy density function.

Truesdell and Noll [16] concluded that when applied to incompressible isotropic materials, the Baker-Ericksen inequalities are satisfied by guaranteeing the positivity of the first derivative of the strain energy density function (W) with respect to the first strain invariant (I) and the non-negativity of the first derivative of with respect to the second train invariant (II). These conditions were analytically determined for the models analyzed in this work.

It is important to note that, in some cases, better stress-strain fittings are achieved if the Baker-Ericksen inequalities are neglected; however there is no mathematical guarantee that outside the strain range used to calibrate the model the material will not behave badly. When complex simulations take place, there can occur particular regions in which the material strains are higher than those for which its parameters were calibrated, and in these cases it is very important to guarantee that at least its mechanical behavior does not violate any law of physics.

The aim of this paper is to apply the Baker-Ericksen inequalities to the equations of five distinct hyperelastic models, write a procedure to retrieve their constitutive parameters satisfying the inequalities, and then fit these models against three different sets of experimental data (simple tension, biaxial tension and pure shear) from two different elastomers samples. Treloar [8] and unfilled silicone rubber [10] experimental data were used in all tests. An optimizing technique that uses data from one or more sets of experimental tests simultaneously (multi-criteria optimization) and obtains the optimum constitutive parameters that minimize the error between experimental and theoretical results is used. These tests also allowed to verify if a single tension test along with the Baker-Ericksen inequalities can deliver results comparable in quality with the ones obtained by multi-test fitting.

2 Constitutive Parameters Optimization Technique

In order to guarantee good results when analyzing rubber-like materials, the analyst must be sure that the available experimental data to be fitted to a model represents the major type of deformation of the analyzed component. For a few simple cases, that should not represent a problem, but when a component is subjected to more complex deformation states, the best solution is to calibrate the hyperelastic model to data from more than one experimental test.

It was shown by Hoss [7] and Stumpf [14] that predicting the behavior of an elastomer in a deformation mode different than the one used in the fitting can lead to inaccurate results. Depending on the hyperelastic model, sometimes the predictions do not even show a physically plausible behavior [7], and many times lead to numerical problems when the constitutive constants so obtained are used in a finite element software.

In order to overcome this problem, the best solution is to adopt a methodology for fitting the hyperelastic model to more than one set of experimental data simultaneously. It is easy to use any combination of two or more different stress-strain tests (usually simple tension, biaxial tension, pure shear, simple shear and compression tests) to obtain the constitutive parameters needed for most hyperelastic models. First it is necessary to know the analytical relationship between stress and strain for simple cases of deformation (homogeneous deformation). These relationships depend uniquely on the equation of the hyperelastic model and the deformation itself and Figs. 1, 2 and 3 along with Eqs. (1), (2) and (3) show the classic cases used in this work (λ is the stretch) [9]:

$$\sigma_1 = t_T = 2\left(\lambda - \frac{1}{\lambda^2}\right)\left(\frac{\partial W}{\partial I} + \frac{1}{\lambda}\frac{\partial W}{\partial II}\right) \tag{1}$$

$$\sigma_1 = \sigma_2 = t_B = 2\left(\lambda - \frac{1}{\lambda^5}\right)\left(\frac{\partial W}{\partial I} + \lambda^2\frac{\partial W}{\partial II}\right) \tag{2}$$

$$\sigma_1 = t_P = 2\left(\lambda - \frac{1}{\lambda^3}\right)\left(\frac{\partial W}{\partial I} + \frac{\partial W}{\partial II}\right) \tag{3}$$

The fitting procedure is well known. By subtracting the theoretical stresses from the experimental values (Fig. 4), we obtain the error function to be minimized:

$$E = e_T + e_P + e_B = \sum_{i=1}^{n_T}\left(t_{T_i} - t_{E_i}\right)_T^2 + \sum_{j=1}^{n_P}\left(t_{T_j} - t_{E_j}\right)_P^2 + \sum_{k=1}^{n_B}\left(t_{T_k} - t_{E_k}\right)_B^2 \tag{4}$$

where n_T, n_P and n_B are the number of points in available single tension, pure shear and biaxial tension experimental data respectively, t_T and t_E are the theoretical and experimental values for the engineering stresses respectively, while the sub-indexes T, B and P refer to axial tension, biaxial tension and pure shear tests, respectively.

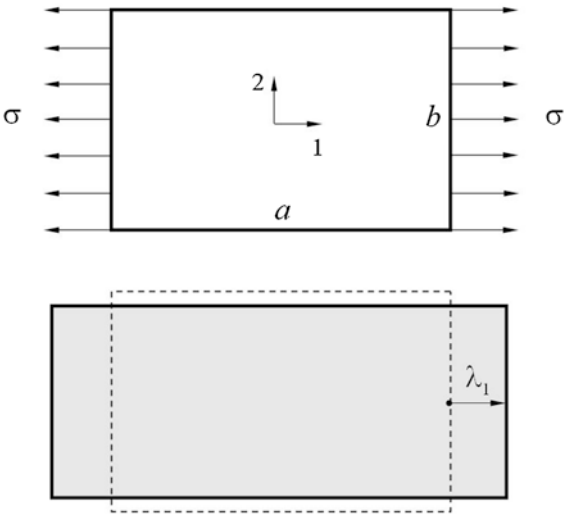

Fig. 1 Simple tension case of deformation—Eq. (1)

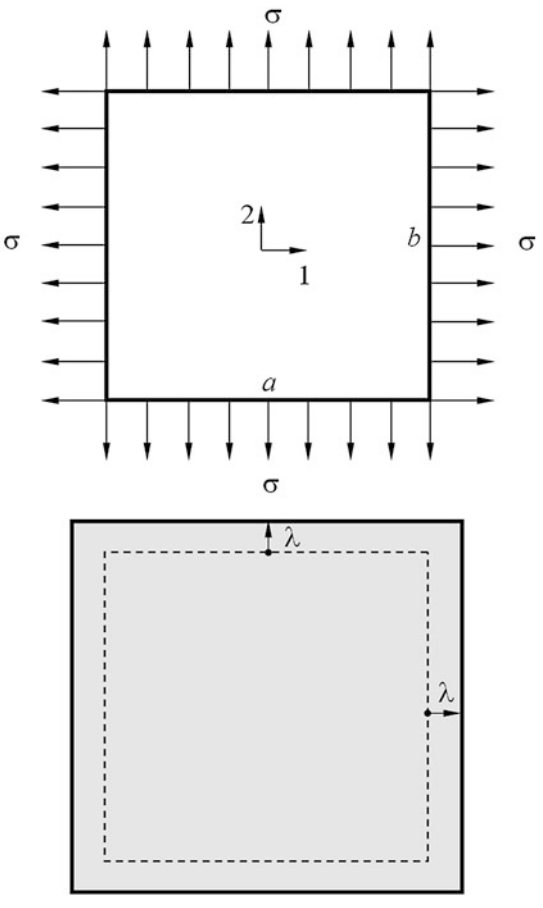

Fig. 2 Biaxial tension case of deformation—Eq. (2)

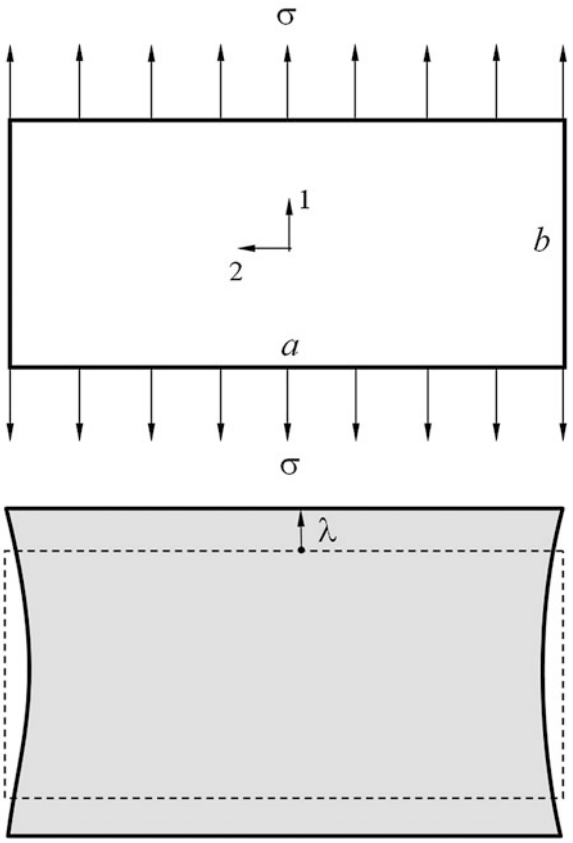

Fig. 3 Pure shear case of deformation—Eq. (3)

The problem lies now in obtaining the constitutive coefficients that minimize the error function E:

$$\min_{\mathbf{C}} E(\mathbf{C}) \tag{5}$$

where $E(\mathbf{C})$ is the error function in terms of the set of constitutive coefficients $\mathbf{C}$.

This methodology consists in an optimization technique, since it obtains the optimum set of coefficients for any hyperelastic model that will lead to the minimum error between experimental and theoretical results for two or more distinct sets of data simultaneously. It is also possible to assign weights to each term on the right side of Eq. (4) in order to take into account the prevailing deformation stress on the real component or the reliability of the experimental data used.

Compared to the classical methodology in which for each different deformation case a particular set of constitutive parameters is obtained, the multi-test methodology presents great advantage, since one single set of constants is used for any deformation case, or combination of them.

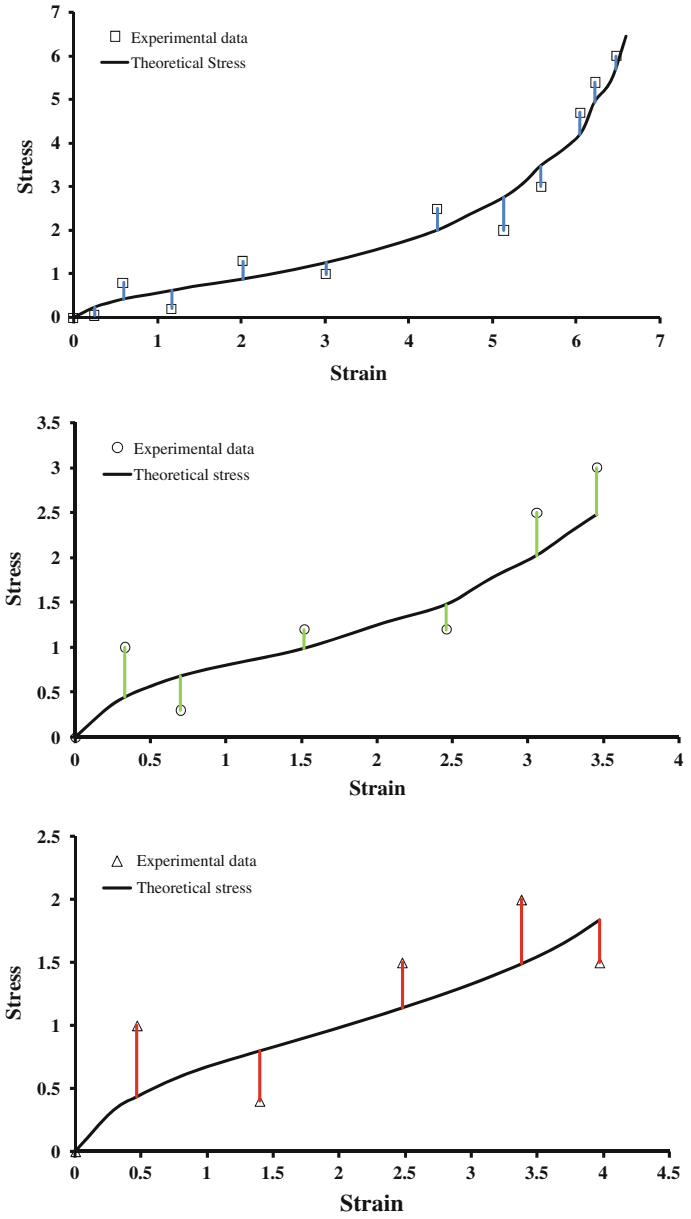

Fig. 4 Deviations between experimental and theoretical results obtained for (*top* to *bottom*): simple tension, biaxial tension, and pure shear

If no constraints are imposed to the set of constants **C**, this can be solved as an unconstrained optimization problem, but in this work, due to the conditions imposed by the Baker-Ericksen inequalities, the problem has to be evaluated as a constrained optimization case.

3 Imposing the Inequalities to the Models

In order to apply the Baker-Ericksen inequalities to a given hyperelastic model, it is first necessary to obtain its derivatives with respect to the first and second strain invariants. After that, the conditions to be satisfied by the parameters of each model are analytically developed and inserted into the optimization procedure.

The following models and their respective restrictions were analyzed in this work:

- Hoss-Marczak/HMI-LS—The strain energy function for this model is given by [7]:

$$W = \frac{\alpha}{\beta}\left(1 - e^{-\beta(I-3)}\right) + \frac{\mu}{2b}\left[\left(1 + \frac{b(I-3)}{n}\right)^{n} - 1\right] \tag{6}$$

$$\frac{\partial W}{\partial I} = \alpha e^{-\beta(I-3)} + \frac{\mu}{2}\left(1 + \frac{b(I-3)}{n}\right)^{n-1} > 0 \tag{7}$$

$$\frac{\partial W}{\partial II} = 0 \tag{8}$$

where α, β, μ, b and n are constitutive parameters and I is the first strain invariant.

As seen in the inequality of the Eq. (7), it is not possible just by inspection to determine analytically the restrictions to be applied to the parameters of the HMI-LS model. This inequality has to be checked at each point along the stress-strain data.

- Hoss-Marczak/HMI-HS—The strain energy function for this model is a variation of the one in Eq. (6) [7]:

$$W = \frac{\alpha}{\beta}\left(1 - e^{-\beta(I-3)}\right) + \frac{\mu}{2b}\left[\left(1 + \frac{b(I-3)}{n}\right)^{n} - 1\right] + C_2 \ln\left(\frac{II}{3}\right) \tag{9}$$

$$\frac{\partial W}{\partial I} = \alpha e^{-\beta(I-3)} + \frac{\mu}{2}\left(1 + \frac{b(I-3)}{n}\right)^{n-1} > 0 \tag{10}$$

$$\frac{\partial W}{\partial II} = \frac{C_2}{II} \geq 0 \tag{11}$$

where C_2 is an additional parameter (not present in Eq. (6)) and II is the second strain invariant.

The first derivative in Eq. (10) is the same of the HM-LS model in Eq. (7), so the same approach was used to check the model parameters. Equation (11) however, shows clearly a restriction imposed to the parameter C_2:

$$C_2 \geq 0 \tag{12}$$

- 3-terms Yeoh—The well known strain energy function for this model is Yeoh [18]:

$$W = C_1(I-3) + C_2(I-3)^2 + C_3(I-3)^3 \tag{13}$$

where C_1, C_2 and C_3 are constitutive parameters. Its derivatives with respect to the first and second strain invariants are, respectively:

$$\frac{\partial W}{\partial I} = C_1 + 2C_2(I-3) + 3C_3(I-3)^2 > 0 \tag{14}$$

$$\frac{\partial W}{\partial II} = 0 \tag{15}$$

Although Eqs. (14 and 15) are not the only possible conditions to satisfy the Baker-Ericksen inequalities in this case, they were chosen to guarantee the positivity of the parameters C_1, C_2 and C_3 in the Yeoh model.

Therefore, in order to ensure the satisfaction of the Baker-Ericksen inequalities in the Yeoh model, its parameters have to fulfill the following conditions:

$$C_1 > 0, \quad C_2 > 0, \quad C_3 > 0 \tag{16}$$

- Fung—A simple, two parameter strain energy function given by [5]:

$$W = \frac{\mu}{2b}\left(e^{b(I-3)} - 1\right) \tag{17}$$

where μ and b are fitting constitutive parameters. The first derivative with respect to the strain invariant is:

$$\frac{\partial W}{\partial I} = \frac{\mu}{2} e^{b(I-3)} > 0 \tag{18}$$

One should note that the term $(I-3)$ is always positive, provided there is a deformation, and so is the exponential term $e^{b(I-3)}$. Thus the only condition necessary to satisfy the Baker-Ericksen inequalities in the Fung model is:

$$\mu > 0 \tag{19}$$

- Pucci-Saccomandi—This model provides reasonably good predictions with the following strain energy function [13]:

$$W = -\frac{\mu\, J_L}{2} \ln\left(1 - \frac{I-3}{J_L}\right) + C_2 \ln\left(\frac{II}{3}\right) \tag{20}$$

where C_2, μ and J_L are the constitutive parameters.

The first derivative of the Pucci-Saccomandi model with respect to the first strain invariant is found to be:

$$\frac{\partial W}{\partial I} = \frac{\mu}{2\left(1 - \frac{I-3}{J_L}\right)} > 0 \tag{21}$$

An initial condition inherent to this model is that the parameter J_L should always be higher than the term $(I-3)$. Therefore the term between parentheses in the denominator is always positive. This leads to the condition:

$$\mu > 0 \tag{22}$$

The derivative of W with respect to the second strain invariant leads to the second condition for the Pucci-Saccomandi model:

$$C_2 \geq 0 \tag{23}$$

For each model analyzed in this work, two codes were written: one concerning the analytical equation for the error to be minimized as presented in the optimization methodology and another containing the restrictions imposed by the Baker-Ericksen inequalities as detailed in this section.

4 Experimental Data

The experimental data used in this work was obtained from simple tension (T), biaxial tension (B) and pure shear (P) tests in samples of natural rubber—NR [8] and unfilled silicone—USR [10]. Figures 5 and 6 show the experimental stress-strain curves for these materials under the three cases of loading.

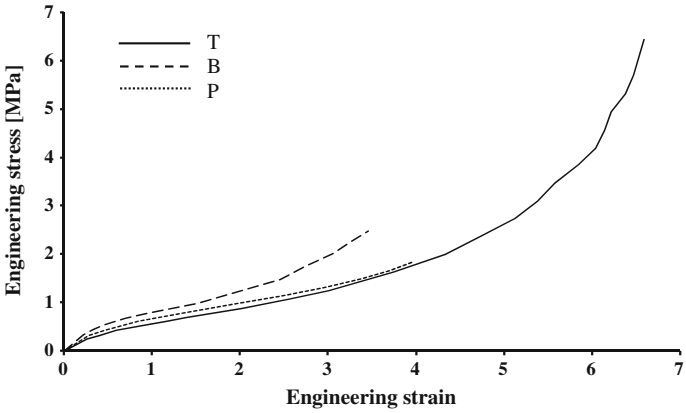

Fig. 5 Treloar experimental data for natural rubber [8]

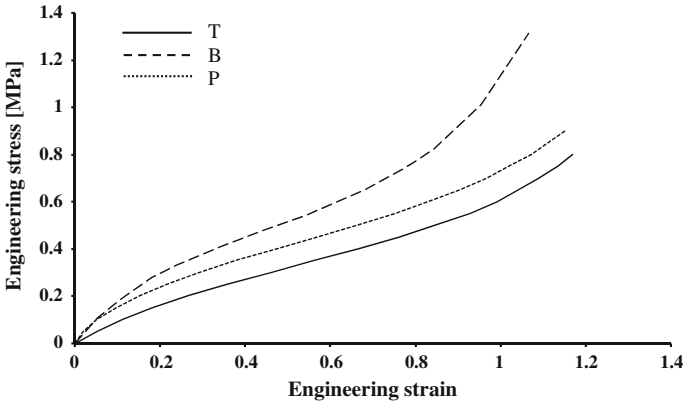

Fig. 6 Experimental data for the USR samples [10]

5 Results

Figures 7, 8, 9, 10, 11, 12, 13, 14, 15 and 16 show the experimental results (symbols) and theoretical results for both material samples used in this work along with Hoss-Marczak, Yeoh, Fung and Pucci-Saccomandi models. The sets of coefficients listed in the labels of the figures satisfy their respective inequalities, as determined by Eqs. (7), (12), (16), (19), (22) and (23).

Results obtained when the methodology was applied to the HMI-LS model for the NR and USR data are shown in Figs. 7 and 8, along with the coefficients obtained in each case. Good agreement between experimental and theoretical values

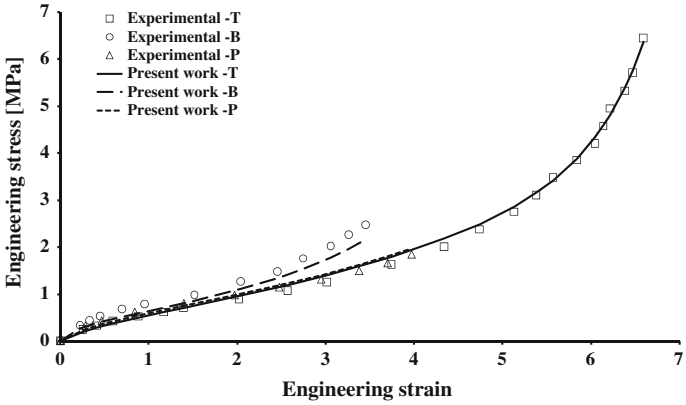

Fig. 7 Treloar's NR experimental data and HMI-LS model. Optimized parameters: $\alpha = 0.153$, $\beta = -0.0106$, $b = 0.166$, $n = 24.8$, $\mu = 1.73\text{E-}4$

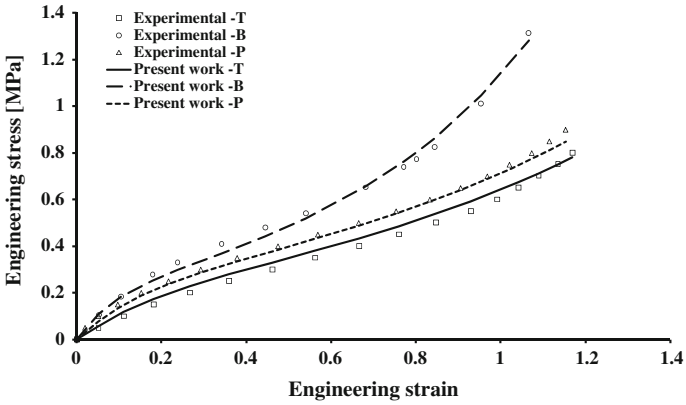

Fig. 8 USR experimental data and HMI-LS model. Optimized parameters: $\alpha = 0.120$, $\beta = -0.167$, $b = 1.03$, $n = 0.25$, $\mu = 0.166$

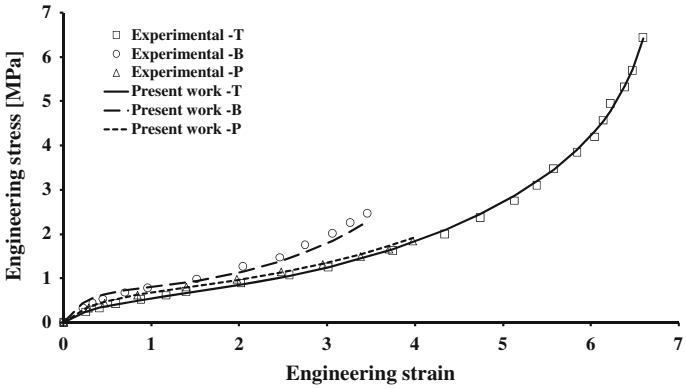

Fig. 9 Treloar's experimental data and HMI-HS model. Optimized parameters: $\alpha = 0.112$, $\beta = -0.0208$, $b = 31.2$, $n = 14.7$, $\mu = 0$, $C_2 = 0.337$

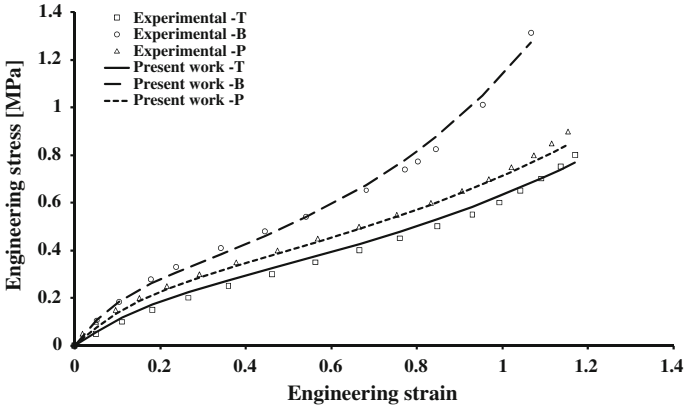

Fig. 10 USR experimental data and HMI-HS model. Optimized parameters: $\alpha = 0.121$, $\beta = -0.161$, $b = 0.537$, $n = 0.112$, $\mu = 0.142$, $C_2 = 0.0407$

is evident, but similar results for the HMI-HS model are better, as shown in Figs. 9 and 10.

Results for the 3-terms Yeoh model are presented in Figs. 11 and 12. Again, good agreement is observed between experimental data and theoretical predictions.

When applied to the Fung model, the methodology also led to similarly good quantitative and qualitative results, in spite of the simplicity of Fung's model. These results are plotted in Figs. 13 and 14.

Figures 15 and 16 show analog results when analyzing the Pucci-Saccomandi model. Once again, good agreement between experimental data and theoretical predictions is verified.

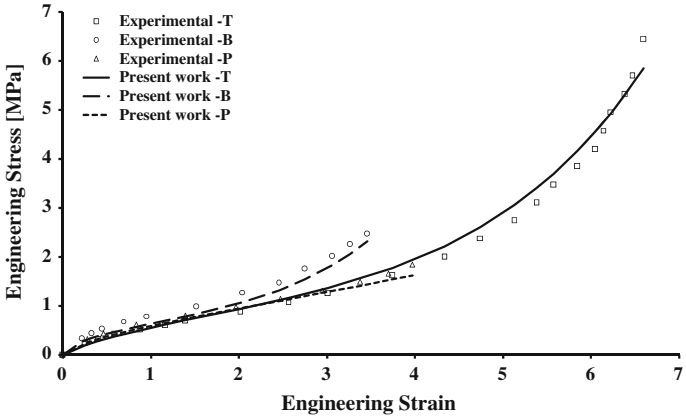

Fig. 11 Treloar's experimental data and 3-terms Yeoh model. Optimized parameters: $C_1 = 0.159$, $C_2 = 0$, $C_3 = 2.51\text{E-}5$

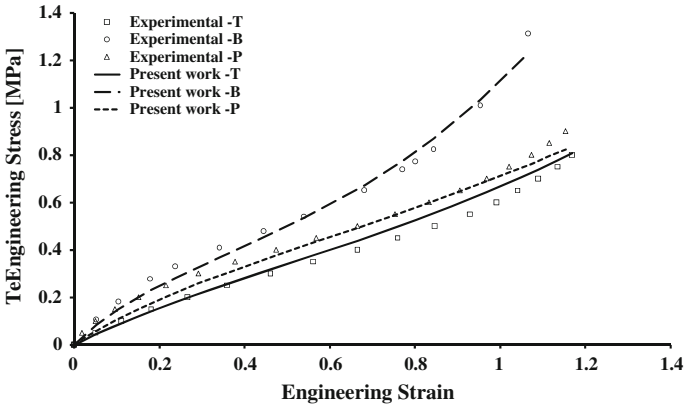

Fig. 12 USR experimental data and 3-terms Yeoh model. Optimized parameters: $C_1 = 0.152$, $C_2 = 7.83\text{E-}3$, $C_3 = 6.73\text{E-}4$

Besides ensuring a physically plausible behavior, the inclusion of additional constraints given by the Baker-Ericksen inequalities narrows the feasible domain of viable constitutive parameters during the fitting process. But another important advantage the inequalities provide, and possibly not yet reported in the open literature, is the potential generation of constitutive constants better than the ones obtained in single or multi-test fittings.

For the sake of comparison of the classical prediction methodology usually used in industry—when the chosen model is fitted against a single loading case—and the ones obtained when the inequalities are considered, a number of numerical tests were performed. In the former case good predictions are obviously expected for the

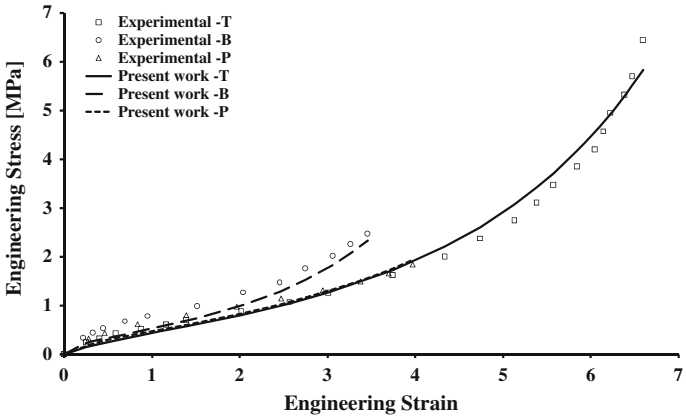

Fig. 13 Treloar's experimental data and Fung model. Optimized parameters: $\mu = 0.240$, $b = 0.0212$

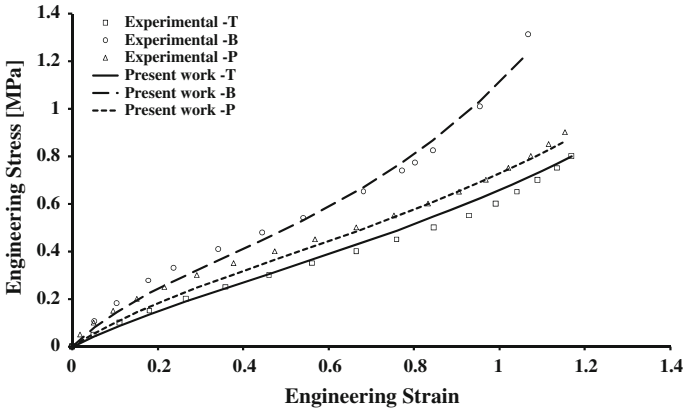

Fig. 14 USR experimental data and Fung model. Optimized parameters: $\mu = 0.289$, $b = 0.132$

loading case used to calibrate the model, but usually there is no guarantee that the predictions for other load cases will be acceptable (and quite commonly are not). That is, even if a model fits accurately with a single set of experimental data, caution should be taken when using these parameters to simulate an elastomer component subjected to different or combined loadings.

The comparisons presented below show that the inclusion of the inequalities can lead to very good predictions to all load cases. Although not yet investigated, their consideration can lead to good predictions even if only one single set of experimental data is used to calibrate the model.

First, using the classical least square technique and the well known SQP optimization method, the fitting algorithm was extended to take all restrictions into

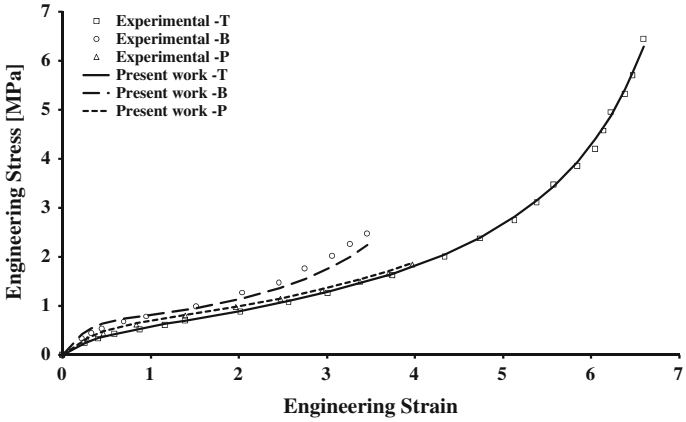

Fig. 15 Treloar's experimental data and Pucci-Saccomandi model. Optimized parameters: $\mu = 0.254$, $J_L = 82.3$, $C_2 = 0.294$

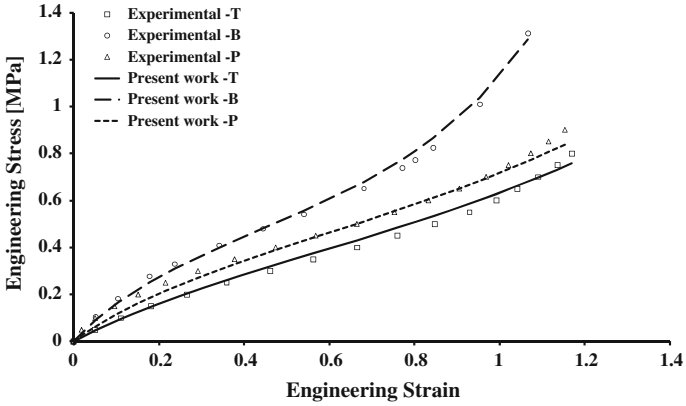

Fig. 16 USR experimental data and Pucci-Saccomandi model. Optimized parameters: $\mu = 0.282$, $J_L = 13.5$, $C_2 = 0.0621$

account and solved using the Matlab optimization routine called *fmincon* [17]. Then the HMI-LS model was calibrated against the data for axial tension using the USR sample. The parameters obtained were used to *predict* the model behavior under the *other two cases of deformation*: biaxial tension and pure shear. In a second example, the model was fitted against the data for biaxial tension of the USR sample and the constants used to *predict* its behavior under single tension and pure shear. The last case shows the results when the model was fitted against pure shear data and the *predicted* behaviors for single tension and biaxial tension were analyzed. Figures 17, 18 and 19 summarize the comparisons.

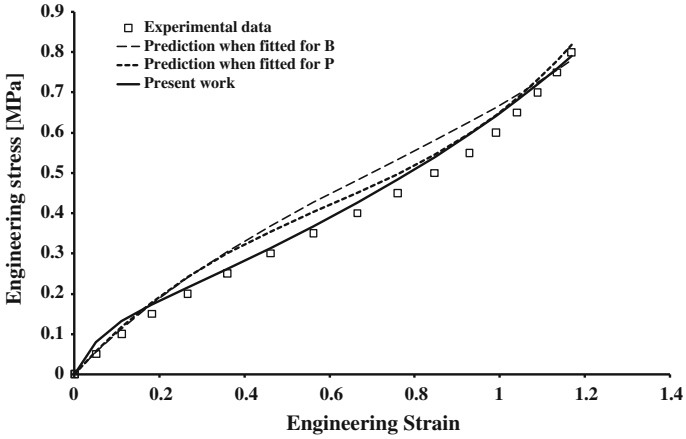

Fig. 17 Prediction of the behavior of USR samples under axial deformation when the constants of the HMI-LS model are fitted against biaxial tension, pure shear and the proposed method (Eqs. (4 and 5) + inequalities)

In Fig. 17, the *predictive behaviors* for axial tension deformation of USR sample using the HMI-LS model fitted against biaxial tension only, pure shear only, and using Eqs. (4 and 5) but considering the inequalities (present methodology).

In Fig. 18, the experiment was repeated to check the predicted biaxial behavior using the HMI-LS model fitted against biaxial tension only, pure shear only, and the present methodology.

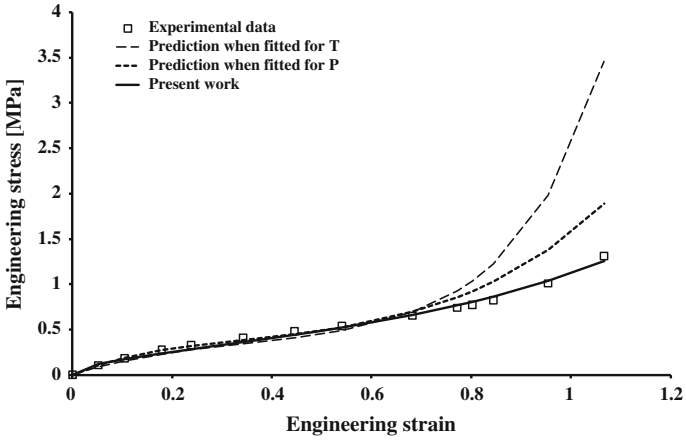

Fig. 18 Prediction of the behavior of USR samples under biaxial deformation when the constants of the HMI-LS model are fitted against single tension, pure shear and the proposed method (Eqs. (4 and 5) + inequalities)

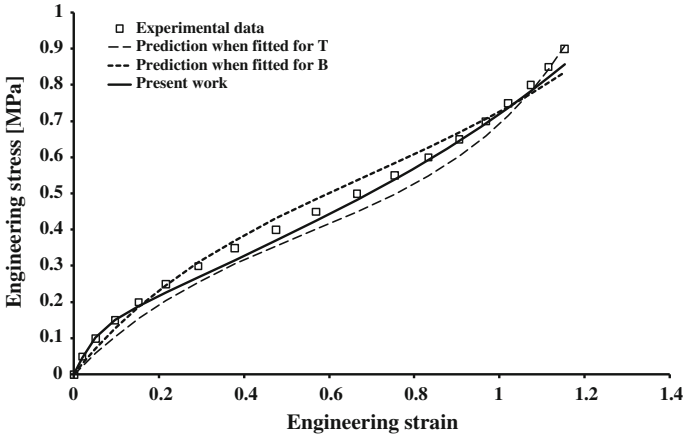

Fig. 19 Prediction of the behavior of USR samples under shear deformation when the constants of the HMI-LS model are fitted against single tension, pure shear, and the proposed method (Eqs. (4 and 5) + inequalities)

Finally, Fig. 19 shows a comparison of the *predictive behaviors* for USR sample under pure shear deformation when it is fitted against single tension only, biaxial tension only and when applied the proposed method, again for the HMI-LS model.

For the three cases, the optimization methodology proposed delivered better predictions than the ones obtained by any case of calibration against a single set of data. It should be pointed out that for each plot in Figs. 17, 18 and 19, a different set of constants was necessary when applying the classical least square technique [11], whereas for the proposed methodology, a single set of constants is used to plot all three graphs.

6 Conclusions

This work investigated a methodology to obtain constitutive parameters for hyperelastic materials by means of a constrained optimization technique. The constraints imposed to the parameters were derived analytically after applying the Baker-Ericksen inequalities to each hyperelastic model. In three out of five models, analytical constraints were obtained, but for the HMI models, it was necessary to check them along the strain range.

The optimization technique was based in the work of Stumpf [14] which uses experimental data originated from two or more distinct cases of deformation simultaneously. Therefore an optimum set of constitutive coefficients is obtained in such a way that it minimizes error between experimental and theoretical results for all deformation modes considered.

Experimental data from to three different deformation cases (simple tension, biaxial tension and pure shear) and two different elastomers samples (Treloar set of data and unfilled silicone rubber) were used to calibrate five different hyperelastic models (HMLSI, HMHSI, 3-terms Yeoh, Fung and Pucci-Saccomandi) and the results were presented in Sect. 5. In all cases, the sets of coefficients satisfied the restrictions imposed by the Baker-Ericksen inequalities.

As one can conclude from Figs. 7, 8, 9, 10, 11, 12, 13, 14, 15 and 16, theoretical results fitted the experimental data of the three cases of deformation accurately in all cases, which is very unlikely to observe when a model is calibrated for a single deformation case and its fitted parameters are used to predict the elastomer´s behavior for a distinct case, as demonstrated in the final part of Sect. 5.

Moreover, these coefficients also satisfy the Baker-Ericksen inequalities, which guarantees that, for all ranges of strain—and not only for that the model was fitted to—these materials will behave in a physically plausible way.

The methodology is also characterized by its flexibility, since through modification of Eq. (4) by including or eliminating the desired terms, the user can suit the method to the available experimental data, making it capable to be used to any combination of deformation cases and any hyperelastic model.

References

1. Baker, M., Ericksen, J.L.: Inequalities Restricting the Form of the Stress-Deformation Relation for Isotropic Elastic Solids and Reiner-Rivlin Fluids. J. Wash. Acad. Sci. **44**, 33–35 (1954)
2. Ball, J.M.: Convexity Conditions and Existence Theorems in NonlinearElasticity. Arch. Ration. Mech. Anal. **63**, 337–403 (1977)
3. Balzani, D., Neff, P., Schröder, J., Holzapfel, G.A.: A polyconvex framework for soft biological tissues. Adjustment to experimental data. Int. J. Solids Struct. **43**, 6052–6070 (2006)
4. Bilgili, E.: Restricting the Hyperelastic Models for Elastomers Based on Some Thermodynamical, Mechanical and Empirical Criteria. J. Elastom. Plast. **36**, 159–175 (2004)
5. Fung, Y.C.B.: Elasticity of soft tissues in sample elongation. Am. J. Physiol. **213**, 1532–1544 (1967)
6. Hartmann, S., Neff, P.: Polyconvexity of Generalized Polynomial-TypeHyperelastic Strain Energy Functions for Near-Incompressibility. Int. J. Solids and Struct. 40, 2767–2791 (2003)
7. Hoss, L., Stumpf, F.T., de Bortoli, D., Marczak, R.J.: Constitutive models for rubber-like materials: comparative analysis, goodness of fitting measures, and proposal of a new model. In: International Rubber Conference, IRCO (2011)
8. Jones, D., Treloar, L.: The properties of rubber in pure homogeneous strain. J. Phys. D Appl. Phys. **8**, 1285–1304 (1975)
9. Marczak, R.J., Gheller, J.J., Hoss, L.: Characterization of Elastomers for Numerical Simulation. Centro Tecnológico de Polímeros SENAI, São Leopoldo (2006) (in Portuguese)
10. Meunier, L., Chagnon, G., Favier, D., Orgeás, L., Vacher, P.: Mechanical experimental characterization and numerical modelling of an unfilled silicone rubber. Polym. Testing **27**, 765–777 (2008)
11. Nelder, J.A., Mead, R.: A simplex method for function minimization. Comput. J. **7**, 308–313 (1965)
12. Ogden, R.W.: Non-Linear Elastic Deformations. Dover Publications, NewYork (1984)

13. Pucci, E., Saccomandi, G.: A note on the Gent model for rubber-like materials. Rubber Chem. Technol. **75**, 839–851 (2002)
14. Stumpf, F.T.: Assessment of a hyperelastic model for incompressible materials: analysis of restrictions, numerical implementation and optimization of the constitutive parameters. M.Sc. Dissertation, UFRGS, Porto Alegre (2009) (in Portuguese)
15. Truesdell, C.: The main unsolved problem in finite elasticity theory. Z. Angew. Math. Phys. **36**, 97–103 (1956) (in German)
16. Truesdell, C., Noll, W.: The nonlinear Field Theories of Mechanics Flügge's Handbuch der Physik, vol. III/3. Springer, Berlin/Heidelberg (1965)
17. Venkataraman, P.: Applied Optimization with MATLAB Programming. Willey (2009)
18. Yeoh, O.H.: Characterization of Elastic Properties of Carbon Black FilledRubber Vulcanizates. Rubber Chem. Tech. **63**, 792–805 (1990)